

# Understanding and predicting the Gulf of Mexico ocean dynamics

**Edited by**

Julio Sheinbaum, Eric Chassignet, Steven L. Morey  
and Ruoying He

**Published in**

Frontiers in Marine Science





## FRONTIERS EBOOK COPYRIGHT STATEMENT

The copyright in the text of individual articles in this ebook is the property of their respective authors or their respective institutions or funders. The copyright in graphics and images within each article may be subject to copyright of other parties. In both cases this is subject to a license granted to Frontiers.

The compilation of articles constituting this ebook is the property of Frontiers.

Each article within this ebook, and the ebook itself, are published under the most recent version of the Creative Commons CC-BY licence. The version current at the date of publication of this ebook is CC-BY 4.0. If the CC-BY licence is updated, the licence granted by Frontiers is automatically updated to the new version.

When exercising any right under the CC-BY licence, Frontiers must be attributed as the original publisher of the article or ebook, as applicable.

Authors have the responsibility of ensuring that any graphics or other materials which are the property of others may be included in the CC-BY licence, but this should be checked before relying on the CC-BY licence to reproduce those materials. Any copyright notices relating to those materials must be complied with.

Copyright and source acknowledgement notices may not be removed and must be displayed in any copy, derivative work or partial copy which includes the elements in question.

All copyright, and all rights therein, are protected by national and international copyright laws. The above represents a summary only. For further information please read Frontiers' Conditions for Website Use and Copyright Statement, and the applicable CC-BY licence.

ISSN 1664-8714  
ISBN 978-2-8325-4743-4  
DOI 10.3389/978-2-8325-4743-4

## About Frontiers

Frontiers is more than just an open access publisher of scholarly articles: it is a pioneering approach to the world of academia, radically improving the way scholarly research is managed. The grand vision of Frontiers is a world where all people have an equal opportunity to seek, share and generate knowledge. Frontiers provides immediate and permanent online open access to all its publications, but this alone is not enough to realize our grand goals.

## Frontiers journal series

The Frontiers journal series is a multi-tier and interdisciplinary set of open-access, online journals, promising a paradigm shift from the current review, selection and dissemination processes in academic publishing. All Frontiers journals are driven by researchers for researchers; therefore, they constitute a service to the scholarly community. At the same time, the *Frontiers journal series* operates on a revolutionary invention, the tiered publishing system, initially addressing specific communities of scholars, and gradually climbing up to broader public understanding, thus serving the interests of the lay society, too.

## Dedication to quality

Each Frontiers article is a landmark of the highest quality, thanks to genuinely collaborative interactions between authors and review editors, who include some of the world's best academicians. Research must be certified by peers before entering a stream of knowledge that may eventually reach the public - and shape society; therefore, Frontiers only applies the most rigorous and unbiased reviews. Frontiers revolutionizes research publishing by freely delivering the most outstanding research, evaluated with no bias from both the academic and social point of view. By applying the most advanced information technologies, Frontiers is catapulting scholarly publishing into a new generation.

## What are Frontiers Research Topics?

Frontiers Research Topics are very popular trademarks of the *Frontiers journals series*: they are collections of at least ten articles, all centered on a particular subject. With their unique mix of varied contributions from Original Research to Review Articles, Frontiers Research Topics unify the most influential researchers, the latest key findings and historical advances in a hot research area.

Find out more on how to host your own Frontiers Research Topic or contribute to one as an author by contacting the Frontiers editorial office: [frontiersin.org/about/contact](https://frontiersin.org/about/contact)

# Understanding and predicting the Gulf of Mexico ocean dynamics

## Topic editors

Julio Sheinbaum — Centro de Investigación Científica y de Educación Superior de Ensenada (CICESE), Mexico

Eric Chassignet — Florida State University, United States

Steven L. Morey — Florida Agricultural and Mechanical University, United States

Ruoying He — North Carolina State University, United States

## Citation

Sheinbaum, J., Chassignet, E., Morey, S. L., He, R., eds. (2024). *Understanding and predicting the Gulf of Mexico ocean dynamics*. Lausanne: Frontiers Media SA.  
doi: 10.3389/978-2-8325-4743-4

## Table of contents

- 05 **Editorial: Understanding and predicting the Gulf of Mexico ocean dynamics**  
Steven L. Morey, Ruoying He, Eric P. Chassignet and Julio Sheinbaum
- 08 **Dispersion of subsurface lagrangian drifters in the northeastern Gulf of Mexico**  
Cathrine Hancock, Kevin Speer,  
Joao Marcos Azevedo Correia de Souza and Steven L. Morey
- 25 **Characteristics of Eulerian mesoscale eddies in the Gulf of Mexico**  
Yingli Zhu and Xinfeng Liang
- 45 **Generation of high-frequency topographic Rossby waves in the Gulf of Mexico**  
Alexis Johnson Exley, Kathleen A. Donohue, D. Randolph Watts,  
Karen L. Tracey and Maureen A. Kennelly
- 61 **Influence of Loop Current and eddy shedding on subseasonal sea level variability along the western Gulf Coast**  
Toshiaki Shinoda, Philippe Tissot and Anthony Reisinger
- 78 **Influence of Caribbean eddies on the Loop current system evolution**  
Nektaria Ntaganou, Vassiliki Kourafalou, Francisco Javier Beron-Vera,  
Maria Josefina Olascoaga, Matthieu Le Hénaff and  
Yannis Androulidakis
- 93 **Impact of upstream variability on the Loop Current dynamics in numerical simulations of the Gulf of Mexico**  
Rémi Laxenaire, Eric P. Chassignet, Dmitry S. Dukhovskoy and  
Steven L. Morey
- 109 **Influence of the Caribbean Sea eddy field on Loop Current predictions**  
Matthieu Le Hénaff, Vassiliki H. Kourafalou, Yannis Androulidakis,  
Nektaria Ntaganou and HeeSook Kang
- 119 **Assessment of predictability of the Loop Current in the Gulf of Mexico from observing system experiments and observing system simulation experiments**  
Dmitry S. Dukhovskoy, Eric P. Chassignet, Alexandra Bozec and  
Steven L. Morey
- 143 **Predicting the Loop Current dynamics combining altimetry and deep flow measurements through the Yucatan Channel**  
Gaston Manta, Giovanni Durante, Julio Candela, Uwe Send,  
Julio Sheinbaum, Matthias Lankhorst and Rémi Laxenaire
- 156 **Characteristics of submesoscale eddy structures within mesoscale eddies in the Gulf of Mexico from 1/48° ECCO estimates**  
Paul A. Ernst, Bulusu Subrahmanyam, Corinne B. Trott and  
Alexis Chaigneau



- 174 **Stratification variability in the Yucatan Channel and its relationship with the Loop Current System**  
Susana Higuera-Parra, Efraín Moreles, Erick R. Olvera-Prado and Jorge Zavala-Hidalgo
- 193 **Variability of the southern Gulf of Mexico and its predictability and stochastic origin**  
Efraín Moreles
- 210 **Dynamical interactions between Loop Current and Loop Current Frontal Eddies in a HYCOM ensemble of the circulation in the Gulf of Mexico**  
Xingchen Yang, Matthieu Le Hénaff, Brian Mapes and Mohamed Iskandarani
- 229 **Contribution of the wind and Loop Current eddies to the circulation in the western Gulf of Mexico**  
Erick R. Olvera-Prado, Steven L. Morey and Eric P. Chassignet



## OPEN ACCESS

EDITED AND REVIEWED BY  
Ming Li,  
University of Maryland, United States

\*CORRESPONDENCE  
Steven L. Morey  
✉ steven.morey@fam.u.edu

RECEIVED 13 March 2024

ACCEPTED 18 March 2024

PUBLISHED 28 March 2024

## CITATION

Morey SL, He R, Chassignet EP and  
Sheinbaum J (2024) Editorial:  
Understanding and predicting the  
Gulf of Mexico ocean dynamics.  
*Front. Mar. Sci.* 11:1400560.  
doi: 10.3389/fmars.2024.1400560

## COPYRIGHT

© 2024 Morey, He, Chassignet and Sheinbaum.  
This is an open-access article distributed under  
the terms of the [Creative Commons Attribution  
License \(CC BY\)](#). The use, distribution or  
reproduction in other forums is permitted,  
provided the original author(s) and the  
copyright owner(s) are credited and that the  
original publication in this journal is cited, in  
accordance with accepted academic  
practice. No use, distribution or reproduction  
is permitted which does not comply with  
these terms.

# Editorial: Understanding and predicting the Gulf of Mexico ocean dynamics

Steven L. Morey<sup>1\*</sup>, Ruoying He<sup>2</sup>, Eric P. Chassignet<sup>3</sup>  
and Julio Sheinbaum<sup>4</sup>

<sup>1</sup>School of the Environment, Florida A&M University, Tallahassee, FL, United States, <sup>2</sup>Department of Marine, Earth, and Atmospheric Sciences, North Carolina State University, Raleigh, NC, United States, <sup>3</sup>Center for Ocean-Atmospheric Prediction Studies, Florida State University, Tallahassee, FL, United States, <sup>4</sup>Departamento de Oceanografía Física, Centro de Investigación Científica y de Educación Superior de Ensenada (CICESE), Ensenada, Mexico

## KEYWORDS

Gulf of Mexico, loop current, loop current eddies, ocean forecasting, Yucatan Channel

## Editorial on the Research Topic

### Understanding and predicting the Gulf of Mexico ocean dynamics

The Gulf of Mexico circulation has been a focus of oceanographic research for well over a century due to its early importance in maritime transportation and naval interests, expansion of petroleum industry activity since the mid-20<sup>th</sup> century, and emerging understanding of its importance to regional ecosystems, weather and climate. Over the past several years, a number of research programs have funded significant efforts to advance understanding of and forecasting capabilities for the Gulf of Mexico circulation, including the Loop Current (LC) and its associated eddies (comprising the Loop Current System – LCS), and deep-water dynamics. This research accelerated following the 2010 Deepwater Horizon oil spill with the establishment of the Gulf of Mexico Research Initiative (GOMRI, 2010–2020) and, more recently, of the National Academies of Sciences, Engineering, and Medicine (NASEM) Gulf Research Program (GRP) funded by settlement funds in the aftermath of this disaster. The 2018 consensus study report from the GRP's Committee on Advancing Understanding of Gulf of Mexico Loop Current Dynamics (NASEM, 2018) outlined critical gaps in the understanding and ability to accurately predict the LCS. Although the LCS dominates the upper layer circulation in the Gulf, this report also highlighted the importance of the subsurface and deep layer circulation for the LCS documented by previous investigations that were funded by industry, the Bureau of Ocean Energy Management (BOEM), and its predecessor, the Minerals Management Service (MMS).

This Research Topic was envisioned as a venue in which to collect and highlight advances in understanding and predicting the Gulf of Mexico circulation that have come from recent studies, including collaborative research programs aimed at addressing the gaps identified in the 2018 Consensus Study Report. One such program is the GRP's Understanding Gulf Ocean Systems (UGOS) initiative, which focuses on improving forecasts of the physical dynamics of the open Gulf of Mexico in space and time scales useful for the reduction of risks to offshore energy exploration and production, as well as for other challenges such as forecasting hurricane intensification and managing fisheries. Much

of the research published in this Research Topic is the result of collaborative efforts among academic, industry, governmental, and international partners, highlighting the advantages of collaborative team science approaches to understanding complex systems such as Gulf of Mexico dynamics.

The fourteen articles contained within this Research Topic provide new insights into the Gulf of Mexico circulation, including the connectivity between upper and deep circulation and dynamics that impact LC behavior, which can be applied to enhance forecasting through modeling and observational strategies. The articles can generally be grouped into themes that include: characterization of the meso- and submeso-scale upper layer circulation features, upstream conditions in the Yucatan Channel and Caribbean Sea, circulation in the western Gulf and connections to the LCS, subsurface and deep layer circulation and the connection with the upper layer circulation, and impacts of observations on improving long-range forecasts. The results presented in these works can collectively lead to improvements in our understanding and predictive capabilities of the Gulf of Mexico circulation and the ecosystems, climate and weather that it impacts.

Advances in numerical models and satellite observations have led to a more comprehensive characterization of the spatio-temporal variability of the LCS. Satellite altimeters have long provided measurements of the sea level anomalies associated with mesoscale features. The growing suite of satellite observations and the roughly 3-decade record length was used by [Zhu and Liang](#) to discover modes of variability, including seasonal signals, in the Loop Current Eddies (LCEs) and smaller cyclonic Loop Current Frontal Eddies. Enhancements in numerical model performance through increased availability of computing power, including the ability to run large numbers of simulations and higher resolution grids, make them well suited for elucidating the role of dynamical processes at scales smaller than the mesoscale that has typically been studied in the Gulf. In this issue, [Yang et al.](#) use ensembles of model runs with perturbed initial conditions to show the importance of West Florida cyclonic eddies in governing the LCE separation dynamics. [Ernst et al.](#) use a high-resolution (2 km) model reanalysis to characterize the submesoscale eddies and their contribution to the overall eddy kinetic energy, demonstrating potential capabilities of new swath altimeter missions like SWOT (Surface Water Ocean Topography) for observing the Gulf.

A number of studies over the past couple decades have aimed to connect variability upstream in this western boundary current system, namely the Yucatan Current in the Yucatan Channel and eddies in the Caribbean Current, with LCS dynamics including LC extension and eddy separations. Five articles in this issue ([Higuera-Parra et al.](#), [Manta et al.](#), [Le Hénaff et al.](#), [Laxenaire et al.](#), and [Ntaganou et al.](#)) add to the evidence that understanding the upstream conditions can enhance predictability of the LCS. These studies used numerical models and observations by moored instruments and satellites to show the impacts of eddy-induced vorticity fluxes and shifts in the Yucatan Current position on the Loop Current and eddy detachments, potentially leading to prediction methods and highlighting the importance of accurate representation of these dynamics in model forecasts.

As LCEs migrate westward after detachment, they influence circulation in the western part of the basin. [Olvera et al.](#) use numerical model experiments to demonstrate these contributions from LCEs to circulation in the northern, central, and southern Gulf of Mexico, with LCEs contributing to low-frequency modulation of the wind-driven circulation. The LCEs and their high pressure anomalies are similarly shown to induce low-frequency sea level variations along the western boundary of the Gulf of Mexico by [Shinoda et al.](#) Though not directly connected with the LCS, upper and deep layer coupling in the southern Gulf of Mexico is investigated using a numerical model by [Moreles](#).

The LC and a detaching LCE interacted with oil from the Deepwater Horizon spill, transporting the oil over long distances at the surface and within the water column. To better understand the subsurface dispersion in the northern Gulf, [Hancock et al.](#) analyze trajectories of 400m floats and numerical model results to characterize subsurface dispersion and the impacts on the dispersion from mesoscale features in the De Soto Canyon region. [Exley et al.](#) analyze measurements from an array of 24 current and pressure recording inverted echo sounders (CPIES) in the LC region to provide new understanding of the coupling and energy transfer from the surface to deep Gulf, generating topographic Rossby waves that radiate westward in the basin.

Finally, [Dukhovskoy et al.](#) present results from a suite of numerical model experiments to evaluate the impacts of observations from a multitude of platforms, including the CPIES array and satellite measurements, on the model forecast capability. Together, the knowledge contained in these articles combining observational and model results can guide a comprehensive approach to improving prediction of the Gulf of Mexico.

The editors thank all authors that contributed to this Research Topic and the Frontiers editorial staff that made this issue possible. The editors hope that the readers find this collection of articles useful for continued advancement toward a greater understanding and skillful prediction of the Gulf of Mexico system.

## Author contributions

SM: Writing – original draft. RH: Writing – review & editing. EC: Writing – review & editing. JS: Writing – review & editing.

## Funding

The author(s) declare that financial support was received for the research, authorship, and/or publication of this article. The authors prepared this editorial with support of the National Academies of Sciences, Engineering, and Medicine Gulf Research Program, Understanding Gulf Ocean Systems III award number 2000013149. SM was additionally supported by the National Oceanic and Atmospheric Administration Office of Education, Educational Partnership Program with Minority-Serving Institutions award #NA21SEC4810004 (NOAA Center for Coastal and Marine Ecosystems-II).



## Conflict of interest

The authors declare that the research was conducted in the absence of any commercial or financial relationships that could be construed as a potential conflict of interest.

## Publisher's note

All claims expressed in this article are solely those of the authors and do not necessarily represent those of their affiliated organizations,

or those of the publisher, the editors and the reviewers. Any product that may be evaluated in this article, or claim that may be made by its manufacturer, is not guaranteed or endorsed by the publisher.

## Author disclaimer

The content is solely the responsibility of the authors and does not necessarily represent the official views of the Gulf Research Program, the National Academies of Sciences, Engineering, and Medicine, or the U.S. Department of Commerce, NOAA.

## Reference

National Academies of Sciences, Engineering, and Medicine (2018). *Understanding and Predicting the Gulf of Mexico Loop Current: Critical Gaps and Recommendations* (Washington, DC: The National Academies Press). doi: 10.17226/24823



## OPEN ACCESS

EDITED BY  
Zhiyu Liu,  
Xiamen University, China

REVIEWED BY  
Qinghua Ye,  
Deltares, Netherlands  
Xinfeng Liang,  
University of Delaware, United States  
Yisen Zhong,  
Shanghai Jiao Tong University, China

\*CORRESPONDENCE  
Cathrine Hancock  
chancock@fsu.edu

†These authors have contributed  
equally to this work and share  
last authorship

SPECIALTY SECTION  
This article was submitted to  
Physical Oceanography,  
a section of the journal  
Frontiers in Marine Science

RECEIVED 20 May 2022  
ACCEPTED 19 July 2022  
PUBLISHED 11 August 2022

CITATION  
Hancock C, Speer K, de Souza JMAC  
and Morey SL (2022) Dispersion of  
subsurface lagrangian drifters in the  
northeastern Gulf of Mexico.  
*Front. Mar. Sci.* 9:949338.  
doi: 10.3389/fmars.2022.949338

COPYRIGHT  
© 2022 Hancock, Speer, de Souza and  
Morey. This is an open-access article  
distributed under the terms of the  
[Creative Commons Attribution License](#)  
(CC BY). The use, distribution or  
reproduction in other forums is  
permitted, provided the original author  
(s) and the copyright owner(s) are  
credited and that the original  
publication in this journal is cited, in  
accordance with accepted academic  
practice. No use, distribution or  
reproduction is permitted which does  
not comply with these terms.

# Dispersion of subsurface lagrangian drifters in the northeastern Gulf of Mexico

Cathrine Hancock<sup>1\*</sup>, Kevin Speer<sup>1,2</sup>,  
Joao Marcos Azevedo Correia de Souza<sup>3†</sup>  
and Steven L. Morey<sup>4†</sup>

<sup>1</sup>Geophysical Fluid Dynamics Institute, College of Arts and Sciences, Florida State University, Tallahassee, FL, United States, <sup>2</sup>Department of Scientific Computing, College of Arts and Sciences, Florida State University, Tallahassee, FL, United States, <sup>3</sup>MetOcean Solutions Ltd., a Division of the Meteorological Service of New Zealand, New Plymouth, New Zealand, <sup>4</sup>School of the Environment, Florida Agricultural and Mechanical University, Tallahassee, FL, United States

The dispersion of subsurface Lagrangian floats by eddies was observed directly in DeSoto Canyon, located in the northeastern Gulf of Mexico. Key elements of dispersion include the capture and release of floats by variations in eddy structure and intensity. Two separate eddy events were revealed through 60-day trajectories from five subsurface drifters deployed at 400 m depth in DeSoto Canyon. A changing background flow in DeSoto Canyon allowed for the contraction and expansion of the eddy's "trap zone," resulting in the capture and release of several drifters deployed in the area. To investigate the variability of dispersion due to this capture-and-release effect, virtual particle tracks from a 5-year numerical model simulation of the Gulf of Mexico were used. Large interannual variability was observed in eddy activity over the 5-year simulation. When coupled with a variable background flow, this greatly affected Lagrangian particle transport within the entire eastern Gulf of Mexico. During years of increased eddy activity, more virtual particles were "captured" from the along-slope flow and "released" offshore, increasing dispersion and residence time within the eastern Gulf of Mexico. The opposite was observed during minimal eddy activity, where more virtual particles remained within the along-slope flow and thus were funneled toward two main exit points out of the eastern Gulf of Mexico. Regions such as DeSoto Canyon with strong topographic constraints, a highly variable background flow, and considerable eddy activity are likely to spread tracers such as nutrients and contaminants over a substantial area due to this capture-and-release effect.

## KEYWORDS

floats, Gulf of Mexico, eddies, dispersion, RAFOS, DeSoto Canyon  
self-organizing maps

# 1 Introduction

Transport pathways in the Gulf of Mexico (GoM) are controlled by large-scale circulation associated with the unstable Loop Current, eddies, bathymetric effects, wind forcing, and boundary-trapped waves. The dominant current in the GoM is the Loop Current, formed from the intrusion of warm Caribbean water into the Gulf across the sill between the Yucatan peninsula and Cuba. From this Loop Current, large eddies are produced, which may detach and dominate the circulation over most of the interior of the Gulf. Frontal instability of the Loop Current is thought to be partly responsible for a complex field of eddies in the northern GoM (Huh et al., 1981; Vukovich and Maul, 1985; Maslo et al., 2020). Most of the time, the Loop Current is south of about 26.5°N (Dukhovskoy et al., 2015). Thus, the Loop Current itself does not impinge on the northern slope region but generates a cascade of smaller-scale motions that subsequently intrude upon the northern Gulf slope and are partly responsible for the eddy activity there (Hamilton et al., 2000; Ohlmann et al., 2001; Ohlmann and Niiler, 2005; Hamilton and Lee, 2005; Hamilton, 2007). In addition, flow along the northern Gulf slope can be forced remotely by Loop Current interaction with the slope further south and east along the Florida escarpment (Oey and Lee, 2002; Hamilton and Lee, 2005; Nguyen et al., 2015; Jouanno et al., 2016; Liu et al., 2018).

In the northeast GoM, wind-driven currents dominate transport on the wide and shallow continental shelf but become only one of several factors controlling transport farther offshore (Weisberg et al., 2005), where mesoscale eddies with scales of 10–100 km are of equal or greater importance (Hamilton and Lee, 2005). Even smaller, submesoscale flow structures are gaining recognition as important components of both upper and deep ocean dispersion (Zhong and Bracco, 2013; Poje et al., 2014; Bracco et al., 2016; Liu et al., 2018).

Cyclonic (anticlockwise) and anticyclonic (clockwise) eddies have frequently been observed in DeSoto Canyon (DSC), located

in the northeastern GoM (Hamilton et al., 2000; Wang et al., 2003; Hamilton, 2007; Hamilton et al., 2015). These eddies, along with wind forcing, have been associated with lower frequency ocean currents energetic at periods of weeks to months (Wang et al., 2003; Hamilton and Lee, 2005; Teague et al., 2006; Carnes et al., 2007; Hallock et al., 2009). Though most of the eddies are formed remotely and intrude upon the northeastern GoM, it has been proposed that some eddies might be locally generated in DSC (Weisberg et al., 2005), due to strong along-slope flow interacting with sharp bends in the bathymetry. In addition to eddy activity, coastally trapped shelf waves have been inferred from mooring data west of DSC (Carnes et al., 2007; Hallock et al., 2009). Potential driving forces are winds along the West Florida Shelf (Carnes et al., 2007) and eddies impacting DSC along the Mississippi–Alabama slope (Hallock et al., 2009).

Numerous observational studies (Hamilton et al., 2000; Wang et al., 2003; Leben, 2005; Liu and Weisberg, 2005; Ohlmann and Niiler, 2005; Hamilton, 2007; Hamilton et al., 2011; Liu et al., 2016; Furey et al., 2018; Perez-Brunius et al., 2018, to name a few) and numerical simulations (Morey et al., 2005; Nguyen et al., 2015; Bracco et al., 2016) have shown that the flow in the northeastern GoM is complex. This flow is often characterized by high temporal and spatial variability, which allows variable shear flows, as well as high and low vorticity environments, to exist on a range of scales. Eddies in such an environment will experience varying trap zone sizes (Shapiro et al., 1997), leading to the capture and/or release of particles as the eddies propagate through this fluctuating background flow. In this manner, eddies can transport particles away from preferred flow pathways, which are often constrained by ocean bathymetry at depth (Weisberg et al., 2011), and into the interior of the basin.

We postulate that the capture-and-release effect of eddies in a variable background flow affects particle dispersion by transporting particles away from depth-constrained along-slope pathways. This allows particles to spread more uniformly throughout the northeastern GoM and increases their residence time within the eastern GoM. To explore this hypothesis, we will use subsurface RAFOS drifter data from the eastern GoM, as well as output from a 5-year Regional Ocean Modeling System (ROMS) simulation over the entire GoM.

The paper is organized as follows. RAFOS drifter data and an overview of the ROMS model simulation are described in Materials and methods, respectively. A brief outline of self-organizing maps (SOM) is located at the end of Materials and methods, followed by results and a discussion.

## 2 Materials and methods

Lagrangian surface and subsurface drifter track data are usually employed in a statistical fashion to observe ocean currents and estimate turbulence and diffusivity within specific

**Abbreviations:** BMU, best matching unit; CICESE, Ensenada Center for Scientific Research and Higher Education; CFRS, Climate Forecast System Reanalysis; DSC, DeSoto Canyon; EKE, eddy kinetic energy; GEBCO, General Bathymetric Chart of the Oceans; GLAD, Grand Lagrangian Deployment; GLORYS, global eddy-permitting ocean reanalysis; GoM, Gulf of Mexico; HYCOM, Hybrid Coordinate Ocean Model; LC, loop current; LCE, loop current eddy; LCS, loop current system; MKE, mean kinetic energy; MITgcm, Massachusetts Institute of Technology global circulation model; QE, quantitative error; ROMS, Regional Ocean Modeling System; SCULP II, Surface Current and Lagrangian Drift Program; SOM, self-organizing maps; TE, topographic error; TPXO, Oregon State University TOPEX/Poseidon Global Inverse Solution; USGS, US Geological Survey; WFS, West Florida Shelf.



flow regions (LaCasce, 2008; Salle et al., 2008; Balwada et al., 2016; Balwada et al., 2021). In this paper, we consider the tracks of five subsurface RAFOS drifters, deployed in DSC over approximately 60 days (15 June 2012–05 August 2012). These drifters were part of the Deep-C Dispersion Experiment in the Eastern Gulf of Mexico to investigate the dispersion in DSC and the northeastern GoM (Hancock and Speer, 2013). To expand upon the results from this novel RAFOS drifter experiment, we use the output from a 5-year free-running version of the ROMS data assimilative counterpart over the entire GoM (Maslo et al., 2020).

## 2.1 RAFOS float data

Thirty-six autonomous drifters, called RAFOS drifters, were deployed at 11 locations in DSC in May of 2012 (Figure 1), as part of the Deep-C Dispersion Experiment in the Eastern Gulf of Mexico (Hancock and Speer, 2013). The RAFOS float is an acoustically tracked subsurface drifter (Rossby et al., 1986) programmed to listen for coded acoustic signals from distant moored sound sources. Using the measured arrival times of the sound signal and the speed of sound in water, the positions of the drifters are determined by triangulation. The drifters are ballasted to drift at a fixed pressure, hence depth, for a year. Their 400-m-drift depth is deep enough to be below direct surface layer effects yet shallow enough to be deployed well

within the canyon. This was the first experiment of its kind focused on the continental slope region in the northern GoM. Temperature and pressure records are obtained along with position, as actual depths can differ from the ballasted depth due to errors and changes in weight over the course of the mission. The median depth of the drifters over the experiment was 419 m, with a range from 343 to 486 m.

Position fixes were obtained three times per day in order to resolve higher frequency motion. Apparent in some tracks is small-scale motion that are resolved inertial oscillations. In general, the accuracy of the position is expected to be about 1–2 km, although it can be worse at times when the float has a poor position relative to the sound sources or when it lies in a sound shadow. Sources were deployed to ensure tracking within DSC itself, which means other distant locations were less well covered with acoustic RAFOS signals.

Float deployments close to the seafloor, here the continental slope, are particularly risky since small ballasting errors of a few grams can translate into many meters of depth change, and touching a muddy bottom can change the weight and lead to failure. Due partly to this effect, of the 36 drifters deployed, 20 returned usable data, producing a total of 3,663 float-days of data. See Hancock and Speer (2013) for the full float report and Speer (2013) for the data.

All RAFOS floats are used when calculating the pseudo-Eulerian flow field in DSC. As most of the floats had left DSC after 100 days, we used only the first 100 days of RAFOS float

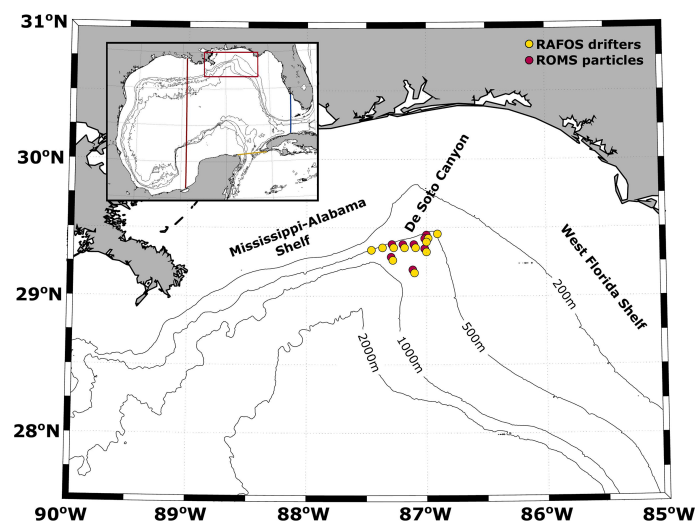


FIGURE 1

Map of the northeastern GoM with a map of the entire GoM in the top left-hand corner. The red rectangle on the full GoM map indicates the extent of the northeastern GoM (28°N–30°N, 85°W–90°W) as used during the SOM analysis. Red, yellow, and blue lines indicate the border between the eastern GoM and western GoM, Caribbean, and Atlantic, respectively, for the particle ending location calculation in Section 3.4 and Figure 12. Isobaths are shown in black at 200, 500, 1,000, and 2,000 m. Yellow and red circles indicate RAFOS drifter and ROMS virtual particle deployment locations, respectively.

data. For the capture and release of RAFOS floats by eddies, however, we focus on the trajectories of five specific RAFOS floats, which were captured by two eddies in DSC.

## 2.2 ROMS model output

Initially, this ROMS simulation was developed to provide the background solution for a 4DVAR data assimilative run to generate a GoM ocean reanalysis product. For this study, we employ 4 years of daily mean output from the free-running version, which is used to investigate the effect of eddies on virtual particle spreading and pathways within the eastern GoM.

ROMS is a 3D primitive equation ocean model employing hydrostatic and Boussinesq approximation (see [Shchepetkin and McWilliams \(2005\)](#); [Shchepetkin and McWilliams \(2009\)](#) and [www.myroms.org](http://www.myroms.org) for a full description of the model). The model is applied to the GoM and part of the Caribbean Sea using a grid with ~5 km horizontal resolution. It contains  $327 \times 375$  computational cells and 36 vertical levels, extending from 97.7°W to 79°W and from 15.6°N to 30.54°N ([Maslo et al., 2020](#); [Morey et al., 2020](#)). A nonlinear, free running (i.e., no data assimilation) simulation was integrated with forcing from 2010 to 2014 ([Maslo, 2020](#)). The bathymetry combines information from the “General Bathymetric Chart of the Oceans” (GEBCO), data from NOAA, proprietary data from PEMEX, and other observations collected during several cruises performed by the [Ensenada Center for Scientific Research and Higher Education \(CICESE\)](#). The need to smooth the bathymetry to avoid pressure-gradient-associated errors is a well-known problem of sigma coordinate models and can have an impact on the simulated deep and near-bottom circulations. To minimize this problem, an interactive method was used ([Sikiric et al., 2009](#)), where smoothing is only applied to the locations where spurious bottom currents generated by pressure gradient errors are observed. This method preserves a good representation of bathymetric features important to this study, such as the shelf break and DSC.

Hourly atmospheric forcing is provided by the Climate Forecast System Reanalysis (CFSR) ([Dee et al., 2014](#)). A bulk formulation scheme was used to calculate the heat, water, and energy fluxes at the surface ([Fairall et al., 1996](#)). The contribution from 21 rivers was included as point sources in the model domain. Daily measured water flux values provided by the U.S. Geological Survey (USGS) are used for the Mississippi and the Atchafalaya rivers, while climatological values reproducing the annual cycle are used for the Mexican rivers. In addition, 11 tidal constituents obtained from the Oregon State University TOPEX/Poseidon Global Inverse Solution (TPXO) ([Egbert and Erofeeva, 2002](#)) were introduced as a separate spectral forcing at the boundaries to the free surface and barotropic velocity, and as tidal potential at every grid point.

Initial and daily open boundary conditions are obtained from the “Global Eddy Permitting Ocean Reanalysis” 2 version 3 by Mercator Ocean—GLORYS2v3. Clamped conditions are applied at the southern and eastern boundaries, while a combination of radiative boundary conditions with nudging towards the GLORYS results is used at the northern boundary. Though the model is forced by prescribed surface and boundary conditions for the years 2010–2014, the fact that this simulation is not constrained by data assimilation means that the interior circulation features (e.g., the Loop Current and eddy field) behave stochastically and are not expected to replicate actual conditions from 2010 to 2014 (in the remaining text, reference to the simulation time periods will indicate the time periods of model forcing).

The ROMS hydrodynamics for this simulation was validated by [Estrada-Allis et al. \(2020\)](#) and [Maslo et al. \(2020\)](#), using velocity measurements from moorings and Lagrangian observations. This simulation was also compared to output from two additional numerical simulations, the Massachusetts Institute of Technology general circulation model (MITgcm) and the Hybrid Coordinate Ocean Model (HYCOM), over the same time period ([Morey et al., 2020](#)). Results demonstrated that ROMS was able to produce realistic surface and deep circulation in the GoM.

Virtual particle tracking in the ROMS simulation was done offline using the Dormand–Prince method ([Dormand and Prince, 1980](#); [Kimura, 2009](#)). Since our primary interest is to supplement our sparse RAFOS results, all virtual particles are forced to stay at 400 m similar to our RAFOS deployment. Virtual particles were seeded daily at eight of the 11 RAFOS deployment locations ([Figure 1](#)) and advected horizontally for a year, using daily mean horizontal velocities from the ROMS simulation result. Due to RAFOS deployments occurring close to the slope and the horizontal ROMS model grid spacing employed, three of the RAFOS deployment locations were in water shallower than 400m and could not be used. Output was in the format of daily latitude and longitude positions for each virtual particle (see [Maslo, 2020](#), for data). To validate the accuracy of virtual particle tracking, we subsampled ROMS virtual particles released in May 2012 and compared them to the RAFOS floats deployed in the same timeframe. Of the 248 virtual particles deployed, 20 were chosen at random, for 1,000 realizations. Both RAFOS floats and ROMS virtual particles were binned into a geographical grid of 0.25° longitude by 0.125° latitude and subsequently counted. Despite ROMS being a free-running model, and therefore not replicating actual conditions from 2012, we have good agreement between the float data and the mean virtual particle output ([Supplementary Figure S1](#)). Based on this result, and previous validations of ROMS model circulation, we presume the model output to be acceptable for further analysis.

## 2.3 Self-organizing maps

The goal of our research is to extract particle dispersion patterns and analyze their temporal variations. To this end, we use SOM, developed by Kohonen (1982), Kohonen (1998); Kohonen (2001); Kohonen (2013) and Vesanto et al. (2000). The SOM method is an artificial neural network based on unsupervised learning that performs nonlinear cluster analysis by mapping high-dimensional data onto a two-dimensional output space. Unlike variance-preserving EOFs, SOM preserves topology and naturally orders patterns most closely matching the original dataset (Liu and Weisberg, 2005). In other words, the SOM network architecture can be stretched and twisted but not cut or folded, and nodes will preserve connections to neighboring nodes, though distances between them can change (Supplementary Figure S2). However, SOM requires a predefined network architecture, which leads to user subjectivity when defining map size and shape. Results from SOM can therefore be strongly dependent on the initial architecture and parameter choices. Despite this, SOM has found widespread use across various disciplines as a pattern recognition and classification tool (Kaski et al., 1998; Oja et al., 2003; Liu et al., 2006; Liu and Weisberg, 2011; Vilibic et al., 2015; Liu et al., 2016; Meza-Padilla et al., 2019). For an in-depth explanation of the SOM technique, including the training process and parameter choices for oceanography, we refer the reader to Liu et al. (2006); Liu et al. (2016).

In our study, the spatial and temporal analysis was based on 36-time steps (i.e., monthly composites of virtual particle distribution in the northeastern GoM from 3 years of ROMS model output, see Supplementary Figure S2) and 4,100 grid points (i.e., a geographical grid of 0.05° latitude by 0.05° longitude over the northeastern GoM, see Figure 1), respectively. In the first step of the SOM training process, nodes are distributed randomly on a two-dimensional space, based on the multidimensional input data (Supplementary Figure S2). Successive steps then proceed iteratively between input data and SOM, until the nodes approach the best representation of the input data. This is achieved by finding the best matching unit (BMU), defined as the minimum Euclidian distance between the node weights and original input data, after each iteration. The BMU and neighboring nodes are modified towards the input data, allowing similar patterns to be mapped closer together and dissimilar patterns farther apart. Supplementary Figure S2 illustrates the SOM process visually, where the input is a 2D array of monthly composites of virtual particle distribution and the output is  $N$  maps of virtual particle distributions.

Several SOM parameters controlling the initialization, iteration, and final output are tunable. Liu et al. (2006)

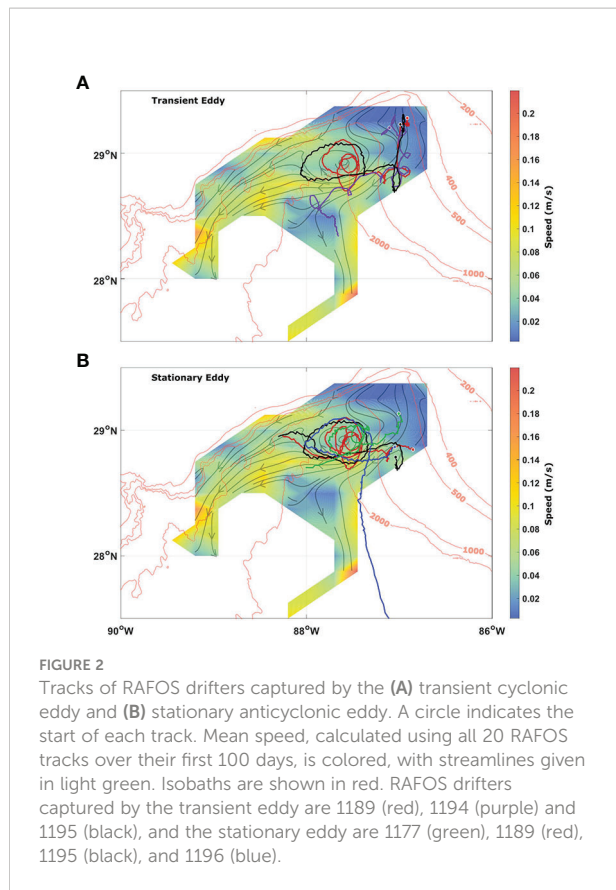
suggested a set of SOM parameters for practical application based on their evaluation of the tool. We follow their suggestions on the parameter choice for initialization, learning rate, and neighborhood function. In addition, the user must specify the SOM map size, which is an empirical process determining how much detail is available for the analysis. This means a trade-off exists between compressing information into a manageable size and accuracy (Liu et al., 2006). We chose a rectangular grid with approximately 30 nodes, calculated using the following formula:  $5 \times \sqrt{\text{number of samples}}$  [Vesanto et al. (2000)], and a hexagonal lattice to avoid directional preference (Kohonen, 2001). To determine the map grid arrangement, we used the ratio of the two largest eigenvalues of the input data to set the ratio of grid side lengths ( $9 \times 3$ ). The actual side lengths were then set such that their product approximated the number of nodes calculated above (i.e., 27). Sensitivity tests were performed with varying map grid arrangements, the number of nodes, and training length, where each scenario was run multiple times to ensure stability and consistency of the results. To further quantify the quality of our final maps, we used two error estimates provided by the SOM toolbox: average quantization error (QE) and topographic error (TE). The QE quantifies how much detail is being learned by the SOM, and TE measures the projection quality. For our analysis, QE and TE were 0.014 and 0.02, respectively, which indicate reliable maps. The SOM MATLAB Toolbox 2.0 by Vesanto et al. (2000) was used, which we downloaded from the Laboratory of Information and Computer Science at the Helsinki University of Technology (<http://www.cis.hut.fi/somtoolbox>).

## 3 Results

### 3.1 Eddies in DSC and the northeastern GoM

Five RAFOS drifters are captured by eddies in DSC, one transient cyclone moving with the background flow (Figure 2A) and another stationary anticyclone just south of the 1000-m-depth contour (Figure 2B). Drifter tracks are overlaid pseudo-Eulerian velocities (shown in dark pastel green), which were calculated on a geographical grid of 0.25° longitude by 0.125° latitude, using all RAFOS drifter tracks over their first 100 days. The transient cyclone captures one drifter (purple track in Figure 2A) within the upper part of DSC, close to the drifter deployment location, and travels southward with the background flow. As the cyclone enters an area with reduced background flow, it briefly captures two more drifters (red and black tracks in Figure 2A), before moving westward. Evident in the streamlines is the stationary anticyclone, which captures four of the drifters (red, black, green, and blue tracks in Figure 2B). Upon the drifters' release from the stationary anticyclone, three

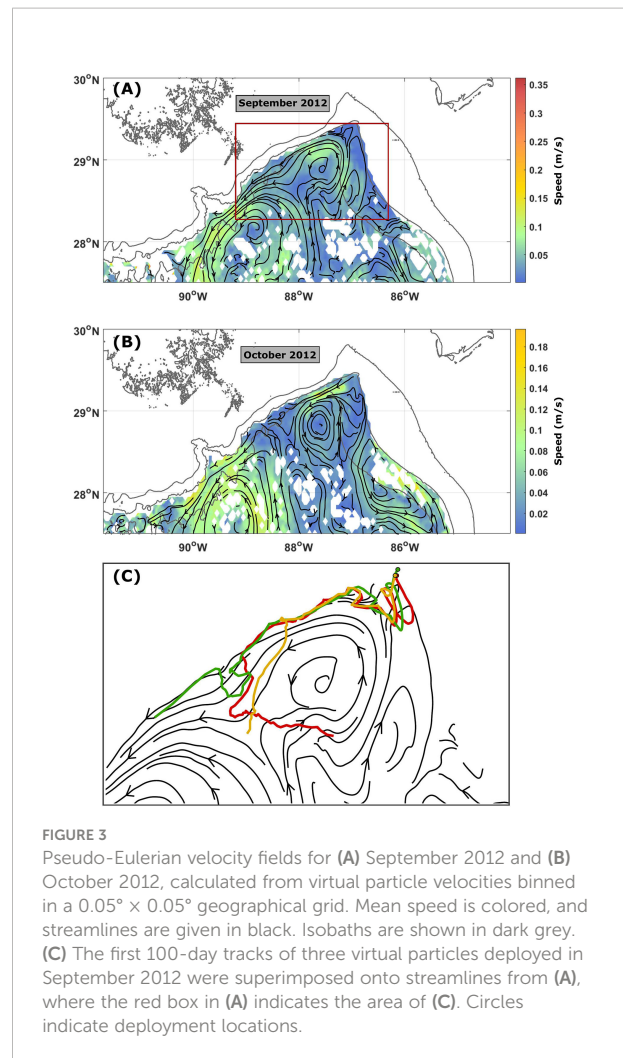




continue westward (red, green, and black tracks), whereas one travels south (blue track).

Based on RAFOS trajectories, we estimated the transient cyclone to be  $O(10\text{ km})$  in diameter and therefore too small to be detected by satellite remote sensing measurements, such as sea surface height and temperature anomalies. Although the stationary anticyclone is at the detection limit with a diameter of  $\sim 40\text{ km}$ , it is not distinguishable by satellite altimetry either. This could be because it is a subsurface eddy with weak surface expression. No other supplementary data, such as mooring arrays and/or hydrographic profiles, are available for this time period.

ROMS virtual particle tracks show similar structures throughout all five model years, with eddies ranging in size from  $O(10\text{ km})$  to  $O(100\text{ km})$  within the northeastern GoM. In fact, a stationary eddy is often seen at the base of DSC, in a similar location as that identified by the RAFOS floats data. Calculating velocities from the year-long virtual particle trajectories and binning these into a geographical grid ( $0.05^\circ$  longitude by  $0.05^\circ$  latitude), we constructed monthly pseudo-Eulerian velocity fields for 2011–2013. These illustrate the presence of semistationary eddies in the northeastern GoM (Figures 3A, B). For transient eddies, single virtual particle trajectories show their presence in DSC (Figure 3C).



### 3.2 Circulation in the northeastern GoM

The Loop Current System (LCS) wields a significant influence on subsurface circulation in the northeastern GoM and DSC. Monthly pseudo-Eulerian velocity fields, calculated from year-long virtual particle trajectories and binned into a geographical grid of  $0.05^\circ \times 0.05^\circ$ , show strong eastward along-slope flow in 2010 and 2011 (Figure 4), corresponding to years dominated by a LCS that extends northwestward toward the Mississippi Canyon (Liu et al., 2016). Hamilton and Lee (2005) observed a similar correlation between LSC location and along-slope flow direction, attributing it to potential vorticity conservation. During late spring and early summer of 2011, the LCS extends northeastward toward DSC, which is clearly seen in the monthly pseudo-Eulerian velocity field (Figure 4). Again, Hamilton and Lee (2005) found evidence of a Loop Current Frontal Eddy intruding over the slope, affecting upper-layer along-slope flow patterns. In contrast, 2012's flow field is much weaker, with an along-slope flow predominantly directed

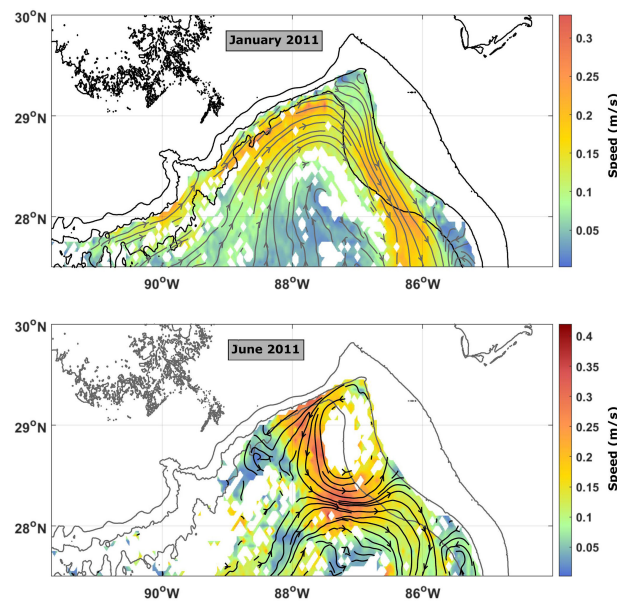


**FIGURE 4**  
Pseudo-Eulerian velocity fields for (top) January 2011 and (bottom) June 2011, calculated from virtual particle velocities binned in a  $0.05^\circ \times 0.05^\circ$  geographical grid. Mean speed is colored, and streamlines are given in black. Isobaths are shown in dark grey.

westward (Figures 3A, B). Multiple eddies were also present throughout the northeastern GoM. Although 2012 saw the shedding of two Loop Current Eddies (LCE), these moved quickly westward, and the Loop Current (LC) was retracted for large portions of the year (Liu et al., 2016). The flow in 2013 was a mixture between 2010–2011 and 2012, with the mean along-slope flow equally directed eastward and westward (not shown).

Eddy activity in the northeastern GoM is evident through the monthly pseudo-Eulerian velocity fields (Figures 3, 4). However, to better quantify the interannual variability in eddy activity, we calculated the yearly mean and eddy kinetic energy (MKE and EKE, respectively) for 2011–2013, using the following formula:

$$\text{MKE} = \frac{(\bar{u}^2 + \bar{v}^2)}{2} \quad (1)$$

$$\text{EKE} = \frac{1}{N} \sum_{i=1}^N \frac{[(u_i - \bar{u})^2 + (v_i - \bar{v})^2]}{2} \quad (2)$$

Here, the bar denotes the time mean, and  $N$  is the number of months. The calculation was performed for each  $0.05^\circ \times 0.05^\circ$  grid box within the northeastern GoM over 12 months. To identify the persistence of eddy activity, Figure 5 shows the ratio of EKE to the total kinetic energy (EKE+MKE) as a percentage for each year. Elevated levels of EKE along the West Florida Shelf (WFS) and Mississippi–Alabama slopes in 2011 are most likely due to variability in the along-slope flow. Previous work has

suggested several causes for this variability, such as wind forcing, the LCS, and eddy activity (Wang et al., 2003; Hamilton and Lee, 2005; Teague et al., 2006; Carnes et al., 2007; Hallock et al., 2009). The year 2011 also exhibits high EKE along  $87^\circ\text{W}$  and  $88^\circ\text{W}$ , which is probably due to the northward extension of the LCS in late spring and early summer of that year. In comparison, 2012 has elevated EKE levels throughout most of the northeastern GoM, with noticeably lower values on the WFS and Mississippi–Alabama slopes. This correlates to monthly pseudo-Eulerian velocity maps, which display abundant eddy activity within the whole northeastern GoM during most months. Similar to the monthly pseudo-Eulerian velocity fields, 2013 exhibits high EKE both along the slopes and within the interior, indicating a mixture of high eddy activity and variable along-slope flows.

### 3.3 Virtual particle dispersion in the northeastern GoM

To investigate pathways out of DSC and the northeastern GoM, we again use the year-long virtual particle trajectories and  $0.05^\circ \times 0.05^\circ$  geographical grid, counting the number of virtual particles in each grid cell for each month, normalized by the total number of virtual particles in the basin. Figure 6 shows results from 2 months with abundant (Figure 6A) and marginal (Figure 6B) eddy activity, respectively. When there is considerable eddy activity in the northeastern GoM (defined

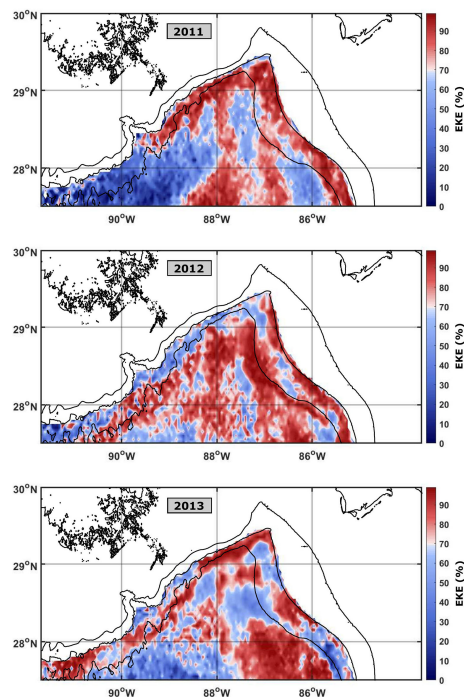


FIGURE 5

Ratio of EKE to total kinetic energy (EKE+MKE) in each grid cell, represented as a percentage for 2011 (top), 2012 (middle), and 2013 (bottom) in the northeastern GoM. EKE and MKE are calculated from virtual particle velocities binned in a  $0.05^\circ \times 0.05^\circ$  geographical grid, for each year separately. Isobath is shown in black.

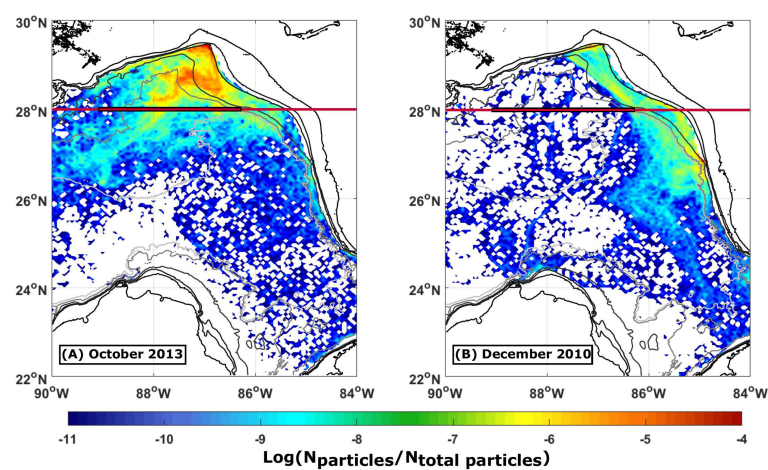


FIGURE 6

Density of virtual particles in each grid cell normalized by the total number of virtual particles in the domain, represented on a log scale for (A) October 2013 and (B) December 2010. Isobaths are shown with black and gray lines. The red line indicates  $28^\circ\text{N}$ , and the black outlined section indicates water depths greater than 1,500 m along  $28^\circ\text{N}$ .

here as north of 28°N), virtual particles are dispersed within the entire northeastern basin, such as in October 2013 (Figure 6A). However, whenever eddy activity is at a minimum, virtual particles are more confined to the slopes bordering either the WFS (Figure 6B) or the Mississippi–Alabama Shelf, dependent on the predominant direction of the along-slope flow.

To further illustrate these pathways out of the northeastern GoM and how they fluctuate in time, we explore the longitude at which virtual particles move south across 28°N (red line in Figure 6) as a function of time (Figure 7). There are significant differences both within and between years. During the latter part of 2010, most virtual particles exited east of 87°W, whereas 2012 reveals the opposite flow pattern, with most virtual particles exiting west of 87°W. If we define 86.5°W–89°W as the interior basin with a water depth greater than 1,500 m (the black outlined portion of the red line in Figure 6) and consider the total number of virtual particles crossing 28°N at that location, we can examine the cumulative effect of variable eddy activity (Figure 7A). Although we see singular months with a sizable particle density crossing 28°N in the interior basin during 2010–2011, half of the months exhibit particle densities less than the lowest values found in 2012–2013. On a yearly timescale, 2010–2011 had a third less virtual particles crossing 28°N in locations where the water depth is greater than 1,500 m, compared to 2012–2013 (Figure 7A). In other words, more virtual particles were confined to slope regions during 2010–2011 than in 2012–2013.

How are these particle pathways connected to the dynamics occurring in the northeastern GoM? To answer this question, we use the SOM method to extract particle dispersion patterns over the model years 2011–2013 in the area 28°N–30°N, 85°W–90°W (red box in Figure 1). In order to reduce errors associated with the SOM technique, we settled on a  $[9 \times 3]$  hexagonal grid of nodes. SOM maps (i.e., nodes) and BMUs (i.e., the SOM map that best describes the dataset at each time step) associated with each of the model years 2011, 2012, and 2013 are grouped in separate figures (Figures 8–10), whereas the full map of nodes in the hexagonal grid can be found in the [Supplementary Material](#) ([Supplementary Figures S3 and S4](#)). Six of the SOM maps never occurred during model years 2011–2013 (maps 8, 11–14, and 17). Of the remaining SOM maps, we notice differences between 2011 and 2012–2013. During 2011, we predominantly observed variations of eastward flow along the WFS and reduced eddy activity occurring in maps 1, 18, 19, 20, and 21 (Figure 8). A composite of these SOM maps illustrates this exiting flow pattern (Figure 11A), which occurs 58% of the time in 2011. This agrees with the EKE (Figure 5) and monthly pseudo-Eulerian velocity fields (Figure 4) for 2011, which show reduced eddy activity and increased along-slope variability. In contrast, westward flow along the Mississippi–Alabama shelf dominates in 2012 (maps 4, 6, 16, 25, and 26), with an increased eddy activity in the northeastern GoM (Figure 9). The year 2013 shows similar increased eddy activity as 2012, though with a mixture of eastward and westward along-shelf flow patterns

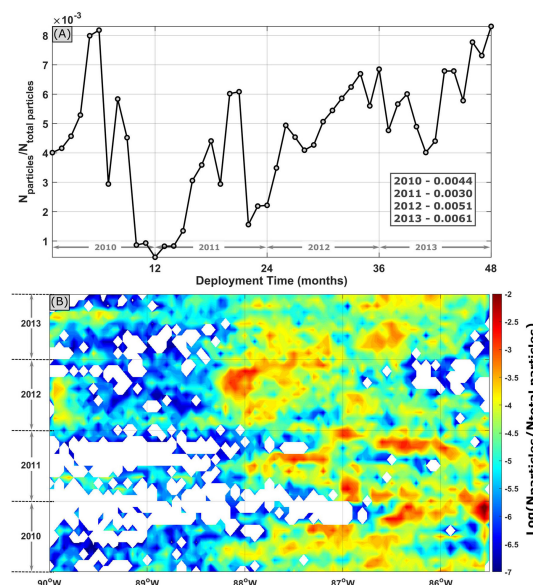


**FIGURE 7**  
**(A)** Virtual particle density, normalized by the total number of virtual particles in the domain, moving south across 28°N in water depths greater than 1,500 m (defined as 86.5°W–89°W, the section of the red line at 28°N outlined in black in Figure 6), as a function of months from deployment. The inset box gives the mean for each year. **(B)** Virtual particle density, normalized by the total number of virtual particles in the domain, moving south across 28°N as a function of longitude and time, is represented on a log scale.



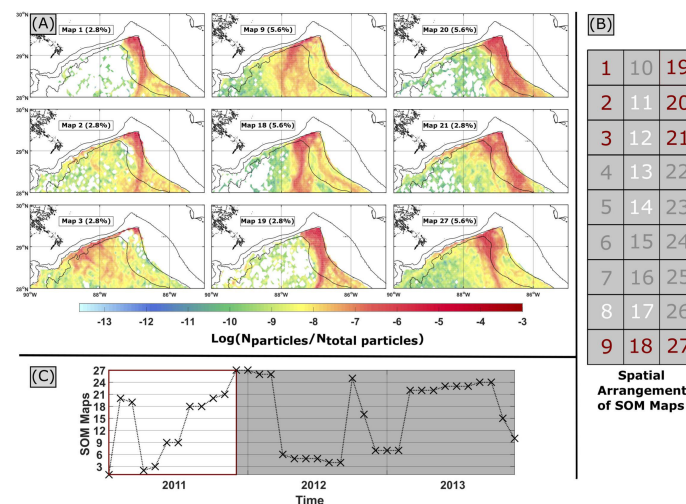


FIGURE 8

(A) SOM maps presenting virtual particle density in each grid cell, normalized by the total number of virtual particles in the domain, for 2011, represented on a log scale. Isobaths are shown in black. (B) The user specified spatial arrangement of SOM maps for the analysis, where the white, red, and gray numbers represent SOM maps that never occur, occur in 2011, and do not occur in 2011, respectively. (C) The BMU for each month, where the white area signifies 2011.

(Figure 10). Again, we created a composite of the SOM maps where mixing occurs in 2012–2013 (this will be termed “eddy mixing”), shown in (Figure 11B). Eddy mixing occurs 75% of the time during 2012–2013, which is corroborated by the EKE (Figure 5) and monthly pseudo-Eulerian velocity fields (Figure 3) for 2012–2013. We observe a similar pattern in particle recirculation, with increased virtual particles within 3 km of their initial deployment location during 2012–2013, compared to 2010–2011 (Table 1).

### 3.4 Virtual particle residence time in the eastern GoM

Given the above variations in virtual particle pathways exiting DSC, how do these control (1) the Lagrangian dispersion of virtual particles out of the eastern GoM and (2) virtual particle residence times in the eastern GoM? To answer both questions, we expand our view and investigate virtual particles that leave the eastern GoM. For this analysis, we divide our area into four sections: (1) the Atlantic (east of 82°W), (2) the western GoM (west of 92°W), (3) the Caribbean (south of 22°N), and (4) the eastern GoM (see Figure 1). Once a virtual particle leaves the eastern GoM, it is considered to be at its final destination. At the end of a virtual particle’s 1-year drift, if it has not exited the eastern GoM, this is considered its final destination. Approximately 3% of virtual particles re-entered the eastern GoM, almost exclusively from the western GoM, over the entire 4 years. Since we are primarily concerned with virtual particle pathways within and out of the eastern GoM, excluding the re-

entry of virtual particles should not affect our analysis. We also want to note that, though the natural divide between the eastern and western sections of the GoM is located around 90°W, several virtual particles entering the region between 90°W and 92°W reversed direction before crossing 92°W and traveled back into the eastern GoM. To ensure these virtual particles were not identified as entering the western GoM, we set the divide at 92°W. Figure 12 shows virtual particles exiting the eastern GoM as a function of deployment month, throughout the model years 2010–2013. An increase in Lagrangian dispersion into the Atlantic (blue line) occurs during model years 2010–2011, whereas the reverse happens in model years 2012–2013 (purple line). Regarding the western GoM, 2012 sees a modest increase in Lagrangian particle dispersion into the western GoM (red line). We observe a similar distinction between 2010–2011 and 2012–2013 in virtual particle residence times (Figure 13), with an average 50-day shorter mean residence time in 2010–2011 compared to 2012–2013.

## 4 Discussion

As shown analytically by Flierl (1981) and numerically by Shapiro et al. (1997), a variable background flow will change an eddy’s trap zone, allowing it to capture and release particles throughout the eddy’s lifetime. This means that the time a particle travels within an eddy is based on how close that particle is to the eddy’s core compared to the strength of the background flow. For a highly variable background flow, individual particles can be mixed along an eddy’s path

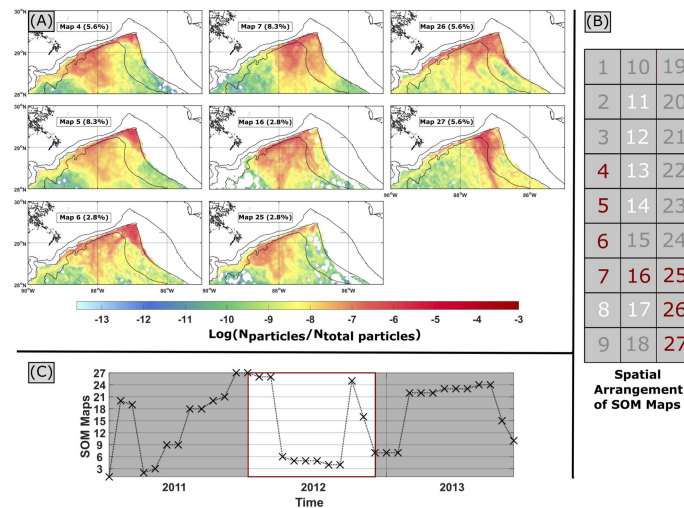


FIGURE 9  
Same as Figure 8, but for 2012.

through the capture-and-release principle, instead of being transported with the eddy until it decays. Although it is hard to quantify this type of mixing on a large scale, it can become important in areas where flow is highly constrained, such as DSC and the northeastern GoM. Mean flow at 400 m in DSC and the northeastern GoM is often confined to the continental slope, flowing either eastwards or westward along isobaths (Teague et al., 2006; Carnes et al., 2007; Hamilton et al., 2000; Hamilton and Lee, 2005). The along-isobath flows parallel to the West Florida and Mississippi–Alabama shelves transport particles to exit pathways into the Atlantic and western GoM, respectively. These exit pathways are located (a) at the western edge of the

Florida Straits and (b) southwest of the Mississippi Canyon (Figure 14). RAFOS drifter tracks (Figure 2) illustrated how eddies can capture drifters and transport them across isobaths into the basin interior. Based on novel Lagrangian observations we postulate that eddies transport particles away from depth-constrained along-slope pathways, affecting their dispersion and residence times in the eastern GoM.

To draw together the larger-scale consequences of the eddy ejection effect, let us assume minimal eddy activity in the northeastern GoM, which means that flow at 400 m depth in DSC will primarily occur along isobaths. If this along-slope flow is directed eastward, it will transport virtual particles to the

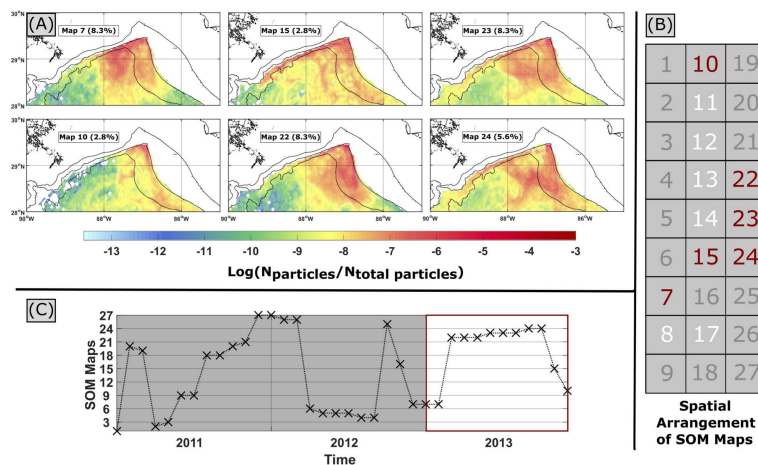


FIGURE 10  
Same as Figure 8, but for 2013.



TABLE 1 Number of ROMS virtual particles within 3 km of their deployment sites.

Months	2010	2011	2012	2013
1	24 (1%)	39 (1%)	249 (9%)	177 (6%)
2	10 (<1%)	4 (<1%)	158 (5%)	153 (5%)
3	4 (<1%)	7 (<1%)	131 (5%)	168 (6%)
4	0 (<1%)	6 (<1%)	83 (3%)	111 (4%)
5	1 (<1%)	6 (<1%)	51 (2%)	120 (4%)
6	8 (<1%)	2 (<1%)	39 (1%)	68 (2%)

This calculation is for model years 2010–2013 and is given as a function of months from deployment. Percentage of the total number of virtual particles is given in parenthesis.

western edge of the Florida Straits where a majority of floats will exit into the Atlantic (Figures 11A, 12). Years with reduced eddy activity would see an increase in virtual particles exiting the eastern GoM, as well as a reduction in their residence times within the eastern GoM. This is consistent with model output from the years 2010–2011 (Figures 4, 5), which shows (a) an increase in the number of virtual particles exiting the northeastern GoM confined to the continental slope (Figures 7, 8), (b) an increase in the number of virtual particles exiting the eastern GoM into the Atlantic (Figure 12), and (c) a decrease in virtual particle residence time in the eastern GoM (Figure 13). However, if eddies populate the northeastern GoM, some virtual particles will be captured and transported away from the along-slope flows and into the basin interior (Figures 11B, 12). This will increase virtual particle residence times in the eastern GoM as well as reduce the number of virtual particles exiting the eastern GoM within their 1-year drift. Again, this is consistent with model output from the years

2012 to 2013 (Figures 3, 5), with (a) a spread in longitudes where virtual particles exit the northeastern GoM (Figures 7, 9, 10), (b) a decrease in the number of virtual particles exiting the eastern GoM (Figure 12), and (c) an increase in virtual particle residence time in the eastern GoM (Figure 13). Examples of virtual particle tracks for times with reduced and increased eddy activity in the northeastern GoM are shown in Figure 14.

Given the above modeling results, the LCS and eddies seem to dominate subsurface circulation in the northeastern GoM. It is therefore not surprising that neither virtual particle pathways nor virtual particle residence times show any significant seasonal signal throughout the model years 2010–2014, as both are dependent on the total flow at any one point. There is, however, significant interannual variability, which better reflects the temporal behavior of the LCS. In fact, Wang et al. (2003) established a connection between the location of the northern LC front and near-surface flows over the lower Alabama slope. It is thought that part of the eddy activity in

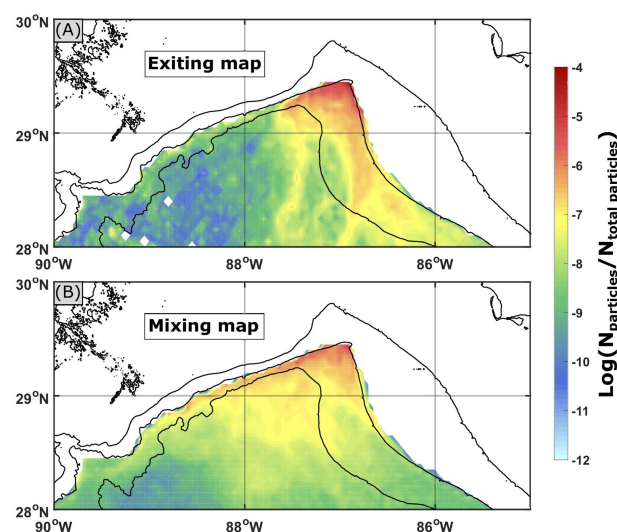


FIGURE 11

Composite of SOM maps to show typical exiting (A) and eddy mixing (B) flow patterns. Exiting and eddy mixing flow patterns are calculated as a mean of SOM maps [1, 18–21] and [4–7, 23–24, 26–27] (see Figures 5–7), respectively. The exiting flow pattern occurred 58% of the time in 2011, whereas the eddy mixing flow pattern occurred 75% of the time in 2012–2013. Isobaths are shown in black.

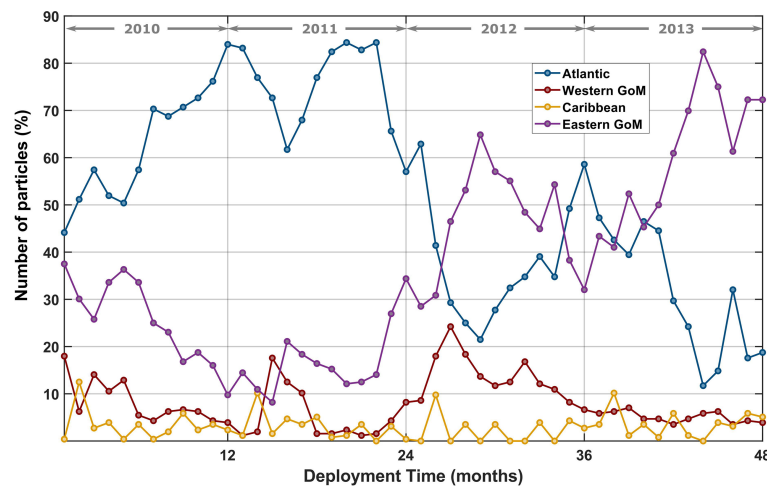


FIGURE 12

ROMS virtual particles' final destination as a function of deployment month, divided into the Atlantic (blue line), western GoM (red line), Caribbean (yellow line), and eastern GoM (purple line). Regions are defined as follows: Atlantic is east of 82°W, western GoM is west of 92°W, the Caribbean is south of 22°N, and eastern GoM is within the bounds of 22°N–30°N and 82°W–92°W (see Figure 1). Once a virtual particle exits the eastern GoM into one of the three locations, that location is considered its final destination. If after a virtual particle's 1-year drift it has not exited into one of the three locations, the eastern GoM is considered its final destination.

the northeastern GoM is generated by the LCS and advected into the region (Hamilton et al., 2000; Ohlmann et al., 2001; Ohlmann and Niiler, 2005; Hamilton and Lee, 2005; Hamilton, 2007). There does, however, seem to be a preference for eddies along the Mississippi slope, which could be a reflection of bathymetric structures, such as canyons and headlands, in this region. Such structures could force the along-slope current to meander, setting the stage for eddy generation

through potential vorticity conservation. Since the LCS seems to affect the along-slope current's strength and direction, this could directly affect eddy generation in this area. DSC has also been suggested as a site for local eddy generation due to sharp bends in the bathymetry (Weisberg et al., 2005).

Although subsurface flow in the northeastern GoM is typically found to be constrained by bathymetry at depth, five RAFOS drifters showed across-isobath movement. If eddies can

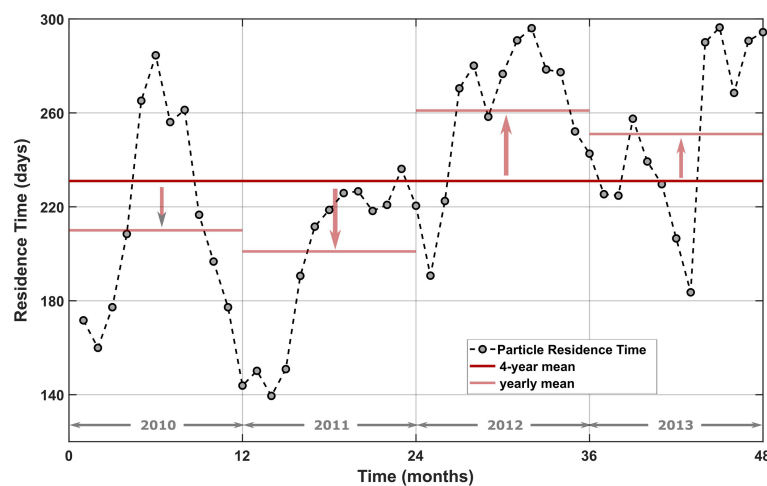


FIGURE 13

Residence time (days) of virtual particles in the eastern GoM as a function of deployment month. The solid red line shows the 4-year mean, whereas the light red lines show yearly means with arrows indicating offset from the 4-year mean.

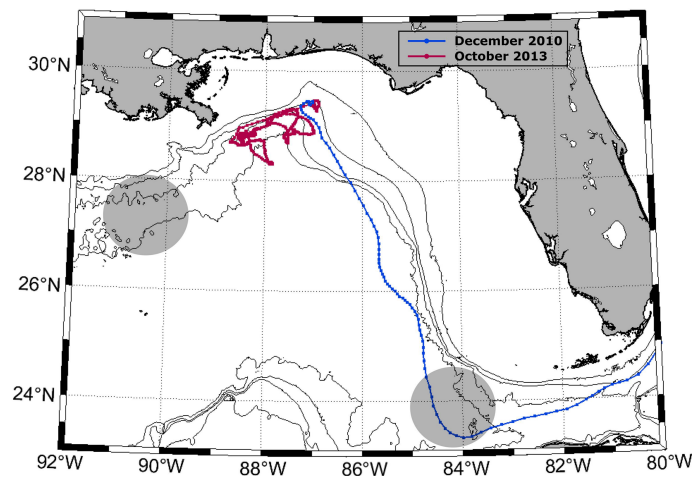


FIGURE 14

Example virtual particle tracks for times with reduced (blue) and increased (red) eddy activity in the northeastern GoM. Gray-shaded areas located at the western edge of the Florida Straits and southwest of Mississippi Canyon denote particle exit points into the Atlantic and western GoM, respectively. Isobaths and coastlines are shown in black.

pull particles from preferred along-slope pathways and into the interior, this will modulate particle dispersion (Figure 14). Thus, the magnitude of eddy activity in the northeastern GoM not only affects particle dispersion in the northeastern GoM but residence times in the eastern GoM as well.

Similar to subsurface drifter data, surface float data in the northeastern GoM, notably from the *Surface Current and Lagrangian Drift Program* (SCULP II) and the *Grand Lagrangian Deployment* (GLAD), shows mesoscale eddies as an important dynamical feature affecting cross-slope flow (Ohlmann and Niiler, 2005; Poje et al., 2014; Hamilton et al., 2015; Mariano et al., 2016) and dispersion (LaCasce and Ohlmann, 2003; Poje et al., 2014). LaCasce and Ohlmann (2003) found evidence for super diffusive dispersion in surface waters using the SCULP II floats, with exponential growth over length scales of 50 km. Their results suggested a spectral continuum of eddies affecting relative dispersion, where eddies of a given scale affected dispersion of the same scale. Both LaCasce and Ohlmann (2003) and Ledwell et al. (2016) found evidence of exponential stretching of tracers into long filaments, despite the study sites being located at the surface and 1,100 m depth, respectively. Near DSC, surface velocity seems to be set by a combination of wind forcing, the energetic eddy field, and the northern LC front (Wang et al., 2003; Hamilton and Lee, 2005; Mariano et al., 2016). Given this complex flow pattern, float tracks are heavily dependent on the dynamical features present and, consequently, their deployment conditions. In fact, Poje et al. (2014) found residence times in DSC could vary from a week to a month, due to this. Both surface floats and subsurface floats observe transient and stationary eddy features in DSC during their deployment (Hamilton and Lee, 2005; Ohlmann

and Niiler, 2005; Hancock and Speer, 2013). The eddy activity in DSC seems to homogenize the upper-layer potential vorticity, removing dynamical barriers for cross-slope flow (Hamilton and Lee, 2005). However, whereas surface floats move offshore and into the Atlantic within 90 days, subsurface virtual particles take an average of 230 days to reach the Atlantic (Figure 13). This difference is possibly due to the lack of direct wind forcing on the subsurface virtual particles.

The northeastern GoM, which includes the Mississippi-Alabama and WFS shelves and slopes as well as DSC, exhibits complex ecosystems defined by high biodiversity and substantial biomass. An important aspect of this is the plume of nutrient-rich low-salinity water from the Mississippi River outflow. Morey et al. (2003a), Morey et al. (2003b) and Schiller et al. (2011) showed using numerical simulations that this low salinity water can be transported off the shelf through a combination of wind forcing and mesoscale eddies in DSC. DSC is a natural pathway for particle transport across the slope, connecting deeper waters with shelf waters along the northeastern GoM. Hamilton and Lee (2005) found evidence of smaller-scale eddies near DSC, which could cause strong cross-slope velocities. These cross-slope velocities thus control the transport of contaminants, such as subsurface oil from the Deepwater Horizon accident, onto the slope and shelf, as well as nutrient-rich Mississippi plume waters off the shelf.

Regions such as DSC, with a highly variable background flow and considerable eddy activity, are likely to spread particles over a substantial area due to the capture-and-release effect of eddies. Eddies can draw tracers into long filaments, which preserves maximum concentrations and gradients better than simple

lateral diffusion. Realizing this can aid in containment strategies for future anthropogenic contamination spills.

Although our research has shown the importance of eddy activity in the northeastern GoM, specifically with regard to particle dispersion and residence times, it suffers from several limitations. The main shortcomings are as follows: (a) the length of the numerical simulation, (b) virtual particle deployment confined to a singular location, and (c) a virtual particle's inability to move vertically in the water column. The length of our simulation was 5 years, with 4 years of virtual particle tracking. With longer simulation times, for example, 20 years, more robust statistics would be available for the analysis. In particular, the SOM method would greatly benefit from an order of magnitude increase in timesteps. As the model output was intended to expand upon the float data, the virtual particle deployment and tracking were configured with the RAFOS experiment in mind. For more comprehensive statistics, particularly relating to the movement of particles into and through DSC, deployment locations should have included sites exterior to DSC, such as its western and eastern flanks. In addition, virtual particles were unable to move vertically in the water column, again to replicate the RAFOS experiment. Understanding the three-dimensional movement of particles in DSC, in particular the connection between the shelf, slope, and deep waters, is beneficial to ecosystem research on the northeastern continental shelf and slope. Future research in the northeastern GoM could start by remedying these noted shortcomings and thus forming a more coherent picture of the dynamics controlling subsurface flow, its variability, and its connectivity to the slope and shelf.

## Data availability statement

The datasets presented in this study can be found in online repositories. The names of the repository/repositories and accession number(s) can be found below: <https://deep-c.coaps.fsu.edu/data> (Deep-C Consortium), and <https://gfdi.fsu.edu/research/research-data> (Geophysical Fluid Dynamics Institute, FSU).

## Author contributions

CH tracked and analyzed the RAFOS float data, analyzed the ROMS virtual particle output, created figures, and wrote the manuscript. KS supplied the RAFOS float data and contributed to the analysis and editing of the manuscript. JS supplied the ROMS model output and contributed to manuscript editing. SM contributed to the analysis methods and editing of the manuscript. All authors listed have made a substantial, direct, and intellectual contribution to the work and approved it for publication.

## Funding

This work was funded by the National Academy of Sciences through the Gulf Research Program grant award 2000006422, and GoMRI and the Deep-C consortium through award SA-12-12/GoMRI-008.

## Conflict of interest

Author JS is employed by MetOcean Solutions Ltd.

The remaining authors declare that the research was conducted in the absence of any commercial or financial relationships that could be construed as a potential conflict of interest.

## Publisher's note

All claims expressed in this article are solely those of the authors and do not necessarily represent those of their affiliated organizations, or those of the publisher, the editors and the reviewers. Any product that may be evaluated in this article, or claim that may be made by its manufacturer, is not guaranteed or endorsed by the publisher.

## Supplementary material

The Supplementary Material for this article can be found online at: <https://www.frontiersin.org/articles/10.3389/fmars.2022.949338/full#supplementary-material>

### SUPPLEMENTARY FIGURE 1

Dominant pathways represented by number of floats/virtual particles in each grid cell ( $0.25^\circ$  longitude  $\times$   $0.125^\circ$ ) on a  $\log_{10}$  scale for (top) RAFOS floats and (bottom) ROMS virtual particles deployed during May 2012. For this calculation, floats/virtual particles were not permitted to re-enter the northeastern box once they have exited it. Isobaths are shown in black.

### SUPPLEMENTARY FIGURE 2

A schematic illustrating the SOM process. For our analysis, monthly virtual particle distribution maps (I) were reshaped into a 2D array for all time steps (II) and used as input for the SOM. The user creates the initial SOM map configuration (III) by selecting the network architecture (i.e., number of maps, lattice shape, initialization parameters etc.). At each timestep, the input data is used to modify the SOM maps (IV), by incrementally moving similar maps closer to the input data. Once the final modifications have been completed, the output data is converted from a 2D array into N maps of virtual particle distributions (V). Along with the N maps, SOM produces a timeseries indicating which SOM map best matches the data (best matching unit, BMU) at each timestep (not shown).

### SUPPLEMENTARY FIGURE 3

SOM maps presenting virtual particle density in each grid cell, normalized by total number of virtual particles in the domain, for 2011–2013, represented on a log scale. Map number and percentage of occurrence is given in the top left of each map and isobaths are shown in gray.

### SUPPLEMENTARY FIGURE 4

The BMU for each month, from 2011–2013, associated with the SOM maps in Figure S3.

## References

- Balwada, D., LaCasce, J. H., Speer, K. G., and Ferrari, R. (2021). Relative dispersion in the antarctic circumpolar current. *J. Phys. Ocean.* 51, 553–574. doi: 10.1175/JPO-D-19-0243.1
- Balwada, D., Speer, K. G., LaCasce, J. H., Owens, W. B., Marshall, R., and Ferrari, R. (2016). Circulation and stirring in the southeast pacific ocean and the Scotia Sea sectors of the Antarctic circumpolar current. *J. Phys. Ocean.* 46, 2005–2027. doi: 10.1175/JPO-D-15-0207.1
- Bracco, A., Choi, J., Joshi, K., Luo, H., and McWilliams, J. C. (2016). Submesoscale currents in the northern Gulf of Mexico: Deep phenomena and dispersion over the continental slope. *Ocean. Model.* 101, 43–58. doi: 10.1016/j.ocemod.2016.03.002
- Carnes, M. R., Teague, W. J., and Jarosz, E. (2007). Low-frequency current variability observed at the shelfbreak in the northeastern Gulf of Mexico: November 2004– may 2005. *Cont. Shelf. Res.* 28 (3), 399–423. doi: 10.1016/j.csr.2007.10.005
- Dee, D. P., Balmaseda, M., Balsamo, G., Engelen, R., Simmons, A. J., and Thépaut, J. N. (2014). Toward a consistent reanalysis of the climate system. *Bull. Am. Meteorol. Soc.* 95 (8), 235–248. doi: 10.1175/BAMS-D-13-00043.1
- Dormand, J. R., and Prince, P. J. (1980). A family of embedded runge-kutta formulae. *J. Comput. Appl. Math.* 6, 19–26. doi: 10.1016/0771-050X(80)90013-3
- Dukhovskoy, d.S., Leben, R. R., Chassignet, E. P., Hall, C. A., Morey, S. L., and Nedbor-Gross, R. (2015). Characterization of the uncertainty of loop current metrics using a multidecadal numerical simulation and altimeter observations. *Deep-Sea. Res. I.* 100, 140–158. doi: 10.1016/j.dsr.2015.01.005
- Egbert, G. D., and Erofeeva, S. Y. (2002). Efficient inverse modeling of barotropic ocean tides. *J. Atmos. Ocean. Technol.* 19 (2), 183–204. doi: 10.1175/1520-0426(2002)019<0183:EIMOB>2.0.CO;2
- Estrada-Allis, S. H., Pardo, J. S., de Souza, J. M. A. C., Ortiz, C. E. E., Tapia, I. M., and Herrera-Silveira, J. A. (2020). Dissolved inorganic nitrogen and particulate organic nitrogen budget in the Yucatan shelf: driving mechanisms through a physical-biochemical coupled model. *Biogeosciences* 17, 1087–1111. doi: 10.5194/bg-17-1087-2020
- Fairall, C. W., Bradley, E. F., Rogers, D. P., Edson, J. B., and Young, G. S. (1996). Bulk parametrization of air-sea fluxes for tropical ocean-global atmosphere coupled-ocean atmosphere response experiment. *J. Geophys. Res.* 101, 3747–3764. doi: 10.1029/95JC03205
- Flierl, G. R. (1981). Particle motions in Large-amplitude wave fields. *Geophys. Astrophys. Fluid. Dyn.* 18 (1–2), 39–74. doi: 10.1080/03091928108298773
- Furey, H., Bower, A., Perez-Brunius, P., Hamilton, P., and Leben, R. R. (2018). Deep eddies in Gulf of Mexico observed with floats. *J. Phys. Ocean.* 48 (11), 2703–2719. doi: 10.1175/JPO-D-17-0245.1
- Hallock, Z. R., Teague, W. J., and Jarosz, E. (2009). Subinertial slope-trapped waves in the northeastern Gulf of Mexico. *J. Phys. Ocean.* 39, 1475–1485. doi: 10.1175/2009JPO3925.1
- Hamilton, R. (2007). Deep-current variability near the sigsbee escarpment in the gulf of Mexico. *J. Phys. Oceanogr.* 37, 708–726. doi: 10.1175/JPO2998.1
- Hamilton, P., Berger, T. J., Churchill, J. H., Leben, R. R., Lee, T. N., Singer, J. J., et al. (2000). *De soto canyon eddy intrusion study. final report. volume II: Technical report* (New Orleans, LA: U.S. Dept. of the Interior, Minerals Management Service, Gulf of Mexico OCS Region), 275pp.
- Hamilton, P., Donohue, K. A., Leben, R. R., Lugo-Fernandez, A., and Green, R. E. (2011). *Monitoring and modeling the deepwater horizon oil spill: A record breaking enterprise* Vol. 195. Eds. Y. Liu, A. MacFadyen, Z.-G. Ji and R. H. Weisberg (Washington, DC: AGU), 117–130. “Loop Current Observations During Spring and Summer of 2010: Description and Historical Perspective”. doi: 10.1029/2011GM001116
- Hamilton, P., and Lee, T. N. (2005). “Eddies and jets over the slope of the northeast Gulf of Mexico,” in *Circulation in the gulf of Mexico: Observations and models*, vol. 161. Eds. W. Sturges and A. Lugo-Fernandez (Washington DC: AGU), 123–142. doi: 10.1029/161GM010
- Hamilton, P., Speer, K., Snyder, R., Wienders, N., and Leben, R. R. (2015). Shelf break exchange events near the de soto canyon. *Cont. Shelf. Res.* 110, 25–38. doi: 10.1016/j.csr.2015.09.021
- Hancock, C., and Speer, K. (2013). “Lateral dispersion in the de soto canyon region. gulf of Mexico RAFOS float data report, may 2012–may 2013,” in *Florida State university marine field group report 13-4* (Tallahassee, FL: Florida State University), 149 [https://gfdi.fsu.edu/sites/g/files/upcnu521/files/Cathrine%20Reports%20RAFOS\\_report\\_F2.pdf](https://gfdi.fsu.edu/sites/g/files/upcnu521/files/Cathrine%20Reports%20RAFOS_report_F2.pdf).
- Huh, O. K., Wiseman, W. J., and Rouse, L. J. Jr. (1981). Intrusion of loop current waters onto the West Florida continental shelf. *J. Geophys. Res.* 86 (C5), 4186–4192. doi: 10.1029/JC086C05p04186
- Jouanno, J., Ochoa, J., Pallás-Sanz, E., Sheinbaum, J., Andrade-Canto, F., Candela, J., et al. (2016). Loop current frontal eddies: Formation along the campeche bank and impact of coastally trapped waves. *J. Phys. Ocean.* 46, 3339–3363. doi: 10.1175/JPO-D-16-0052.1
- Kaski, S., Kangas, J., and Kohonen, T. (1998). Bibliography of self-organizing map (SOM) papers: 1981–1997. *Neural Comput. Surv.* 1, 102–350 [http://www.cis.hut.fi/research/som-bibl/vol1\\_4.pdf](http://www.cis.hut.fi/research/som-bibl/vol1_4.pdf).
- Kimura, T. (2009). On dormand-prince method. *Jpn. Malaysia. Tech. Instit.* 40, 1–9.
- Kohonen, T. (1982). Self-organized formation of topologically correct feature maps. *Biol. Cybernet.* 43 (1), 59–69. doi: 10.1007/BF00337288
- Kohonen, T. (1998). The self-organizing map. *Neurocomputing* 21, 1–6. doi: 10.1016/S0925-2312(98)00030-7
- Kohonen, T. (2001). *Self-organizing maps, 3rd ed* Vol. 30 (Berlin, Springer Ser). Inf. Sci.
- Kohonen, T. (2013). Essentials of the self-organizing map. *Neural Networks* 37, 52–65. doi: 10.1016/j.neunet.2012.09.018
- LaCasce, J. H. (2008). Statistics from lagrangian observations. *Prog. In. Ocean.* 77, 1–29. doi: 10.1016/j.poocean.2008.02.002
- LaCasce, J. H., and Ohlmann, C. (2003). Relative dispersion at the surface of the gulf of Mexico. *J. Mar. Res.* 61, 285–312. doi: 10.1357/002224003322201205
- Leben, R. R. (2005). “Altimeter-derived loop current metrics,” in *Circulation of the gulf of Mexico: Observations and models*, vol. 161. Eds. W. Sturges and A. Lugo-Fernandes (Washington, DC: AGU), 181–201. doi: 10.1029/161GM15
- Ledwell, J. R., He, R., Xue, Z., DiMarco, S. F., Spencer, L. J., and Chapman, P. (2016). Dispersion of tracer in the deep Gulf of Mexico. *J. Geophys. Res. Ocean.* 121, 1110–1132. doi: 10.1002/2015JC011405
- Liu, G., Bracco, A., and Passow, U. (2018). The influence of mesoscale and submesoscale circulation on sinking particles in the northern gulf of Mexico. *Elem. Sci. Anth.* 6 (36), 1–16. doi: 10.1525/elementa.292
- Liu, Y., and Weisberg, R. H. (2005). Patterns of ocean current variability on the West Florida shelf using the self-organizing map. *J. Geophys. Res.* 110, C06003. doi: 10.1029/2004JC002786
- Liu, Y., and Weisberg, R. H. (2011). “A review of self-organizing map applications in meteorology and oceanography,” in *Self-organizing maps-applications and novel algorithms design*. Ed. J. I. Mwasiagi (Rijeka, Croatia: InTech), 253–272 <http://www.intechopen.com/books/self-organizing-maps-applications-and-novel-algorithm-design/a-review-of-self-organizing-map-applications-in-meteorology-and-oceanography>.
- Liu, Y., Weisberg, R. H., and Moores, C. N. K. (2006). Performance evaluation of the self-organizing map for feature extraction. *J. Geophys. Res. Ocean.* 111 (C5), C05018. doi: 10.1029/2005JC003117
- Liu, Y., Weisberg, R. H., Vignudelli, S., and Mitchum, G. T. (2016). Patterns of loop current system and regions of sea surface height variability in the eastern gulf of Mexico revealed by the self-organizing maps. *J. Geophys. Res. Ocean.* 121, 2347–2366. doi: 10.1002/2015JC011493
- Mariano, A. J., Ryan, E. H., Huntley, H. S., Laurindo, C. C., Coelho, E., Griffa, A., et al. (2016). Statistical properties of surface velocity field in the northern gulf of Mexico sampled by GLAD drifters. *J. Geophys. Res. Ocean.* 121, 5193–5216. doi: 10.1002/2015JC011569
- Maslo, A. (2020) *Data from: Particle tracks from the regional ocean modelling system (ROMS) experiment in the Gulf of Mexico*. FSU server. Available at: <http://gfdi.fsu.edu/research/research-data>.
- Maslo, A., Souza, J. M. A. C., Andrade-Canto, F., and Outerelo, J. R. (2020). Connectivity of deep waters in the Gulf of Mexico. *J. Mar. Sys.* 203, 103267–103299. doi: 10.1016/j.jmarsys.2019.103267
- Meza-Padilla, R., Enriquez, C., Liu, Y., and Appendini, C. M. (2019). Ocean circulation in the Western Gulf of Mexico using self-organizing maps. *J. Geophys. Res.* 124 (6), 4152–4167. doi: 10.1029/2018JC014377
- Morey, S. L., Gopalakrishnan, G., Pallás Sanz, E., Correia De Souza, J. M. A., Donohue, K., Pérez-Brunius, P., et al. (2020). Assessment of numerical simulations of deep circulation and variability in the gulf of Mexico using recent observations. *J. Phys. Ocean.* 50 (4), 1045–1064. doi: 10.1175/JPO-D-19-0137.1
- Morey, S. L., Martin, P. J., O'Brien, J. J., Wallcraft, A. A., and Zavala-Hidalgo, J. (2003a). Export pathways for river discharged fresh water in the northern gulf of Mexico. *J. Geophys. Res.* 108 (C10), 3303. doi: 10.1029/2002JC001674
- Morey, S. L., Schroeder, W. W., O'Brien, J. J., and Zavala-Hidalgo, J. (2003b). The annual cycle of riverine influence in the eastern Gulf of Mexico. *Geophys. Res. Lett.* 30 (16), 1867. doi: 10.1029/2003GL017348



- Morey, S. L., Zavala-Hidalgo, J., and O'Brien, J. J. (2005). "The seasonal variability of continental shelf circulation in the northern and western Gulf of Mexico from a high-resolution numerical model," in *Circulation in the Gulf of Mexico: Observations and models*, vol. 161. Eds. W. Sturges and A. Lugo-Fernandez (Washington, DC: AGU), 203–218. doi: 10.1029/161GM16
- Nguyen, T.-T., Morey, S. L., Dukhovskoy, D. S., and Chassignet, E. P. (2015). Nonlocal impacts of the loop current on cross-slope near-bottom flow in the northeastern Gulf of Mexico. *Geophys. Res. Lett.* 42, 2926–2933. doi: 10.1002/2015GL063304
- Oey, L., and Lee, H. (2002). Deep eddy energy and topographic rossby waves in the Gulf of Mexico. *J. Phys. Ocean.* 32, 3499–3527. doi: 10.1175/1520-0485(2002)032<3499:DEEATR>2.0.CO;2
- Ohlmann, J. C., and Niiler, P. P. (2005). Circulation over the continental shelf in the northern Gulf of Mexico. *Prog. In. Ocean.* 64 (1), 45–81. doi: 10.1016/j.pocean.2005.02.001
- Ohlmann, J. C., Niiler, P. P., Fox, C. A., and Leben, R. R. (2001). Eddy energy and shelf interactions in the Gulf of Mexico. *J. Geophys. Res.* 106 (C5), 2605–2620. doi: 10.1029/1999JC000162
- Oja, M., Kaski, S., and Kohonen, T. (2003). Bibliography of self-organizing map (SOM) papers: 1998–2001 addendum. *Neural Comput. Surv.* 3, 1–156. [https://www.cis.hut.fi/research/som-bibl/NCS\\_vol3\\_1.pdf](https://www.cis.hut.fi/research/som-bibl/NCS_vol3_1.pdf)
- Pérez-Brunius, P., Furey, H., Bower, A., Hamilton, P., Candela, J., Garcia-Carrillo, P., et al. (2018). Dominant circulation patterns of the deep Gulf of Mexico. *J. Phys. Ocean.* 48, 511–529. doi: 10.1175/JPO-D-17-0140.1
- Poje, A. C., Ozgokmen, T. M., Lipphardt, B. L., Haus, B. K., Ryan, E. H., Haza, A. C., et al. (2014). Submesoscale dispersion in the vicinity of the deepwater horizon spill. *PNAS* 111 (35), 12693–12698. doi: 10.1073/pnas.1402452111
- Rossby, T., Dorson, D., and Fontaine, J. (1986). The RAFOS system. *J. Atmos. Ocean. Technol.* 3, 672–679. doi: 10.1175/1520-0426(1986)003<0672:TRS>2.0.CO;2
- Sallee, J. B., Speer, K., Morrow, R., and Lumpkin, R. (2008). An estimate of Lagrangian eddy statistics and diffusion in the mixed layer of the southern ocean. *J. Mar. Res.* 66, 441–463. doi: 10.1357/002224008787157458
- Schiller, R. V., Kourafalou, V. H., Hogan, P., and Walker, N. D. (2011). The dynamics of the Mississippi river plume: Impact of topography, wind and offshore forcing on the fate of plume waters. *J. Geophys. Res.* 116 (C06029), 1–22. doi: 10.1029/2010JC006883
- Shapiro, G. I., Barton, E. D., and Meschanov, S. L. (1997). Capture and release of Lagrangian floats by eddies in shear flow. *J. Geophys. Res. Ocean.* 102 (C13), 27887–27902. doi: 10.1029/97JC02386
- Shchepetkin, A. F., and McWilliams, J. C. (2005). The regional oceanic modeling system (ROMS): a split-explicit, free-surface, topography-following-coordinate oceanic model. *Ocean. Model.* 9 (4), 347–404. doi: 10.1016/j.ocemod.2004.08.002
- Shchepetkin, A. F., and McWilliams, J. C. (2009). Correction and commentary for ocean forecasting in terrain-following coordinates: Formulation and skill assessment of the regional ocean modeling system by haidvogel et al., *J. comp. phys.* 227, 35953624. *J. of. Comp. Phy.* 228 (24), 8985–9000. doi: 10.1016/j.jcp.2009.09.002
- Sikiric, M. D., Janekovic, I., and Kuzmic, M. (2009). A new approach to bathymetry smoothing in sigma-coordinate ocean models. *Ocean. Modell.* 29, 128–136. doi: 10.1016/j.ocemod.2009.03.009
- Speer, K. (2013). Data from: RAFOS float data collected as part of the Gulf of Mexico Research Initiative (GoMIR): Dispersion Experiment in the De Soto Canyon Region, Gulf of Mexico, by the Marine Field Group (MFG), Florida State University (FSU). Deep-C Data Center. (2013). <https://deep-c.coaps.fsu.edu/data/tabular/drifters>.
- Teague, W. J., Jarosz, E., Carnes, M. R., Mitchell, D. A., and Hogan, P. J. (2006). Low-frequency current variability observed at the shelfbreak in the northeastern gulf of Mexico: May–october. *Cont. Shelf. Res.* 26 (20), 2559–2582. doi: 10.1016/j.csr.2006.08.002
- Vesanto, J., Himberg, J., Alhoniemi, E., and Parhankangas, J. (2000). *SOM toolbox for Matlab 5, report* (Finland: Helsinki Univ. of Technol.).
- Vilibic, I., Mihanovic, H., Kuspilic, G., Ivcevic, A., and Milun, V. (2015). Mapping of oceanographic properties along a middle Adriatic transect using self-organizing maps. *Estuar. Coast. Shelf. Sci.* 163, 84–92. doi: 10.1016/j.ecss.2015.05.046
- Vukovich, F. M., and Maul, G. A. (1985). Cyclonic eddies in the Eastern gulf of Mexico. *J. Phys. Ocean.* 15, 105–117. doi: 10.1175/1520-0485(1985)015<0105:CEITEG>2.0.CO;2
- Wang, D.-P., Oey, L.-Y., Ezer, T., and Hamilton, P. (2003). Near-surface currents in de soto canyon, (1997–1999): Comparison of current meters, satellite observations, and model simulation. *J. Phys. Ocean.* 33, 313–326. doi: 10.1175/1520-0485(2003)033<0313:NSCIDC>2.0.CO;2
- Weisberg, R. H., He, R., Liu, Y., and Virmani, J. I. (2005). "West Florida shelf circulation on synoptic, seasonal and interannual time scales," in *Circulation in the Gulf of Mexico: Observations and models*, vol. 161. Eds. W. Sturges and A. Lugo Fernandez (Washington, DC: AGU), 325–347. doi: 10.1029/161GM23
- Weisberg, R. H., Zheng, L. L., and Kiu, Y. Y. (2011). "Tracking subsurface oil in the aftermath of the deepwater horizon well blowout," in *Monitoring and modeling the deepwater horizon oil spill: A record-breaking enterprise*. Eds. Y. Liu, A. Macfadyen, Z.-G. Ji and R. H. Weisberg (Washington, DC: AGU), 205–215. doi: 10.1029/2011GM001131
- Zhong, Y., and Bracco, A. (2013). Submesoscale impacts on horizontal and vertical transport in the Gulf of Mexico. *J. Geophys. Res. Oceans.* 118, 5651–5668. doi: 10.1002/jgrc.20402





## OPEN ACCESS

## EDITED BY

Ruoying He,  
North Carolina State University,  
United States

## REVIEWED BY

Wei Huang,  
Oak Ridge National Laboratory (DOE),  
United States  
Yonggang Liu,  
University of South Florida,  
United States  
Xavier Carton,  
Université de Bretagne Occidentale,  
France

## \*CORRESPONDENCE

Yingli Zhu  
✉ zhuyingliouc@gmail.com

## SPECIALTY SECTION

This article was submitted to  
Physical Oceanography,  
a section of the journal  
Frontiers in Marine Science

RECEIVED 01 November 2022

ACCEPTED 05 December 2022

PUBLISHED 15 December 2022

## CITATION

Zhu Y and Liang X (2022)  
Characteristics of Eulerian mesoscale  
eddies in the Gulf of Mexico.  
*Front. Mar. Sci.* 9:1087060.  
doi: 10.3389/fmars.2022.1087060

## COPYRIGHT

© 2022 Zhu and Liang. This is an open-access article distributed under the terms of the [Creative Commons Attribution License \(CC BY\)](https://creativecommons.org/licenses/by/4.0/). The use, distribution or reproduction in other forums is permitted, provided the original author(s) and the copyright owner(s) are credited and that the original publication in this journal is cited, in accordance with accepted academic practice. No use, distribution or reproduction is permitted which does not comply with these terms.

# Characteristics of Eulerian mesoscale eddies in the Gulf of Mexico

Yingli Zhu\* and Xinfeng Liang

School of Marine Science and Policy, University of Delaware, Lewes, DE, United States

Although numerous studies on Eulerian mesoscale eddies with closed contours of sea surface height (SSH) or streamline have been conducted in the Gulf of Mexico (GoM), a comprehensive study on their temporal and spatial characteristics is still lacking. In this study, we combine three eddy detection algorithms to detect Eulerian eddies from the 26-year SSH record in the GoM and examine their characteristics. We find distinct characteristics between Loop Current Eddies (LCEs), Loop Current Frontal Eddies (LCFEs), and mesoscale eddies that are not directly related to the Loop Current (LC). Many characteristics of LCEs and LCFEs in the eastern GoM are closely related to the LC. More LCFEs are formed in January to July than in August to December, likely related to the seasonal variation of the northward penetration of the LC. However, the formation of non-LCFE cyclonic eddies shows a biannual variability, which could be linked to the position and strength of the background current in the western GoM. Nevertheless, the seasonal variability of the Eulerian eddies shows large uncertainties (not significant at the 95% confidence level). Low-frequency (interannual to multidecadal) variability is also detected. In the eastern GoM, the extent of northward penetration of the LC can affect the generation of LCFEs and result in low-frequency variations. In the western GoM, the low-frequency variability of eddy occurrence and amplitude could be related to the surface circulation strength.

## KEYWORDS

Gulf of Mexico, loop current, mesoscale eddies, eddy characteristics, background currents

## 1 Introduction

Mesoscale eddies, which are usually demonstrated as closed contours of sea surface height (SSH) or streamline, are ubiquitous in the Gulf of Mexico (GoM). Different types of eddies have been identified, such as anticyclonic Loop Current Eddies (LCEs), cyclonic Loop Current Frontal Eddies (LCFEs), and eddies that are not directly related to the Loop Current (LC). Those eddies with closed contours of SSH and streamline are usually called Eulerian eddies. These eddies are important for explaining surface mesoscale anomalies

of temperature and salinity (e.g., Meunier et al., 2018; Brokaw et al., 2019), and can potentially affect the bottom currents in the GoM (e.g., Zhu and Liang, 2020). For example, the bottom currents are closely related to the upper-layer mesoscale eddies in the GoM (e.g., Tenreiro et al., 2018; Zhu and Liang, 2020). Besides, those eddies can modify the atmospheric environment. In particular, hurricanes in the GoM can be intensified when encountering warm-core rings by absorbing a large amount of heat from eddies (e.g., Bosart et al., 2000; Hong et al., 2000). Therefore, it is useful to examine the characteristics of the mesoscale eddies in the GoM.

Various measurements, including drifters, gliders, mooring, and satellite data, have been used to characterize eddies in the GoM (e.g., Elliott, 1982; Paluszkiwicz et al., 1983; Kirwan et al., 1984; Vukovich and Maul, 1985; Lewis et al., 1989; Hamilton, 1992; Hamilton et al., 1999; Hamilton, 2007; Rivas et al., 2008; Rudnick et al., 2015; Meunier et al., 2018; Zhang et al., 2019). Some eddy characteristics, such as diameter and propagation speed, have been reported in previous studies. In the eastern GoM, where the LC is the dominant circulation feature, LCEs with a warm and salty core are shed irregularly from the LC through dynamic instability (e.g., Hurlburt and Thompson, 1980; Pichevin and Nof, 1997; Sturges and Leben, 2000; Liu et al., 2016; Yang et al., 2020). The shedding time of LCEs has been shown to be related to the seasonal winds in the GoM and the Caribbean Sea (Chang and Oey, 2012) and fluctuations from the Caribbean Sea (Murphy et al., 1999; Oey et al., 2003; Chang and Oey, 2012; Chang and Oey, 2013). LCEs have a diameter of 200 to 400 km, a surface swirling speed exceeding  $0.5 \text{ m s}^{-1}$ , and an average propagating speed of 2 to 5  $\text{km day}^{-1}$  (e.g., Elliott, 1982; Kirwan et al., 1984; Vukovich and Crissman, 1986; Kirwan et al., 1988). The LCE path occupies a broad band in the center of the basin with a mean west-southwest track (Hamilton et al., 1999; Meza-Padilla et al., 2019). When LCEs travel to the western GoM and encounter the western boundary, companion cyclones can be generated (Smith and David, 1986; Vidal et al., 1992; Frolov et al., 2004).

In addition to LCEs, mesoscale cyclonic eddies (CEs) with relatively small diameters of 80 to 150 km have also been detected in the GoM (Vukovich and Maul, 1985; Hamilton, 1992; Vukovich, 2007; Le Hénaff et al., 2014; Jouanno et al., 2016). The commonly seen CEs in the eastern GoM are cold-core LCFEs that are formed on the LC's periphery as a result of the barotropic and baroclinic instabilities (e.g., Vukovich and Maul, 1985; Fratantoni et al., 1998; Zavala-Hidalgo et al., 2003; Chérubin et al., 2006; Donohue et al., 2016a; Jouanno et al., 2016; Maslo et al., 2020; Yang et al., 2020). The topographic vortex stretching can play a role in the intensification of LCFEs (Le Hénaff et al., 2012; Le Hénaff et al., 2014). Also, eddies with a median radius of 30 km have been observed on the northern GoM slope from drifter orbits and hydrographic surveys (e.g., Hamilton, 2007). The small-scale slope eddy activity was

speculated to be related to the LC extension and LCE detachment (Nickerson et al., 2022). Some eddies on the northern GoM slope that are not likely related to the LC have also been observed (Hamilton, 1992; Hamilton et al., 2002). Besides, Caribbean eddies can squeeze into the GoM through the Yucatan Channel (Murphy et al., 1999; Huang et al., 2013; Huang et al., 2021), but the eddy number is relatively small. Nevertheless, most previous studies only focus on the LCEs and LCFEs, while characteristics of other types of mesoscale eddies in the GoM have not been comprehensively described.

Although some temporal and spatial distributions of eddy characteristics have been obtained from the absolute dynamic topography (ADT) maps or along-track SSH anomalies, they are based on short-period altimeter data with record lengths of 2 to 4 years (Leben and Born, 1993; Brokaw et al., 2020) or are focused on one specific type of eddy, such as the LCE (e.g., Leben, 2005; Hall and Leben, 2016) or LCFE (Le Hénaff et al., 2014). For example, by tracking SSH contour (17 cm) and its breaking from the LC in the GoM, LCE separations have been determined over the first 12-year (Leben, 2005) and 20-year altimetry period (Hall and Leben, 2016). A significant peak in the timing of LCE separation in August and September and a less significant peak in February and March have been observed (Vukovich, 2012; Hall and Leben, 2016). An increasing number of LCEs in the decade 2001–2010 was also found (Vukovich, 2012; Lindo-Atichati et al., 2013). The previous studies indicate that the mesoscale eddies vary with season and over long time scale. The seasonal and interannual variabilities of mesoscale eddies are important and closely related to that of the large-scale circulation, from which eddies obtain energy (e.g., Yang et al., 2020). As the dominant circulation system in the eastern GoM, the LC has been shown to be more intrusive from January to July on the seasonal time scale (Hamilton et al., 2014) and from 2002 to 2006 than in 1993 on the interannual time scale (Alvera-Azcárate et al., 2009). The climate variability in the GoM has been related to remote climate forcing such as El Niño–Southern Oscillation (ENSO) and North Atlantic Oscillation (NAO) (e.g., Rodríguez-Vera et al., 2019). Therefore, the eddy activity in the GoM could be affected by various climate modes, such as ENSO (e.g., Philander, 1990), NAO (e.g., Wallace and Gutzler, 1981), and Atlantic Meridional Mode (AMM) (e.g., Chiang and Vimont, 2004). However, characteristics of different types of eddies in the GoM, such as propagation, seasonal, and low-frequency (interannual to multidecadal) variability, are not clear and need more examination. Nowadays, with the satellite observed SSH data that span almost 30 years, we can conduct a more comprehensive analysis of the characteristics of mesoscale eddies in the GoM.

It should be noted that two distinct definitions of mesoscale eddies exist, reflecting the nature of mesoscale features presented in different studies. The mesoscale eddies detected with the Eulerian methods are mostly defined as mesoscale features

with closely SSH or streamline. SSH provides geostrophic streamlines. These methods have been widely used and greatly advanced our understanding of the dynamics and impacts of mesoscale eddies over the past few decades. However, the Eulerian eddies may not have material coherent structure, depend on the frames and the observer (e.g., Haller, 2005; Peacock et al., 2015) and can change form and exchange material with ambient fluid. In contrast, Lagrangian eddies or Lagrangian coherent vortex (e.g., Haller, 2005; Andrade-Canto et al., 2020) have material boundaries that withstand stretching or diffusion. They are therefore important for tracking the transport of ocean materials (Bello-Fuentes et al., 2021; Andrade-Canto and Beron-Vera, 2022; Andrade-Canto et al., 2022). In this study, we focused on the mesoscale features with closed SSH or streamlines that can be detected with Eulerian methods. These eddies can be considered as propagating signals/perturbation even though the material and vortex are not necessarily conserved during the eddy propagating. We specifically named the mesoscale eddies presented in this study Eulerian eddies.

To detect and describe Eulerian eddies, a variety of automatic Eulerian eddy detection and tracking algorithms have been developed. Chelton et al. (2007) used the physical Okubo-Weiss (OW) parameter (Okubo, 1970; Weiss, 1991) to detect mesoscale eddies. Geometric properties, such as the closed SSH or streamline contours, have also been used to define eddy domains (e.g., Chaigneau et al., 2008; Chelton et al., 2011; Faghmous et al., 2015; Le Vu et al., 2018). Moreover, hybrid methods that combine the physical parameters and geometric properties have been proposed to discern mesoscale eddies (Kang and Curchitser, 2013; Halo et al., 2014). The 17-cm SSH contour has also been widely used to define the LC front, and separation events of LCE are identified by breaking of the 17-cm tracking contour with no later reattachment (Leben, 2005; Hall and Leben, 2016). Different eddy detection algorithms have their advantages and drawbacks. For example, the OW method is sensitive to the noise in the SSH data, and the approaches that use geometrical properties are sensitive to the interval searching for closed contours (Le Vu et al., 2018; Lian et al., 2019).

In this study, to find Eulerian eddies that are less sensitive to the Eulerian eddy detection algorithms, a method that combines three previously used Eulerian eddy detection algorithms is developed and applied to the 26-year SSH maps in the GoM. Characteristics of Eulerian mesoscale eddies in the GoM are derived by examining the eddies detected with the new method. The paper is organized as follows: data and details of the eddy detection and tracking algorithms are presented in section 2. Characteristics of the detected eddies, including basic eddy characteristics, seasonal and low-frequency variabilities of eddies are reported in section 3. Conclusions and discussions are given in section 4.

## 2 Data and methods

### 2.1 Data

Statistical and comprehensive analyses of eddies over the whole GoM using *in situ* data and satellite infrared or ocean color data are difficult (e.g., Vukovich, 2007). *In situ* data cannot give continuous monitoring over the whole GoM. The nearly uniform sea surface temperature (SST) in summer and the extensive cloud cover hinder us from discerning eddies from the satellite infrared or ocean color maps (e.g., Vukovich and Maul, 1985; Sturges and Leben, 2000). In contrast, altimeter observed SSH data are available in all weather conditions and are the most complete source of detecting mesoscale eddies (e.g., Liu et al., 2011). Altimetry products were used to characterize the spatial patterns of the LC system variation in the GoM based on a machine learning method (e.g., Liu et al., 2016; Weisberg et al., 2017; Nickerson et al., 2022), but due to the limited number of the characteristic patterns chosen, the mesoscale eddies were not fully represented. Delayed time 2018 (DT2018) gridded ADT data (Taburet et al., 2019) from two altimeter satellites (twosat product) provided by the Copernicus Climate Change Service (C3S) were used for eddy detection and the subsequent examination of eddy characteristics. DT2018 gridded ADT data from multiple satellites (allsat product) provided by the Copernicus Marine Environment Monitoring Service (CMEMS) were also used for the discussion of the influence of satellite sampling on eddy detection. The ADT data span from 1 January 1993 to 13 May 2019 with a daily time interval. ADT data rather than sea level anomalies (SLAs) were selected because artificial eddies could be identified in SLAs (e.g., Laxenaire et al., 2018; Pegliasco et al., 2021). Note that although the spatial resolution of the ADT provided is 0.25 degrees, its effective spatial resolution is controlled by many factors, such as the along-track smoothing and the spatial correlation scale (Pujol et al., 2016). Satellite altimetry products were demonstrated to slightly outperform the numerical models in the GoM (Liu et al., 2014).

To examine the effective spatial resolution of the gridded ADT product in the GoM, TOPEX/Poseidon (T/P) along-track ADT data from 2 January 1996 to 3 December 1999 were compared with the twosat gridded ADT data (Figure 1). Gridded ADT data were first linearly interpolated to the ground tracks shown in Figure 1A. The wavenumber spectra of the along-track and interpolated ADT data along one sample T/P track were then calculated and averaged over the selected T/P period (Figure 1B). Compared to the along-track ADT, the spectrum of the gridded ADT decreases by 50% at the wavelength of 200 km, which represents the effective spatial resolution of the gridded ADT data in the GoM. This finding is consistent with the spatial correlation scales used in the gridded product processing (Pujol et al., 2016) and corresponds to an e-folding scale of about 37 km for an individual eddy (Chelton

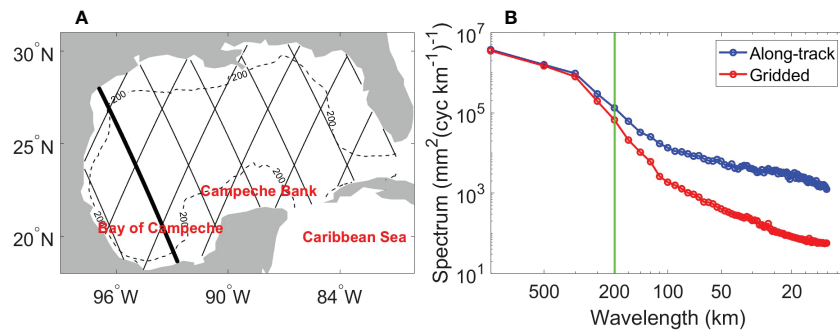


FIGURE 1

(A) Ground tracks of the TOPEX/Poseidon satellite in the GoM. The thick black line represents the track along which the wavenumber spectrum of ADT was estimated. The dashed black line represents the 200-m isobath. (B) Wavenumber spectrum of along-track and gridded ADT along the track marked by the thick black line in (A). The vertical green line marks the wavelength of 200 km.

et al., 2011). The interpretation of filter cutoff wavelength in terms of the corresponding eddy scale is based on eddy shape that is approximated as an axially symmetric Gaussian structures (Chelton et al., 2011). Chelton et al. (2011) showed that a half-power point at a wavelength of  $2^\circ$  corresponds to a Gaussian feature in space with an e-folding scale of  $0.37^\circ$ . Therefore, the gridded ADT product in the GoM can only resolve eddies with a radius larger than 37 km, and eddies with a radius smaller than 37 km are not considered in this study. The gridded products cannot capture the small-scale eddies (Amores et al., 2018). It should be noted that eddies that lie in the “diamond-shaped” area between the satellite tracks cannot be fully resolved. The eddy amplitude could be underestimated due to the smoothing during the data generation process. We focus on the spatial and temporal variability when we examine the eddy amplitude.

ADT data were further processed before they were used to detect eddies. First, since altimetry observations near the coast are less reliable and more than 30% of along-track data are not available for the mapping of the gridded product at locations less than 30 km away from the coast (Saraceno et al., 2008; Castelao and He, 2013), ADT data at grid points that are 30 km or less away from the coast were discarded. However, it should be noted that the quality of altimetry data gets worse in shallower water (Liu et al., 2012). Second, to make eddy features stand out from the large-scale background SSH field, a two-dimensional spatial filter with a cut-off wavelength of 1000 km was applied to the gridded ADT data. The spatial filtering removes the large-scale variability of SSH that is dominated by the seasonal steric height, which is similar to removing the daily spatial average ADT over the deep-water GoM. Third, because the LC has a shape of a loop, which is different from isolated mesoscale eddies but might be recognized as eddy by the eddy detection algorithms, the LC was isolated so that no eddy was considered within the LC. Leben (2005) used the 17-cm contour of ADT to define the LC front. As the mean reference SSH field in this study was different

from that used in Leben (2005), we used the 25-cm contour of the SSH anomalies to define the LC front. Because we would like to eliminate the spatially uniform variability of SSH in the GoM, the SSH anomalies with the spatially mean SSH removed were used to find the LC front. The northern boundary of the LC obtained using the 25-cm contour of SSH anomalies shows similar variability as that reported in Leben (2005). Eulerian eddy detection and tracking algorithms were then applied to the high-passed ADT fields.

Other variables were also explored to explain some of the detected eddy characteristics. The global atlas of the first-mode Rossby radius of deformation (Chelton et al., 1998) was used to calculate the standard first-mode Rossby wave propagation velocity,  $c = -\beta R^2$ , where  $\beta$  is the meridional variation of the Coriolis parameter and  $R$  is the first-mode Rossby radius of deformation. Moreover, the multivariate ENSO index (MEI V2) (Zhang et al., 2019), NAO index (Hurrell, 1995), and AMM index (Chiang & Vimont, 2004) were used to examine possible relationships between the eddy activity in the GoM and climate modes.

## 2.2 Eddy detection and tracking algorithms

An approach that combines three Eulerian eddy detection algorithms proposed by Faghmous et al. (2015); Le Vu et al. (2018), and Halo et al. (2014) was developed to detect Eulerian mesoscale eddies in the GoM. The three algorithms represent different approaches of automatic eddy detection and hereafter are referred to as F15, L18, and H14, respectively. In the F15 algorithm, eddies are defined as features of closed-contour SSH with one extremum of SSH. The eddy center is at the location with extremum SSH. The H14 algorithm combines the OW parameter and geometrical properties of SSH. It identifies eddy



as contained within a close loop of SSH and dominated by vorticity with the negative OW parameter. The eddy center is the mean position of the identified eddy. The L18 algorithm is a hybrid method based on physical parameters and geometrical properties of the velocity field. The eddy is contained within closed streamlines around an eddy center with a local maximum normalized angular momentum. The differences between the three eddy detection algorithms are that closed SSH contours are used in F15 and H14, while closed streamlines are used in L18. The eddy center is defined differently in the three algorithms and is associated with the SSH extremum location, mean position of eddy, and the local maximum normalized angular momentum in F15, H14, and L18, respectively.

Due to the limited resolution of the gridded ADT field, a minimum of 9 pixels was used in the F15 algorithm and a minimum eddy radius of 37 km was used in the other two algorithms. The threshold value of nine pixels was selected in the F15 algorithm because it corresponds to a square area that is occupied by the smallest eddy with a radius of 37 km. Also, a minimum eddy amplitude of 2 cm was applied due to the accuracy of the SSH product (Pujol et al., 2016). The three eddy detection algorithms were implemented to the high-passed ADT field, yielding daily mesoscale eddies. An example of the detected eddies on 20 March 1995, as marked by the black circles in Figures 2A–C, shows that some eddies can be detected by one algorithm but cannot be detected by the others. The three algorithms, F15, L18, and H14, gave rise to a total of 67016, 65852, and 55309 anticyclonic eddies (AEs), and a total of 93054,

93118, and 86077 CEs in the GoM over the examined period, respectively. The daily mean area occupied by AEs in F15, L18, and H14 is  $1.91\text{e}5\text{ km}^2$ ,  $2.42\text{e}5\text{ km}^2$  and  $9.57\text{e}4\text{ km}^2$ , respectively; while the daily mean area occupied by CEs in F15, L18, and H14 is  $2.1\text{e}5\text{ km}^2$ ,  $2.45\text{e}5\text{ km}^2$ , and  $1.14\text{e}5\text{ km}^2$ , respectively. The H14 algorithm yields the smallest eddy size and the least eddy number, suggesting the H14 algorithm is more restrictive than the other two algorithms. Moreover, to examine the influence of the spatial filtering that removes the large-scale variability of SSH on eddy detection, we run the eddy detection algorithms on the unfiltered ADT field and compare the eddy numbers with those from the filtered ADT field. A total of 139867, 148309 and 125886 eddies are found in F15, L18, and H14, respectively, which are less than 158970, 160070 and 141386 eddies when the filtered ADT field is used (Eddy number and area are listed in Table S1 in the supplementary material). The differences of eddy numbers obtained from the filtered and unfiltered ADT fields are from 7% to 12% of the total eddy number. Therefore, the spatial filtering can make eddy features stand out from the large-scale background ADT field.

We focus on the Eulerian mesoscale eddies that can be detected by at least two algorithms. Eddies from the most recently developed L18 algorithm were used as basis eddies. For each basis eddy, if common eddy pixels were found in H14 or F15, the eddy was considered and kept for further processing. There are 10% of AEs and 7% of CEs detected by L18 that were removed based on the comparison of outputs of the three algorithms. Mesoscale eddies are selected in this way so that

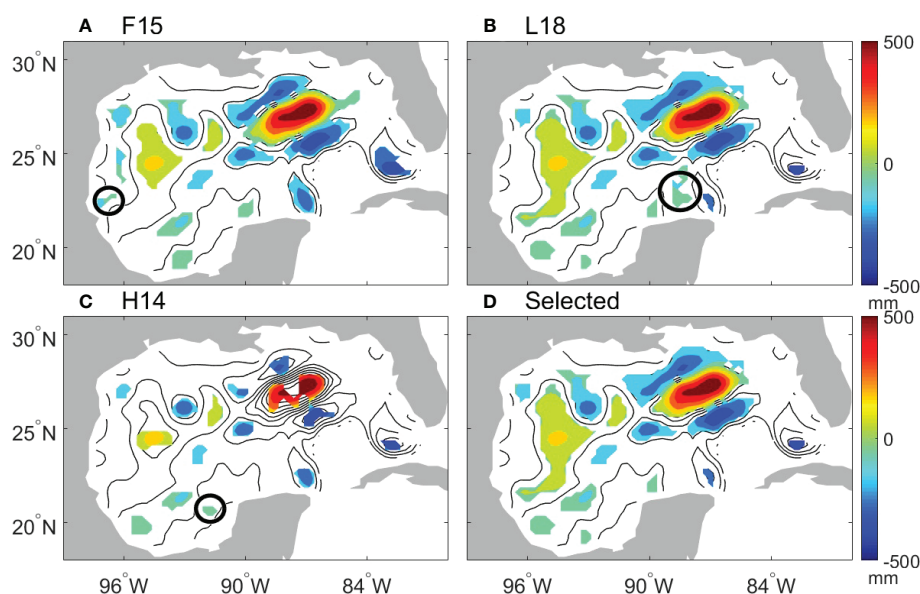


**FIGURE 2**  
Snapshots of the high-passed ADT (contours) and detected eddies (color shading) on 20 March 1995. Eddies were detected by (A) F15 algorithm, (B) L18 algorithm, (C) H14 algorithm, and (D) eddies were selected by a combination of the three algorithms. The black circle in (A–C) encloses the eddy that was detected by one algorithm but not detected by the other two algorithms.

we have more confidence in the detected eddies than that given by one algorithm, but they are less restrictive than those given by the H14 method. [Figures 2A–C](#) show an example of eddies on 20 March 1995 detected by F15 algorithm, L18 algorithm and H14 algorithm, respectively. The black circles in [Figures 2A–C](#) enclose the eddy that was detected by one algorithm but not detected by the other two algorithms. An example of selected eddies on 20 March 1995 is shown in [Figure 2D](#), and the selected eddies are those that were detected by at least two algorithms.

The resulting eddies were then tracked with an algorithm that was also used in [Le Vu et al. \(2018\)](#). First, each detected eddy  $e_i$  at the last time step  $t$  is associated with the closest eddy  $e_j$  of the same sign detected at the previous time step  $t-dt$  in a given search area. The maximum search distance  $D_{ij}$  is then given by  $D_{ij} = C(1 + dt)/2 + \langle R_{max} \rangle(j) + R_{max}(i)$ , where  $\langle R_{max} \rangle(j)$  is the mean speed-based radius of  $e_j$  averaged during the five preceding steps of its track, while  $R_{max}(i)$  is the speed-based radius of  $e_i(t)$  that corresponds to the eddy radius with maximum mean azimuthal velocity. The speed parameter  $C$  is a constant value of 6.5 km/day that is one typical upper bound of eddy propagation speed used in the maximum search distance  $D_{ij}$  ([Le Vu et al., 2018](#)). When no eddies are found in the search area,  $e_i(t)$  is identified as a new eddy. When several eddies are found in the search area,  $e_i$  will be associated with  $e_j$ , which minimizes one cost function:

$$\epsilon_{ij} = \sqrt{\left[ \frac{d_{ij}}{D_{ij}(T_c)} \right]^2 + \left[ \frac{\Delta R}{\langle R \rangle(j) + R(i)} \right]^2 + \left[ \frac{\Delta Ro}{\langle Ro \rangle(j) + Ro(i)} \right]^2 + \left( \frac{dt}{2T_c} \right)^2}$$

where  $d_{ij}$  is the distance between  $e_i$  and  $e_j$ ;  $D_{ij}(T_c)$  is the distance  $D_{ij}$  at the correlation time ( $T_c=10$  days);  $\Delta R$  and  $\Delta Ro$  are the radius and the Rossby number difference between  $e_i$  and  $e_j$ , respectively;  $\langle R \rangle(j)$  and  $\langle Ro \rangle(j)$  are the mean radius and the mean Rossby number of the eddy  $e_j$  averaged during the five preceding steps, respectively; the eddy radius is defined as the radius of the circle equivalent to the eddy area. The dimensionless cost function is used to compare physical similarity between eddy pairs. The terms under the root square represent the relative distance between eddy centers, the relative difference between eddy radius, the relative difference between the intensity characterized by Rossby number and the relative difference of temporal separation, respectively. Eddy merging and splitting due to eddy-eddy interactions are considered in this tracking algorithm. Because the temporal correlation scales of gridded ADT data are about 30 days at latitudes of the GoM ([Pujol et al., 2016](#)), only eddies with a lifetime greater than 30 days are examined in this study. Although there are eddies with lifetime shorter than 30 days, the gridded SSH data are not independent on timescales shorter than 30 days and are not sufficient to detect the short-lived eddies.

AEs were further grouped into LCEs and non-LCE AEs. LCEs are AEs that were generated east of 92°W, were dead west of 90°

W, translated westward for more than 2 degrees, and had eddy amplitude at the birth time larger than 0.12 m and have a lifespan of more than 60 days. The eddy amplitude was defined as the difference between the SSH on the contour of maximum rotation speed and maximum or minimum SSH in the eddy. Because the LC may experience detachment and reattachment during the formation of LCE, the identified LCE may lose tracking and new eddies were identified. Therefore, AEs that were formed east of 92°W with amplitude larger than 0.2 m and with the distance between eddy center and the LC front being less than 250 km were considered as LCEs as well. The threshold values used in the definition of LCEs were chosen by comparing detected AEs with the SSH maps that show separations of LCEs from the LC. A total of 51 LCE trajectories were found. Among the 35 LCEs with industry names, separation dates of 28 LCEs are less than 1 month different from those reported by [Hall and Leben \(2016\)](#). There are 376 non-LCE AE trajectories. CEs were further grouped into LCFEs and non-LCFE CEs. Based on the CE trajectories, LCFEs are CEs that have the distance between the eddy center and the LC front be less than 200 km in the first 20 days after the generation. LCFEs defined in this way propagate along the LC front during their lifetimes. Non-LCFEs are CEs that are not identified as LCFEs. There are 297 LCFE trajectories and 447 non-LCFE CE trajectories (Number of eddy trajectory is listed in [Table S2](#) in the supplementary material).

## 3 Results

### 3.1 Eddy frequency and propagation

[Figure 3](#) shows the percentages of months when eddy birth, death, and presence were observed over the observation period. The months of eddy birth and death were the times when eddies were first and last detected, respectively. LCEs were mostly generated in the northwestern tip of the LC ([Figure 3A](#)), were mostly dissipated in the western GoM, and some of them could reach the western boundary of the GoM ([Figure 3B](#)). They traveled from the east to the southwest in a broad meridional band, consistent with the broad paths of LCEs revealed in previous studies (e.g., [Vukovich and Crissman, 1986](#); [Hamilton et al., 1999](#); [Vukovich, 2007](#)). Therefore, it is more frequent to observe LCEs in the band from the east to the southwest ([Figure 3C](#)).

LCFEs were mostly generated east of Campeche Bank, in the northern and eastern LC ([Figure 3D](#)), and they were more likely to dissipate in the eastern LC ([Figure 3E](#)). LCFEs traveled mainly in the eastern GoM because they were closely tied to the LC. LCFEs generated around the Campeche Bank did not travel or lost tracks along the western part of the LC. In the eastern part of the LC, LCFEs traveled along the southward flowing LC. These are consistent with the previous conclusion that LCFE motions along the northern and eastern LC were decoupled from the



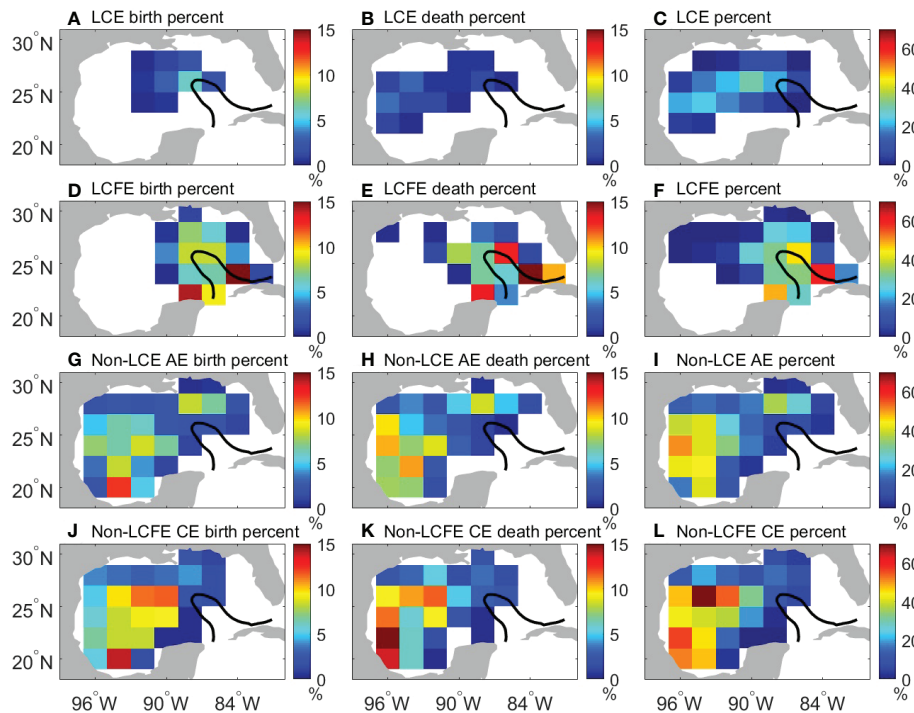


FIGURE 3

(A, D, G, J) The percentage of months when eddy birth was observed from January 1993 to April 2019. (B, E, H, K) The percentage of months when eddy death was observed. (C, F, I, L) The percentage of months when the presence of eddy was observed. LCEs, LCFEs, non-LCE AEs, non-LCFE CEs are shown in (A–C), (D–F), (G–I), and (J–L), respectively. The black line represents the 25-cm contour of temporal mean SSH anomalies from 1993 to 2019.

LCFE motions along the southwestern LC (Walker et al., 2009; Donohue et al., 2016a; Donohue et al., 2016b; Hamilton et al., 2016). LCFEs were most frequently found east of Campeche Bank and in the eastern LC (Figure 3F). A large fraction of LCFEs has been reported on the eastern flank of the Campeche Bank (Zavala-Hidalgo et al., 2003; Le Hénaff et al., 2014; Jouanno et al., 2016).

In contrast to the LCEs and LCFEs that were directly related to the instability of the LC in the eastern GoM, non-LCE AEs and non-LCFE CEs were mostly generated in the western GoM, especially in the central-western GoM and in the Bay of Campeche (Figures 3G, J). They were prone to dissipate along the western boundary of the GoM (Figures 3H, K). The non-LCE AEs and non-LCFE CEs are mostly in the western GoM and do not affect the eastern GoM. The presence frequencies of these eddies are also the highest west of 92°W (Figures 3I, L).

Although dynamic instabilities of large-scale currents have been reported to be important for the aforementioned spatial pattern of eddy generation (e.g., Sturges and Leben, 2000; Zavala-Hidalgo et al., 2003; Chérubin et al., 2006; Donohue et al., 2016a; Jouanno et al., 2016; Maslo et al., 2020; Yang et al., 2020), the eddy-topography interaction and eddy-eddy interaction could play a role in generating new eddies (Smith

and David, 1986; Vidal et al., 1992; Biggs et al., 1996; Frolov et al., 2004). The eddy-eddy interaction including eddy splitting and merging was also considered in this study following Le Vu et al. (2018). When a characteristic shared contour encloses two eddy centers and the mean velocity along the shared contour reaches a maximum value larger than the maximum velocity of at least one eddy, the two eddies inside the shared contour experience eddy interaction. If such a characteristic shared contour is detected and there is only one trajectory before the eddy interaction period, a splitting event is considered. New eddies due to splitting accounts for 15.4% of the total generated eddies. Only 2 LCEs and 16 LCFEs were generated by splitting. However, 80 non-LCE AEs and 82 non-LCFE CEs were generated by splitting and account for 7% of the total generated eddies, respectively. Most non-LCE AEs and non-LCFE CEs due to eddy splitting were scattered in the western GoM (Figure 4A). In addition to eddy splitting, LCEs could induce eddies along their periphery during the traveling period because of the relatively large current shear around LCEs or when they encounter the western boundary of the GoM. Figure 4B shows the center locations of eddies that were generated along LCE periphery. There are 14 non-LCE AEs and 118 non-LCFE CEs (10% of the total generated eddies) that

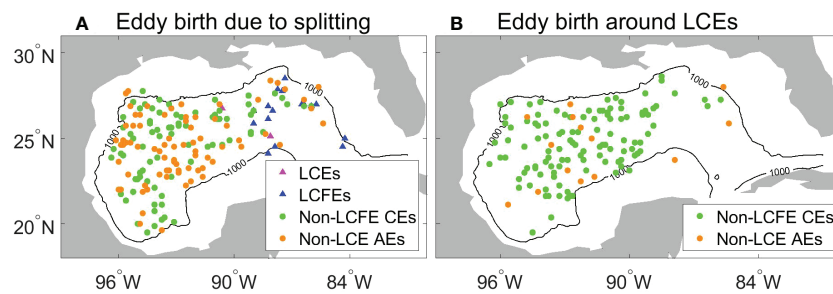


FIGURE 4

(A) Locations of generated eddies due to splitting. (B) Locations of generated eddies within LCE radius plus 100 km.

are likely related to LCEs, showing no particular pattern. Only a small number of CEs were generated along the western boundary of GoM as LCEs arrived there, suggesting that the interaction between LCEs and topography plays a relatively small role in creating new eddies. The dominance of CEs that are possibly induced by LCEs is consistent with the fact that the current shear along LCE periphery is mainly cyclonic.

Moreover, eddy propagation velocities were estimated by least-squares fitting the positions of eddy centers as a function of time in overlapping 30-day segments of each eddy's trajectory. Figure 5 shows the mean eddy propagation speeds and directions. Mean eddy propagating speeds are highly variable in the GoM. Specifically, LCEs have large traveling speeds in the

central-western GoM that can be as large as 5 km/day (Figure 5A). The mean propagating direction of LCEs is southwestward in the central GoM and bifurcates north and south when LCEs encounter the western boundary of GoM. LCFEs propagate along the LC front and large propagation speeds are found in the eastern part of the LC (Figure 5B) that are related to the advection of the LC. Non-LCE AEs and non-LCFE CEs have large propagation speeds in the southwest of the GoM and the dominant propagation direction of the two types of eddies is to the west (Figures 5C, D). The eddy speeds in the western GoM have a similar magnitude as the first-mode Rossby wave propagation speeds (Chelton et al., 2011). However, it should be noted that eddy speeds larger than the first-mode

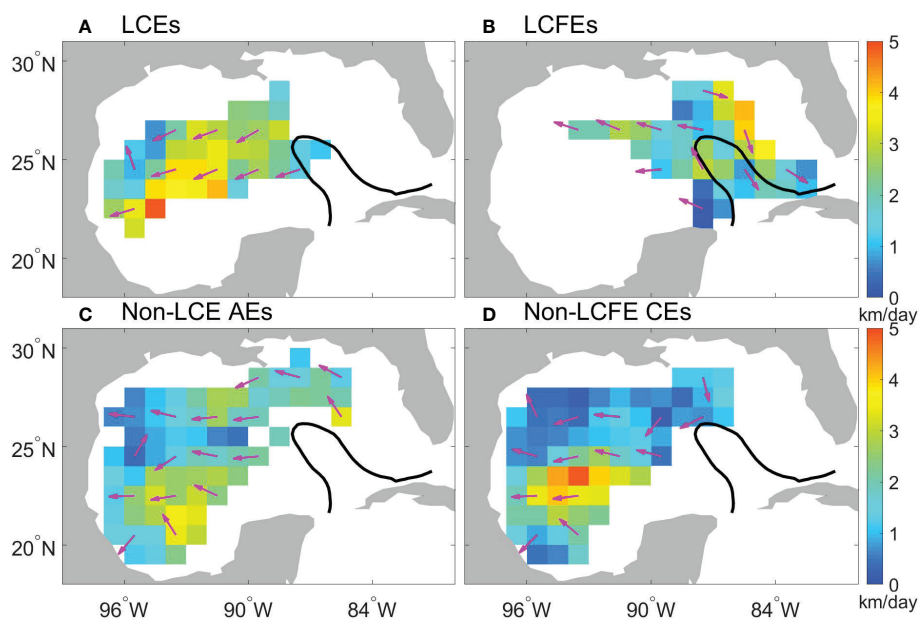


FIGURE 5

Mean eddy propagation speeds (color shading) and directions (magenta arrows) for (A) LCEs, (B) LCFEs, (C) non-LCE AEs, and (D) non-LCFE CEs. The thick black line represents the 25-cm contour of temporal mean SSH anomalies from 1993 to 2019.

Rossby wave propagation speeds by more than  $1 \text{ km day}^{-1}$  were also found, which might be related to the background circulation, or in the case of CEs caused by the swirl velocities of a large LCE.

### 3.2 Basic eddy characteristics

Distributions of some basic eddy characteristics derived from the mean values along eddy trajectories are presented in Figures 6A–D, and the distribution of eddy lifetime is shown in Figure 6E. Apparent differences between the four types of eddies appear in their amplitude, scale, relative vorticity, and maximum rotational speed (Figures 6A–D). LCEs have the largest mode values of eddy amplitude, LCFEs have a smaller eddy amplitude, and non-LCE AEs and non-LCFE CEs have the smallest mode values of eddy amplitude (Figure 6A). The distributions of the eddy scale, defined as the radius with the maximum rotational speed (Chelton et al., 2011), show that LCEs have the largest scale and that the other three types of eddies have smaller and similar mode values of eddy scale (Figure 6B). The distributions of the relative vorticity, and maximum rotational speed show that LCEs and LCFEs have larger magnitudes of mode values than those of non-LCE AEs and non-LCFE CEs (Figures 6C, D). Nearly 25.1% of AEs have a lifetime longer than 100 days. About 16.7% of CEs can live longer than 100 days (Figure 6F).

Because the temporal correlation scale of gridded ADT data is about 30 days, the obtained eddy amplitude, scale, and maximum rotational speed were mapped into monthly data on

two-degree grids. To illustrate their spatial distributions, the temporal mean eddy characteristics on spatial grids are shown in Figure 7. Eddy characteristics within the LC are not considered in this study because SSH fields within the LC region were removed. Mean values of the LCE amplitude, scale, and maximum rotational speed are large northwest of the LC where LCEs were shed from the LC (Figures 7A–C) and are much larger than those of the other three types of eddies. The larger amplitude of LCEs is expected due to their larger size even with a rotational speed comparable to smaller eddies. LCFEs have relatively large amplitude and rotational speed in the southeastern part of the LC (Figures 7D, F), in agreement with previous estimates that LCFEs have larger amplitude and rotational speed in the northern and eastern side of the LC than on the western side (e.g., Le Hénaff et al., 2014). Compared to the eddy amplitude and rotational speed, the LCFE scale is relatively uniform (Figure 7E). In contrast to LCEs and LCFEs, non-LCE AEs and non-LCFE CEs show relatively small spatial variations of amplitude, scale, and rotational speed (Figures 7G–I). The spatial patterns of the eddy amplitude, scale, and maximum rotational speed are not likely related to the eddy number distributions (Figures 3, Figure 7).

### 3.3 Monthly climatology of eddies

Monthly climatology of eddy number was obtained and expressed in percentage of the total generated eddies (Figure 8). The seasonal peak of LCE birth in September and

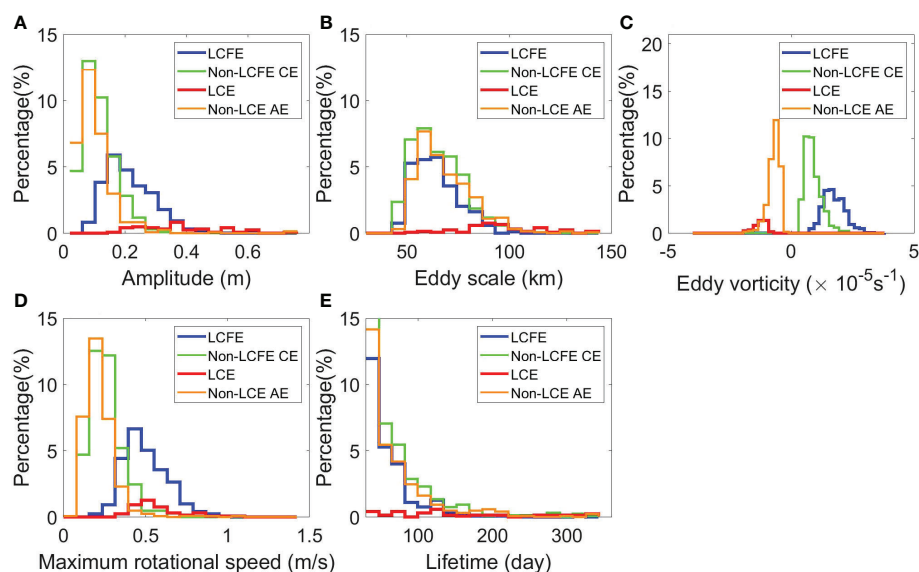


FIGURE 6  
Histograms of basic eddy characteristics: (A) amplitude (m), (B) eddy scale (km), (C) eddy relative vorticity ( $\text{s}^{-1}$ ), (D) maximum rotational speed (m/s), (E) lifetime (day).

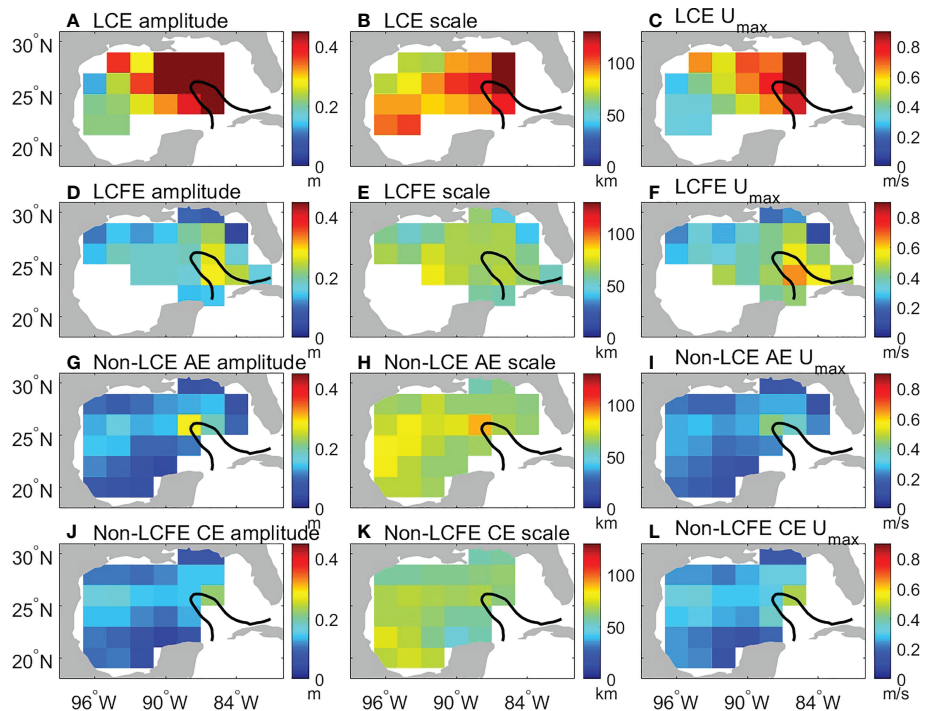


FIGURE 7

Eddy mean amplitude (m) for (A) LCEs, (D) LCFEs, (G) non-LCE AEs, and (J) non-LCFE CEs. Eddy mean scale (km) for (B) LCEs, (E) LCFEs, (H) non-LCE AEs, and (K) non-LCFE CEs. Eddy mean maximum rotational speed (m/s) for (C) LCEs, (F) LCFEs, (I) non-LCE AEs, and (L) non-LCFE CEs. The black line represents the 25-cm contour of temporal mean SSH anomalies from 1993 to 2019.

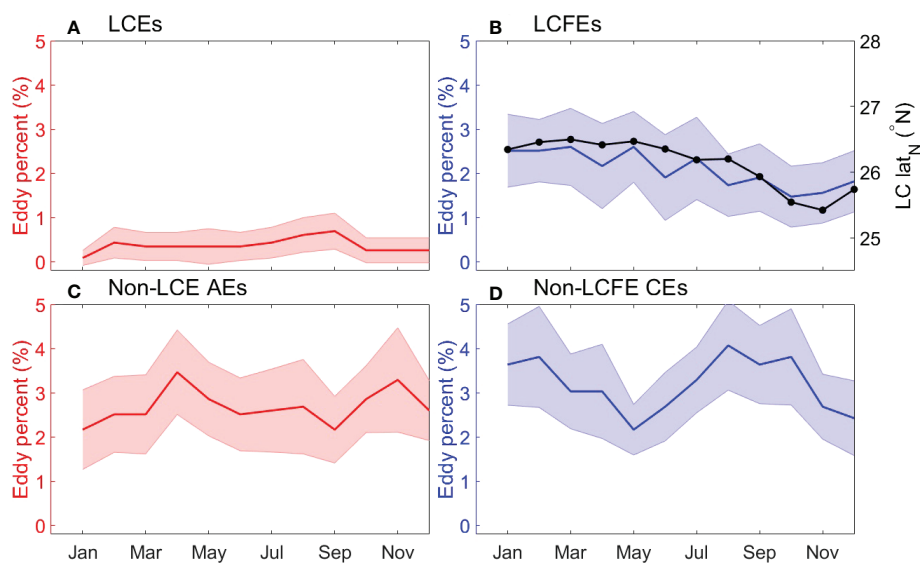


FIGURE 8

(A) The percentage of birth number of LCEs relative to the total eddy birth number. (B) The percentage of birth number of LCFEs relative to the total birth number. The black line in (B) represents the monthly climatology of the LC position. (C) The percentage of birth number of non-LCE AEs relative to the total birth number. (D) The percentage of birth number of non-LCFE CEs relative to the total birth number. The shading denotes the 95% confidence level represented by two times standard deviation of eddy percentage in each month.

the secondary peak in February are observed (Figure 8A), which are consistent with that reported by Hall and Leben (2016). The seasonal variation of LCEs is the smallest compared to the other three types of eddies and is not significant at the 95% confidence level. The nonsignificant seasonal variability of LCE separation may be partially related to the physical processes that do not have apparent seasonal variability but can affect the LCE separation. For example, fluctuations such as mesoscale eddies from the Caribbean Sea (Murphy et al., 1999; Oey et al., 2003; Huang et al., 2021) can influence the LCE separation.

Compared to LCEs, more LCFEs are observed and the birth number of LCFEs is larger in January to July than in October to December (Figure 8B). The magnitude of the seasonal variation of LCFEs is close to 1% of the total eddy birth number, but it is still not significant at the 95% confidence level. Because LCFEs are generated along the LC peripheral, the extent of northern penetration of the LC may be one important factor for the LCFE generation. The seasonal variation of the northern boundary of the LC is shown to have a similar variation as that of LCFEs (Figure 8B). Hamilton et al. (2014) also showed that altimeter-derived LC northern-boundary latitude is relatively high from January through about July and low in September and October. The more northward the LC penetrates, the more LCFEs are generated.

The seasonal variations of non-LCE AEs and non-LCFE CEs are relatively large, but differences of eddy number between most

months are not significant at the 95% confidence level due to large uncertainties (Figures 8C, D). The number of non-LCFE CEs is small in May and December and is large in February and August (Figure 8D), indicating a biannual variability. Compared to the non-LCFE CEs, the seasonal variation of non-LCE AEs has a different phase and a smaller amplitude (Figure 8C). Both the background currents and eddy-eddy interaction might be important for the seasonality of the two types of eddies. Figure 9 shows the monthly climatology of the eddy numbers of non-LCE AEs and non-LCFE CEs that were induced by eddy splitting and LCEs. The seasonal variations of AEs and CEs induced by splitting and LCEs are small and are not significant at the 95% confidence level. It should be noted that their seasonal variations are much smaller and more random than those shown in Figures 8C, D. Therefore, the seasonal variations of non-LCE AEs and non-LCFE CEs (Figures 8C, D) are not related to eddy-eddy interaction represented by eddy splitting and the effect of LCEs and could be likely related to the background currents. It is noted that the seasonal variations of the eddies are not robust. The large uncertainties of the seasonal variations of eddies are likely related to the multiple factors that can influence the large-scale background circulation such as the LC. In the eastern GoM, the seasonal variability of the LC can be modulated both by wind forcing over the northwestern Caribbean Sea and GoM (Chang and Oey, 2012; Chang and Oey, 2013) and by mesoscale variability in the Caribbean Sea (Murphy et al., 1999; Oey

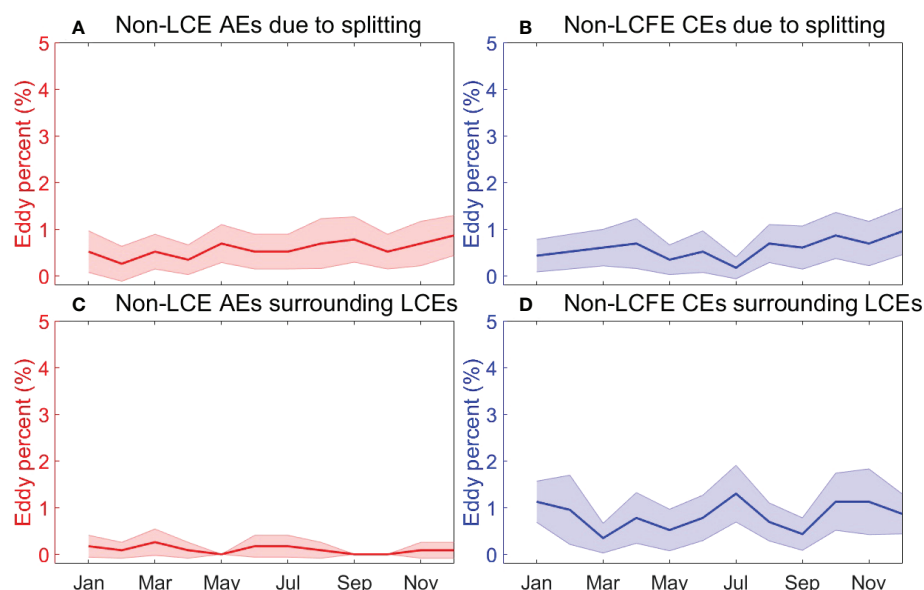


FIGURE 9

(A) The percentage of non-LCE AEs generated due to splitting relative to the total generated eddies. (B) The percentage of non-LCFE CEs generated due to splitting relative to the total generated eddies. (C) The percentage of non-LCE AEs generated within LCE radius plus 100 km relative to the total generated eddies. (D) The percentage of non-LCFE CEs generated within LCE radius plus 100 km relative to the total generated eddies. The shading denotes the 95% confidence level represented by two times standard deviation of eddy percentage in each month.



et al., 2003). In the western GoM, both the irregular LCEs and seasonal wind forcing contribute to the circulation that is partially important for the eddy generation (e.g., Sturges, 1993).

To further show spatial patterns of the monthly climatology of generated eddies, the locations of eddy centers were mapped on two-degree grids (Figure 10). Figures 10A–D shows the generation locations of LCEs and the mean position of the LC in February, May, August, and November (the generation locations of LCEs in 12 months are shown in Figure S1 in the supplementary material). The LC has a more northward penetration in February and May than in August and November but more LCEs are formed at the northwestern tip of the LC in August than in other months, suggesting no clear linkage between the generation of LCEs and the LC northern boundary can be built. However, more LCFEs can be found in the northern LC in February and May when the LC makes more penetration than in August and November when the LC makes less penetration (Figures 10E–H) (the generation locations of LCFEs in 12 months are shown in Figure S2 in the supplementary material). Therefore, a more northward penetration of the LC favors the generation of LCFEs.

Compared to LCEs and LCFEs that are closely related to the LC, the generation of non-LCE AEs and non-LCFE CEs is scattered over the whole GoM and is mainly in the western GoM (Figures 10I–P) (the generation locations of non-LCE AEs

and non-LCFE CEs in 12 months are shown in Figures S3 and S4 in the supplementary material). The contours of current speed gradient in Figures 10I–P indicate the position of strong background currents. The generation locations of eddies tend to move with the seasonal movement of strong currents, from which eddies may obtain energy. However, non-LCE AEs do not show a significant change in the birth number between different months, which is also indicated in Figure 8C. It is noted that the number of non-LCFE CEs is more likely related to the strength of the background currents (Figures 10M–P). More non-LCFE CEs were generated along the boundary of strong currents in February and August and fewer non-LCFE CEs were generated in May and November. The current speeds and directions in the four months are highlighted and shown in Figure 11 (the current speeds and directions are shown in Figure S5 in the supplementary material). The background currents in western GoM are stronger in February and August than in May. The mean currents in the central western GoM flow westward approximately at 22–23°N and eastward at 25–27°N, forming an anticyclonic circulation pattern. It is noted that the currents change direction with season along the western boundary. Therefore, the non-LCFE CEs were more likely formed along the periphery of the strong anticyclonic circulation pattern in the western GoM. It is noted that the eddy generation location varies within the strong-current region and sometimes few eddies are

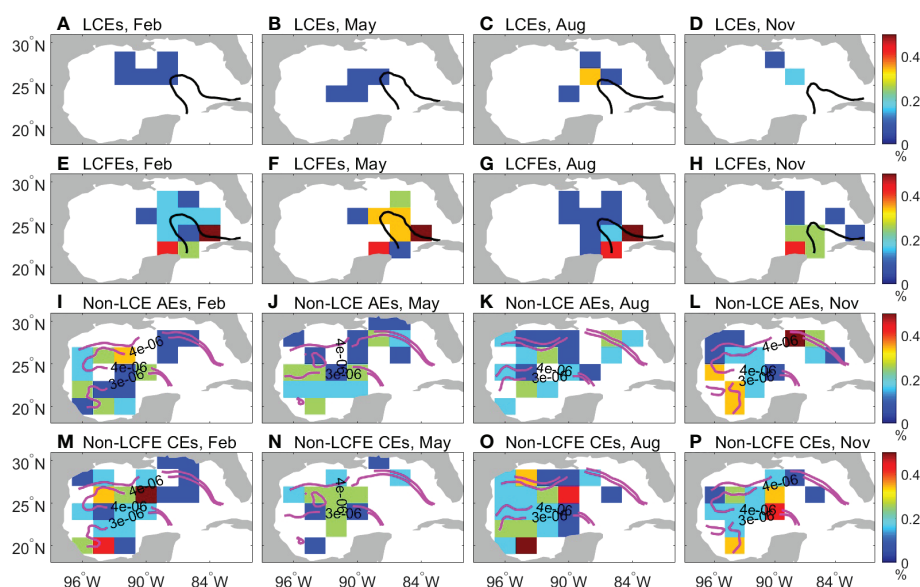


FIGURE 10

(A–D) LCE percentage relative to the total generated eddies in (A) February, (B) May, (C) August, and (D) November. (E–H) LCFE percentage relative to the total generated eddies in (E) February, (F) May, (G) August, and (H) November. (I–L) Non-LCE AE percentage relative to the total generated eddies in (I) February, (J) May, (K) August, and (L) November. (M–P) Non-LCFE CE percentage relative to the total generated eddies in (M) February, (N) May, (O) August, and (P) November. The black lines in (A–H) represent the mean position of the LC in February, May, August, and November, respectively. The magenta lines in (I–P) represent the monthly climatology of current speed gradient in February, May, August, and November, respectively.



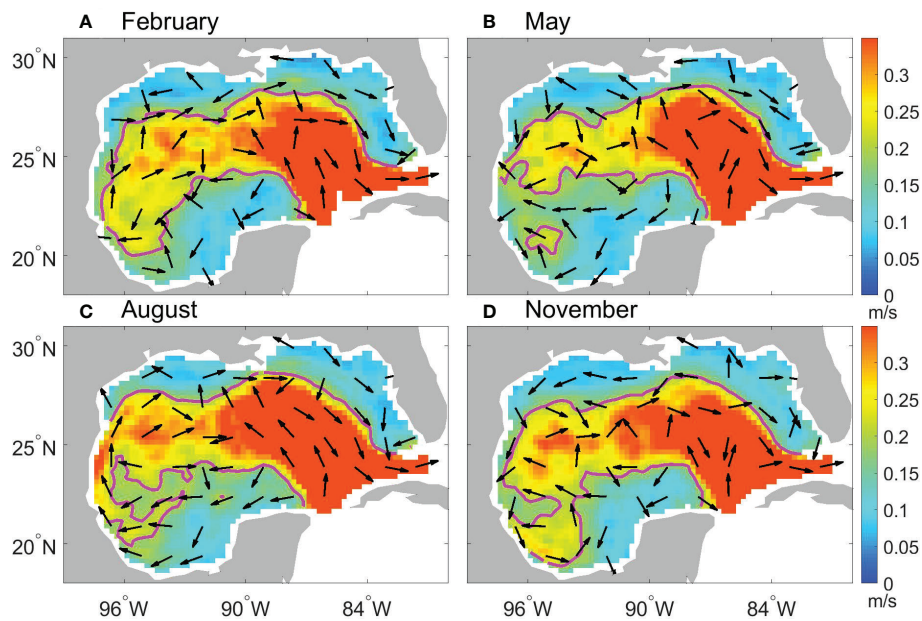


FIGURE 11

Current speeds (m/s, color shading) climatology and mean current direction (arrows) in the GoM in (A) February, (B) May, (C) August, and (D) November. The magenta contour denotes the current speed of 0.2 m/s.

generated. One possible reason is that the large-scale background current can influence the eddy generation but is not the only factor that determines the eddy generation location and other factors such as wind stress play some role.

In addition to the seasonality observed in the eddy birth number, the seasonal variability of eddy amplitude at the time of eddy birth was examined. The monthly climatology of median eddy amplitude is presented in Figure 12. Since eddy amplitude

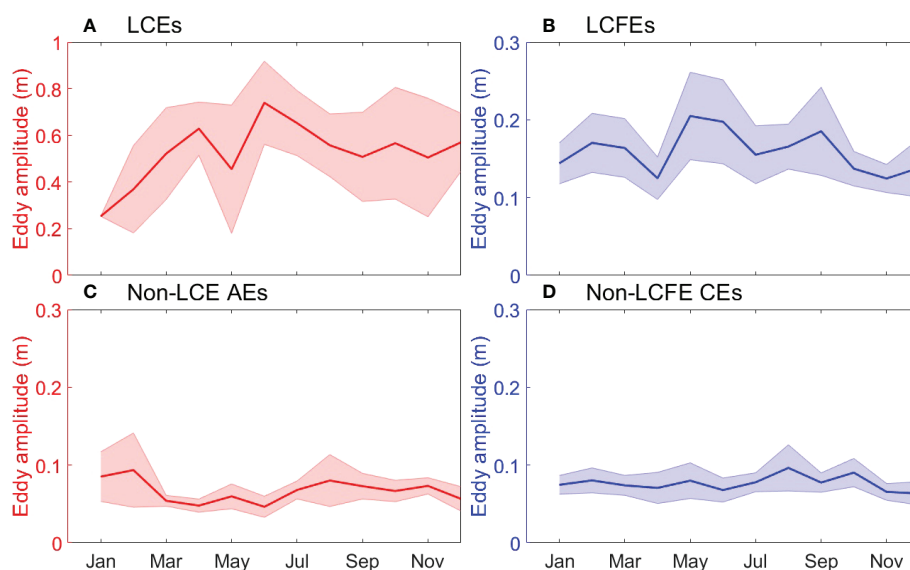


FIGURE 12

Monthly climatology of eddy amplitude of (A) LCEs, (B) LCFEs, (C) non-LCE AEs, and (D) non-LCFE CEs when they were generated. The shading denotes the 95% confidence level represented by two times standard deviation of amplitude.

is not normally distributed, median eddy amplitude was used to mitigate the potential influence of amplitude outliers. Compared to the seasonal variability of eddy number, the seasonal variability of eddy amplitude is less apparent. This is because eddy amplitude is defined as the difference between the SSH on the contour of maximum rotation speed and maximum or minimum SSH in the eddy. In the LCEs and LCFEs region, SSH variations are dominated by intra-seasonal oscillations, not by annual cycles or seasonal variations (Liu et al., 2016; Weisberg et al., 2017). LCEs and LCFEs have relatively larger monthly variations and uncertainties than non-LCE AEs and non-LCFE CEs. It should be noted that the seasonal variation of LCE amplitude may not be reflected from the relatively short record because it was estimated from a relatively small number of LCEs that is less than 6 in most months.

### 3.4 Low-frequency variability of eddies

To examine the low-frequency variability of eddies, annual variations of eddy birth number and amplitude were obtained. Figure 13 shows the annual variations of the birth number of eddies. The generation of LCEs is relatively rare and shows a weak variability (Figure 13A). The other three types of eddies indicate a larger variability. A linear regression model that includes a linear trend, ENSO index, NAO index, and AMM index was applied to the annual eddy number. An increasing number of LCEs over 2001–2010 has been found in previous studies (Vukovich, 2012; Lindo-Atichati et al., 2013). Nevertheless, no long-term variability of other types of eddies has been reported. The linear trends of the annual birth number of LCEs, LCFEs, non-LCE AEs, and non-LCFE CEs from 1993 to 2018 are  $3.5 \times 10^{-2} \pm 3.3 \times 10^{-2}$  ( $\pm 1\sigma$ )  $\text{year}^{-1}$ ,  $-0.2 \pm 0.17$  ( $\pm 1\sigma$ )

$\text{year}^{-1}$ ,  $-0.06 \pm 0.11$  ( $\pm 1\sigma$ )  $\text{year}^{-1}$ , and  $0.05 \pm 0.11$  ( $\pm 1\sigma$ )  $\text{year}^{-1}$ , respectively. These linear trends are not significant at the 95% confidence level. LCFEs have the largest decreasing trend that is not significant, which is likely related to the negative trend of the northern boundary of the LC that is  $-1.7 \times 10^{-2} \pm 1.7 \times 10^{-2}$  ( $\pm 1\sigma$ )  $\text{degree year}^{-1}$ . Regression coefficients of the three climate indices are not significant as well. For the four types of eddies, the coefficients of determination of the three climate indices are less than 0.08. Therefore, only a small portion of eddy number variance can be explained by the three climate modes, indicating that the role of the remote climate variability in changing the eddy activity in the GoM is relatively small or cannot be detected from the linear model.

In the eastern GoM, the low-frequency variability of eddy number is likely related to that of the LC. Figure 13B shows the annual mean variation of the northern boundary position of the LC that particularly follows the variation of LCFEs. Correlation between the birth number of LCEs and the northern boundary position of the LC is small and not significant (Correlation coefficient  $r=0.38$ ), therefore, the extent of LC penetration plays a relatively small role in the separation of LCEs. However, the LCFE number and the northern boundary position of the LC are correlated with a significant correlation coefficient of 0.76, indicating that the LCFE number increases with the northward penetration of the LC on the interannual to multidecadal time scale. The extent of northward penetration of the LC is important for the LCFE generation although previous studies have shown that perturbations coming from the Caribbean Sea (Huang et al., 2013) and the topography of the northern Campeche (Chérubin et al., 2006) also contribute to the eddy activity along the western edge of the LC.

For the non-LCE AEs and non-LCFE CEs, the eddy numbers also show large annual mean variations (Figures 13C, D). Since

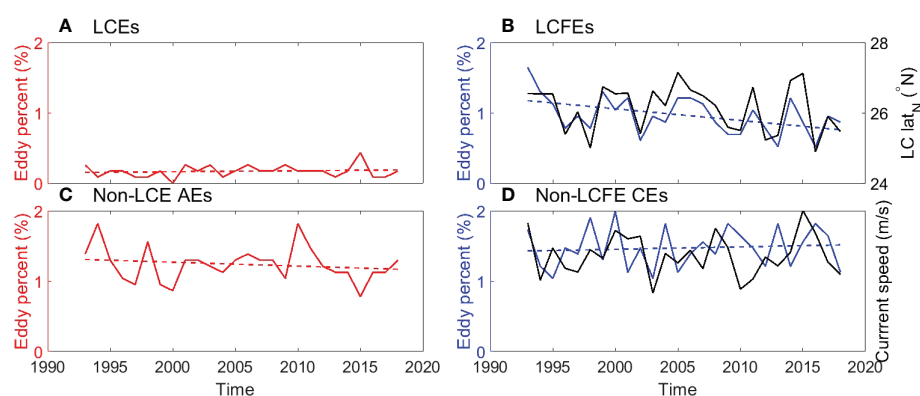


FIGURE 13

Annual number of generated (A) LCEs, (B) LCFEs, (C) non-LCE AEs and (D) non-LCFE CEs and is expressed as percentage of the total new eddy from 1993 to 2018. The black line represents the annual mean northern boundary ( $^{\circ}\text{N}$ ) of the LC in (B) and the annual mean current speed (m/s) in the western GoM in (D). The dashed lines represent linear trend of generated eddies.

the background current strength could be important in affecting the low-frequency eddy activity (Chen et al., 2011), birth numbers of non-LCE AEs and non-LCFE CEs, which were mostly formed in the western GoM, were compared with the surface current speed averaged in the western GoM (Figure 13D). The non-LCE AE number is anticorrelated with the mean surface current speed in the western GoM ( $r=-0.42$ ). The non-LCFE CE number is correlated with the mean surface current speed in the western GoM ( $r=0.33$ ). But the correlation values are not significant at the 95% confidence level.

In addition to the influence of background currents, the eddy-eddy interaction that includes eddy splitting and eddy formation related to LCEs is considered as well. The annual mean variability of eddies due to eddy-eddy interaction is relatively weak. After removing the eddies induced by eddy splitting and LCEs, the correlations between non-LCE AE number, non-LCFE CE number, and the mean surface current speed in the western GoM are  $-0.38$  and  $0.32$ , respectively. The eddy-eddy interaction has little effect on the relationship between western eddies and the background flows. Since a much smaller number of eddies due to eddy splitting and LCEs are found along the western boundary (Figure 4) where LCEs could interact with the topography (e.g., Vidal et al., 1992), the eddy-topography interaction is not important for the low-frequency variability of eddies.

The relationship between the eddy number and the strength of the circulation in the western GoM was further examined with composite analysis. The mean current speeds and flow directions during the periods with more non-LCFE CEs and fewer non-LCFE CEs are shown in Figure 14. When the annual number of non-LCFE CEs is one standard deviation larger than the average eddy number, strong mean anticyclonic circulation is observed in the western GoM. When the annual number of non-LCFE CEs is one standard deviation smaller than the average eddy number, weak mean anticyclonic circulation is observed in the

western GoM. However, over the period with more non-LCE AEs weak mean anticyclonic circulation is observed in the western GoM. Over the period with fewer non-LCE AEs strong mean anticyclonic circulation is observed in the western GoM. Therefore, the strength of the background circulation could play a role in influencing the low-frequency variability of eddy number.

Eddy amplitude in the GoM exhibits low-frequency variability as well. To mitigate the potential influence of amplitude outliers, the median amplitude of eddies at the time of birth in each year was selected for the analysis of the low-frequency variability of eddy amplitude (Figure 15). LCEs show the largest annual variation of eddy amplitude (Figure 15A) that was obtained from a small number of LCEs (Figure 13A). The amplitude variation of LCFEs is weaker than that of LCEs but is larger than those of non-LCE AEs and non-LCFE CEs (Figure 15B). The variations of LCE and LCFE amplitude are not closely related to the northern boundary of the LC with small correlations, suggesting the extent of the LC penetration is not an important factor for the eddy amplitude at the time of birth. For non-LCE AEs and non-LCFE CEs, the eddy amplitude at the time of birth seems to be related to the strength of background currents in the western GoM (Figures 15C, D) but with a nonsignificant positive correlation of  $0.47$ .

## 4 Conclusions and discussions

In this study, we present characteristics of the Eulerian mesoscale eddies in the GoM, including their spatial distributions, seasonal and low-frequency variabilities. As expected, many eddy characteristics in the eastern GoM are closely related to the LC, which sheds large and strong LCEs and develops small-scale LCFEs (e.g., Le Hénaff et al., 2014; Brokaw et al., 2020). Compared to LCEs and LCFEs, non-LCE AEs and

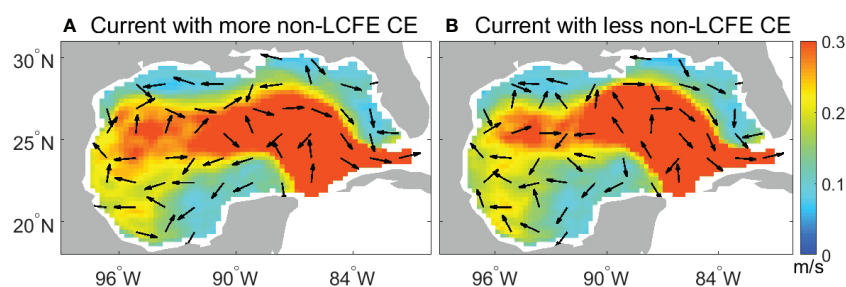


FIGURE 14

Composite of current speeds in the GoM (A) during the period with more generated non-LCFE CEs (annual number of non-LCFE CEs is larger than mean value plus one standard deviation), and (B) during the period with fewer non-LCFE CEs (annual number of non-LCFE CEs is smaller than mean value minus one standard deviation). Arrows denote the mean current direction.

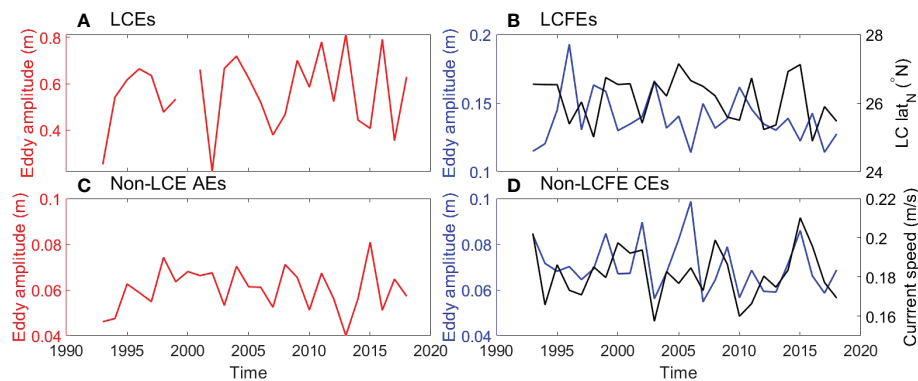


FIGURE 15

Annual median amplitude (m) of the (A) LCEs, (B) LCFEs, (C) non-LCE AEs and (D) non-LCFE CEs when they were generated. The black line represents the annual mean northern boundary ( $^{\circ}$ N) of the LC in (B) and the annual mean current speed (m/s) in the western GoM in (D).

non-LCFE CEs are mainly formed in the central-western GoM, tend to dissipate along the western boundary, and have smaller amplitude, relative vorticity magnitude, and rotational speed. Temporally mean propagation speeds are high in the eastern part of the LC and the southwestern GoM.

The temporal variability of eddy occurrence and amplitude, which is less reported in the literature, shows manifest spatial patterns and dramatic differences between LCEs, LCFEs, non-LCE AEs, and non-LCFE CEs. This study indicates a biannual variability of LCE separation with large uncertainties that is similar to that found in a shorter record by Hall and Leben (2016). However, the seasonality in LCE formation is not significant, while Hall and Leben (2016) suggested that the seasonal peak in LC eddy separation events in August and September was significant. The seasonal variabilities of birth numbers of the other three types of eddies are also not significant at the 95% confidence level. Nevertheless, LCFEs and non-LCFE CEs show more apparent seasonal patterns than LCEs and non-LCE AEs. More LCFEs are observed from January to July, while more non-LCFE CEs are found in February and August. Fewer LCFEs are observed from August to December, while fewer non-LCFE CEs are found in May and December. Moreover, the seasonal variability of eddy amplitude at the time of eddy birth is more random than that of eddy number. Similar to the temporal mean characteristics, the seasonal variability of eddy amplitude of LCEs and LCFEs at the time of eddy birth is much larger than that of non-LCE AEs and non-LCFE CEs. On the low-frequency time scale, although an increasing number of LCEs in the decade 2001–2010 has been found in previous studies (Vukovich, 2012; Lindo-Atichati et al., 2013), the linear trends of LCEs and other three types of eddies obtained in this study are not significant at the 95% confidence level.

The seasonal and low-frequency variabilities described above could be closely related to the large-scale background circulations such as the LC, eddy-eddy interaction, and eddy-topography interaction. On the seasonal time scale, the extent of northward penetration of the LC is important for LCFE generation but not for their amplitude. The position and strength of background currents in the western GoM are likely important for the formation of non-LCFE CEs and non-LCE AEs that are mostly formed in the western GoM. On the low-frequency band (interannual to multidecadal), LCFE number is related to the extent of northward penetration of the LC in the eastern GoM. In the western GoM, the surface circulation strength could be important for the low-frequency variability of eddy occurrence and amplitude, which is also found in other oceans (e.g., Chen et al., 2011). In contrast, the eddy-eddy interaction that includes eddy splitting and the effect of LCEs and the eddy-topography interaction give rise to a relatively small number of eddies and play a small role in the temporal variability of eddies.

Note that the Eulerian eddies examined in this study are interpreted as mesoscale perturbations with closely SSH or streamlines, which reflect the generation, propagation, and dissipation of these signals rather than coherent mass. The characteristics of these Eulerian eddies are useful information for the description of the upper-ocean mesoscale variabilities that possess different temperature and salinity and that may exert significant influence on the bottom currents (Brokaw et al., 2020; Zhu and Liang, 2020). Nevertheless, the Eulerian eddies were detected without considering the conservation of material within them. The material within the eddy might exchange with the ambient fluid and might be different during the propagation process. Therefore, the detected and traced eddies examined in

this study cannot be directly used to infer the transport of ocean mass, temperature, salinity, and other materials. In cases of examining ocean material transport within mesoscale eddies, Lagrangian methods that consider the conservation of boundary materials should be used (e.g., [Andrade-Canto et al., 2020](#)). The Lagrangian coherent vortex is different from the Eulerian eddies in the objective definition of coherent structure that is frame-independent and observer-independent. Eddy characteristics based on the Lagrangian methods can be done and compared with the results obtained with the Eulerian methods in our future work.

In addition to the limitation of eddy detection and tracking algorithms, satellite sampling could affect the detection of the mesoscale activity ([Le Traon and Dibarbouré, 1999](#)) and the LC statistics ([Dukhovskoy et al., 2015](#)). The allsat ADT product was derived from a varying number of altimeters and was useful for examining the influence of satellite sampling on eddy detection. Mesoscale eddies were detected with the algorithm developed by [Le Vu et al. \(2018\)](#) from the allsat ADT product and were compared with those detected from the twosat ADT. From 1 January 1993 to 31 December 1999 when twosat and allsat ADT data were mainly derived from 2 altimeters, 41388 and 41343 eddies were detected from the twosat and allsat ADT data respectively, suggesting that 0.1% of eddies was not detected in allsat ADT. From 1 January 2000 to 13 May 2019 when the allsat ADT data were mainly derived from 3 or more altimeters, 117582 and 117359 eddies were detected from the twosat and allsat ADT data respectively, suggesting that 0.2% of eddies was less detected in allsat ADT than in twosat ADT. The satellite sampling has a relatively small effect on the detection of eddies in the GoM.

In this study, we focus on describing the characteristics of the Eulerian mesoscale eddies in the GoM, and some characteristics such as the temporal and spatial patterns of eddies still need further dynamical explanations. Previous studies indicate that mesoscale eddies in the eastern GoM likely arise from dynamic instabilities, such as barotropic and baroclinic instabilities (e.g., [Vukovich and Maul, 1985](#); [Pichevin and Nof, 1997](#); [Sturges and Leben, 2000](#); [Zavala-Hidalgo et al., 2003](#); [Chérubin et al., 2006](#); [Donohue et al., 2016a](#); [Yang et al., 2020](#)). In the future, dynamic analyses such as eddy energy may shed light on the detailed mechanisms of the temporal and spatial variability of mesoscale eddies in the GoM.

## Data availability statement

Publicly available datasets were analyzed in this study. This data can be found here: The daily DT2018 ADT data ([Taburet](#)

[et al., 2019](#)) from two altimeter satellites used for eddy detection was provided by the C3S (<https://cds.climate.copernicus.eu/cdsapp#!/dataset/satellite-sea-level-global?tab=form>). Besides, the daily DT2018 ADT data from multi-mission altimeter satellites used to examine the influence of satellite sampling on eddy detection is SEALEVEL\_GLO\_PHY\_L4\_REP\_OBSERVATIONS\_008\_047 that was produced and provided by CMEMS ([https://resources.marine.copernicus.eu/product-detail/SEALEVEL\\_GLO\\_PHY\\_L4\\_MY\\_008\\_047/INFORMATION](https://resources.marine.copernicus.eu/product-detail/SEALEVEL_GLO_PHY_L4_MY_008_047/INFORMATION)). TOPEX/Poseidon (T/P) along-track ADT data from 2 January 1996 to 3 December 1999 were used to examine the effective spatial resolution of the gridded ADT product in the GoM and were provided by CMEMS. Since the eddy traveling speeds were compared with the first-mode baroclinic Rossby wave speeds, the atlas of the first-baroclinic Rossby radius of deformation was also used and downloaded at [https://ceoas.oregonstate.edu/rossby\\_radius](https://ceoas.oregonstate.edu/rossby_radius) ([Chelton et al., 1998](#)). The multivariate ENSO index (MEI V2) (e.g., [Zhang et al., 2019](#)) from National Oceanic and Atmospheric Administration (NOAA) Physical Sciences Laboratory, NAO index ([Hurrell, 1995](#)) from NOAA Climate Prediction Center, and AMM index ([Chiang and Vimont, 2004](#)) from University of Wisconsin were used to examine possible relationships between the eddy activity in the GoM and climate modes. The MEI, NAO index, and AMM index were downloaded at <https://psl.noaa.gov/data/climateindices/list/>.

## Author contributions

YZ and XL designed the experiments and YZ carried them out. YZ prepared the manuscript with contributions from XL. All authors contributed to the article and approved the submitted version.

## Funding

The work was supported in part by the National Aeronautics and Space Administration through Grant 80NSSC20K0757.

## Acknowledgments

The preprint of the work was submitted for public discussion online ([Zhu and Liang, 2022](#)) and the authors acknowledge comments from two reviewers and Dr. Francisco Beron-Vera. The authors thank three reviewers for their constructive comments and suggestions.



## Conflict of interest

The authors declare that the research was conducted in the absence of any commercial or financial relationships that could be construed as a potential conflict of interest.

## Publisher's note

All claims expressed in this article are solely those of the authors and do not necessarily represent those of their affiliated

organizations, or those of the publisher, the editors and the reviewers. Any product that may be evaluated in this article, or claim that may be made by its manufacturer, is not guaranteed or endorsed by the publisher.

## Supplementary material

The Supplementary Material for this article can be found online at: <https://www.frontiersin.org/articles/10.3389/fmars.2022.1087060/full#supplementary-material>

## References

- Alvera-Azcárate, A., Barth, A., and Weisberg, R. H. (2009). The surface circulation of the Caribbean Sea and the gulf of Mexico as inferred from satellite altimetry. *J. Phys. Oceanogr.* 39 (3), 640–657. doi: 10.1175/2008JP03765.1
- Amores, A., Jordà, G., Arsouze, T., and Le Sommer, J. (2018). Up to what extent can we characterize ocean eddies using present-day gridded altimetric products? *J. Geophysical Res.: Oceans* 123, 7220–7236. doi: 10.1029/2018JC014140
- Andrade-Canto, F., and Beron-Vera, F. J. (2022). Do eddies connect the tropical Atlantic ocean and the gulf of Mexico? *Geophysical Res. Lett.*, 49, e2022GL099637. doi: 10.1029/2022GL099637
- Andrade-Canto, F., Beron-Vera, F. J., Goni, G. J., Karrasch, D., Olascoaga, M. J., and Triñanes, J. (2022). Carriers of sargassum and mechanism for coastal inundation in the Caribbean Sea. *Phys. Fluids* 34 (1), 016602. doi: 10.1063/5.0079055
- Andrade-Canto, F., Karrasch, D., and Beron-Vera, F. J. (2020). Genesis, evolution, and apocalypse of loop current rings. *Phys. Fluids* 32 (11), 116603. doi: 10.1063/5.0030094
- Bello-Fuentes, J., García-Nava, F., Andrade-Canto, H. F., Durazo, R., Castro, R., and Yarbuh, I. (2021). Retention time and transport potential of eddies in the northwestern gulf of Mexico. *Cienc. Marinas* 47 (2):71–88. doi: 10.7773/cm.v47i2.3116
- Biggs, D. C., Fargion, G. S., Hamilton, P., and Leben, R. R. (1996). Cleavage of a gulf of Mexico loop current eddy by a deep water cyclone. *J. Geophysical Res.: Oceans* 101 (C9), 20629–20641. doi: 10.1029/96JC01078
- Bosart, L. F., Bracken, W. E., Molinari, J., Velden, C. S., and Black, P. G. (2000). Environmental influences on the rapid intensification of hurricane opal (1995) over the gulf of Mexico. *Monthly Weather Rev.* 128 (2), 322–352. doi: 10.1175/1520-0493(2000)128<0322:EIOTRI>2.0.CO;2
- Brokaw, R. J., Subrahmanyam, B., and Morey, S. L. (2019). Loop current and eddy-driven salinity variability in the gulf of Mexico. *Geophysical Res. Lett.* 46 (11), 5978–5986. doi: 10.1029/2019GL082931
- Brokaw, R. J., Subrahmanyam, B., Trott, C. B., and Chaigneau, A. (2020). Eddy surface characteristics and vertical structure in the gulf of Mexico from satellite observations and model simulations. *J. Geophysical Res.: Oceans* 125 (2), e2019JC015538. doi: 10.1029/2019JC015538
- Castelao, R. M., and He, R. (2013). Mesoscale eddies in the south Atlantic bight. *J. Geophysical Res.: Oceans* 118 (10), 5720–5731. doi: 10.1002/jgrc.20415
- Chaigneau, A., Gizolme, A., and Grados, C. (2008). Mesoscale eddies off Peru in altimeter records: Identification algorithms and eddy spatio-temporal patterns. *Prog. Oceanogr.* 79 (2), 106–119. doi: 10.1016/j.pocan.2008.10.013
- Chang, Y.-L., and Oey, L.-Y. (2012). Why does the loop current tend to shed more eddies in summer and winter? *Geophysical Res. Lett.* 39 (5):L05605. doi: 10.1029/2011GL050773
- Chang, Y.-L., and Oey, L.-Y. (2013). Loop current growth and eddy shedding using models and observations: Numerical process experiments and satellite altimetry data. *J. Phys. Oceanogr.* 43 (3), 669–689. doi: 10.1175/JPO-D-12-0139.1
- Chelton, D. B., deSzoeke, R. A., Schlax, M. G., El Naggar, K., and Siwertz, N. (1998). Geographical variability of the first baroclinic rossby radius of deformation. *J. Phys. Oceanogr.* 28 (3), 433–460. doi: 10.1175/1520-0485(1998)028<0433:GVOTFB>2.0.CO;2
- Chelton, D. B., Schlax, M. G., and Samelson, R. M. (2011). Global observations of nonlinear mesoscale eddies. *Prog. Oceanogr.* 91(2), 167–216. doi: 10.1016/j.pocan.2011.01.002
- Chelton, D. B., Schlax, M. G., Samelson, R. M., and de Szoeke, R. A. (2007). Global observations of large oceanic eddies. *Geophysical Res. Lett.* 34 (15):L15606. doi: 10.1029/2007GL030812
- Chen, G., Hou, Y., and Chu, X. (2011). Mesoscale eddies in the south China Sea: Mean properties, spatiotemporal variability, and impact on thermohaline structure. *J. Geophys. Res.* 116, C06018. doi: 10.1029/2010JC006716
- Chérubin, L. M., Morel, Y., and Chassignet, E. P. (2006). Loop current ring shedding: The formation of cyclones and the effect of topography. *J. Phys. Oceanogr.* 36 (4), 569–591. doi: 10.1175/JPO2871.1
- Chiang, J. C. H., and Vimont, D. J. (2004). Analogous pacific and Atlantic meridional modes of tropical atmosphere–ocean variability. *J. Climate* 17 (21), 4143–4158. doi: 10.1175/JCLI4953.1
- Donohue, K., Watts, D., Hamilton, P., Leben, R., and Kennelly, M. (2016a). Loop current eddy formation and baroclinic instability. *Dyn. Atmos. Oceans* 76, 195–216. doi: 10.1016/j.dynatmoce.2016.01.004
- Donohue, K. A., Watts, D. R., Hamilton, P., Leben, R., Kennelly, M., and Lugo-Fernández, A. (2016b). Gulf of Mexico loop current path variability. *Dyn. Atmos. Oceans* 76, 174–194. doi: 10.1016/j.dynatmoce.2015.12.003
- Dukhovskoy, D. S., Leben, R. R., Chassignet, E. P., Hall, C. A., Morey, S. L., and Nedbor-Gross, R. (2015). Characterization of the uncertainty of loop current metrics using a multidecadal numerical simulation and altimeter observations. *Deep Sea Res. Part I: Oceanographic Res. Papers* 100, 140–158. doi: 10.1016/j.dsr.2015.01.005
- Elliott, B. A. (1982). Anticyclonic rings in the gulf of Mexico. *J. Phys. Oceanogr.* 12 (11), 1292–1309. doi: 10.1175/1520-0485(1982)012<1292:ARITGO>2.0.CO;2
- Faghmous, J. H., Frenger, I., Yao, Y., Warmka, R., Lindell, A., and Kumar, V. (2015). A daily global mesoscale ocean eddy dataset from satellite altimetry. *Sci. Data* 2, 150028. doi: 10.1038/sdata.2015.28
- Fratantoni, P. S., Lee, T. N., Podesta, G. P., and Muller-Karger, F. (1998). The influence of loop current perturbations on the formation and evolution of tortugas eddies in the southern straits of florida. *J. Geophysical Res.: Oceans* 103 (C11), 24759–24779. doi: 10.1029/98JC02147
- Frolov, S. A., Sutyryn, G. G., Rowe, G. D., and Rothstein, L. M. (2004). Loop current eddy interaction with the western boundary in the gulf of Mexico. *J. Phys. Oceanogr.* 34 (10), 2223–2237. doi: 10.1175/1520-0485(2004)034<2223:ICEIWT>2.0.CO;2
- Haller, G. (2005). An objective definition of a vortex. *J. Fluid mechanics* 525, 1–26. doi: 10.1017/S0022112004002526
- Hall, C. A., and Leben, R. R. (2016). Observational evidence of seasonality in the timing of loop current eddy separation. *Dynamics Atmospheres Oceans* 76, 240–267. doi: 10.1016/j.dynatmoce.2016.06.002
- Halo, I., Backeberg, B., Penven, P., Ansgore, I., Reason, C., and Ullgren, J. (2014). Eddy properties in the Mozambique channel. a comparison between observations and two numerical ocean circulation models. *Deep Sea Res. Part II: Topical Stud. Oceanogr.* 100, 38–53. doi: 10.1016/j.dsr2.2013.10.015
- Hamilton, P. (1992). Lower continental slope cyclonic eddies in the central gulf of Mexico. *J. Geophysical Res.: Oceans* 97 (C2), 2185–2200. doi: 10.1029/91JC01496
- Hamilton, P. (2007). Eddy statistics from lagrangian drifters and hydrography for the northern gulf of Mexico slope. *J. Geophysical Res.: Oceans* 112 (C9):C09002. doi: 10.1029/2006JC003988

- Hamilton, P., Berger, T. J., and Johnson, W. (2002). On the structure and motions of cyclones in the northern gulf of Mexico. *J. Geophysical Res.: Oceans* 107 (C12), 1–11. doi: 10.1029/1999JC000270
- Hamilton, P., Donohue, K., Hall, C., Leben, R. R., Quian, H., Sheinbaum, J., et al. (2014). *Observations and dynamics of the loop current (Tech. rep. no. OCS study BOEM 2015-006)* (New Orleans, LA: U.S. Dept. of the Interior, Bureau of Ocean Energy Management, Gulf of Mexico OCS Region).
- Hamilton, P., Fargion, G. S., and Biggs, D. C. (1999). Loop current eddy paths in the Western gulf of Mexico. *J. Phys. Oceanogr.* 29 (6), 1180–1207. doi: 10.1175/1520-0485(1999)029<1180:LCEPIT>2.0.CO;2
- Hamilton, P., Lugo-Fernández, A., and Sheinbaum, J. (2016). A loop current experiment: Field and remote measurements. *Dyn. Atmos. Oceans* 76, 156–173. doi: 10.1016/j.dynatmoce.2016.01.005
- Hong, X., Chang, S. W., Raman, S., Shay, L. K., and Hodur, R. (2000). The interaction between hurricane opal, (1995) and a warm core ring in the gulf of Mexico. *Monthly Weather Rev.* 128 (5), 1347–1365. doi: 10.1175/1520-0493(2000)128<1347:TIBHOA>2.0.CO;2
- Huang, M., Liang, X., Zhu, Y., Liu, Y., and Weisberg, R. H. (2021). Eddies connect the tropical Atlantic ocean and the gulf of Mexico. *Geophysical Res. Lett.* 48, e2020GL091277. doi: 10.1029/2020GL091277
- Huang, H., Walker, N. D., Hsueh, Y., Chao, Y., and Leben, R. R. (2013). An analysis of loop current frontal eddies in a 1/6° Atlantic ocean model simulation. *J. Phys. Oceanogr.* 43 (9), 1924–1939. doi: 10.1175/JPO-D-12-0227.1
- Hurlburt, H. E., and Thompson, J. D. (1980). A numerical study of loop current intrusions and eddy shedding. *J. Phys. Oceanogr.* 10 (10), 1611–1651. doi: 10.1175/1520-0485(1980)010<1611:ANSOLC>2.0.CO;2
- Hurrell, J. W. (1995). Decadal trends in the north Atlantic oscillation and relationships to regional temperature and precipitation. *Science* 269, 676–679. doi: 10.1126/science.269.5224.676
- Jouanno, J., Ochoa, J., Pallás-Sanz, E., Sheinbaum, J., Andrade-Canto, F., Candela, J., et al. (2016). Loop current frontal eddies: Formation along the campeche bank and impact of coastally trapped waves. *J. Phys. Oceanogr.* 46 (11), 3339–3363. doi: 10.1175/JPO-D-16-0052.1
- Kang, D., and Curchitser, E. N. (2013). Gulf stream eddy characteristics in a high resolution ocean model. *J. Geophysical Res.: Oceans* 118 (9), 4474–4487. doi: 10.1002/jgrc.20318
- Kirwan, A. D., Lewis, J. K., Indest, A. W., Reinersman, P., and Quintero, I. (1988). Observed and simulated kinematic properties of loop current rings. *J. Geophysical Res.: Oceans* 93 (C2), 1189–1198. doi: 10.1029/JC093iC02p01189
- Kirwan, A. D., Merrell, W. J., Lewis, J. K., and Whitaker, R. E. (1984). Lagrangian Observations of an anticyclonic ring in the western gulf of Mexico. *J. Geophysical Res.: Oceans* 89 (C3), 3417–3424. doi: 10.1029/JC089iC03p03417
- Laxenaire, R., Speich, S., Blanke, B., Chaigneau, A., Pegliasco, C., and Stegner, A. (2018). Anticyclonic eddies connecting the western boundaries of Indian and Atlantic oceans. *J. Geophysical Res.: Oceans* 123, 7651–7677. doi: 10.1029/2018JC014270
- Leben, R. R. (2005). *Altimeter-derived loop current metrics, circulation in the gulf of Mexico: Observations and models* (Washington, DC: American Geophysical Union (AGU), 181–201. doi: 10.1029/161GM15
- Leben, R. R., and Born, G. H. (1993). Tracking loop current eddies with satellite altimetry. *Adv. Space Res.* 13 (11), 325–333. doi: 10.1016/0273-1177(93)90235-4
- Le Hénaff, M., Kourafalou, V. H., Dussurget, R., and Lumpkin, R. (2014). Cyclonic activity in the eastern gulf of Mexico: Characterization from along-track altimetry and *in situ* drifter trajectories. *Prog. Oceanogr.* 120, 120–138. doi: 10.1016/j.pocean.2013.08.002
- Le Hénaff, M., Kourafalou, V. H., Morel, Y., and Srinivasan, A. (2012). Simulating the dynamics and intensification of cyclonic loop current frontal eddies in the gulf of Mexico. *J. Geophysical Res.: Oceans* 117 (C2), C02034. doi: 10.1029/2011JC007279
- Le Traon, P. Y., and Dibarboure, G. (1999). Mesoscale mapping capabilities of multiple-satellite altimeter missions. *J. Atmospheric Oceanic Technol.* 16 (9), 1208–1223. doi: 10.1175/1520-0426(1999)016<1208:MMCOMS>2.0.CO;2
- Le Vu, B., Stegner, A., and Arsouze, T. (2018). Angular momentum eddy detection and tracking algorithm (AMEDA) and its application to coastal eddy formation. *J. Atmospheric Oceanic Technol.* 35 (4), 739–762. doi: 10.1175/JTECH-D-17-0010.1
- Lewis, J. K., Kirwan, A. D., Jr., and Forristall, G. Z. (1989). Evolution of a warm-core ring in the gulf of Mexico: Lagrangian observations. *J. Geophysical Res.: Oceans* 94 (C6), 8163–8178. doi: 10.1029/JC094iC06p08163
- Lian, Z., Sun, B., Wei, Z., Wang, Y., and Wang, X. (2019). Comparison of eight detection algorithms for the quantification and characterization of mesoscale eddies in the south China Sea. *J. Atmospheric Oceanic Technol.* 36 (7), 1361–1380. doi: 10.1175/JTECH-D-18-0201.1
- Lindo-Atchati, D., Bringas, F., and Goni, G. (2013). Loop current excursions and ring detachments during 1993–2009. *Int. J. Remote Sens.* 34 (14), 5042–5053. doi: 10.1080/01431161.2013.787504
- Liu, Y., Weisberg, R. H., Hu, C., Kovach, C. C., and Riethmüller, R. R. (2011). “Evolution of the loop current system during the deepwater horizon oil spill event as observed with drifters and satellites,” in *Monitoring and modeling the deepwater horizon oil spill: A record-breaking enterprise*. Eds. Y. Liu, A. Macfadyen, Z.-G. Ji and R. H. Weisberg. (Washington DC: American Geophysical Union). doi: 10.1029/2011GM001127
- Liu, Y., Weisberg, R. H., Vignudelli, S., and Mitchum, G. T. (2014). Evaluation of altimetry-derived surface current products using Lagrangian drifter trajectories in the eastern gulf of Mexico. *J. Geophys. Res. Oceans* 119, 2827–2842. doi: 10.1002/2013JC009710
- Liu, Y., Weisberg, R. H., Vignudelli, S., and Mitchum, G. T. (2016). Patterns of the loop current system and regions of sea surface height variability in the eastern gulf of Mexico revealed by the self-organizing maps. *J. Geophysical Res.: Oceans* 121, 2347–2366. doi: 10.1002/2015JC011493
- Liu, Y., Weisberg, R. H., Vignudelli, S., Roblou, L., and Merz, C. R. (2012). Comparison of the X-TRACK altimetry estimated currents with moored ADCP and HF radar observations on the West Florida shelf. *Adv. Space Res.* 50, 1085–1098. doi: 10.1016/j.asr.2011.09.012
- Maslo, A., Azevedo Correia de Souza, J. M., and Pardo, J. S. (2020). Energetics of the deep gulf of Mexico. *J. Phys. Oceanogr.* 50 (6), 1655–1675. doi: 10.1175/JPO-D-19-0308.1
- Meunier, T., Pallás-Sanz, E., Tenreiro, M., Portela, E., Ochoa, J., Ruiz-Angulo, A., et al. (2018). The vertical structure of a loop current eddy. *J. Geophysical Res.: Oceans* 123 (9), 6070–6090. doi: 10.1029/2018JC013801
- Meza-Padilla, R., Enriquez, C., Liu, Y., and Appendini, C. (2019). Ocean circulation in the western gulf of Mexico using self-organizing maps. *J. Geophysical Res.: Oceans* 124, 4152–4167. doi: 10.1029/2018JC014377
- Murphy, S. J., Hurlburt, H. E., and O'Brien, J. J. (1999). The connectivity of eddy variability in the Caribbean Sea, the gulf of Mexico, and the Atlantic ocean. *J. Geophysical Res.: Oceans* 104 (C1), 1431–1453. doi: 10.1029/1998JC000010
- Nickerson, A. K., Weisberg, R. H., and Liu, Y. (2022). On the evolution of the gulf of Mexico loop current through its penetrative, ring shedding and retracted states. *Adv. Space Res.* 69 (11), 4058–4077. doi: 10.1016/j.asr.2022.03.039
- Oey, L.-Y., Lee, H.-C., and Schmitz, W. J. (2003). Effects of winds and Caribbean eddies on the frequency of loop current eddy shedding: A numerical model study. *J. Geophysical Res.: Oceans* 108 (C10). doi: 10.1029/2002JC001698
- Okubo, A. (1970). Horizontal dispersion of floatable particles in the vicinity of velocity singularities such as convergences. *Deep Sea Res.* 17 (3), 445–454. doi: 10.1016/0011-7471(70)90059-8
- Paluszkievicz, T., Atkinson, L. P., Posmentier, E. S., and McClain, C. R. (1983). Observations of a loop current frontal eddy intrusion onto the West Florida shelf. *J. Geophysical Res.: Oceans* 88 (C14), 9639–9651. doi: 10.1029/JC088iC14p09639
- Peacock, T., Froyland, G., and Haller, G. (2015). Introduction to focus issue: Objective detection of coherent structures. *Chaos* 25, 087201. doi: 10.1063/1.4928894
- Pegliasco, C., Chaigneau, A., Morrow, R., and Dumas, F. (2021). Detection and tracking of mesoscale eddies in the Mediterranean Sea: A comparison between the Sea level anomaly and the absolute dynamic topography fields. *Adv. Space Res.* 68 (2), 401–419. doi: 10.1016/j.asr.2020.03.039
- Philander, S. G. (1990). *El Niño, la niña, and the southern oscillation* (London: Academic).
- Pichevin, T., and Nof, D. (1997). The momentum imbalance paradox. *Tellus A: Dynamic Meteorol. Oceanogr.* 49 (2), 298–319. doi: 10.3402/tellusa.v49i2.14484
- Pujol, M.-I., Faugère, Y., Taburet, G., Dupuy, S., Pelloquin, C., Ablain, M., et al. (2016). DUACS DT2014: the new multi-mission altimeter data set reprocessed over 20 years. *Ocean Sci.* 12 (5), 1067–1090. doi: 10.5194/os-12-1067-2016
- Rivas, D., Badan, A., Sheinbaum, J., Ochoa, J., and Candela, J. (2008). Vertical velocity and vertical heat flux observed within loop current eddies in the central gulf of Mexico. *J. Phys. Oceanogr.* 38 (11), 2461–2481. doi: 10.1175/2008JP03755.1
- Rodriguez-Vera, G., Romero-Centeno, R., Castro, C. L., and Castro, V. M. (2019). Coupled interannual variability of wind and Sea surface temperature in the Caribbean Sea and the gulf of Mexico. *J. Climate* 32, 4263–4280. doi: 10.1175/JCLI-D-18-0573.1
- Rudnick, D. L., Gopalakrishnan, G., and Cornuelle, B. D. (2015). Cyclonic eddies in the gulf of Mexico. observations by underwater gliders and simulations by numerical model. *J. Phys. Oceanogr.* 45 (1), 313–326. doi: 10.1175/JPO-D-14-0138.1
- Saraceno, M., Strub, P. T., and Kosro, P. M. (2008). Estimates of sea surface height and near-surface alongshore coastal currents from combinations of altimeters and tide gauges. *J. Geophysical Res.: Oceans* 113 (C11), C11013. doi: 10.1029/2008JC004756

- Smith, I., and David, C. (1986). A numerical study of loop current eddy interaction with topography in the Western gulf of Mexico. *J. Phys. Oceanogr.* 16 (7), 1260–1272. doi: 10.1175/1520-0485(1986)016<1260:ANSOLC>2.0.CO;2
- Sturges, W. (1993). The annual cycle of the western boundary current in the gulf of Mexico. *J. Geophys. Res.* 98 (C10), 18053–18068. doi: 10.1029/93JC01730
- Sturges, W., and Leben, R. (2000). Frequency of ring separations from the loop current in the gulf of Mexico: A revised estimate. *J. Phys. Oceanogr.* 30 (7), 1814–1819. doi: 10.1175/1520-0485(2000)030<1814:FORSFT>2.0.CO;2
- Taburet, G., Sanchez-Roman, A., Ballarotta, M., Pujol, M.-I., Legeais, J.-F., Fournier, F., et al. (2019). DUACS DT2018: 25 years of reprocessed sea level altimetry products. *Ocean Sci.* 15, 1207–1224. doi: 10.5194/os-15-1207-2019
- Tenreiro, M., Candela, J., Sanz, E. P., Sheinbaum, J., and Ochoa, J. (2018). Near-surface and deep circulation coupling in the western gulf of Mexico. *J. Phys. Oceanogr.* 48 (1), 145–161. doi: 10.1175/JPO-D-17-0018.1
- Vidal, V. M. V., Vidal, F. V., and Peírez-Molero, J. M. (1992). Collision of a loop current anticyclonic ring against the continental shelf slope of the western gulf of Mexico. *J. Geophysical Res.: Oceans* 97 (C2), 2155–2172. doi: 10.1029/91JC00486
- Vukovich, F. M. (2007). Climatology of ocean features in the gulf of Mexico using satellite remote sensing data. *J. Phys. Oceanogr.* 37 (3), 689–707. doi: 10.1175/JPO2989.1
- Vukovich, F. M. (2012). Changes in the loop current's eddy shedding in the period 2001–2010. *Int. J. Oceanogr.* 18. doi: 10.1155/2012/439042
- Vukovich, F. M., and Crissman, B. W. (1986). Aspects of warm rings in the gulf of Mexico. *J. Geophysical Res.: Oceans* 91 (C2), 2645–2660. doi: 10.1029/JC091iC02p02645
- Vukovich, F. M., and Maul, G. A. (1985). Cyclonic eddies in the Eastern gulf of Mexico. *J. Phys. Oceanogr.* 15 (1), 105–117. doi: 10.1175/1520-0485(1985)015<0105:CEITEG>2.0.CO;2
- Walker, N., Leben, R., Anderson, S., Feeney, J., Coholan, P., and Sharma, N. (2009). *Loop current frontal eddies based on satellite remote sensing and drifter data* (Tech. rep. no. OCS study MMS 2009-023) (New Orleans, LA: U.S. Dept. of the Interior, Minerals Management Service, Gulf of Mexico OCS Region).
- Wallace, J. M., and Gutzler, D. S. (1981). Teleconnections in the geopotential height field during the northern hemisphere winter. *Monthly Weather Rev.* 109 (4), 784–812. doi: 10.1175/1520-0493(1981)109<0784:TITGHF>2.0.CO;2
- Weisberg, R. H., Zheng, L., and Liu, Y. (2017). On the movement of deepwater horizon oil to northern gulf beaches. *Ocean Model.* 111, 81–97. doi: 10.1016/j.ocemod.2017.02.002
- Weiss, J. (1991). The dynamics of enstrophy transfer in two-dimensional hydrodynamics. *Physica D: Nonlinear Phenomena* 48 (2), 273–294. doi: 10.1016/0167-2789(91)90088-Q
- Yang, Y., Weisberg, R. H., Liu, Y., and San Liang, X. (2020). Instabilities and multiscale interactions underlying the loop current eddy shedding in the gulf of Mexico. *J. Phys. Oceanogr.* 50 (5), 1289–1317. doi: 10.1175/JPO-D-19-0202.1
- Zavala-Hidalgo, J., Morey, S. L., and O'Brien, J. J. (2003). Cyclonic eddies northeast of the campeche bank from altimetry data. *J. Phys. Oceanogr.* 33 (3), 623–629. doi: 10.1175/1520-0485(2003)033<0623:CENOTC>2.0.CO;2
- Zhang, T., Hoell, A., Perlwitz, J., Eischeid, J., Murray, D., Hoerling, M., et al. (2019). Towards probabilistic multivariate ENSO monitoring. *Geophys. Res. Lett.* 46, 10532–10540. doi: 10.1029/2019GL083946
- Zhang, Y., Hu, C., Liu, Y., Weisberg, R. H., and Kourafalou, V. H. (2019). Submesoscale and mesoscale eddies in the florida straits: Observations from satellite ocean color measurements. *Geophysical Res. Lett.* 46 (22), 13262–13270. doi: 10.1029/2019GL083999
- Zhu, Y., and Liang, X. (2020). Coupling of the surface and near-bottom currents in the gulf of Mexico. *J. Geophysical Res. Oceans* 125, e2020JC016488. doi: 10.1029/2020JC016488
- Zhu, Y., and Liang, X. (2022). *Characteristics of robust mesoscale eddies in the gulf of Mexico* (Munich, Germany: EGU sphere). doi: 10.5194/egusphere-2022-789



## OPEN ACCESS

## EDITED BY

Julio Sheinbaum,  
Centro de Investigación Científica y de  
Educación Superior de Ensenada  
(CICESE), Mexico

## REVIEWED BY

Zhengguang Zhang,  
Ocean University of China, China  
Junbiao Tu,  
Tongji University, China

## \*CORRESPONDENCE

Alexis Johnson Exley  
✉ [ajohnson1@uri.edu](mailto:ajohnson1@uri.edu)

## SPECIALTY SECTION

This article was submitted to  
Physical Oceanography,  
a section of the journal  
Frontiers in Marine Science

RECEIVED 20 September 2022

ACCEPTED 07 December 2022

PUBLISHED 22 December 2022

## CITATION

Johnson Exley A, Donohue KA,  
Watts DR, Tracey KL and Kennelly MA  
(2022) Generation of high-frequency  
topographic Rossby waves in  
the Gulf of Mexico.  
*Front. Mar. Sci.* 9:1049645.  
doi: 10.3389/fmars.2022.1049645

## COPYRIGHT

© 2022 Johnson Exley, Donohue,  
Watts, Tracey and Kennelly. This is an  
open-access article distributed under  
the terms of the [Creative Commons  
Attribution License \(CC BY\)](https://creativecommons.org/licenses/by/4.0/). The use,  
distribution or reproduction in other  
forums is permitted, provided the  
original author(s) and the copyright  
owner(s) are credited and that the  
original publication in this journal is  
cited, in accordance with accepted  
academic practice. No use,  
distribution or reproduction is  
permitted which does not comply with  
these terms.

# Generation of high-frequency topographic Rossby waves in the Gulf of Mexico

Alexis Johnson Exley\*, Kathleen A. Donohue,  
D. Randolph Watts, Karen L. Tracey and Maureen A. Kennelly

Graduate School of Oceanography, University of Rhode Island, Narragansett, RI, United States

The Loop Current Eddy (LCE) separation cycle energizes deep circulation in the eastern Gulf of Mexico, transferring energy from the surface intensified Loop Current (LC) to the typically quiescent lower layers. To document the generation and radiation of deep energy during this cycle, an array of 24 current and pressure recording inverted echo sounders (CPIES) is deployed in the region 89°W to 86°W, 25°N to 27.5°N with the intent to capture circulation near bathymetric features thought to be important for current-topographic interactions: Campeche Bank, Mississippi Fan, and West Florida Shelf. During the nearly two-year deployment, June 2019 to May 2021, three LCE separation events are observed, during which energy injected into the deep Gulf organizes into two distinct frequency bands ( $1/100 - 1/20 \text{ days}^{-1}$  and  $1/20 - 1/10 \text{ days}^{-1}$ ). High-frequency variability dominates the array's northwest corner in the vicinity of the Mississippi Fan. Wave properties are consistent with topographic Rossby Waves (TRWs) with wavelengths of 150 – 300 km. Their generation coincides with each LCE separation and is attributed to an upper-lower layer resonant coupling between surface meanders and the sloping topography of the Mississippi Fan. TRWs captured by the CPIES array will likely intensify as wavelengths shorten in steeper topography along propagation pathways towards the Sigsbee Escarpment, generating hazardous currents with the potential to disrupt oil and gas operations in the region.

## KEYWORDS

topographic Rossby waves, Gulf of Mexico, Loop Current, deep energy propagation, inverted echo sounders, deep currents

## 1 Introduction

A number of societal factors motivate the need for improved forecasting and a better understanding of Gulf of Mexico Loop Current (LC) system dynamics: extensive energy sector operations in the Gulf, rapidly intensifying tropical storms in response to warming Gulf waters, sea level rise along the densely-populated Florida coast and downstream



impacts on the Gulf Stream (Hirschi et al., 2019). The LC dominates upper-layer circulation in the Gulf. It enters through the Yucatan Channel and exits through the Florida Straits, evolving from a port-to-port mode to an extended mode, penetrating up over the Mississippi Fan. Occasionally, the LC pinches off and sheds a large 200 – 400 km Loop Current Eddy (LCE) which can detach and reattach multiple times before a final separation and subsequent westward translation across the Gulf. The deep layers of the eastern Gulf (>1000 m) have been characterized as relatively quiescent during the port-to-port mode. In contrast, when the LC advances, the deep circulation is energized through topographic interactions and LC instabilities (Donohue et al., 2016).

In the early 1990s, oil and gas operators recognized that bursts of strong deep currents arrive along the deep continental slope without warning. Prompted by this risk to operations, a series of observational studies were funded by Minerals Management Service, now Bureau of Ocean and Energy Management (BOEM) to directly measure and diagnose these deep currents. Hamilton (1990) attributes these strong bottom-intensified fluctuations with frequencies between  $1/40 - 1/20 \text{ days}^{-1}$  to topographic Rossby waves (TRWs). Coherence between sites suggests a westward propagation with group velocity of about  $9 \text{ km day}^{-1}$  hypothesized to originate under LC meanders over the Mississippi Fan. Hamilton and Lugo-Fernandez (2001) builds upon this work using observations from Sigsbee Escarpment where lower-layer variability is found to be higher frequency ( $1/20 - 1/10 \text{ days}^{-1}$ ) and exceptionally more energetic than in other regions of the deep Gulf.

Oey and Lee (2002) establishes a direct link between the LCE separation process and TRWs by using a numerical simulation of the Gulf of Mexico. Deep variability is consistent with observations with spectral peaks in the  $1/100 - 1/20 \text{ day}^{-1}$  frequency band. This work identifies regions where a sufficient topographic slope to support the propagation of TRWs coincides with both bottom intensification and significant eddy kinetic energy in the equivalent periodicity band. Energy paths produced by a TRW ray-tracing model align with these TRW active regions along the northern slope of the Gulf and, when traced backward, are found to originate under the LC and LCEs. This work establishes the LC as an energy source for TRWs propagating along the northern slope of the Gulf of Mexico.

A major finding from numerical results is the funneling of ray paths towards the Sigsbee Escarpment (Oey and Lee, 2002), resulting from the presence of deep currents and wave refractions over steep topography. This region therefore plays an important role in determining downstream propagation as refraction will alter wave characteristics and can locally intensify the currents. Observations of lower-layer currents at the escarpment are made by Hamilton (2007) using an array of five moorings deployed along and just straddling the slope. High energy fluctuations typical of TRWs with dominant frequencies of  $1/14 - 1/8 \text{ days}^{-1}$  and maximum speeds nearing  $100 \text{ cm s}^{-1}$  are

measured with high coherence along and at the base of the escarpment. Only very high energy events are able to penetrate inshore of the escarpment, confirming that steep topography acts as a barrier by refracting and possibly reflecting high-frequency energy back into the deep Gulf. Another significant result from Hamilton's work is a relatively persistent, yet distinct series of wave trains traveling through the escarpment, all with unique frequencies occurring during different stages of the LC shedding process. This provides evidence that energy transfer can occur under a number of dynamic conditions and originate from many locations across the eastern Gulf.

While ray tracing evinces a link between the LC and TRWs (Oey and Lee, 2002; Hamilton, 2007), the dynamics by which that energy transfers to lower layers remains an outstanding question. A complicating factor is that deep energy likely originates from many different locations around the eastern Gulf. A relatively well documented process is the generation of deep energy through baroclinic instabilities in growing upper layer Loop Current meanders during LCE separation. Below the main thermocline, this eddy kinetic energy (EKE) manifests as anticyclones and cyclones with frequencies in the  $1/100 - 1/40 \text{ day}^{-1}$  band (Donohue et al., 2016). A number of studies attribute the radiation of energy away from the baroclinic instability regions to westward propagating TRWs. Oey (2008) uses a high resolution numerical model to study the generation of deep eddies by baroclinic instabilities, concluding that TRWs are excited by a simple linear eddy-wave coupling mechanism over shoaling topography. Hamilton (2009) argues that observed coherence between upper and lower layer relative vorticity fluctuations in the  $1/35 - 1/20 \text{ day}^{-1}$  frequency band, where the lower layer leads upper meanders by a  $90^\circ$  phase offset, is characteristic of a baroclinic instability mechanism. Further evidence is provided by Hamilton et al. (2019) who use an aggregate of floats in the Gulf to observe a significant increase in deep EKE generated intermittently by meanders of the LC and LCE detachments, similar to what is observed by Donohue et al. (2016). They argue that radiation of this energy through TRWs is supported by observations of large amplitude, rectilinear oscillations just west of a retracting LC or departing LCE.

A hypothesis of TRW generation suggests that LC interactions with topography triggers a transfer of energy to the lower layer, generating perturbations through potential vorticity adjustments over a sloping bottom depth (Malanotte-Rizzoli et al., 1987; Hamilton, 1990). Viable topographic features in the Gulf of Mexico include the Mississippi Fan and the continental slope surrounding West Florida Shelf and Campeche Bank. This mechanism is thought to generate energy across a broad range in frequencies and is frequently proposed as a TRW forcing mechanism in the Gulf owing to observations of characteristic motion with frequencies spanning  $1/100 - 1/10 \text{ days}^{-1}$  (Hamilton, 1990; Hamilton and Lugo-Fernandez, 2001; Hamilton, 2007). A similar mechanism that likely works in concert with LC pulsations over topography is a



potential vorticity adjustment in response to a squashing of the lower layer by an advancing LC front. [Hamilton et al. \(2019\)](#) observes a number of anticyclones north of the Campeche Bank that intensify under the northward extension of the LC and dissipate once the LC becomes stationary or retreats. They hypothesize that deep anticyclones are dispersed into radiating TRWs once the lower layer compression stops but are unable to detect the radiation from observations.

Another deep energy generation mechanism that has been proposed to radiate TRWs in the Gulf is an upper-lower layer resonant coupling first described by [Malanotte-Rizzoli et al. \(1995\)](#). This theory suggests that deep energy will be generated by an upper layer meander that has a frequency and wavenumber that projects onto the TRW dispersion relation local to the bottom slope and stratification. Resulting lower layer flows will couple to the upper, generating TRWs of equivalent frequency and wavelength that are free to propagate away from the coupling region. [Pickart \(1995\)](#) shows this is a viable generation mechanism for TRWs observed by a mooring array off Cape Hatteras. Offshore of this region, Gulf Stream meanders are predominantly eastward, so in order for coupling to occur, strongly sloped bathymetry must be oriented in a northerly (meridional) direction to generate an eastward component of phase speed at depth. Observed  $1/40\text{-day}^{-1}$  TRWs are traced backward to a region of the Gulf Stream where the most commonly occurring meanders have a matching frequency and fit one component of the dispersion relation. In the Gulf of Mexico, meanders in the LC are analogous to the Gulf Stream and while many studies have proposed this theory as a TRW generation mechanism, none have been able to identify the coupling and subsequent propagation.

While observations of the deep circulation in Gulf of Mexico have increased substantially, a number of questions related to TRW pathways and generation mechanisms remain unanswered. An array of 24 bottom mounted current and pressure recording inverted echo sounders (CPIES) located across the eastern Gulf of Mexico is ideally positioned to address a number of these unknowns. This array, funded by the National Academies of Science, Engineering and Medicine under the Understanding Gulf Ocean Systems initiative (UGOS), was deployed from June 2019 to May 2021 and expanded to the north, west, and south beyond the BOEM funded Observations and Dynamics of the Loop Current (DynLoop) PIES array recovered in 2011. This work will focus on propagation and generation mechanisms of the high-frequency ( $1/20 - 1/10 \text{ day}^{-1}$ ) energy observed by the array.

## 2 Data and methods

The array consists of 24 CPIES mounted on the seafloor in the central Gulf of Mexico ([Figure 1](#)) for nearly two years, June 2019 - May 2021. Extending from  $25^{\circ}\text{N}$  to  $27.5^{\circ}\text{N}$ ,  $86^{\circ}\text{W}$  to  $89^{\circ}\text{W}$ , instruments are spaced approximately 60 km apart, a distance chosen based on known correlation length scales from previous Gulf experiments. The array allows for mapping of the circulation at mesoscale resolution and its size is designed to cover the entire LCE detachment area while expanding upon the DynLoop PIES array recovered in 2011 ([Hamilton et al., 2015](#)).

The inverted echo sounder emits a sound pulse at 12 kHz and measures the acoustic round trip travel time from the sea

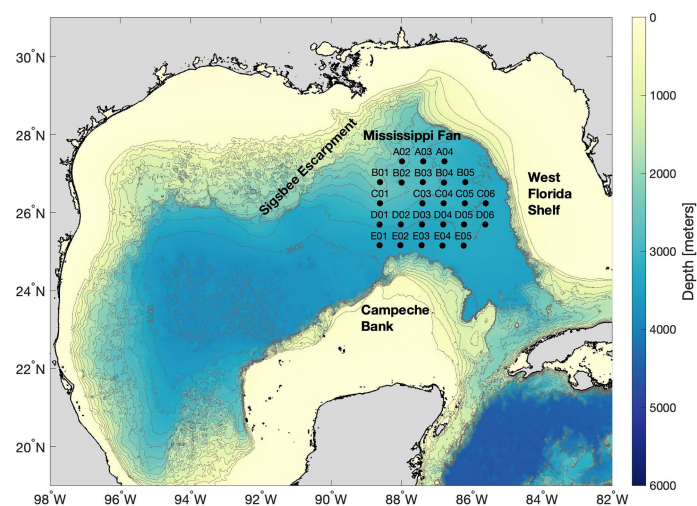


**FIGURE 1**  
The Understanding Gulf Ocean Systems array comprised of 24 CPIES deployed June 2019 and recovered May 2021 in the eastern Gulf of Mexico. Locations of the CPIES are denoted by black circles and labeled. Bathymetry is contoured every 250 meters.

floor to the surface and back,  $\tau$  (Watts and Rossby, 1977). Using empirical relationships developed with historical hydrography,  $\tau$  provides an estimate of the vertical temperature, salinity and density structure. The IES was configured for four pulses every 10 minutes and data are processed through a two step windowing and median filtering process to get hourly measurements (Kennelly et al., 2022). Housed within the instrument, a pressure gauge measures bottom pressure every 30 minutes. Tidal signals are removed following Munk and Cartwright (1966) and pressures are dedrifted and leveled to the same geopotential surface as in Donohue et al. (2010). As in Donohue et al. (2010) a basin wide signal, termed common mode, is removed. Both  $\tau$  and pressure are 72-hour low pass filtered and subsampled at 12-hour increments.

Current magnitude and direction are measured outside the bottom boundary layer at 50 m from the seafloor. Samples are taken every 30 minutes. The record is corrected for the local magnetic declination and the sound speed applicable to each instrument depth. Corrected zonal and meridional velocities are subsequently 72-hour low pass filtered and subsampled at 12-hour increments. A thorough description of CPIES instrumentation, data processing,  $\tau$ -derived fields and mapping techniques may be found in Donohue et al. (2010) and, for PIES in the Gulf, Hamilton et al. (2015)

To convert  $\tau$  measurements to profiles of temperature, salinity and specific volume anomaly, we utilize the Gravest Empirical Mode (GEM) representation (Meinen and Watts, 2000). The GEM exploits the relationship between the integrated speed of sound to known profiles of temperature and salinity from historical hydrography to create a look up table for measured  $\tau$  values. Detailed treatment of the Gulf of Mexico GEM can be found in Hamilton et al. (2015) and Donohue et al. (2016). The Gulf of Mexico GEM was originally established for the Exploratory Study of Deepwater Currents in the Gulf of Mexico (Donohue et al., 2006) expanded upon for the DynLoop study (Hamilton et al., 2015) and now expanded upon further for the UGOS Initiative. Previously, the hydrographic data set accumulated for the Gulf of Mexico GEM consisted of 1136 casts, extending to at least 1000 dbar and representing about 30 years of sampling (Hamilton et al., 2015). The most recent update includes 98 CTD casts taken during deployment, telemetry and recovery and an additional 9984 Argo profiles spanning 2003 to 2021. The GEM is now based upon 11218 hydrocasts, of which more than 4400 extend to 2000 dbar.

Absolute sea surface height is calculated by summing a reference level sea surface height,  $SSH_{ref}$ , with a baroclinic sea surface height,  $SSH_{bcb}$ . Reference level sea surface height is bottom pressure divided by gravity and bottom density:  $SSH_{ref} = P_{ref}/\rho_{bg}$ . Baroclinic sea surface height is geopotential height referenced to zero at the bottom divided by gravity, where geopotential is estimated from measured  $\tau$  and the empirical lookup table for specific volume anomaly:  $SSH_{bcb} = \phi_{bcb}/g$ . Together we obtain the absolute sea surface height as

$$SSH_{abs} = SSH_{ref} + SSH_{bcb}$$

This calculation of sea surface height from CPIES has been shown to compare well to a long track altimetric SSH anomaly data in the Gulf of Mexico (Hamilton et al., 2015; Donohue et al., 2016).  $SSH_{ref}$  and  $SSH_{bcb}$  are mapped at 12-hour intervals using objective analysis techniques (Bretherton et al., 1976). For this application, bottom pressure maps are created using inputs from both pressure and near-bottom velocities (Watts et al., 2001). This multivariate optimal interpolation approach constrains pressure and velocity to be geostrophic and the addition of the velocity sharpens gradients. As described in Hamilton et al. (2015), two-stage mapping is applied to both  $SSH_{ref}$  and  $SSH_{bcb}$ . For  $SSH_{ref}$ , first a 20-day low-passed field is mapped with correlation length scale of 70 km. Then an anomaly field is mapped with a correlation scale of 65 km. For  $SSH_{bcb}$ , the data are first 40-day low passed and mapped with a 170 km correlation length scale and the anomaly is mapped with a 60 km correlation length scale.

Near real time sea surface height data from Copernicus Marine Service provide a wider regional context of the upper-ocean circulation during the study period. The gridded altimeter product is estimated by optimal interpolation, merging data from all altimeter missions: Jason-3, Sentinel-3A, HY-2A, Saral/AltiKa, Cryosat-2, Jason-2, Jason-1, T/P, ENVISAT, GFO, and ERS1/2. This global mapped daily product has 25 km horizontal resolution. In this product, the position of the LC is indicated by a single 0.65 cm contour, a SSH value closely aligned with the edge of the LC. This contour is used to calculate Loop Current area, a metric used to quantify the extension of the LC into the Gulf. Detachment of LCEs is identified as a breaking of the 0.65 cm SSH contour and an abrupt decline in LC area.

### 3 Regional circulation June 2019 – May 2021

Three LCEs, Sverdrup Thor and Ursa, separate from the core of the LC during the CPIES deployment. The final detachment of Eddy Sverdrup occurs just days into the deployment and thus only a small portion of the LCE separation process is observed. We therefore mainly focus on the subsequent two LCE separations, Eddy Thor and Eddy Ursa. While both LCEs eventually separate and propagate off to the west, the events are notably distinct in a number of ways. This includes the number of preliminary detachments, pinch off locations, position of large meanders in both the LC and on the periphery of detached eddies and the generation and propagation of deep energy across the array. To illustrate these differences during the LC separation events and highlight the relationship between upper layer fluctuations and deep energy, maps of  $SSH_{ref}$  (deep pressure scaled as sea surface height) and LC position are plotted at five to eight day intervals spanning the time of LC advancement to final separation (Figures 2, 3).

### 3.1 Eddy Thor: January to July 2020

The LC extends into the central Gulf and over the Mississippi Fan until the first detachment of LCE Thor in mid-to-late January, 2020 (Figure 2). During this period, a few small amplitude perturbations are observed in the deep fields with some indication of topographically controlled propagation; note the progression of a low pressure band from northeast corner of the array from January 1st - January 8th. Nevertheless, deep energy remains weak during the first detachment and reattachment. Perturbations intensify after the first detachment of Thor which occurs to the south of the array in early February. During this time, a sizable meander appears along the northern edge of the LCE which continues to grow even after the LCE reattaches in mid-March. Beneath the meander trough, a deep cyclone intensifies and is accompanied by a strengthening anticyclone, indicating deep energy generation presumably

through baroclinic instability. These deep perturbations begin to dissipate in late March followed by the final separation of LCE Thor, which pinches off in the southeast corner of the array and quickly propagates off to the west and outside the array. A small surface anticyclone is shed from the LC in mid-April once the LCE has fully separated. It propagates along the West Florida Shelf, just outside the periphery of the array and does not appear to generate any notable perturbations in the deep. By mid-June, Thor has propagated away, the LC has retracted and the deep returns to a nearly quiescent state.

### 3.2 Eddy Ursa: January to May 2021

The LC propagates onto the Mississippi Fan in January, 2021 and remains in the extended state until it begins to pinch in on itself in early February (Figure 3). During this time, deep fields

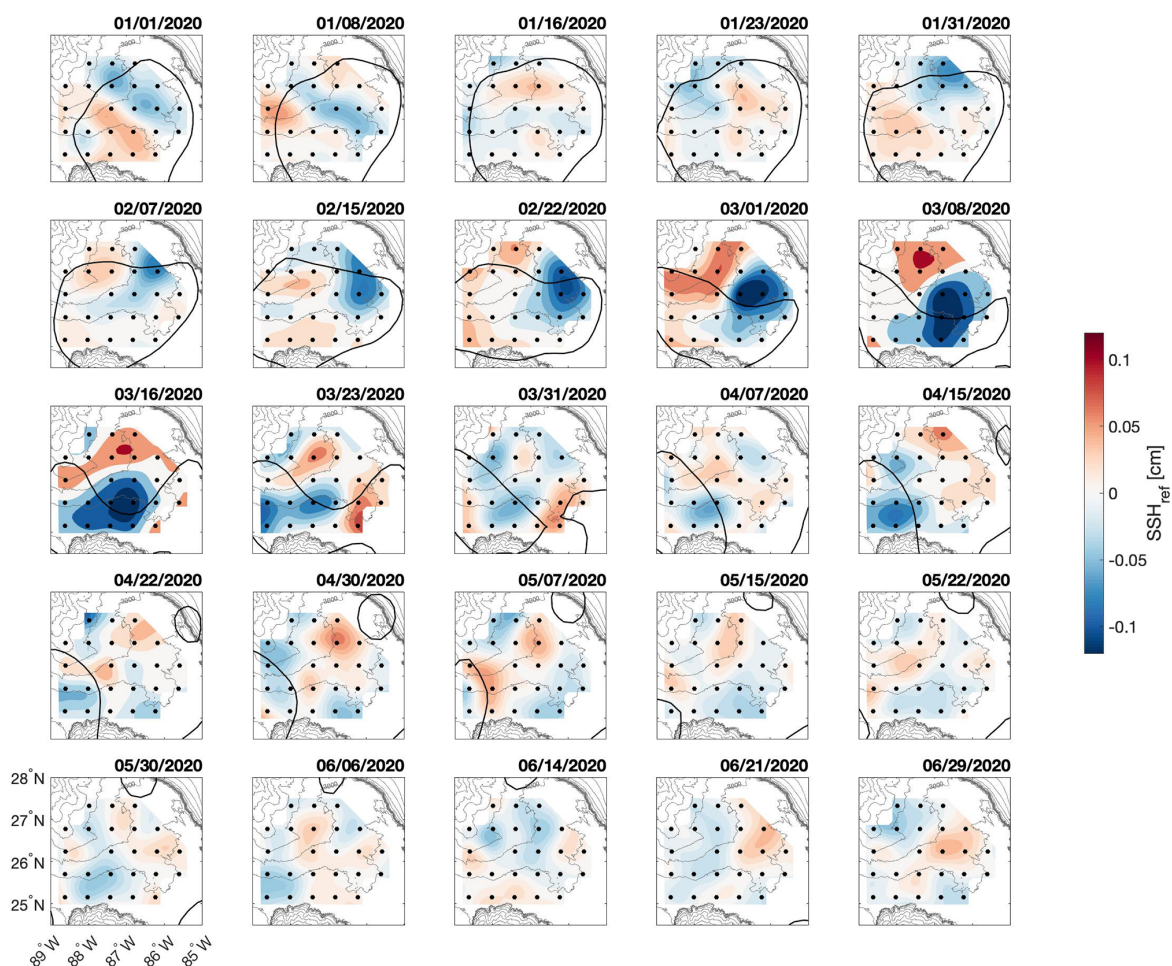


FIGURE 2  
Mapped deep pressure fields,  $SSH_{ref}$ , at seven to eight-day intervals during LCE Thor shedding event, January-June 2020. The bold SSH contour represents the location of the LC. CRIES locations are marked by black circles and bathymetry is contoured in light gray every 250 meters.



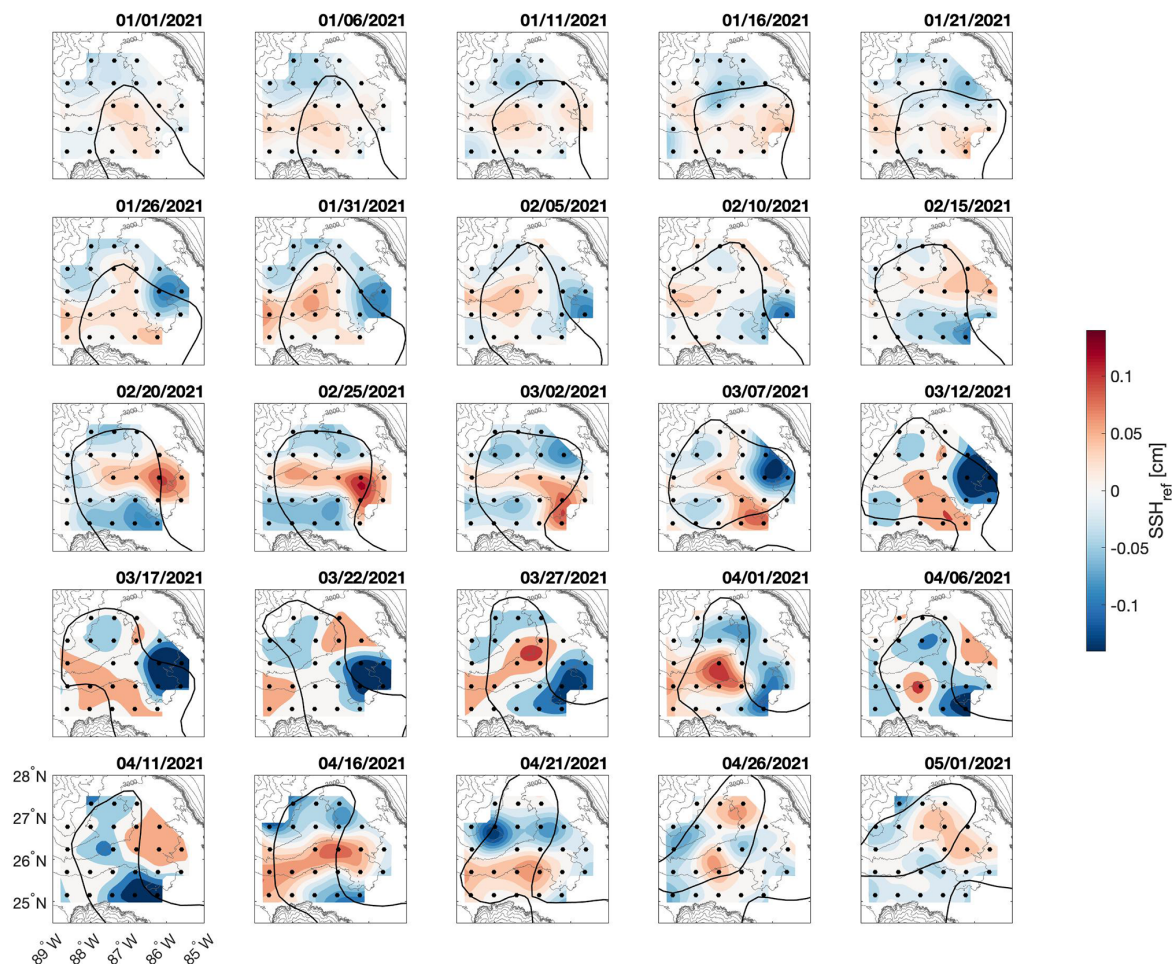


FIGURE 3  
Mapped deep pressure fields  $SSH_{ref}$  at five-day intervals during LCE Ursa shedding event, January–May 2021. The bold SSH contour represents the location of the LC at each time step. CPIES locations are marked by black circles and bathymetry is contoured in light gray every 250 meters.

are fairly quiescent with a small amplitude cyclone intensifying under the meander trough associated with the necking down phase of the separation. This deep low travels southward under the meander until it propagates outside the array. In late February, an anticyclone appears under this eastward arm of the LC just downstream of the meander crest, a possible indication of a brief baroclinic instability setup before the LC pinches in on itself in early March. The LCE briefly detaches, during which a larger amplitude cyclone begins to form under the eastern side of the eddy. The amplitude of this perturbation continues to grow while it remains relatively in place and the LCE reattaches. For the remainder of the study period, the LC is characterized by large fluctuating meanders. In the deep, the large amplitude cyclone propagates southward beneath the meander trough and is eventually accompanied by a strong anticyclone in late March. This setup precedes the development of a steep meander in the LC which initiates a pinching off phase

until the end of our study period when the array is recovered in early May. During this time, amplitudes of the deep perturbations are decreasing as these layers of the eastern Gulf return to their relatively quiescent state.

## 4 Deep energy distribution

In the eastern Gulf the LC and the detachment of LCEs are the main suppliers of energy to the deep, generating deep EKE through baroclinic instabilities and forcing TRWs along the continental slope. The CPIES array captures the generation of deep EKE, calculated as  $\frac{1}{2}(u'^2 + v'^2)$  where primes denote deviation from the time mean, under the mean position of the eastward arm of the LC (Figure 4A). Time-averaged EKE peaks between approximately 25°–27°N, 86°–87°W, similar but slightly west of what was observed by Donohue et al. (2016).

A band of slightly intensified EKE extends out along 26°N suggesting a pathway of deep energy propagation. The time-averaged velocity field also identifies similar features to Donohue et al. (2016), including a deep cyclone centered near 26.8°N, 86°W, slightly north of previous observations, and a broad anticyclonic circulation around 26°N, 87.6°W. Another cyclone is centered near 26.9°N, 88°W, a region outside the bounds of the previous array. The influence of LCE separation events on deep energy is evident from the array-averaged deep EKE, peaking during each detachment (Figures 4B, C). During the first few days of deployment, Eddy Sverdrup separates from the LC corresponding to a sharp decline in energy, followed by a

slower decline over the subsequent months. The formation of Thor is unique as the deep EKE fields remain weak as the LC advances and Thor detaches for the first time. It seems likely that the deep EKE generated during the first detachment isn't captured within the array as the detachment point is south of the array. Deep EKE does peak just prior to reattachment and declines again after the final separation. During LCE Ursa formation, deep energy increases during the first necking-down phase of separation and remains high throughout the remainder of the study period.

The spectral content of energy generated in the deep layers of the Gulf is found to vary across the array, organized into two

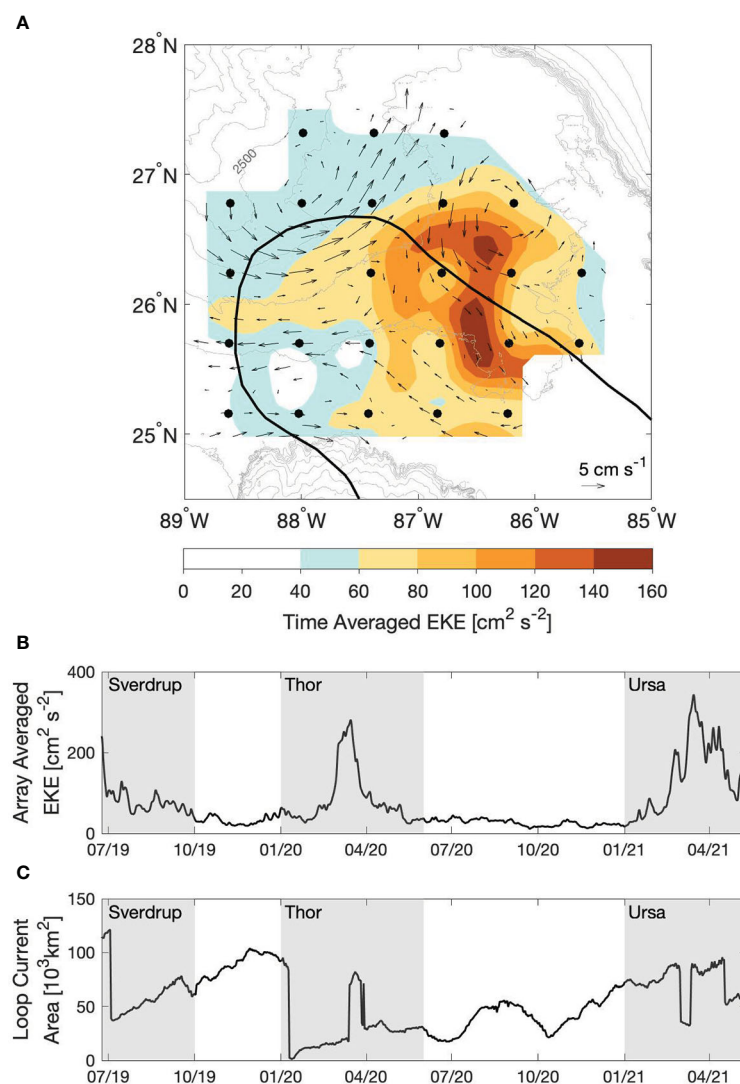


**FIGURE 4**  
Deep eddy kinetic energy and current vectors (A), time averaged over the study period. The bold SSH contour represents the mean position of the LC. CPIES are denoted by black circles and bathymetry is contoured in gray every 250 meters. The array-averaged eddy kinetic energy (B) is compared against the LC Area (C), derived from satellite SSH. Formation time-frames for LC Eddies Sverdrup, Thor and Ursa are highlighted by gray boxes.



distinct frequency bands (Figure 5). The southeastern region of the array is dominated by low frequency fluctuations within the  $1/100 - 1/20 \text{ day}^{-1}$  band and devoid of energy at higher frequencies. Much less low frequency energy is found in the northwestern portion of the array which is instead characterized by a distinct peak between  $1/20 - 1/10 \text{ days}^{-1}$ . Motivated by these discrete spectral bands of  $\text{SSH}_{ref}$ , the distribution of variance is mapped as a function of frequency (Figure 6). While nearly an order of magnitude smaller, spatial variance in the  $1/100 - 1/20 \text{ day}^{-1}$  band reflects that of the total distribution. Variance peaks near  $26^\circ\text{N}$ ,  $86^\circ\text{W}$ , centered slightly east of the region of maximum EKE and north of the mean position of the LC. Another region of enhanced low frequency variance is also found along the southeast edge of

the array. This overall pattern is similar to what was identified by Donohue et al. (2016) and attributed to deep eddies generated by instabilities under meanders of the LC. In contrast, a band of high-frequency ( $1/20 - 1/10 \text{ day}^{-1}$ ) variance is found along the base of the Mississippi Fan while almost no variance is found in the southeast corner of the array where the low frequencies had maxima. Maximum variance in the  $1/20 - 1/10 \text{ day}^{-1}$  band is about an order of magnitude smaller than that of the low frequency, with maximum values near  $26.2^\circ\text{N}$ ,  $88.4^\circ\text{W}$ .

We focus here on the deep high-frequency energy which did not receive attention in previous DynLoop studies. We hypothesize that the band of  $\text{SSH}_{ref}$  variability along the base of the Mississippi Fan is representative of propagating TRWs. Energetic TRWs within this frequency band have been shown to

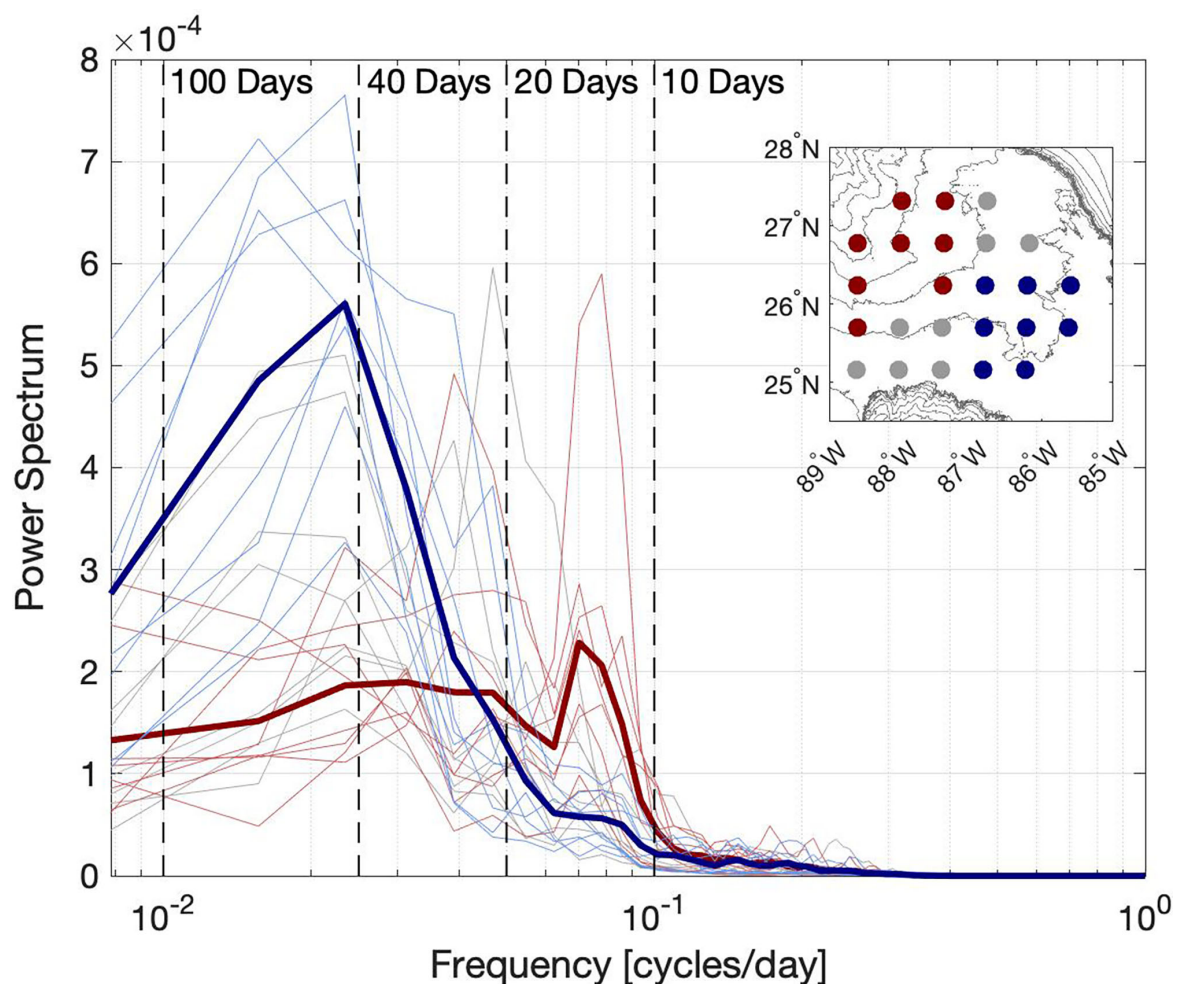


FIGURE 5

Variance-preserving spectra for CPIES bottom pressures,  $\text{SSH}_{ref}$  in the southeastern (blue) and northwestern corner of the array (red). Remaining instruments are in gray. Individual instruments are in light shades and area averages are in dark bold colors. Frequency limits, labeled by their corresponding period, are denoted by dashed vertical lines. Inset identifies sites in the southeastern (blue), northwestern (red) and remaining groups.

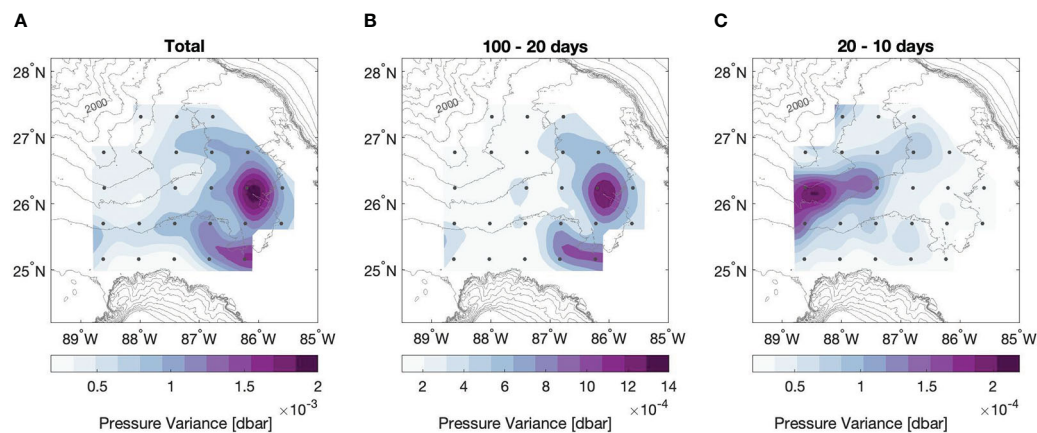


FIGURE 6

Deep pressure variance across all frequency bands (A), in the  $1/100 - 1/20 \text{ day}^{-1}$  frequency band (B) and in the  $1/20 - 1/10 \text{ day}^{-1}$  frequency band (C). Variance range is unique to each panel, decreasing from left to right. CPIES locations are marked by black circles and bathymetry is contoured in light gray every 250 meters.

dominate deep current variability at the Sigsbee Escarpment and, when traced backward are found to radiate from this region of high variability (Hamilton, 2007). These new UGOS observations progress further and indicate, as shown next, that TRWs can originate within the LCE formation region and propagate towards the escarpment.

## 5 Deep energy radiation

To diagnose the origin of observed high-frequency spatial variability propagating along the base of the Mississippi Fan, we consider characteristics of TRWs derived from the dispersion relation and linear wave equations. TRWs are bottom trapped, meaning the amplitude of fluctuations increases with depth and is strongest just outside the bottom boundary layer. The degree of bottom trapping is inversely proportional to the wavelength, stratification and bottom slope (e.g. Pickart, 1995). Phase and group velocity in the northern hemisphere are to the right of increasing water depth, with phase velocity mainly along the direction of increasing water depth. Group velocity is roughly perpendicular to phase velocity, generally oriented along bathymetric contours. TRWs are refracted by a change in the magnitude of bottom slope such that group velocity trends slightly upslope in regions of weak bottom slope, and alternatively is more nearly along the bathymetry in regions of steeper slope.

While the instruments do not provide any vertical information to identify evidence of bottom trapping, the horizontal resolution of the CPIES array allows us to explore phase and group characteristics in relation to bathymetry. A complex EOF analysis (CEOF) is used to diagnose dominant

spatial and temporal patterns of the high-frequency propagation across the array. The CEOF is applied to the full two-year record of  $1/20 - 1/10 \text{ day}^{-1}$  band-passed  $\text{SSH}_{ref}$  to produce a normalized spatial amplitude, phase propagation and temporal amplitude coefficients (Figure 7). Propagation is in the direction of increasing phase and is only plotted in regions where the normalized spatial amplitude is greater than 0.3. A similar use of a Hilbert transform to compute CEOFs from a scalar field can be found in Trenberth and Shin (1984). We focus exclusively on the first mode, accounting for 51% of the variance.

The normalized spatial amplitude (Figure 7A) identifies a propagation pathway similar to what is observed by the high-frequency variance distribution (Figure 6C). Propagation is from the northeast corner of the array to the southwest, bending around the topography of the Mississippi Fan. Amplitude is the highest along the western side of the array, near  $26.2^\circ\text{N}$ ,  $88.4^\circ\text{W}$ . The phase gradient illustrates the magnitude and direction of phase propagation across the array. The largest phase speeds are found along the northern side of the array where the bathymetric slope begins to steepen along the Mississippi Fan. In a narrow region near  $88.0^\circ\text{W}$  (sites A02 and B02) propagation is to the south-southeast, turning westward along the band of highest amplitude and slowing as it approaches  $88.7^\circ\text{W}$  along the western side of the array. Variance ellipses of the  $1/20 - 1/10 \text{ day}^{-1}$  band-passed near bottom velocities at each CPIES site again illustrate how little high-frequency energy is found in the southeast corner of the array. In contrast, in the northwest corner, ellipses are rectilinear with the principal axis generally oriented along the bathymetry.

We identify a number of characteristics from the high-frequency CEOF that agree with TRW linear ray theory. The phase propagation around the Mississippi Fan in the region of

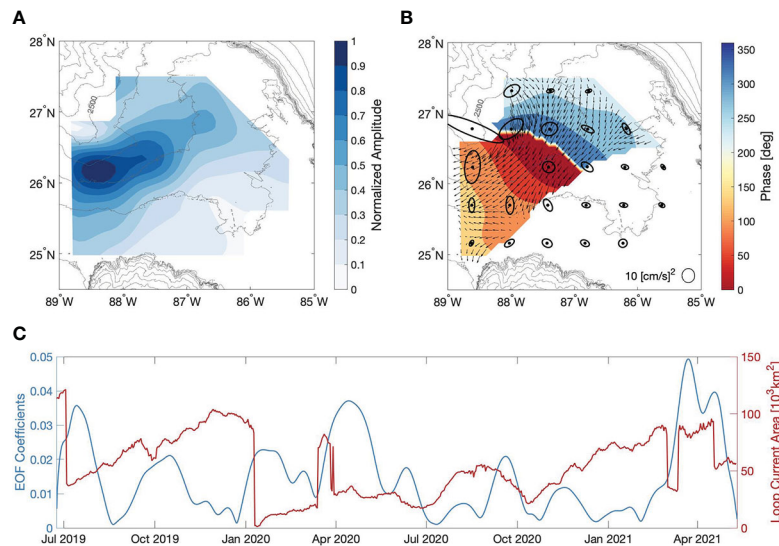


FIGURE 7

Normalized spatial amplitude (A) and phase in degrees (B) derived from CEOF of  $1/20 - 1/10 \text{ day}^{-1}$  band-passed reference sea surface height,  $\text{SSH}_{ref}$ , during the full two year deployment. Phase is plotted for regions where the spatial amplitude is greater than 0.3. Propagation direction indicated by the phase gradient (arrows). CPIES locations are marked by closed black circles surrounded by  $1/20 - 1/10 \text{ day}^{-1}$  band-passed variance ellipses. Bathymetry is contoured every 250 meters. CEOF amplitude time series (C; blue) and LC Area (C; red) derived from satellite altimetry.

significant spatial amplitude is clearly oriented with shallow water to the right. Within this region, over the steepening bathymetric slope of the Mississippi Fan, the maximum TRW frequency,  $\omega \geq (N|\Delta h|)/\tanh(Nhk/f)$ , is  $1/10 \text{ days}^{-1}$  and therefore able to support these high frequency observations. In contrast, maximum frequencies in the southeast corner of the array, where observed  $1/20 - 1/10 \text{ day}^{-1}$  variance is weak, range from  $1/30 - 1/40 \text{ days}^{-1}$  owing to the more gradual bathymetric slope. Within the high amplitude region, we also identify a number of CPIES sites where the direction of phase propagation is oriented perpendicular to the principal axis of the independently measured variance ellipses, confirming a plane-wave like propagation. Additionally, the steepest bathymetric slope coincides with the largest phase speeds in the northern portion of the array around  $27^\circ\text{N}$ ,  $88^\circ\text{W}$ . Here, we find phase direction oriented more offshore and variance ellipses roughly aligned with bathymetry. Approximate wavelengths of  $150 - 300 \text{ km}$  with phase speeds of  $10 - 12 \text{ km d}^{-1}$  are estimated from the phase gradient, values consistent with both linear wave theory and observations of TRWs with frequencies in the  $1/100 - 1/10 \text{ day}^{-1}$  range in the Gulf of Mexico.

The time series of EOF coefficients (Figure 7C) illustrates peaks in high-frequency energy are closely associated with the LC cycle, where an abrupt decline in LC area indicates a shedding event. We find three major peaks in  $1/20 - 1/10 \text{ day}^{-1}$  energy, each following a LCE formation event, in July 2019, April 2020 and March – May 2021. This suggests the LCE shedding process is responsible for generating high-frequency

TRWs. We also find a peak in high-frequency energy near Jan-Feb 2020, after the first separation of LCE Thor. The area-averaged EKE, dominated by low frequencies, did not have a peak at this time (Figure 4). Additional smaller peaks are found throughout the study period, such as Oct 2019 and Oct 2020, appearing to be dissociated with the LCE separation process and sometimes occurring when the LC is in a retracted state. These remotely-generated TRW wave trains could arise from LC interaction with topography or baroclinic instabilities that occur outside the array.

## 6 Deep energy generation

It is well understood that energy injected into the deep Gulf by the LC propagates along the northern continental slope as TRWs (Oey and Lee, 2002; Hamilton, 2007; Hamilton, 2009). The dynamics by which energy is transferred to the deep remains difficult to observe, a consequence of numerous generation mechanisms that can act in different locations across the eastern Gulf. Baroclinic instabilities under the eastward meandering arm of the LC has been shown to generate significant eddy kinetic energy in the deep (Donohue et al., 2016), produced by a forced upper/deep coupling. The process by which this energy reorganizes and radiates into freely propagating TRWs remains to be understood. It has been proposed that these deep eddies organize into TRWs through linear eddy-wave coupling (Oey, 2008), and while

observations have not confirmed this process, [Hamilton et al. \(2019\)](#) uses characteristic Lagrangian float behavior to argue that energy is radiated away from the baroclinic instability regions as TRWs. Deep eddy generation through potential vorticity adjustments in response to LC advancement over the Mississippi Fan or compression of the lower layer by the LC front has been shown to produce deep energy in numerical models ([Le Hénaff et al., 2012](#)) and in float observations ([Hamilton et al., 2019](#)). Energy radiation by TRWs is hypothesized but not confirmed by observations. Finally, an upper-lower layer resonant coupling has been shown to generate TRWs originating from eastward meanders in the Gulf Stream ([Pickart, 1995](#)). Numerous studies have speculated that meanders of the LC, analogous to the Gulf Stream, should generate TRWs, however observations have not yet confirmed this coupling.

Unlike observations of TRWs, which have been confirmed across the Gulf, observations of their generation mechanisms are much more difficult. Few studies have conclusively linked generation to propagation, a consequence of the difficulty in observing these episodic and non-stationary processes by moorings and Lagrangian floats. Our array, ideally situated across the eastern Gulf of Mexico, is at an advantage to capture the transfer of energy and subsequent propagation of these bottom trapped waves.

We focus here on deep energy generation during the period of LCE Ursa formation and detachment. We focus only on a single time period for a few reasons: 1) the Ursa detachment produces the highest amount of energy in the  $1/20 - 1/10 \text{ day}^{-1}$  frequency band, 2) generation and propagation appears local to the array during this time period, 3) previous detachments generate deep energy across and outside the array with high variability in both time and space and 4) by focusing on a single time period we aim to isolate a single generation mechanism.

During LCE Ursa formation, the first advancement of the LC onto the Mississippi Fan does not generate strong fluctuations in the  $1/20 - 1/10 \text{ day}^{-1}$  frequency band ([Figure 8](#)). It is not until the first necking-down phase of separation, sometime around February 20th, that small amplitude perturbations are observed around the western perimeter of the LC. These perturbations increase in magnitude over the next few days corresponding to the initial detachment of LCE Ursa. Following reattachment on March 12th, deep, high-frequency fluctuations intensify under a strong meander of the LC in the northeast corner of the array and propagate as wave-like (alternating high-low  $\text{SSH}_{\text{ref}}$ ) perturbations to the west-southwest around the Mississippi Fan. This pattern continues through the second necking down phase, until around April 21st when the eastern arm pinches in on itself over the southern portion of the array. The pattern of propagation from the northeast corner of the array resembles that of [Figure 7](#), suggesting this high-frequency energy can be attributed to TRWs.

A coupled upper and lower layer CEOF calculated during the time period of LCE Ursa formation and separation (January

– May 2021) is used to illustrate cohesive fluctuations and phase propagation jointly in upper ocean meanders and deep perturbations. The upper field is represented as  $\text{SSH}_{\text{bcb}}$  and the lower as  $\text{SSH}_{\text{ref}}$ . Both full time series are band-passed filtered in the  $1/20 - 1/10 \text{ day}^{-1}$  frequency band, scaled by their respective variance and concatenated into a single input for the CEOF. The output is remapped into the four panels shown in [Figure 9](#). In the upper layer, we find highest spatial amplitudes ([Figure 9A](#): dark gray) around the perimeter of the LC and the briefly detached LCE Ursa (LC position plotted in purple in the upper panels). The phase ([Figure 9B](#)) follows the same pattern, propagating anticyclonically around the LC. In the lower layer ([Figure 9C](#)), a clear propagation path is observed from the northeast corner of the array, bending around the Mississippi Fan and exiting the array around  $26.5^\circ\text{N}$ . A peak in deep spatial amplitude is also found to the south near  $25.4^\circ\text{N}$ ,  $86.8^\circ\text{W}$ . Phase propagation ([Figure 9C](#)) is generally southwest in the high amplitude region around the Mississippi Fan. The blue highlighting in [Figures 9A, B](#) identifies areas where fluctuations in both the upper and the lower layers have coincident heightened amplitude. The observations demonstrate coherent motion in both layers. The coherence in this region is also confirmed by direct squared coherence and wavelet cross spectra, all showing the same phase offsets (not shown).

This type of coupling resembles the [Malanotte-Rizzoli et al. \(1995\)](#) theory of forcing TRWs *via* upper-lower layer resonant coupling. We hypothesize that a near-resonance response is observed in the northeast corner of the array, during short-duration events in which upper layer  $\text{SSH}_{\text{bcb}}$  meanders propagate with wavenumber and frequency that approximately matches the TRW dispersion relation. This excites fluctuations of similar wavelength and frequency in  $\text{SSH}_{\text{ref}}$ . When the event evolves away from near-resonant coupling, the deep ocean is nearly unforced and the fluctuations radiate away around the Mississippi Fan as free, unforced TRWs. We will therefore refer to the ‘generation’ and ‘propagation’ regions as the blue highlighted and dark gray regions, respectively, in the lower spatial amplitude coupled CEOF plot ([Figure 9C](#)).

To show that this type of resonant coupling can generate TRWs in the Gulf Stream region, [Pickart \(1995\)](#) requires both the frequency and zonal wavelength of the TRWs to match that of the meanders. Additionally, surface meanders must project onto the TRW dispersion relation which, because Gulf Stream meanders are predominantly eastward, requires sufficient northerly orientation of bathymetry at the coupling site to rotate the TRW dispersion relation enough to create an eastward component of phase speed. Here, we have band-passed both  $\text{SSH}_{\text{bcb}}$  and  $\text{SSH}_{\text{ref}}$  confining the frequency of both the upper and lower layer fluctuations to the  $1/20 - 1/10 \text{ day}^{-1}$  band. In this case we require a component of the lower phase speed to match the upper and map onto the TRW dispersion relation local to the bottom slope. The coupled TRW dispersion relation, first derived



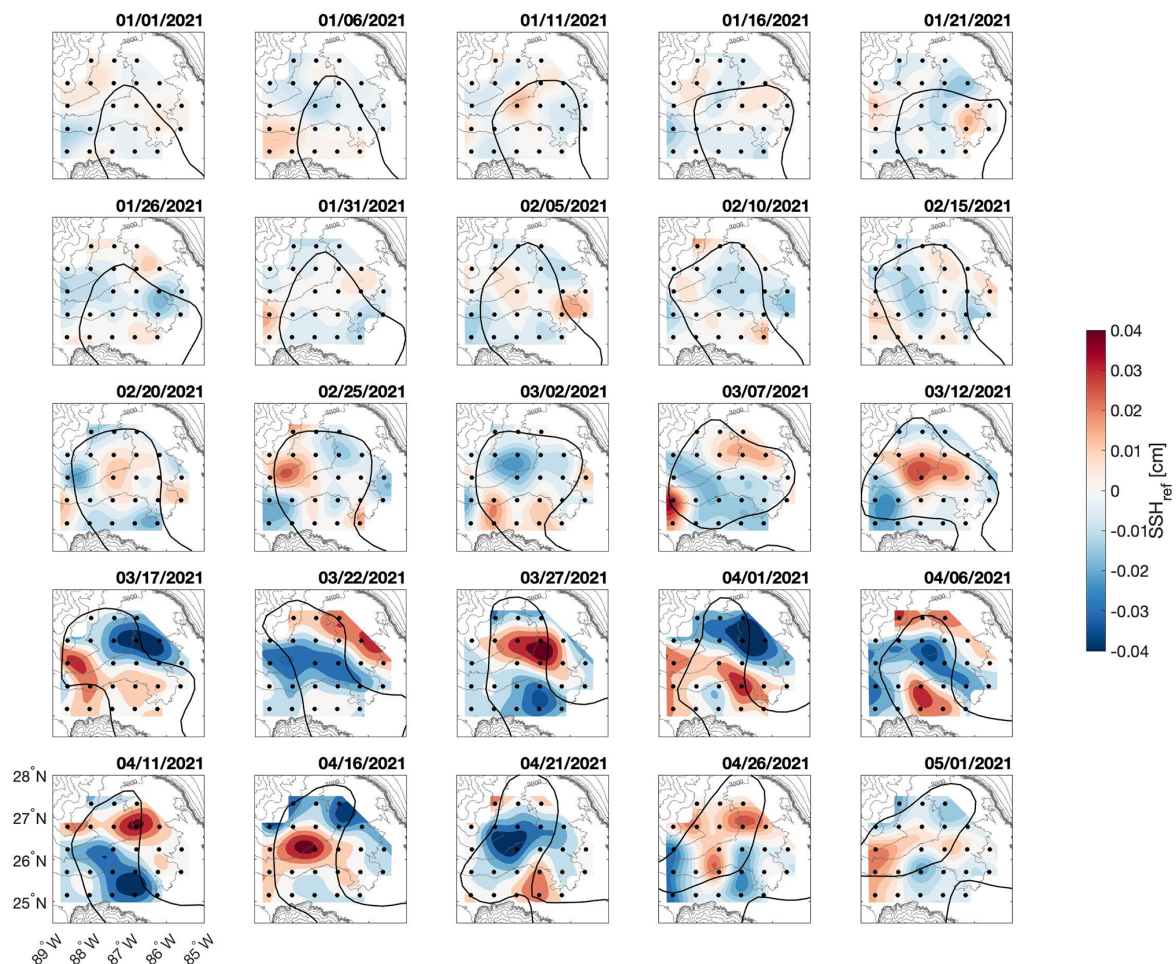


FIGURE 8  
Mapped  $SSH_{ref}$  at five-day intervals during LCE Ursa shedding event, January–May 2021.  $SSH_{ref}$  is band-passed with a  $1/20 - 1/10 \text{ day}^{-1}$  filter. The bold SSH contour represents the location of the LC at each time step. CPIES locations are marked by black circles and bathymetry is contoured in light gray every 250 meters.

by Rhines (1970) is:

$$\lambda^2 = \frac{N^2}{f^2} (k^2 + l^2 + \frac{\beta k}{\omega})$$

$$\omega = \frac{N^2(h_y k - h_x l)}{f \lambda \tanh(\lambda h)}$$

where  $k$  and  $l$  are the meridional and zonal wavenumbers,  $[h_x, h_y]$  is the topographic slope,  $h$  is the local bottom depth,  $\omega$  is the wave frequency and  $N$  is the buoyancy frequency. Here, a constant value of  $N = 15 \times 10^{-4} \text{ s}^{-1}$  is used, chosen to reflect numerous deep CTD casts across the array. Additionally, the bathymetry is smoothed using a 60-km Gaussian filter to emphasize large bathymetric features expected to influence the

generation and propagation of deep waves of wavelength greater than 150 km.

The dispersion relation is calculated by numerically solving for meridional wavenumbers given a range of zonal wavenumbers for a  $1/16\text{-day}^{-1}$  wave at each bathymetric grid point in a 60-km square box around each CPIES location (Figure 10). This results in a unique dispersion relationship for each bathymetric slope (while keeping frequency and stratification constant) within the 60-km box, giving us the range in dispersion curves for each site in Figure 10. Standard deviation of the zonal and meridional wavenumbers, derived from the coupled CEOF phase, within a 60-km square box around each CPIES site is plotted together with the family of local dispersion curves. In the generation region (blue), both the upper and lower wavevectors are plotted on the dispersion to



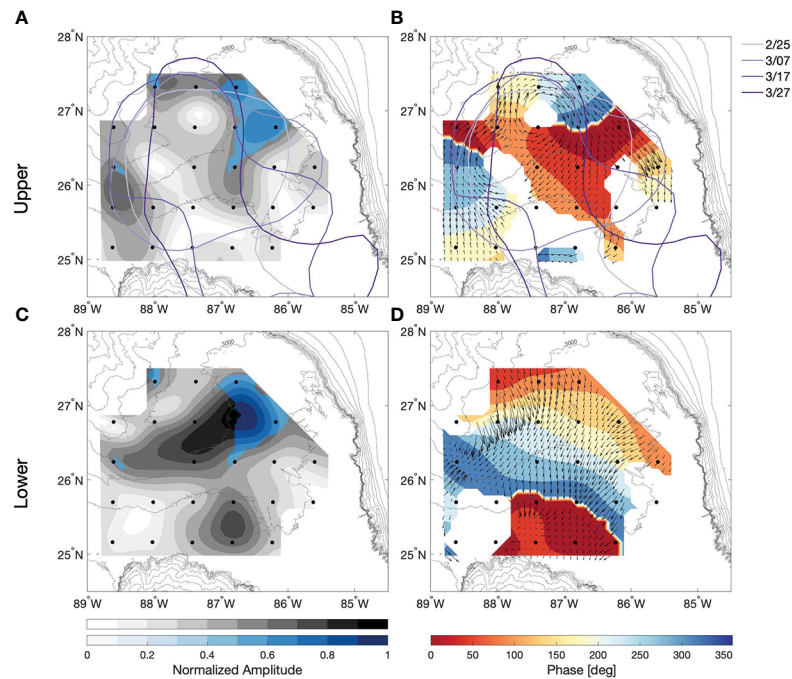


FIGURE 9

Coupled CEOF from  $1/20 - 1/10 \text{ day}^{-1}$  band-passed baroclinic sea surface height,  $SSH_{bcb}$  (upper) and reference sea surface height,  $SSH_{ref}$  (lower) during LCE Ursa detachment. Normalized spatial amplitude is on the left panels (A, C) and phase in degrees is on the right (B, D). Normalized amplitude is plotted in color only where both the upper and lower exceed 0.4. Phase is plotted only in regions where the spatial amplitude is greater than 0.3. The position of the LC, determined from SSH satellite altimetry, is contoured every 10 days during Ursa detachment on the upper panels. Bathymetry is contoured in gray every 250 meters.

identify evidence of resonant coupling. In the propagation region (gray), only the lower wavenumber standard deviation is plotted on the dispersion as these waves should be unforced and uncoupled from the surface. Smoothing the bathymetry and calculating the dispersion curves as well as the wavenumbers over a 60-km area was done to capture TRW response to bathymetric features on the order of the observed wavelength. This smoothing is comparable to that done in Oey and Lee (2002). For comparison purposes, the same analysis was done with 30-km smoothing and a 30-km square box (for both dispersion and wavenumbers) and did not yield significantly different results (not shown).

In the propagation region (Figure 10; gray dispersion diagrams), TRWs are supported for a wide range of wavenumbers. Sites B03 and C03 fall within the band of highest spatial amplitude, appearing to be dominated by TRWs during this time period. The orientation of bathymetry at B03 is northerly while C03 is more northeasterly, allowing for some contrast between the dispersion curves. However, the lower layer southwesterly phase propagation observed from the array falls within the range of TRW dispersion curves suggesting propagation is supported at both locations. On the northern edge of the propagation region, site B02 is located near a bend in bathymetry, generating numerous dispersion curves

which support the south to southeastward TRW phase propagation observed. At site C01, bathymetry is aligned nearly east-west and varies only slightly within the 60-km square box, minimizing variance of the dispersion curves. Wavenumbers  $[k, l]$  however, are centered close to  $[0, 0]$  with a relatively large standard deviation in both the zonal and meridional directions. While some of this propagation maps onto the dispersion relation, the large variability indicates more than one process is controlling deep perturbations at site C01.

In the generation region (Figure 10; blue dispersion diagrams), we aim to identify evidence for both TRW propagation and upper-lower layer near-resonant coupling. As in the propagation region, lower layer wavenumbers (orange crosses) are required to map onto the dispersion curve to illustrate that observed perturbations can be attributed to TRWs. Additionally, wavenumbers of upper layer meanders (purple crosses) must, at the very least, have a component in common with lower layer fluctuations and map onto the dispersion curves to satisfy the requirements of near-resonant coupling. In an idealized framework, upper and lower layer wavenumbers would perfectly match each other. However, owing to the variability of the system and likely intermittent coupling over the Ursa time period, we believe a common wavenumber component provides adequate evidence for

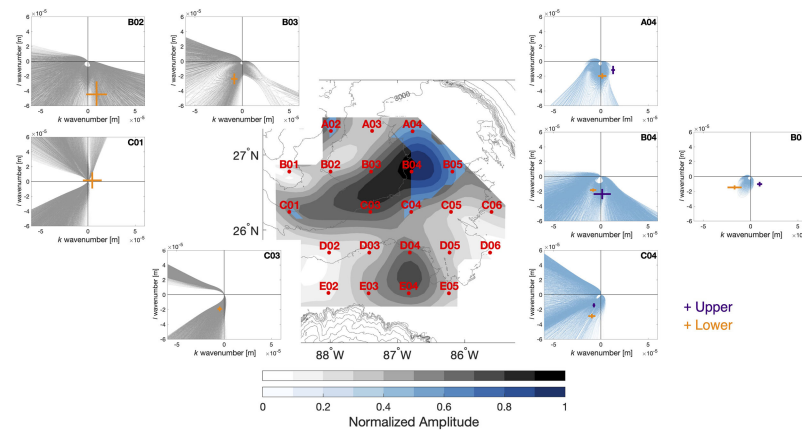


FIGURE 10

Central panel: normalized spatial amplitude from the coupled CEOF of the  $1/20 - 1/10 \text{ day}^{-1}$  band-passed reference sea surface,  $SSH_{ref}$ , during LCE Ursa detachment (same as Figure 9C). CPIPE locations are marked in red and labeled. Bathymetry is contoured in gray every 250 meters. Outside panels: the TRW dispersion curves calculated for each bathymetric slope within a 60-km square kilometer box around the corresponding CPIPE sites. To calculate the dispersion relationship, frequency ( $\omega = 1/15 \text{ day}^{-1}$ ) and stratification ( $N = 15 \times 10^{-4} \text{ s}^{-1}$ ) are kept constant across the array and bathymetry is smoothed using a 60-km Gaussian filter. The dispersion relations plotted in blue correspond to sites that fall within the blue region on the spatial amplitude (central) plot and represent regions where we hypothesize TRWs have been generated. The dispersion relations plotted in gray correspond to sites within the region of high spatial amplitude where we hypothesize TRWs are freely propagating. Orange and purple crosses represent the standard deviation of the  $SSH_{ref}$  (lower) and  $SSH_{bcb}$  (upper), respectively, wavevectors local to the corresponding CPIPE location.

coupling. Site B04 exemplifies this type of coupling. The upper and lower wavenumbers fall very close to each other, nearly overlapping in the meridional direction with similar magnitude, and also map onto the TRW dispersion relationship. Based on both the joint CEOF and comparison to the dispersion relationship, we believe the strongest coupling is occurring at site B04. At sites A04, C04 and B05, upper and lower wavenumbers share a component in common (mainly southward) suggesting coupling is likely more intermittent at these sites. Coupling may not result in TRWs at site B05 where wavenumbers do not map onto the dispersion curves.

We believe observations from site C01 support a combination of both free and forced waves at this location. Given that spatial amplitude is high and topography appears to act as a wave guide to funnel TRWs through C01 and out the western side of the array, we expected deep phase propagation to fit the dispersion relationship well. However, during both Ursa and other time periods, projection of the local wavenumber onto the dispersion curve is only within the standard deviation limits. This is likely because not only are TRWs propagating through this location but they are also being generated in this region, resulting in both free and forced waves. There is some evidence of coupling from the joint upper-lower layer CEOF (Figure 9C) and just south of C01 there is agreement in phase propagation.

A similar analysis is completed during the time period of LCE Thor to identify TRW pathways and generation regions. A few notable differences between Thor and Ursa made it difficult to draw any definitive conclusions about the origin of high-frequency

perturbations observed during Thor. There are two distinct peaks in high-frequency energy associated with each of the detachments over the Thor time period. During the first time period, the generation region appears to be north of the array with perturbations traveling southward before bending around the Mississippi Fan and exiting the array near site C01. We believe a similar coupling mechanism could be responsible for these TRWs, associated with meanders in either the LC or detached LCE. However, because generation is outside the array, the coupled CEOF (not shown) identifies only a single region, site C01, where high amplitudes of both upper and lower layer coincide providing further evidence for a mix of free and forced waves at this location.

## 7 Summary and conclusions

An array of 24 CPIPEs deployed in the eastern Gulf of Mexico from June 2019 – May 2021 is well positioned to observe the generation and propagation of TRWs associated with the LC and LCEs. During the two year deployment, three LCEs separate from the core of the LC. Each LCE formation and detachment is associated with a peak in deep eddy kinetic energy under the eastward arm of the LC. This energy is found to organize into two distinct frequency bands,  $1/100 - 1/20 \text{ days}^{-1}$  and  $1/20 - 1/10 \text{ days}^{-1}$ , with the high-frequency band dominating over the Mississippi Fan in the northwest corner of the array. We believe this energy to be associated with TRWs generated by LC or LCE interactions with the Mississippi Fan.

A CEOF analysis of  $1/20 - 1/10 \text{ day}^{-1}$  band-passed  $\text{SSH}_{ref}$  over the full deployment period identifies a number of characteristics that satisfy linear TRW theory: phase propagation to the right of increasing water depth, current velocity variance ellipses perpendicular to the direction of phase velocity in regions where spatial amplitude is high and a larger phase speed oriented down-slope in regions of steeper bathymetric slope. Additionally, wavelengths of 150 – 300 km are estimated from the phase gradient, values consistent with both linear wave theory and previous observations in the Gulf of Mexico. The time series of EOF coefficients reveals peaks in  $1/20 - 1/10 \text{ day}^{-1}$  energy just following each LCE detachment event as well as a number of smaller peaks seemingly disassociated with the separation process and sometimes occurring during a retracted LC state.

Results from the CEOF analyses strongly suggest observed high-frequency propagation following roughly around the topography of the Mississippi Fan can be attributed to TRWs. This is in agreement with previous works that have identified TRWs at numerous locations across the northern continental slope of the Gulf (Hamilton, 1990; Hamilton and Lugo-Fernandez, 2001; Hamilton, 2007). While many of these studies suggest the LC or LCEs as the source of this deep energy, conclusively linking generation to propagation has proved difficult. A coupled high-frequency  $\text{SSH}_{ref}$  (lower layer) and  $\text{SSH}_{bcb}$  (upper layer) CEOF during the LCE Ursa formation and detachment time period identifies a TRW propagation region extending from an area where both upper and lower layers exhibit cohesive high amplitude fluctuations. Suggestive of an upper-lower layer resonant coupling mechanism, this is likely a region where high-frequency energy is being generated and radiating away as TRWs within the band of high CEOF amplitude. This region, extending south-southwest and wrapping along the Mississippi Fan suggests the path of group energy propagation. The along path decrease in amplitude likely results from the dispersion of TRW contributions within this band of wavelengths and frequencies.

To illustrate generation by coupling and TRW propagation, wave characteristics are mapped onto the linear dispersion relationship within a 60-km region around each CPIES site. Within the  $\text{SSH}_{ref}$  high amplitude fluctuation region, or the propagation region, wavenumbers fit the dispersion curve well, confirming observed perturbations can be attributed to TRWs. In the generation region, upper-lower layer resonant coupling is identified by matching, or having at least one component in common,  $\text{SSH}_{ref}$  and  $\text{SSH}_{bcb}$  wavenumbers that both map onto the local dispersion curve. In the northeast corner of the array, where the joint CEOF illustrates coherent upper and lower layer fluctuations, site B04 exhibits strong evidence for near-resonance coupling between the upper and lower layers. Coupling is likely more intermittent at the remainder of the sites, where upper and lower wavenumbers share a southward

wavenumber. These results provide sufficient evidence for the near-resonant coupling hypothesis.

The CPIES array has identified propagation pathways of high-frequency TRWs around the Mississippi Fan. We believe these waves, generated across the eastern Gulf of Mexico, are likely funneled out of the western side of the array and towards the Sigsbee Escarpment, a known active TRW region. A combination of ray tracing and continuous long term deep current measurements at the Escarpment has the potential to connect generation and propagation within the array to deep hazardous currents that can interfere with energy sector operations.

## Data availability statement

The CPIES datasets analyzed for this study can be found in the GRIIDC data repository <https://data.gulfresearchinitiative.org/>. Specifically, vertical acoustic round trip travel time: <https://data.gulfresearchinitiative.org/data/U1.x852.000:0005> and DOI:10.72664B13NKBA, vertical profiles of temperature, salinity and geopotential anomaly: <https://data.gulfresearchinitiative.org/data/U1.x852.000:0007> and DOI:10.7266G E30701Z, bottom pressure: <https://data.gulfresearchinitiative.org/data/U1.x852.000:0004> and DOI:10.7266BZ9B3C54, and bottom current meter data: <https://data.gulfresearchinitiative.org/data/U1.x852.000:0003> and DOI:10.7266K4ZF1T9Z. The mapped altimeter SSH product can be found at [https://resources.marine.copernicus.eu/product-detail/SEALEVEL\\_GLOP\\_HY4\\_NRT\\_OBSE\\_RVATIONS08046/INFORMATION](https://resources.marine.copernicus.eu/product-detail/SEALEVEL_GLOP_HY4_NRT_OBSE_RVATIONS08046/INFORMATION).

## Author contributions

AJE, KD, and DW contributed to conception and design of the study. KT and MK processed and organized the database. AJE performed the statistical analysis and wrote the first draft of the manuscript. All authors contributed to manuscript revision, read, and approved the submitted version.

## Funding

Funding for this project was provided by the National Academy of Science, Engineering and Medicine Grant 2000009943.

## Acknowledgments

The authors would like to thank the Captain, Tad Berkey, and crew of the R/V Pelican for the successful deployment and recovery of the array. We also acknowledge instrument development and careful planning and preparation by Erran

Sousa and Laura Reed. This paper has benefited from the thoughtful comments from the editor, Julio Sheinbaum.

## Conflict of interest

The authors declare that the research was conducted in the absence of any commercial or financial relationships that could be construed as a potential conflict of interest.

## References

- Bretherton, F. P., Davis, R. E., and Fandry, C. (1976). A technique for objective analysis and design of oceanographic experiments applied to MODE-73. *Deep Sea Res.* 23, 559–582. doi: 10.1016/0011-7471(76)90001-2
- Donohue, K. A., Hamilton, P., Leaman, K., Leben, R., Prater, M., Waddell, E., et al. (2006). *Exploratory study of deepwater currents in the gulf of Mexico, volume 2: Technical report* (Tech. rep., United States. Minerals Management Service. Gulf of Mexico OCS Region). Available at: <https://digital.library.unt.edu/ark:/67531/metadc955399/>.
- Donohue, K. A., Watts, D., Hamilton, P., Leben, R., and Kennelly, M. (2016). Loop current eddy formation and baroclinic instability. *dyn. atmos. Oceans* 76, 195–216. doi: 10.1016/j.dynatmoce.2016.01.004
- Donohue, K. A., Watts, D. R., Tracey, K. L., Greene, A. D., and Kennelly, M. (2010). Mapping circulation in the kuroshio extension with an array of current and pressure recording inverted echo sounders. *J. Atmos. Oceanic Technol.* 27, 507–527. doi: 10.1175/2009JTECHO686.1
- Hamilton, P. (1990). Deep currents in the gulf of Mexico. *J. Phys. Oceanogr.* 20, 1087–1104. doi: 10.1175/1520-0485(1990)020<1087:DCITGO>2.0.CO;2
- Hamilton, P. (2007). Deep-current variability near the sigsbee escarpment in the gulf of Mexico. *J. Phys. Oceanogr.* 37, 708–726. doi: 10.1175/JPO2998.1
- Hamilton, P. (2009). Topographic rossby waves in the gulf of Mexico. *Prog. Oceanogr.* 82, 1–31. doi: 10.1016/j.pocan.2009.04.019
- Hamilton, P., Bower, A., Furey, H., Leben, R., and Pérez-Brunius, P. (2019). The loop current: Observations of deep eddies and topographic waves. *J. Phys. Oceanogr.* 49, 1463–1483. doi: 10.1175/JPO-D-18-0213.1
- Hamilton, P., Donohue, K., Hall, C., Leben, R., Quian, H., Sheinbaum, J., et al. (2015). *Observations and dynamics of the loop current* (Tech. rep., US Department of the Interior, Bureau of Ocean Energy Management, Gulf of Mexico OCS Region). Available at: <https://digital.library.unt.edu/ark:/67531/metadc955416/>.
- Hamilton, P., and Lugo-Fernandez, A. (2001). Observations of high speed deep currents in the northern gulf of Mexico. *Geophys. Res. Lett.* 28, 2867–2870. doi: 10.1029/2001GL013039
- Hirschi, J. J.-M., Frajka-Williams, E., Blaker, A. T., Sinha, B., Coward, A., Hyder, P., et al. (2019). Loop current variability as trigger of coherent gulf stream transport anomalies. *J. Phys. Oceanogr.* 49, 2115–2132. doi: 10.1175/JPO-D-18-0236.1
- Kennelly, M., Tracey, K., Donohue, K., and Watts, D. R. (2022). *PIES and CPIES data processing manual* (Tech. rep., University of Rhode Island Graduate School of Oceanography). Available at: [https://digitalcommons.uri.edu/cgi/viewcontent.cgi?article=1037&context=physical\\_oceanography\\_techrpts](https://digitalcommons.uri.edu/cgi/viewcontent.cgi?article=1037&context=physical_oceanography_techrpts).
- Le Hénaff, M., Kourafalou, V. H., Morel, Y., and Srinivasan, A. (2012). Simulating the dynamics and intensification of cyclonic loop current frontal eddies in the gulf of Mexico. *J. Geophys. Res.* 117. doi: 10.1029/2011JC007279
- Malanotte-Rizzoli, P., Dale, B. H., and Young, R. E. (1987). Numerical simulation of transient boundary-forced radiation. part I: The linear regime. *J. Phys. Oceanogr.* 17, 1439–1457. doi: 10.1175/1520-0485(1987)017<1439: NSOTBF>2.0.CO;2
- Malanotte-Rizzoli, P., Hoggi, N. G., and Young, R. E. (1995). Stochastic wave radiation by the gulf stream: Numerical experiments. *Deep Sea Res.* 42, 389–423. doi: 10.1016/0967-0637(95)00001-M
- Meinen, C. S., and Watts, D. R. (2000). Vertical structure and transport on a transect across the north Atlantic current near 42°N: Time series and mean. *J. Geophys. Res.* 105, 21869–21891. doi: 10.1029/2000JC900097
- Munk, W. H., and Cartwright, D. E. (1966). Tidal spectroscopy and prediction. *Philos. Trans. R. Soc. London* 259, 533–581. doi: 10.1098/rsta.1966.0024
- Oey, L. (2008). Loop current and deep eddies. *J. Phys. Oceanogr.* 38, 1426–1449. doi: 10.1175/2007JPO3818.1
- Oey, L., and Lee, H. (2002). Deep eddy energy and topographic rossby waves in the gulf of Mexico. *J. Phys. Oceanogr.* 32, 3499–3527. doi: 10.1175/1520-0485(2002)032<3499:DEEATR>2.0.CO;2
- Pickart, R. S. (1995). Gulf stream-generated topographic rossby waves. *J. Phys. Oceanogr.* 25, 574–586. doi: 10.1175/1520-0485(1995)025<0574:GSTRW>2.0.CO;2
- Rhines, P. (1970). Edge-, bottom-, and rossby waves in a rotating stratified fluid. *Geophys. Fluid Dyn.* 1, 273–302. doi: 10.1080/03091927009365776
- Trenberth, K. E., and Shin, W.-T. K. (1984). Quasi-biennial fluctuations in sea level pressures over the northern hemisphere. *Monthly Weather Rev.* 112, 761–777. doi: 10.1175/1520-0493(1984)
- Watts, D. R., Qian, X., and Tracey, K. L. (2001). Mapping abyssal current and pressure fields under the meandering gulf stream. *J. Atmos. Oceanic Technol.* 18, 1052–1067. doi: 10.1175/1520-0426(2001)018<1052:MACAPF>2.0.CO;2
- Watts, D. R., and Rossby, H. T. (1977). Measuring dynamic heights with inverted echo sounders: Results from MODE. *J. Phys. Oceanogr.* 7, 345–358. doi: 10.1175/1520-0485(1977)007<0345:MDHWIE>2.0.CO;2

## Publisher's note

All claims expressed in this article are solely those of the authors and do not necessarily represent those of their affiliated organizations, or those of the publisher, the editors and the reviewers. Any product that may be evaluated in this article, or claim that may be made by its manufacturer, is not guaranteed or endorsed by the publisher.



## OPEN ACCESS

## EDITED BY

Eric Chassignet,  
Florida State University, United States

## REVIEWED BY

Nektaria Ntaganou,  
Florida State University, United States  
Matthieu Le Hénaff,  
University of Miami, United States

## \*CORRESPONDENCE

Toshiaki Shinoda  
✉ toshiaki.shinoda@tamucc.edu

## SPECIALTY SECTION

This article was submitted to  
Physical Oceanography,  
a section of the journal  
Frontiers in Marine Science

RECEIVED 20 September 2022

ACCEPTED 12 December 2022

PUBLISHED 09 January 2023

## CITATION

Shinoda T, Tissot P and Reisinger A  
(2023) Influence of Loop Current and  
eddy shedding on subseasonal sea  
level variability along the western G  
ulf Coast.  
*Front. Mar. Sci.* 9:1049550.  
doi: 10.3389/fmars.2022.1049550

## COPYRIGHT

© 2023 Shinoda, Tissot and Reisinger.  
This is an open-access article  
distributed under the terms of the  
[Creative Commons Attribution License  
\(CC BY\)](https://creativecommons.org/licenses/by/4.0/). The use, distribution or  
reproduction in other forums is  
permitted, provided the original  
author(s) and the copyright owner(s)  
are credited and that the original  
publication in this journal is cited, in  
accordance with accepted academic  
practice. No use, distribution or  
reproduction is permitted which does  
not comply with these terms.

# Influence of Loop Current and eddy shedding on subseasonal sea level variability along the western Gulf Coast

Toshiaki Shinoda<sup>1\*</sup>, Philippe Tissot<sup>2</sup> and Anthony Reisinger<sup>2</sup>

<sup>1</sup>Department of Physical and Environmental Sciences, Texas A&M University – Corpus Christi, Corpus Christi, TX, United States, <sup>2</sup>Conrad Blucher Institute, Texas A&M University – Corpus Christi, Corpus Christi, TX, United States

Mechanisms that generate subseasonal (1–2 months) events of sea level rise along the western Gulf Coast are investigated using the data collected by a dense tide gauge network: Texas Coastal Ocean Observation Network (TCOON) and National Water Level Observation Network (NWLON), satellite altimetry, and high-resolution (0.08°) ocean reanalysis product. In particular, the role of Loop Current and eddy shedding in generating the extreme sea level rise along the coast is emphasized. The time series of sea level anomalies along the western portion of the Gulf Coast derived from the TCOON and NWLON tide gauge data indicate that a subseasonal sea level rise which exceeds 15 cm is observed once in every 2–5 years. Based on the analysis of satellite altimetry data and high-resolution ocean reanalysis product, it is found that most of such extreme subseasonal events are originated from the anti-cyclonic (warm-core) eddy separated from the Loop Current which propagates westward. A prominent sea level rise is generated when the eddy reaches the western Gulf Coast, which occurs about 6–8 months after the formation of strong anti-cyclonic eddy in the central Gulf of Mexico. The results demonstrate that the accurate prediction of subseasonal sea level rise events along the Gulf Coast with the lead time of several months require a full description of large-scale ocean dynamical processes in the entire Gulf of Mexico including the characteristics of eddies separated from the Loop Current.

## KEYWORDS

sea level rise, Gulf Coast, Loop Current, Gulf of Mexico, subseasonal variability, eddy shedding



# 1 Introduction

Global mean sea level (SL) rise has been estimated during the past decades based on tide-gauge observations. The rise is caused primarily by two factors related to global warming: the thermal expansion of sea water and the added water from melting land ice (IPCC, 2022). The advance of satellite altimetry in recent years has provided the opportunity to detect spatial differences of long-term SL change. Recent studies indicate that SL rise is not geographically uniform because of changes in atmospheric and oceanic circulations (e.g., Unnikrishnan and Shanker, 2007; Miline et al., 2009; Woodworth et al., 2009; Han et al., 2010; Ezer et al., 2013; Han et al., 2014). Areas along the coastlines of the Gulf of Mexico, and particularly the northwest portion of the basin, are experiencing significantly higher rates of relative SL rise due to large rates of subsidence (Wang et al., 2020) as compared to the global mean. As large industrial infrastructure and millions of people reside in these low-lying coastal regions, a small increase in SL will have substantial impacts on people's lives including increased frequencies and expanses of flooding.

In addition to the long-term changes, coastal SL fluctuates substantially on relatively short time scales from hours to few months. Such SL rises include those associated with astronomical tides, storm surges, waves, and other atmospheric and oceanic processes. As the mean (or background) SL is rising as a result of global warming, it will become much easier for coastal flooding to occur due to relatively short-term SL rise events. For example, recent studies suggest that an increase in high-tide or clear-sky flooding started about two decades ago is growing rapidly in recent years as a result of mean SL rise, and it is likely that this type of coastal flooding will continue to grow over the coming years and decades (e.g., Sweet et al., 2021). For example, the number of high-tide flooding days per year along the western Gulf Coast has more than doubled over the past 30 years (Sweet et al., 2021).

The long-term increase of flooding caused by SL rise events can also arise from the changes in amplitude and frequency of short-term SL fluctuations themselves. For example, occurrence of strong land falling storms could be increased due to the global warming (IPCC, 2022). Recent studies suggest that strong winds associated with land-falling atmospheric river (AR) events cause a substantial SL rise along the US west coast which exceeds 50 cm (Shinoda et al., 2019). As frequency and intensity of ARs will be changing under a warming climate (e.g., Espinoza et al., 2018; O'Brien et al., 2021), AR-associated SL extreme events may increase in the future. Moreover, such short-term SL rise events are not cancelled out by the opposite change (SL drop events), changes in AR frequency could in turn impact the long-term SL changes including their trend. Accordingly, it is crucial to understand processes that control short-term SL rise events

along the coast for both adaptation strategies for coastal flooding as well as future projections of coastal SL changes.

Previous studies suggest that large-scale dynamical processes over the open ocean area could largely impact SL rise along the coast on a variety of time scales (e.g., Ezer et al., 2013; Chen et al., 2015; Qiu et al., 2015; Minobe et al., 2017; Feng et al., 2022). For example, a significant portion of intraseasonal variability in SL anomalies along the east coast of Philippine is attributed to Rossby waves propagated from the tropical north Pacific (Chen et al., 2015), and local wind forcing may play a minor role during which the remote forcing largely affects the coastal SL. The importance of remote forcing for determining coastal SL changes on longer time scales has been also demonstrated for both western and eastern sides of continents (Minobe et al., 2017; Feng et al., 2022). Hence, these studies suggest that ocean dynamical processes originated from remote areas must be considered to understand the mechanisms controlling the coastal SL.

Although the Gulf Coast SL has been monitored for a long time period, physical processes that control the SL variability are not well understood. Since the Loop Current, which is part of the strong western boundary current of the north Atlantic subtropical gyre, is located near the Gulf Coast, ocean dynamical processes could be a primary factor in controlling the western and northern Gulf Coast SL on various time scales. Because of the high velocity of the Loop Current, the average SL across the current axis varies substantially. The SL inside of the Loop is about 80 cm higher than the outside of the Loop, which is associated with the thermocline depth variation of about 150–200 m (e.g., Maul, 1977; Shay et al., 2000). The Loop Current reveals large variability of its position. It occasionally extends northward around 29°N, reaching as north as the continental shelf in the northeast Gulf of Mexico (e.g., Wiseman and Dinnel, 1988; Leben, 2005; Schmitz et al., 2005). When extended, the Loop Current often sheds an anti-cyclonic eddy (e.g., Cochran, 1972; Vukovich, 1995; Sturges and Leben, 2000). The anti-cyclonic eddy separated from the Loop Current moves westward with the speed of about 0.08–0.2 m/s (Elliott, 1982; Coats, 1992; Shay et al., 1998). The size (diameter) of the eddy can be about 200 to 400 km, and extends down to a depth of about 1000 m (e.g., Mooers and Maul, 1998). After the release of the anti-cyclonic eddy, the Loop Current changes its path, which flows almost directly to the Florida strait with a small meander.

Because of the substantial variations of the Loop Current path near the central Gulf Coast, its variability could directly influence near-shore sea surface height (SSH) around the northern Gulf Coast. In addition, the Loop Current variability and eddy shedding as discussed above could influence near-shore SSH around the western Gulf Coast. In particular, some of the strong anti-cyclonic eddies separated from the Loop Current often propagate westward all the way to the western part of Gulf

Coast, which may result in SL fluctuations along the western Gulf Coast. However, the relation between ocean dynamical processes such as the Loop Current variability and eddy shedding and the Gulf Coast SL is still unclear.

As in most areas along the US coastline, the Gulf Coast SL fluctuates substantially on a variety of time scales. While previous studies documented long-term trends in the Gulf Coast SL (e.g., Boon et al., 2018), extreme SL rise events on the time scale shorter than seasonal (except that caused by hurricanes) have not been well documented, and physical processes that control such events are not well understood. Our analysis of tide gauge data along the western Gulf Coast indicates that such extreme SL rise events on the time scale of 1–2 months often occur. This study investigates physical processes that contribute to SL variations in the Gulf Coast and Gulf of Mexico on the subseasonal (1–2 months) time scale. A particular emphasis is given to the role of ocean dynamics in such SL rise events along western Gulf Coast areas, which are examined through the combined analysis of satellite altimeter, *in-situ* tide-gauge, and ocean reanalysis data.

## 2 Data and methods

### 2.1 Observational data and reanalysis product

Primary data sets used in this study are described in the following.

#### 2.1.1 Texas Coastal Ocean Observing Network (TCOON)

The Texas Coastal Ocean Observation Network (TCOON) (Rizzo et al., 2014) is a uniquely dense coastal network of scientific data collection platforms operated following National Ocean Service standards complementing the stations of the National Water Level Observation Network (NWLON). SL time series from 23 tide gauges along the Texas coast were processed (Figure 1). Eighteen of these stations are part of the TCOON while five stations are part of the NWLON. All stations are maintained to the same standards with similar instrumentation.

Because of the exceptionally dense network of tide-gauge data along the coast, it is possible to distinguish between local and large-scale impacts. For example, there are spatial differences in local tidal dynamics, local wind pattern, river runoff, and the influence of complex bathymetry, besides the different rates of subsidence. The large-scale influence will be detected based on the comparison of the data from a number of stations along the coast. The estimated SL will be explained through examining processes relevant to large-scale oceanic and atmospheric variability.

#### 2.1.2 HYCOM reanalysis

The high-resolution global ocean reanalysis data set “GOFS 3.1: 41-layer HYCOM + NCODA Global 1/12° Reanalysis”, created by the US Navy’s operational Global Ocean Nowcast/Forecast System (Metzger et al., 2014), is used in this study. The system employs the 0.08° Hybrid Coordinate Ocean Model (HYCOM; Bleck, 2002) as an ocean model component, and

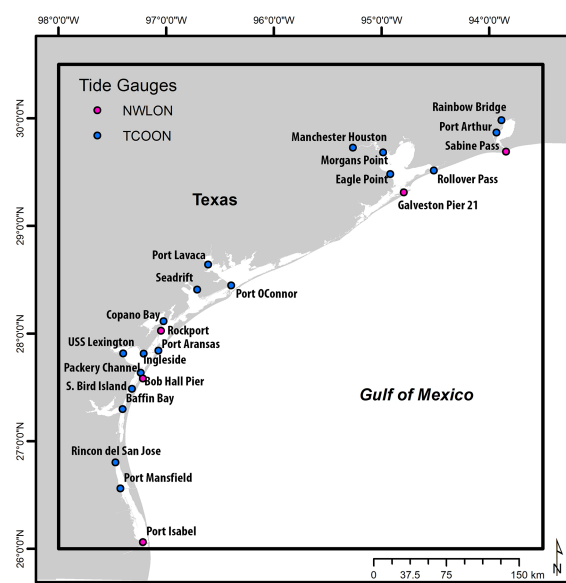


FIGURE 1

A map of TCOON and NWLON tide gauge stations. The rectangular box indicates the area used for calculating average winds.

*in-situ* and satellite data are assimilated through the Navy Coupled Ocean Data Assimilation (NCODA; Cummings and Smedstad, 2013). This reanalysis product is referred to as “HYCOM reanalysis” hereafter.

HYCOM, NCODA and the data assimilation method are explained here briefly, as the details are described in other papers (Bleck, 2002; Cummings and Smedstad, 2013; Helber et al., 2013; Metzger et al., 2014). The global HYCOM used in this study is eddy-resolving, in which the horizontal resolution is  $0.08^\circ$  at the equator. HYCOM is forced by surface forcing fields derived from coupled reanalysis products, the Climate Forecast System Reanalysis (CFSRV1; Saha et al., 2010) and Climate Forecast System Version 2 (CFSV2; Saha et al., 2014). The ocean data assimilated by NCODA include satellite-derived SSH, sea surface temperature (SST), sea ice concentration, *in situ* surface and subsurface temperature and salinity observations. The HYCOM/NCODA system uses synthetic temperature profiles derived from the Improved Synthetic Ocean Profile (ISOP; Helber et al., 2013). The ISOP is constructed at a given location by projecting satellite-derived SSH and SST downward from the surface using statistical relationships. In this study, the daily and monthly mean ocean velocity and SSH data for the period of 1994–2015 are used. HYCOM has been extensively used for simulations of upper ocean structure and circulations in the Gulf of Mexico (e.g., Chassignet et al., 2005; Zamudio and Hogan, 2008). Also, in the last several years, the HYCOM reanalysis has been validated extensively, including the coastal SL variations (e.g., Yu et al., 2015; Thoppil et al., 2016; Shinoda et al., 2019; Shinoda et al., 2020).

### 2.1.3 Satellite data and other reanalysis products

Satellite altimeter data obtained from Archiving, Validation, and Interpretation of Satellite Oceanographic data (AVISO) for the period 1994–2015 are used to monitor the variability of Loop Current and the associated eddy formation. Daily SSH data are provided on a  $0.25^\circ \times 0.25^\circ$  grid. Surface winds at 10 m height from CFSRV1 for the period of 1994–2010 and CFSV2 for the period of 2011–2015 are used. The horizontal resolution of CFSRV1 (CFSV2) is  $0.3125^\circ$  ( $0.205^\circ$ ). These wind data sets are used to force HYCOM for creating the HYCOM reanalysis product.

## 2.2 Data processing

The individual SL time series are processed to remove the variability associated with their respective weather and tidal forcings as well as their local vertical land motion. The magnitude of the vertical land motion can be important, with a large spatial variability along the Texas coast. The short term, hours to seasonal, SL dynamic varies substantially depending on the location within the study area. The tidal range is on the order of 20–30 cm along the shores of the Gulf of Mexico and decreases

rapidly along ship channels and within the bays and estuaries. The tidal influence becomes insignificant in the Laguna Madre. Similarly high frequency weather forcings, including the passage of cold fronts influence bays, estuaries and lagunas differently, then the nearshore waters of the Gulf of Mexico. Within embayments or along the intracoastal waterway where many tide gauges are located, hourly SL changes are largely driven by weather forcings and the distance from the nearest pass or ship channel connecting the respective water bodies to the Gulf of Mexico. This high frequency variability is however not significant for the present study as monthly time series are computed by averaging out high frequency variability.

Hourly SLs measured relative to their respective station datums were downloaded for the period 1993–2017. The number of gaps in the time series was small for all stations, and gaps were left unfilled. Then monthly averages are computed to remove the high frequency influences of the local tides and weather driven changes. A monthly mean was computed for stations only if at least 90% of the hourly records was available. The seasonal cycle is computed individually and removed from the monthly time series for each station. The resulting time series are used to estimate the locations’ relative SL linear trends. The respective trends are then removed from the respective locations’ time series (Zervas et al., 2013). The values of relative SL trends range from 3 to 14 mm/yr. The processed individual locations’ time series are highly correlated. The mean of the correlation coefficients for all locations with respect to the mean is 0.95 and the individual correlation coefficients are at least 0.89. Thus the average time series of all TCOON and NWLON stations are adequate to quantify the oceanic signal for the western Gulf Coast.

The anomalies of SSH from AVISO and SSH and surface currents from the HYCOM reanalysis are calculated by subtracting the climatological seasonal cycle for the 1994–2015 period. The linear trend in anomalies of SSH and surface currents is removed. The anomalies of surface winds from CFSRV1 (CFSV2) are calculated by subtracting the climatological seasonal cycle for the 1994–2010 (2011–2015) period.

## 3 Results

### 3.1 Time series of SL along the western Gulf Coast

Figure 2 shows the time series of monthly average SL anomaly measured by TCOON and NWLON tide gauges. Although the time series is the average of 23 stations, large fluctuations of the SL anomalies, which exceeds 5 cm are frequently found every year for both positive and negative anomalies, with the standard deviation (STD) of 6.8 cm. In addition, the extreme SL rise which exceeds 15 cm ( $2.2 \times \text{STD}$ ) are found once in 2–5 years. During 1994–2015, six of such extreme

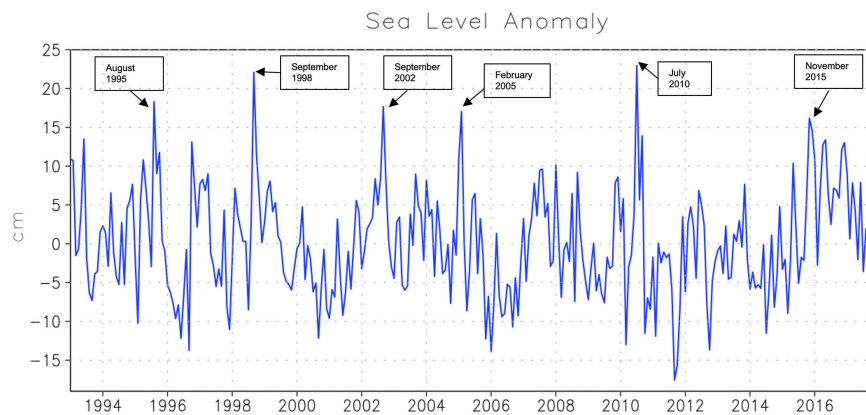


FIGURE 2  
Time series of monthly mean sea level anomalies (cm) derived from the 23 study tide gauge stations.

events are observed, and two of them exceed 20 cm ( $2.9 \times \text{STD}$ ). There is not specific seasonality in the timing of these extreme events. Given that the study tide stations cover relatively large areas which span the entire Texas coast, it is expected that these extreme SL rise events are caused by oceanic and atmospheric processes which are on the scale larger than 100–200 km. Note that the time series in different areas of the Texas coast are very coherent at least for these extreme SL rise events (not shown).

In contrast to positive anomalies, the extreme events of the negative anomalies are not often found. The negative anomalies exceeded 15 cm only once during the 22-year period, but the negative anomalies larger than 5 cm last relatively longer time. For example, the negative SL anomaly of 5–10 cm is found more than 6 months in 1996.

The asymmetry of negative and positive anomalies is further demonstrated in the histogram of monthly SL anomalies (Figure 3). The distribution is positively skewed with the skewness of 0.38. The negative values of 2.0–5.6 cm range are most frequently found, and thus the peak value during extreme SL rise events relative to the normal (most frequently found) values are larger than the peak values of anomaly.

In this study, we investigate the six extreme SL rise events identified from the TCOON and NWLON SL time series by comparing them with the large-scale ocean and atmospheric circulations. In particular, variability of SL and ocean circulations in the entire Gulf of Mexico during these events will be thoroughly described to elucidate the possible causes of such extreme SL rise events.

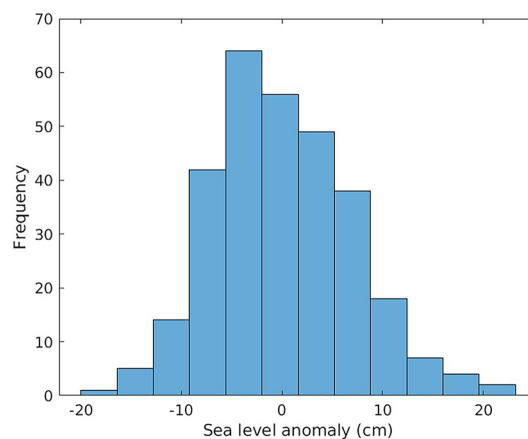


FIGURE 3  
Histogram of monthly mean sea level anomalies (cm). Mean values of all tide gauge stations shown in Figure 1 are used.

### 3.2 Comparison with local wind forcing

Figure 4 compares the time series of the sea level anomaly (Figure 4A) with those of the speed of anomalous winds (Figure 4B) and surface wind anomaly (Figure 4C) averaged over the area 98°W–93.5°W, 26°N–29.5°N (box area in Figure 1), which cover the almost entire TCOON and NWLON tide gauge stations. The correlation coefficients of SL anomalies with zonal wind anomalies (−0.24) and meridional wind anomalies (−0.24) are statistically significant, and the sign of the correlation is consistent with SL fluctuations driven by the along-shore wind stress since the northeasterly winds can generate coastal downwelling and thus SL rise. However, correlations are very weak and it is difficult to visually identify the similarity between the wind and SL variations. This suggests that while local wind variations affect the subseasonal

SL fluctuations to some extent or during some periods, they are not the major factor that controls the overall subseasonal SL variations in this region. In particular, there are no obvious strong local wind events during the extreme SL rise events. Hence, other oceanic or atmospheric processes may cause most of the extreme SL rise events observed in this region.

### 3.3 Comparisons with large-scale SL variations and ocean circulations

#### 3.3.1 Event in 2002

Figure 5A displays the SSH anomalies for the entire Gulf of Mexico during September 2002 when a peak of SL rise is found in the TCOON SL time series (Figure 2). The positive SSH

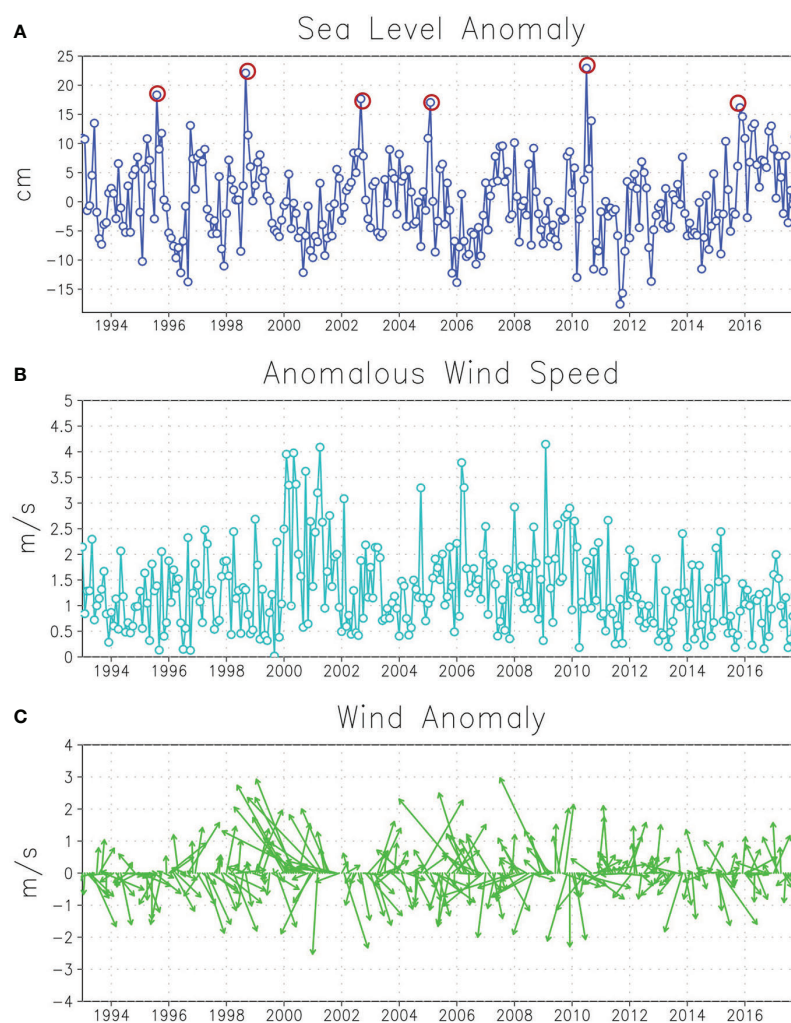


FIGURE 4

(A) Time series of monthly mean sea level anomalies (cm) derived from tide gauge measurements of 23 study stations. The time series are the same as those in Figure 2. (B) Time series of anomalous surface wind speed averaged over the area 98°W–94°W, 25°N–29.5°N (box area in Figure 1). The anomalous wind speed is calculated by average zonal and meridional wind anomalies. The wind data from CFSR and CFSV2 are used. (C) Same as (B) except for surface vector winds.



anomalies are found along the western Gulf Coast which covers most of the areas of TCOON tide gauge stations. The SSH anomalies along the coast are connected to the high SSH anomaly centered around 24°N–25°N, 96°W, which extends to further east around 93°W. The spatial distribution of SSH along the coast measured by AVISO is very similar to those in the HYCOM reanalysis (Figure 5B), and thus the HYCOM reanalysis could be used to describe SSH and upper ocean currents during the period of SL rise events. It should be noted that a similar agreement of SSH between the AVISO and HYCOM reanalysis are evident in other periods of SL rise events, as will be shown in the following sections.

Surface current anomalies during this period from the HYCOM reanalysis is shown in Figure 5C. The high SSH anomalies connected to the western Gulf Coast SL rise are associated with the strong anti-cyclonic circulations. These

anti-cyclonic circulations are connected to the southward surface currents along the coast all the way to around 29°N. Since the southward coastal current around 25°N–27°N is directly connected to the circulation in the eastern part of the anti-cyclonic eddy, a large meander of southward flow is evident. Near the coast around 24°N, the very narrow southward current is found while the anomalous northward currents associated with the anti-cyclonic eddy is located very close to the coast. The northward currents on the western side of the eddy are much narrower and weaker than southward currents on the eastern side of the eddy, suggesting that the eddy is interacting with the coast during this period and the western part of the eddy including anomalous northward currents are affected by the coast. The spatial pattern of these surface currents suggests that strong eastward currents on the northern side of the eddy located around 25°N–26°N largely influence the generation of

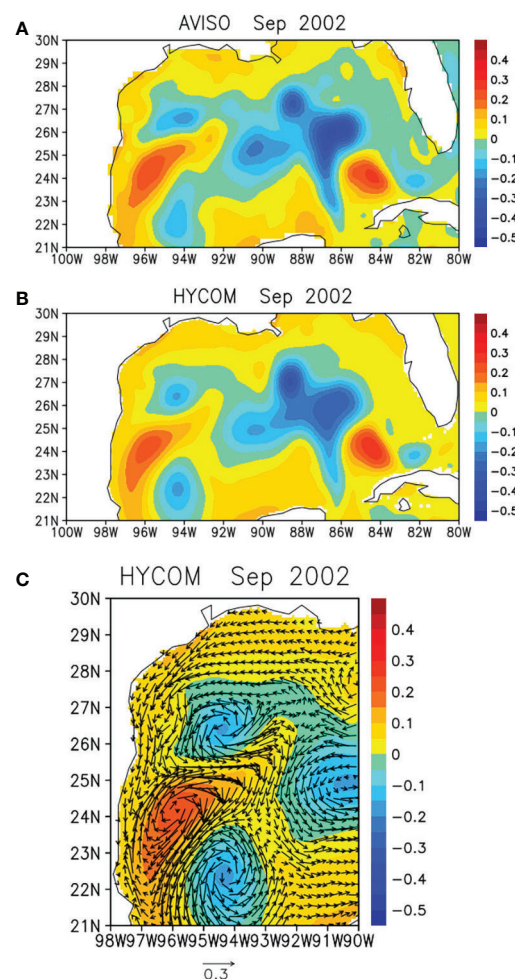


FIGURE 5

(A) Monthly mean SSH anomalies in the Gulf of Mexico in September 2002 derived from AVISO. (B) Same as (A) except for SSH anomalies from the HYCOM reanalysis. (C) SSH (shading) and surface currents (arrows) anomalies in September 2002 derived from the HYCOM reanalysis.

the anomalous southward coastal currents (and thus high SL at the coast) in the area of TCOON tide gauge stations when the eddy reaches near the coast.

These circulation patterns such as a large meander of coastal currents is consistent with previous theoretical studies on the processes associated with on-shore movement of anti-cyclonic eddy (e.g., Isoda, 1996; Frolov et al., 2004). Also, it is indicated that the area of influence along the coast by the anti-cyclonic eddy is 2–3 times as large as the eddy size based on the idealized numerical model simulations (Isoda, 1996; Frolov et al., 2004). Hence an anticyclonic eddy with the horizontal scale (diameter) of 200–300 km could be sufficient to influence SL rise in large areas along the western Gulf Coast. However, the detailed dynamics associated with the interaction between eddies, coastal currents and SL such as the coastal circulation induced by eddies are complex (e.g., Nof, 1984). In addition, the bottom topography (continental shelf) may further impact the eddy-induced coastal circulations (e.g., Frolov et al., 2004; An and McDonald, 2005; Vic et al., 2015). For example, the idealized numerical model simulations suggest that a cyclonic eddy could be formed north of the anti-cyclonic eddy with the presence of continental slope (Frolov et al., 2004), which is consistent with the circulation pattern in Figure 5C. Further theoretical studies are necessary to fully describe coastal processes associated with on-shore movement of an anti-cyclonic eddy.

To identify the origin of the anti-cyclonic eddy centered around 24°N–25°N, 96°W near the western Gulf Coast in September, 2002 which is associated with the coastal SL rise event, the SSH anomaly fields of the entire Gulf of Mexico derived from AVISO is described from the early 2002 to the peak period (Figure 6, left panels). The positive SSH anomalies near the coast in September can be traced back to those in the north central Gulf of Mexico around 90°W–93°W, 26°N–27°N in February. These large positive SSH anomalies centered around 92°W, 26.5°N in February extend to the east and south all the way to 24°N, which includes the area inside of the Loop Current (Figure 6, right panels). These positive anomalies split in March, and the western portion of the anomalies farther move to the west around 94°W, 25°N in May. Then the SSH anomalies with the size of ~200–300 km are completely separated from the eastern portion in June, and the western portion of the separated anomalies reach the coast in September, which is connected to the high SSH along the coast. These variations of SSH measured by AVISO are very similar to those from HYCOM reanalysis (Figure 6, middle panels), suggesting that upper ocean currents associated with these SSH anomalies can be realistically described using the HYCOM reanalysis.

The variations of upper ocean currents during February–September 2002 are displayed in right panels of Figure 6. During February, the Loop Current is extended northwestward in which the northern edge reaches around 27°N, 93°W. In March, the two anti-cyclonic circulations centered around 89°W, 26°N and

93°W, 26°N associated with high SSH are evident, and these anti-cyclonic circulations are separated from the high SSH in the southern portion of the basin. In May, these two anti-cyclonic circulations are merged, and continue to move westward. The center of the anti-cyclonic circulations is found around 94°W–24.5°N in June, and the western portion of the circulation reaches the Gulf Coast in September. During March–September, the anti-cyclonic circulations associated with high SSH are clearly isolated from surroundings and their westward propagation is evident. Note that the southward current right near the coast around 23°N–24°N in September shown in Figure 5 exists in the total field, but it is not found in Figure 6 due to the narrow width.

To further elucidate the Loop Current phase transition between February and March 2002, the detailed SSH and surface currents during early 2002 when the anti-cyclonic eddy is generated are fully described (Figure 7). The northwestward extension of the Loop Current started in late January, and the current continues to extend by February 10. The anti-cyclonic eddies started to separate from the Loop Current in mid-February. Then the two anti-cyclonic eddies are almost separated from the Loop Current by February 28, and the Loop Current retracted to the south after the eddy shedding. In early March, two anti-cyclonic eddies (also called Loop Current Eddies) originally separated from the Loop Current (eddy shedding) become completely isolated in the central Gulf of Mexico.

It should be noted that local anomalous winds in the area of TCOON tide gauge stations during the peak period of this extreme SL rise event are cyclonic and northwesterly along the coast (Figure S1, Figure 4), which are somewhat favorable for the downwelling (SL increase). However, the direction of the wind anomalies is not along-shore since the zonal component is positive (0.35 m/s, westerly) although the southward component of about 2 m/s is observed (Figure S1, Figure 4). Also, the strength of the anomalous winds (~2.2 m/s for the area average) is not at all extreme (Figure S1, Figure 4). Hence, the contribution of the local winds is expected to be very minor for the SL rise event during this period.

### 3.3.2 Event in 2015

The same analysis described in the previous section has been carried out for the period of the SL rise event observed in November 2015. The results are very similar to those for the 2002 event. Figure 8 shows the SSH and surface current anomalies from AVISO and HYCOM reanalysis in November 2015 when the SL anomalies from TCOON reach the peak value. The circulation patterns and SSH anomalies near the western Gulf Coast are similar to those during the 2002 event. The anti-cyclonic circulation around 25°N, 96°W is connected to southward alongshore currents. The southward along-shore currents north of the anti-cyclonic eddy directly flow towards

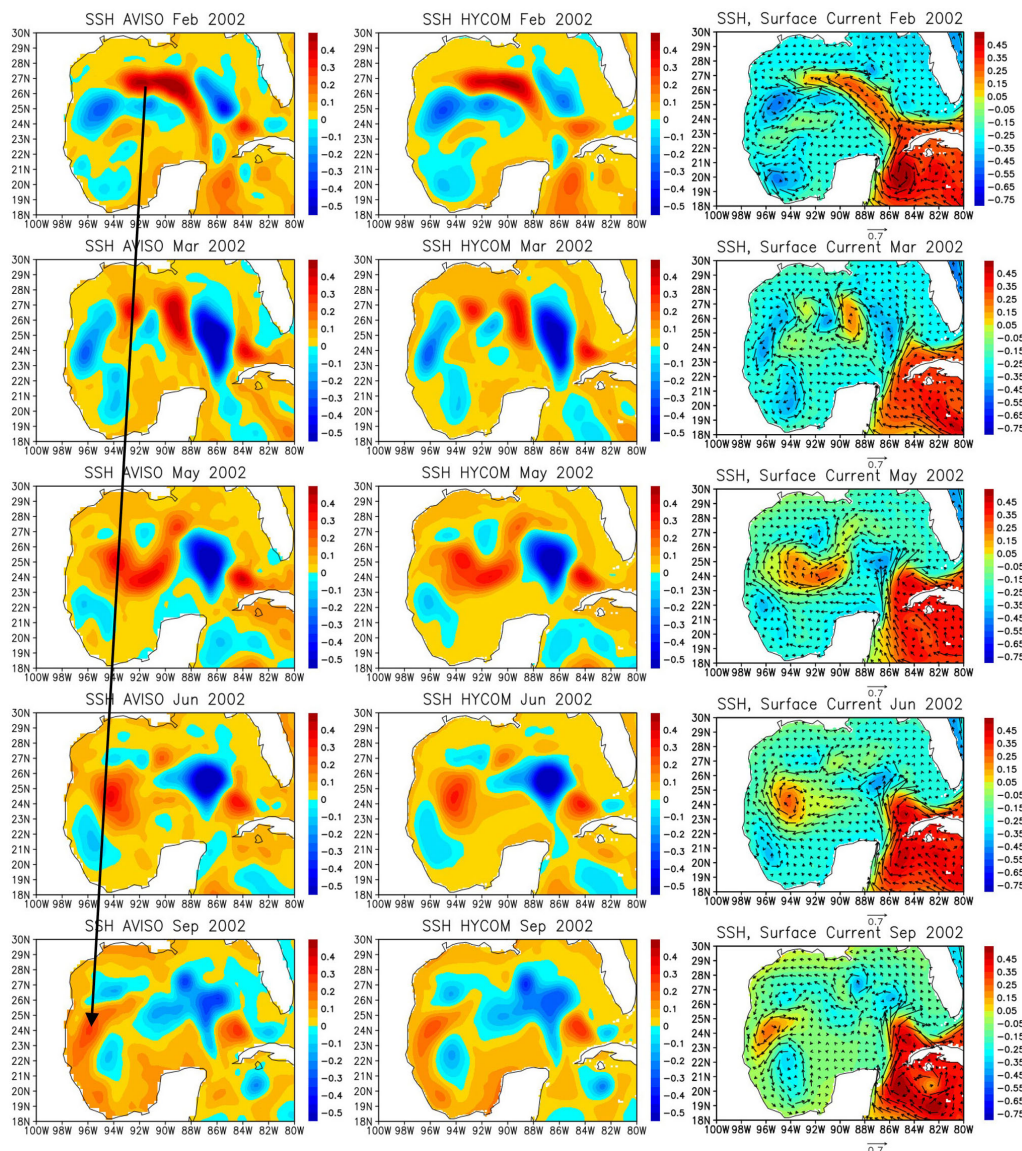


FIGURE 6

Left panels: SSH anomalies in February, March, May, June, and September, 2002 derived from AVISO. Middle panels: Same as left panels except for SSH anomalies derived from the HYCOM reanalysis. Right panels: Same as middle panels except for surface currents and SSH (total).

the eastern side of the eddy, and thus a large meander of the southward currents is evident as the eddy moves close to the coast. The narrow southward currents right near the coast on the western side of the eddy are also evident in November. The anomalous SSH from the HYCOM reanalysis is consistent with that from the satellite altimeter measurements.

The anti-cyclonic eddy near the western Gulf Coast in November can be traced back to the eddy shedding during April 2015 (Figure 9). The loop Current was extended to around 28°N in April, and eddies separated from the Loop Current split to three isolated eddies in June. Two of those eddies on the western side

moved westward and merged in September during which the western edge of the eddy is very close to the coast. The western portion of the eddy reached the coast in November when the SL rise reveals the maximum value. As in the 2002 SL rise event, the anti-cyclonic eddy separated from the Loop Current is shown to contribute to the extreme SL rise event in 2015.

In addition to the eddy on the western side of the basin which propagated westward, another strong anti-cyclonic eddy in the northern Gulf of Mexico may also have contributed to this SL rise event (Figure 9). During April–June, the Loop Current Eddy splits into two eddies, and the eddy on the western side



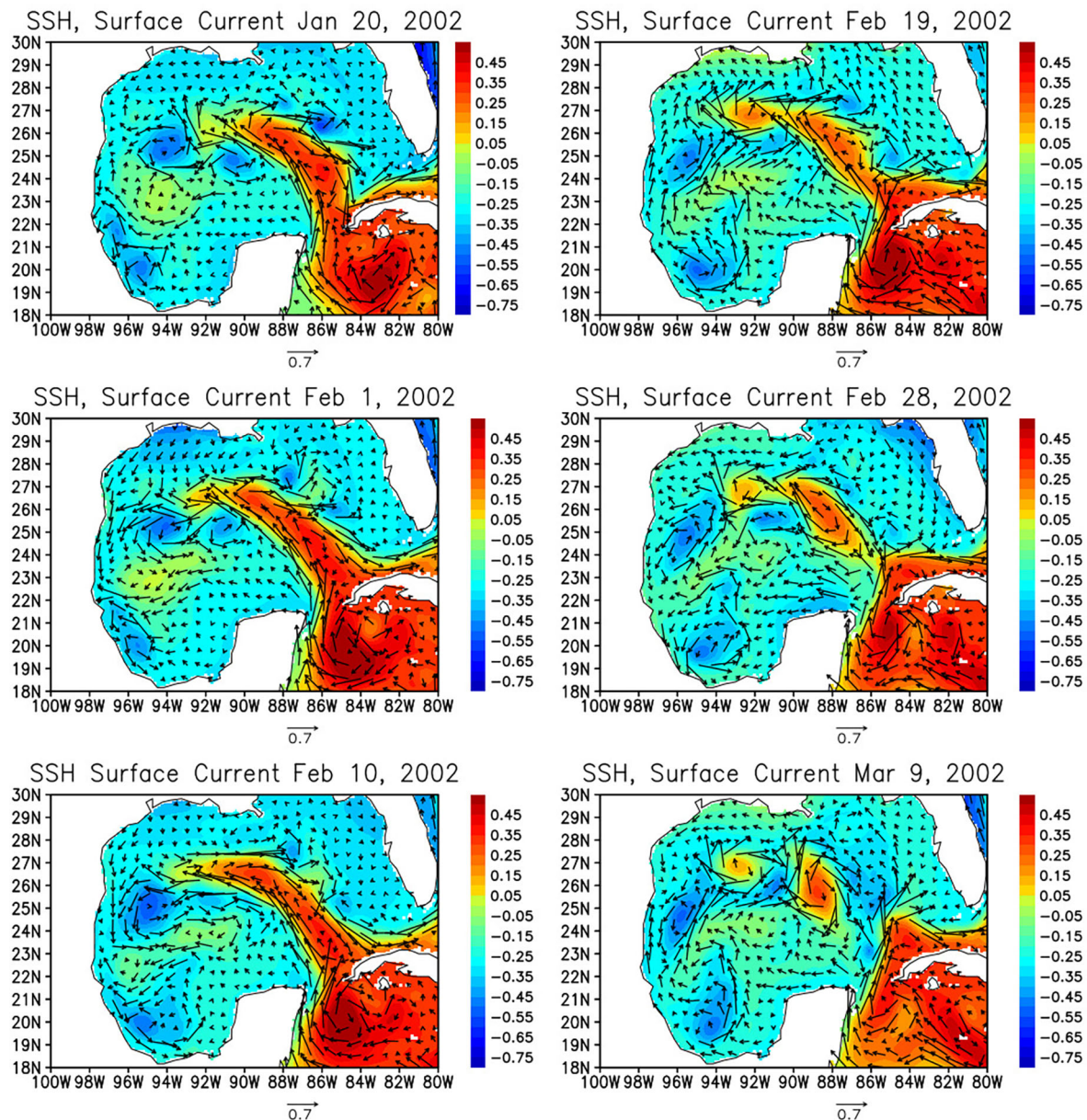


FIGURE 7

Surface currents (arrows) and SSH (shading) in January 20, February 1, 10, 19, 28, and March 9, 2002 derived from the HYCOM reanalysis.

moved westward and affected SL in the western Gulf Coast as described above. The eddy on the eastern side moved slowly northwestward in June–September. In September–November, the eddy further splits into two eddies, and the one on the northwestern side moved further northwestward and the northern edge of the eddy reached the central Gulf Coast in November. The SSH anomalies along the coast spread to the western side, which appears to affect the SL rise along the western Gulf Coast. The direction of the spreading of SL anomalies are consistent with the coastal trapped waves (e.g.,

Adams and Buchwald, 1969; Gill and Clarke, 1974; Brink, 1991). However, it is difficult to detect the propagation of those waves in this case only from the available data. Previous observational studies reported that the phase speed of coastal trapped waves along the western Gulf Coast is about 4 m/s (Dubranna et al., 2011; Rivas, 2017). The high temporal and spatial resolutions of the data near the coast is required to detect such fast waves propagating through the short distance in this case.

The local wind forcing does not help to generate SL rise during this event (Figure S1). The winds in the western Gulf

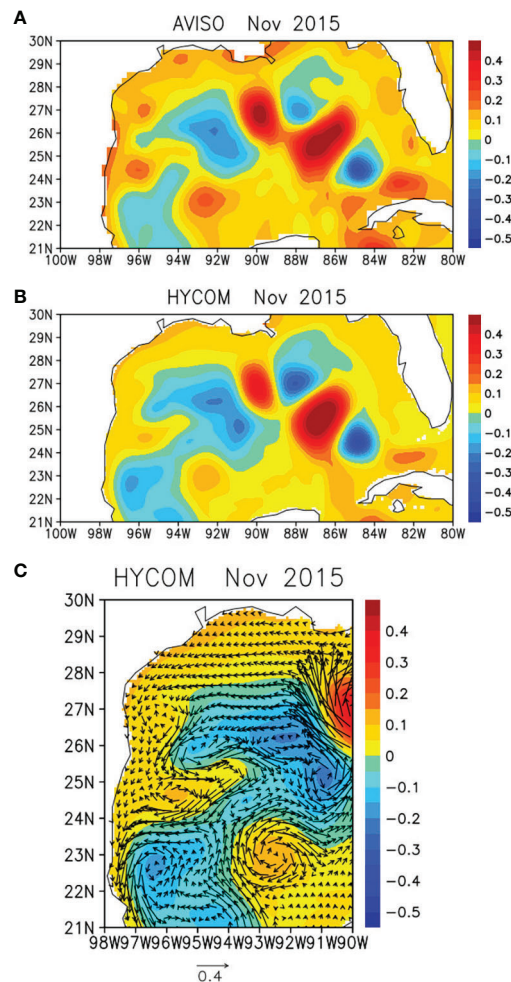


FIGURE 8  
Same as Figure 5 except for November 2015.

coast are predominantly easterlies, and the along-shore component is very small in the entire Texas coast.

### 3.3.3 Event in 2010

Figure 10 shows The SSH and surface wind anomalies in July 2010 when the peak of SL anomaly from the TCOON data occurred. While the satellite-derived SSH shows the high positive anomaly along the Gulf Coast, anti-cyclonic eddies near the coast similar to those observed during the 2002 and 2015 events are not clearly evident. Although the same analysis for the 2002 and 2015 events described above are conducted, a significant contribution of eddies moved from the remote areas to the coastal SL rise is not identified during this event (not shown). Instead, the strong along-shore wind anomalies which are favorable for the SL rise (downwelling) are found almost the entire coastal areas in the western and northern Gulf Coast. Anomalous SL rise are found all the way to the west Florida

coast. Since the SL fluctuations propagate westward as Kelvin or coastal trapped waves along the southern coast, the SL rise in the western Gulf Coast generated by local winds may not be recovered quickly. Hence, the large scale anomalous along-shore winds which cover the western and northern Gulf Coasts can maintain the SL rise in the western Gulf Coast for a relatively long time. Note that the anti-cyclonic eddy located around 96°W, 22.5°N in July, which appears to impinge on the shelf, and this eddy may have also contributed to maintain high SL along the coast. Note also that this eddy cannot be traced back directly to Loop Current Eddy shedding (not shown), and thus it seems to be developed locally in the western Gulf of Mexico

### 3.3.4 Event in 1995

An extreme SL rise event is observed in the mid-summer of 1995 in which the peak value is found in August (Figure 2). The westward movement of the anti-cyclonic eddy and its influence



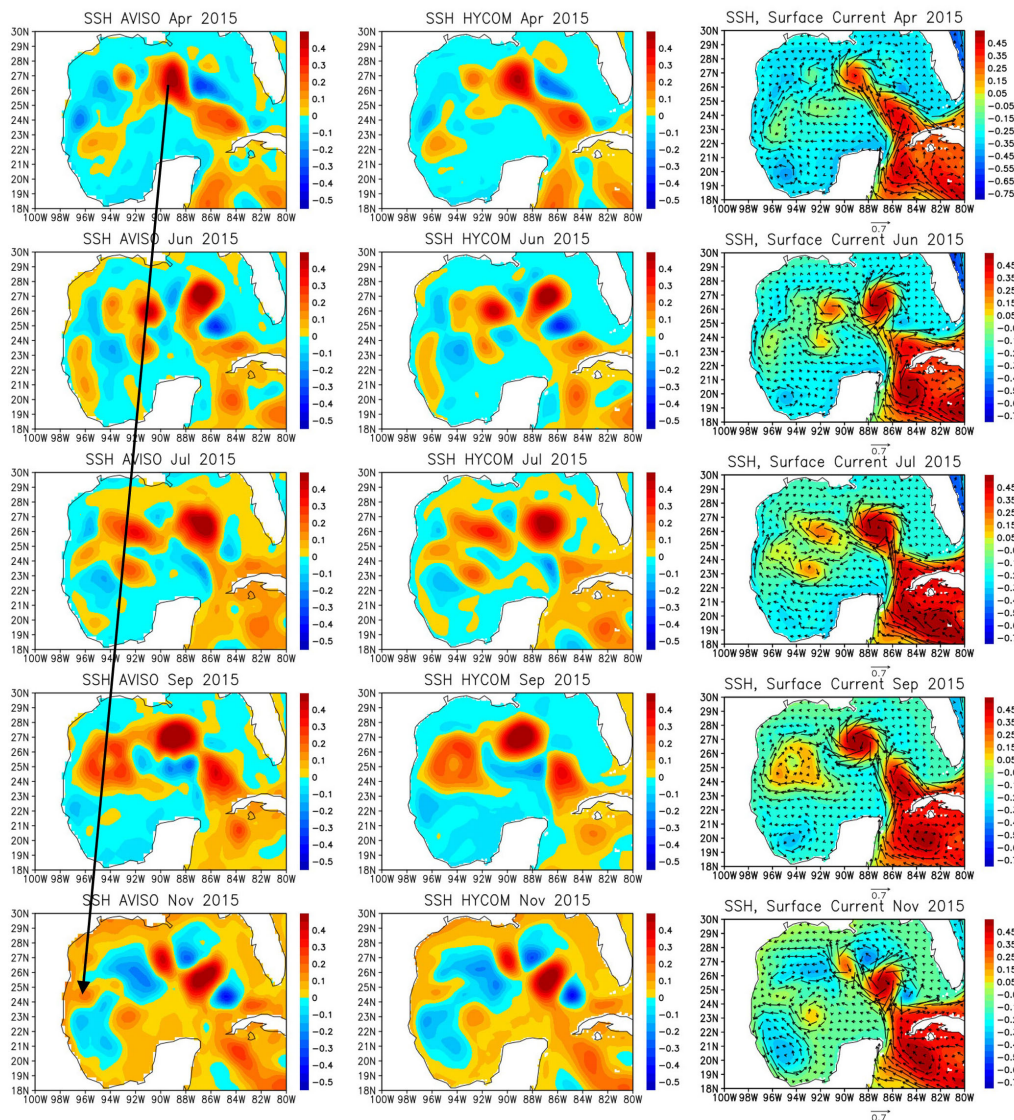


FIGURE 9  
Same as Figure 6 except for April, June, July, September, and November 2015.

on the coastal SL is evident (Figure 11). However, during the peak period in August, the anti-cyclonic circulation associated with positive SSH anomalies near the center of the eddy is somewhat weaker compared to those in the 2002 and 2015 SL rise events. Although the positive SSH anomalies moved from the central Gulf of Mexico are connected to the SL rise along the coast, the eddy is located farther offshore about  $4^\circ$  from the coast.

During this period, there is another anti-cyclonic eddy located around  $94^\circ\text{W}$ ,  $24^\circ\text{N}$  in August, which may have contributed to this SL rise event. This eddy was stronger in July and appears to start interacting with the coast (Figure 11 right panel). This eddy can be traced back to the eddy separated from the Loop Current before January 1995, which was located around

$93^\circ\text{W}$ ,  $25^\circ\text{N}$  in January. Since this eddy is connected to high SL along the coast in July–August (Figure 11, left panel), it may have contributed to the SL rise event. However, the eddy is also located offshore about  $3^\circ$  from the coast, and thus other factors probably contribute to this SL rise event during this period.

Figure 12 shows the surface wind anomalies in August 1995. The anomalous northeasterly and northerly winds which are along-shore direction in the entire areas of TCOON stations are clearly evident. However, the anomalous alongshore winds are confined in the western portion of the Gulf Coast (compared to 2010 events in Figure 10), and thus these winds alone may not cause the extreme SL rise event. Hence, the analysis of winds and ocean circulations suggests that a combination of anti-cyclonic

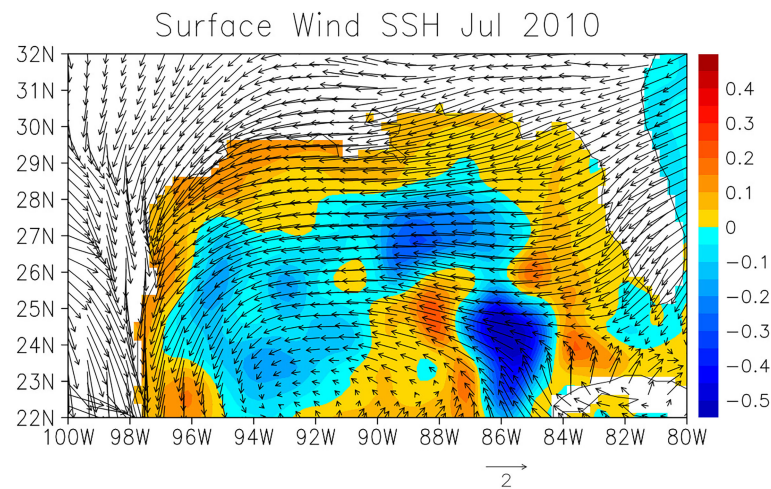


FIGURE 10  
Anomalies of surface winds (arrows) and SSH (shading) from AVISO in July 2010.

eddies originated from eddy shedding and the anomalous along-shore winds generates the SL rise event during this period.

### 3.3.5 Summary of all events

The same analysis described above is carried out for periods of all six SL rise events identified in the TCOON time series. Eddy shedding and subsequent westward movement of anti-cyclonic eddy is shown to contribute to the SL rise along the western Gulf Coast during the events in September 1998 and February 2005 (Figure S2, Figure S3). Table 1 summarizes the major physical processes that contribute to the SL rise events which include the period of eddy shedding. In five out of six events, anti-cyclonic eddies originated from eddy shedding of the Loop Current contribute to the SL rise. This suggests that ocean dynamics play an important role in generating extreme SL rise events at least on the subseasonal time scale.

The eddy shedding occurs 6-8 months before the peak SL rise in the western Gulf Coast. Hence, the information on the variability of Loop Current and eddy shedding such as the location and strengths of anti-cyclonic eddy several months in advance could help to predict the SL rise along the western Gulf Coast. Although not all eddies separated from the Loop Current affect the Gulf Coast SL rise events, the results at least suggest that the accurate prediction of the ocean circulations in the entire Gulf of Mexico is necessary for the accurate forecast of coastal SL rise event with the lead time of several months.

## 4 Summary and discussions

Oceanic and atmospheric processes that generate subseasonal sea level (SL) rise events along the western Gulf

Coast are investigated using Texas Coastal Ocean Observing Network (TCOON) and National Water Level Observation Network (NWLON) tide gauge data, the high-resolution (0.08°) ocean reanalysis, surface winds from the reanalysis, and satellite altimetry data. The time series of SL measured by TCOON and NWLON indicates that SL in the western Gulf Coast varies substantially on the subseasonal time scale. In particular, extreme subseasonal SL rise events which exceed 15 cm are observed once in every 2-5 years. The results indicate that most of such extreme subseasonal events are originated from the warm core anti-cyclonic eddy separated from the Loop Current which propagates westward. The anti-cyclonic eddies then reach the western Gulf Coast, resulting in prominent SL rise which lasts about 1-2 months. While the local wind forcing in the western Gulf Coast does not show extreme values and only weakly correlated, the analysis also suggests that large-scale along-shore winds over the entire western and northern Gulf Coast can cause such extreme SL rise events.

The results indicate that extreme SL rise events occur about 6-8 months after a strong anti-cyclonic eddy is formed by eddy shedding in the central Gulf of Mexico. Hence, the large-scale ocean circulations in the Gulf of Mexico needs to be monitored well to accurately predict the SL rise in the western Gulf of Mexico with the lead time of several months. In other words, the information of the ocean variability in the central Gulf of Mexico may help improve the SL prediction in the Gulf Coast. However, it is still a major challenge to predict the behavior of separated eddies including their westward movement. In general, the strong eddies separated from the Loop Current move westward, and some of the strong eddies are evident until they reach the western coast, resulting in generating the coastal SL rise. However, the behavior of the Loop Current Eddies are often



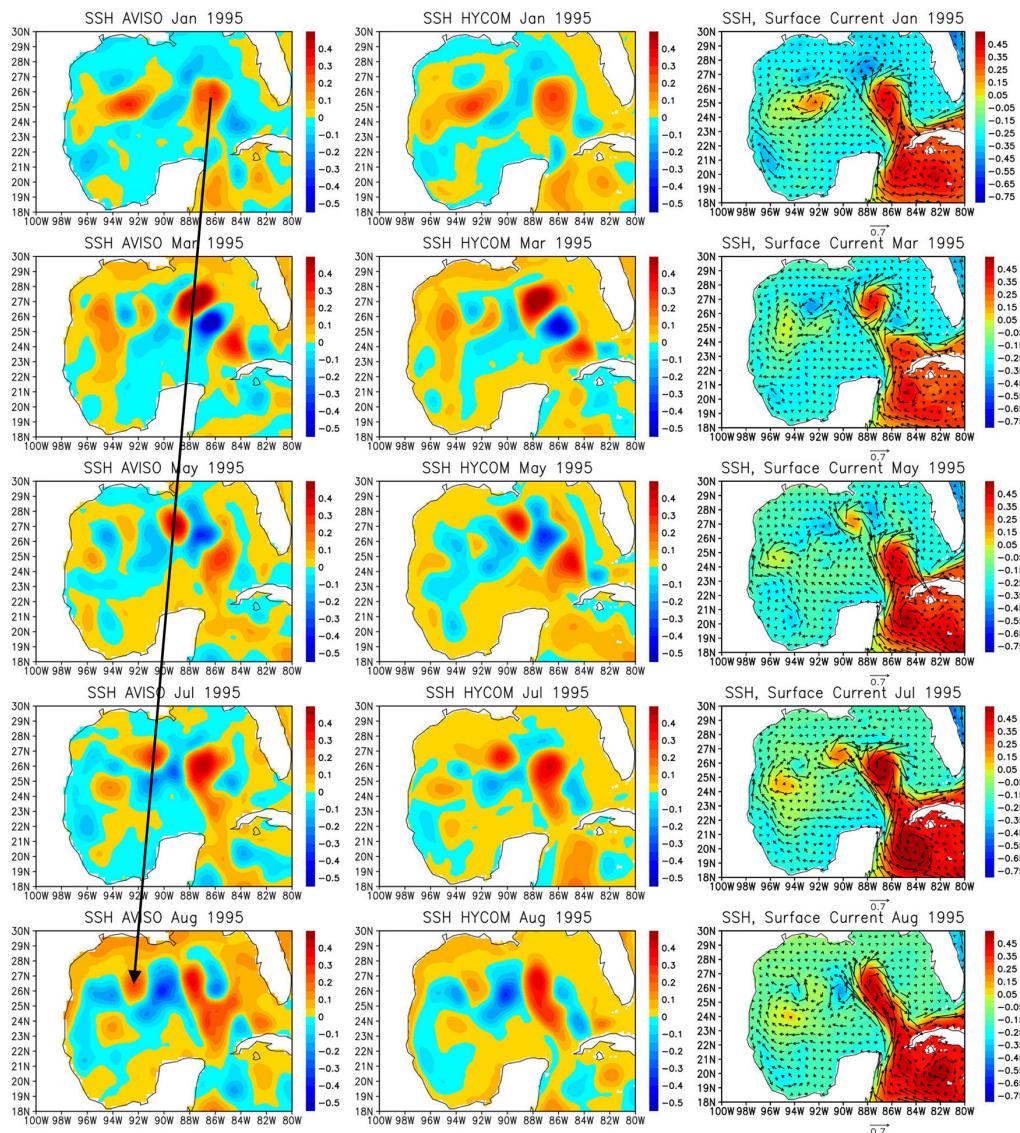


FIGURE 11  
Same as Figure 6 except for January, March, May, July, and August, 1995.

complex. As shown in the several examples in this study, eddies sometimes split to multiple eddies or merge with other eddies, and their strength changes substantially during the westward movement. These variations are determined by a combinations of different processes including internal ocean variability, the effect of atmospheric forcing and the large-scale ocean circulation. It is still unclear whether such detailed behavior of eddy movement is predictable, and the accurate prediction of strength and location of eddies at least requires further improvement of ocean component in the prediction system.

The results suggest that some of the SL events are caused by a combination of eddy-shedding and local wind forcing near the coast. However, the relative importance of these processes cannot

be quantified based only on the data analyses. A numerical modeling study is necessary to further quantify the physical processes that cause SL rise events. For example, sensitivity simulations of ocean model in which the anomalous wind forcing is removed could isolate the impact of ocean dynamics. Further studies using high-resolution numerical experiments which can adequately resolve the coastal SL fluctuation are necessary to isolate and quantify key physical processes.

In this study, physical processes associated with only extreme SL rise events are discussed. While the dominant processes that contribute to such extreme events could be identified, smaller SL rise events of about 10 cm are frequently observed in the western Gulf Coast. However, it is difficult to

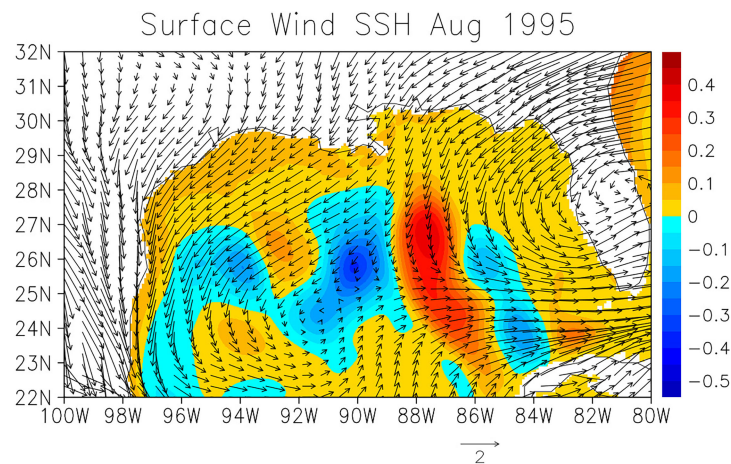


FIGURE 12  
Same as Figure 10 except for August, 1995.

identify dominant processes that cause such events. Many SL rise events with such magnitude may be caused by a combination of multiple processes. In the western Gulf of Mexico, eddy activity is relatively high, and mesoscale and submesoscale eddies are often observed. Although these eddies may not be as strong as the warm-core eddies generated through eddy shedding, weaker eddies may still influence SL along the coast. Since smaller fluctuations of SL are caused by these oceanic processes as well as atmospheric forcing such as along-shore winds, it is difficult to fully identify all physical processes associated with subseasonal SL fluctuations only from the available data. In particular, high-resolution data near the coast are required to adequately resolve the variability caused by coastal processes. As the higher resolution satellite-derived SL will become available from SWOT (Surface Water Ocean Topography) mission (e.g., Wang et al., 2018) in coming years, such data may provide useful information for the further study of coastal SL variations.

The analysis of TCOON and NWLON data indicates that the SL time series are positively skewed. The possible reason could be the asymmetry of cyclonic and anti-cyclonic eddies in the western portion of Gulf of Mexico. Because of the asymmetry

of eddy separation processes from the Loop Current, more anti-cyclonic eddies are found in the western Gulf of Mexico, while more cyclonic eddies are evident in the eastern Gulf of Mexico (e.g., Vukovich, 2007). The frequent influence of anti-cyclonic eddies on western Gulf Coast SL may result in skewed distribution of SL anomalies at the coast.

The Loop Current is part of the western boundary current connected to Gulf Stream, and thus it is part of the upper branch of the Atlantic Meridional Overturning Circulation (AMOC). Recent studies suggest that the AMOC is changing in a warming climate (e.g., Liu et al., 2017; Boers, 2021), and thus it is expected that the behavior of the Loop Current including its strength, frequency of eddy shedding, the strength and location of anti-cyclonic rings separated from the Loop Current will be changing in the coming decades. Such changes may influence the skewness of the SL anomaly distribution, and it may in turn affect the longer-term variation of the coastal SL through the skewness changes. Hence, understanding the dynamics of long-term changes in the Loop Current strength and its impact on eddy shedding is crucial for the future SL projection along the Gulf Coast.

TABLE 1 Periods of extreme SL rise events and associated major processes.

Period of peak SL rise	Major processes
August 1995	Eddy Shedding (January 1995), Along-shore winds
September 1998	Eddy Shedding (January 1998)
September 2002	Eddy Shedding (February 2002)
February 2005	Eddy Shedding (August 2004)
July 2010	Along-shore winds
November 2015	Eddy Shedding (May 2015)



## Data availability statement

The original contributions presented in the study are included in the article/[Supplementary Material](#). Further inquiries can be directed to the corresponding author.

## Author contributions

TS conceived the idea and designed and performed most of the analysis. PT and AR contributed to complete the analysis of TCOON data. TS wrote the paper, and other co-authors assisted in writing it. All authors contributed to the article and approved the submitted version.

## Funding

TS acknowledges support from NOAA Grant NA17OAR4310256 and DOD Grant W911NF-20-1-0309. PT acknowledges support from the National Science Foundation award 2019758.

## References

- Adams, J. K., and Buchwald, V. T. (1969). The generation of continental shelf waves. *J. Fluid Mech.* 35, 815–826.
- An, B. W., and McDonald, N. R. (2005). Coastal currents and eddies and their interaction with topography. *Dynamics Atmospheres Oceans* 40, 237–253. doi: 10.1016/j.dynatmoce.2005.04.002
- Bleck, R. (2002). An oceanic general circulation model framed in hybrid isopycnal-Cartesian coordinates. *Ocean Model.* 4, 55–88. doi: 10.1016/S1463-5003(01)00012-9
- Boers, N. (2021). Observation-based early-warning signals for a collapse of the Atlantic meridional overturning circulation. *Nat. Climate Change* 11, 680–688. doi: 10.1038/s41558-021-01097-4
- Boon, J. D., Mitchell, M., Loftis, J. D., and Malmquist, D. L. (2018). *Anthropocene Sea level change: A history of recent trends observed in the U.S. East, gulf, and West coast regions. special report in applied marine science and ocean engineering (SRAMSOE) no. 467* (Virginia Institute of Marine Science, William & Mary). doi: 10.21220/V5T17T
- Brink, K. H. (1991). Coastal-trapped waves and wind-driven currents over the continental shelf. *Annu. Rev. Fluid Mech.* 23, 389–412.
- Chassignet, E. P., Hurlburt, H. E., Smedstad, O. M., Barron, C. N., Ko, D. S., Rhodes, R. C., et al. (2005). “Assessment of ocean data assimilative systems in the Gulf of Mexico using ocean color,” in *AGU monograph “New developments in the circulation of the Gulf of Mexico*, vol. Vol. 161. Eds. W. Sturges and L.-. Fernandez (AGU, Washington DC), pp 87–pp100.
- Chen, X., Qiu, B., Cheng, X., et al. (2015). Intra-seasonal variability of pacific-origin sea level anomalies around the Philippine archipelago. *J. Oceanogr.* 71, 239–249. doi: 10.1007/s10872-015-0281-9
- Coats, D. A. (1992). “The loop current,” in *In the physical oceanography of the U.S. Atlantic and Eastern Gulf of Mexico*, U.S. dept of the interior, mineral management service, *Atlantic OCS region*. Eds. J. D. Milliman and E. Imamura (Herndon, Va.), Chapter 6.
- Cochrane, J. D. (1972). “Separation of an anticyclone and subsequent developments in the loop current, (1969),” in *Contributions on the physical oceanography of the Gulf of Mexico*. Eds. L. R. A. Capurro and J. L. Reid (Houston, Texas: Gulf Publishing Co.), 91–106.
- Cummings, J. A., and Smedstad, O. M. (2013). “Variational data assimilation for the global ocean,” in *Data assimilation for atmospheric, oceanic and hydrologic applications*, vol. Vol. II). (Springer Berlin Heidelberg), 303–343. doi: 10.1007/978-3-642-35088-7
- Dubranca, J., Pérez-Brunius, P., López, M., and Candela, J. (2011). Circulation over the continental shelf of the western and southwestern Gulf of Mexico. *J. Geophys. Res.* 116, C08009. doi: 10.1029/2011JC007007
- Elliott, B. A. (1982). Anti-cyclonic rings in the Gulf of Mexico. *J. Phys. Oceanogr.* 12, 1292–1309.
- Espinoza, V., Waliser, D. E., Guan, B., Lavers, D. A., and Ralph, F. M. (2018). Global analysis of climate change projection effects on atmospheric rivers. *Geophys. Res. Lett.* 45 (9), 4299–4308. doi: 10.1029/2017GL076968
- Ezer, T., Atkinson, L. P., Corlett, W. B., and Blanco, J. L. (2013). Gulf stream's induced sea level rise and variability along the U.S. mid-Atlantic coast. *J. Geophys. Res.* 118 (2), 685–697. doi: 10.1002/jgrc.20091
- Feng, X., Shinoda, T., and Han, W. (2022). Topographic trapping of the lee win current and its impact on the Ningaloo Niño. *J. Climate*. doi: 10.1175/JCLI-D-22-0218.1
- Frolov, S. A., Sutyryn, G. G., Rowe, G. D., and Rothstein, M. (2004). Loop current eddy interaction with the Western boundary in the Gulf of Mexico. *J. Phys. Oceanogr.* 34, 2223–2237. doi: 10.1175/1520-0485(2004)034<2223:LCEIWT>2.0.CO;2
- Gill, A. E., and Clarke, A. J. (1974). Wind-induced upwelling, coastal currents and sea-level changes. *Deep-Sea Res.* 21, 325–345.
- Han, W., Meehl, G. A., Hu, A., Alexander, M., Yamagata, T., Yuan, D., et al. (2014). Intensification of decadal and multi-decadal sea level variability in the western tropical pacific during recent decades. *Clim. Dyn.* 43, 1357–1379. doi: 10.1007/s00382-013-1951-1
- Han, W., Meehl, G. A., Rajagopalan, B., Fasullo, J., Hu, A., Lin, J., et al. (2010). Patterns of Indian ocean sea level change in a warming climate. *Nat. Geosci* 3, 546–550. doi: 10.1038/NGEO901
- Helber, R. W., Townsend, T. L., Barron, C. N., Dastugue, J. M., and Carnes, M. R. (2013). Validation test report for the improved synthetic ocean profile ( ISOP ) system. *Part I : Synthetic Profile Methods and. NRL Memo. Rep.*, 1–6.
- IPCC (2022). “Climate change 2022: Impacts, adaptation, and vulnerability,” in *Contribution of working group II to the sixth assessment report of the intergovernmental panel on climate change*. Eds. H.-O. Pörtner, D. C. Roberts, M. Tignor, E. S. Poloczanska, K. Mintenbeck, A. Alegria, M. Craig, S. Langsdorf, S. Löschke, V. Möller, A. Okem and B. Rama (Cambridge University Press).

## Conflict of interest

The authors declare that the research was conducted in the absence of any commercial or financial relationships that could be construed as a potential conflict of interest.

## Publisher's note

All claims expressed in this article are solely those of the authors and do not necessarily represent those of their affiliated organizations, or those of the publisher, the editors and the reviewers. Any product that may be evaluated in this article, or claim that may be made by its manufacturer, is not guaranteed or endorsed by the publisher.

## Supplementary material

The Supplementary Material for this article can be found online at: <https://www.frontiersin.org/articles/10.3389/fmars.2022.1049550/full#supplementary-material>

- Isoda, Y. (1996). Interaction of a warm eddy with the coastal current at the eastern boundary area in the tsushima current region. *Continental Shelf Research* 16, 1149–1163. doi: 10.1016/0278-4343(95)00057-7
- Leben, R. R. (2005). “Altimeter-derived loop current metrics,” in *Circulation in the Gulf of Mexico: Observations and models, geophys*, vol. 161. Eds. W. Sturges and A. Lugo-Fernandez (AGU, Washington, D. C.), 181–201.
- Liu, W., Xie, S.-P., Liu, Z., and Zhu, J. (2017). Overlooked possibility of a collapsed Atlantic Meridional Overturning Circulation in warming climate. *Science Adv.* 3, e1601666. doi: 10.1126/sciadv.1601666
- Maul, G. A. (1977). The annual cycle of the gulf loop current, part I: Observations during a one-year time series. *J. Mar. Res.* 35, 29–47.
- Metzger, J. E., Smedstad, O. M., Thoppil, P. G., Hurlburt, H. E., Cummings, J. A., Wallcraft, A. J., et al. (2014). US Navy operational global ocean and Arctic ice prediction systems. *Oceanography* 27, 32–43. doi: 10.5670/oceanog.2014.66
- Miline, G. A., Gehrels, W. R., Hughes, C. W., and Tamisiea, M. E. (2009). Identifying the causes of sea-level change. *Nature. Geosci.* 2, 471–478. doi: 10.1038/ngeo544
- Minobe, S., Terada, M., Qiu, B., and Schneider, N. (2017). Western Boundary sea level: a theory, rule of thumb, and application to climate models. *J. Phys. Oceanogr.* 47 (5), 957–977. doi: 10.1175/JPO-D-16-0144.1
- Moore, C. N. K., and Maul, G. A. (1998). “Intra-americas Sea circulation,” in *The Sea*, vol. Vol. 11. Eds. K. H. Brink and A. R. Robinson (NY: John Wiley), pp.183–pp.208.
- Nof, D. (1984). On the interaction between thin isolated eddies and longshore currents. *J. Phys. Oceanogr.* 14, 125–137.
- O’Brien, T. A., et al. (2021). Increases in future AR count and size: Overview of the ARTMIP tier 2 CMIP5/6 experiment. *JGR-Atmosphere* 127, e2021JD036013. doi: 10.1029/2021JD036013
- Qiu, B., Chen, S., Wu, L., and Kida, S. (2015). Wind- versus eddy-forced regional sea level trends and variability in the north pacific ocean. *J. Climate* 28, 1561–1577.
- Rivas, D. (2017). Wind-driven coastal-trapped waves off southern tamaulipas and northern veracruz, western Gulf of Mexico, during winter 2012–2013. *Estuar. Coast. Shelf Sci.* 185, 1–10. doi: 10.1016/j.ecss.2016.12.002
- Rizzo, J., Tissot, P., and Duff, S. (2014). The Texas coastal ocean observation network. *2014 Oceans - St. John's*. doi: 10.1109/OCEANS.2014.7003131
- Saha, S., Moorthi, S., Pan, H.-L., Wu, X., Wang, J., Nadiga, S., et al. (2010). The NCEP climate forecast system reanalysis. *Bull. Amer. Meteor. Soc.* 91, 1015.1057. doi: 10.1175/2010BAMS3001.1
- Saha, S., Moorthi, S., Wu, X., Wang, J., Nadiga, S., Tripp, P., et al. (2014). The NCEP climate forecast system version 2. *J. Climate* 27, 2185–2208. doi: 10.1175/JCLI-D-12-00823.1
- Schmitz, Biggs, D. C., Lugo-Fernandez, A., Oey, L.-Y., and Sturges, W. (2005). “A synopsis of the circulation in the Gulf of Mexico and on its continental margins,” in *Circulation in the Gulf of Mexico: Observations and models, geophysical monographs series*. Eds. W. T. Sturges and A. Lugo-Fernandez (Washington DC: American Geophysical Union), 11–29. doi: 10.1029/161GM03
- Shay, L. K., Goni, G. J., and Black, P. G. (2000). Effects of a warm oceanic feature on hurricane opal. *Mon. Wea. Rev.* 128, 1366–1138. doi: 10.1175/1520-0493(2000)128<1366:EOAWOF>2.0.CO;2
- Shay, L. K., Mariano, A. J., Jacob, S. D., and Ryan, E. H. (1998). Mean and near-inertial ocean current response to hurricane Gilbert. *J. Phys. Oceanogr.* 28 (5), 858–889. doi: 10.1175/1520-0485(1998)028<0858:MANIOC>2.0.CO;2
- Shinoda, T., Han, W., Zamudio, L., and Feng, X. (2020). Influence of atmospheric rivers on the leewind current system. *Clim. Dyn.* 54, 4263–4277. doi: 10.1007/s00382-020-05228-z
- Shinoda, T., Zamudio, L., Guo, Y., Metzger, E. J., and Fairall, C. (2019). Ocean variability and air-sea fluxes produced by atmospheric rivers. *Sci. Rep.* 9. doi: 10.1038/s41598-019-38562-2
- Sturges, W., and Leben, R. (2000). Frequency of ring separations from the loop current in the Gulf of Mexico: A revised estimate. *J. Phys. Oceanogr.* 30, 1814–1818.
- Sweet, W., Dusek, G., Carbin, G., Marra, J., Marcy, D., and Simon, S. (2021). *2019 state of U.S. high tide flooding with a 2020 outlook* (NOAA Technical Report NOS CO-OPS 092). doi: 10.1175/1520-0485(2000)030<1814:FORSFT>2.0.CO;2
- Thoppil, P. G., Metzger, E. J., Hurlburt, H. E., Smedstad, O. M., and Ichikawa, H. (2016). The current system east of the Ryukyu islands as revealed by a global ocean reanalysis. *Prog. Oceanogr.* 141, 239–258. doi: 10.1016/j.pocean.2015.12.013
- Unnikrishnan, A. S., and Shanker, D. (2007). Are sea-level-rise trends along the coasts of north Indian ocean consistent with global estimate? *Global Planet. Change* 57, 301–307. doi: 10.1016/j.gloplacha.2006.11.029
- Vic, C., Roulet, G., Capet, X., Carton, X. J., Molemaker, M. J., and Gula, J. (2015). Eddy-topography interactions and the fate of the Persian gulf outflow. *J. Geophys. Res. Oceans Wiley-Blackwell* 120 (10), 6700–6717. doi: 10.1002/2015JC011033
- Vukovich, F. M. (1995). An updated evaluation of the loop currents eddy shedding frequency. *J. Geophys. Res.* 100, 8655–8659. doi: 10.1029/95JC00141
- Vukovich, F. M. (2007). Climatology of ocean features in the Gulf of Mexico using satellite remote sensing data. *J. Phys. Oceanogr.* 37, 689–707. doi: 10.1175/JPO2989.1
- Wang, J., Fu, L.-L., Qiu, B., Menemenlis, D., Farrar, J. T., Chao, Y., et al. (2018). An observing system simulation experiment for the calibration and validation of the surface water and ocean topography sea surface height measurement using in-situ platforms. *J. Atmos. Oceanic Technol.* 35, 281–297. doi: 10.1175/JTECH-D-17-0076.1
- Wang, G., Zhou, X., Wang, K., Ke, X., Zhang, Y., Zhao, R., et al. (2020). GOM20: A stable geodetic reference frame for subsidence, faulting, and Sea-level rise studies along the coast of the Gulf of Mexico. *Remote Sens.* 12 (3), 350. doi: 10.3390/rs12030350
- Wiseman, W. J., Jr., and Dinnel, S. P. (1988). Shelf current near the mouth of the Mississippi river. *J. Phys. Oceanogr.* 18 (9), 1287–1291. doi: 10.1175/1520-0485(1988)018<1287:SCNTMO>2.0.CO;2
- Woodworth, P. L., White, N. J., Jevrejeva, S., Holgate, S. J., Church, J. A., Ghrels, W. R., et al. (2009). Evidence for the acceleration of sea level on multi-decade and century time scales. *Int. J. Climatol.* 29, 777–789.
- Yu, Z., Metzger, E. J., Thoppil, P., Hurlburt, H. E., Zamudio, L., Smedstad, O. M., et al. (2015). Seasonal cycle of volume transport through kerama gap revealed by a 20-year global HYbrid coordinate ocean model reanalysis. *Ocean Model.* 96, 203–213. doi: 10.1016/j.ocemod.2015.10.012
- Zamudio, L., and Hogan, P. (2008). Nesting the Gulf of Mexico in Atlantic HYCOM: Oceanographic processes generated by hurricane Ivan. *Ocean Modeling* 21, 106–125. doi: 10.1016/j.ocemod.2007.12.002
- Zervas, C., Gill, S., and Sweet, W. (2013). Estimating vertical land motion from long-term tide gauge records. *NOAA Tech. Rep. NOS CO-OPS* 65, 22.



## OPEN ACCESS

## EDITED BY

Julio Sheinbaum,  
Centro de Investigación Científica y de  
Educación Superior de Ensenada  
(CICESE), Mexico

## REVIEWED BY

Heriberto Vazquez,  
University of California, San Diego,  
United States  
Gabriela Athié,  
Universidad de Veracruz, Mexico

## \*CORRESPONDENCE

Nektaria Ntaganou  
✉ nntaganou@fsu.edu

## †PRESENT ADDRESS

Nektaria Ntaganou,  
Center for Ocean-Atmospheric  
Prediction Studies, Florida State  
University, Tallahassee, FL, United States

## SPECIALTY SECTION

This article was submitted to  
Physical Oceanography,  
a section of the journal  
Frontiers in Marine Science

RECEIVED 03 June 2022

ACCEPTED 13 January 2023

PUBLISHED 27 January 2023

## CITATION

Ntaganou N, Kourafalou V, Beron-Vera FJ,  
Olascoaga MJ, Le Hénaff M and  
Androulidakis Y (2023) Influence of  
Caribbean eddies on the Loop current  
system evolution.  
*Front. Mar. Sci.* 10:961058.  
doi: 10.3389/fmars.2023.961058

## COPYRIGHT

© 2023 Ntaganou, Kourafalou, Beron-Vera,  
Olascoaga, Le Hénaff and Androulidakis. This  
is an open-access article distributed under  
the terms of the [Creative Commons  
Attribution License \(CC BY\)](#). The use,  
distribution or reproduction in other  
forums is permitted, provided the original  
author(s) and the copyright owner(s) are  
credited and that the original publication in  
this journal is cited, in accordance with  
accepted academic practice. No use,  
distribution or reproduction is permitted  
which does not comply with these terms.

# Influence of Caribbean eddies on the Loop current system evolution

Nektaria Ntaganou <sup>1\*†</sup>, Vassiliki Kourafalou<sup>1</sup>,  
Francisco Javier Beron-Vera<sup>1</sup>, Maria Josefina Olascoaga<sup>1</sup>,  
Matthieu Le Hénaff<sup>2,3</sup> and Yannis Androulidakis<sup>1,4</sup>

<sup>1</sup>Department of Ocean Sciences, Rosenstiel School of Marine, Atmospheric, and Earth Science, University of Miami, Miami, FL, United States, <sup>2</sup>Cooperative Institute for Marine and Atmospheric Studies (CIMAS), University of Miami, Miami, FL, United States, <sup>3</sup>Atlantic Oceanographic and Meteorological Laboratory (AOML), NOAA, Miami, FL, United States, <sup>4</sup>Department of Civil Engineering, Laboratory of Maritime Engineering and Maritime Works, Aristotle University of Thessaloniki, Thessaloniki, Greece

The Loop Current (LC) system dynamics are an essential component of the processes influencing circulation and transport in the Gulf of Mexico (GoM). The LC evolution is influenced by various factors, including the rich eddy field of the region and the flow exchange through the Yucatan Strait with the neighboring Caribbean Sea. These factors contribute to the complexity of the LC and, as a result, to the limitations in the predictability of the system. The focus of this study is to further elucidate the evolution of the LC, by quantifying the influence of coherent eddy fluxes originating in the Caribbean Sea. This is achieved by employing the Lagrangian-Averaged Vorticity Deviation (LAVD) method, an objective metric to evaluate eddy coherence in the Caribbean Sea that allows, for the first time, to quantify at different depths the evolution of coherent Caribbean eddies through the Yucatan Channel towards the GoM. The physical connectivity between the Caribbean Sea and the GoM is addressed using Lagrangian techniques to analyze processes that take place south of the Yucatan Channel and help quantify their strong relationship with the GoM eddy field. Coherent anticyclonic vorticity fluxes, as well as the net coherent anticyclonic volume transport between the Caribbean Sea and the GoM are associated with Loop Current Eddy (LCE) detachments through direct connectivity between the coherent Caribbean anticyclones and the forming LCE. The findings have important implications for understanding and predicting the LC system and the physical connectivity processes between the GoM and the Caribbean Sea.

## KEYWORDS

Lagrangian-Averaged Vorticity Deviation, eddy detection and tracking, HYCOM, Gulf of Mexico, Yucatan Channel

## 1 Introduction

Understanding and predicting the Loop Current (LC) variability in the Gulf of Mexico (GoM) has been an ongoing effort, mainly due to the rich eddy field of the region (Androulidakis et al., 2014; Le Hénaff et al., 2014) and the irregular behavior of the Loop Current Eddy (LCE) shedding cycles (Vukovich and Maul, 1985; Lugo-Fernández, 2007). Many studies have focused on the processes that take place within the GoM interior and are

tied to the LCE shedding events, such as the intensification and baroclinic instability of frontal cyclones (Schmitz, 2005; Chérubin et al., 2006; Le Hénaff et al., 2012; Donohue et al., 2016). Others have investigated processes in the Caribbean Sea connected to the variability of the LC system, such as wind effects and eddy influence (Oey et al., 2003; Athié et al., 2012; Androulidakis et al., 2021), as well as vorticity flux through the Yucatan Channel (Candela et al., 2002; Oey, 2004; Androulidakis et al., 2021).

In this study, we aim to investigate how the mesoscale eddy field in the northwestern Caribbean Sea may contribute to the LC evolution. We approach the problem by focusing on the interaction between the dominant processes in the GoM (namely LC phase transition from extended to retracted through LCE shedding events) and eddies that originate in the Caribbean Sea and pass through the Yucatan Channel. The effects of Caribbean eddies on the LC variability have not been studied as extensively as the processes that take place in the GoM interior. However, previous studies have shown the importance of including the processes upstream (south of the Yucatan Channel) to further understand the GoM dynamics. The recent study by Androulidakis et al. (2021) showed that the anticyclonic relative vorticity south of the Yucatan Channel is correlated to the eastward tilt of the LC axis and associated with the eastward shift of the Yucatan Current position at the base of the LC, with a lag of 5–10 days. Furthermore, according to the authors, the presence of anticyclonic eddies in the northwestern Caribbean Sea coincides with retracted LC phases, whereas the absence of such eddies usually coincides with extended LC phases. Androulidakis et al. (2021) used Eulerian analysis on altimetry-derived data and drifter trajectories to identify anticyclonic eddies in the northwestern Caribbean Sea, as well as limited Lagrangian analysis using the “geodesic eddy detection”, a method to objectively detect coherent material eddies (Haller and Beron-Vera, 2013; Haller and Beron-Vera, 2014), which they applied on numerical model near-surface velocities. The geodesic eddy detection method identifies fluid regions with the same averaged material stretching (to the first order), that experience no filamentation under advection (Haller and Beron-Vera, 2013; Haller and Beron-Vera, 2014). Their results confirmed that surface anticyclonic relative vorticity flux at the Yucatan Channel is present mostly during retracted LC phases. We here aim to expand on these findings, by performing a different Lagrangian analysis, based on vorticity, the “Lagrangian-Averaged Vorticity Deviation” (LAVD, Haller et al., 2016), that was used in Androulidakis et al. (2021) to identify near-surface coherence of only one particular Caribbean Anticyclone (CarA). LAVD, unlike the geodesic method, is associated with regions of high vorticity and tangential boundary filamentation is allowed. In the present study, LAVD is applied on model velocities in the entire water column, to identify eddies south of the Yucatan Channel.

The anticyclonic Caribbean eddies were first mentioned in Murphy et al. (1999), who performed a modeling study on the connectivity of the mesoscale field among the Caribbean Sea, the GoM, and the Atlantic Ocean. The authors argued that there is statistically significant correlation between eddies that form in the easternmost Caribbean Sea and the LCE shedding events. They also noticed interactions between the anticyclonic Caribbean eddies and the LC main body, after the Caribbean eddies enter the GoM through the Yucatan Channel. The concept of connectivity between the tropical Atlantic Ocean and the GoM was also discussed in the

recent study by Huang et al. (2021). The authors, using satellite products of altimetry, sea surface salinity, and chlorophyll, argued that freshwater from the tropical Atlantic can be transported to the GoM through mesoscale features that travel through the Lesser Antilles to the Caribbean Sea. The freshwater input from the tropical Atlantic can impact the variability of the GoM dynamics, adding to the complexity of the system (Huang et al., 2021). Oey et al. (2003) in their modeling study, using Eulerian estimates, suggested that the LCE shedding cycles are subject to wind-induced transport fluctuations of the Yucatan Current and the presence of anticyclonic eddies originating in the Caribbean Sea. More specifically, they showed that anticyclonic activity in the northwestern Caribbean Sea promotes longer LCE shedding intervals, while wind-induced transport fluctuations are connected to shorter LCE shedding intervals. Garcia-Jove et al. (2016), in their modeling study, showed that Caribbean anticyclones are associated with LCE detachments but noted that they are not the primary driver of the detachments. Instead, the authors argue that instabilities that take place in the Campeche Bank and the LC extension are the primary mechanism for LCE detachments and/or final separations. However, Athié et al. (2012) argued that another factor connected to the LC evolution and LCE shedding is the eastward shift of the Yucatan Current, caused by cyclonic eddies generated south of the Yucatan Current, right before LCE detachments. Candela et al. (2002), using data from a mooring array of Acoustic Doppler Current Profilers (ADCPs) across the Yucatan Channel, calculated the potential vorticity flux that enters the GoM and concluded that LCE shedding events follow periods of cyclonic vorticity flux at the Yucatan Channel. Gopalakrishnan et al. (2013) also showed that LCE separations are associated with cyclonic vorticity at the YC and frontal eddy intensification on the eastern side of the LC. Following the study by Candela et al. (2002); Oey (2004) also studied the Eulerian vorticity flux through the Yucatan Channel with respect to LC variability, using both observations across the Yucatan Channel, satellite SSH, and model simulations. Based on their results, conversely to Candela et al. (2002), anticyclonic vorticity flux at the Yucatan Channel triggers LCE shedding events or promotes retracted LC phases.

The variability of the LC has also been studied with respect to transport at the Yucatan Channel. Lin et al. (2009) in their modeling study, argued that the maximum vertically integrated transport occurs during retracted LC phases, particularly after LCE shedding events, whereas the minimum values occur during extended LC phases. Focusing on the deep flow in the Yucatan Channel, Bunge et al. (2002) found that the deep transport at the Yucatan Channel is correlated with both the LC northern extension and the expansion of the LC area, suggesting that the Yucatan Undercurrent might also contribute to the LC variability. Similarly to Athié et al. (2012); Sheinbaum et al. (2016) found that eastward shifts of the Yucatan Current core are related to vorticity perturbations originating in the Caribbean Sea and are evident before LCE detachments. However, they claim that such connections are not always apparent, as there are other factors that influence the variability of the LC and the LCE shedding cycles. They also tried to establish a correlation between the transport at the Yucatan Channel and the vorticity fluctuations from the Caribbean Sea, but this was inconclusive due to the high variability of the Yucatan current system and the limited amount of available data. Furthermore, Abascal et al. (2003), based on



observations at the Yucatan Channel, showed that the variability of the flow at the Yucatan Channel is mostly governed by both anticyclonic and cyclonic eddies.

Overall, the dynamics of the LC evolution that are governed by processes at the Yucatan Channel as well as the Caribbean Sea and the GoM cannot be explained based on a specific mechanism. Many processes can be simultaneously responsible for the variability of the LC system, such as the meteorological conditions of the region, eddy activity, fluctuations in the Yucatan transport, both in upper and deeper layers, through shifts of the Yucatan Current, and vorticity perturbations in the two basins as well as across the Yucatan Channel (Athié et al., 2020).

The main objective of this study is to focus on one process, specifically to investigate the effects of the mesoscale activity upstream of the Yucatan Channel (northwestern Caribbean Sea) on the LC system evolution, expanding on the findings by Androulidakis et al. (2021). This is done using a robust Lagrangian eddy detection methodology that identifies vortices objectively based on the vorticity of the fluid mass (Haller et al., 2016). We will discuss the LC dynamics with respect to vorticity fluxes at the Yucatan Channel, which are attributed to coherent eddies that originate in the Caribbean Sea in tandem with the LC variability, using a 7-year period of model data. We will also focus on individual case studies of detected coherent eddies that coincide with both retracted and extended LC phases, to explore how the connectivity between the two basins is associated with the LC evolution and coherent Caribbean eddies variability.

The model configuration and the eddy-tracking methodology are presented in Section 2. The results are included in Section 3. A brief concluding summary is provided in Section 4.

## 2 Methodology

### 2.1 Model description

The numerical simulation output data are obtained from the Hybrid Coordinate Ocean Model (HYCOM; [hycom.org](https://hycom.org); Bleck, 2002; Halliwell, 2004). The model domain covers the north Atlantic, the Gulf of Mexico, and the Caribbean Sea from 98° W to 20° W and from 5° S to 45° N (Figure 1A), at 1/25° horizontal resolution and 35 hybrid vertical layers (ATL-HYCOM 1/25). Depending on the topographic characteristics and the vertical structure, the hybrid vertical coordinates are optimized to best represent the ocean dynamics of the area. The distribution of the vertical coordinates is isobaric in the mixed layer and in very shallow areas, terrain-following at the continental shelf, and isopycnal in the stratified ocean interior (Bleck, 2002). The current configuration (ATL-HYCOM 1/25) uses initial and boundary conditions from the Global HYCOM (GLB-HYCOM), at 1/12° horizontal grid resolution and 32 hybrid vertical layers (Androulidakis et al., 2016). The atmospheric forcing is obtained from the Navy Operational Global Atmospheric Prediction System (NOGAPS) and the Navy Global Environmental Model (NAVGEM). The model performance was evaluated in Androulidakis et al. (2016) and Kourafalou et al. (2016) who showed good agreement between the model output and *in situ* and satellite observations. ATL-HYCOM 1/25 has also served as a Nature

Run for Observing System Simulation Experiments OSSEs, designed to improve model skill, and was further evaluated in Halliwell et al. (2017). The configuration is free-running (no data assimilation) and appropriate for the process-oriented purposes of this study. Furthermore, since the model domain covers both the Caribbean Sea and the GoM, it is suitable for analyzing processes that take place in both regions as well as inter-basin exchanges (Androulidakis et al., 2021). For our analysis, we focus on a 7-year period (2010–2016) to investigate the relationship between the mesoscale eddy variability in the northwestern Caribbean Sea and the LC evolution.

### 2.2 Detection of coherent eddies

In our Lagrangian analysis, we aim to detect eddy structures in the Caribbean Sea that pass through the Yucatan Channel, interacting with the predominant mesoscale features in the GoM. We employ an eddy-detecting methodology, the Lagrangian-Averaged Vorticity Deviation (LAVD), developed by Haller et al. (2016), who defined Lagrangian rotationally coherent vortices from relative vorticity. As vortices are often considered regions of vorticity maxima or minima (Haller, 2005; Haller et al., 2016), efforts have been made toward defining a vortex based on that property. Haller (2005) reviewed such definitions, according to which vortices are characterized by closed streamlines that remain invariant under Galilean transformations, such as the *Q-criterion* (Hunt et al., 1988), the *Okubo-Weiss criterion* (Okubo, 1970; Weiss, 1991), and the  $\lambda_2$ -*criterion* (Jeong and Hussain, 1995). However, these criteria do not remain invariant under rotational transformations, hence the notion of objectivity, which is necessary for a generalized vortex definition, is not satisfied. Objectivity is achieved when vortices remain the same under transformations to different frames of reference (Haller, 2005). Haller et al. (2016) overcame the difficulties of defining coherent vortices from vorticity, mainly the lack of objectivity, and showed that even though vorticity is not objective, meaning that the vorticity tensor is not invariant under changes of observers, the LAVD is, in fact, an objective field. The LAVD is defined as:

$$LAVD_{t_0}^{t_0+T}(x_0) := \int_{t_0}^{t_0+T} |\omega(F_{t_0}^t(x_0), t) - \bar{\omega}(t)| dt \quad (1)$$

where  $\omega$  is the relative vorticity,  $\bar{\omega}$  the spatial mean relative vorticity, and  $F_{t_0}^t(x_0)$  is the flow map, which is defined as the mapping from the initial position  $x_0$  at time  $t_0$  to some later position  $x(t; x_0, t_0)$  at time  $t = t_0 + T$ . According to the LAVD-based definition, the centers of rotationally coherent vortices are characterized by local LAVD maxima and the boundaries are the outermost closed convex level surfaces of LAVD. Each LAVD level set is composed of fluid particles that complete the same total material rotation relative to the mean material rotation of the whole fluid mass (Haller et al., 2016). This definition along with the objective nature of their detection method makes them robust indicators of the mesoscale eddy field in oceanic flows (Haller, 2005). Unlike geodesically detected eddies, eddies detected using the LAVD approach are allowed to experience filamentation. However, filamentation is observed to typically develop tangentially, without global breakaway. As it is based on vorticity, the method described by Haller et al. (2016) may be regarded as oceanographically more

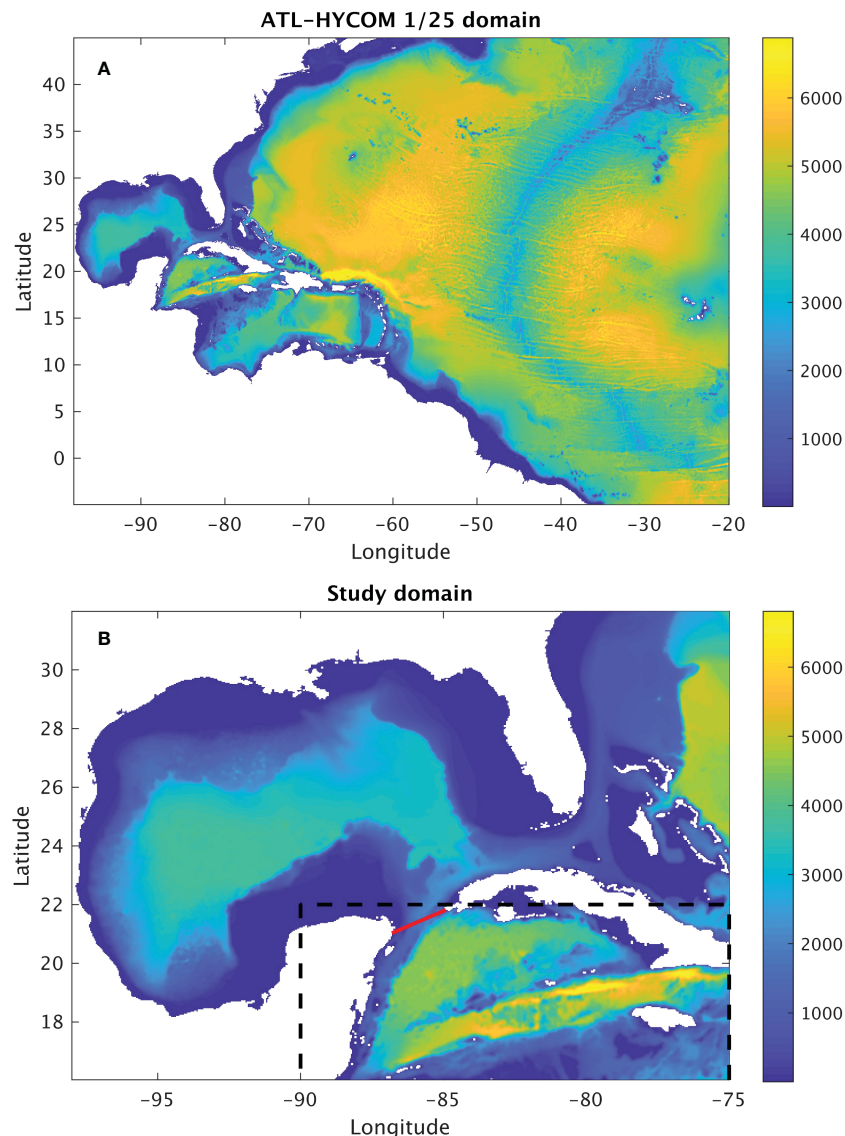


FIGURE 1

(A) ATL-HYCOM model domain and bathymetry (m), (B) Study domain that includes the northwestern Caribbean Sea and the Gulf of Mexico (GoM). The red line marks the Yucatan Channel and the box represents the area where LAVD was computed.

appealing than the geodesic method, which produces similar results with some caveats, such as the sensitivity to parameters during computation (Andrade-Canto et al., 2020). Tarshish et al. (2018) expanded on this issue and focused on developing an index that classifies coherent structures detected using the LAVD method into three categories based on their coherency; strictly, moderately, and weakly coherent. Using different values for convexity deficiency, they calculated the mean and median coherency indices for the coherent structures detected based on a certain convexity deficiency. The large variation of their results supported their argument on the highly sensitive nature of the LAVD method regarding the tuning of the computational parameters.

However, despite the limitations, the LAVD method is considered a robust method to identify Lagrangian coherent eddies; the study by Beron-Vera et al. (2013), with the use of concrete examples, expanded on the advantages of using an observer-independent method for eddy detection as opposed to the classic SSH-based eddy detection.

Moreover, Liu et al. (2019), who quantified the material coherence of Eulerian SSH eddies and rotationally coherent Lagrangian vortices detected using the LAVD method, showed that SSH eddies are highly leaky and do not maintain their material coherence over the detection time interval, as opposed to the Lagrangian coherent vortices that were detected based on the LAVD method. They also showed that the SSH eddies may be coherent in their core, but they also may not, making SSH eddies almost indiscernible from any other body of water in the ocean, in terms of material coherence.

We applied the LAVD method in the northwestern Caribbean Sea (16° N - 22° N, 90° W - 75° W, Figure 1B) to assess eddy coherence during the study period, using the velocity fields from ATL-HYCOM 1/25, in each of the 35 layers of the model to allow for eddy detection at depth. In our calculations, the convexity deficiency was set at  $10^{-2}$ . Lower convexity deficiency led to very few coherent eddies in the region of interest. According to the study by Tarshish et al. (2018), the value of the convexity deficiency chosen in the present study ( $10^{-2}$ )

relates to coherency indices that indicate the identification of coherent structures that are not highly leaky. Although the authors developed their methodology based on outputs from a different numerical model, they argue that it should be applicable to data from other numerical models, as well. The LAVD is calculated every 15 days and integration time  $T$  was set to 15 days, a time period that is sufficient for detecting coherent mesoscale eddies using either observational or realistic model data (Beron-Vera et al., 2018; Androulidakis et al., 2021).

## 2.3 Advection of coherent boundaries and isopycnal particles

After coherence is established, the boundaries are advected to examine their pathways and physical connectivity with the GoM. The boundaries are advected as contour points using ODE45 in MATLAB and Dritschel's curvature interpolation (Dritschel, 1988). We will be using the term "boundary" for individual coherent contours and the term "eddy" when we refer to a group of boundaries in different layers that correspond to the same structure. Eddy coherence, using the LAVD method, has only been applied in fields from realistically forced, high-resolution model in Androulidakis et al. (2021), to examine the coherence and advection of anticyclonic Caribbean eddies (Caribbean anticyclones - CarAs) at the surface, as they approached the Yucatan Channel. The calculation of LAVD at depth using horizontal velocity fields at different layers from such a model to investigate eddy coherence throughout the entire water column is a novel approach, which to our knowledge, has not been applied in previous studies.

To better track the evolution of coherent structures, 2D Lagrangian particle experiments were also performed, with releases in two different layers either inside or in the vicinity of coherent boundaries. The particles were advected using the boundary advection method that is described in the previous paragraph.

## 2.4 Potential vorticity fluxes

We calculate potential vorticity (PV) fluxes at the Yucatan Channel attributed to coherent structures in the Caribbean Sea as an indicator of physical connectivity between the two basins. The potential vorticity is defined as:

$$PV = (fz + \nabla \times u) \cdot \nabla \left( -g \frac{\rho}{\rho_0} \right) = PV_1 PV_2 \quad (2)$$

where  $f$  is the Coriolis parameter,  $z$  is the unit vector of the  $z$ -coordinate,  $u$  is the velocity vector from which we take into consideration only the zonal and meridional components,  $g$  is the gravitational acceleration,  $\rho$  is the potential density, and  $\rho_0$  is the reference density. The term  $PV_1$  represents the absolute vorticity, and  $PV_2$  represents the gradient of buoyancy. We compute the transport of PV ( $\Phi$ ) by rotationally coherent eddies as:

$$\Phi = \frac{\overline{PV_\gamma} A}{T} \quad (3)$$

where  $\overline{PV_\gamma}$  is the mean PV inside the coherent boundary,  $A$  is the area enclosed by the boundary, and  $T$  is the coherence time scale. This formula was also used by Androulidakis et al. (2021) to calculate surface relative vorticity fluxes of geodesic eddy boundaries (Haller and Beron-Vera, 2013; Haller and Beron-Vera, 2014). We will discuss the PV fluxes of all the boundaries that traverse through the Yucatan Channel and into the GoM. For our analysis we will only show the fluxes attributed to PV induced by horizontal shear, which is given by:  $PV_{hshear} = -\frac{g}{\rho_0} \left( \frac{\partial v}{\partial x} - \frac{\partial u}{\partial y} \right) \frac{\partial \rho}{\partial z}$ , a term derived from Eq. (2).

The PV induced by vertical shear is two orders of magnitude smaller than the horizontal shear induced PV and the planetary vorticity is unrelated to changes in the LC, as discussed by Candela et al. (2002), who calculated Eulerian PV fluxes based on velocity measurements at the Yucatan Channel.

## 3 Results

### 3.1 LC Variability and mesoscale eddy coherence in the Caribbean Sea

We examine eddy coherence in the northwestern Caribbean Sea with respect to LC evolution by only accounting for the coherent eddies that traverse through the Yucatan Channel (Figure 1B) upon 15 days of advection. Figure 2 shows the area of only the largest boundaries (diameter  $\geq 90$  km), normalized by the area of the largest boundary ( $A_{max}$ ), that were detected south of the Yucatan Channel (Figure 1B) throughout the 7-year period along with the LC northern extension. Boundaries that are smaller than 90 km in diameter have been omitted for clarity. The dots that are assigned on the same dates usually represent parts of one eddy with coherent signature in multiple model layers, because an eddy with a coherent signature in various model layers consists of a group of coherent boundaries vertically. Thus, if multiple of these coherent boundaries have a

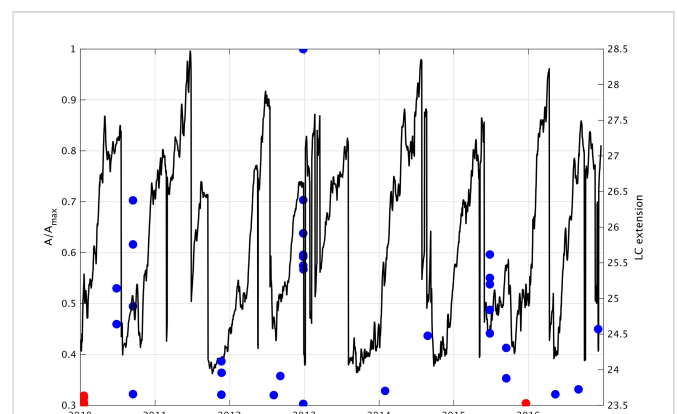


FIGURE 2

Left y-axis: Normalized area of largest coherent boundaries (diameter  $\geq 90$  km), detected in the northwestern Caribbean Sea and crossed the Yucatan Channel from 2010 to 2016. The blue and red dots represent coherent anticyclonic and cyclonic boundaries, respectively. Right y-axis: LC northernmost extension (black line), based on the position of the 17-cm SSH anomaly contour from 2010 to 2016. The dots' projection onto the x-axis corresponds to the dates that the boundaries are identified as coherent in the northwestern Caribbean Sea and mark the first day of advection.

diameter  $\geq 90$  km, they will represent a different dot on the same date. 86% of the coherent boundaries with diameter  $\geq 90$  km that are identified in the northwestern Caribbean Sea are anticyclonic, with the largest one reaching the diameter of 165 km. This boundary is part of an anticyclonic eddy that was identified as coherent in multiple layers of the model and was evident a few days before a LCE went through several detachments and reattachments prior to its final separation on August 2, 2013. Such pattern is evident in 50% of the detachments, in which anticyclonic coherent eddies with diameter  $\geq 90$  km were detected before LCE detachments or final separations (such as June 2010 and May 2016). In 70% of the instances where the LC was retracted, anticyclonic coherent boundaries with diameter  $\geq 90$  km are also evident (such as December 2011 and June 2015), while the cyclonic ones do not seem to follow a particular pattern.

Eddy coherence was evaluated throughout the entire water column (list of approximate layer depths in Table 1), and coherent boundaries were detected from layer 1 to layer 20 ( $\approx 650$  m) (Figure 3A). No coherent boundaries were detected below layer 20 in the time period of 2010–2016. More specifically, more coherent anticyclonic boundaries than cyclonic ones were detected in all layers (up to layer 19) except for layer 20 where only a few cyclonic boundaries were detected (Figure 3A). The larger number of the coherent anticyclonic boundaries in all layers suggests that coherent anticyclonic eddies in the region are more likely to have a deeper signature than the cyclonic ones. However, overall, the polarity does not play a role on the depth to which the eddies can be detected, since both cyclonic and anticyclonic boundaries are present down to  $\approx 650$  m. Taking a closer look only at the boundaries with diameter  $\geq 90$  km, a total of 32 large anticyclones were detected (down to  $\sim 200$  m), much higher than the total number of 4 cyclonic boundaries (down to  $\sim 100$  m), throughout the 7-year period (Figure 3B). Such finding indicates that large coherent anticyclones are deeper and dominate the region in comparison with the cyclonic structures of equivalent size. The actual number of 3D eddies (grouping of boundaries at different layers with similar coordinates that represent parts of an individual eddy) is not calculated and would be outside of the scope of the study, since we do not focus on the number of eddies or boundaries but on the effect of the total volume and vorticity fluxes.

Figures 4A, B show the total anticyclonic volume in each of the 15-day period ( $T = 15$  days: LAVD assessment period) of all the structures that were detected crossing the Yucatan Channel, down to layer 20 ( $\approx 650$  m) and at surface, along with the LC extension, respectively. The discrete values of the anticyclonic volume of coherent boundaries are calculated at time  $t_0$  in the entire water column (Figure 4A) and at surface (Figure 4B). The volume of each boundary is computed by multiplying the area of the boundary by the layer thickness. The total anticyclonic volume attributed to coherent boundaries at the surface is two orders of magnitude smaller than the respective volume of coherent boundaries down to layer 20, with the pattern being similar in both cases (Figures 4A, B). However, coherence assessment in the entire water column provides a more comprehensive picture on the presence of LAVD vortices and their interaction with the LC system, since detection in the surface layer accounts for about 50% of the total flux occurrences. Thus, coherent boundaries that represent coherent eddies may appear at depths below the surface and would be unaccounted for if only the surface

TABLE 1 List of approximate layer depth ranges for the region south of the Yucatan Channel and north of 18° N.

Layer#	Depth(m)
1	~2
2	~6
3	~12
4	~30
5	~40
6	~40
7	~70-100
8	~100-150
9	~150-200
10	~200
11	~200-250
12	~250-300
13	~300-350
14	~350-400
15	~400-450
16	~450-500
17	~500-550
18	~550-600
19	~600-650
20	~650-800
21	~800-900
22	~900-950
23	~950-1000
24	~1000-1100
25	~1100-1200
26	~1200-1300
27	~1300-1500
28	~1500-2000
29	~2000-3500
30	~3500-4000
31	~4000-4500
32	~4000-4500
33	~4000-4500
34	~4000-4500
35	~4000-4500

circulation was analyzed. However, it should be noted that the presence of noise in the surface layer can contribute to a failure in the LAVD method to identify vortices, hence the lower number of coherent boundaries detected in layer 1.

Focusing on the at-depth coherence assessment, the largest values of anticyclonic volume ( $\geq 10^6 \text{ m}^3$ ) are mostly evident when the LC is



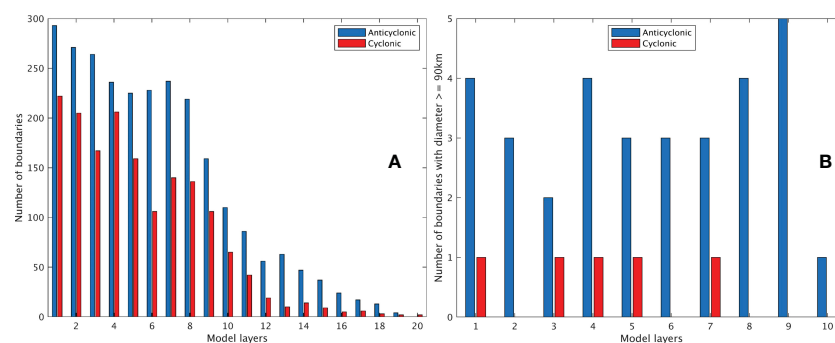


FIGURE 3

(A) Total number of anticyclonic (blue) and cyclonic (red) boundaries in each model layer (layers 1–20;  $\sim 650$  m), detected in the northwestern Caribbean and passed through the Yucatan Channel and (B) similar to (A) but for boundaries with diameter  $\geq 90$  km that are detected in model layers 1–10 (layer 10  $\sim 200$  m).

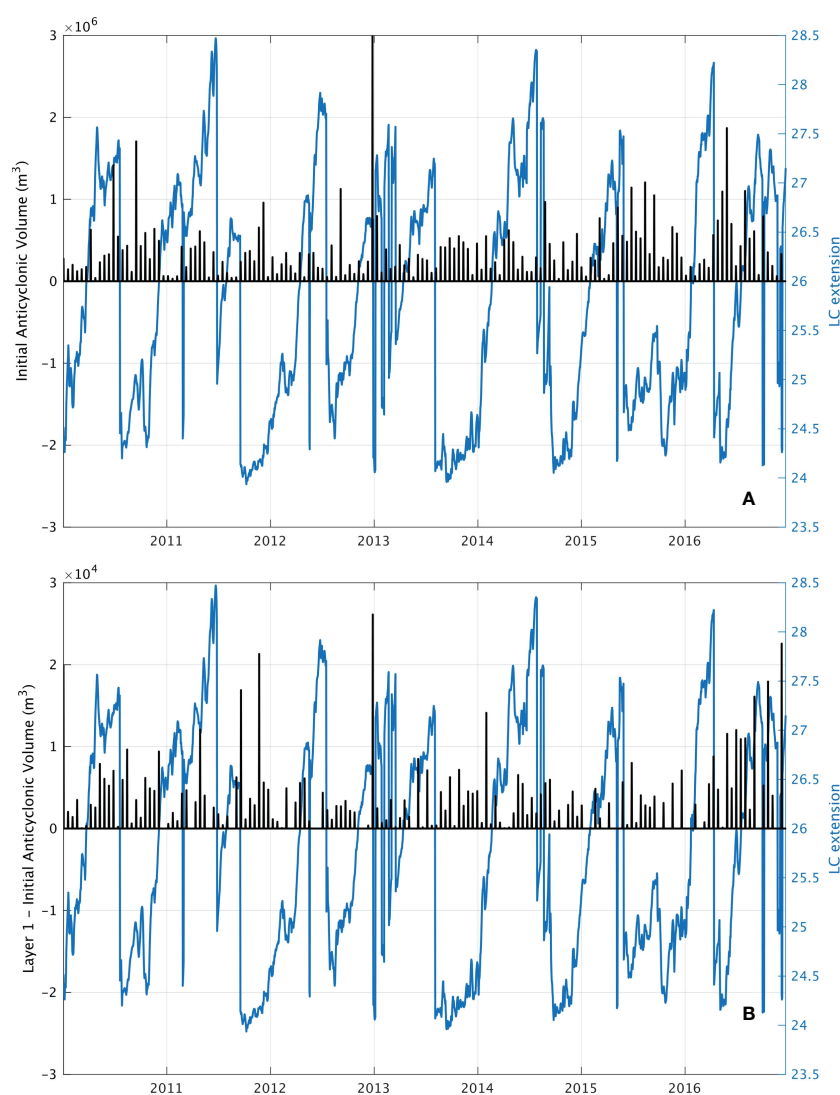


FIGURE 4

Initial volume of anticyclonic, coherent boundaries (black bars) that were detected in the northwestern Caribbean Sea and crossed the Yucatan Channel (max total volume:  $300 \text{ km}^3$ ), along with the LC northernmost extension (blue line) (A) in the entire water column and (B) at the surface.

retracted or before LCE detachments (Figure 4A), indicating that large coherent anticyclones are associated with retracted LC phases (Androulidakis et al., 2021). This finding is in agreement with the result presented in Figure 2, in which the normalized areas of the largest anticyclonic coherent boundaries are also associated to retracted LC phases. After grouping all the identified coherent boundaries based on their polarity, the anticyclonic eddies that cross the Yucatan Channel tend to also be larger than the cyclonic ones in terms of total initial volume (not shown). The 7-year mean coherent anticyclonic volume that originates in the northwestern Caribbean Sea and ends up being advected into the GoM is  $\sim 20 \text{ km}^3$ , whereas the mean cyclonic one is  $\sim 13 \text{ km}^3$ .

### 3.2 Potential vorticity fluxes through the Yucatan Channel

Figure 5 shows the discretized horizontal shear induced PV flux, calculated for every coherent boundary and summed over the total number of detected boundaries in all layers of the model that propagate into the GoM, along with the LC extension from 2010 to 2016. The PV flux is summed over the 20 layers of the model in which coherence was detected and it is computed within the boundaries that cross the red line in Figure 1B. The coherent PV flux values are normalized by the maximum value of the examination period. The largest coherent PV fluxes are anticyclonic (negative values) and, in 5 cases, intensified anticyclonic PV fluxes are evident before LCE detachments or final separations (such as June 2010 and December 2012, Figure 5). This suggests that the presence of anticyclonic eddies in the northwestern Caribbean Sea is connected to the LC evolution and more specifically to the LCE detachments or separations. Furthermore, large anticyclonic fluxes are evident during retracted LC phases (Figure 5) and along with the findings from Figure 4 indicate that the coherent anticyclonic activity in the northwestern Caribbean Sea promotes retracted LC phases, in agreement with Androulidakis et al. (2021). The Eulerian study by Oey et al. (2003) showed that anticyclonic activity in the Caribbean Sea is also associated with retracted LC phases, although a direct comparison to our results would not be optimal due to the lagrangian nature of our study. On the other hand, Candela et al. (2002), in their Eulerian study, showed that cyclonic vorticity flux is present before LCE detachments. In our study, there are a couple of cases (i.e., 2015, 2016) out of a total of 9, where cyclonic activity is pronounced right before the start of LCE shedding events (Figure 5). Nonetheless, the values are not as large as the largest anticyclonic vorticity flux values. However, larger cyclonic PV fluxes ( $>0.2$ ) do occur in other instances (years 2013 and 2014) as well, when the LC is extended, about 45–50 days before LCE detachments/separations. This is a considerably larger time interval than the coherence assessment time interval selected in the present study (15 days), thus establishing a relationship between intensified cyclonic PV fluxes and LCE detachments is not trivial. The controversy in the results as well as the high variability of the system indicated that a statistical approach using a longer time series of data may be needed to further elucidate the relationship between the coherent eddy activity in the Caribbean and the LC evolution.

During extended LC phases,  $\sim 35\%$  of the normalized coherent PV flux values are in the bin range between 0 and 0.1, indicating weak coherent mesoscale activity in the northwestern Caribbean (Figure 6). The rest of the occurrence frequencies during extended LC phases are equally distributed in positive and negative PV flux values, except for a 7% of increased negative PV flux values occurring only when the LC is extended (north of  $26^\circ \text{ N}$ ). This is possibly connected to intensified anticyclonic activity before LCE detachments, as presented in Figure 5. On the other hand, during retracted LC phases (south of  $26^\circ \text{ N}$ ), almost 70% of the coherent PV flux values are negative, a finding that agrees with Androulidakis et al. (2021), who argued that anticyclonic surface relative vorticity attributed to geodesic eddies was more pronounced when the LC is retracted.

### 3.3 Case studies of coherent eddies and 2D Lagrangian particle experiments

We now focus on specific case studies of coherent Caribbean anticyclones associated with different LC phases.

#### 3.3.1 Coherent anticyclones during extended LC phases

It is shown that anticyclonic coherent PV fluxes are often present before LCE detachments or final separations (Figure 5). On June 26, 2010 (Figure 7), the increased anticyclonic PV flux is attributed to one coherent anticyclone with multilayer signature starting at the depth of  $\sim 100 \text{ m}$  just south of the Yucatan Channel and extending down to the depth of  $200 \text{ m}$  (layers 7 ( $\approx 70\text{--}100\text{m}$ ), 8 ( $\approx 100\text{--}150\text{m}$ ), and 9 ( $\approx 150\text{--}200\text{m}$ )). This anticyclone is particularly large with area and diameter of  $1.15 \times 10^4 \text{ km}^2$  and  $\sim 120 \text{ km}$ , respectively, in the uppermost layer (layer 7 in Figure 7). The size is decreasing from layer 7 to layer 9, with a total decrease of 89% of the initial area at layer 9 compared to layer 7.

We will be discussing the evolution of the anticyclonic boundary only in the uppermost layer, as all three detected boundaries evolve in a similar way. Figure 8 shows the evolution of the vortex

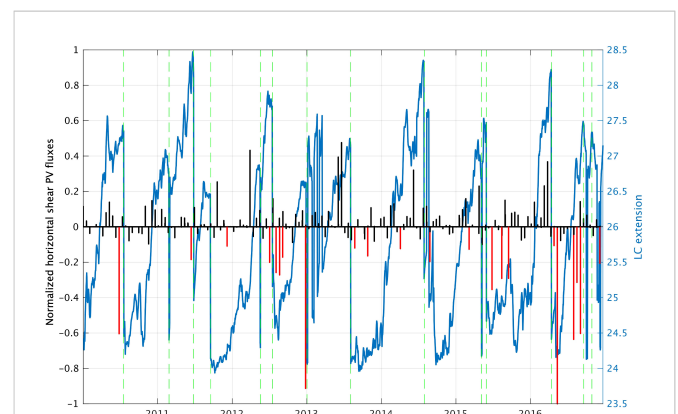


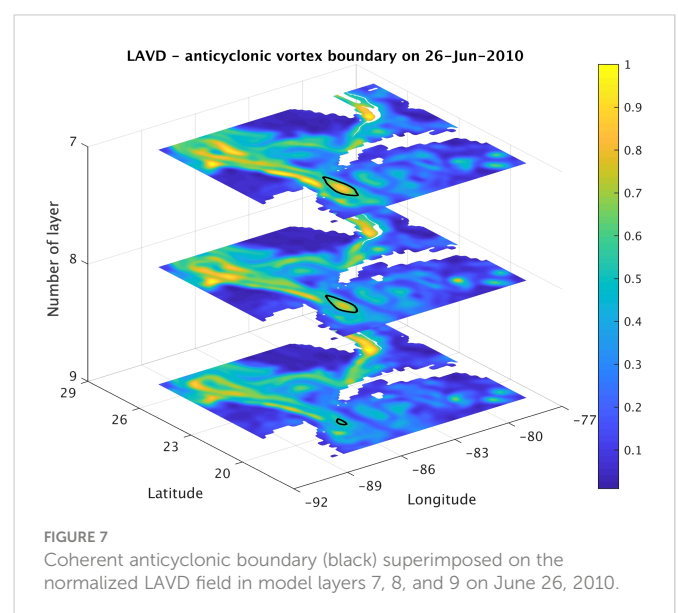
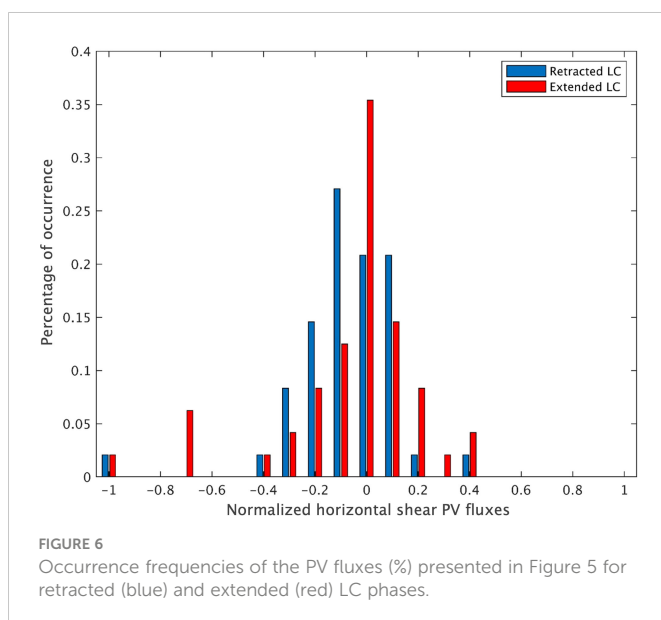
**FIGURE 5**  
Normalized horizontal shear PV fluxes (black and red bars) of coherent boundaries detected south of the Yucatan Channel and propagated into the GoM, along with the LC northernmost extension (blue line). The red bars indicate values  $\leq -0.1$ . The dashed green lines mark the LCE detachments/final separations.

superimposed on SSH fields for up to 35 days from the day of detection (Jun 26, 2010, [Figure 8A](#)), along with the evolution of the LCE boundary ([Figures 8A–D](#)). After the coherent boundary enters the GoM, it quickly undergoes filamentation, exhibiting two pathways (July 15, 2010; [Figure 8B](#)). The first pathway wraps around the forming LCE, while part of the initial filament gets advected eastward, following the southern part of the LC towards the entrance of the Straits of Florida ([Figure 8B](#)). On July 20, 2010, the filament undergoes stretching, with its northern part continuously wrapping around the newly formed LCE ([Figure 8C](#)), until it is fully detached from the main LC body on July 30, 2010 ([Figure 8D](#)). Such evolution indicates that the coherent anticyclonic boundary detected south of the Yucatan Channel, contributes to the detached LCE, through the advection of anticyclonic Caribbean waters into the GoM. From an Eulerian point of view, [Oey \(2004\)](#) suggested that anticyclonic Potential Vorticity flux anomaly through the Yucatan Channel is associated with almost all the LCE shedding events in their 13-year modeling study period. However, the association of our findings with the results from [Oey \(2004\)](#) is not feasible, since [Oey \(2004\)](#) calculated the PV fluxes in the Eulerian sense along a line in the Yucatan Channel and we calculate PV fluxes from closed coherent eddy contours which were computed from a lagrangian perspective.

The LCE was detected coherent by July 15, 2010 ([Figure 8B](#)). The coherent LCE undergoes some tangential filamentation on July 20, 2010 ([Figure 8C](#)), that further develops by July 30, with the boundary exhibiting more filamentation as time progresses ([Figure 8D](#)). Throughout this period, the boundary of the LCE encloses the high SSH values that indicate the presence of an anticyclonic eddy, objectively marking the boundaries of that eddy. These might differ from the traditional tracking of the LCE and LC boundaries, based on the 17-cm SSH contour anomaly, proposed by [Leben \(2005\)](#) ([Beron-Vera et al., 2018; Andrade-Canto et al., 2020](#)).

The above findings suggest that the anticyclonic Caribbean eddy enters the GoM and wraps around the newly detected coherent LCE. This suggests that the LCE formation is associated with the coherent

anticyclonic vorticity fluxes through the Yucatan Channel. To better elucidate the evolution of both coherent structures, we present Lagrangian particle experiments; 1250 isopycnal particles were released inside the Caribbean eddy in layer 7, located at the depth of approximately 70–100 m (layer of detection for both Caribbean anticyclone and LCE). In particular, the particles were released in the center of the Caribbean eddy, covering ~10% of the total boundary area ([Figure 9A](#)), and were advected for a total of 45 days. As shown in [Figures 9B–D](#), the particles are advected northward along with the black contour and are finally traced inside the coherent boundary that marks the LCE (magenta colors). More specifically, 70% of the particles are found inside the LCE boundary from July 15, 2010 to August 9, 2010 ([Figures 9B–D](#)). The rest of the particles are still located within the black contour that originates in the coherent Caribbean anticyclone ([Figures 9B, C](#)). As a result, the particles that end up inside the LCE boundary outnumber the ones just outside of it, as shown in [Figure 9E](#), that shows the positions of all 1250 particles in the 45-day period. Since the majority of the Caribbean waters originating in the core of the Caribbean anticyclone, represented by the Lagrangian particles, are advected into the LCE, it is suggested that in this case, the LCE detachment is facilitated by an anticyclonic incoherent filament originating from a coherent Caribbean anticyclone present under an extended LC. Identical experiments were conducted in layers 8 and 9 (~150–200m), where both the Caribbean anticyclone and the LCE were detected coherent and exhibited similar results in terms of the evolution of their boundaries, as well the percentage of particles that were traced inside the LCE after being released in the center of the Caribbean anticyclone (not shown). The process of a coherent eddy originating in a non-coherent filament is discussed in [Wang et al. \(2015\)](#), who showed that material vortices in the Agulhas region are formed by mostly south Atlantic incoherent water and then traverse through the subtropical gyre. In our case, the incoherent water tracked by isopycnal particles ([Figures 9A–D](#)) may partially originate in the coherent Caribbean anticyclone that underwent filamentation after



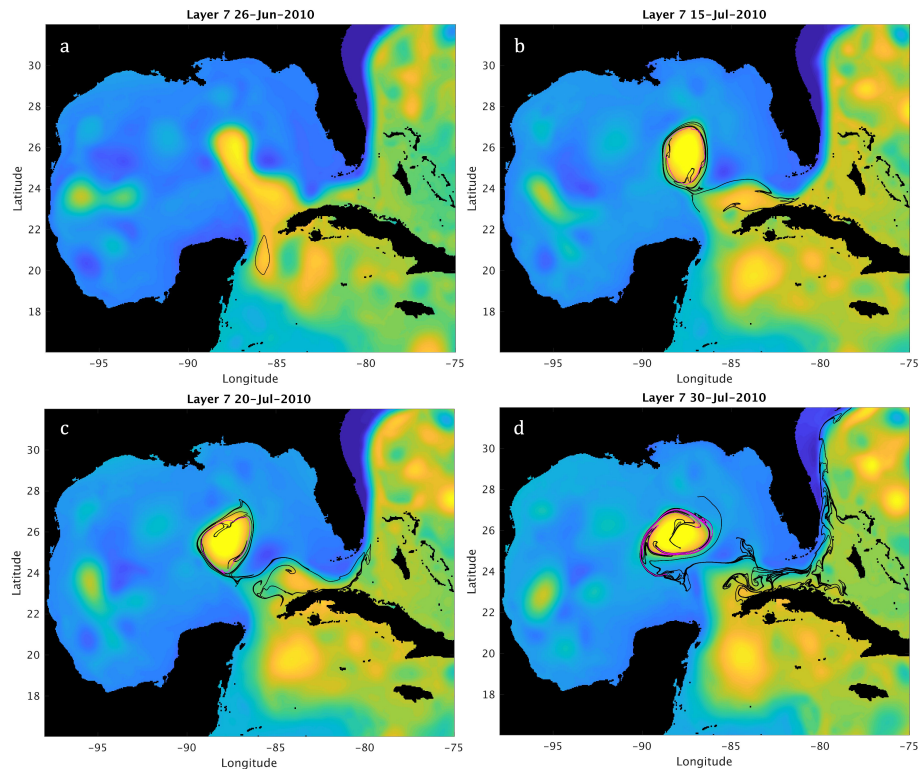


FIGURE 8

Snapshots of the evolution of the LCE boundary (magenta contours) and coherent anticyclonic boundary (black contours) detected south of the Yucatan Channel along with the, superimposed on model SSH for (A) June 26, 2010; day of coherent Caribbean anticyclonic boundary detection, (B) July 15, 2010; just after the LCE was detected coherent (magenta contours), and (C, D) 5 and 15 days later, respectively.

entering the GoM. However, this hypothesis needs further testing by advecting of the coherent LCE contour (Figure 8B) backward in time.

Neighboring seeding locations were also tested, to quantify the connectivity between the surrounding Caribbean waters and the LCE (Figures 10A, C, E). 1250 particles were released east of the anticyclonic boundary (Figure 10A), 2000 along the Yucatan Strait (Figure 10C), and 1000 particles on the eastern part of the Yucatan Strait (Figure 10E). All particles were advected for 45 days and their evolution from the day of each deployment until the advection end day, for each one of the different locations is shown in Figures 10B, D, F respectively. In the experiments presented in Figures 10A, E about 10% of the initial number of particles were traced in the LCE boundary, exhibiting weaker connectivity compared to the seeding case inside the core of the Caribbean anticyclone (Figure 9A), in which the equivalent percentage was 70%. Even weaker connectivity is suggested by the experiment presented in Figure 10C, where only 5% of the particles end up in the LCE contour. The particles that did not end up in the LCE boundary (Figures 10B, D, F), either recirculate in the northwestern Caribbean Sea, with the most intense recirculation being evident in Figure 10A, or are advected in the southeastern (Figures 10B, D, F) and northern GoM (Figure 10F), before exiting toward the Atlantic Ocean. The recirculation in the Caribbean Sea is not evident in the experiment presented in Figure 9, supporting the hypothesis of stronger connectivity between the core of the coherent Caribbean anticyclone and the newly formed LCE before this detachment event.

### 3.3.2 Coherent anticyclones during retracted LC phases

Intensified anticyclonic PV is also evident during retracted LC phases (Figure 5), in agreement with Androulidakis et al. (2021), where surface anticyclonic relative vorticity was calculated, based on geodesic eddies (Haller and Beron-Vera, 2013; Haller and Beron-Vera, 2014) detected in the Caribbean Sea. We now examine a case study of a coherent anticyclone present just south of the Yucatan Channel on June 24, 2015 (Figure 11). The anticyclone is detected coherent down to layer 12 ( $\approx 250\text{--}300\text{m}$ ), starting from the layer 2, as shown in Figure 11. The area of the boundaries, marking the outermost part of the eddy, decreases with depth by 90% of the maximum value, except for a small increase of 7% from layer 2 to layer 3. The diameter of the eddy decreases from  $\sim 122\text{km}$  at layer 2, to just  $18\text{km}$  at the depth down to which an anticyclonic coherent boundary is present.

The evolution of the anticyclonic boundary in layer 2 (the uppermost layer where the anticyclone was detected coherent) is shown in Figure 12 and is quite different from the case study of an extended LC (Section 3.3.1). The LAVD vortex (Figure 12A) transforms into a non-coherent filament (Figure 12B), which undergoes stretching and more filamentation (Figure 12C) but is quickly advected in the Straits of Florida and the Atlantic Ocean (July 19, 2015, Figure 12D). Similar particle experiments to the ones presented in Figure 8 were performed for this case as well. More specifically, 1250 particles were released in the core of the anticyclone in layer 2 ( $\sim 6\text{m}$ ). The particle-release experiment shows that all the



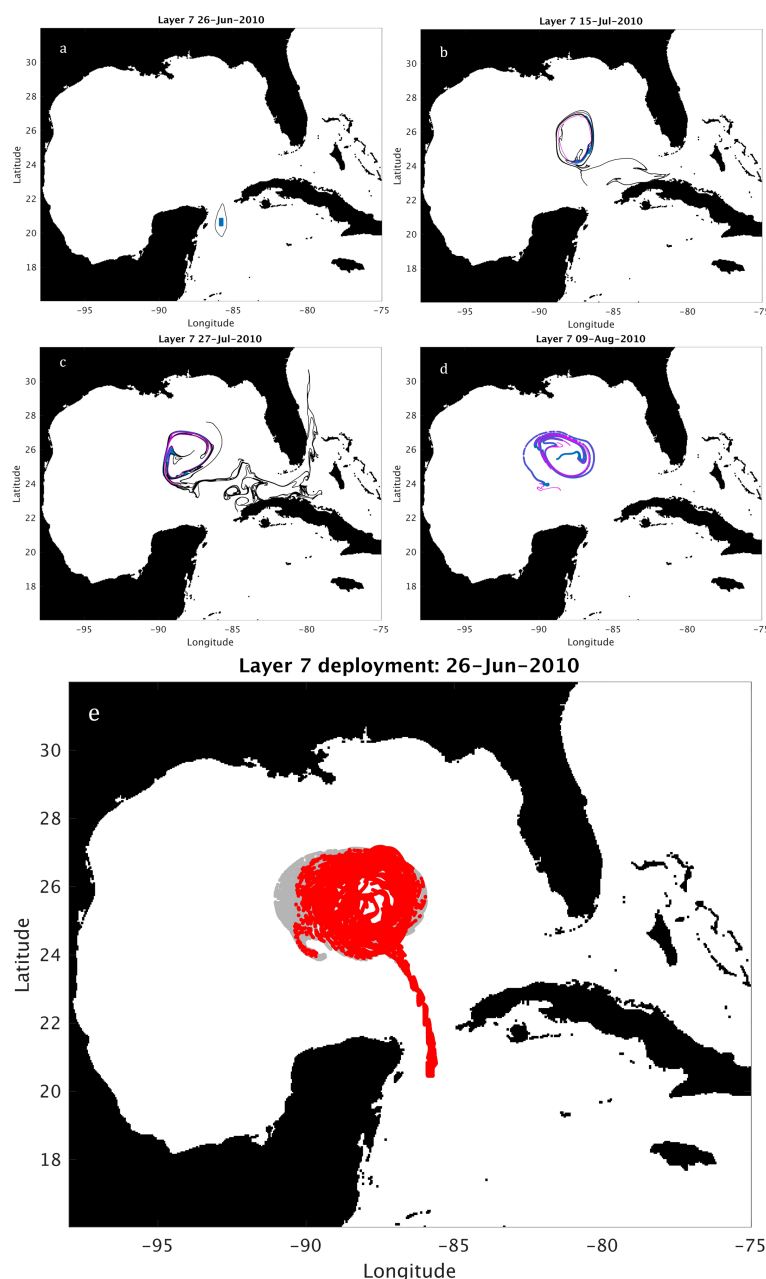


**FIGURE 9**  
 (A-D) Snapshots of Lagrangian particle advection, along with the evolution of both the Caribbean anticyclone (black contours) and the LCE boundary (magenta contours). (E) Particle evolution; the blue colors represent trajectories that were traced inside the LCE contour at the end of the 45-day experiment and the gray colors mark trajectories that were traced outside the LCE contour.

particles released in the core of the anticyclone (Figure 12A) are located east of 81°W on July 19 (Figure 12D), suggesting that these particles exit the GoM. The rapid advection of the coherent eddy while the LC is retracted is an indicator of strong physical connectivity between the Caribbean Sea and the Atlantic Ocean, conversely to the case presented in Figure 8, under an extended LC phase. While the LC is extended and before a LCE is detached from the main body, there is strong physical connectivity between the Caribbean Sea and the GoM, with most of the Caribbean waters (70% percent of total particles released) originating in the core of the

coherent Caribbean anticyclone being advected into the LCE. Our results agree with the study by Androulidakis et al. (2021), where the physical connectivity between the Caribbean Sea and the GoM was also studied by releasing Lagrangian particles in the northwestern Caribbean Sea. The authors note that during extended LC phases with no Caribbean anticyclonic eddy presence, the majority of the particles are advected in the GoM, whereas when the Caribbean anticyclones are present and the LC retracted, the majority of the particles is directly advected to the Atlantic Ocean, with only a small percentage of them reaching higher latitudes in the inner GoM. The authors also

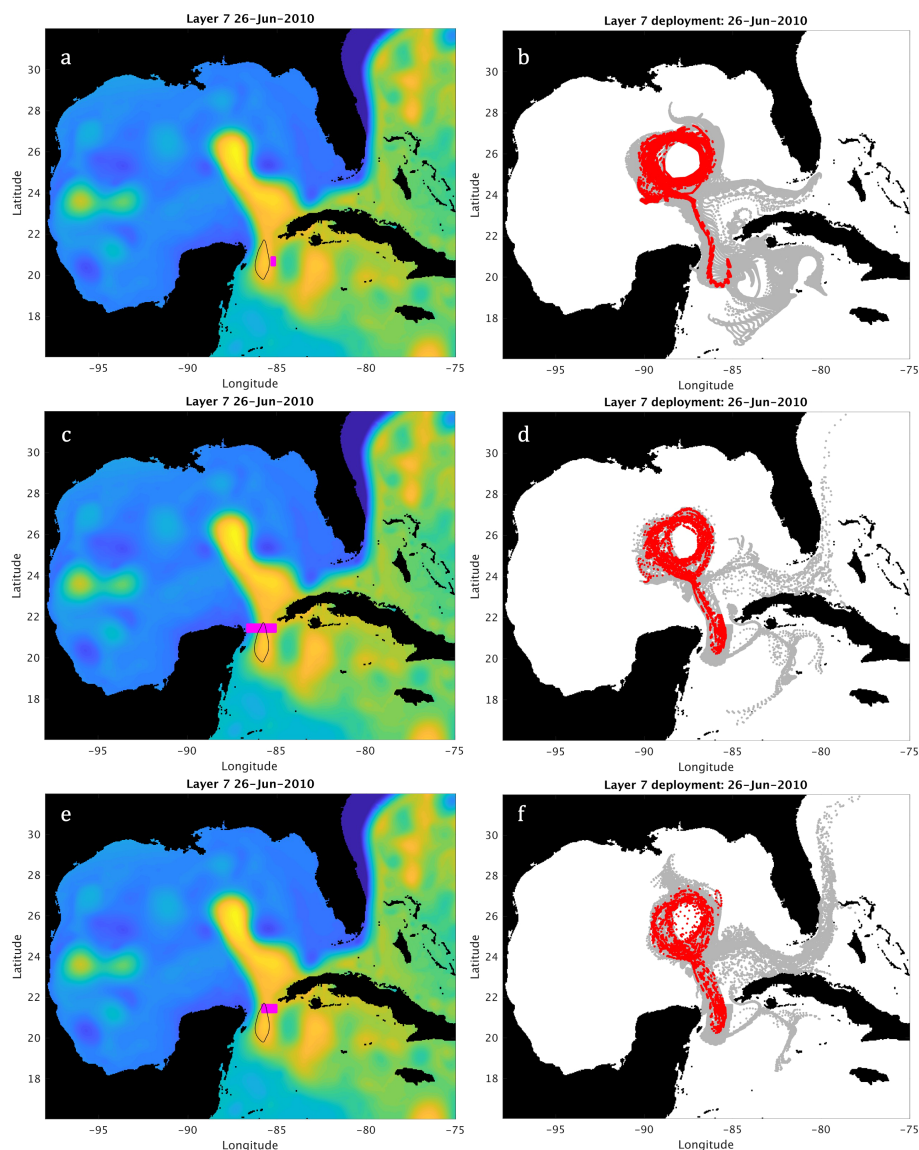


FIGURE 10

(A, C, E) Snapshots of seeding locations of Lagrangian particles (magenta boxes) and initial detection location of Caribbean anticyclone (black contour) superimposed on SSH. (B, D, F) Particle locations for each of the three particles experiments in panel (A, C, E), respectively. The red colors represent particles that were traced inside the LCE contour at the end of each 45-day experiment and the gray colors mark particles that were traced outside the LCE contour.

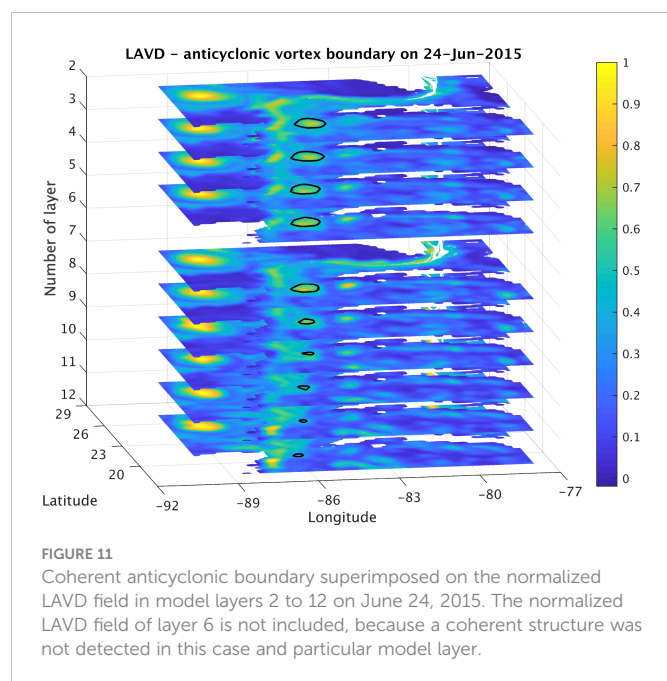
show the evolution of a coherent Caribbean anticyclone in the case of a retracted LC, in which the filament that originated in the coherent anticyclone traces another coherent vortex inside the retracted LC (Figure 11; Androulidakis et al., 2021).

Overall, our results show that the coherent eddy activity in the northwestern Caribbean Sea is associated with the LC phase transition and LCE shedding. More specifically, coherent anticyclonic fluxes that enter the GoM through the Yucatan Channel promote retracted LC phases, either by being evident during retracted LC phases or by facilitating LCE detachments and final separations. Coherent anticyclones with multi-layer signature in the Caribbean Sea can directly be associated with the water mass that

comprises a LCE or are indicators of physical connectivity between the Caribbean Sea and the Atlantic Ocean during retracted LC phases.

## 4 Summary and conclusions

We have evaluated eddy coherence in the Caribbean Sea and explored the interactions with extended and retracted LC phases, to assess the physical connectivity between the Caribbean Sea and the Gulf of Mexico (GoM), as well as processes that take place south of the Yucatan Channel, evolve through the channel, and influence the LC evolution.



We approached the assessment of the mesoscale eddy field by applying the Lagrangian-Averaged Vorticity Deviation (LAVD) method for eddy identification, based on the relative vorticity of the fluid mass, a robust method for objectively identifying coherent eddy

centers and boundaries (Haller et al., 2016). Eddy coherence was assessed throughout the entire water column for a 7-year period (2010–2016), using the velocity fields from the high-resolution, free-running ATL-HYCOM 1/25. The identified eddy boundaries were then advected forward in time and their evolution is examined. As the purpose of this study is to investigate the inter-basin exchanges between the Caribbean Sea and the GoM, only the boundaries that pass through the Yucatan Channel were included in the analysis.

Eddies were detected in the northwestern Caribbean Sea over the upper  $\approx 650\text{m}$ , while their polarity does not play a role on the depth to which either cyclones or anticyclones are detected. However, a larger number of anticyclonic boundaries was detected in the deeper layers, indicating that anticyclones are more coherent with depth than the cyclones, as in the upper layers.

We further calculated depth-integrated coherent PV fluxes from closed coherent eddy contours that traverse through the Yucatan Channel. Such calculations, based on a Lagrangian point of view, differ from calculating Eulerian PV fluxes from velocity data at the Yucatan Channel, as is common in Eulerian studies. Our results suggest that the depth-integrated coherent anticyclonic PV flux at the Yucatan Channel is associated with retracted LC phases. During extended LC phases the coherent anticyclonic activity in the Caribbean Sea is generally weak. However, the majority of the instances where depth-integrated coherent anticyclonic PV fluxes are evident during extended LC phases is prior to LCE detachments. This happens in 5 out of 9 cases within 15 days prior to the start of LCE shedding events, suggesting that

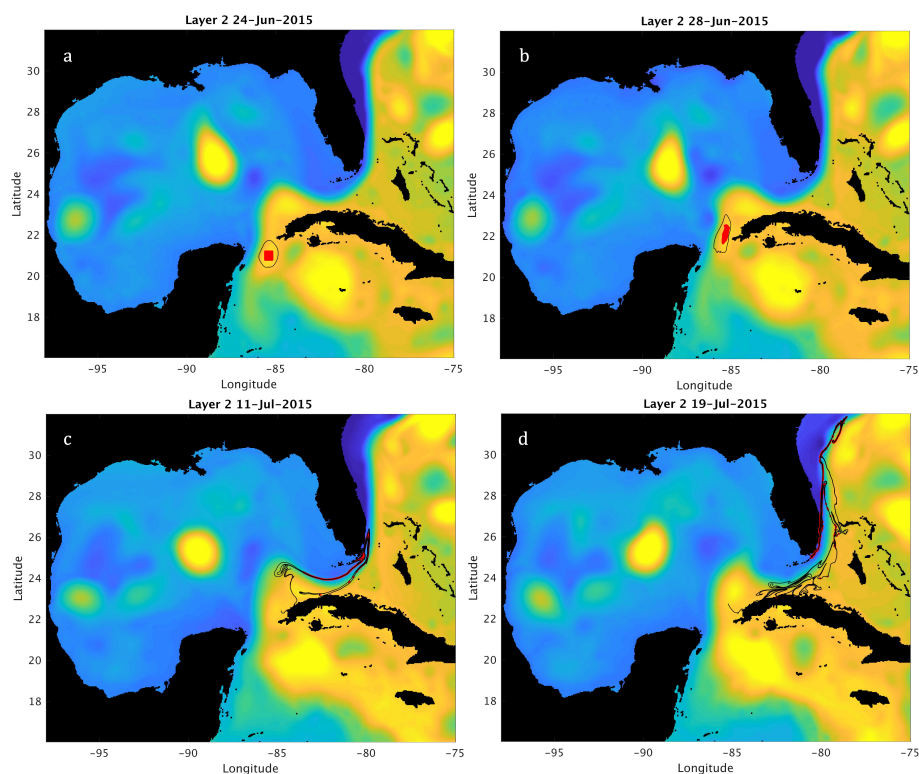


**FIGURE 12** Snapshots of the coherent LCE anticyclone detected south of the Yucatan Channel (black contours), during a retracted LC phase, superimposed on model SSH. The red box in panel (A) represents the seeding location of Lagrangian particles on June 24, 2015, and the red dots in panels (B) June 28, 2015, (C) July 11, 2015, and (D) July 19, 2015 represent the particle locations after advection.

the presence of coherent Caribbean anticyclones may be linked to one of the mechanisms controlling the LC evolution.

Case studies during a retracted LC phase and during an extended LC phase (prior to LCE shedding) suggest that the physical connectivity between the Caribbean Sea and the GoM differs depending -among other factors- on the LC extension. In the case of a retracted LC, non-coherent filaments that originate in coherent anticyclones in the Caribbean Sea are quickly advected toward the Straits of Florida, indicating weak connectivity with the GoM interior.

While our findings generally agree with Androulidakis et al. (2021), who tied the presence of Caribbean anticyclones to retracted LC phases, our results further indicate that strong anticyclonic activity in the Caribbean Sea can also be present prior to LCE detachments. In particular, a case study from June 2010 showed that non-coherent anticyclonic filaments originating in a coherent Caribbean anticyclone trace the coherent LCE. Furthermore, isopycnal particles seeded in the core of the Caribbean anticyclone are mostly being advected in the core of the coherent LCE. Such event can lead to direct connectivity between the core of the Caribbean anticyclone and the formed LCE prior to its detachment from the main LC body. The anticyclonic filaments advected in the GoM can also be traced in other anticyclonic structures in the GoM, also known as Cuban Anticyclones (CubANs), located in the northern coast of Cuba (Kourafalou et al., 2017), a case also reported by Androulidakis et al. (2021). The physical connectivity between the Caribbean eddies and the LCEs that may travel throughout the GoM may also have significant biochemical implications, affecting the quality and ecological characteristics of remote offshore and coastal areas.

Overall, our findings suggest that the coherent eddy activity in the northwestern Caribbean Sea affects the GoM mesoscale dynamics. The complexity of the LC system, however, necessitates accounting for a wide range of mechanisms to fully elucidate the underlying dynamics and further work is needed to characterize the extent to which each mechanism contributes to the overall dynamics of the region.

## Data availability statement

The raw data supporting the conclusions of this article will be made available by the authors, without undue reservation.

## References

- Abascal, A. J., Sheinbaum, J., Candela, J., Ochoa, J., and Badan, A. (2003). Analysis of flow variability in the Yucatan channel. *J. Geophys. Res. Ocean.* 108, 1–18. doi: 10.1029/2003JC001922
- Andrade-Canto, F., Karrasch, D., and Beron-Vera, F. J. (2020). Genesis, evolution, and apocalypse of loop current rings. *Phys. Fluids* 32, 116603. doi: 10.1063/5.0030094
- Androulidakis, Y., Kourafalou, V., Halliwell, G., Le Hénaff, M., Kang, H., Mehari, M., et al. (2016). Hurricane interaction with the upper ocean in the Amazon-Orinoco plume region. *Ocean Dyn.* 66, 1559–1588. doi: 10.1007/s10236-016-0997-0
- Androulidakis, Y. S., Kourafalou, V. H., and Le Hénaff, M. (2014). Influence of frontal cyclone evolution on the 2009 (Ekman) and 2010 (Franklin) loop current eddy detachment events. *Ocean Sci.* 10, 947–965. doi: 10.5194/os-10-947-2014
- Androulidakis, Y., Kourafalou, V., Olascoaga, M. J., Beron-Vera, F. J., Le Hénaff, M., Kang, H., et al. (2021). Impact of Caribbean anticyclones on loop current variability. *Ocean Dyn.* 71, 935–956. doi: 10.1007/s10236-021-01474-9
- Athié, G., Candela, J., Ochoa, J., and Sheinbaum, J. (2012). Impact of Caribbean cyclones on the detachment of loop current anticyclones. *J. Geophys. Res. Ocean.* 117, 1–16. doi: 10.1029/2011JC007090
- Athié, G., Sheinbaum, J., Candela, J., Ochoa, J., Pérez-Brunius, P., and Romero-Arteaga, A. (2020). Seasonal variability of the transport through the yucatan channel from observations. *J. Phys. Oceanogr.* 50, 343–360. doi: 10.1175/JPO-D-18-0269.1
- Beron-Vera, F. J., Olascoaga, M. J., Wang, Y., Triñanes, J., and Pérez-Brunius, P. (2018). Enduring Lagrangian coherence of a loop current ring assessed using independent observations. *Sci. Rep.* 8, 1–12. doi: 10.1038/s41598-018-29582-5
- Beron-Vera, F. J., Wang, Y., Olascoaga, M. J., Goni, G. J., and Haller, G. (2013). Objective detection of oceanic eddies and the agulhas leakage. *J. Phys. Oceanogr.* 43, 1426–1438. doi: 10.1175/JPO-D-12-0171.1
- Bleck, R. (2002). An oceanic general circulation model framed in hybrid isopycnal-Cartesian coordinates. *Ocean Model.* 4, 219. doi: 10.1016/S1463-5003(01)00017-8

## Author contributions

NN designed the study, performed all the data analyses, all necessary calculations, and wrote the manuscript. FB-V contributed to the conception of the study and provided the LAVD code draft. VK provided the HYCOM data. VK, MO, and MLH contributed to the conception of the study and provided input throughout the process. YA provided input during the data analyses process. All authors contributed to the article and approved the submitted version.

## Acknowledgments

This research was made possible by a grant from the National Academy of Sciences, Engineering, and Medicine (Gulf Research Program UGOS #2000011056). ML received partial support for work on this publication by NOAA/AOML and was supported in part under the auspices of the Cooperative Institute for Marine and Atmospheric Studies (CIMAS), a cooperative institute of the University of Miami and NOAA (agreement NA20OAR4320472). The authors also acknowledge partial financial support by Prof. Eric Chassignet (FSU) and the Center for Ocean-Atmospheric Prediction Studies (COAPS). We greatly appreciate the comments of two reviewers, which helped improve the manuscript.

## Conflict of interest

The authors declare that the research was conducted in the absence of any commercial or financial relationships that could be construed as a potential conflict of interest.

## Publisher's note

All claims expressed in this article are solely those of the authors and do not necessarily represent those of their affiliated organizations, or those of the publisher, the editors and the reviewers. Any product that may be evaluated in this article, or claim that may be made by its manufacturer, is not guaranteed or endorsed by the publisher.



- Bunge, L., Ochoa, J., Badan, A., Candela, J., and Sheinbaum, J. (2002). Deep flows in the Yucatan channel and their relation to changes in the loop current extension. *J. Geophys. Res. Ocean.* 107, 1–7. doi: 10.1029/2001JC001256
- Candela, J., Sheinbaum, J., Ochoa, J., Badan, A., and Leben, R. (2002). The potential vorticity flux through the Yucatan channel and the loop current in the gulf of Mexico. *Geophys. Res. Lett.* 29, 16-1-16-4. doi: 10.1029/2002GL015587
- Chérubin, L. M., Morel, Y., and Chassignet, E. P. (2006). Loop current ring shedding: The formation of cyclones and the effect of topography. *J. Phys. Oceanogr.* 36, 569–591. doi: 10.1175/JPO2871.1
- Donohue, K. A., Watts, D. R., Hamilton, P., Leben, R., and Kennelly, M. (2016). Loop current eddy formation and baroclinic instability. *Dyn. Atmos. Ocean.* 76, 195–216. doi: 10.1016/j.dynatmoce.2016.01.004
- Dritschel, D. G. (1988). Contour surgery: A topological reconnection scheme for extended integrations using contour dynamics. *J. Comput. Phys.* 77, 240–266. doi: 10.1016/0021-9991(88)90165-9
- García-Jové, M., Sheinbaum, J., and Jouanno, J. (2016). Sensitivity of loop current metrics and eddy detachments to different model configurations: The impact of topography and Caribbean perturbations. *Atmosfera* 29, 235–265. doi: 10.20937/ATM.2016.29.03.05
- Gopalakrishnan, G., Cornuelle, B. D., and Hoteit, I. (2013). Adjoint sensitivity studies of loop current and eddy shedding in the gulf of Mexico. *J. Geophys. Res. Ocean.* 118, 3315–3335. doi: 10.1002/jgrc.20240
- Haller, G. (2005). An objective definition of a vortex. *J. Fluid Mech.* 525, 1–26. doi: 10.1017/S0022112004002526
- Haller, G., and Beron-Vera, F. J. (2013). Coherent Lagrangian vortices: The black holes of turbulence. *J. Fluid Mech.* 731, 1–10. doi: 10.1017/jfm.2013.391
- Haller, G., and Beron-Vera, F. J. (2014). Addendum to “Coherent Lagrangian vortices: The black holes of turbulence”. *J. Fluid Mech.* 755, 1–4. doi: 10.1017/jfm.2014.441
- Haller, G., Hadjighasem, A., Farazmand, M., and Huhn, F. (2016). Defining coherent vortices objectively from the vorticity. *J. Fluid Mech.* 795, 136–173. doi: 10.1017/jfm.2016.151
- Halliwell, G. R. (2004). Evaluation of vertical coordinate and vertical mixing algorithms in the HYbrid-coordinate ocean model (HYCOM). *Ocean Model.* 7, 285–322. doi: 10.1016/j.ocemod.2003.10.002
- Halliwell, G. R., Mehari, M. F., Le Hénaff, M., Kourafalou, V. H., Androulidakis, I. S., Kang, H. S., et al. (2017). North Atlantic ocean OSSE system: Evaluation of operational ocean observing system components and supplemental seasonal observations for potentially improving tropical cyclone prediction in coupled systems. *J. Oper. Oceanogr.* 10, 154–175. doi: 10.1080/1755876X.2017.1322770
- Huang, M., Liang, X., Zhu, Y., Liu, Y., and Weisberg, R. H. (2021). Eddies connect the tropical Atlantic ocean and the gulf of Mexico. *Geophys. Res. Lett.* 48, 1–10. doi: 10.1029/2020GL091277
- Hunt, J. C. R., Wray, A., and Moin, P. (1988). Eddies, streams, and convergence zones in turbulent flows. *Cent. Turbul. Res. Proc. Summer Progr.* 193–208.
- Jeong, J., and Hussain, F. (1995). On the identification of a vortex. *J. Fluid Mechanics* 285, 69–94. doi: 10.1017/S0022112095000462
- Kourafalou, V. H., Androulidakis, Y. S., Halliwell, G. R., Kang, H. S., Mehari, M. M., Le Hénaff, M., et al. (2016). North Atlantic ocean OSSE system development: Nature run evaluation and application to hurricane interaction with the gulf stream. *Prog. Oceanogr.* 148, 1–25. doi: 10.1016/j.poccean.2016.09.001
- Kourafalou, V., Androulidakis, Y., Le Hénaff, M., and Kang, H. S. (2017). The dynamics of Cuba anticyclones (CubANs) and interaction with the loop Current/Florida current system. *J. Geophys. Res. Ocean.* 122, 7897–7923. doi: 10.1002/2017JC012928
- Leben, R. R. (2005). Altimeter-derived loop current metrics. *Geophys. Monogr. Ser.* 161, 181–201. doi: 10.1029/161GM15
- Le Hénaff, M., Kourafalou, V. H., Dussurget, R., and Lumpkin, R. (2014). Cyclonic activity in the eastern gulf of Mexico: Characterization from along-track altimetry and *in situ* drifter trajectories. *Prog. Oceanogr.* 120, 120–138. doi: 10.1016/j.poccean.2013.08.002
- Le Hénaff, M., Kourafalou, V. H., Morel, Y., and Srinivasan, A. (2012). Simulating the dynamics and intensification of cyclonic loop current frontal eddies in the gulf of Mexico. *J. Geophys. Res. Ocean.* 117, 1–20. doi: 10.1029/2011JC007279
- Lin, Y., Greatbatch, R. J., and Sheng, J. (2009). A model study of the vertically integrated transport variability through the Yucatan channel: Role of loop current evolution and flow compensation around Cuba. *J. Geophys. Res. Ocean.* 114, 1–14. doi: 10.1029/2008JC005199
- Liu, T., Abernathey, R., Sinha, A., and Chen, D. (2019). Quantifying eulerian eddy leakiness in an idealized model. *Journal of geophysical research: Oceans.* 124, 8869–8886. doi: 10.1029/2019JC015576
- Lugo-Fernández, A. (2007). Is the loop current a chaotic oscillator? *J. Phys. Oceanogr.* 37, 1455–1469. doi: 10.1175/JPO3066.1
- Murphy, S. J., Hurlburt, H. E., and O'Brien, J. J. (1999). The connectivity of eddy variability in the Caribbean Sea, the gulf of Mexico, and the Atlantic ocean. *J. Geophys. Res. Ocean.* 104, 1431–1453. doi: 10.1029/1998JC900010
- Oey, L. Y. (2004). Vorticity flux through the Yucatan channel and loop current variability in the gulf of Mexico. *J. Geophys. Res. C Ocean.* 109, 1–10. doi: 10.1029/2004JC002400
- Oey, L. Y., Lee, H. C., and Schmitz, W. J. (2003). Effects of winds and Caribbean eddies on the frequency of loop current eddy shedding: A numerical model study. *J. Geophys. Res. C Ocean.* 108, 22–21. doi: 10.1029/2002JC001698
- Okubo, A. (1970). Horizontal dispersion of floatable particles in the vicinity of velocity singularities such as convergences. *Deep. Res. Oceanogr. Abstr.* 17, 445–454.
- Schmitz, W. J. (2005). Cyclones and westward propagation in the shedding of anticyclonic rings from the loop current. *Geophys. Monogr. Ser.* 161, 241–261. doi: 10.1029/161GM18
- Sheinbaum, J., Athié, G., Candela, J., Ochoa, J., and Romero-Arteaga, A. (2016). Structure and variability of the Yucatan and loop currents along the slope and shelf break of the Yucatan channel and campeche bank. *Dyn. Atmos. Ocean.* 76, 217–239. doi: 10.1016/j.dynatmoce.2016.08.001
- Tarshish, N., Abernathey, R., Zhang, C., Dufour, C., Frenger, I., and Griffies, St. (2018). Identifying Lagrangian coherent vortices in a mesoscale ocean model. *Ocean Model.* 130, doi: 10.1016/j.ocemod.2018.07.001
- Vukovich, F. M., and Maul, G. A. (1985). Cyclonic eddies in the eastern Gulf of Mexico. *J. Phys. Oceanogr.* 15, 105–117. doi: 10.1175/1520-0485(1985)015<0105:CEITEG>2.0.CO;2
- Wang, Y., Olascoaga, M. J., and Beron-Vera, F. J. (2015). Coherent water transport across the south Atlantic. *Geophys. Res. Lett.* 42, 4072–4079. doi: 10.1002/2015GL064089
- Weiss, J. (1991). The dynamics of enstrophy transfer in two-dimensional hydrodynamics. *Phys. D Nonlinear Phenom.* 48, 273–294. doi: 10.1016/0167-2789(91)90088-Q



## OPEN ACCESS

## EDITED BY

Arun Chakraborty,  
Indian Institute of Technology Kharagpur,  
India

## REVIEWED BY

Hari Warrior,  
Indian Institute of Technology Kharagpur,  
India  
Dezhou Yang,  
Institute of Oceanology (CAS), China  
Terry Eugene Whittedge,  
Retired, Fairbanks, AK, United States

## \*CORRESPONDENCE

Rémi Laxenaire

✉ remi.laxenaire@univ-reunion.fr

## SPECIALTY SECTION

This article was submitted to  
Physical Oceanography,  
a section of the journal  
Frontiers in Marine Science

RECEIVED 26 October 2022

ACCEPTED 20 January 2023

PUBLISHED 02 February 2023

## CITATION

Laxenaire R, Chassignet EP,  
Dukhovskoy DS and Morey SL (2023)  
Impact of upstream variability on the Loop  
Current dynamics in numerical simulations  
of the Gulf of Mexico.  
*Front. Mar. Sci.* 10:1080779.  
doi: 10.3389/fmars.2023.1080779

## COPYRIGHT

© 2023 Laxenaire, Chassignet, Dukhovskoy  
and Morey. This is an open-access article  
distributed under the terms of the [Creative  
Commons Attribution License \(CC BY\)](#). The  
use, distribution or reproduction in other  
forums is permitted, provided the original  
author(s) and the copyright owner(s) are  
credited and that the original publication in  
this journal is cited, in accordance with  
accepted academic practice. No use,  
distribution or reproduction is permitted  
which does not comply with these terms.

# Impact of upstream variability on the Loop Current dynamics in numerical simulations of the Gulf of Mexico

Rémi Laxenaire<sup>1,2,3\*</sup>, Eric P. Chassignet<sup>1</sup>, Dmitry S. Dukhovskoy<sup>1,4</sup>  
and Steven L. Morey<sup>1,5</sup>

<sup>1</sup>Center for Ocean-Atmospheric Prediction Studies, Florida State University, Tallahassee, FL, United States, <sup>2</sup>Laboratoire de Météorologie Dynamique, LMD-IPSL, UMR, École Polytechnique, ENS, CNRS, Paris, France, <sup>3</sup>Laboratoire de l'Atmosphère et des Cyclones (LACy, UMR 8105 CNRS, Université de la Réunion, Météo-France), Université de La Réunion, Saint-Denis de La Réunion, France, <sup>4</sup>National Oceanic and Atmospheric Administration, National Weather Service, National Centers for Environmental Prediction, College Park, MD, United States, <sup>5</sup>School of the Environment, Florida Agricultural and Mechanical University, FSH Science Research Center, Tallahassee, FL, United States

The Loop Current (LC), which is the main mesoscale dynamic feature of the Gulf of Mexico (GoM), has a major impact on the circulation and its variability in the interior Gulf. The LC is a highly variable and dynamic feature. It changes shape from a short jet connecting the two openings of the GoM in an almost straight line ("retracted phase") to a long loop invading most of the eastern part of the GoM ("extended phase"). When it is in the extended phase, it can shed large anticyclonic eddies, called Loop Current Eddies, which then migrate to the western GoM. In this study, the processes controlling the LC dynamics are investigated using two multi-decadal simulations of the Gulf of Mexico HYbrid Coordinate Ocean Model differing in their open boundary conditions (BCs) and altimetry-derived gridded fields. The LC in the simulation with BCs derived from monthly climatology state variables frequently remains in its retracted phase significantly longer than observed. In contrast, the duration of the retracted phase is notably shorter in the simulation in which the BCs have realistic daily variability. By examining the flow properties through the Yucatan Channel from which the LC originates, we find that increased intensity of this current and a westward shift of the mean core is associated with the LC transitions from the retracted to the extended phase. This transition is accompanied by an increase of both cyclonicity of the flow in the west and anticyclonicity in the east of the core of this jet. Moreover, the number of anticyclonic eddies entering in the GoM through the Yucatan Channel is significantly higher when the LC extends in the GoM. Consequently, this study demonstrates the importance of realistic flow variability at the lateral boundaries for accurate simulation of the LC system in a model, and reveals characteristics of the upstream flow associated with different LC behavior that can potentially aid in forecasting the LC system.

## KEYWORDS

Gulf of Mexico, Loop Current, ocean modeling, eddies (oceanic), mesoscale processes

# 1 Introduction

The Gulf of Mexico (GoM) is a marginal sea of the Atlantic Ocean partially closed by the United States, the United Mexican States, and the Republic of Cuba. It has an average depth of 1615 m with a maximum depth of 4400 m. The GoM is connected in the south to the Caribbean Sea *via* the Yucatan Channel (YC) (threshold depth of about 2000 m) and in the east to the Atlantic Ocean *via* the Strait of Florida (SF) (threshold depth shallower than 1000 m). The main oceanic circulation feature in the GoM is an intense surface jet (up to more than 1 m/s in the upper 800 m), called the Loop Current (LC), which originates in the YC and exits the Gulf through the SF. This current is, like the Gulf Stream, a branch of the western boundary current system of the North Atlantic Ocean and has an average transport between 23 and 31 Sv (e.g., Baringer & Larsen, 2001; Candela et al., 2002; Johns et al., 2002; Sheinbaum et al., 2002; Candela et al., 2019). The LC undergoes large variations as its shape varies from a short jet connecting the two GoM openings (YC and SF) in an almost direct port-to-port fashion (hereafter “retracted phase”) to a long loop invading most the eastern part of the GoM (hereafter “extended phase”) (e.g. seminal work of Reid, 1972). Episodically, the LC sheds large warm-core anticyclonic rings (radius about 200–400 km) called Loop Current eddies (LCEs) (e.g., Cochrane, 1972; Elliott, 1982; Vukovich, 1995; Leben, 2005; Dukhovskoy et al., 2015), but the LC dynamics are also characterized by smaller scale variability that includes meanders (e.g., Vukovich et al., 1979; Ezer et al., 2003; Donohue et al., 2016), and frontal eddies – both cyclonic (e.g., Vukovich & Maul, 1985; Walker et al., 2009; Jouanno et al., 2016) and anticyclonic (e.g., Hamilton et al., 2000; Leben, 2005).

The time interval between two LCE detachments, commonly called the eddy separation period, varies from a few weeks to more than a year and a half (Vukovich, 1995; Sturges & Leben, 2000; Leben, 2005; Schmitz, 2005; Dukhovskoy et al., 2015). Once formed, LCEs propagate westward from the central part of GoM to its western boundary where they slowly dissipate (Leben, 2005). This is in contrast to the frontal eddies that dissipate rapidly as they propagate along the LC (Leben, 2005). Overall, the LC system is the most dominant feature in the Gulf, despite a non-negligible wind-induced circulation (Sturges & Blaha, 1976; Elliott, 1982; Sturges et al., 1993; Olvera-Prado, 2019). In addition, variability in the LC generates topographic Rossby waves (Oey, 2008; Hamilton, 2009) and is correlated with deep water exchanges through the YC. An increase in volume of the LC when it expands is compensated by a the deep outflow in the YC and vice-versa after a shedding event (Maul, 1977; Bunge et al., 2002; Ezer et al., 2003; Lee & Mellor, 2003; Chang & Oey, 2011; Nedbor-Gross et al., 2014). The LC and associated LCEs have been the subject of numerous studies, starting with *in-situ* observations (Leipper, 1970; Behringer et al., 1977; Maul, 1977) and, with the advent of satellites, synoptic views of surface fields such as temperature (e.g., Maul, 1975) and sea surface height (SSH) (e.g., Leben, 2005). Altimetric sensors are unaffected by cloud cover and several methods have been developed to track the LC and its associated eddies from SSH fields, ranging from simple methods such as identification of the maximum horizontal gradient of SSH (e.g., Lindo-Atichati et al., 2012; Lindo-Atichati et al., 2013) or of an empirical demeaned SSH contour (e.g. 17 cm for Leben, 2005) to

more complex techniques using a Kalman filter (Dukhovskoy et al., 2015) or connecting cells associated with the highest absolute surface velocities (Hirschi et al., 2019).

Many studies have attempted to explain the mechanisms controlling the shape of the LC and associated eddy separation. It is not chaotic (Lugo-Fernández, 2007) and idealized numerical models (Hurlburt & Thompson, 1980) together with analytical models (Pichevin & Nof, 1997; Nof & Pichevin, 2001; Nof, 2005) have shown that the detachment of LCEs has a natural separation period controlled by horizontal shear instability and the  $\beta$ -effect and thus that the detachment mechanism does not require external perturbations. However, these studies, as well as those using more complex numerical models and observations, have also shown that the eddy separation period can be modulated by external factors. Several studies emphasized the importance of the GoM inflows and outflows such as their relative magnitude (Pichevin & Nof, 1997; Weisberg & Liu, 2017; Moreles et al., 2021), their fluctuations (Oey et al., 2003; Sturges et al., 2010), their stratification (Moreles et al., 2021) and their vorticity (Candela et al., 2002; Oey, 2004). Vorticity was found to be modulated by mesoscale activity, such as cyclones in the GoM that can either block the invasion of the LC in the Gulf (Schmitz, 2005; Zavala-Hidalgo et al., 2006) or favor the release of LCE (Chérubin et al., 2006), as well as Caribbean Anticyclones (Murphy et al., 1999; Candela et al., 2002; Oey et al., 2003; Athié et al., 2012; Garcia-Jove et al., 2016; Androurlidakis et al., 2021; Ntaganou et al., ), or deep eddies (Welsh & Inoue, 2000; Oey, 2008) that influence the dynamic of the LC.

In this paper, we demonstrate the importance of inflow variability on the LC retracted and extended phases by comparing two multi-decadal GoM simulations, identical except for their open boundary conditions (climatological versus realistically variable). We show that the addition of daily realistic variability from daily to interannual time scales does eliminate the unrealistically long period of LC retracted phases found in the simulations with climatological BCs (Dukhovskoy et al., 2015). We also find that when the LC tends to invade the GoM, the flow across the YC satisfies the following conditions when compared to the mean state:

- Maximum velocity shifted westward, directed toward the north-west and of higher magnitude, leading to higher horizontal shear and vorticity on both sides of the jet.
- Stronger vertical shear close to the surface and weaker subsurface between 200 and 800 m.
- Higher transport toward the GoM in the upper layer of the YC compensated by transport toward the Caribbean in the lower layers.
- Higher number of mesoscale eddies entering in the GoM (both polarity) in the main core of the LC, but with a lower number of cyclones in the vicinity of the Mexican coast. A larger number of anticyclonic eddies is also found to enter the GoM when the LC area increases.

This paper is organized as follows. In section 2, the configurations of the two numerical simulations are described in detail and the altimeter product used for validation is introduced. Two new objective methods to identify the LC and LCE ejections are also presented at the end of this section. The results section is divided in

two parts. In subsection 3.1, the new objective methods are applied to the numerical simulations and the altimeter dataset to describe the difference in the shape of the LC. The flow properties through the YC are then analyzed in subsection 3.2 to unveil the impact of its variability on the LC evolution in the GoM. Finally, the results are discussed and summarized in the last section.

## 2 Methodology and data

### 2.1 Numerical experiments

The Hybrid Coordinate Ocean Model (HYCOM, Bleck, 2002; Chassignet et al., 2003) is configured for the Gulf of Mexico domain (Figure 1A) with a horizontal resolution of  $1/25^\circ$  (Dukhovskoy et al., 2015). There are 20 hybrid layers in the vertical that are representative of the density range of water masses in the GoM and western Caribbean. Most of the vertical resolution is located in the upper ocean to resolve the vertical structure of the flow through the Yucatan Channel and the Straits of Florida. The model bathymetry is derived

from the Naval Research Laboratory Digital Bathymetry Data Base 2-minute resolution (NRL DBDB2; [https://www7320.nrlssc.navy.mil/DBDB2\\_WWW](https://www7320.nrlssc.navy.mil/DBDB2_WWW)) and Monthly climatology river inflow is prescribed at 40 locations along the coast. Both simulations are initialized from a 5-year spin-up run that started from the Generalized Digital Environmental Model 3.0 (GDEM) climatology and forced with atmospheric fields from the Fleet Numerical Meteorology and Oceanography Center's Navy Operational Global Atmospheric Prediction System (NOGAPS) (Rosmond et al., 2002). Following spin-up, the atmospheric forcing (10-m wind speed, vector wind stress, 2-m air temperature, 2-m atmospheric humidity, surface shortwave and longwave heat fluxes, and precipitation) is derived from hourly fields of the Climate Forecast System Reanalysis (CFSR) (Saha et al., 2010). Surface latent and sensible heat fluxes, along with evaporation, are calculated using Kara et al. (2000) bulk formulas. For specific details on the numerical choices, the reader is referred to Dukhovskoy et al. (2015).

The two configurations analyzed in this paper are identical, except that one has monthly climatological boundary fields at the open boundaries (hereafter ClimBC) and the other has boundary

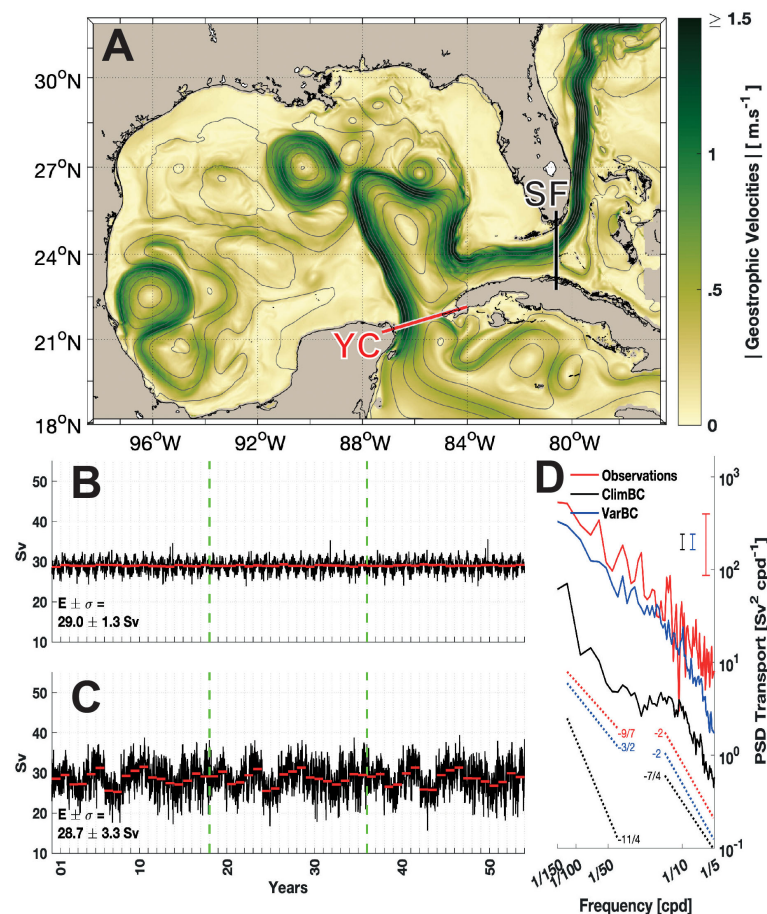


FIGURE 1

(A) Geographic area of the simulation showing the SSH isolines (SSH increment of 10 cm) and speed (background color) on the first day of the VarBC simulation. The Yucatan Channel (YC) and Straits of Florida (SF) are indicated by red and black sections, respectively, in the upper panel. Transport through the YC in ClimBC (B) and VarBC (C) simulations. Each red line in panels b and c indicates the annual averages, and the green vertical dashed lines separate the three integration cycles. In panels (B, C), the total average (E) and associated standard deviation ( $\sigma$ ) are indicated. (D) Power spectral density of transport across the YC in the 54-year simulations (ClimBC in black and VarBC in blue) and over 4 years of CANEK (Athié et al., 2015; Sheinbaum et al., 2016; Candela et al., 2019; Athié et al., 2020) mooring measurements (red). Vertical bars indicate the 95% confidence intervals and dashed lines are the slopes for each dataset.



conditions with daily variability (VarBC). In the ClimBC simulation, the boundary conditions are derived from a bi-weekly climatology produced by four years (2000–2003) of a HYCOM Atlantic free-running (non-assimilative) simulation at 1/12<sup>th</sup>; therefore, the fields imposed at the lateral boundaries have no interannual nor daily variability and reproduce the seasonal cycle only (Dukhovskoy et al., 2015). The boundary conditions for the VarBC experiment are derived from the ClimBC open boundary conditions by adding T, S, U daily anomalies to the time-averaged T, S, U fields of ClimBC as follows:

$$T(x, y, z, t) = [T_{rnl}(x, y, z, t) - \overline{T_{rnl}(x, y, z, t)}] + \overline{T_{clm}} \quad (1)$$

Where  $T_{clm}$  is the temperature from the climatology and  $T_{rnl}$  from the reanalysis and where  $\overline{\phantom{x}}$  indicate a temporal mean. The daily anomalies are derived from the 0.08° HYCOM reanalysis (19.0 and 19.1) for the period 1993–2010 (Chassignet et al., 2009; Metzger et al., 2014).

Both simulations are integrated for 54 years by repeating three times 18 years of atmospheric forcing derived from the CFSR hourly fields as detailed in Dukhovskoy et al. (2015). The ends of the 18-year forcing time series are blended by temporal interpolation of the last three days towards the forcing fields on the first day in order to avoid jumps in the forcing fields between the 18-year cycles. The ocean fields are integrated continuously during these 54 years.

Different time scales at the BCs result in notable variability of the YC transports in the ClimBC and VarBC simulations (1b and c). In the VarBC experiment, one can clearly see the 18-year repeat cycle due to the recycled ocean boundary conditions every 18 years as well as the high and low frequency variability not present in ClimBC. The estimates of the YC transport (mean  $\pm \sigma$ ) derived from the two simulations ( $29 \pm 1.3$  Sv and  $28.7 \pm 3.3$  Sv) are only slightly higher than the transport ( $27.5 \pm 11.3$  Sv) computed from roughly 4 years (July 10 2012 to August 07 2016) of CANEK mooring data (Athié et al., 2015; Sheinbaum et al., 2016; Candela et al., 2019; Athié et al., 2020). The 4-year observation-derived transport is within the range of the mean transport estimates from the simulations (note that the observed transport standard deviation includes tides that are not present in the numerical simulations). To illustrate how a 4-year transport estimate can vary over a 54-year time period, the Yucatan transport was computed from 4-year overlapping segments shifted by 1 year over all 54 years of the VarBC experiment. We found that in about 25% of these segments the 4-year modeled YC transport estimates were below the observed 4-year transport of 27.5 Sv. To quantify the impact of adding higher frequency variability, we computed the power spectral density (PSD) of the transport for the two simulations and for the CANEK data (Figure 1D). To smooth the signal, multiple PSD are computed over temporal blocks of 365 days with 50% overlap and averaged to obtain confidence intervals following Thomson & Emery (2014). We focus on the frequency band that is well resolved by the 4-year period of observations. VarBC exhibits a lower PSD than the observations, but the overall shape is similar. The ClimBC PSD, on the other hand is much lower and has a significantly different shape for lower frequencies with a sharp decrease in the PSD slope in the frequency band between about 1/150 and 1/50 cpd that is smoother in VarBC or the observations.

Therefore, with more realistic variability of the BCs, the transport variability has more energy for a wide frequency band ranging from interannual variability (Figures 1B, C) to higher frequency such as daily and weekly variability (Figure 1D).

## 2.2 Satellite altimetry data

In order to compare the model fields of elevation and velocity to observations, Absolute Dynamic Topography (ADT) maps, derived from satellite altimetry, were analyzed. 1/4° SSH and the associated surface geostrophic velocities are extracted for the Gulf of Mexico for 26 years (from 01/01/1993 to 31/12/2018) from the global daily multi-mission altimeters DUACS DT2014 (Pujol et al., 2016). These 1/4° fields, built from an optimal spatial and temporal interpolation of along-track data, are made available by the European maritime service Copernicus ([www.marine.copernicus.eu](http://www.marine.copernicus.eu)). Because of the interpolation, the effective spatial resolution is coarser than 1/4° and is on the order of a 150–250 km wavelength in the Atlantic Ocean at the latitude of the GoM (Ballarotta et al., 2019). Following Chelton et al. (2019; 2011) who showed that eddy characteristic can be estimated as around 25% of the wavelength, we could expect to resolve an eddy radius of 40–60 km. Thus, the 1/4° fields have sufficient spatial resolution to permit the investigation of the mesoscale dynamics of the LC and LCEs which have a typical radius of more than 100 km (e.g., Leben, 2005).

## 2.3 LC/LCE tracking

In order to compare the dynamics of the LC and LCE in model simulations and observational datasets, one requires an objective definition of the LC/LCE front independent of the dataset being analyzed. Two new objective methods inspired by eddy detection algorithms were developed to automatically track the LC front and identify LCE separation events.

### 2.3.1 Detection of the Loop Current front

One of the commonly used definitions of the LC front is based on some threshold value of demeaned SSH field such that the contour continuously tracks the LC from the YC to the Straits of Florida [e.g., a threshold of 0.17 m was used in Leben (2005) and Dukhovskoy et al. (2015)]. This definition is, however, sensitive to the choice of the SSH contour and may result in different LC front position and shape as well as differences in the LCE shedding events for different SSH contours. An alternative definition of the LC front, proposed here, tracks the streamline, associated with maximum geostrophic velocity magnitude, that connects the YC to the SF (respectively the red and black lines in Figure 1A). This method, which is hereafter referred to as the <V> method, is described and validated in the Supplementary Material. It assumes that the LC current is mostly in geostrophic balance (e.g., Leben, 2005; Lindo-Atichati et al., 2013; Dukhovskoy et al., 2015) and that the outer limit of the LC is in the vicinity of the core of the jet (e.g., Lindo-Atichati et al., 2013; Dukhovskoy et al., 2015; Hirschi et al., 2019).

### 2.3.2 Identification of Loop Current Eddy separation events

Most automated methods identify a LC eddy separation as a jump in the length of the LC front. We developed a new method based on the detection of the dynamic structure associated with closed contours of SSH by taking advantage of recent threshold-free eddy detection algorithms that take into account both merging and splitting events (e.g., Laxenaire et al., 2018; Le Vu et al., 2018). We track the position of anticyclonic recirculation within the LC (e.g., Molinari et al., 1977; Lewis & Kirwan, 1987; Hall & Leben, 2016) identified as an eddy by such algorithms. This recirculation is tracked over time allowing the identification of an eddy separation event as the date at which this recirculation becomes an isolated eddy in the GoM. During the eddy separation event, the trajectory linking the center of the recirculation and of the LCE crosses the LC as the LC front retracts. With this method, one can keep track of detachment and reattachment events and it is therefore possible to identify when a LCE reattaches to the LC without having to set *a priori* a temporal threshold, nor needing an operator as in Leben (2005). The effectiveness of the method, which uses the TOEddies eddy detection algorithm (Chaigneau et al., 2011; Pegliasco et al., 2015; Laxenaire et al., 2018), was evaluated by comparing the ring separation event dates to the ones obtained by Hall & Leben (2016) using the 17 cm contour method of Leben (2005). In the period from 1 January 1993 to 11 September 2015, 36 events are identified by TOEddies and 32 by Hall & Leben (2016). The 4 additional events identified by TOEddies are among the smallest and least durable with an average LCE radius of 44 km and a lifetime after LC separation of

75 days (the average radius is 115 km with an average lifetime of 285 days).

Overall, these two procedures [Leben (2005) and TOEddies] give very similar results for large LCEs with the only difference being that the TOEddies method, being threshold-free, can detect smaller LCE ejections not identified by the method of Leben (2005).

## 3 Results

### 3.1 Comparison of LC and LCE metrics

In this subsection, we summarize metrics for the Loop current derived from the two multi-decadal HYCOM experiments and the altimetry maps to document the impact of the boundary conditions. The metrics are: LC length, LCE shedding period, LCE radius, and duration of the retracted phases. The metrics are computed over the last two cycles only (36 years), with the first cycle considered as an adjustment period.

#### 3.1.1 LC statistics

The length of the LC front is a traditional measure of its extension in the GoM (Hirschi et al., 2019). Indeed, Leben (2005) has shown that its length is strongly correlated with many other variables such as its surface area, volume, and maximum longitudinal and latitudinal extensions. The length of the LC ( $\ell_{LC}$ ), computed using the method described in 2.3.1, is normalized by the beeline distance ( $B_D$ ) between the positions of the front (Figure 2) in the YC and the SF (Equation 2).

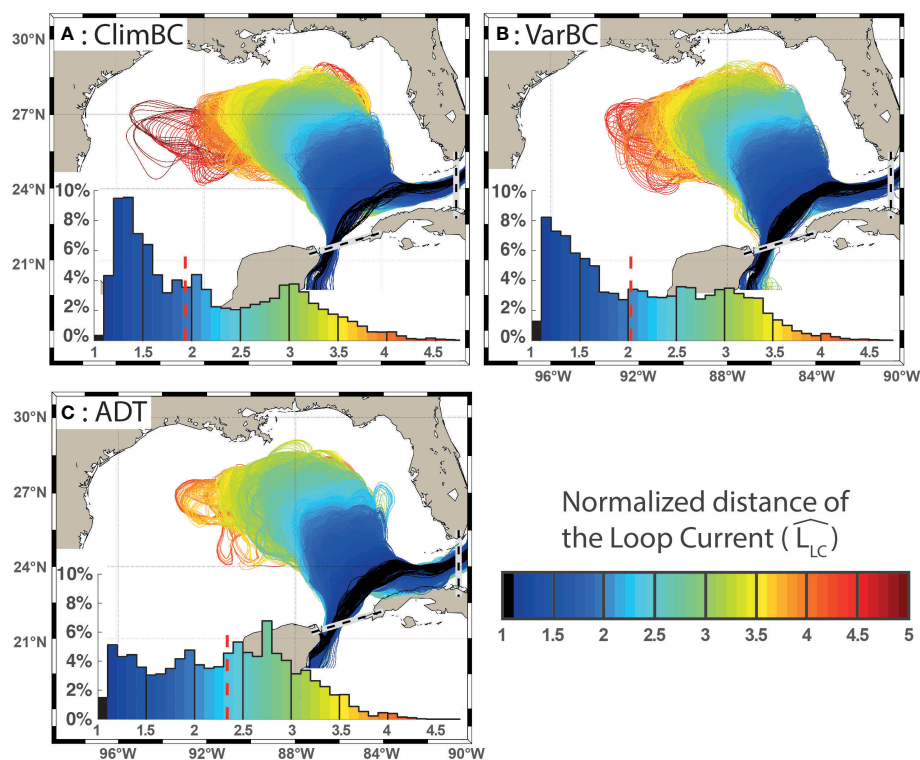


FIGURE 2

Shape of the LC for the last two cycles of ClimBC and VarBC (A, B) and of the ADT (C). The histogram of  $L_{LC}$  distribution (percentage) is displayed in the lower left corner of each panel. The color represents the normalized  $L_{LC}$  length both in maps and histograms as described in the lower right panel of this figure. .

$$L_{LC} = \frac{1}{B_D} \oint dl \quad (2)$$

The geographic position and histograms of  $L_{LC}$  for the three datasets are plotted in Figure 2. Overall, the mean shape of the Loop Current is very similar in the three datasets for  $L_{LC} < 3.5$  (blue, green and yellow contours), which is about 90% of the time. The mean and the median  $L_{LC}$  are close, ranging from 1.9 to 2.3, with slightly higher values in the ADT maps. However, the histograms (Figure 2) show that the most frequent value for  $L_{LC}$  is 2.8 in the altimeter maps versus 1.4 and 1.2 in ClimBC and VarBC, respectively. Thus, in the simulations, the LC spends more time in a retracted phase (i.e. low  $L_{LC}$ ) than in the altimetry. In all cases, there is a bimodal distribution, but the first mode (low LC value) is much more pronounced in the simulations. As surmised, the  $L_{LC}$  is highly correlated with the LC surface area with a correlation coefficient ( $R$ ) greater than 0.98.

Furthermore, Figure 2 demonstrates that the LC extends further west in ClimBC than in VarBC. This is confirmed by the normalized histograms for the western and northern extensions of the LC displayed in Figure 3 (grey for ClimBC and cyan for VarBC). Overall, the two distributions are close to each other, but as already pointed out by Dukhovskoy et al. (2015) for ClimBC, while the distributions of the maximum western longitude of the LC have similar statistics to the altimeter-derived data, the distribution of the maximum northern latitude is more strongly bimodal in the model simulations than in the data.

### 3.1.2 LCE statistics

The LCE statistics are presented in terms of number of shedding events per year, eddy separation period, and eddy radius in Table 1. In the ClimBC simulation, very long eddy separation intervals occur substantially more often than in the observations or in the VarBC simulation. In 20% of the cases, the separation period exceeds 18 months in ClimBC compared to only a few percent both in the VarBC experiment and in the altimetry. The number of LCEs per year ranges from 1.2 to 1.6, giving an average eddy separation period of 7.3 to 9.4 months. This range encompasses the mean period of 8 months (243.3

days) obtained by Hall & Leben (2016) from CCAR data over the first 20 years of altimetry measurements. The shortest eddy separation period is in the ADT fields (7.3 months) and the longest is in the ClimBC simulation (9.4 months). The differences are not significant when compared to the 95% confidence interval (CI) ranging from 1.6 to 2.9 months, but the VarBC eddy separation period is closer to the ADT fields than ClimBC. In terms of eddy size, the HYCOM simulations generate LCEs with a mean radius slightly larger than in the altimeter fields, but the differences are not significant. However, the LCE with radii smaller than 100 km represent a larger portion of the ADT eddies than for the simulations. The difference is less pronounced for the larger eddies with radius greater than 150 km.

### 3.1.3 Retracted phases

The retracted phases, i.e., the periods when the LC does not penetrate inside the GoM are identified as events where the  $L_{LC}$  remains below 2.3 (i.e., largest average  $L_{LC}$  computed from the three datasets) for at least 4 months [i.e. about half of the average eddy separation period; see Table 1 and Hall & Leben (2016)]. The 4-month minimum in the retracted phase effectively filters out cases when the transient decrease of  $L_{LC}$  is followed by a sharp increase in the case of the detachment and reattachment of a LCE. This is illustrated in Figure 4 where the LCE separations and retracted phases are identified in the time series of  $L_{LC}$  for the three datasets. The average  $L_{LC}$  for the retracted phases is 1.5.

The statistics for the retracted phases are given in Table 2. The frequency of these events is quite similar among the datasets. However, if we consider the percentage of time that the LC is in a retracted phase, the modeled LC spends more time in a retracted phase than in the observed ADT fields. The differences are quite significant since the LC is in a retracted position about 25% of the time in the ADT fields while it is more than 40% in the simulations. The average duration for the retracted phase is longest in the ClimBC experiment (19.4 versus 11.6 for VarBC and 8.6 months for ADT). The duration of the retracted phases is significantly different in ClimBC at the 95% level using a Kolmogorov-Smirnov test with two samples (Massey, 1951).

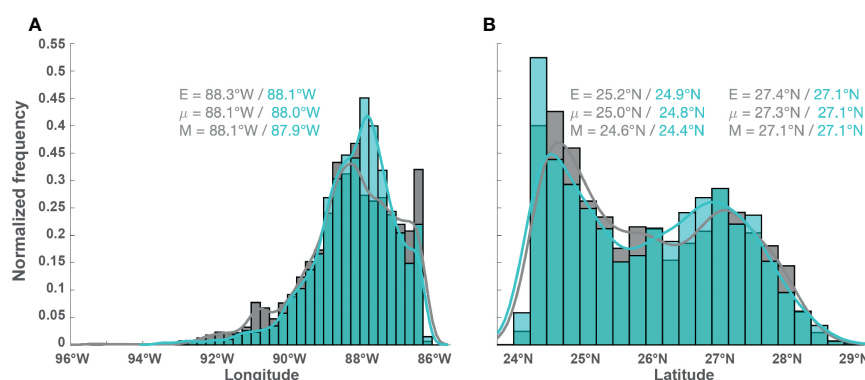


FIGURE 3

Normalized histograms (bars) and associated kernel density estimates (solid lines) of the Loop Current (LC) western extension (A) and northern extension (B) with  $1/4^\circ$  binning derived from the last two cycles of ClimBC (grey) and VarBC (cyan). The statistics of each mode of the bimodal distribution of the northern extension are provided. The estimates of the mean (E), median ( $\mu$ ), and mode (M) are shown in all the panels. The plain lines indicate the kernel probability density estimates (Rice, 1995).

**TABLE 1** Frequency, eddy shedding period, and LCE radii for ADT, ClimBC, and VarBC.

Dataset	Freq /yr	Period (months)		Radius (km)		
		Mean	>18	Mean	>100	>150
ADT	1.6	$7.3 \pm 1.6$	2%	$106 \pm 11$	52%	14%
ClimBC	1.2	$9.4 \pm 2.9$	19%	$117 \pm 09$	73%	11%
VarBC	1.4	$8.0 \pm 1.7$	6%	$114 \pm 10$	71%	17%

## 3.2 Relation between LC properties and flow across the YC

In this subsection, the characteristics of the Yucatan Current (surface velocity, vertical flow structure) during the LC expansion and retracted phases are analyzed.

### 3.2.1 Flow properties during retracted phase

The YC flow characteristics during the LC retracted are compared to the properties during the month following their end when the LC expands in ClimBC (Figure 5) and VarBC (Figure 6) experiments. The meridional velocities across the YC are extracted (Panel A in Figures 5, 6) and the percentages of time spent in a specific cell by a velocity range versus longitude are computed separately for the two periods of interest, i.e., during the retracted phase and for the month after its end (Panels b and c in Figures 5, 6). In both simulations, there is a clear difference in the mean velocity profile between the two periods with a higher maximum velocity shifted to the west in the periods after the retracted phases when the LC starts to invade the GoM. The variability of the velocity profile is higher during the retracted phases, possibly because of the higher number of days used to compute the percentages, but also because the Loop current position is not steady when in retracted position as it can be seen in Figure 4. The difference in variability between ClimBC and VarBC is especially noticeable when comparing the panels b to d in Figures 5,

6. The variability is substantially smaller in ClimBC in the months following the retracted periods.

To compare the surface meridional velocity distribution along the YC section between these two phases, anomalies are constructed by subtracting Panel B from Panel C (Panel D in Figures 5, 6). The position of the current found more often during the extension phase than during the retracted phase is in red and the opposite is blue. After a retracted phase, the average velocity profile has a higher maximum velocity and the surface meridional velocity distribution is shifted to the west. It is the same at 100 m (Panel E in Figures 5, 6), but with less variability, indicating that the surface signature extends at depth. Note that the results are very similar between ClimBC and VarBC, except that there is a larger spread in the differences in VarBC than in ClimBC because of the higher variability prescribed at the boundaries.

In order to quantify the differences between and after the retracted phases, the daily surface velocity profiles are used to calculate a) the value and position of the maximum velocity ( $V_{max}$  and  $X_{V_{max}}$ ), b) the vorticity west and east of this maximum (Vort West and East), as well as c) the cumulative east-west surface velocity over 1 m (1D Transport). Vorticity is computed using the first half of the velocity slopes near the maximum speed to capture the core of the LC jet. Figure 7 displays all these different variables in one diagram for the surface. The distribution of values during the two periods (retracted phases and after retracted phases) can then be compared to each other. For example, the median of the  $V_{max}$  distribution at the surface after retracted phases is higher than the ~ 65th percentile of the complete time series (75th percentile in ClimBC and 68th percentile in VarBC). By contrast, this value is slightly less than the 40th percentile during retracted phases. Further examination of these diagrams show that the periods of retracted phases are associated with a) low values of  $V_{max}$ , b) a position of the main LC core shifted to the east, and c) a lower cyclonicity (anticyclonicity) west (east) of the LC core. There is no noticeable difference in surface transport (1D Transport). Once the retracted phases end, there is a shift in these variables to a) high values of  $V_{max}$ , b) a position of the main LC core

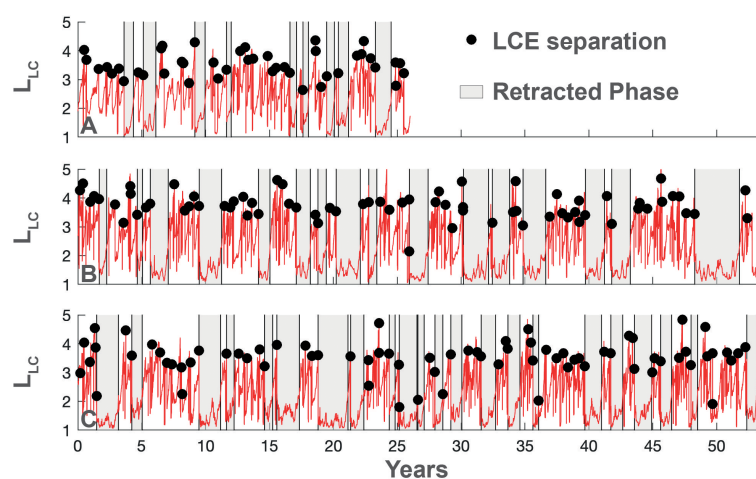


**FIGURE 4**

Time series of  $L_{LC}$ , separation of LCE and retracted phases in ADT (A), ClimBC (B) and VarBC (C). In b and c, the first cycle of 18 years is not analyzed in this section.



**TABLE 2** Number per year, fraction of the time series and duration of the retracted phases for the three data sets (last two cycles for ClimBC and VarBC).

Dataset Name	Number per year	Fraction of the time series	Duration (E $\pm$ CI)
ADT	0.3/yr	25%	8.6 $\pm$ 2.2 mo
ClimBC	0.3/yr	45%	19.4 $\pm$ 6.0 mo
VarBC	0.4/yr	43%	11.6 $\pm$ 2.8 mo

The Mean (E) and associated Confidence Interval (CI) at 95% of the duration of the retracted phases are indicated.

shifted to the west, and c) higher cyclonicity (anticyclonicity) west (east) of the LC core. The same method was applied to the velocity field at 100 m resulting in a very similar behavior suggesting that it is not a process limited to the surface.

### 3.2.2 Link between flow properties and evolution of the LC area

In the previous section, the relationship between the retracted and extending states of the LC system and the flow through the YC was analyzed. In this section, we make an attempt to generalize these results by extending the analysis to periods when the LC is in the extended phase and invades the GoM and when it retracts shrinking in size. These phases are identified as in [Nedbor-Gross et al. \(2014\)](#) by calculating the time derivative of the LC surface ( $d_t A$ ) at time  $t$  by subtracting the mean area of the previous 10 days from the mean area of the next 10 days (20-day time interval).  $d_t A > 0$  implies expansion and  $d_t A < 0$  retraction.

The anomalies of the Yucatan flow properties from the time averaged fields as functions of the sign of  $d_t A$  are shown in [Figure 8](#) for ClimBC and in [Figure 9](#) for VarBC. The first three rows of each figure highlight the changes in hydrographic properties (temperature,

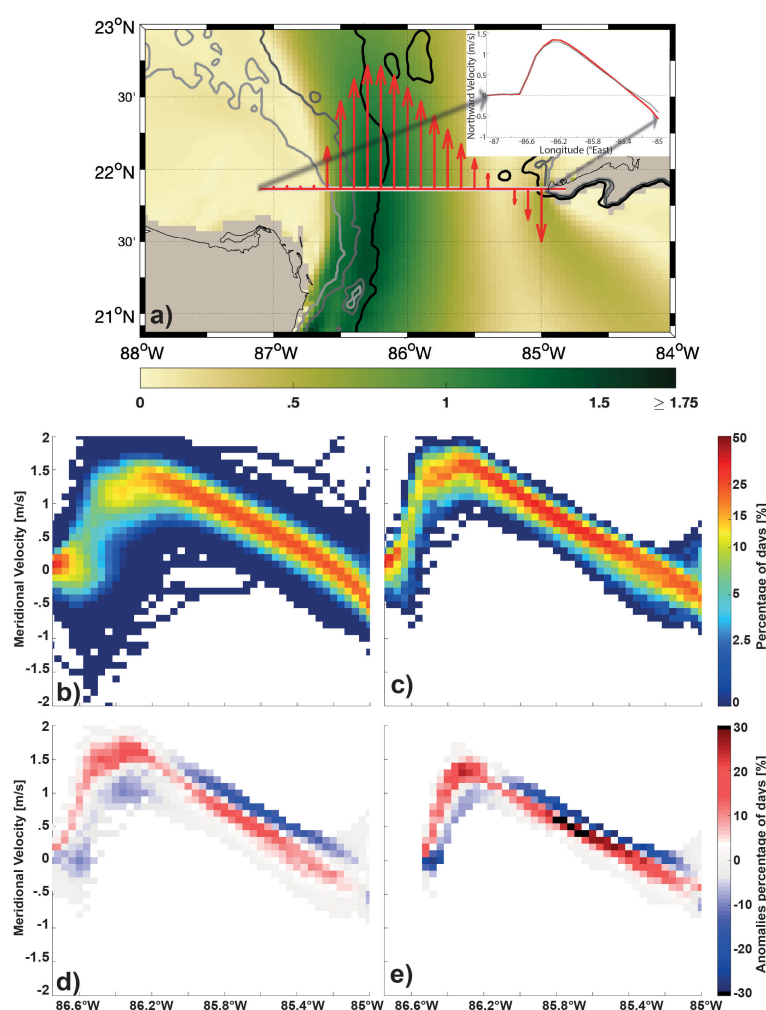


**FIGURE 5**

(A) Time averaged surface meridional velocity across the YC from the Campeche Bank to Cuba in ClimBC. Distribution of the time averaged surface meridional velocity along the section in ClimBC is drawn in red in the upper right corner of the panel and the one of VarBC is in grey (B) Occurrence (percentage of time) of meridional velocity (vertical axis) along the YC section (longitudes along the section are on X axis) during the LC retracted phase and (C) during the first month of the LC extension phase; Occurrence of meridional velocity distribution during retracted phase minus that of the month following their end (vertical axis) along the YC section (longitudes along the section are on X axis) at the surface (D) and at 100 m (E).

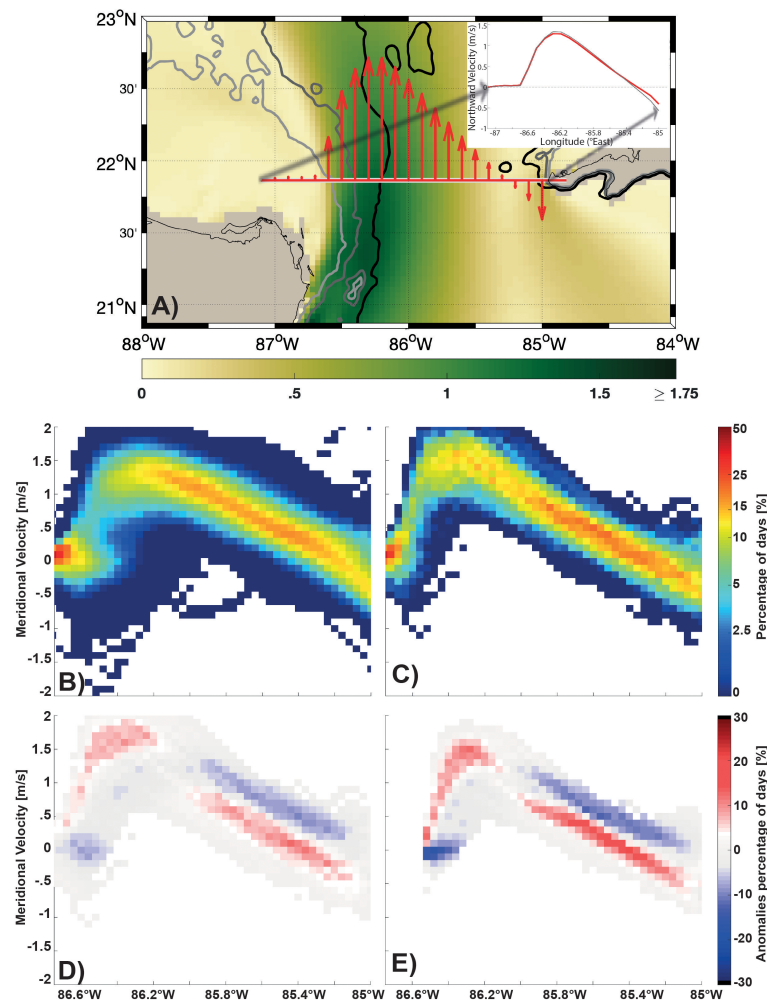


FIGURE 6

Same as in Figure 5 for VarBC, except that the distribution of the time averaged surface meridional velocity along the section in VarBC is drawn in red in the upper right corner of the panel and the one of ClimBC is in grey.

salinity, density) of the flow across the YC with respect to the sign of  $d_t A$ . These figures show that the westward shift of the LC core leading to the expansion of the LC is, in the center of the YC, associated with warmer and saltier water than the temporal mean. It results in lighter

water entering the GoM in the center of the section whereas the opposite occurs at its lateral boundaries and close to the surface.

The westward drift and higher intensity of the maximum of the meridional velocity in the LC jet when it invades the GoM, identified

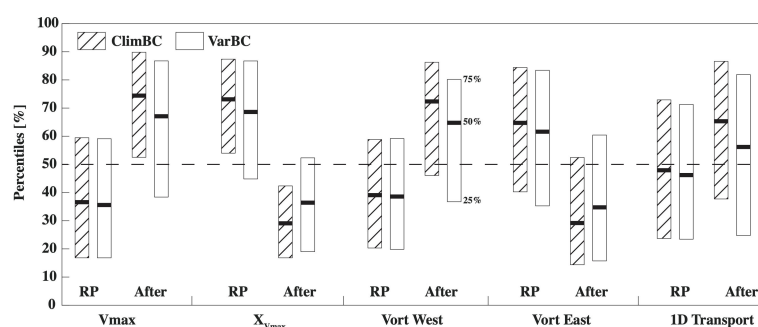


FIGURE 7

The box diagrams showing the median (thick black line) and the interquartile range (the top and bottom lines of the boxes) for: the maximum surface meridional velocity along the section shown in Figure 5A; position of the maximum velocity ( $V_{max}$  and  $X_{Vmax}$ ) along this section; the vorticity west and east of this maximum (Vort West and East) and of the cumulative surface velocity over 1 m (1D Transport) at the surface relative to the total time series (percentiles in the vertical axis) during the retracted phases (RP) and the month following the end of these phases (After). Note that  $X_{Vmax}$  is increasing toward the East. Hatched boxplots represent ClimBC and clear boxes represent VarBC.

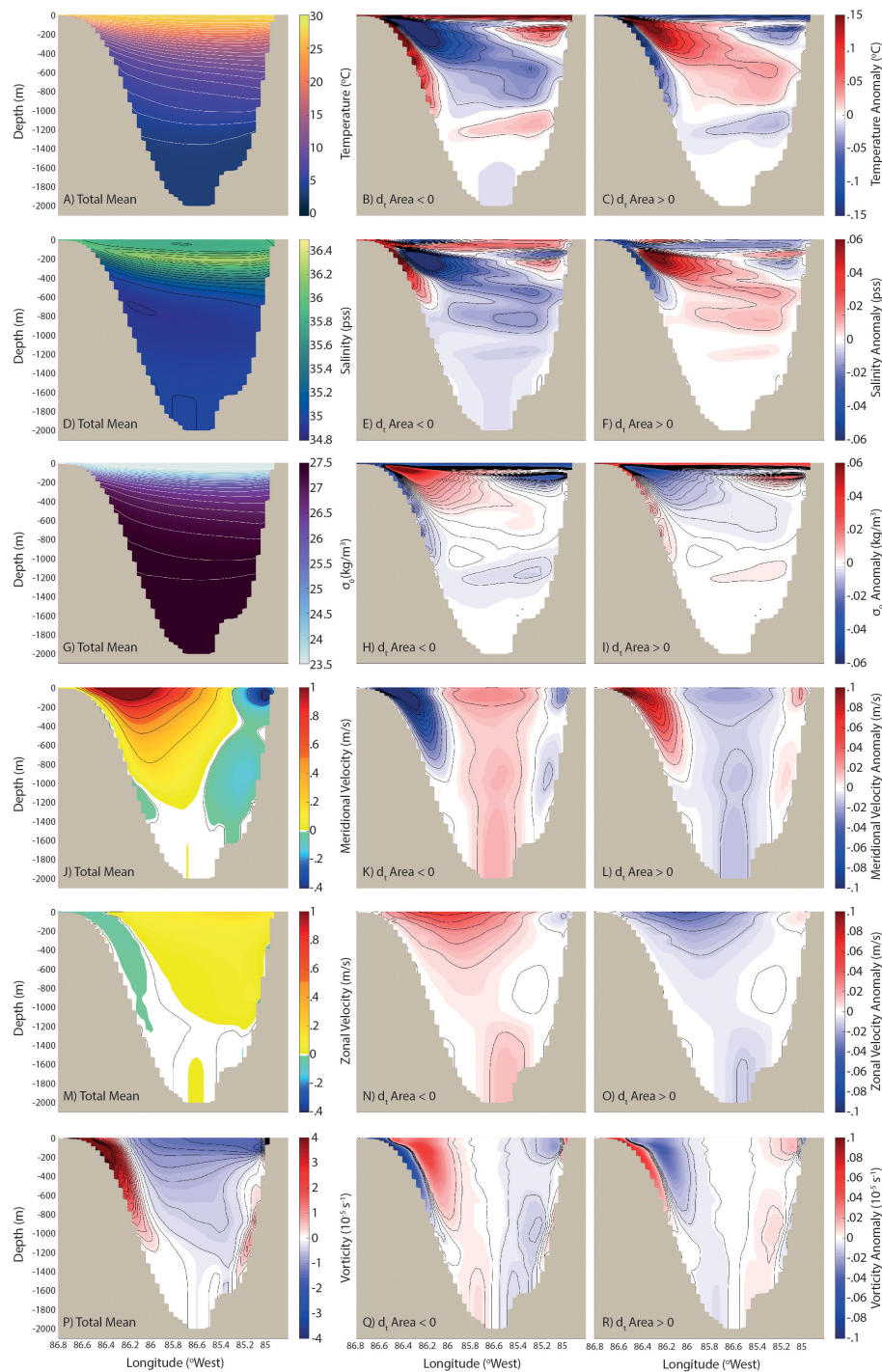


FIGURE 8

From the first to the last row, the fields of temperature, salinity, density, meridional, zonal velocities and vorticity respectively through the YC in the ClimBC simulation. The complete mean fields of these variables are shown in the first column and the associated mean anomalies when the LC “shrinks” and “grows” across the GoM are provided in the second and third columns respectively.

in the previous subsection, can be seen in panels J to L of Figures 8, 9. The zonal displacement of the maximum velocity is quite strong in the upper 1000 m, especially close to the western boundary, with a higher transport in the upper layer (Table 3). In the center of the current, meridional velocity anomalies are negative throughout the complete water column during expansion, which generates in the lower layer an outward flow (Table 3) as extensively discussed by

different authors (Maul, 1977; Bunge et al., 2002; Ezer et al., 2003; Lee & Mellor, 2003; Chang & Oey, 2011; Nedbor-Gross et al., 2014). This is true for both ClimBc and VarBc (see summary in Table 3). The changes in the zonal component of the current through the YC (Panels M to O) indicate that, when the LC invades the GoM, the velocity core is shifted to the northwest (northeast when the LC retracts). Finally, as pointed out in the previous subsection, the

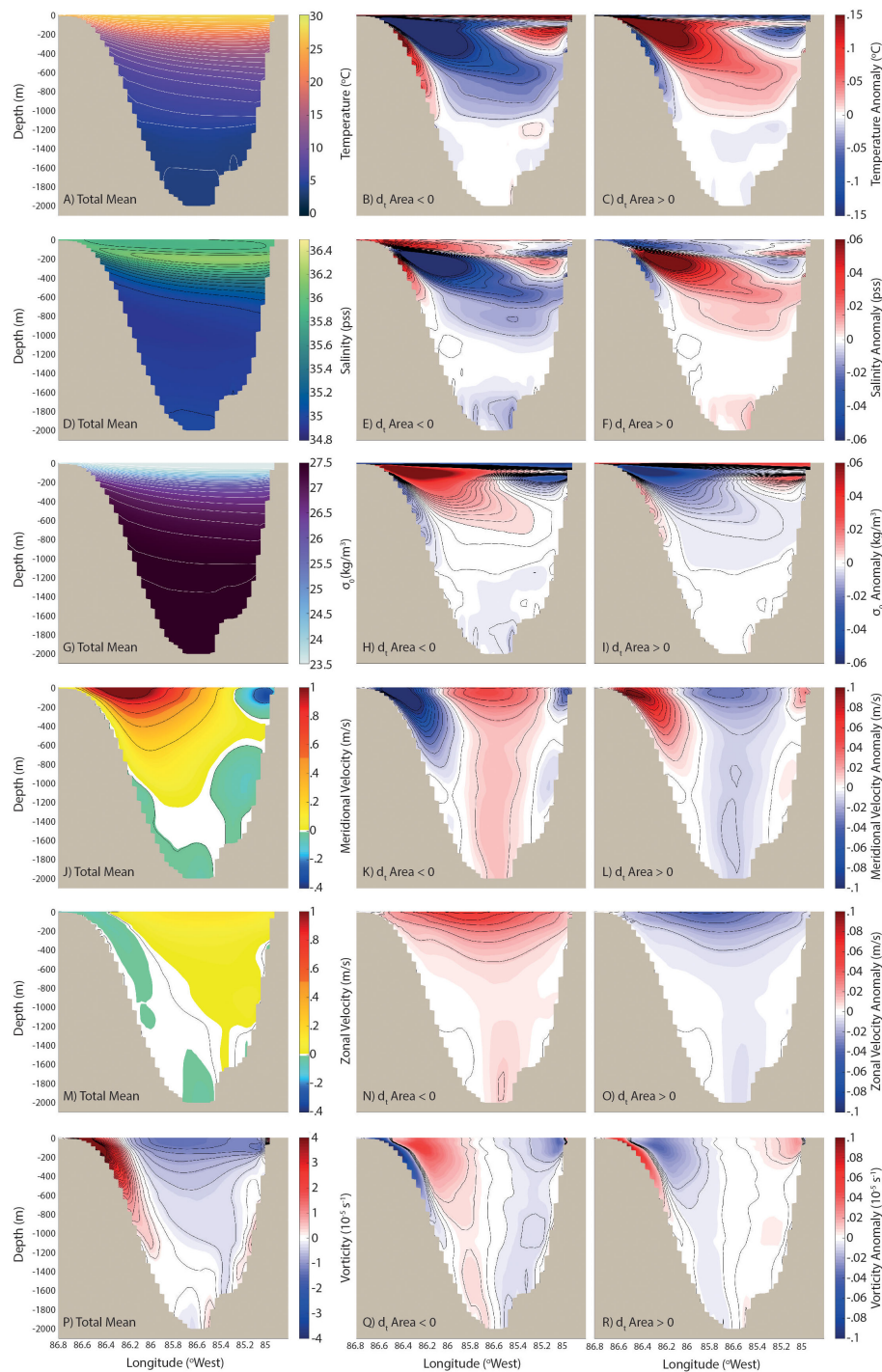


FIGURE 9  
Same as Figure 8 for VarBC.

displacement of the main core of the jet and its intensification lead to higher anticyclonic shear to the east of the LC and higher cyclonic shear to the west. The detachment of the main core along the island of Cuba during the “growth” of the LC leads to small areas of positive vorticity that are visible in the eastern part of the channel. Overall, the results obtained by comparing particular phases of the LC clearly illustrates how the flow properties across the YC change when the LC invades the GoM as opposed to when it retracts.

### 3.2.3 Eddies in the Yucatan channel and the Loop Current

As discussed by many authors (e.g., [Murphy et al., 1999](#); [Candela et al., 2002](#); [Oey et al., 2003](#); [Athié et al., 2012](#); [Androulidakis et al., 2021](#)), the properties of the LC can be modulated by the entry of coherent patches of vorticity into the GoM. In this subsection, we characterize and quantify the eddies entering the GoM by applying the TOEddies algorithm of [Laxenaire et al. \(2018\)](#) on the SSH



**TABLE 3** Average transport through the YC. The mean values are calculated either using the full period or both periods with a different sign of the time derivation of the LC area in the GoM ( $d_t A$ ). The lower layer is identified as HYCOM layers below which the time averaged transport is close to zero.

		ClimBC			VarBC		
		Total	$d_t A < 0$	$d_t A > 0$	Total	$d_t A < 0$	$d_t A > 0$
		(100%)	(42%)	(58%)	(100%)	(41%)	(59%)
	Total	29.6 Sv	29.7 Sv	29.5 Sv	29.3 Sv	29.4 Sv	29.3 Sv
Transport	Upper Layer	29.5 Sv	29.0 Sv	29.8 Sv	29.3 Sv	28.9 Sv	29.6 Sv
	Lower Layer	0.1 Sv	0.7 Sv	-0.3 Sv	<0.1 Sv	0.5 Sv	-0.3 Sv

contours (Table 4). The eddies are separated into two categories when they enter the Gulf of Mexico *via* the Yucatan Channel, either west or east of the maximum mean surface velocity (see the velocity distribution across the Yucatan Channel in Figures 5, 6). We find that all the anticyclones enter the GoM east of maximum velocity and that there are more anticyclones entering the GoM during the LC extension vs the LC retraction. On the other hand, we find that there are more cyclones entering the GoM west of maximum velocity when the LC is retracting and more entering to the east when the LC is growing. Most of those cyclones enter to the east of the maximum velocity enter near Cuba, providing a positive vorticity influx. There are significant differences between the two simulations with about 3 times more anticyclones entering the GoM in VarBC than in ClimBC; but both simulations have approximately the same number of cyclones. This indicates that cyclones are more likely to be formed locally south of Cuba while anticyclones are more likely to be injected in the model domain *via* the open boundary conditions.

Androulidakis et al. (2021) named the anticyclones south of the Yucatan Channel, CARibbean Anticyclones (CARAs), and, as in their study, we note that when the LC retracts, a large CARA is often found south of the LC while one anticyclone is often found south of Cuba when the LC expands (not shown). Here, we go one step further by documenting the origin and fate of these eddies. To do this, we track the eddies entering the area depicted by a polygon (in gray in Figure 10). Figure 10 shows that the CARAs originate mainly from two distinct areas, Caribbean Sea (black trajectories) and an area between the northwestern tip of the main island of Cuba and the Isle of Youth (blue trajectories). Most of the anticyclones exit north into the GoM (green trajectories), but a small portion recirculates within the Caribbean Sea (black trajectories). In both simulations, there are more anticyclonic eddies entering the polygon than exiting which indicates that merging events occur prior to entering the GoM. As already stated, there are more anticyclonic eddies entering the GoM in

VarBC than in ClimBC since eddies can enter the southern boundary in VarBC *via* the open boundary conditions. We do find that anticyclonic eddies entering the GoM are somewhat linked to an increase in the LC area as shown in Table 4, but overall there is no obvious correlation between the LC dynamics and the eddies entering or exiting the GoM. However, it is worth noting that, from the blue trajectories in Figure 10, more eddies appear to drift from east to west (entering) that the inverse (exiting) the polygon, suggesting that the CARAs upstream of the GoM discussed by Androulidakis et al. (2021) mainly leave this area to enter the GoM.

## 4 Discussion and summary

In this study, we document the impact of boundary conditions (BC) on the the Loop Current (LC) evolution and associated LC eddy (LCE) formation. The importance of inflow variability on the LC retracted and extended phases is demonstrated by comparing two multi-decadal GoM simulations, identical except for their open boundary conditions (climatological versus variable). We show that the addition of daily interannual variability does eliminate the unrealistically long period of LC retracted phases found in the climatological simulations (Dukhovskoy et al., 2015).

To unveil the processes explaining the differences between the numerical simulations, a detailed study of the structure of flows entering the Gulf of Mexico through the Yucatan Channel is performed. It shows that the LC tends to extend into the GoM when the flow across the YC satisfies the following conditions when compared to the mean state:

- Maximum velocity shifted westward, directed toward the north-west and of higher magnitude, leading to higher horizontal shear and vorticity on both side of the jet.

**TABLE 4** Number of eddies entering the GoM through the YC. The mean values are calculated either using the full period or both periods with a different sign of the time derivation of the LC area in the GoM ( $d_t A$ ). Anticyclones (ACY) and cyclones (CY) are studied separately depending on whether they cross the YC west of the maximum velocity or east.

		ClimBC			VarBC		
		Total	$d_t A < 0$	$d_t A > 0$	Total	$d_t A < 0$	$d_t A > 0$
		(100%)	(42%)	(58%)	(100%)	(41%)	(59%)
	ACY east	0.9/yr	0.5/yr	1.2/yr	3.3/yr	2.8/yr	3.7/yr
Eddies	CY east	0.5/yr	0.3/yr	0.6/yr	0.4/yr	0.2/yr	0.5/yr
	CY west	0.5/yr	0.7/yr	0.3/yr	0.5/yr	0.6/yr	0.4/yr

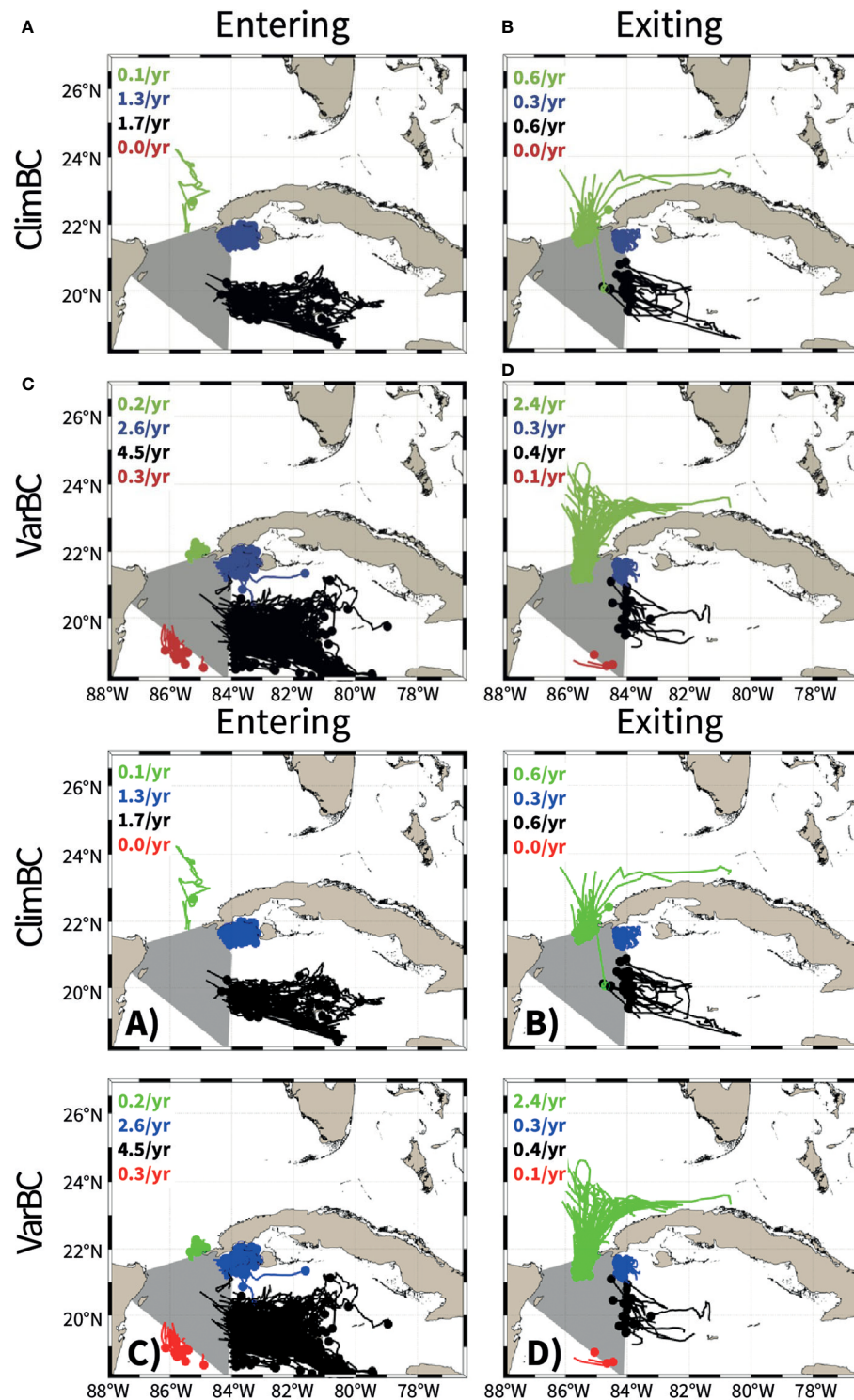


FIGURE 10

Origin (Entering, A, C) and termination (Exiting, B, D) of the Caribbean Anticyclones in ClimBC (A, B) and VarBC (C, D). The eddies are separated if they enter/exit the area of interest by north (green), east (blue), south (black) and west (red) routes. The numbers in the upper left corner of each panel indicate the number of structures per year, with the color indicating the route followed.

- Stronger vertical shear close to the surface and weaker subsurface between 200 and 800 m.
- Higher transport toward the GoM in the upper layer of the YC compensated by transport toward the Caribbean in the lower layers.
- Higher number of mesoscale eddies entering in the GoM (both polarity) in the main core of the LC, but with a lower number of cyclones in the vicinity of the Mexican coast. A larger number of anticyclonic eddies is also found to enter the GoM when the LC area increases.

The link between the westward displacement of the LC velocity core and change of LC area in the GoM was first documented by Nedbor-Gross et al. (2014) following the work of Athié et al. (2012) who identified such displacement in relation to LCE shedding. When investigating the relationship between the LC area and the time integration of the deep YC transport, Nedbor-Gross et al. (2014) showed that, when the LC area is larger than its 75th percentile, the YC transport profile shifts west and that, when the LC area is below the 25th percentile, the YC transport profile shifts east and broadens. The Nedbor-Gross et al. (2014) results are in agreement with the results presented in this paper as well as those of Androulidakis et al. (2021). One can therefore envision that assimilation of the Yucatan Channel velocity profile could lead to substantial improvements in the forecasting of the Loop Current evolution.

Furthermore, Candela et al. (2002) and Oey (2004) surmise that an influx of cyclonic potential vorticity flux anomaly extends the Loop Current and influx of anticyclonic potential vorticity flux anomaly “triggers” a retraction. These vorticity fluxes are controlled by the intensity of the current near the surface at the western portion of the YC where the cyclonic horizontal shear of Ertel’s potential vorticity are maximum (see the upper right panel of Figure 2 of Oey (2004)). On the other hand, the theory of the momentum imbalance paradox (Pichevin & Nof, 1997; Nof & Pichevin, 2001; Nof, 2005) states that the fraction of the flux transferred to the bulb should increase when the anticyclonicity of the input flux increases (e.g. discussion of parameter  $\alpha$  in Nof (2005)). These two results *a priori* may appear to be contradictory, but they are consistent with our findings which show that an increase in LC maximum velocity not only leads to a higher cyclonicity in the western part of the LC, but also higher anticyclonicity in the core of the eastern part of the LC.

Mesoscale dynamics in the Caribbean Sea upstream of the Loop Current as a possible important factor on Yucatan flow variability and LC dynamics has been discussed in many studies (e.g., Murphy et al., 1999; Candela et al., 2002; Abascal et al., 2003; Oey et al., 2003; Athié et al., 2012; Garcia-Jove et al., 2016; Androulidakis et al., 2021). In particular, Garcia-Jove et al. (2016) showed that Caribbean eddies activity directly impact the LCE separation period, and thus LC dynamics, by suppressing these eddies in numerical simulations *via* increasing viscosity in the Caribbean Sea. Furthermore, Androulidakis et al. (2021) documented a relation between the presence of CARibbean Anticyclones (CARAs) upstream of the GoM and phases of the LC. They showed that, when a CARA lies south of the YC, the LC tend to be retracted and the inverse is found when it expands. We obtained the same results (not shown) and focused on the fluxes of eddies in the CARAs area. The number of eddies entering in the GoM increases when the LC extends. While the cyclones are formed locally, anticyclonic eddies can originate far from the Caribbean Sea and are thus more numerous in VarBC where they can be formed at the boundary of the domain due to the variable boundary conditions. These results are in agreement with the work of Huang et al. (2021) which demonstrate that anticyclonic eddies in the western tropical Atlantic Ocean can enter the Gulf of Mexico and thus are a direct product of variable boundary conditions.

The choice of the boundary conditions (monthly climatology versus realistic variability added to the climatology) does not have a

significant impact on the periodicity of the LC eddy formation, but when interannual daily perturbations are added at the boundaries, the durations of the retracted phases are significantly shorter and better agree with altimetry-derived LC statistics than when using climatological boundary conditions. The added variability impacts the dynamics of the flow across the YC and associated eddies which are strongly linked to the dynamics of the LC and explains the differences found in the simulations. However, with so many different parameters impacting the dynamics of the LC, it is a complicated task to clearly identified a predominant factor. Therefore, while this study of the sensitivity of the LC to the BCs (primarily, the inflow variability) confirmed the importance of the latter, further analysis with other simulations such as with constant BCs or different atmospheric forcings could be studied to reveal other mechanisms acting on the LC dynamics such as, for example, frequency of the LCE shedding.

## Data availability statement

The raw data supporting the conclusions of this article will be made available by the authors, without undue reservation.

## Author contributions

All authors designed the study. DD and SM ran the numerical simulations. RL performed the data analysis and, with EC, wrote the first version of the article. All the authors contributed to the article and approved the submitted version.

## Funding

We acknowledge support from the Gulf Research Program of the National Academies of Sciences, Engineering, and Medicine under award numbers 2000009966 and 2000013149. The content is solely the responsibility of the authors and does not necessarily represent the official views of the Gulf Research Program or the National Academies of Sciences, Engineering, and Medicine. We also acknowledge support from the Office Naval Research (ONR) Grant N00014-19-1-2671

## Acknowledgments

The HYCOM simulations were performed on supercomputers at the US Navy DoD Supercomputing Resource Center (DSRC) in Stennis Space Center, Mississippi, using computer time provided by the US DoD High Performance Computing Modernization Program. The gridded altimeter products were produced by SSALTO/DUACS and distributed by the Copernicus Marine Environment Monitoring Service. We acknowledge Dr. Gabriela Athie de Velasco, Dr. Julio Candela and Dr. Julio Sheinbaum who shared the ADCP data from the CANEK program.

## Conflict of interest

The authors declare that the research was conducted in the absence of any commercial or financial relationships that could be construed as a potential conflict of interest.

## Publisher's note

All claims expressed in this article are solely those of the authors and do not necessarily represent those of their affiliated

organizations, or those of the publisher, the editors and the reviewers. Any product that may be evaluated in this article, or claim that may be made by its manufacturer, is not guaranteed or endorsed by the publisher.

## Supplementary material

The Supplementary Material for this article can be found online at: <https://www.frontiersin.org/articles/10.3389/fmars.2023.1080779/full#supplementary-material>

## References

- Abascal, A., Sheinbaum, J., Candela, J., Ochoa, J., and Badan, A. (2003). Analysis of flow variability in the Yucatan Channel. *J. Geophys. Res.* 108, 3381. doi: 10.1029/2003JC001922
- Androulidakis, Y., Kourafalou, V., Le Hénaff, M., Kang, H., and Ntaganou, N. (2021). The role of mesoscale dynamics over northwestern Cuba in the loop current evolution in 2010, during the deepwater horizon incident. *J. Mar. Sci. Eng.* 9, 188. doi: 10.3390/jmse9020188
- Androulidakis, Y., Kourafalou, V., Olascoaga, M. J., Beron-Vera, F. J., Le Hénaff, M., Kang, H., et al. (2021). Impact of Caribbean anticyclones on Loop Current variability. *Ocean dynamics*, 71 (9), 935–956. doi: 10.1007/s10236-021-01474-9
- Athié, G., Candela, J., Ochoa, J., and Sheinbaum, J. (2012). Impact of Caribbean cyclones on the detachment of loop current anticyclones. *J. Geophys. Res.: Oceans* 117, C03018. doi: 10.1029/2011JC007090
- Athié, G., Sheinbaum, J., Candela, J., Ochoa, J., Pérez-Brunius, P., and Romero-Arteaga, A. (2020). Seasonal variability of the transport through the Yucatan channel from observations. *J. Phys. Oceanogr.* 50, 343–360. doi: 10.1175/jpo-d-18-0269.1
- Athié, G., Sheinbaum, J., Leben, R., Ochoa, J., Shannon, M. R., and Candela, J. (2015). Interannual variability in the Yucatan channel flow. *Geophys. Res. Lett.* 42, 1496–1503. doi: 10.1002/2014GL062674
- Ballarotta, M., Ubelmann, C., Pujol, M.-I., Taburet, G., Fournier, F., Legeais, J.-F., et al. (2019). On the resolutions of ocean altimetry maps. *Ocean Sci.* 15, 1091–1109. doi: 10.5194/os-15-1091-2019
- Baringer, M. O., and Larsen, J. C. (2001). Sixteen years of Florida current transport at 27° N. *Geophys. Res. Lett.* 28, 3179–3182. doi: 10.1029/2001GL013246
- Behringer, D. W., Molinari, R. L., and Festa, J. F. (1977). The variability of anticyclonic current patterns in the gulf of Mexico. *J. Geophys. Res.* (1896-1977) 82, 5469–5476. doi: 10.1029/JC082i034p05469
- Bleck, R. (2002). An oceanic general circulation model framed in hybrid isopycnal-Cartesian coordinates. *Ocean Model.* 4, 55–88. doi: 10.1016/S1463-5003(01)00012-9
- Bunge, L., Ochoa, J., Badan, A., Candela, J., and Sheinbaum, J. (2002). Deep flows in the Yucatan channel and their relation to changes in the loop current extension. *J. Geophys. Res.: Oceans* 107, 26–1–26–7. doi: 10.1029/2001JC001256
- Candela, J., Ochoa, J., Sheinbaum, J., López, M., Pérez-Brunius, P., Tenreiro, M., et al. (2019). The flow through the gulf of Mexico. *J. Phys. Oceanogr.* 49, 1381–1401. doi: 10.1175/jpo-d-18-0189.1
- Candela, J., Sheinbaum, J., Ochoa, J., Badan, A., and Leben, R. (2002). The potential vorticity flux through the Yucatan channel and the loop current in the gulf of Mexico. *Geophys. Res. Lett.* 29, 16–1–16–4. doi: 10.1029/2002GL015587
- Chaigneau, A., Marie, L. T., Gérard, E., Carmen, G., and Oscar, P. (2011). Vertical structure of mesoscale eddies in the eastern south pacific ocean: A composite analysis from altimetry and argo profiling floats. *J. Geophys. Res.: Oceans* 116, C11025. doi: 10.1029/2011JC007134
- Chang, Y.-L., and Oey, L.-Y. (2011). Loop current cycle: Coupled response of the loop current with deep flows. *J. Phys. Oceanogr.* 41, 458–471. doi: 10.1175/2010JPO4479.1
- Chassignet, E. P., Hurlburt, H. E., Metzger, E. J., Smedstad, O. M., Cummings, J. A., Halliwell, G. R., et al. (2009). US GODAE: Global ocean prediction with the HYbrid coordinate ocean model (HYCOM). *Oceanography* 22, 64–75. doi: 10.5670/oceanog.2009.39
- Chassignet, E. P., Smith, L. T., Halliwell, G. R., and Bleck, R. (2003). North Atlantic simulations with the hybrid coordinate ocean model (HYCOM): Impact of the vertical coordinate choice, reference pressure, and thermobaricity. *J. Phys. Oceanogr.* 33, 2504–2526. doi: 10.1175/1520-0485(2003)033<2504:naswth>2.0.co;2
- Chelton, D. B., Schlax, M. G., and Samelson, R. M. (2011). Global observations of nonlinear mesoscale eddies. *Prog. Oceanogr.* 91, 167–216. doi: 10.1016/j.pocean.2011.01.002
- Chelton, D. B., Schlax, M. G., Samelson, R. M., Farrar, J. T., Molemaker, M. J., McWilliams, J. C., et al. (2019). Prospects for future satellite estimation of small-scale variability of ocean surface velocity and vorticity. *Prog. Oceanogr.* 173, 256–350. doi: 10.1016/j.pocean.2018.10.012
- Chérubin, L. M., Morel, Y., and Chassignet, E. P. (2006). Loop current ring shedding: The formation of cyclones and the effect of topography. *J. Phys. Oceanogr.* 36, 569–591. doi: 10.1175/jpo2871.1
- Cochrane, J. D. (1972). *Separation of an anticyclone and subsequent developments in the loop current*, (1969). Contributions on the Physical Oceanography of the Gulf of Mexico LRA Capurio, JL Reid Vol. 2 (Texas A&M University Oceanographic Studies), 91–106.
- Donohue, K., Watts, D., Hamilton, P., Leben, R., Kennelly, M., and Lugo-Fernández, A. (2016). Gulf of Mexico loop current path variability. *Dynamics Atmospheres Oceans* 76, 174–194. doi: 10.1016/j.dynatmoce.2015.12.003
- Dukhovskoy, D. S., Leben, R. R., Chassignet, E. P., Hall, C. A., Morey, S. L., and Nedbor-Gross, R. (2015). Characterization of the uncertainty of loop current metrics using a multidecadal numerical simulation and altimeter observations. *Deep Sea Res. Part I: Oceanographic Res. Papers* 100, 140–158. doi: 10.1016/j.dsr.2015.01.005
- Elliott, B. A. (1982). Anticyclonic rings in the gulf of Mexico. *J. Phys. Oceanogr.* 12, 1292–1309. doi: 10.1175/1520-0485(1982)012<1292:aritgo>2.0.co;2
- Ezer, T., Oey, L.-Y., Lee, H.-C., and Sturges, W. (2003). The variability of currents in the Yucatan channel: Analysis of results from a numerical ocean model. *J. Geophys. Res.: Oceans* 108, 3012. doi: 10.1029/2002JC001509
- García-Jové, M., Sheinbaum, J., and Jouanno, J. (2016). Sensitivity of loop current metrics and eddy detachments to different model configurations: The impact of topography and Caribbean perturbations. *Atmosfera* 29, 235–265. doi: 10.20937/ATM.2016.29.03.05
- Hall, C. A., and Leben, R. R. (2016). Observational evidence of seasonality in the timing of loop current eddy separation. *Dynamics Atmospheres Oceans* 76, 240–267. doi: 10.1016/j.dynatmoce.2016.06.002
- Hamilton, P. (2009). Topographic rossby waves in the gulf of Mexico. *Prog. Oceanogr.* 82, 1–31. doi: 10.1016/j.pocean.2009.04.019
- Hamilton, P., Berger, T., Singer, J., Waddell, E., Churchill, J., Leben, R., et al. (2000). *DeSoto canyon eddy intrusion study, final report, volume II* (New Orleans, LA: OCS Study MMS 2000-080, US Dept. of the Interior, Minerals Management Service). Tech. rep., Rep.
- Hirschi, J. J.-M., Frajka-Williams, E., Blaker, A. T., Sinha, B., Coward, A., Hyder, P., et al. (2019). Loop current variability as trigger of coherent gulf stream transport anomalies. *J. Phys. Oceanogr.* 49, 2115–2132. doi: 10.1175/jpo-d-18-0236.1
- Huang, M., Liang, X., Zhu, Y., Liu, Y., and Weisberg, R. H. (2021). Eddies connect the tropical Atlantic ocean and the gulf of Mexico. *Geophys. Res. Lett.* 48, e2020GL091277. doi: 10.1029/2020GL091277
- Hurlburt, H. E., and Thompson, J. D. (1980). A numerical study of loop current intrusions and eddy shedding. *J. Phys. Oceanogr.* 10, 1611–1651. doi: 10.1175/1520-0485(1980)010<1611:ansolc>2.0.co;2
- Johns, W. E., Townsend, T. L., Frantoni, D. M., and Wilson, W. D. (2002). On the Atlantic inflow to the Caribbean Sea. *Deep Sea Res. Part I: Oceanographic Res. Papers* 49, 211–243. doi: 10.1016/S0967-0637(01)00041-3
- Jouanno, J., Ochoa, J., Pallàs-Sanz, E., Sheinbaum, J., Andrade-Canto, F., Candela, J., et al. (2016). Loop current frontal eddies: Formation along the campeche bank and impact of coasts trapped waves. *J. Phys. Oceanogr.* 46, 3339–3363. doi: 10.1175/jpo-d-16-0052.1
- Kara, A. B., Rochford, P. A., and Hurlburt, H. E. (2000). Efficient and accurate bulk parameterizations of air-sea fluxes for use in general circulation models. *J. Atmospheric Oceanic Technol.* 17, 1421–1438. doi: 10.1175/1520-0426(2000)017<1421:EAABPO>2.0.CO;2
- Laxenaire, R., Speich, S., Blanke, B., Chaigneau, A., Pegliasco, C., and Stegner, A. (2018). Anticyclonic eddies connecting the Western boundaries of Indian and Atlantic oceans. *J. Geophys. Res.: Oceans* 123, 7651–7677. doi: 10.1029/2018JC014270
- Leben, R. R. (2005). *Altimeter-derived loop current metrics* (American Geophysical Union (AGU), Eds. Sturges, W. Lugo-Fernandez, A. 181–201. doi: 10.1029/161GM15



- Lee, H.-C., and Mellor, G. L. (2003). Numerical simulation of the gulf stream system: The loop current and the deep circulation. *J. Geophys. Res.: Oceans* 108, 3043. doi: 10.1029/2001JC001074
- Leipper, D. F. (1970). A sequence of current patterns in the gulf of Mexico. *J. Geophys. Res.* (1896-1977) 75, 637–657. doi: 10.1029/JC075i003p00637
- Le Vu, B., Stegner, A., and Arsouze, T. (2018). Angular momentum eddy detection and tracking algorithm (AMEDA) and its application to coastal eddy formation. *J. Atmospheric Oceanic Technol.* 35, 739–762. doi: 10.1175/JTECH-D-17-0010.1
- Lewis, J. K., and Kirwan, A. D. Jr. (1987). Genesis of a gulf of Mexico ring as determined from kinematic analyses. *J. Geophys. Res.: Oceans* 92, 11727–11740. doi: 10.1029/JC092iC11p11727
- Lindo-Atichati, D., Bringas, F., and Goni, G. (2013). Loop current excursions and ring detachments during 1993–2009. *Int. J. Remote Sens.* 34, 5042–5053. doi: 10.1080/01431161.2013.787504
- Lindo-Atichati, D., Bringas, F., Goni, G., Muhling, B., Muller-Karger, F., and Habtes, S. (2012). Varying mesoscale structures influence larval fish distribution in the northern gulf of Mexico. *Mar. Ecol. Prog. Ser.* 463, 245–257. doi: 10.3354/meps09860
- Lugo-Fernández, A. (2007). Is the loop current a chaotic oscillator? *J. Phys. Oceanogr.* 37, 1455–1469. doi: 10.1175/jpo3066.1
- Massey, J. F. Jr. (1951). The kolmogorov-smirnov test for goodness of fit. *J. Am. Stat. Assoc.* 46, 68–78. doi: 10.1080/01621459.1951.10500769
- Maul, G. (1975). An evaluation of the use of the earth resources technology satellite for observing ocean current boundaries in the gulf stream system. *Technical Report (Environmental Research Laboratories)*.
- Maul, G. A. (1977). The annual cycle of the gulf loop current part i: Observations during a one-year time series. *J. Mar. Res.* 35, 29–47.
- Metzger, E. J., Smedstad, O. M., Thoppil, P. G., Hurlburt, H. E., Cummings, J. A., Wallcraft, A. J., et al. (2014). US Navy operational global ocean and Arctic ice prediction systems. *Oceanography* 27, 32–43. doi: 10.5670/oceanog.2014.66
- Molinari, R. L., Baig, S., Behringer, D. W., Maul, G. A., and Legeckis, R. (1977). Winter intrusions of the loop current. *Science* 198, 505–507. doi: 10.1126/science.198.4316.505
- Moreles, E., Zavala-Hidalgo, J., Martínez-López, B., and Ruiz-Angulo, A. (2021). Influence of stratification and Yucatan current transport on the loop current eddy shedding process. *J. Geophys. Res.: Oceans* 126, e2020JC016315. doi: 10.1029/2020JC016315
- Murphy, S. J., Hurlburt, H. E., and O'Brien, J. J. (1999). The connectivity of eddy variability in the Caribbean Sea, the gulf of Mexico, and the Atlantic ocean. *J. Geophys. Res.: Oceans* 104, 1431–1453. doi: 10.1029/1998JC900010
- Nedbor-Gross, R., Dukhovskoy, D. S., Bourassa, M. A., Morey, S. L., and Chassignet, E. P. (2014). Investigation of the relationship between the Yucatan channel transport and the loop current area in a multidecadal numerical simulation. *Mar. Technol. Soc. J.* 48, 15–26. doi: 10.4031/MTSJ.48.4.8
- Nof, D. (2005). The momentum imbalance paradox revisited. *J. Phys. Oceanogr.* 35, 1928–1939. doi: 10.1175/JPO2772.1
- Nof, D., and Pichevin, T. (2001). The ballooning of outflows. *J. Phys. Oceanogr.* 31, 3045–3058. doi: 10.1175/1520-0485(2001)031<3045:tboo>2.0.co;2
- Ntaganou, N., Kourafalou, V., Beron-Vera, F., Olascoaga, M., Le Henaff, M., and Androulidakis, I. (2023). Influence of Caribbean eddies on the loop current system evolution. *Submitted to Front. Mar. Sci.* 10, 961058. doi: 10.3389/fmars.2023.961058
- Oey, L.-Y. (2004). Vorticity flux through the Yucatan channel and loop current variability in the gulf of Mexico. *J. Geophys. Res.: Oceans* 109, C10004. doi: 10.1029/2004JC002400
- Oey, L.-Y. (2008). Loop current and deep eddies. *J. Phys. Oceanogr.* 38, 1426–1449. doi: 10.1175/2007jpo3818.1
- Oey, L.-Y., Lee, H.-C., and Schmitz, W. J. Jr. (2003). Effects of winds and Caribbean eddies on the frequency of loop current eddy shedding: A numerical model study. *J. Geophys. Res.: Oceans* 108, 3324. doi: 10.1029/2002JC001698
- Olvera-Prado, E. R. (2019). *Contribution of wind and loop current eddies to the circulation in the Western gulf of Mexico* (Doctoral dissertation, The Florida State University). Ph.D. thesis.
- Pegliasco, C., Chaigneau, A., and Morrow, R. (2015). Main eddy vertical structures observed in the four major Eastern boundary upwelling systems. *J. Geophys. Res.: Oceans* 120, 6008–6033. doi: 10.1002/2015JC010950
- Pichevin, T., and Nof, D. (1997). The momentum imbalance paradox. *Tellus A* 49, 298–319. doi: 10.1034/j.1600-0870.1997.t01-1-00009.x
- Pujol, M.-I., Faugère, Y., Taburet, G., Dupuy, S., Pelloquin, C., Ablain, M., et al. (2016). DUACS DT2014: the new multi-mission altimeter data set reprocessed over 20 years. *Ocean Sci.* 12, 1067–1090. doi: 10.5194/os-12-1067-2016
- Reid, R. (1972). A simple dynamic model of the loop current. *Contributions on the Physical Oceanography of the Gulf of Mexico* 2, 157–159.
- Rice, J. (1995). *Mathematical statistics and data analysis. duxbury advanced series* (Belmont, CA, USA: Duxbury Press, Wadsworth Publishing Company).
- Rosmond, T., Teixeira, J., Peng, M., Hogan, T., and Pauley, R. (2002). Navy operational global atmospheric prediction system (NOGAPS): Forcing for ocean models. *Oceanography* 15 (1), 99–108. doi: 10.5670/oceanog.2002.40
- Saha, S., Moorthi, S., Pan, H.-L., Wu, X., Wang, J., Nadiga, S., et al. (2010). The NCEP climate forecast system reanalysis. *Bull. Am. Meteorological Soc.* 91, 1015–1058. doi: 10.1175/2010bams3001.1
- Schmitz, W. J. Jr. (2005). *Cyclones and westward propagation in the shedding of anticyclonic rings from the loop current*. Circulation in the Gulf of Mexico: Observations and Models Eds. Sturges, W., and Lugo-Fernandez, A. (American Geophysical Union (AGU)), 241–261. doi: 10.1029/161GM18
- Sheinbaum, J., Athié, G., Candela, J., Ochoa, J., and Romero-Arteaga, A. (2016). Structure and variability of the Yucatan and loop currents along the slope and shelf break of the Yucatan channel and campeche bank. *Dynamics Atmospheres Oceans* 76, 217–239. doi: 10.1016/j.dynatmoce.2016.08.001
- Sheinbaum, J., Candela, J., Badan, A., and Ochoa, J. (2002). Flow structure and transport in the Yucatan channel. *Geophys. Res. Lett.* 29, 10–1–10–4. doi: 10.1029/2001GL013990
- Sturges, W., and Blaha, J. P. (1976). A western boundary current in the gulf of Mexico. *Science* 192, 367–369. doi: 10.1126/science.192.4237.367
- Sturges, W., Evans, J. C., Welsh, S., and Holland, W. (1993). Separation of warm-core rings in the gulf of Mexico. *J. Phys. Oceanogr.* 23, 250–268. doi: 10.1175/1520-0485(1993)023<0250:sowcri>2.0.co;2
- Sturges, W., Hoffmann, N. G., and Leben, R. R. (2010). A trigger mechanism for loop current ring separations. *J. Phys. Oceanogr.* 40, 900–913. doi: 10.1175/2009JP04245.1
- Sturges, W., and Leben, R. (2000). Frequency of ring separations from the loop current in the gulf of Mexico: A revised estimate. *J. Phys. Oceanogr.* 30, 1814–1819. doi: 10.1175/1520-0485(2000)030<1814:forsft>2.0.co;2
- Thomson, R. E., and Emery, W. J. (2014). “Chapter 5 - time series analysis methods,” in *Data analysis methods in physical oceanography (Third edition)*. Eds. R. E. Thomson and W. J. Emery (Boston: Elsevier), 425–591. Third edition edn. doi: 10.1016/B978-0-12-387782-6.00005-3
- Vukovich, F. M. (1995). An updated evaluation of the loop current's eddy-shedding frequency. *J. Geophys. Res.: Oceans* 100, 8655–8659. doi: 10.1029/95JC00141
- Vukovich, F. M., Crissman, B. W., Bushnell, M., and King, W. J. (1979). Some aspects of the oceanography of the gulf of Mexico using satellite and *in situ* data. *J. Geophys. Res.: Oceans* 84, 7749–7768. doi: 10.1029/JC084iC12p07749
- Vukovich, F. M., and Maul, G. A. (1985). Cyclonic eddies in the Eastern gulf of Mexico. *J. Phys. Oceanogr.* 15, 105–117. doi: 10.1175/1520-0485(1985)015<0105:ceiteg>2.0.co;2
- Walker, N. D., Leben, R., Anderson, S., Feeney, J., Coholan, P., and Sharma, N. (2009). *Loop current frontal eddies based on satellite remote-sensing and drifter data* Vol. 88 (U.S. Dept. of the Interior, Minerals Management Service, Gulf of Mexico OCS Region, OCS Study MMS 2009-023, New Orleans, LA).
- Weisberg, R. H., and Liu, Y. (2017). On the loop current penetration into the gulf of Mexico. *J. Geophys. Res.: Oceans* 122, 9679–9694. doi: 10.1002/2017JC013330
- Welsh, S. E., and Inoue, M. (2000). Loop current rings and the deep circulation in the gulf of Mexico. *J. Geophys. Res.: Oceans* 105, 16951–16959. doi: 10.1029/2000JC900054
- Zavala-Hidalgo, J., Morey, S., O'Brien, J., and Zamudio, L. (2006). On the loop current eddy shedding variability. *Atmósfera* 19 (1), 41–48.



## OPEN ACCESS

## EDITED BY

Steven L. Morey,  
Florida Agricultural and Mechanical  
University, United States

## REVIEWED BY

Wei Huang,  
Oak Ridge National Laboratory (DOE),  
United States  
Terry Eugene Whittedge,  
Retired, Fairbanks, AK, United States  
Gilles Reverdin,  
Centre National de la Recherche  
Scientifique (CNRS), France

## \*CORRESPONDENCE

Matthieu Le Hénaff  
✉ [mlehenaff@earth.miami.edu](mailto:mlehenaff@earth.miami.edu)

## SPECIALTY SECTION

This article was submitted to  
Physical Oceanography,  
a section of the journal  
Frontiers in Marine Science

RECEIVED 21 December 2022

ACCEPTED 06 March 2023

PUBLISHED 20 March 2023

## CITATION

Le Hénaff M, Kourafalou VH,  
Androulidakis Y, Ntaganou N and Kang H  
(2023) Influence of the Caribbean Sea eddy  
field on Loop Current predictions.  
*Front. Mar. Sci.* 10:1129402.  
doi: 10.3389/fmars.2023.1129402

## COPYRIGHT

© 2023 Le Hénaff, Kourafalou, Androulidakis,  
Ntaganou and Kang. This is an open-access  
article distributed under the terms of the  
[Creative Commons Attribution License  
\(CC BY\)](https://creativecommons.org/licenses/by/4.0/). The use, distribution or  
reproduction in other forums is permitted,  
provided the original author(s) and the  
copyright owner(s) are credited and that  
the original publication in this journal is  
cited, in accordance with accepted  
academic practice. No use, distribution or  
reproduction is permitted which does not  
comply with these terms.

# Influence of the Caribbean Sea eddy field on Loop Current predictions

Matthieu Le Hénaff<sup>1,2\*</sup>, Vassiliki H. Kourafalou<sup>3</sup>,  
Yannis Androulidakis<sup>3,4</sup>, Nektaria Ntaganou<sup>3,5</sup>  
and HeeSook Kang<sup>1,2</sup>

<sup>1</sup>Cooperative Institute for Marine and Atmospheric Studies (CIMAS), University of Miami, Miami, FL, United States, <sup>2</sup>National Oceanic and Atmospheric Administration (NOAA) Atlantic Oceanographic and Meteorological Laboratory (AOML), Miami, FL, United States, <sup>3</sup>Rosenstiel School, University of Miami, Miami, FL, United States, <sup>4</sup>Department of Civil Engineering, Laboratory of Maritime Engineering and Maritime Works, Aristotle University of Thessaloniki, Thessaloniki, Greece, <sup>5</sup>Center for Ocean-Atmospheric Prediction Studies (COAPS), Florida State University, Tallahassee, FL, United States

Previous studies have shown how the passage of eddies from the Caribbean Sea (CS) to the Gulf of Mexico (GoM) can impact the Loop Current (LC) system, in particular the detachments of LC Eddies (LCEs). Here we used numerical modeling to investigate the impact of the eddy field in the CS on LC predictions. We used a HYCOM ocean model configuration of the North Atlantic at 1/12° resolution to perform two data-assimilative experiments: one in which all available observations were assimilated (*Ref*), and one in which all available observations were assimilated except in the CS, where climatological altimetry values were assimilated instead of actual observations, leading to dampening the mesoscale activity there (*NoCarib*). These experiments took place in 2015, when the LC was very active with several LCE detachments, re-attachments, and separations. Each of these experiments was used to initialize 28 60-day forecast simulations every 10 days. In terms of model Sea Surface Height (SSH), the forecasts initialized with the *Ref* experiment had, on average, lower errors than the forecasts initialized with the *NoCarib* experiment in the southeastern part of the GoM, with a peak during the 31–40 day forecast period. More importantly, the errors in predicting the date of the next LCE detachment or separation were smaller in the forecasts initialized from the more realistic *Ref* experiment. Finally, the forecasts initialized by the *NoCarib* experiment showed a much higher level of false negatives predictions, meaning that no LCE detachment was predicted whereas a detachment actually happened. Overall, 68% of LCE detachments were predicted with an error smaller than 15 days in the forecasts initialized from the more realistic *Ref* experiment, but only 32% in the forecasts initialized from the *NoCarib* experiment, stressing the importance of the CS eddy field for predicting the LC evolution. These findings have implications on the GoM predictability, highlighting the need to either run data-assimilative models covering both the GoM and the CS, or pay particular attention to accurate boundary conditions for limited-area GoM models.

## KEYWORDS

Gulf of Mexico, Loop Current, Caribbean Sea, mesoscale eddies, ocean forecast

# 1 Introduction

The Loop Current (LC) is the main dynamical feature in the Gulf of Mexico (GoM). Characterizing and predicting the state of the LC has important implications, as it affects all ranges of ocean-related processes in the GoM, from larval connectivity to pollution transport or oil platform operations (e.g. [Lara-Hernández et al., 2019](#); [Le Hénaff et al., 2012a](#); [Kaiser and Pulsipher, 2007](#)). This led the National Academy of Sciences, Engineering, and Medicine to implement the Understanding Gulf Ocean Systems (UGOS) initiative as part of its Gulf Research Program, to support research related to ocean observations and modeling in the GoM to improve the understanding and forecasting of the LC dynamics. This study focuses on the forecasting aspect, using numerical methods to examine the influence of the Caribbean Sea eddy field.

The LC is a component of the North Atlantic western boundary current, upstream of the Gulf Stream. It enters the GoM in the south, through the Yucatan Channel between the Yucatan Peninsula in Mexico and the western tip of Cuba, and it exits the GoM to the east, through the Straits of Florida between Florida, in the US, and the northern coast of Cuba. Inside the GoM, the shape of the LC evolves in a peculiar way, from a retracted, or port-to-port, position in which the LC flows almost directly from the Yucatan Channel to the Straits of Florida, to an extended position in which the LC reaches the edge of the northeastern GoM continental shelf, before turning anticyclonically toward the GoM exit in the southeast of the basin.

When it is fully extended, the LC sheds an anticyclonic eddy called a Loop Current Eddy (LCE). LCEs are large eddies, with a diameter of 300 to 400 km at separation, and it takes about 8 months for LCEs to reach the western boundary of the GoM, at which stage their initial diameter decreased by 55% ([Vukovich, 2007](#)). Eventually, LCEs break apart after colliding with the continental shelf of the western GoM, or through the interactions with local mesoscale eddies ([Vidal et al., 1992](#); [Lipphardt et al., 2008](#)). The shedding of an LCE leads to the sudden southward shift of the LC to its retracted position. The LC can experience several temporary detachments and reattachments of an LCE before the final separation ([Schmitz, 2005](#); [Le Hénaff et al., 2012b](#); [Le Hénaff et al., 2014](#)). The period between two LCE separations, called the LC separation period, varies from a few weeks to 18 months, with the dominant modes at 6, 9 and 11 months, and a mean value close to 9 months ([Leben, 2005](#); [Dukhovskoy et al., 2015](#)).

The physical mechanisms inside the GoM that explain the behavior of the LC have been the topics of many studies. A reference analytical study was performed by [Pichevin and Nof \(1997\)](#), who characterized the LC as a low-density water mass entering a basin of higher density, the GoM, from the south, which is forced to turn east under the Coriolis force. The authors demonstrate that there is no steady state possible for such a flow, which they identify as the imbalance paradox, and that, as a result, the current must shed eddies that will then drift westward under the beta effect. Using a comparable analytical framework, [Lugo-Fernández \(2018\)](#) found that the LC intrusion is due to an initial transport imbalance at the entrance of the GoM that creates a volume storage inside the LC. This storage in turns creates a sea-level difference across the LC that reinforces the northward flow

into the LC ([Lugo-Fernández, 2018](#)). In parallel with these analytical studies, model studies have suggested that the LCE shedding process involves mixed barotropic and baroclinic instabilities ([Hurlburt and Thompson, 1980](#); [Hurlburt and Thompson, 1982](#); [Chérubin et al., 2006](#)). Recently, observations confirmed that baroclinic instabilities contribute to the meandering of the LC and intensify during the LCE shedding process ([Donohue et al., 2016a](#); [Donohue et al., 2016b](#)). The meandering of the LC is closely associated with the presence of cyclonic frontal eddies along its edge. These frontal eddies are usually observed to be more developed on the eastern flank of the LC, where they often contribute to the necking-down of the LC and to the initial detachment of an LCE ([Schmitz, 2005](#); [Le Hénaff et al., 2014](#); [Hiron et al., 2020](#)). Frontal eddies are also observed on the western side of the LC, where they are also found to contribute to the LCE shedding ([Zavala-Hidalgo et al., 2003](#)).

At the entrance of the GoM, in the Yucatan Channel, the total transport incoming into the GoM was found to be 27.6 Sv on average, based on mooring observations ([Candela et al., 2019](#)). Mooring observations also suggested that periods of cumulative anticyclonic vorticity fluxes are associated with phases of extension of the LC, whereas periods of cumulative cyclonic vorticity fluxes are associated with the retraction of the LC, which sometimes coincide with the shedding of an LCE ([Candela et al., 2002](#)). On the other hand, using numerical modeling and observations, [Oey \(2004\)](#) suggested that cyclonic vorticity flux anomalies coming through the Yucatan Channel are associated with the extension of the LC, whereas anticyclonic vorticity flux anomalies are associated with the triggering of the LC retraction or LCE shedding. [Oey \(2004\)](#) also stressed that further research is necessary to better assess these mechanisms.

Compared to the GoM interior and the Yucatan Channel that have been extensively investigated, and although directly upstream of the LC, the Caribbean Sea (CS) has received little attention in the LC problem. [Oey et al. \(2003\)](#), using modeling, found that the variations in the wind-induced transport into the CS tend to shorten the LC shedding interval in the GoM, whereas the presence of anticyclonic eddies in the CS tend to increase it. Similarly, [Garcia-Jove et al. \(2016\)](#) found that suppressing eddies in the CS in their ocean model tends to reduce the number of LCE separations. Using observations, [Athié et al. \(2012\)](#) found that cyclonic eddies present in the CS and entering the GoM on the western side of the incoming LC are often involved in the LCE separation process. [Chang and Oey \(2012\)](#) found that the seasonal variations in wind patterns in the CS, with strong trade winds in summer and winter, favor the shedding of LCEs during those seasons. [Androulidakis et al. \(2021\)](#) found, using observations and numerical models, that the passage of anticyclonic eddies from the CS to the GoM in the Yucatan Channel is more common during retracted LC phases, and that such passages tend to precede, by 5 to 10 days, an eastward shift of the LC in the Yucatan Channel and a retraction of the LC in the GoM. This agrees with [Sheinbaum et al. \(2016\)](#) who, using mooring observations, found that eastward shifts of the main current in the Yucatan Channel appear to be associated with vorticity perturbations coming from the CS and tended to precede eddy detachments.

However, they stressed that the significance of these vorticity perturbations on the shedding process remain to be determined.

In this study, we aim to quantify to what extent the eddy activity in the CS influences the LC shedding process inside the GoM and its prediction. To do so, we implemented numerical experiments that consist of two series of ocean forecasts, one with realistic initial conditions, and one in which the mesoscale eddy activity in the CS has been dampened. The experiments took place in 2015, a year when the LC was very active with several LCE detachments, re-attachments, and separations. Following this introduction (Section 1), Section 2 presents the model and the experimental set-up, Section 3 describes our results, and Section 4 provides a discussion and the conclusions.

## 2 Methods

### 2.1 Model

For our numerical experiments, we used the Hybrid Coordinate Ocean Model (HYCOM, Bleck, 2002; Chassignet et al., 2003; Halliwell, 2004). The model was implemented over the North Atlantic (Figure 1). This model configuration is similar to the Observing System Simulated Experiment (OSSE) system forecast model described in detail in Halliwell et al. (2017a). In particular, the model grid has a  $1/12^\circ$  ( $0.08^\circ$ ) horizontal resolution and 26 hybrid vertical levels, which is comparable to most global operational ocean systems. One difference with Halliwell et al. (2017a) is that the model is forced at the surface by the NAVy Global Environmental Model (NAVgEM) that replaced the Navy Operational Global Atmospheric Prediction System (NOGAPS). Similar to the configuration introduced by Halliwell et al. (2017a), the model is implemented with a data assimilation filter that is based on a statistical interpolation scheme. The details of the data assimilation filter are described by Halliwell et al. (2014). The forecast error

covariance statistics necessary for the data assimilation step are estimated using a multi-year free running simulation of the same model. This model configuration has been fully evaluated by Halliwell et al. (2017a) and implemented to perform several OSSEs in the North Atlantic (Halliwell et al., 2017a; Halliwell et al., 2017b; Halliwell et al., 2020).

### 2.2 Experimental set-up

First, the model was run to perform a hindcast of the year 2015. The initial conditions on January 1<sup>st</sup>, 2015, were taken from an unconstrained simulation running since January 1<sup>st</sup>, 2013, which was initialized from the Levitus climatology. In that 2015 reference experiment, called *Ref*, the model assimilated the following observations: along-track absolute dynamic topography (ADT) altimetry data from the Copernicus Marine Environment Monitoring Service (CMEMS, formerly AVISO), which is comparable to the model sea surface height (SSH), sea surface temperature (SST) from satellites (Multi-Channel Sea Surface Temperature, MCSST), drifters, buoys and ships of opportunity, and finally vertical profiles of temperature and/or salinity from Argo floats, ocean gliders, moorings, and expendable bathythermographs (XBTs).

A second experiment was then performed (namely *NoCarib*), which is identical to the *Ref* experiment except for the observations that were assimilated in the CS. In all other areas of the model domain, the observations that were assimilated are the same as in the *Ref* experiment, i.e. available along-track altimetry, SST, and vertical profiles of temperature and/or salinity. In the CS, the only observations that were assimilated were along-track climatological ADT altimetry data. The climatological ADT dataset was estimated by averaging, for each day of a calendar year, altimetry-derived

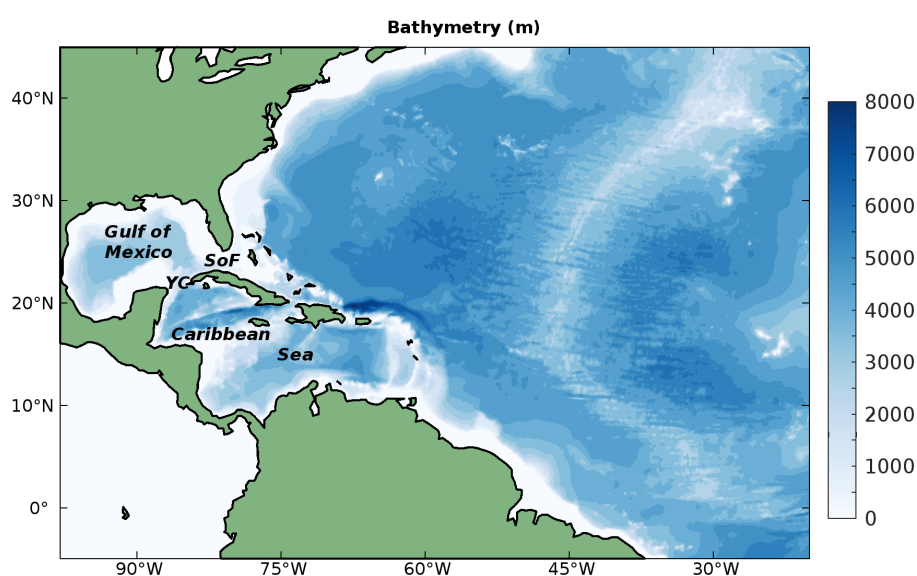


FIGURE 1  
Model domain and bathymetry of the North Atlantic used in this study, with the main toponyms mentioned in the text (YC, Yucatan Channel; SoF, Straits of Florida).



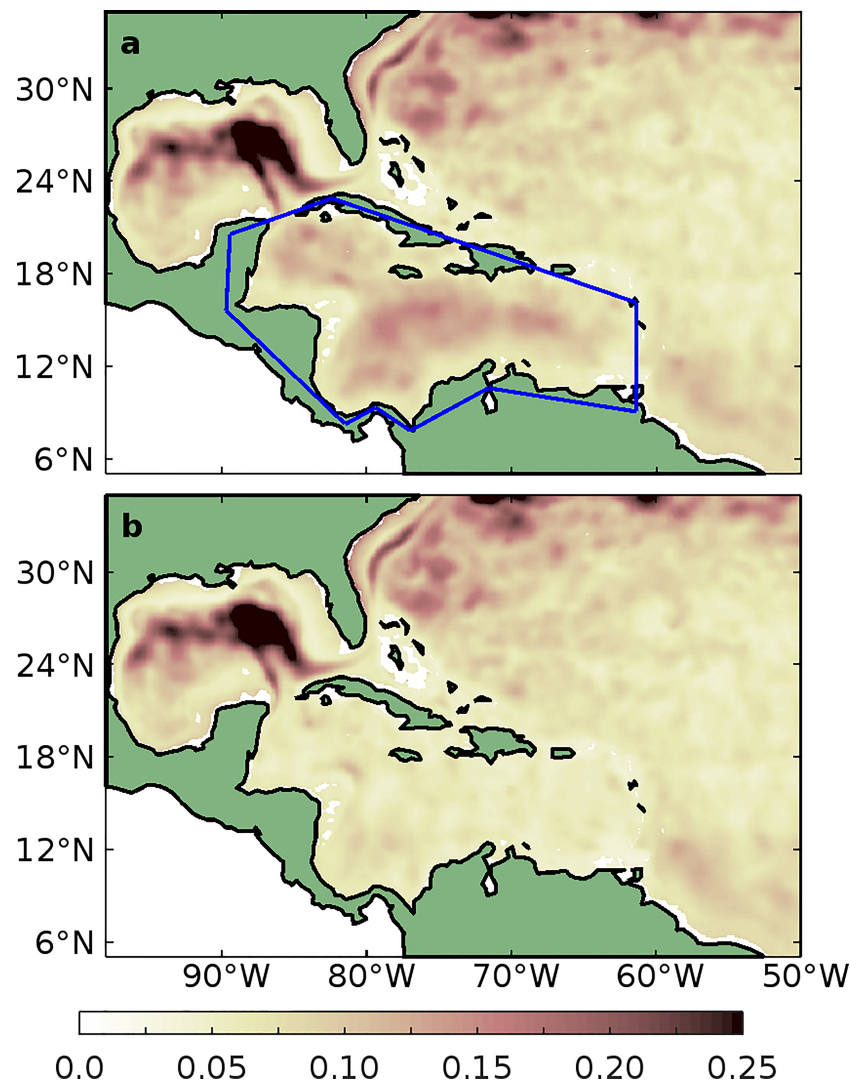


FIGURE 2

Temporal standard deviation in simulated Sea Surface Height (SSH, in meters) in the: (A) *Ref* and (B) *NoCarib* experiments during 2015. The blue box in (A) represents the extent of the Caribbean Sea in which the only assimilated observations in the *NoCarib* experiment were climatological SSH data. Please see text for details about the *Ref* and *NoCarib* experiments.

mapped ADT observed from 1993 to 2019. Climatological ADT values interpolated at the same day of the year and at the same locations as the actual along-track observations in 2015 were assimilated in the CS in the *NoCarib* experiment. Because the space and time variability in ADT (or SSH) is the signature of ocean mesoscale activity, replacing the actual altimetry observations with climatological values in the data that were assimilated leads to dampening the mesoscale activity in the model. This is visible on Figure 2, which shows the maps of the temporal standard deviation in model SSH estimated for the whole year in the *Ref* and *NoCarib* experiments. We clearly see that the standard deviation in SSH in the CS in the *NoCarib* experiment is close to 0, whereas in the *Ref* experiment it is much larger.

From these two data-assimilative experiments, we then ran a series of forecast simulations to investigate to what extent the presence or absence of eddy activity in the CS impact the LC predictions. For each experiment, we initiated 60-day forecasts

every 10 days, starting on day 30 of 2015 to allow for data assimilation to constrain the ocean state from the initial conditions. The last forecast was initiated on day 300 and ended on day 360 at the end of 2015. This corresponds to 28 forecast simulations per experiment, i.e. 56 forecast simulations in total (*Ref* and *NoCarib* together). We analyzed the daily model outputs from these model experiments and forecasts.

## 2.3 Analysis of model outputs

The first analysis of model outputs is based on the root-mean square error (RMSE) of the model SSH with respect to the daily mapped ADT altimetry observations from CMEMS. Since the observed mapped ADT field has a 0.25° spatial resolution, whereas the model grid has a resolution of 0.08°, the model SSH values were first smoothed and

interpolated onto the same grid as the mapped ADT observations, by averaging the model SSH over three grid intervals, i.e.  $0.24^\circ$ , which is very close to the resolution of the observed ADT, in both latitudinal and longitudinal directions around each ADT grid point. Then, since the mean SSH level in the HYCOM model is arbitrary, both the model SSH and the observed ADT fields need to be corrected before they can be compared. For the model SSH, this was done by removing, at each grid point, the temporal mean of the SSH from the realistic, data-assimilated *Ref* experiment over the whole of 2015. For the observations, this was done by removing, at each grid point, the temporal mean of the observed ADT over the whole of 2015. The RMSE in each ensemble of forecasts was estimated after completion of these steps.

The second analysis of model outputs is based on the evolution of the LC contour. We estimated the contour of the LC, for each daily output of each model forecast, by identifying the contour of the 17 cm anomaly in SSH with respect to the basin average, following the approach by Leben (2005). We did the same with the altimetry observations using the daily mapped ADT. We then used these daily LC contours to derive the time series of the northernmost extension of the LC, in the model forecasts and in the observations. Because an LCE detachment or separation is associated with the sudden retraction of the LC, any drop, from one day to the next, of the LC northern extension time series by 0.3 degree in latitude or more was considered to mark an LCE detachment. We verified visually that this threshold allows capturing actual LCE detachments by examining the time evolution of the SSH maps. For each of the 60-day forecast period, we estimated the day of the first eddy detachment or separation, if any, in the model forecasts as well as in the actual LC state observed by altimetry.

### 3 Results

#### 3.1 Impact of the CS eddy field on the model SSH

We first compare the realism of the SSH field forecasted from both the *Ref* and *NoCarib* experiments in terms of RMSE. Figure 3 shows the

RMSE in forecasted SSH derived from the 28 forecast cycles initialized from the *Ref* experiment, for various forecast periods. As expected, we see the RMSE growing with time in the eastern GoM, associated with the LC. Because of its peculiar, highly non-linear behavior, and the difficulty in predicting it, the LC is associated with the largest RMSE in the region. Figure 4 shows the same RMSE but for the forecasts initialized from the *NoCarib* experiment. Similar to the forecasts from the *Ref* experiment, the RMSE is growing with time in the LC region within the GoM. One difference is that, in the initial forecast periods at 1 to 10 days and 11 to 20 days (Figures 3A, B, 4A, B), the RMSE of the forecasts initialized from the *NoCarib* experiment is slightly larger in the CS, with values reaching 0.15 to 0.2 m compared to values generally lower than 0.1 m in the *Ref* experiment. This is expected from the fact that the eddy field in the CS has been damped down in the *NoCarib* experiment. As a result, the forecasts are initialized with a non-realistic state and the errors in SSH are present from the start. For longer forecasts beyond 20 or 30 days, the RMSE levels appear to be comparable in the forecasts initialized from both experiments, with local differences that will now be discussed.

The differences between the RMSE achieved in the ensembles of forecasts initialized from both hindcast experiments are more visible on Figure 5. We clearly see, in the initial 1-10 day forecast period (Figure 5A), the large, positive RMSE difference ( $RMSE_{NoCarib} - RMSE_{Ref}$ ) in the CS, which means that the forecasts initialized from the *Ref* experiment are closer to the observed ocean state than the forecasts initialized from the *NoCarib* experiment. As mentioned earlier, this RMSE difference stems from the perturbation strategy. The RMSE difference in the CS in that period is especially large in the eastern and western parts of the CS where the bathymetry is deep, which is where the signature of mesoscale eddies is expected to be large. During that same 1-10 day forecast period, the RMSE difference is small in the GoM, although the positive RMSE difference in the western part of the CS extends in the southeastern GoM, associated with water masses advected into the GoM. During the following forecast periods, at 11-20 and 21-30 days (Figures 5B, C), the RMSE difference tends to reduce in amplitude in the CS, as the memory of the different initial conditions constrained with data assimilation tends to

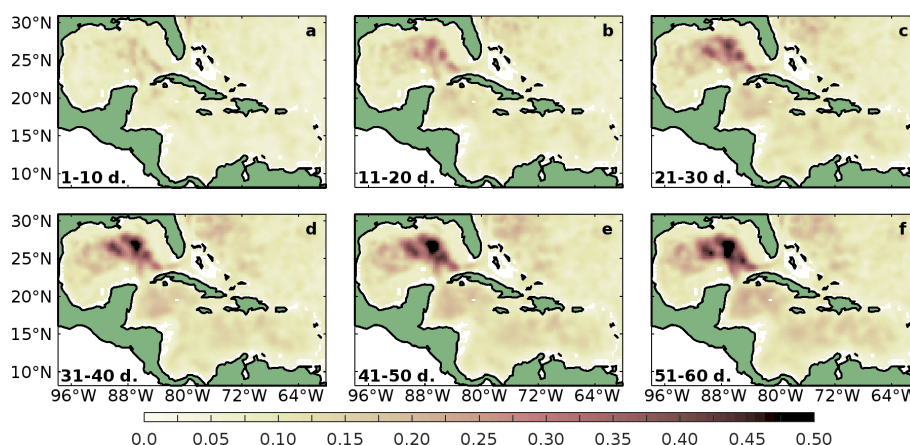


FIGURE 3

Root-mean square error in simulated Sea Surface Height (SSH, in meters) derived from the 28 forecast cycles initialized from the *Ref* experiment, averaged for the following forecast periods: (A) 1-10 days, (B) 11-20 days, (C) 21-30 days, (D) 31-40 days, (E) 41-50 days, and (F) 51-60 days.

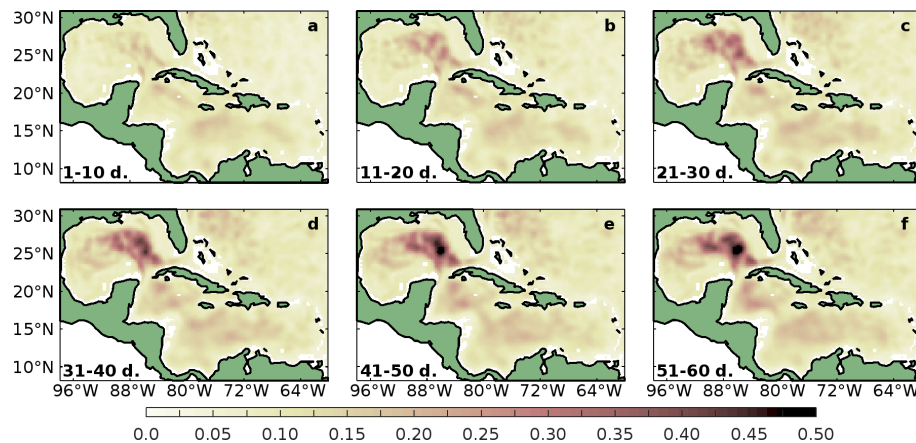


FIGURE 4  
Same as Figure 3 but for the *NoCarib* experiment.

wane. On the other hand, during those periods the RMSE difference grows in the GoM, with positive differences in the southeastern GoM just north of the Yucatan Channel, whereas the RMSE difference is negative in other parts of the deep eastern GoM. This pattern is more pronounced in the 31-40 day forecast period (Figure 5D), during which the RMSE difference is positive in the eastern GoM between the Yucatan Channel and 25°N, whereas it is negative in other parts of the deep eastern and central GoM. In the CS, the RMSE difference remains positive in the eastern part of the basin, but it is more mixed in the western part of the basin south of the Yucatan Channel, with positive and negative patches. In the 41-50 day forecast period (Figure 5E), the RMSE difference in the GoM remains largely positive between the Yucatan Channel and 25°N, although with a lower amplitude than in the previous period. We also notice the presence of a patch of negative RMSE difference close to the Straits of Florida, which was present in the previous forecast period but moved southward between both periods. In the CS, the RMSE difference

remains positive in the eastern part of the basin, whereas, in the western part, a patch of negative RMSE difference is seen making its way into the Yucatan Channel toward the GoM. During the 51-60 day forecast period (Figure 5F), that patch merges with the patch of negative RMSE difference that was present in the southeastern GoM in the previous period, leading to a large portion of negative RMSE difference in the GoM just north of the Yucatan Channel. A patch of positive RMSE difference is still present in the eastern GoM around 25°N.

The forecast experiments show that, in the absence of a mesoscale eddy field in the CS in the initial conditions, the forecasted SSH tends to degrade with time in the southeastern GoM, with the largest signature in RMSE difference reached during the 31-40 day forecast period. However, in other parts of the eastern and central GoM, the forecasted SSH appears to have similar or even reduced errors with respect to the reference case, associated with negative RMSE differences. This suggests that the expected negative impact of dampening the CS mesoscale eddy field on the

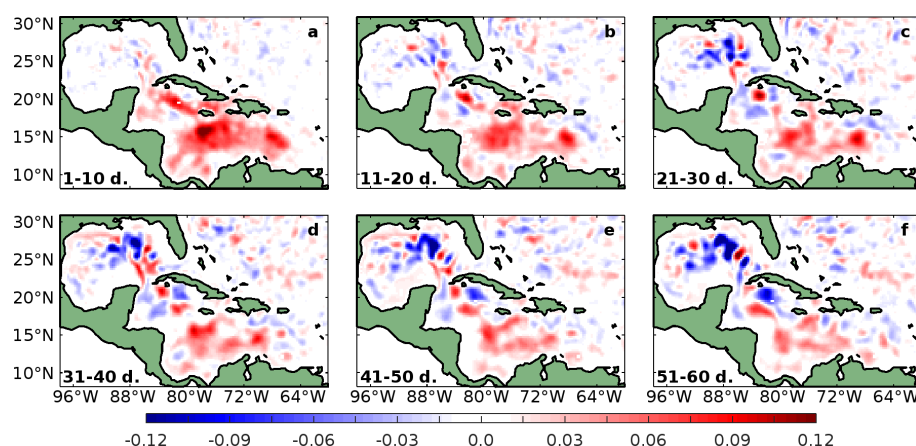
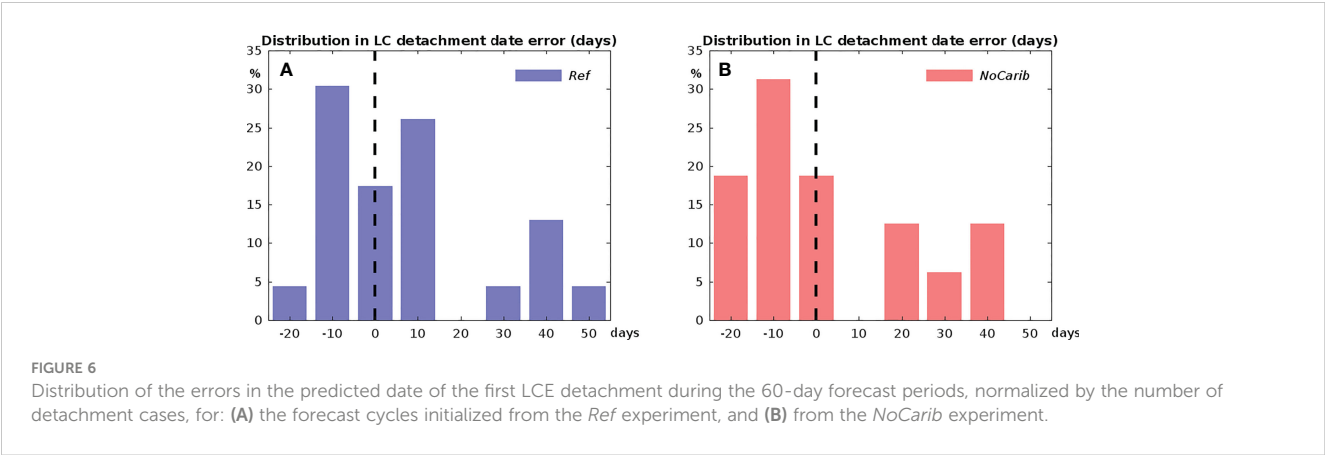


FIGURE 5  
Differences in simulated SSH root-mean square errors (in meters) between the forecast cycles initialized from the *NoCarib* experiment and from the *Ref* experiment ( $RMSE_{NoCarib} - RMSE_{Ref}$ ), averaged for the same forecast periods as in Figures 3, 4. Positive values indicate higher RMSE in the *NoCarib* experiment.



GoM SSH forecast is strongest, on average, at the region between the Yucatan Channel and 25°N, where the core of the LC is usually located.

3.2 Impact of the CS eddy field on LCE shedding

Although the RMSE in SSH in the eastern GoM is a relevant metric to analyze the ocean dynamical processes associated with the LC system, it is not the most adapted to analyze the LCE shedding events, which is the focus of this study. We thus now consider the impact of dampening the CS eddy field on the forecast of the LCE shedding events, using the day of the first LCE detachment, as described in Section 2.3, in each model forecast period.

Figure 6 presents the normalized distribution of the errors in the day of the first detachment, estimated for each forecast period for all forecasts initialized by both the *Ref* and the *NoCarib* experiments. The error was estimated by comparing the day of the first LCE detachment in a given forecast with the day of an actual LCE detachment identified using altimetry in that same forecast period. A negative error indicates that the model forecasted an LCE detachment after it was actually observed, whereas a positive error indicates that the model forecasted an LCE detachment before it was actually observed. The distributions were normalized by the total number of LCE detachments taking place in each ensemble, which differ from the total number of observed LCE detachments, as will be examined later. Figure 6A shows that the errors in the LCE detachment date in the forecasts initialized from the *Ref*

experiment range from -20 to 50 days, with 74% of the forecasted LC detachments associated with errors between -15 and 15 days. On the other hand, the errors in the LCE detachment date in the forecasts initialized from the *NoCarib* experiment are less often close to 0 (Figure 6B), with 50% of the forecasted LC detachments with errors between -15 and 15 days. Thus, the LCE detachment dates in the forecasts initialized with realistic ocean conditions in the CS (*Ref* forecasts) are more often close to the observed detachment dates than in the absence of the CS mesoscale eddy field (*NoCarib* forecasts).

In addition to the errors in the LCE detachment date, we examined the cases in which a detachment was incorrectly predicted to take place or not. These errors include the false positive LCE detachment predictions, i.e. cases for which an LCE detachment was predicted by the model forecasts within the 60-day forecast period but was not actually observed, and the false negative LCE detachment predictions, i.e. cases for which an LCE detachment was not predicted within the 60-day forecast period but was actually observed. Table 1 shows that the level of false positive cases is identical in both ensembles of forecast (3 out of 28 cycles), but the level of false negative cases is much larger in the forecasts initialized from the *NoCarib* experiment (9) than in the forecasts initialized from the *Ref* experiment (2). This means that, in the absence of the CS eddy field in the initial conditions, the model tends to underestimate the number of LCE detachment events within the 60 days of the forecast period.

Considering both the normalized distribution of the errors in the LCE detachment dates and the level of false negative LCE detachment predictions, 68% of the actual LCE detachments were predicted with an error of 15 days or less in the forecasts initialized

TABLE 1 False positive and false negative cases in the prediction of the date of the first LCE detachment during the 28 60-day forecast periods, for the forecast cycles initialized from the *Ref* experiment and from the *NoCarib* experiment.

Initial conditions for the forecasts	<i>Ref</i>	<i>NoCarib</i>
False positive (LCE detachment predicted but not observed)	3	3
False negative (LCE detachment not predicted but observed)	2	9

bold character stress that it is remarkable.



from the *Ref* experiment, but only 32% in the forecasts initialized from the *NoCarib* experiment.

## 4 Discussion and conclusions

In this study, we performed two data-assimilative experiments in the North Atlantic using the HYCOM model at 1/12° resolution, one assimilating all available observations (*Ref*) and one assimilating all available observations except in the Caribbean Sea (CS), where only climatological altimetry data were assimilated, leading to the dampening of the eddy activity there (*NoCarib*). These two experiments were used to initialize 28 forecasts of 60-day length for each case, totaling 56 forecast experiments. In terms of Sea Surface Height (SSH), the forecasts initialized with the *Ref* experiment had, on average, lower errors than the forecasts initialized with the *NoCarib* experiment in the southeastern part of the Gulf of Mexico (GoM) north of the Yucatan Channel, with a peak during the 31–40 day forecast period. In addition, in the absence of mesoscale eddy activity in the CS in the initial conditions, the errors in the predicted date of a Loop Current (LC) Eddy detachment tend to be larger, whereas these errors are more centered around zero in the forecasts initialized with the realistic, *Ref* experiment. More importantly, the rate of false predictions of an absence of a detachment, whereas a detachment was actually observed, is much larger in the forecasts initialized with dampened mesoscale eddy activity in the CS. As a result, 68% of actual Loop Current Eddy (LCE) detachments were predicted with an error of 15 days or less in the forecasts initialized with the *Ref* experiment, but only 32% in the forecasts initialized from the *NoCarib* experiment.

Our results show the importance of the eddy field in the CS for the prediction of the LC system. In terms of SSH, the absence of the CS eddy field leads to degrading the forecasts in the southeastern GoM, which was expected, although this is not necessarily the case in large portions of the eastern and central GoM. This result is associated with outlier members of the ensemble of forecasts initialized with the *Ref* experiment, in which the LC retracts after shedding an LCE, whereas in the observations the LCE either detaches much later or the LC reattaches after the LCE detachment. This led to large discrepancies in SSH in the model forecasts in the area where the extended LC usually evolves, i.e. north of 25°N in the eastern and central GoM. In the other ensemble initialized with the *NoCarib* experiment, in the same cases the LC tends to remain extended, consistent with the high rate of false negative LCE detachment predictions derived from that ensemble. For these cases, the discrepancies in SSH in the model forecasts are significantly smaller than in the ensemble initialized with the *Ref* experiment, leading to the patches of negative RMSE difference seen on Figure 5.

The smaller error in the LCE detachment date for the forecasts initialized with the *Ref* experiment rather than the *NoCarib* experiment shows that the eddy field is important for the timing of the LCE detachment. This result is in agreement with Androulidakis et al. (2021), who showed that the passage of anticyclonic Caribbean Eddies from the CS to the GoM tend to precede a retraction of the LC in the GoM, and also with Athié et al.

(2012), who found that cyclonic perturbations or eddies present in the CS and entering the GoM are often involved in the LCE shedding process. Moreover, the large number of false negative cases in the LCE detachment forecasts initialized with the *NoCarib* experiment shows that the eddy activity in the CS is crucial for the LCE detachment process to even happen, not to mention with the correct timing. These false negative forecasts correspond to cases in which no LCE detachment was predicted within the 60-day forecast period, whereas an LCE detachment actually took place. This result is consistent with Oey et al. (2003), who found that the presence of anticyclonic eddies in the Caribbean Sea tended to delay the frequency of LCE shedding by over 5 months, i.e. much longer than the 2-month period of the forecast experiments run here. It is also consistent with Garcia-Jove et al. (2016), who found that suppressing eddies in the CS in their model reduces the number of LCE separations and increases the mean LCE separation interval by about 2 months.

Our study is thus consistent with the few previous studies that discuss the impact of the eddy field in the CS on the GoM dynamics and the LCE shedding process. However, it is the first study, to our knowledge, that addresses this topic from the perspective of ocean model forecasts, and our results clearly show that the eddy field in the CS is essential to the correct prediction of the LCE shedding events and their timing. This result is important for near-real time and operational prediction systems, especially the regional systems focusing on forecasting the GoM and the LC evolution. Such systems have to include a large portion of the CS, constrained with data assimilation, or pay particular attention to accurate boundary conditions from the CS upstream of the GoM, if the LC evolution is to be realistically predicted. This result is of particular importance for applications in the GoM that depend on the correct prediction of the LC state at a range of a few weeks, especially the ones related to the oil industry. Such applications justified the current effort, from the National Academy of Sciences, Engineering, and Medicine to implement its UGOS initiative. Future work along the lines presented here could include a comparable study with a higher resolution model, which would allow examining the impact of the smaller mesoscale and sub-mesoscale processes in the CS on the LC and the GoM dynamics, which is still little known.

## Data availability statement

The raw data supporting the conclusions of this article will be made available by the authors, without undue reservation.

## Author contributions

MLH led the design of the study, performed some of the numerical experiments, and led the analysis of the results. VK helped in the design of the study and in the analysis of the results. YA and NN helped in the analysis of the results. HK performed some of the numerical experiments. ML led the writing of the manuscript, with the help of all co-authors. All authors contributed to the article and approved the submitted version.

## Funding

Research reported in this publication/press release was supported by the Gulf Research Program of the National Academies of Sciences, Engineering, and Medicine under award number 2000011056 and award number 2000013149. Additionally, MLH and HK received partial support by the NOAA Atlantic Oceanographic and Meteorological Laboratory (Miami, FL) and were supported in part under the auspices of the Cooperative Institute for Marine and Atmospheric Studies (CIMAS), a cooperative institute of the University of Miami and NOAA (agreement NA20OAR4320472).

## Acknowledgments

The content is solely the responsibility of the authors and does not necessarily represent the official views of the Gulf Research Program or the National Academies of Sciences, Engineering, and Medicine. This study has been conducted using E.U. Copernicus Marine Service Information; <https://doi.org/10.48670/moi-00148>

## References

- Androulidakis, Y., Kourafalou, V., Olascoaga, M. J., Beron-Vera, F. J., Le Hénaff, M., Kang, H., et al. (2021). Impact of Caribbean anticyclones on loop current variability. *Ocean Dyn.* 71 (9), 935–956. doi: 10.1007/s10236-021-01474-9
- Athié, G., Candela, J., Ochoa, J., and Sheinbaum, J. (2012). Impact of Caribbean cyclones on the detachment of loop current anticyclones. *J. Geophys. Res.* 117 (C3). doi: 10.1029/2011JC007090
- Bleck, R. (2002). An oceanic general circulation framed in hybrid isopycnal-Cartesian coordinates. *Ocean Model.* 4, 55–88. doi: 10.1016/S1463-5003(01)00012-9
- Candela, J., Ochoa, J., Sheinbaum, J., Lopez, M., Perez-Brunius, P., Tenreiro, M., et al. (2019). The flow through the gulf of Mexico. *J. Phys. Oceanogr.* 49 (6), 1381–1401. doi: 10.1175/JPO-D-18-0189.1
- Candela, J., Sheinbaum, J., Ochoa, J. L., Badan, A., and Leben, R. (2002). The potential vorticity flux through the Yucatan channel and the loop current in the gulf of Mexico. *Geophys. Res. Lett.* 29 (22), 2059. doi: 10.1029/2002GL015587
- Chang, Y.-L., and Oey, L.-Y. (2012). Why does the loop current tend to shed more eddies in summer and winter? *J. Geophys. Res.* 39, L05605. doi: 10.1029/2011GL050773
- Chassignet, E. P., Smith, L. T., Halliwell, G. R. Jr., and Bleck, R. (2003). North Atlantic simulation with the HYbrid coordinate ocean model (HYCOM): impact of the vertical coordinate choice, reference density, and thermobaricity. *J. Phys. Oceanogr.* 33, 2504–2526. doi: 10.1175/1520-0485(2003)033<2504:NASWTH>2.0.CO;2
- Chérubin, L. M., Morel, Y., and Chassignet, E. P. (2006). Loop current ring shedding: The formation of cyclones and the effect of topography. *J. Phys. Oceanogr.* 36 (4), 569–591. doi: 10.1175/JPO2871.1
- Donohue, K. A., Watts, D. R., Hamilton, P., Leben, R., and Kennelly, M. (2016a). Loop current eddy formation and baroclinic instability. *Dyn. Atmos. Oceans* 76, 195–216. doi: 10.1016/j.dynatmoce.2016.01.004
- Donohue, K. A., Watts, D. R., Hamilton, P., Leben, R., Kennelly, M., and Lugo-Fernández, A. (2016b). Gulf of Mexico loop current path variability. *Dyn. Atmos. Oceans* 76, 174–194. doi: 10.1016/j.dynatmoce.2015.12.003
- Dukhovskoy, D. S., Leben, R. R., Chassignet, E. P., Hall, C. A., Morey, S. L., and Nedbor-Gross, R. (2015). Characterization of the uncertainty of loop current metrics using a multidecadal numerical simulation and altimeter observations. *Deep Sea Res. Part I Oceanogr. Res. Pap.* 100, 140–158. doi: 10.1016/j.dsr.2015.01.005
- García-Jové, M., Sheinbaum, J., and Jouanno, J. (2016). Sensitivity of loop current metrics and eddy detachments to different model configurations: The impact of topography and Caribbean perturbations. *Atmosfera* 29, 235–265. doi: 10.20937/ATM.2016.29.03.05
- Halliwell, G. R. (2004). Evaluation of vertical coordinate and vertical mixing algorithms in the hybrid-coordinate ocean model (HYCOM). *Ocean Model.* 7, 285–322. doi: 10.1016/j.ocemod.2003.10.002
- Halliwell, G. R., Goni, G. J., Mehari, M. F., Kourafalou, V. H., Baringer, M., and Atlas, R. (2020). OSSE assessment of underwater glider arrays to improve ocean model initialization for tropical cyclone prediction. *J. Atmos. Ocean Technol.* 37 (3), 467–487. doi: 10.1175/JTECH-D-18-0195.1
- Halliwell, G. R., Mehari, M., Le Hénaff, M., Kourafalou, V. H., Androulidakis, Y. S., Kang, H.-S., et al. (2017a). North Atlantic ocean OSSE system: evaluation of operational ocean observing system components and supplemental seasonal observations for potentially improving tropical cyclone prediction in coupled systems. *J. Oper. Oceanogr.* 10 (2), 154–175. doi: 10.1080/1755876X.2017.1322770
- Halliwell, G. R. Jr., Mehari, M., Shay, L. K., Kourafalou, V. H., Kang, H., Kim, H.-S., et al. (2017b). OSSE quantitative assessment of rapid-response prestorm ocean surveys to improve coupled tropical cyclone prediction. *J. Geophys. Res.* 122 (7), 5729–5748. doi: 10.1002/2017JC012760
- Halliwell, G. R., Srinivasan, A., Kourafalou, V. H., Yang, H., Willey, D., Le Hénaff, M., et al. (2014). Rigorous evaluation of a fraternal twin ocean OSSE system in the open gulf of Mexico. *J. Atmos. Ocean Technol.* 31, 105–130. doi: 10.1175/JTECH-D-13-00011.1
- Hiron, L., Jaimes de la Cruz, B., and Shay, L. K. (2020). Evidence of loop current frontal eddy intensification through local linear and nonlinear interactions with the loop current. *J. Geophys. Res.* 125 (4), p.e2019JC015533. doi: 10.1029/2019JC015533
- Hurlburt, H. E., and Thompson, J. D. (1980). A numerical study of loop current intrusions and eddy shedding. *J. Phys. Oceanogr.* 10, 1611–1651. doi: 10.1175/1520-0485(1980)010<1611:ANSOLC>2.0.CO;2
- Hurlburt, H. E., and Thompson, J. D. (1982). “The dynamics of the loop current and shed eddies in a numerical model of the gulf of Mexico,” in *Hydrodynamics of semi-enclosed seas*. Ed. J. C. J. Nihoul (Liege: Elsevier Oceanography Series, Elsevier) 34, 243–297. doi: 10.1016/S0422-9894(08)71247-9
- Kaiser, M. J., and Pulsipher, A. G. (2007). The impact of weather and ocean forecasting on hydrocarbon production and pollution management in the gulf of Mexico. *Energy Policy* 35 (2), 966–983. doi: 10.1016/j.enpol.2006.01.026
- Lara-Hernández, J. A., Zavala-Hidalgo, J., Sanvicente-Añorve, L., and Briones-Fourzán, P. (2019). Connectivity and larval dispersal pathways of panulirus argus in the gulf of Mexico: A numerical study. *J. Sea Res.* 155, 101814. doi: 10.1016/j.seares.2019.101814
- Leben, R. R. (2005). *Altimeter-derived loop current metrics, in circulation in the gulf of Mexico: Observations and models* Vol. 161. Eds. W. Sturges and A. Lugo-Fernandez (Washington, D. C.: AGU), 181–201.
- Le Hénaff, M., Kourafalou, V. H., Dussurget, R., and Lumpkin, R. (2014). Cyclonic activity in the eastern gulf of Mexico: characterization from along-track altimetry and *in situ* drifter trajectories. *Prog. Oceanogr.* 120, 120–138. doi: 10.1016/j.pocean.2013.08.002
- Le Hénaff, M., Kourafalou, V. H., Morel, Y., and Srinivasan, A. (2012b). Simulating the dynamics and intensification of cyclonic loop current frontal eddies in the gulf of Mexico. *J. Geophys. Res.* 117 (C2), C02034. doi: 10.1029/2011JC007279

and 10.48670/moi-00146. The authors also thank four reviewers for their very helpful comments that led to an improved manuscript.

## Conflict of interest

The authors declare that the research was conducted in the absence of any commercial or financial relationships that could be construed as a potential conflict of interest.

The handling editor SM declared a shared consortium with the author MLH at the time of the review.

## Publisher's note

All claims expressed in this article are solely those of the authors and do not necessarily represent those of their affiliated organizations, or those of the publisher, the editors and the reviewers. Any product that may be evaluated in this article, or claim that may be made by its manufacturer, is not guaranteed or endorsed by the publisher.

- Le Hénaff, M., Kourafalou, V. H., Paris, C. B., Helgers, J., Aman, Z. M., Hogan, P. J., et al. (2012a). Surface evolution of the deepwater horizon oil spill patch: combined effects of circulation and wind-induced drift. *Environ. Sci. Technol.* 46, 7267–7273. doi: 10.1021/es301570w
- Lipphardt, B., Poje, A. C., Kirwan, A., Kantha, L., and Zweng, M. (2008). Death of three loop current rings. *J. Mar. Res.* 66 (1), 25–60. doi: 10.1357/002224008784815748
- Lugo-Fernández, A. (2018). Modeling the intrusion of the loop current into the gulf of Mexico. *Dyn. Atmos. Oceans* 84, 46–54. doi: 10.1016/j.dynatmoce.2018.10.003
- Oey, L.-Y. (2004). Vorticity flux through the Yucatan channel and loop current variability in the gulf of Mexico. *J. Geophys. Res.* 109, C10004. doi: 10.1029/2004JC002400
- Oey, L.-Y., Lee, H.-C., and Schmitz, W. J. Jr. (2003). Effects of winds and Caribbean eddies on the frequency of loop current eddy shedding: A numerical model study. *J. Geophys. Res.* 108 (C10), 3324. doi: 10.1029/2002JC001698
- Pichevin, T., and Nof, D. (1997). The momentum imbalance paradox. *Tellus A* 49 (2), 298–319. doi: 10.3402/tellusa.v49i2.14484
- Schmitz, W. J. (2005). “Cyclones and westward propagation in the shedding of anticyclonic rings from the loop current,” in *Circulation in the gulf of Mexico: Observations and models*, vol. 161. Ed. W. Sturges and A. Lugo-Fernandez (Washington, D. C: AGU), 241–261.
- Sheinbaum, J., Athié, G., Candela, J., Ochoa, J., and Romero-Arteaga, A. (2016). Structure and variability of the Yucatan and loop currents along the slope and shelf break of the Yucatan channel and campeche bank. *Dyn. Atmos. Oceans* 76, 217–239. doi: 10.1016/j.dynatmoce.2016.08.001
- Vidal, V. M., Vidal, F. V., and Pérez-Molero, J. M. (1992). Collision of a loop current anticyclonic ring against the continental shelf slope of the western gulf of Mexico. *J. Geophys. Res.* 97 (C2), 2155–2172. doi: 10.1029/91JC00486
- Vukovich, F. M. (2007). Climatology of ocean features in the gulf of Mexico using satellite remote sensing data. *J. Phys. Oceanogr.* 37 (3), 689–707. doi: 10.1175/JPO2989.1
- Zavala-Hidalgo, J., Morey, S. L., and O'Brien, J. J. (2003). Cyclonic eddies northeast of the campeche bank from altimetry data. *J. Phys. Oceanogr.* 33, 623–629. doi: 10.1175/1520-0485(2003)033<0623:CENOTC>2.0.CO;2



## OPEN ACCESS

EDITED BY  
Zhiyu Liu,  
Xiamen University, China

REVIEWED BY  
Wei Huang,  
Oak Ridge National Laboratory (DOE),  
United States  
Alejandro Orfila,  
Spanish National Research Council  
(CSIC), Spain

\*CORRESPONDENCE  
Dmitry S. Dukhovskoy  
✉ dmitry.dukhovskoy@noaa.gov

SPECIALTY SECTION  
This article was submitted to  
Physical Oceanography,  
a section of the journal  
Frontiers in Marine Science

RECEIVED 30 January 2023

ACCEPTED 20 March 2023

PUBLISHED 05 April 2023

## CITATION

Dukhovskoy DS, Chassignet EP, Bozec A  
and Morey SL (2023) Assessment of  
predictability of the Loop Current in the  
Gulf of Mexico from observing system  
experiments and observing system  
simulation experiments.  
*Front. Mar. Sci.* 10:1153824.  
doi: 10.3389/fmars.2023.1153824

## COPYRIGHT

© 2023 Dukhovskoy, Chassignet, Bozec and  
Morey. This is an open-access article  
distributed under the terms of the [Creative  
Commons Attribution License \(CC BY\)](#). The  
use, distribution or reproduction in other  
forums is permitted, provided the original  
author(s) and the copyright owner(s) are  
credited and that the original publication in  
this journal is cited, in accordance with  
accepted academic practice. No use,  
distribution or reproduction is permitted  
which does not comply with these terms.

# Assessment of predictability of the Loop Current in the Gulf of Mexico from observing system experiments and observing system simulation experiments

Dmitry S. Dukhovskoy<sup>1\*</sup>, Eric P. Chassignet<sup>2</sup>, Alexandra Bozec<sup>2</sup>  
and Steven L. Morey<sup>3</sup>

<sup>1</sup>National Oceanic and Atmospheric Administration, National Weather Service, National Centers for Environmental Prediction, Environmental Modeling Center, College Park, MD, United States, <sup>2</sup>Center for Ocean-Atmospheric Prediction Studies, Florida State University, Tallahassee, FL, United States, <sup>3</sup>School of the Environment, Florida A&M University, Tallahassee, FL, United States

This study presents results from numerical model experiments with a high-resolution regional forecast system to evaluate model predictability of the Loop Current (LC) system and assess the added value of different types of observations. The experiments evaluate the impact of surface versus subsurface observations as well as different combinations and spatial coverage of observations on the forecasts of the LC variability. The experiments use real observations (observing system experiments) and synthetic observations derived from a high-resolution independent simulation (observing system simulation experiments). Model predictability is assessed based on a saturated error growth model. The forecast error is computed for the sea surface height fields and the LC frontal positions derived from the forecasts and control fields using two metrics. Estimated model predictability of the LC ranges from 2 to 3 months. Predictability limit depends on activity state of the LC, with shorter predictability limit during active LC configurations. Assimilation of subsurface temperature and salinity profiles in the LC area have notable impact on the medium-range forecasts (2–3 months), whereas the impact is less prominent on shorter scales. The forecast error depends on the uncertainty of the initial state; therefore, on the accuracy of the analysis providing the initial fields. Forecasts with the smallest initial error have the best predictive skills with reliable predictability beyond 2 months suggesting that the impact of the model error is less prominent than the initial error. Hence, substantial improvements in forecasts up to 3 months can be achieved with increased accuracy of initialization.

## KEYWORDS

Gulf of Mexico, loop current, data assimilation, ocean modeling, model skill assessment, predictability



# 1 Introduction

The Gulf of Mexico (GoM) marine basin provides significant economic, ecological, and biological value. The Gulf provides 15% of the total U.S. domestic oil and 1% of natural gas production (Zeringue et al., 2022) with over 3,200 active oil and gas structures (NOAA NCEI Gulf of Mexico Data Atlas, <https://www.ncei.noaa.gov/maps/gulf-data-atlas/atlas.htm?plate=Offshore%20Structures>, accessed 23 January 2023). Accurate and timely forecasts of strong currents associated with the energetic mesoscale features such as the Loop Current (LC) and Loop Current eddies (LCEs) at the offshore production sites are of great importance for oil and gas operations. Improved understanding and predictive capabilities of the LC system have also major implications for hurricane forecasts (Shay et al., 2000), oil spill response and preparedness (Walker et al., 2011; Weisberg et al., 2017), biogeochemical variability (Damien et al., 2021), sustainability of fisheries (Weisberg et al., 2014; Selph et al., 2022), and forecasting sargassum transport and harmful algal blooms (Gower and King, 2011; Liu et al., 2016). The necessity of improved predictability of the LC system from short-range (from a few days to a week) to long-range (3 months and longer) has been emphasized in a call to action by the National Academies of Sciences, Engineering, and Medicine (NASEM, 2018). The importance of this problem has motivated the Understanding Gulf Ocean Systems (UGOS) research initiative (part of the NASEM Gulf Research Program) focused on improving our knowledge and forecasts of the GoM circulation in spatial and time scales useful for a broad community of stakeholders.

A modeling research project conducted by a consortium of university researchers funded by UGOS Phase 1 (UGOS-1) has the overarching goal to achieve greater understanding of the physical processes that control the LC and LCE separation dynamics through advanced data-assimilative modeling and analyses. One of the objectives of the study is to examine the limits of predictability of the LC system using multi-model forward simulations. Several modeling groups conducted coordinated experiments using different data-assimilative modeling systems to test the performance and sensitivity of existing Gulf of Mexico forecasting models and to evaluate long-range prediction capabilities. The numerical experiments included Observing System Experiments (OSEs) and Observing System Simulation Experiments (OSSEs). OSEs apply existing observational data to evaluate the sensitivity of a data assimilative system to different types of observations and their combination (Fujii et al., 2019). In OSSEs, synthetic observations derived from a realistic simulation ("nature run") are used as constraints in data assimilation systems (Lahoz and Schneider, 2014).

The predictability of a model can be defined as the time extent within which the true state can be predicted within some finite error (e.g., Lorenz, 1965; Lorenz, 1984; Krishnamurthy, 2019). Many metrics have been employed to measure the predictability (e.g., DelSole, 2004; Krause et al., 2005). In most studies, the predictability is evaluated based on the square error or mean square error between the predicted state and truth (Lorenz, 1965; Lorenz, 1984; Dalcher and Kalnay, 1987; Oey et al., 2005). The error-based measure of predictability follows a mathematical theory of the growth of initial errors formulated by Lorenz (1965).

According to this theory, the error of the forecast increases with lead-time. The amplification factor of the error is not constant and depends on the model parameters, the initial magnitude of the error, as well as the system itself. Typically, forecast error growth rate is largest at the beginning and then the magnitude of the forecast error levels off, asymptotically approaching the limiting value, called the saturation value. The saturation value is comparable to the expected error of two randomly chosen states of the system (Lorenz, 1965; Dalcher and Kalnay, 1987). This means that when the forecast error approaches the saturation value, its predictive skill is no better than any randomly selected state of the system. The time taken to reach the saturation level has been used as a measure of the predictability of forecasting systems (DelSole, 2004; Krishnamurthy, 2019). Another measure of the model predictability used in atmospheric forecasts is the doubling time of the errors (e.g., Charney et al., 1966; Lorenz, 1982). However, it has been shown that this parameter is not a good measure of error growth and predictability (e.g., Dalcher and Kalnay, 1987).

Some studies compare statistics derived from forecasts and reference states to evaluate model predictive skill. For example, Thoppil et al. (2021) compared RMSE computed from forecasts and from a monthly mean climatology of ocean observations. This work defined that the model has predictive skills if RMSE is lower than RMSE from climatology data. In other studies, the predictability is measured in terms of time when cross-correlation between the forecast and observations drops below a threshold value (e.g., Latif et al., 1998). Boer (2000) used cumulative scaled predictability statistics derived from cross-correlation between the forecast and observations to investigate the predictability of the coupled atmosphere-ocean system on time scales of monthly to decadal. The statistics were compared against threshold values to evaluate model predictability. Many skill scores are referenced with respect to persistence prediction or persistence (Mittermaier, 2008). Alternatively, predictive skill scores can be referenced with respect to a random forecast (Wilks, 2006) or climatology (DelSole, 2004).

The type of predicted characteristics selected for evaluation of the predictability dictates the choice of the metrics. In the GoM, the shape and location of the LC and LCEs are the main predicted characteristics. The model prediction skill assessment is performed by comparing the LC/LCE frontal positions in the forecast and control data set. In many studies, the LC/LCE fronts are defined from the sea surface height (SSH) fields using a threshold value (e.g., 0.17 m in Leben, 2005; 0.45 m in Zeng et al., 2015). Oey et al. (2005) defined forecast frontal positions by contouring the 18°C isotherm at 200 m. Dukhovskoy et al. (2015a) used SSH gradient field to correct the first guess of the LC frontal position derived from the SSH 0.17 m contour. Comparison of the contours or shapes requires special metrics providing robust error estimates that measure dissimilarity of the objects. Oey et al. (2005) used shortest distance from the LC/LCE fronts to several locations in the Gulf derived from the forecasts and observations to deduce the forecast error in frontal position. This metric may provide an acceptable measure of the model forecast skill for the predicted characteristic defined as the shortest distance from the LC/LCE front to specific locations. However, it does not provide information about the shape

of the LC front. In theory, there are an infinite number of possible LC/LCE shapes that will have identical distances to the specified locations. To address this, Dukhovskoy et al. (2015b) tested five metrics for contour and shape comparison and demonstrated that the Modified Hausdorff Distance (MHD) method (Dubuisson and Jain, 1994) exhibits high skill and robustness in quantifying similarity between the objects. This metric has been successfully applied for evaluation of model skill for simulating river plumes (Hiestler et al., 2016). There are other methods specifically designed for contour comparison in geophysical applications that could potentially be applied for LC/LCE frontal position skill assessment (Goessling and Jung, 2018; Melsom et al., 2019).

For most of the documented GoM forecast systems, predictability of the LC position is approximately 3–5 weeks (Oey et al., 2005; Mooers et al., 2012). Forecasting a LCE separation event is a challenging prediction task for GoM circulation models and its predictability is on the order of a month (Mooers et al., 2012). It should be noted that predictability estimates from other model studies are not comparable when different measures of predictability, predicted characteristics, reference state, and type of control data sets are used. Also, predictability characterizes predictive skills of the particular model used for prediction and does not describe the predictability of the process being forecast, although, the process determines the time scale of the model predictability (Krishnamurthy, 2019).

This paper summarizes results of numerical experiments performed using a high-resolution (~2.5 km) regional data-assimilative system to systematically assess the impact of different types of observations on the predictive time scale in the GoM. To evaluate the impact of specific observations (SSH, temperature (T) and salinity (S) profiles, etc.) on the predictive skills of the forecasting system, we perform free-running (no data assimilation) forecasts initialized from the runs that assimilate real observations (OSEs) and synthetic observations derived from a high-resolution independent simulation (OSSEs). Results of the OSEs and OSSEs demonstrate the importance of minimizing the error in the forecast initial fields for accurate forecasts. In its turn, the accuracy of the hindcasts providing initial fields depend on availability of observations and assimilation techniques.

The layout of the paper is as follows. Section 2 describes the data-assimilative system and the methods for model skill assessment. Then, results of the OSEs using various combinations of observations are presented in section 3. In section 4, we use OSSEs and a nature run to further assess the predictability of the forecasting system. Finally, the results are discussed and summarized in section 5.

## 2 Model configuration, nature run, and metrics

### 2.1 The 1/32.5° intra-American seas HYCOM-TSIS

A regional configuration of the HYbrid Coordinate Ocean Model (HYCOM; Bleck, 2002; Chassignet et al., 2003; Halliwell,

2004) is used for the data-assimilative OSEs and OSSEs. The computational grid has uniform 1/32.5° horizontal spacing (~2.5 km) between 98.08°W and 56.08°W and 7.03°N and 31.93°N (Figure 1). The Intra-American seas (IAS HYCOM) domain includes the GoM and the Caribbean Sea. This configuration keeps the open boundaries away from the Gulf reducing the boundary effect on the numerical solution in the GoM, which is the study region. The model bathymetry is a combination of global 1-arc-min ocean depth and land elevation from the U.S. National Geophysical Data Center (ETOPO1; <https://www.ngdc.noaa.gov>) and the 15-arc-second General Bathymetric Chart of the Oceans (GEBCO; [https://www.gebco.net/data\\_and\\_products/gridded\\_bathymetry\\_data/](https://www.gebco.net/data_and_products/gridded_bathymetry_data/)) 2020 grid with local corrections in the Gulf of Mexico. The model employs 30 vertical hybrid layers with potential densities referenced to 2000 db and ranging from 27.10 to 37.17 sigma units. The model is forced with NCEP CFSR and CFSv2 atmospheric fields of air temperature and specific humidity at 2 m, surface net short- and long-wave radiation, precipitation, and 10 m wind stress. Monthly climatological river discharge is prescribed at all major rivers resulting in a negative salt flux at the river sources. A combination of Laplacian and biharmonic mixing is used for horizontal momentum diffusion. The mixing is specified in terms of diffusion velocity, that is  $2.86 \times 10^{-3} \text{ m s}^{-1}$  for Laplacian momentum dissipation,  $5.0 \times 10^{-3} \text{ m s}^{-1}$  for scalar diffusivity, and  $0.01 \text{ m s}^{-1}$  for biharmonic momentum dissipation and layer thickness diffusivity. The K-profile parameterization (KPP; Large et al., 1994) is used for vertical mixing with default values.

For data assimilation of the observations in HYCOM, we use the Tendral Statistical Interpolation System (T-SIS) version 2.0. The interpolation algorithm is based on the Kalman filtering approach with a novel technique for solving the least squares normal equations. The suggested solution uses the information matrix (inverse of the covariance matrix), which significantly reduces computational complexity of calculation of the filter gain matrix. Details of the parameterization of the inverse covariance using Markov random fields are in Srinivasan et al. (2022). In the numerical experiments presented here, different types of oceanographic fields are assimilated as discussed in sections 3 and 4 (OSEs and OSSEs, respectively). All experiments consist of data-assimilative hindcasts simulations (analysis) followed by 3-month free-running forecasts initialized from the analysis fields at specified times.

### 2.2 OSSE nature run

In the OSSE hindcasts (section 4), synthetic observations, derived from another simulation, the so-called nature run (NR), are assimilated in the forecasting system. The NR model is chosen to perform the most statistically realistic simulation of the ocean as possible. The NR should be an unconstrained simulation performed at high resolution using a state-of-the-art general circulation model. For OSSEs to be credible, it is essential that the NR provides the most accurate possible representation of the true system, that is, possess a model climatology and variability with statistical properties that agree with observations to within specified limits.

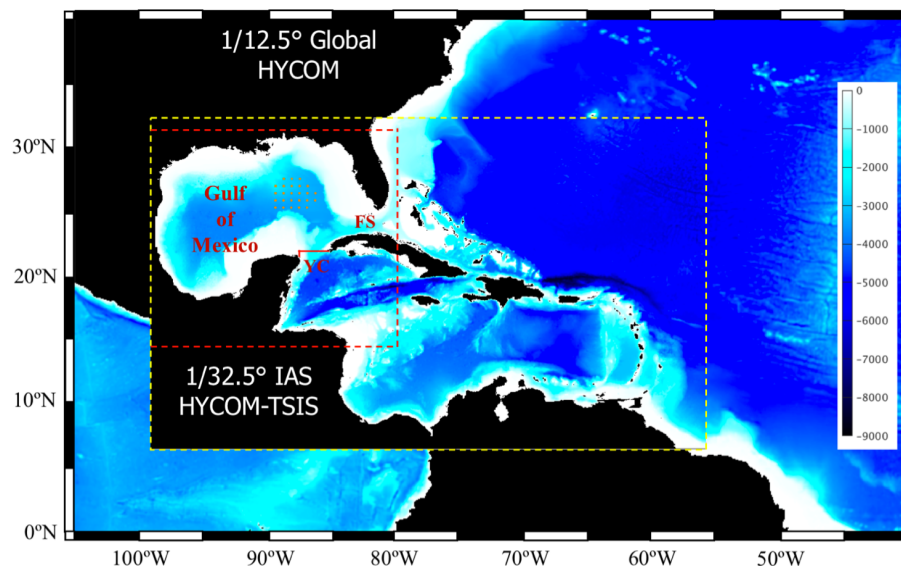


FIGURE 1

Bathymetry map of the computational domain of the 1/32.5° IAS HYCOM-TSIS forecast modeling system (yellow dashed box) nested within the outer model. In OSEs, the domain is nested into the 1/12.5° Global HYCOM reanalysis (GOF3.0). In OSSEs, the domain is nested into the 1/12° GLORYS reanalysis. The red dashed lines delineate the outer boundaries of the NEMO domain providing the nature run fields. The orange bullets in the eastern GoM indicate PIES locations. The Yucatan Channel (YC) and the Florida Straits (FS) are indicated. The red line designates location of the vertical section of the mean along-channel velocities shown in Figure 4.

Here, the NR solution is provided by a GoM simulation performed with the Nucleus for European Modeling of the Ocean program (NEMO.4.0; Madec et al., 2017) ocean model at Centro de Investigación Científica y de Educación Superior de Ensenada (CICESE, Mexico). This model is configured on a 1/108° horizontal grid (~900 m spatial grid spacing) with 75 vertical levels. The model domain is shown in Figure 1 with the dashed red lines. The NR is initialized from the 1/12° GLORYS12 global reanalysis (Lellouche et al., 2021) and is integrated using boundary (surface and lateral) forcing and no assimilation for the period from 1 January 2009 to 31 December 2014. The lateral boundary conditions are derived from the GLORYS12 reanalysis. At the surface, the atmospheric fluxes of momentum, heat and freshwater are computed by bulk formulae using the COARE 3.5 algorithm (Edson et al., 2013). The model is forced with the Drakkar Forcing Field (DFS5.2) atmospheric fields product (Dussin et al., 2016) which is based on the ERA-interim reanalysis and consists of 3-hour fields of wind, atmospheric temperature and humidity, atmospheric pressure at the sea level, and daily fields of long, short wave radiation and precipitation.

## 2.3 Metrics, forecast predictability, and skill assessment

The performance of the data-assimilative runs and forecasts is assessed by two metrics: the root mean square error (RMSE) and the MHD. Both metrics quantify the disagreement between the forecast and the true state and can be used as a measure of predictability and skill assessment of the model simulation.

### 2.3.1 The root mean square error

The RMSE is computed to quantify the difference between spatial distributions of a scalar field from the simulation and the control run, and is computed as

$$E_{RMSE} = \left( \frac{\sum_{i=1}^n (x_i - \tilde{x}_i)^2}{N} \right)^{1/2}, \quad (1)$$

where  $x_i$  is scalar value at the  $i^{\text{th}}$  point in the simulation and  $\tilde{x}_i$  is the value at the corresponding point from the control data field. The comparison is performed for spatial fields; in this case,  $i$  is the grid point index. The RMSE provides a quantitative estimate of the overall agreement between two fields (a forecast and a control field) based on a statistical score (eq. 1). However, for the purposes of this study, more precise assessment of a model run was needed to evaluate the model skill in predicting the LC system in terms of the LC position and shape; therefore, a topological metric, the MHD, is also employed.

### 2.3.2 Modified Hausdorff distance of the loop current front

There are two steps in this skill assessment approach. First, the contours representing the LC and LCE fronts are derived from the SSH fields of a tested simulation and control data (e.g., control model run, altimetry gridded data) following Leben (2005) and Dukhovskoy et al. (2015a). Second, the MHD score ( $D_{MHD}$ ) is computed for the two contours considered as sets of points (A and B)

$$D_{MHD}(A, B) \equiv \max \left\{ \frac{1}{|A|} \sum_{a \in A} d(a, B), \frac{1}{|B|} \sum_{b \in B} d(b, A) \right\}, \quad (2)$$

where  $|A|$  and  $|B|$  are the cardinality of sets  $A$  and  $B$ ,  $d(a, B) \equiv \min_{b \in B} d(a, b)$  and  $d(A, b) \equiv \min_{a \in A} d(a, b)$ . Next, the MHD scores are used for evaluating the predictability skills of the forecast compared to control data. Identical LC frontal positions result in zero MHD. The MHD score increases as the two contours (i.e., the LC frontal positions) become more dissimilar. The MHD units depend on the positional units or can be unitless (normalized distances, for instance). Here, MHD is in km for ease of interpretation.

While MHD is a robust objective metric, measuring dissimilarities in two-dimensional and which can be generalized to N-dimensional fields (Dukhovskoy et al., 2015b), different definitions of the LC front may result in different contours impacting the MHD score and model skill assessment. This is particularly true during LCE detachment and reattachment when the LC shape drastically changes within several hours. As an illustration, the daily mean SSH fields from the NEMO NR and

one of the HYCOM OSSE forecasts are shown for two consecutive dates (Figure 2). The LC front is defined using the 17-cm contour of demeaned SSH shown with the red lines in the upper and middle panels. The bottom panels show the two contours representing the LC fronts from the control field (NR) and the forecast and the MHD score is computed for these contours. At the end of the 3-month HYCOM forecast, the LC shapes from the NR truth and the forecast are notably dissimilar. Yet, there is some agreement in the positioning and size of the LC on April 9, 2012. Between April 9 and the following day, the LC sheds an eddy in the forecast, but not in the NR (Figure 2B). If one were to adopt a definition of the contours that only include the LC, this would result in a drastic increase of the MHD score (or decrease in the prediction skill) for the forecast because the LC is in the retracted position whereas it is in the extended position in the NR. In many cases, a LCE reattaches the LC several days later now causing a sudden decrease in the

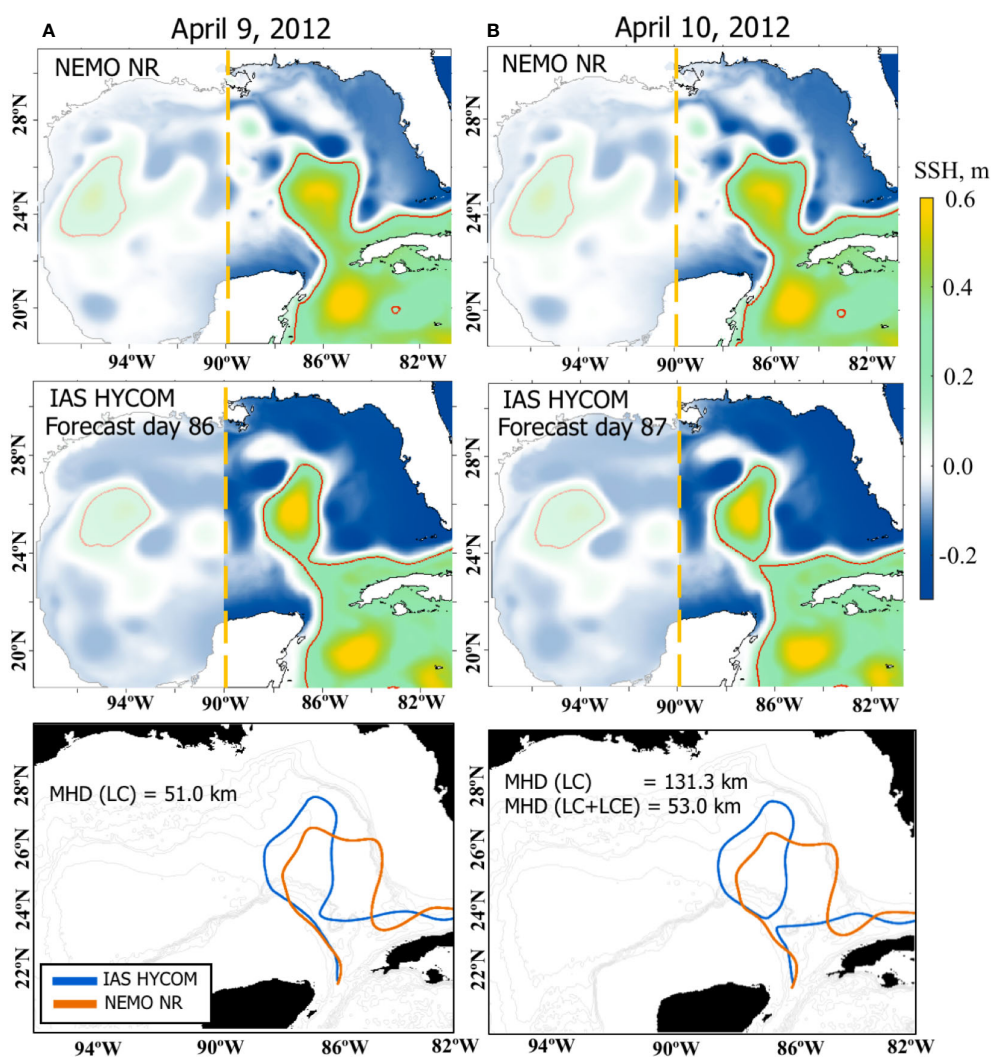


FIGURE 2

The SSH fields and the LC/LCE fronts from the NEMO NR (top row) and one of the 1/32.5° IAS HYCOM OSSE forecasts (middle) for April 9, 2012 (left column, A) and April 10, 2012 (right column, B). The red lines indicate LC/LCE fronts defined as the 17-cm contours of the demeaned SSH. The bottom panels show the LC/LCE fronts used for the MHD calculation with the MHD score listed. For the NR, only LCEs that are in the east of 90°W are considered for the MHD (the eddies that are in the shaded area are ignored). For (B), the two MHD scores of the forecast (blue) are given: for the LC front only and the LC with the LCE fronts combined.



MHD score. In this study, the prediction skill is assessed for the whole LC system that includes LCEs that are within a certain distance to the LC (somewhat similar to Oey et al., 2005). The definition of the predicted characteristics would be different if the predictability of the shedding event were the main focus of this study.

To mitigate the impact of LCE detachment and reattachment on the MHD score, keeping in mind that the focus of the experiment is on the frontal locations for the entire LC system (including eddies) rather than the timing of the LCE shedding, the following approach is used to define the fronts for MHD skill assessment. An automated algorithm tracks the LC and LCEs in the SSH fields similar to Dukhovskoy et al. (2015a). LCEs west of 90°W are discarded (shaded region in Figure 2). For other LCEs, the MHD is computed for all possible combinations of the LCEs (including none) with the LC both for the forecast and the control fields. Then the best (smallest) MHD score is selected. For the case presented in Figure 2B, the combination of the LCE contour with the LC from the forecast yields a smaller MHD score than for the LC alone (53 vs 131.3 km) and, therefore, both the LCE and LC contours from the forecast versus the LC contour from the control field are used for MHD.

### 2.3.3 Assessment of predictability

As mentioned above, two metrics, RMSE and MHD, are used to evaluate the model predictability. The predictability is considered to be lost when the RMSE is comparable to the saturation value. Sensitivity testing of the MHD metric conducted by Dukhovskoy et al. (2015b) demonstrated that the MHD linearly responds to the

linearly increasing error in the shape. Therefore, the idea of saturation value is also applicable to the MHD metric meaning that the MHD score will increase as the dissimilarity between the forecast and the control frontal position, due to forecast error, increases approaching the saturation value. Note that an agreement between the RMSE and MHD scores is expected, however the MHD evaluates only the LC and LCE shapes, whereas RMSE provides a spatially average score for the whole GoM and is less sensitive to mismatch in the LC frontal position in the forecast and the control data.

In order to assess predictability of the forecast system, RMSE and MHD scores are compared against the saturation values. The estimates of the RMSE saturation value ( $RMSE_{\infty}$ ) and MHD saturation value ( $MHD_{\infty}$ ) are derived from the SSH fields of the NEMO NR for 2010 and 2012 (Figure 3). The randomly selected fields are at least 90 days apart from each other to avoid similar states of the SSH. The distributions of  $RMSE_{\infty}$  and  $MHD_{\infty}$  are symmetric and close to normal with similar mean and median. Following Dalcher and Kalnay (1987), 95% of the estimated saturation values ( $RMSE_{\infty} = 0.178$  m and  $MHD_{\infty} = 66.3$  km) are used in our analysis of the forecast experiments for predictability assessment. The estimated  $RMSE_{\infty}$  agrees well with that of Zeng et al. (2015) who used a threshold value of 0.7 for spatial correlation coefficients of predicted and observed SSH to evaluate prediction skill of the forecasts. According to Zeng et al. (2015), the spatial RMSE of SSH exceeded  $RMSE_{\infty}$  for the forecasts with spatial correlation  $<0.7$  (Figure 3 in Zeng et al., 2015).

Model forecast skill is defined as forecast performance relative to the performance of a reference forecast demonstrating added

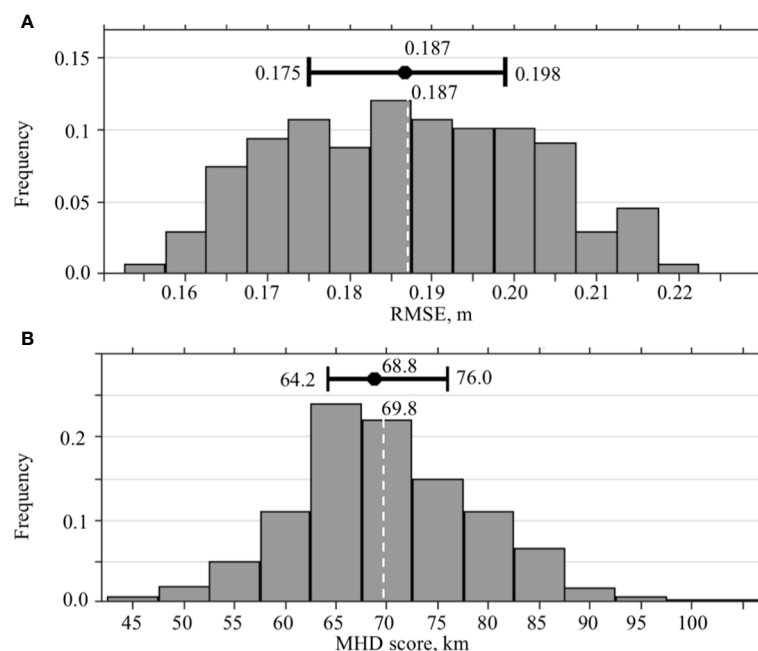


FIGURE 3

Statistics of the RMSE and MHD scores characterizing the saturation value. (A) Distribution of the RMSE between two randomly selected SSH fields from the NEMO NR. (B) Distribution of the MHD scores calculated for the LC/LCE fronts derived from randomly selected SSH fields from the NEMO NR. At the upper part of the diagrams, the median and IQR with the values are shown. The dashed white line is the expected value with the value listed at the top.

value of the forecast (Mittermaier, 2008). If the state of the system at time  $t$  is  $\mathbf{X}(t)$ , where  $\mathbf{X} \in \mathbb{R}^n$ , then persistence prediction at lead time  $\tau$  is  $\mathbf{X}(t + \tau) = \mathbf{X}(t)$ . In our case, persistence is the initial fields of the forecast simulation. Persistence is a useful comparison of the model skill that provides measure of added value relative to some benchmark. However, no conclusion on predictability of the forecast system can be usually drawn from this. Also, skill assessment depends on the choice of the benchmark as a reference state (Niraula and Goessling, 2021).

### 3 Observing system experiments

In this first series of the experiments (OSEs), the IAS HYCOM is nested within the 1/12.5° global HYCOM reanalysis GOF3.0 (Metzger et al., 2014) and hindcasts of the GoM state during the time period from 2009 through 2011 are performed using observational data for constraining the numerical solution used for the forecasts. The OSEs assimilate sea level anomaly (SLA) derived from the satellite altimetry observations (AVISO L3 along-track data downloaded from <https://www.aviso.altimetry.fr/en/data/products/sea-surface-height-products/global.html>), gridded sea surface temperature (SST) fields provided by the Group for High Resolution Sea Surface Temperature (GHRST, downloaded from <https://www.ghrst.org>), and temperature and salinity profiles derived from Argo floats (downloaded from <https://usgodae.org/argo/argo.html>) and pressure inverted echo sounders (PIES, available at <http://www.po.gso.uri.edu/dynamics/dynloop/index.html>) observations collected during the Dynamics of the Loop Current in the U.S. Waters Study from April 2009 to November 2011 (Donohue et al., 2016a). The array consisted of 25 PIES (locations shown in Figure 1), nine full-depth moorings and 7 short near-bottom moorings. Three LC eddies were shed during 2009–2011 ("Ekman" in July 2009, "Franklin" in May 2010, and "Galileo" in June 2011 based on Horizon Marine denomination; <https://www.horizonmarine.com/loop-current-eddies>). The Dynamic of the Loop Current in the U.S. Waters Study observations provide temperature (T) and salinity (S) profiles at mesoscale resolution (30–50 km) within the region spanning 89° W to 85° W, 25° N to 27° N. Vertical profiles of T, S, and density were reconstructed from PIES observations using empirically-derived relations between the round-trip acoustic travel times of the sound pulse emitted from the PIES and historical hydrography (Hamilton et al., 2014; Donohue et al., 2016b). To increase the number of satellite tracks over the GoM and improve the assimilation, the assimilation algorithm used 4-day composite satellite tracks (Envisat, Cryosat, Jason 1 interleaved, and Jason 2) within the domain.

#### 3.1 OSE assimilative hindcasts

Most of the information about the ocean state assimilated into the analysis is derived from the ocean surface fields that are readily observed by remote-sensing instruments. Assessment of the influence of subsurface fields assimilated into the models on the

LC predictability was one of the UGOS-1 main research objectives. Particularly, the focus was on the PIES observations that provide information about subsurface ocean fields in the LC region (Figure 1). To evaluate the added values of the subsurface T/S profiles, two OSEs are conducted using the 1/32.5° IAS HYCOM-TSIS: with and without T/S profiles derived from PIES observations with all other observational fields being assimilated (SLA, SST, and Argo T/S profiles). The OSE hindcasts are compared against the 1/12° global HYCOM reanalysis GOF3.0 (0.08GLB; <https://www.hycom.org/dataserver/gofs-3pt0/reanalysis>) and the 1/25° Gulf of Mexico HYCOM reanalysis (0.04GOM; <https://www.hycom.org/data/gomu0pt04/expt-50pt1>).

The simulated Yucatan volume transport averaged over 2009–2011 is similar in the HYCOM-TSIS OSEs (25.3 Sv with PIES and 25.1 Sv with no PIES) and is only slightly lower than in the 0.08GLB (26.1Sv) and 0.04GOM (25.8 Sv; Figure 4A). The long-term (> 3 months) variability of the transports from the OSE analyses compares well with the reanalysis estimates. This result is expected because the low-frequency variability and the mean Yucatan transport is mostly controlled by the lateral BCs (derived from 0.08GLB). There is a bigger spread in the daily volume transport estimates from the hindcasts and the reanalysis data. The higher-frequency variability is due to local dynamics such as Caribbean eddies propagating along the Yucatan Channel (Murphy et al., 1999; Abascal et al., 2003) and changes in the intensity and position of the currents and countercurrents (Sheinbaum et al., 2002). These processes are less controlled by the BCs in the HYCOM-TSIS where domain boundaries are far away from the Yucatan Channel.

The characteristics of the Yucatan Channel flow derived from the OSE analysis and the reanalysis fields are in good agreement (Figure 4A). The flow structure captures major features of the flow (Figures 4B–E) reported from observations (e.g., Sheinbaum et al., 2002; Abascal et al., 2003). The strong Yucatan current flows northward with the core located in the upper western part of the channel with speeds exceeding  $1 \text{ m s}^{-1}$ . Along the eastern side, there is a strong surface Cuban Countercurrent. Interestingly, the Cuban countercurrent in the HYCOM-TSIS OSEs (Figures 4B, C) is stronger (about  $0.2 \text{ m s}^{-1}$ ) than in both reanalyses (about  $0.1 \text{ m s}^{-1}$ ; Figures 4D, E). Reported mean speeds in the Cuban Countercurrent exceed  $0.2 \text{ m s}^{-1}$  (Abascal et al., 2003), but it has a large interannual variability (Sheinbaum et al., 2002). Deep undercurrents in the western and eastern sides of the channel are also present in the simulations. The Yucatan Undercurrent – the outflow that follows the Yucatan slope between 800 m and the bottom – is only weakly pronounced in the 0.08GLB reanalysis (Figure 4D), but is notable in the OSEs and 0.04GOM reanalysis.

The root mean square error (RMSE) is computed between the SSH fields derived from the OSEs ("PIES" and "noPIES") and from the 0.04GOM reanalysis (Figures 4F, G). From a visual inspection, the impact of the assimilated T/S profiles derived from PIES observations on the SSH is more notable in 2009 and 2010, and less in 2011. For both OSEs, the RMSE has comparable values and spatial distribution over the GoM. During all years, the RMSE of the OSEs is low ( $<0.1 \text{ m}$ ) over the most of the domain, but increases (up to  $0.2 \text{ m}$ ) in the eastern GoM over the LC region. In this region, the

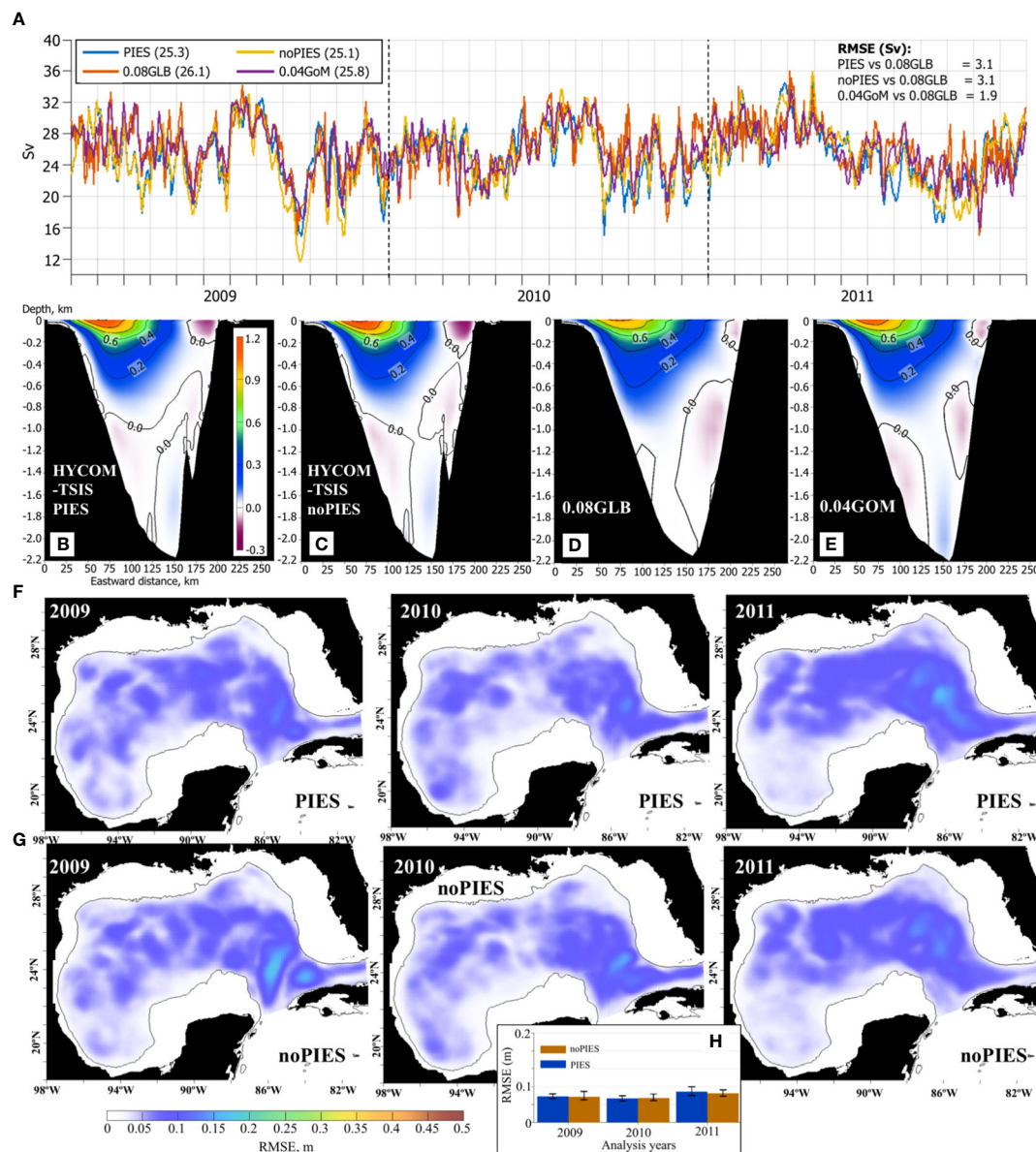


FIGURE 4

(A–E) Flow characteristics in Yucatan Channel from the  $1/32.5^\circ$  IAS HYCOM-TSIS OSEs,  $0.08^\circ$  Global HYCOM+NCODA reanalysis (0.08GLB), and  $0.04^\circ$  Gulf of Mexico HYCOM+NCODA reanalysis (0.04GOM). (A) Yucatan daily volume transport estimates (Sv). The mean volume transports over 2009–2011 are listed in parenthesis in the legend. On the right, RMSE (Sv) of the daily Yucatan transport estimates relative to the 0.08GLB is given. Vertical section of the mean along-channel velocity component ( $\text{m s}^{-1}$ , positive northward) in the Yucatan Channel from: (B) the  $1/32.5^\circ$  IAS HYCOM-TSIS OSE with PIES T/S profiles assimilated in the hindcast; (C)  $1/32.5^\circ$  IAS HYCOM-TSIS OSE without PIES T/S profiles; (D) 0.08GLB reanalysis; (E) 0.04GOM reanalysis. In (B–E), the horizontal axis is eastward distance (km) along the section (the Yucatan Shelf on the left), the vertical axis is depth (km). (F) Annual RMSE between SSH (m) from the OSE analysis runs with assimilated PIES T/S profiles and from the 0.04GOM reanalysis for April 2009 – November 2011 (time interval of the PIES observations). (G) Same as (F) but OSE with no PIES T/S profiles. (H) Median and IQR of the RMSE from “PIES” and “noPIES” OSEs by years.

OSEs exhibit some differences. In 2009 and 2010, the “noPIES” OSE has elevated RMSE in the middle of the LC region (between  $22^\circ\text{N}$  and  $26^\circ\text{N}$ ) that is smaller in the “PIES” OSE. This is the region where LC “necking” occurs before the LC sheds an eddy, the so-called “necking-down” separation (Vukovich and Maul, 1985; Zavala-Hidalgo et al., 2003). Presumably, assimilating PIES observations improves the LC behavior in this region, although the PIES sites are located farther north (Figure 1). In 2011, the “noPIES” OSE has slightly lower RMSE in the LC region compared

to the “PIES” OSE. Spatial RMSE of the SSH in the OSE analysis runs is comparable for all years (Figure 4H).

### 3.2 OSE forecasts

Added value of the PIES T/S profiles to the predictability of the LC system is investigated in 3-month forecast simulations initialized from the “PIES” and “noPIES” OSE hindcasts. The first

3-month forecast starts on May 1, 2009. The other 3-month forecasts are performed at a one-month interval until December 1, 2010, providing twenty 3-month forecasts for each OSE (“PIES” and “noPIES”). The predictive skill of the forecasts is then evaluated based on the RMSE of the daily SSH and the MHD of the LC and LCE contours derived from the forecast daily SSH fields. The forecasts are compared against the 0.04GOM reanalysis.

In both forecast groups, the RMSE increases with time as the forecasts’ accuracy degrades (Figure 5). The most prominent increase of the RMSE is in the LC region and the error is larger in the forecasts initialized from “noPIES” OSE. The growth rate of the mean RMSE is faster during the first several weeks and then slows down as the error approaches the saturation value (Figure 6A), in agreement with the forecast error theory (Lorenz, 1965; Dalcher and Kalnay, 1987). There is a wide spread in the RMSE estimates across the individual forecasts because of the spread in the initial error. Larger errors grow faster resulting in the lower predictive skills and shorter predictability of the forecasts.

The monthly mean RMSE in Figures 5, 6B shows that the forecasts initialized from the OSE assimilating PIES T/S profiles perform slightly better than the “noPIES” forecasts. The median (and the mean) RMSE is less than  $RMSE_{\infty}$  indicating that most forecasts from both groups have not lost predictability by the end of the 3<sup>rd</sup> month of the forecast cycle. A higher percentage of the “PIES” forecasts retain predictability by the end of the forecast cycle (almost 75% “PIES” vs ~63% “noPIES”) suggesting added value of subsurface T/S profiles from PIES assimilated in the OSE analysis. Compared to the persistence RMSE, the forecasts from both groups have similar ratio to persistence skills in the 1<sup>st</sup> month. In the 2<sup>nd</sup> and 3<sup>rd</sup> months, the RMSE of the forecasts is lower than persistence. Our OSE forecasts demonstrate longer predictability when

compared to the results of Zeng et al. (2015) where the number of forecasts that failed to pass the threshold value for skillful prediction quickly increased after 4 weeks. In the OSE forecasts, >75% of “noPIES” forecasts possess predictive skills by the end of the 2<sup>nd</sup> month of the forecast window.

Similar to RMSE, the MHD scores increase with lead time due to degrading accuracy of the forecasts in predicting the LC front (Figure 6C). The growth rate of mean MHD is slower for “PIES” forecasts than for “noPIES” but in both cases, the mean does not exceed  $MHD_{\infty}$  during the 3-month forecast time. Statistics (the median and the IQR) of the MHD scores indicate similar skills in predicting the LC front for both “PIES” and “noPIES” forecasts groups during the 1<sup>st</sup> month (Figure 6D). The difference between the MHD scores for two forecast groups increases in the 2<sup>nd</sup> and 3<sup>rd</sup> months with “PIES” forecasts on average demonstrating better skills. In contrast to the RMSE, more forecasts from both groups (>75% “PIES” and ~70% “noPIES”) still possess predictability by the end of the 3<sup>rd</sup> month. Both forecasts groups barely outperform persistence in predicting the LC front during the 1<sup>st</sup> month, but have markedly better skills in the following months.

## 4 Observing system simulation experiments

In the second series of the experiments (OSSEs), the IAS HYCOM solution is relaxed to the GLORYS12 reanalysis outside of the GoM NEMO NR domain to provide a similar ocean state to that of NEMO along the NEMO domain. In the OSSE hindcasts, the assimilated fields are subsampled from the NR (section 2.2) in a similar fashion to that of the observations (existing or projected), i.e.

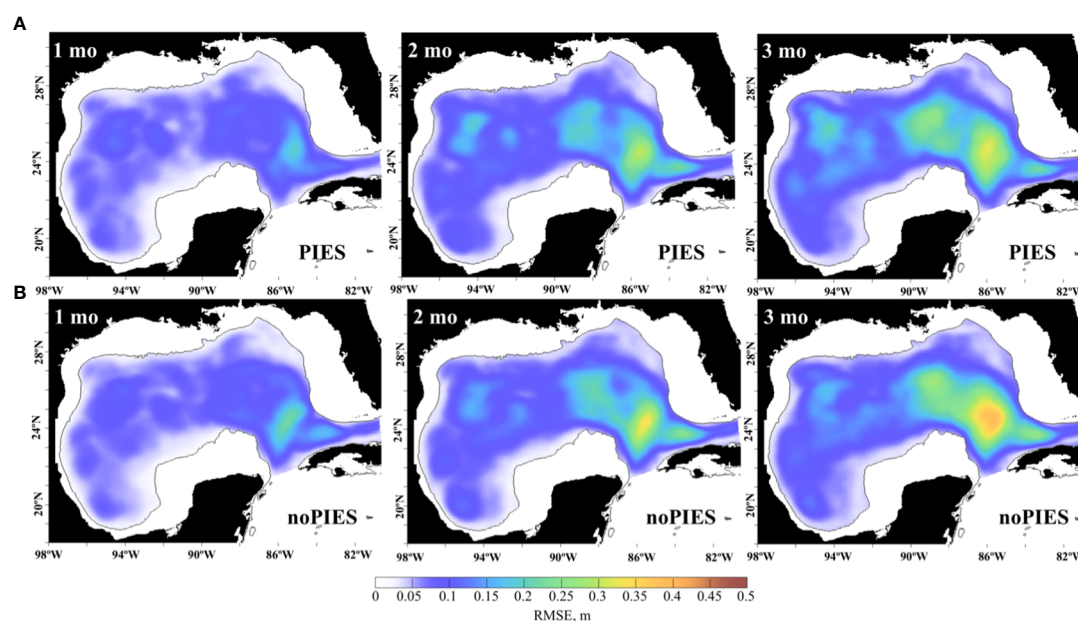


FIGURE 5

Monthly mean RMSE between daily SSH (m) from the OSE 3-month forecasts in 2009–2010 and from the 0.04GOM reanalysis. The forecasts initialized from the OSE with PIES T/S profiles (top row, A) and the OSE with no PIES T/S profiles (bottom row, B). The RMSE is averaged by the forecast months (in columns), so that the monthly statistics are derived from roughly 30 days of 20 forecasts.



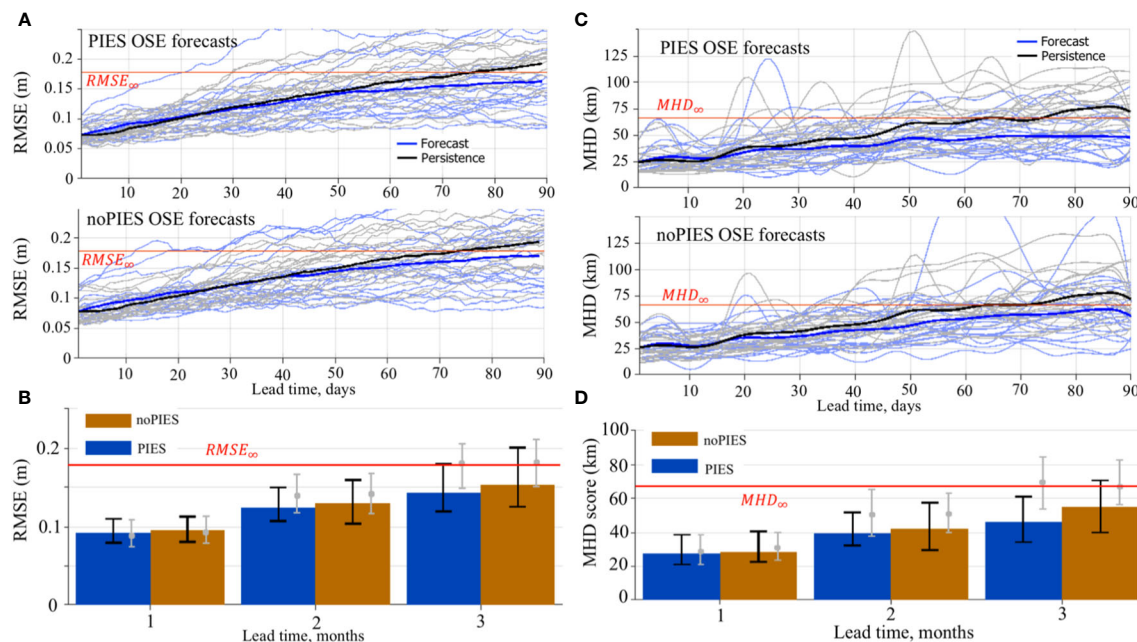


FIGURE 6

(A, B) RMSE (m) between SSH from the forecasts initialized from the “PIES” and “noPIES” OSE analysis runs and SSH from the 0.04GOM reanalysis. (A) RMSE of the individual 3-month forecasts (light blue) and corresponding persistency prediction (grey lines). The bold blue line is the mean RMSE over all individual forecasts. The black is the mean RMSE of persistency forecasts. The horizontal red line indicates  $RMSE_{\infty}$  (95% of the saturation value). (B) The median (the colored bars) and the IQR (the black vertical lines) of the RMSE. The RMSE are grouped by the forecast months. The grey bullet and the vertical lines indicate the median and the IQR of the RMSE between the persistence and the 0.04GOM reanalysis. (C, D) MHD scores (km) of the OSE forecasts. The MHD is computed for the LC/LCE fronts derived from the SSH fields of the OSE forecasts and the 0.04GOM reanalysis. (C) MHD scores of the individual 3-month forecasts (light blue) and corresponding persistency prediction (grey lines). The bold blue line is the mean MHD over all individual forecasts. The black is the mean MHD of persistency forecasts. The horizontal red line indicates  $MHD_{\infty}$ . (D) Median (bars) and the IQR (the black vertical lines) of the MHD scores of the OSE forecasts grouped by the forecast months. The grey bullet and the vertical lines indicate the median and the IQR of the MHD of the persistence.

at the same locations and with the same temporal and spatial frequencies. In this series of experiments, the OSSEs are carried out to assess added value of different types of observations, their location and spatial coverage to the predictability skills of the forecasting systems. During the OSSEs, the nature run solutions are sampled at the space-time locations of satellite SST measurements, along-track SSH, and PIES T/S profiles to form daily synthetic observations for assimilation into the numerical solutions. These OSSEs address the following objectives: (1) assess the sensitivity of the forecasts to the various types of observations currently available; (2) evaluate added value to the forecasts from proposed new types of observations or expansion of observing sites in the eastern GOM; and (3) evaluate predictability of the LC system for idealized cases when the information about the true state is unlimited resulting in smaller error between the true state and analysis. Two time periods representing active and stable LC states are selected from the NR for the OSSE data assimilative hindcasts. During the first time period, June–September 2011, the shape of the LC changes considerably during several detachments and reattachments of the LCEs. By contrast, the LC exhibits small variability with one LCE reattachment during the second time period, January–May 2012. Note that the model states during these time periods do not necessarily represent the true ocean states because the NR is free-running and not data assimilative.

#### 4.1 Design of the OSSE hindcasts

To address the objectives of the OSSEs, nine hindcasts were performed with different set of NR fields assimilated into the 1/32.5° IAS HYCOM-TSIS (Figure 7). The OSSEs can be combined into 3 main groups, following the objectives. The first group of hindcasts (Figures 7A–D) assimilate types of observations commonly used in the operational GoM forecasts as well as the PIES observations that are currently being evaluated for delivering data in near-real-time. Hindcast “AVISO-PIES-SST” represents the case with the most complete set of synthetic observations including 4-day composite SLA from AVISO swath data, T/S profiles from PIES, and SST from GHRSSST gridded fields (Figure 7D). Hindcasts “AVISO-PIES”, “AVISO”, and “AVISO-1” assimilate reduced information: withheld SST (Figure 7C), no T/S profiles and no SST (Figure 7B), SLA from only 1 satellite (Figure 7A).

The second group of OSSE hindcasts evaluates the added value of assimilating additional T/S profiles provided by expanded PIES arrays in the LC region (hindcast “AVISO-extdPIES-SST”, Figure 7E). The expansion of the PIES and mooring sites in the eastern GOM for better observation of the LC and LCE was proposed at the time of UGOS-1. This experiment is similar to hindcast “AVISO-PIES-SST” (Figure 7D), except for the additional PIES T/S profiles that are assimilated during the hindcast.

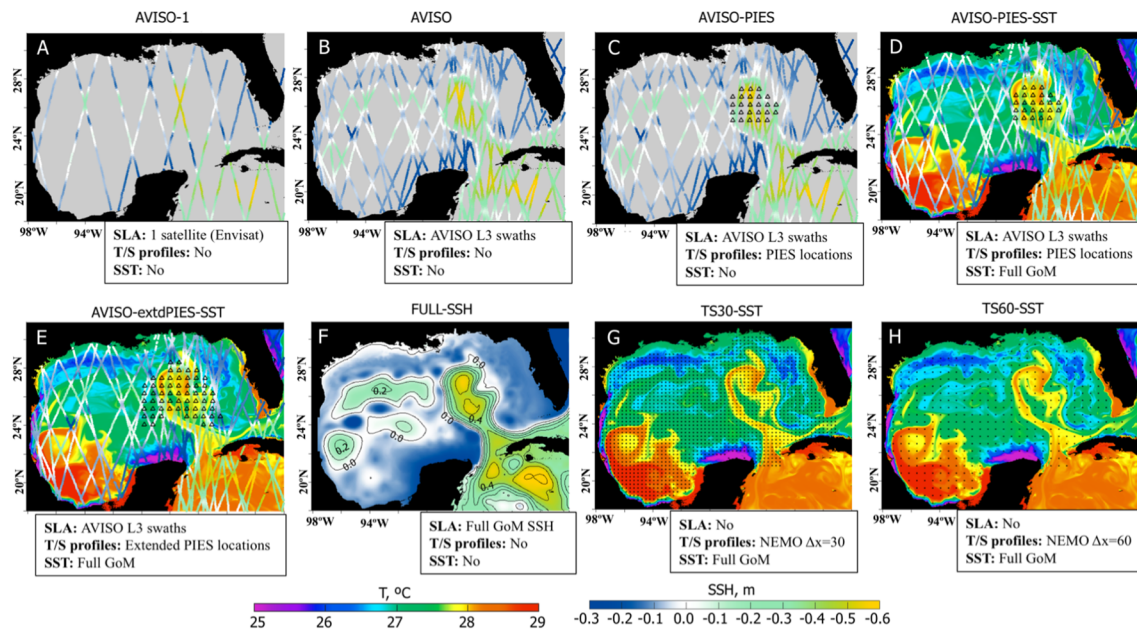


FIGURE 7

Design of the OSSEs. The maps show data fields assimilated into the OSSE hindcasts. Assimilated fields are listed below the maps. (A) SLA from one (Envisat) satellite (4 days composite). The colored lines show NEMO SSH (Nature Run) on June 1, 2011 interpolated into satellite swaths. (B) Same as (A) but all available satellites on the analysis day (4 days composite). (C) Same as (B) additionally with T/S profiles derived from PIES observations. (D) Same as (C) additionally with SST. This experiment replicates the most complete set of observations presently available for assimilated runs. The colored field in the background shows SST from the NEMO NR (June 1, 2011). (E) Same as (D) but with T/S profiles from extended PIES. (F) Full SSH field from the NEMO NR (June 1, 2011). (G) T/S profiles at every 30th NEMO grid point and SST. (H) T/S profiles at every 60th NEMO grid point and SST.

The last group combines idealized cases when unlimited information is available for constraining the  $1/32.5^\circ$  IAS HYCOM simulation. In hindcast “FULL-SSH”, complete information about the sea surface height (SLA from the NR) is provided to the data assimilation algorithm (Figure 7F). In the two other hindcasts (“TS30-SST” and “TS60-SST”), only subsurface T/S fields and SST are assimilated and no SLA fields are used. For these hindcasts, the T/S profiles are derived from the NR at every 30<sup>th</sup> (Figure 7G) and 60<sup>th</sup> (Figure 7H) NEMO grid points in the GoM. Thus, the two hindcasts differ in the density of T/S profiles over the GoM.

The last hindcast (“NEMO-INT”) represents a highly idealized case imitating a perfect assimilation of the 3D ocean state into the forecasting system. There are two sources of errors contributing to forecast error: errors in the initial conditions and errors associated with numerical models used in the forward simulation. In complex forecast systems, these two components cannot be easily separated. One practical way for doing this is to provide perfect initial conditions and evaluate the forecast error growth. In order to substantially reduce the uncertainty in the predictive skills of the model due to errors in the data assimilation process, the NEMO fields are directly interpolated onto the  $1/32.5^\circ$  IAS HYCOM horizontal grid and vertical layers. Outside the NEMO domain (Figure 1), the GLORYS12 fields are interpolated onto the IAS HYCOM grid. This approach significantly reduces the error of the “analysis” (demonstrated in the following section) providing the best possible initial state for the OSSE forecast experiments. Therefore, this experiment provides an estimate of the best

predictive skill for this configuration of the  $1/32.5^\circ$  IAS HYCOM if a perfect initial state could be provided by the analysis. Validation of the SSH, subsurface T/S fields, and the LC frontal position have shown a very close match of the interpolated fields to the NR. Hindcast “NEMO-INT” is not a true analysis run and it is therefore not discussed in the OSSE hindcasts section 4.2. The forecasts initialized from the interpolated NEMO fields are analyzed and compared to the other OSSE forecasts.

## 4.2 Analysis of the OSSE hindcasts

### 4.2.1 RMSE analysis

The RMSE is calculated from the daily SSH fields derived from the HYCOM analysis and NR and averaged over 2011–2012 (Figure 8A). The RMSE maps show conspicuous differences in the OSSEs depending on the amount of information assimilated in the analysis. As expected, the hindcast with the lowest quantity of information (“AVISO-1” using experiments’ notations in Figure 7) demonstrates the poorest performance with high RMSE over the GoM compared to other OSSEs. Whereas, the “TS30-SST” forecast with the most complete set of T/S profiles has the best performance with the overall lowest RMSE. The hindcast “TS60-SST” that assimilates T/S profiles with the coarser spatial coverage (half of “TS30-SST”) has comparable RMSE scores, but the error is elevated along the eastern side of the LC.

Predictive skills of the OSSE hindcasts are compared in terms of the median values of the time-averaged SSH RMSE fields (Figure 8B). The OSSE ranking matches the expectation. The hindcast constrained by the most complete 3D hydrographic fields (“TS30-SST”) has the best performance followed by the hindcast that assimilates 2D SSH provided at every model grid in the GoM (“FULL-SSH”). Then the hindcast performance degrades as the amount of the assimilated information decreases. The hindcast with only 1 AVISO track used as a constraint (“AVISO-1”) has the poorest performance with distinctly higher RMSE. The hindcasts ranked from 4 to 7 have very small difference in the RMSE scores. All these hindcasts have assimilated AVISO SLA, but differ in the assimilation of SST and PIES T/S profiles. The hindcast that assimilates T/S profiles from the extended PIES array has a better skill than that the experiment assimilating data from the actual PIES array, but the difference is too small to be significant.

#### 4.2.2 MHD of the LC and LCE frontal positions

The MHD is computed for the LC and LCE fronts derived from demeaned daily SSH fields to quantify the similarity between the LC fronts in the OSSE analysis runs versus the NR. Examples of the LC and LCE fronts from the NR are shown in Figure 2 (top panels). The OSSE analysis runs are ranked based on the median MHD values (Figure 8C). There is a good agreement between rankings based on the MHD scores and RMSE, respectively. Again, the best performance has the simulations constrained by synthetic T/S profiles at every 30<sup>th</sup> grid point (“TS30-SST”) followed by the “FULL-SSH” and “TS60-SST” hindcasts. The hindcast that assimilates limited SSH information (“AVISO-1”) has the lowest predictive skills. Adding subsurface T/S profiles to the satellite altimetry improves the accuracy of the LC front prediction in the hindcasts. The only difference between the MHD and the RMSE rankings is that “AVISO-PIES” swaps places with “AVISO-

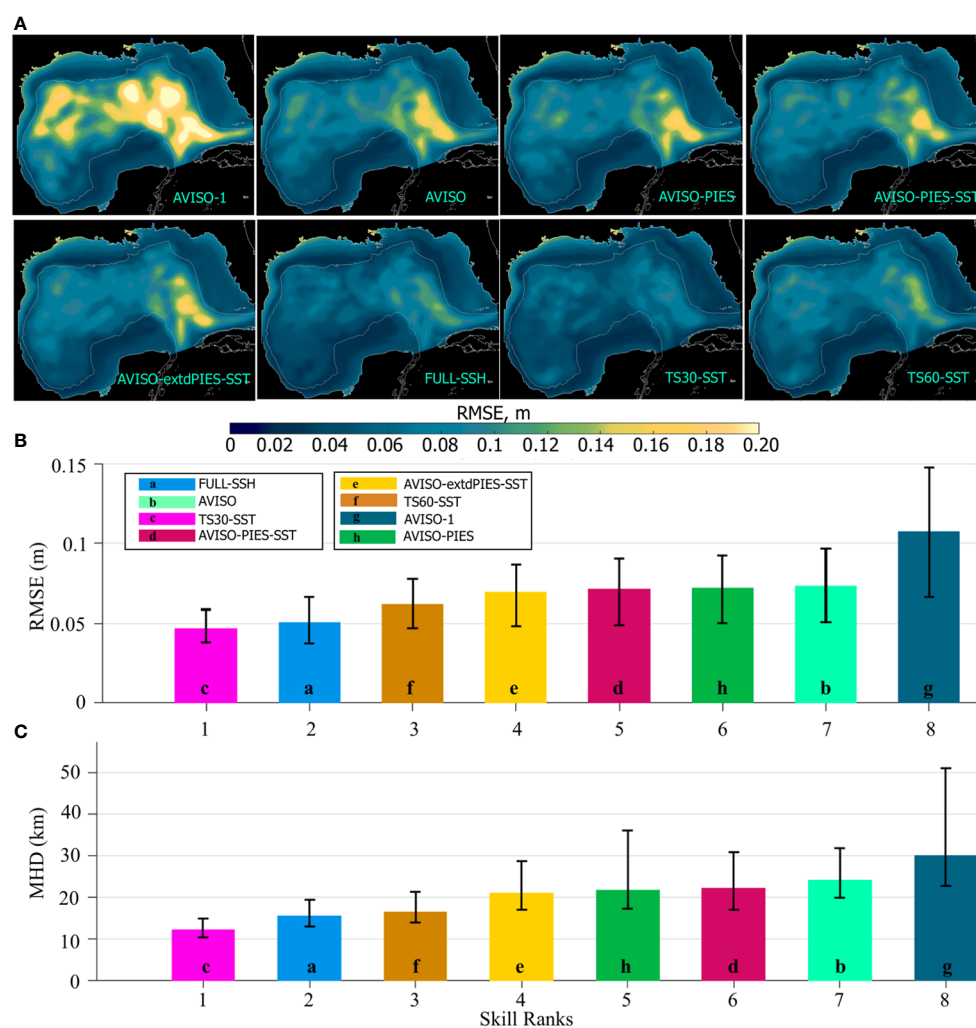


FIGURE 8

(A) Maps of mean RMSE (m) between daily SSH fields from the OSSE analysis runs shown in Figure 7 and from the NR (NEMO). The RMSE is averaged over 2011–2012. The gray contour is the 200-m isobath. The OSSEs are indicated in the maps. (B) RMSE (m) between SSH from the OSSE analysis runs and the NR over the hindcast period (2011–2012). The colored bars show the median RMSE with colors corresponding to the OSSEs. The hindcasts are ranked based on the median RMSE. The vertical black lines indicate the IQR. The letters in the bars are for ease of color identification. (C) MHD scores computed for the LC/LCE contours derived from the OSSE analysis SSH fields versus the NEMO NR. The bars show the median MHD scores by OSSEs. The hindcasts are ranked based on the median MHD score.



PIES-SST”; however, in both metrics the scores of these hindcasts are almost identical making the ranking of these two experiments uncertain.

### 4.2.3 Comparison of subsurface frontal positions

Anticyclonic eddies have a distinct signature in the subsurface hydrographic fields. The LC and LCEs in the GoM are associated with positive temperature anomalies that are tracked down to several hundred meters. Isotherms contouring warm water masses in the subsurface layers effectively delineate LC and LCEs and have been previously used for the LC/LCE identification and model skill assessment (Oey et al., 2005). Here, temperature anomalies at 200 m derived from the OSSEs are compared in order to assess the impact of different fields assimilated in the analysis on subsurface hydrographic fields. Temperature anomalies ( $\Delta T$ ) are computed from the 200 m temperature fields by subtracting the spatial mean. Then,  $\Delta T = 2.5^\circ\text{C}$  is used to contour the LC and LCEs (Figure 9A). Next, the MHD metric is employed to compare the OSSE  $2.5^\circ\text{C}$  contours against the NR for 2011–2012 (Figure 9B). The hindcasts are ranked based on the median of the MHD score. The best and the worst skills are found in the “TS30-SST” and “AVISO-1” hindcasts, respectively, similar to the ranking derived from the SSH contours (Figure 8C). The main difference in the MHD-based ranking between the surface and subsurface frontal positions is a decreased ranking of the “FULL-SSH” hindcast, with the ranking changed from the 2nd best to the 6th. All OSSE analysis runs that assimilate subsurface T/S profiles outperform the hindcasts constrained by the surface fields (“FULL-SSH”, “AVISO”, and “AVISO-1”). The ranking of the “FULL-SSH” analysis is lower (although insignificantly) than both hindcasts assimilating PIES and extended PIES T/S profiles. Note substantially better skill (lower MHD score) of the “AVISO-extdPIES-SST” OSSE compared to “AVISO-PIES-SST” demonstrating added value of the extended PIES array.

### 4.3 Design of the OSSE forecasts

Two time intervals are selected for the OSSE forecast experiments. The first interval, the NR June–September 2011 time period, corresponds to an active or unstable phase of the LC characterized by extended position of the LC with potential LCE detachment (Figures 10A, B, E) or reattachment (Figures 10C, D). During this time period, the LC shape frequently changes due to several detachments and reattachments of LCEs (Figures 10A–E). The second time interval corresponds to the NR January–May 2012 (Figures 10F–J). At the beginning, the LC is in a stable position being retracted towards the Yucatan Channel in January (Figure 10F). During February – early March of 2012, the LC extends farther north (Figures 10G, H) and sheds a LCE in early March. The eddy reattaches to the LC about a week later (Figure 10I). Note that the shape and positioning of the LC in May 2012 is somewhat similar to that in January and February; this would make persistency with initial state from January or February a good forecast of the LC state in May as discussed in section 4.4.

In the following set of numerical experiments, the three-month forecasts are initialized from the following OSSE analysis runs: “FULL-SSH”, “AVISO”, “AVISO-PIES-SST”, “AVISO-extdPIES-SST”, “TS30-SST” (Figure 7), and “NEMO-INT”. For each of these OSSE analysis runs, seven forecasts are initialized one week apart starting from May 1, 2011 until June 15, 2011 and seven forecasts initialized from January 1, 2012 until February 15, 2012. Therefore, there are 12 sets of forecasts (six OSSE group runs during two time intervals) that include seven individual forecasts initialized with a one-week interval and run forward for 3 months.

## 4.4 Analysis of the OSSE forecasts

### 4.4.1 RMSE analysis

The RMSE of the SSH is calculated using daily fields from the OSSE forecasts and from the NEMO NR. All forecasts within the same forecast group have been pooled together to provide monthly average RMSE for months 1 through 3 during 2011 (Figure 11) and 2012 (Figure 12). In all forecasts, the RMSE increases with time with the errors growing fastest in the LC area. In general, the predictability of the forecasts follows expectations dictated by the rankings of the OSSE analysis runs (Figures 8B, C). Forecasts initialized from the state with the smaller error have lower RMSE during the first 2 months and, in some cases, during the 3<sup>rd</sup> month. For example, the performance of the “NEMO-INT” forecasts during the first 2 months is markedly better than all other forecasts, as expected due to the smallest error in the “NEMO-INT” analysis fields providing initial conditions for these forecasts. An interesting aspect of the 2011 RMSE maps is notably smaller errors over the LC region in the “AVISO-extdPIES-SST” during all 3 months of the forecast. The magnitudes and the pattern of the RMSE in these forecasts are similar to that from the “TS30-SST” forecasts that are initialized from the analysis more heavily constrained by the T/S profiles from the NR. Note that the error magnitude over the LC area is smaller in the “AVISO-extdPIES-SST” forecasts than that in the “AVISO-PIES-SST”.

The error growth rate in the forecasts is faster at the beginning of the forecast, then slows down as the error approaches the saturation value (Figure 13A) again in agreement with the forecast error theory (Lorenz, 1965; Dalcher and Kalnay, 1987). The “NEMO-INT” case is different in that the error growth rate is nearly linear during the 3-month time period. This stems from the fact that the initial errors in the “NEMO-INT” are very small ( $<0.01$  compared to 0.05–0.08 in the other forecasts), and the time evolution of the small error is governed by linearized equations (Lorenz, 1965). Therefore, a linear growth rate is expected for small errors as nicely demonstrated by the “NEMO-INT” forecasts.

The performance of the OSSE forecasts is ranked based on the median of the spatially averaged daily RMSE (Figures 13B, C). For the forecasts started in May–June 2011, the ranking during the first month of the forecast matches the expectation assuming that the forecast with the smallest error in the initial state from the analysis provides a more accurate prediction. Therefore, the ranking of the OSSE forecasts would be expected to follow the ranking of the corresponding OSSE analysis runs (Figure 8B). This is true for the



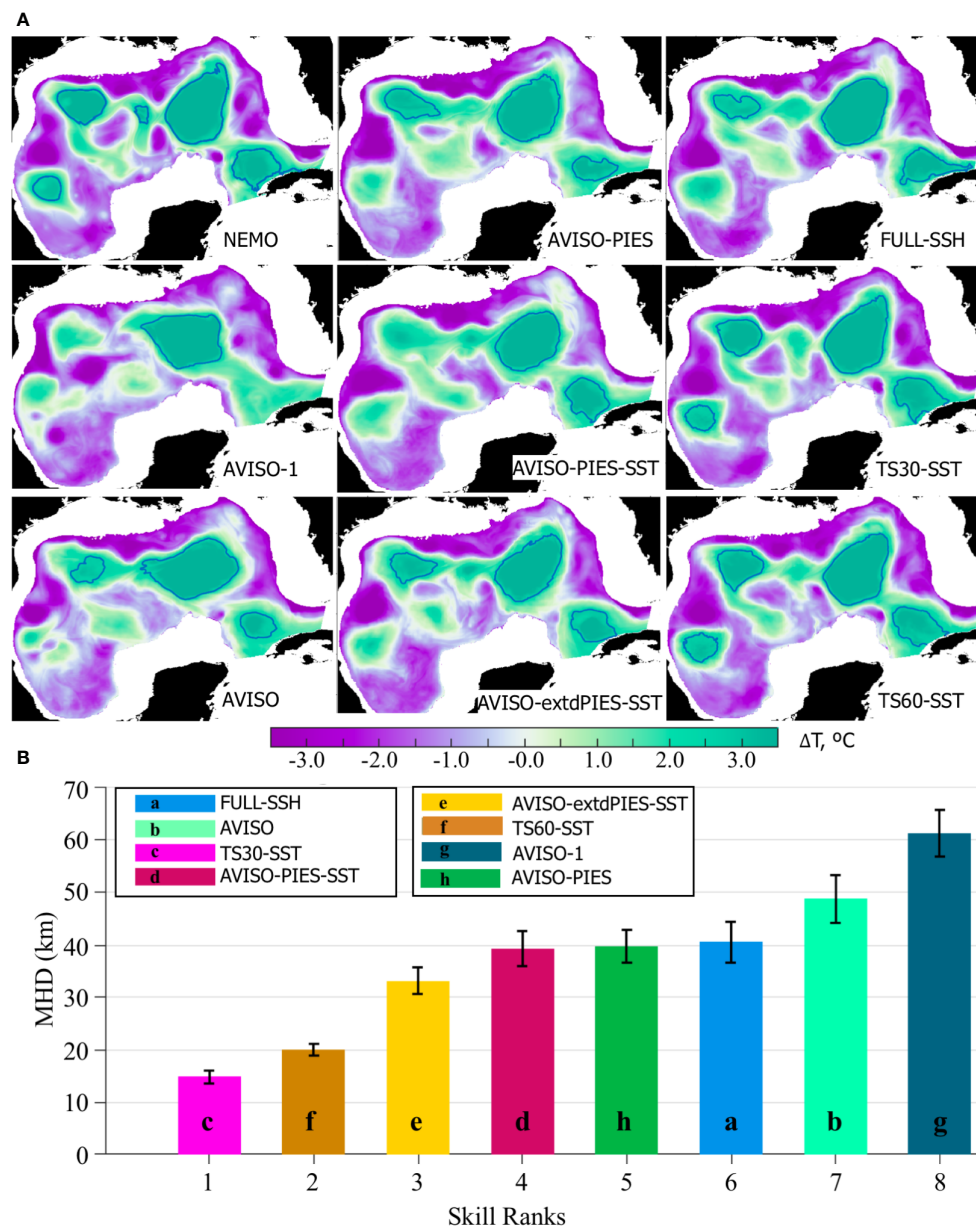


FIGURE 9

(A) Temperature anomaly ( $\Delta T$ ) at -200 m on July 9, 2011 from the NEMO NR and OSSE analysis. The contours delineate  $\Delta T=2.5^{\circ}\text{C}$  isoline that tracks anticyclones and the LC. (B) MHD scores computed for the  $2.5^{\circ}\text{C}$  contours of  $\Delta T$  at -200 m (2011–2012) derived from the OSSE analysis fields and the NEMO NR. The colored bars are the medians with colors corresponding to the OSSE hindcasts. The hindcasts have been ranked based on the median MHD. The vertical black lines on top of the bars indicate the IQR.

1<sup>st</sup> month. The forecasts “NEMO-INT”, initialized from the best initial conditions with the smallest assimilation error (interpolated fields), are ranked first demonstrating significantly smaller RMSE than the other forecasts. The RMSE in this forecast group decreases and is only slightly smaller than the RMSE of the second-best forecast by the end of the forecast period. The “TS30-SST” forecasts have the best second ranking followed by the “FULL-SSH”. The forecasts in these two groups were initialized from the OSSE analysis that assimilated the most complete synthetic observations compared to the other hindcasts. The “AVISO” forecasts have the lowest score, which is expected given substantially smaller amount of information constraining the

solution in the OSSE analysis providing initial state to these forecasts. Therefore, the ranking for the first month demonstrates an expected relation between the accuracy of the initial condition and the quality of the forecast. However, this expected ranking breaks in the second and third months where the “AVISO” forecasts have moved two positions up and the “FULL-SSH” to the end. The order of the forecasts in months 2 and 3 is unexpected and does not agree with the OSSE analysis ranking in Figure 8B. This result shows that the error in the forecasts grows at a different rate, which is evident in Figure 13A.

In 2012, the “NEMO-INT” and “TS30-SST” forecasts also have persistently higher rankings as in 2011. Again, the “FULL-SSH”

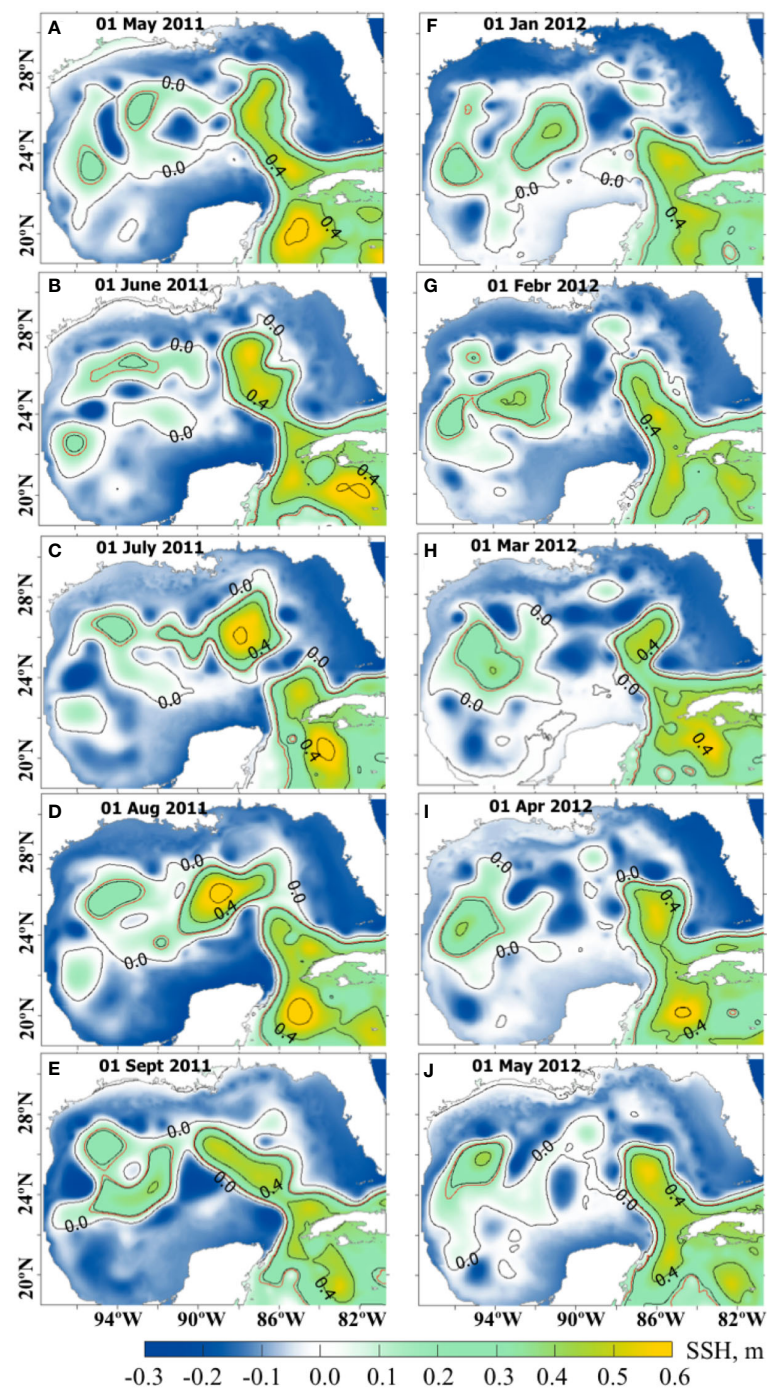


FIGURE 10

Daily SSH fields (m) from the NEMO NR. The left column (A–E) are SSH fields from May (A) – September (E) 2011 corresponding to the active state of the LC with several detachments and reattachments of the LCE. The right column (F–J) are SSH fields from the time interval January (F) – May (J) 2012 during which the LC is in a more stable position. Contours are every 0.2 m starting from 0. The red line is the 0.17 m contour used as a definition of the LC and LCE fronts.

forecasts ranking unexpectedly decreases by the end of the forecast period, whereas “AVISO” forecasts are third best in the second and third months. Rankings of “AVISO-PIES-SST” and “AVISO-extdPIES-SST” are inconsistent. In 2012, the prediction skills of “AVISO-extdPIES-SST” forecasts are not as high as during 2011 when compared to the other forecasts, although the difference in RMSE among some of them is small.

Similar to the OSEs, the OSSEs (except for “NEMO-INT”) struggle to outperform persistence during the 1<sup>st</sup> month in 2011. The only two forecast groups that outperform persistence in terms of the SSH RMSE during all forecast months in 2011 and 2012 runs are “NEMO-INT” and “TS30-SST”. In 2011, the skills of other forecasts are lower than persistence in the 1<sup>st</sup> month, higher in the 3<sup>rd</sup> month, and mixed in the 2<sup>nd</sup> month. In 2012, all forecasts have

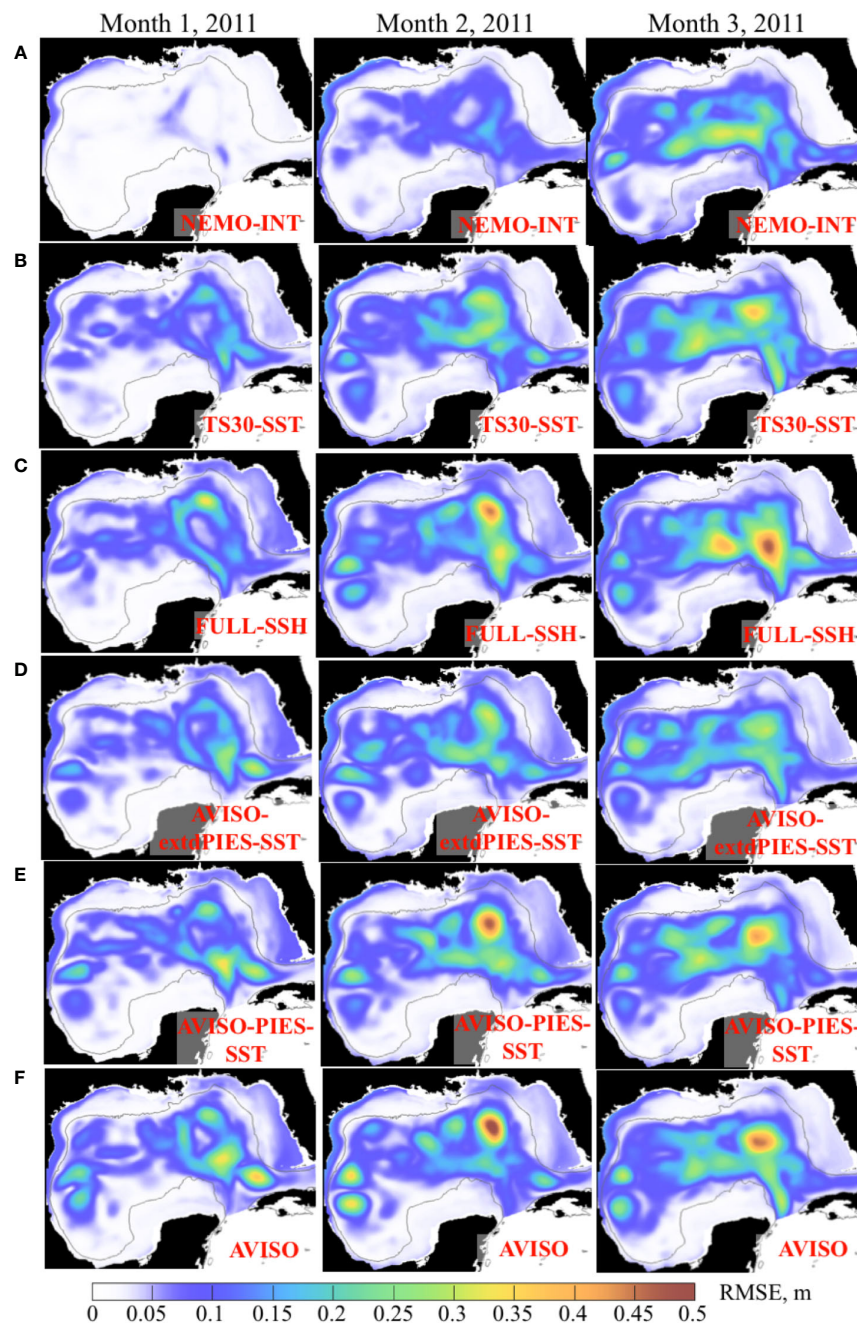


FIGURE 11

Monthly mean RMSE between SSH (m) from the 3-month OSSE forecasts started in May – June 2011 and the NEMO NR. The RMSE for months 1 through 3 are in the columns. The OSSE forecast groups are shown in the rows (A–F) with the forecast names shown in the maps.

better skills than persistence in 1<sup>st</sup> and 2<sup>nd</sup> months. During the 3<sup>rd</sup> month, the forecasts are ranked lower than persistence except for “NEMO-INT” and “TS30-SST”. The persistence-based estimate of the forecast skills is somewhat inconsistent with the assessment of predictability of the forecasts. In all cases (except for “FULL-SSH” in month 3 of 2011), the median RMSE and the upper IQR are less than  $RMSE_{\infty}$  indicating that the model predictive skills exceed 3 months in 75% forecasts.

#### 4.4.2 MHD of the LC and LCE fronts

The forecast skills of the 1/32.5° IAS HYCOM in predicting the LC front are assessed employing the MHD that is computed for the LC and LCE fronts derived from daily SSH fields in the OSSE forecasts and the NR. An example of the LC/LCE contours derived from SSH fields of one of the OSSE forecasts and NR is shown in Figure 14. The MHD scores are computed between the LC/LCE contours from the forecasts and the NR (the MHD score is listed in



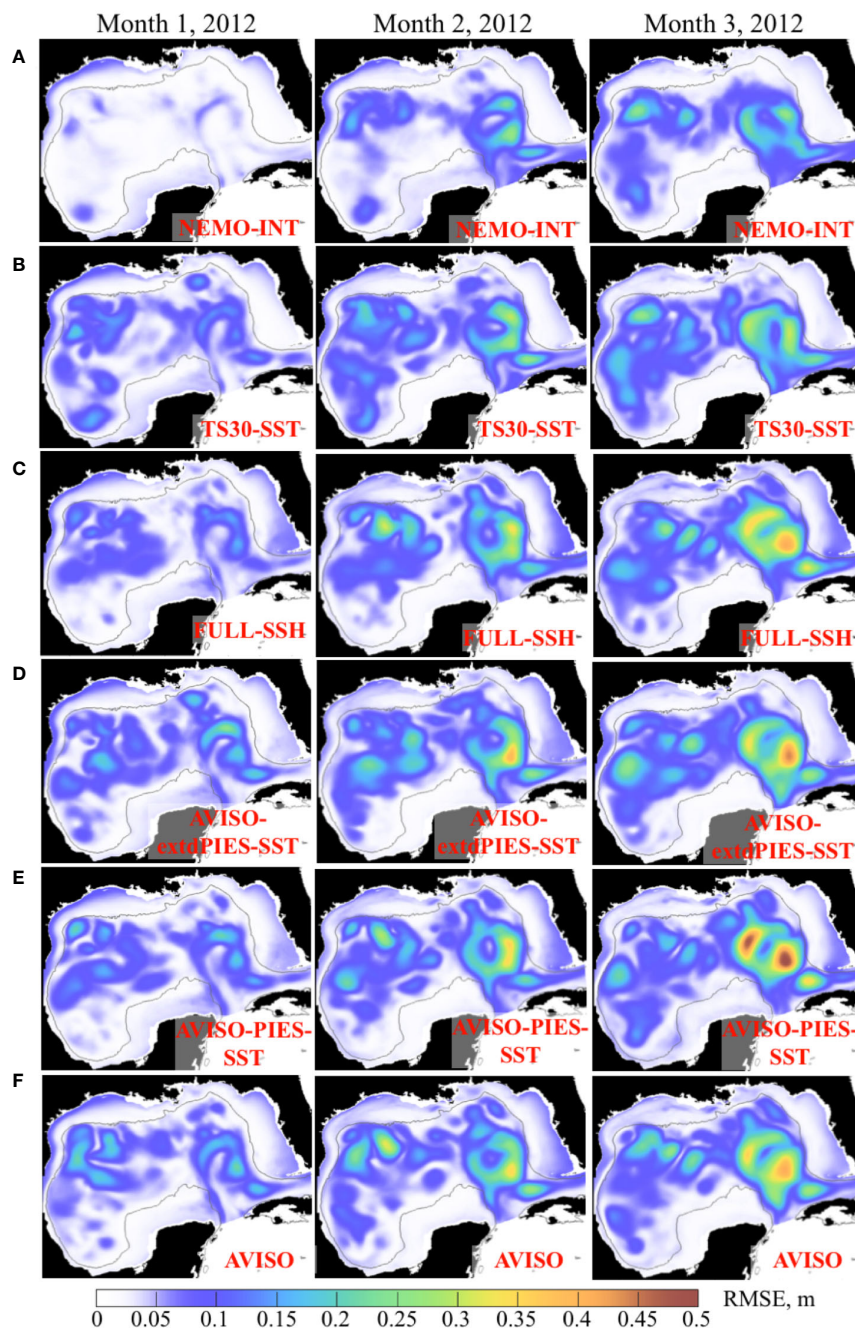


FIGURE 12

Monthly mean RMSE between SSH (m) from the 3-month OSSE forecasts started in January – February 2012 and the NEMO NR. The RMSE for months 1 through 3 are in the columns. The OSSE forecast groups are shown in the rows (A–F) with the forecast names shown in the maps.

blue), as well as between the forecast and the persistence (grey). Scores greater than  $MHD_{\infty}$  (6.3 km) demonstrate a lack of skills in predicting the LC/LCE frontal position.

Compared to the RMSE, the MHD scores of the OSSE forecasts exhibit more oscillating behaviour superimposed on the overall increasing trend (Figure 15A). The oscillations of the MHD scores are due to the rapid changes in the shape of the LC front during eddy detachment–reattachment events, the timing of which is not correctly predicted by the forecast. Nevertheless, the overall trend in the MHD scores meets the expectation and agrees with the RMSE

results. The MHD time series demonstrate degrading forecast skills of predicting the LC frontal position with time. In 2011, the mean MHD of all forecast groups has exceeded or reached  $MHD_{\infty}$  after ~60 days. By contrast, the mean MHD stays below  $MHD_{\infty}$  through the end of the runs for the all forecast groups. The difference in the forecast performance is due to different LC phases (Figure 10). In 2011, the NR LC was active with several eddy detachment–reattachment events. Whereas in 2012, the NR LC was less active resulting in a more accurate forecasts of the LC front. Note the decreasing mean MHD for persistence during 2012 by the end of



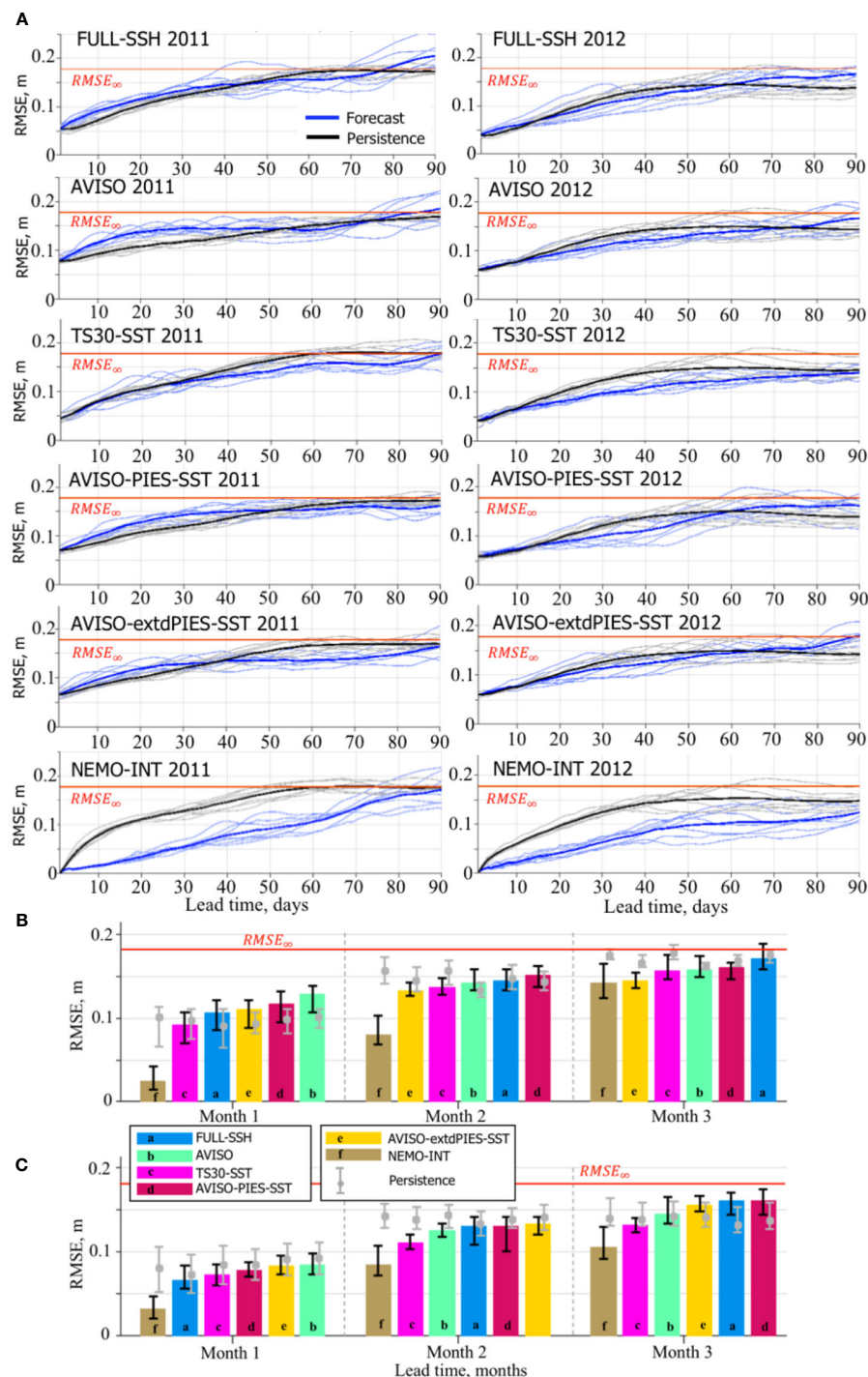


FIGURE 13

RMSE between SSH from the OSSE forecasts and the NR. (A) Daily RMSE for individual forecasts and persistence from the OSSE forecast groups during 2011 (left column) and 2012 (right column). The bold solid lines are the mean RMSE estimates for the forecasts (blue) and persistence (black). The horizontal red line indicates 95% of the saturation value ( $RMSE_{\infty} = 0.178$  m). The bar diagrams (B, C) show median RMSE (m) of the forecasts by the OSSE forecast groups during months 1 through 3 started in May-June 2011 (B) and January-February 2012 (C). Within each month, the OSSE forecast groups are ordered according to the ranks based on the median RMSE. The vertical black lines on top of the bars indicate the IQR. The grey line and the bullet show the IQR and the median, respectively, of the persistence corresponding to the OSSE forecast group. The horizontal red line indicates  $RMSE_{\infty}$ .

the 3-month period in contradiction to the expected increase. The decreasing MHD is a consequence of similar LC shapes at the beginning and end of the forecast time period (Figures 10F, J) by chance making persistence a good prediction of the LC front.

There is a good agreement in the rankings based on the RMSE (Figures 13B, C) and the MHD metrics (Figures 15B, C). “NEMO-INT” forecasts have the best predictive skills and are ranked first for all months in both forecast time periods (2011 and 2012). The



FIGURE 14

Example of the LC/LCE contours (fronts) from one of the OSSE forecasts in each forecast group (in columns) and corresponding contours from the NEMO NR during 2010 (A) and 2011 (B). The blue contours correspond to the OSSE forecasts and the orange contours are from the NR. The grey contours show persistence prediction. In the first row in (A, B), the initial state (day 1) is shown. The LC contours from the OSSE forecasts and persistence coincide demonstrating a perfect match of the initial contours from the “NEMO-INT” and the NR. The numbers are MHD scores for the shown contours from the forecast - NEMO NR (blue) and persistence - NEMO NR (orange).

“TS30-SST” forecasts are second best, in agreement with the expectation. Similar to the RMSE metric, the “FULL-SSH” forecasts quickly lose predictive skills moving to the last (2011) and second last (2012) rankings at the end of the forecast period. By contrast, the “AVISO” forecasts unexpectedly improve rankings in the 2<sup>nd</sup> and 3<sup>rd</sup> months. The “AVISO-extdPIES-SST” forecasts have better predictive skills than the “AVISO-PIES-SST” forecasts after the 1<sup>st</sup> month.

The MHD scores indicate similar predictive skills of the OSSEs, although there is a bigger difference in the performance during the 3<sup>rd</sup> months across OSSEs in 2011 and 2012. During a more active LC (year 2011), predictability of the forecasts is lost during the 3<sup>rd</sup> month in >50% of cases except for the “NEMO-INT”. By contrast, >75% of the OSSE forecasts demonstrate high predictive skills of the LC by the end of the 3<sup>rd</sup> month.

The “NEMO-INT” forecast group is the only one that outperforms persistence in 2011 and 2012, except for the 3<sup>rd</sup> month in 2011 when the scores are similar. In 2011, other forecasts struggle to outperform persistence during the first month and substantially outperform the persistence in the 2<sup>nd</sup> and 3<sup>rd</sup> months. In 2012, the forecasts outperform the persistence for the first two months and underperform during the last month of the forecast window. In 2011, the initial state of the LC quickly evolves into an unstable state in the forecasts, whereas it remains nearly unchanged for several weeks in the NR, as demonstrated by the example in Figure 14A. At the beginning of the forecast, the LC front in the “NETMO-INT” perfectly matches the LC contour in the NR. In the other forecasts, there is a notable difference in the initial LC shapes compared to the NR. In 2011 after 30 days, the forecasts tend to predict LCE shedding (except for the “NEMO-INT” and

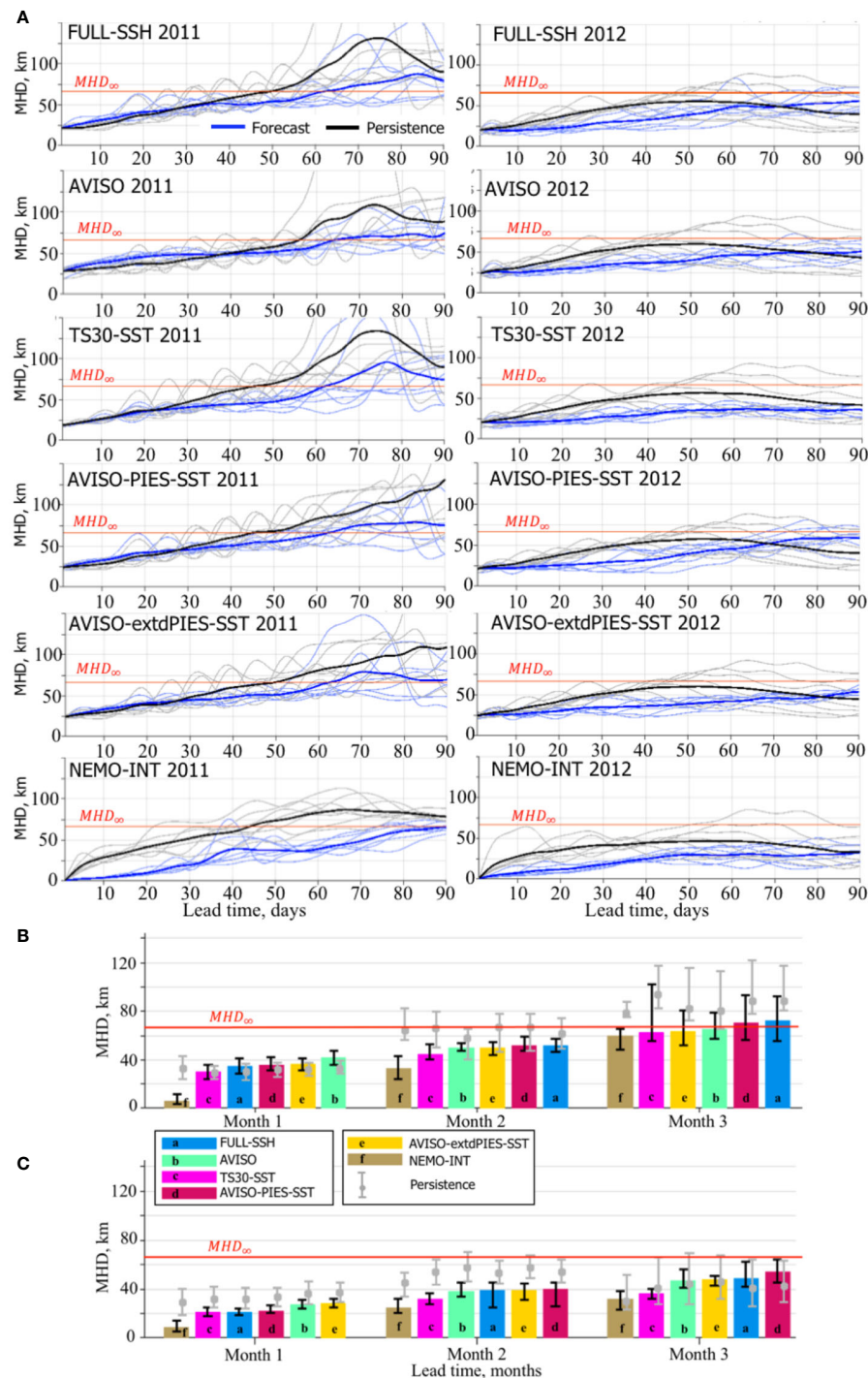


FIGURE 15

MHD scores for LC/LCE fronts derived from OSSE SSH forecasts and the NR. (A) Daily MHD scores for individual forecasts and persistence from the OSSE forecast groups during 2011 (left column) and 2012 (right column). The bold solid lines are the mean MHD scores for the forecasts (blue) and persistence (black). The horizontal red line indicates 95% of the saturation value ( $MHD_{\infty} = 66.3$  m). The bar diagrams (B, C) show median MHD score (km) from forecasts within the forecast group (shown with colors and letters corresponding to the OSSE forecast groups) during forecast months 1 through 3 started in May–June 2011 (A) and January–February 2012 (B). Within each month, the OSSE forecast groups are ranked based on the median MHD score. The vertical black lines on top of the bars indicate the IQR. The grey line and the bullet on the line show the IQR and the median of the persistence corresponding to the OSSE forecasts. The horizontal red line indicates  $MHD_{\infty}$ .

“FULL-SSH”), whereas the LC has not shed an eddy in the NR. In this case, persistence has a better match with the NR in terms of the LC front. By the end of the second month, the LC in the NR sheds an eddy. Now, the forecasts that have predicted an eddy shedding

have a better resemblance with the NR and lower MHD score than those that have not. Persistence, on average, has higher MHD score (lower predictive skill) than the OSSE forecasts because its LC does not change and has not shed an eddy. By the end of the forecast



cycle (day 90), the LC in the NR has an extended shape protruding far west. In fact, the 0.17 m contour combines several small anticyclones that form a chain of intense anticyclonic eddies within the LC. The forecasts (except the “NEMO-INT”) fail to predict exactly this shape of the LC. However, the forecasts have several LCEs that follow the LC extended shape and persistence does not. This explains a better predictive skill for the forecasts during the 3<sup>rd</sup> month.

In 2012, the forecasts follow closely the NR during the 1<sup>st</sup> month, and even after 60 days, most of the forecasts have good predictive skills of the LC frontal position. By the end of the forecast cycle, the forecasts predict eddy shedding or a more extended LC than it is in the NR. Whereas, in the NR the LC returns to a shape that is similar to the initial state. This explains better scores for persistence during the 3<sup>rd</sup> month.

## 5 Discussion

The analyses of the OSEs and OSSEs presented here provide information about time scales of predictability for the 1/32.5° IAS HYCOM-TSIS forecast system. The predictability estimates discussed here depend on the choice of the skill metrics and parameters used for skill assessment. The assessments of predictive skills are based on RMSE and MHD and the concept of saturation value (Lorenz, 1965; Lorenz, 1982). The metrics are compared to the 95% of the saturation values for RMSE and MHD scores ( $RMSE_{\infty}$  and  $MHD_{\infty}$ ) to estimate the model predictability of the LC system. Both OSE and OSSE forecasts demonstrate that the forecast system has predictive skills sufficient for medium-range predictions of the LC system. In the OSEs in >75% the model produces reliable forecasts at least for 2 months with <50% by the end of 3 months. The RMSE and MHD scores averaged over the forecasts approach saturation values by the end of 3 months, suggesting that the limit of the predictability is about 90 days for this system with this set of observations assimilated during the analysis. A similar estimate of the model predictability is suggested by the OSSEs.

As expected, the best predictability is demonstrated by the forecasts initialized from the interpolated NR fields (“NEMO-INT”). Even by the end of the forecast window, >50% of the forecasts still have predictive skills of the LC. The overall forecast error depends on the initial error, the modeling system itself (that defines an “error matrix” controlling the error growth rate, following Lorenz, 1965), and the model error (imperfect model scenario which is different from Lorenz “perfect model”). Results of “NEMO-INT” demonstrate that initial error is the main source of uncertainty in the forecast and the primary contributor to the forecast error. Therefore, minimizing error in the initial forecast fields provides the most prominent improvement of the long-range forecasts of the LC system. Whereas, improvement in the model numerics might have smaller impact on the forecast predictability within the 2–3-month range. After 3 months, model errors dominate suggesting that models with improved ability to simulate the LC system would be needed for reliable long-range forecasts.

The derived estimate of the model predictability is hard to compare with the estimates reported in earlier studies (e.g., Oey et al., 2005; Mooers et al., 2012) because of the disagreement in selected metrics, predicted characteristics, criteria of predictability. Results from our study can be compared to Zeng et al. (2015) who used a different metric for evaluation of predictability, but their selection criterion (based on the spatial cross-correlation) would provide a similar decision on the model predictability in terms of RMSE metric used in our study. Zeng et al. (2015) estimated that reliable forecasts could provide reliable predictions of the LC variability up to 4 weeks and in some cases up to 6 weeks (the duration of their forecast window). The IAS HYCOM-TSIS system described here can provide reliable forecast of the LC system for 2 months and up to 3 months demonstrating better predictability. It should be noted again that the estimated predictability depends on the choice of the predicted characteristics. For example, predicting the LCE shedding events is a more challenging task than predicting the frontal position. The predictability of the shedding events would likely be smaller than 2–3 months.

The OSEs and OSSEs clearly demonstrate that the forecast predictive skills of the LC system are controlled by the magnitude of initial error and the growth rate of the error. The result is in agreement with many previous studies starting from Lorenz (1965). The initial error depends on assimilation techniques and amount of information constraining the numerical solution in the analysis that provides the initial state for the forecast run. In the highly idealized case (“NEMO-INT”) with minimal initial error, the predictive skill of the 1/32.5° IAS HYCOM convincingly exceeds 2 months with very small spread in RMSE and MHD scores across the individual forecasts. The magnitude of the initial error impacts the growth rate of the error. In the presented forecasts, the smaller error has slower growth rate and in the forecast initialized from the interpolated NR fields (“NEMO-INT”), the growth rate is close to linear. The experiments demonstrate different predictive skills for the LC in a stable and unstable phase. In general, the forecasts have shorter predictability for unstable LC.

One of the unexpected results in the OSSEs is the quick decrease of predictive skills in the “FULL-SSH” forecasts (Figures 13B, C, 15B, C). The forecasts are initialized from the analysis constrained by complete SLA fields from the NR producing accurate initial fields (Figures 13A, 15A). Despite the fact that the forecast has small initial error (~0.05 m), the growth rate of the forecast error is on average higher than in the other OSSE forecasts resulting in a lower performance than some other forecasts initialized from less accurate analysis after one month. Also, the “FULL-SSH” forecasts have higher RMSE along the LC front than the “T30-SST” forecasts, which do not use SLA to constrain the SSH. This can be related to errors introduced by the SLA interpolation technique projecting SLA information into subsurface layers. HYCOM-TSIS employs a layerized version of the Cooper and Haines (1996) algorithm to ingest altimetry SLA by adjusting the layer thicknesses of the isopycnic layers using potential vorticity conservation. This approach indirectly impacts the T/S structure in the subsurface layers that is less precise than direct ingestion of T/S profiles in the “TS30-SST”. Therefore, the T/S fields in the “TS30-SST” are better constrained and provide more accurate vertical baroclinic structure



of the mesoscale features in the Gulf resulting in better long-term predictions than in the “FULL-SSH”, which is also true for other forecasts where T/S profiles are directly assimilated (Figure 9B).

The added value of an extended PIES array is demonstrated in the OSSE analysis fields during 2011 and 2012 (Figures 8B, C). Nevertheless, predictive skills of the forecasts with “AVISO-extdPIES-SST” initial fields are different in 2011 and 2012 (Figures 13, 15). This suggests that T/S profiles are useful when they provide information about the baroclinic structure of the LC at critical locations and times. During 2011, synthetic T/S profiles derived at extended PIES locations provide additional information about the LC and LCE shedding improving the forecasts. In 2012, when the LC is in a more stable position, this information is not essential and the added benefit of this information is low. The idea is further supported by the RMSE analysis discussed in section 4.2.1 demonstrating good predictive skills of the “AVISO-extdPIES-SST” forecasts when compared to the other forecasts in 2011, but not in 2012 (Figures 11–13). These results demonstrate that adding more data to a data assimilative system does not always result in notable improvement of the forecasts because data have different informative value for the forecasting system. Collection of observational information and its delivery to the prediction systems can be optimized *via* an automated process of adaptive sampling (Lermusiaux et al., 2006; Lermusiaux et al., 2017) based on optimal timing and location of observational platforms. Adaptive sampling predicts what type of observation available over the sampling time period to be collected and at what location to provide the most critical information for predicted ocean variable (Lermusiaux et al., 2017). Adaptive sampling combined with OSE/OSSEs can be utilized to infer information about the most optimal way to complement existing observational sites with observations collected by autonomous platforms and sensors.

Predictability estimates depend on the choice of skill assessment metrics. In our study, the two metrics we use are based on different norm definitions and focus on different aspects of the analyzed data, yet there is good agreement between them for the model skill assessment. The RMSE is the most utilized metric for model predictability evaluation with its advantages and limitations (e.g., Schneider and Griffies, 1999). The MHD is robust metric that is particularly useful for quantitative comparison of N-dimensional shapes or contours and is useful for comparison of oceanic frontal positions. For best performance, the metric requires unambiguous definition of the contours (fronts) being compared. The LC front definition based on the 0.17 m contours of SSH fields is not optimal for our study because it results in instantaneous substantial changes of the LC frontal position during LC and LCE detachment and reattachment leading to large errors in the forecast if the timing of the process is not exact in the forecast. This artificially degrades the forecast skill. Such definition of the LC front would work best for evaluating predictability of the LCE shedding event using the MHD metric, but it is less useful for our purposes. A better definition of the LC front (e.g., Laxenaire et al., 2023) can provide more consistent scores, thus reducing the spread of the scores in the individual forecasts.

## 6 Summary

The presented study evaluates the forecast skill of the 1/32.5° IAS HYCOM-TSIS based on the OSE/OSSEs. Existing high-resolution models can provide skillful forecasts of the LC system up to 2 months when initialized with near-real time available observations and data assimilation techniques. Predictability limits depend on activity state of the LC, with active LC configurations presenting more challenges for the model forecasts. Results also suggest that substantial improvements in forecasts out to 3 months can be achieved with increased accuracy of initial conditions derived from analysis. This further suggests that the short-range and medium-range (up to 3 months) forecasts of the LC system can be improved through adding observational information and better assimilation techniques. However, adding more observational data does not always improve the forecasts. The numerical experiments have demonstrated the added value of T/S profiles that provide information about vertical baroclinic structure of the mesoscale features in the Gulf. However, the impact of T/S profiles on the forecasts is notable when the information is provided at critical locations and times. In other cases, additional information derived from the T/S profiles has minor impact on the model forecasting skills. Therefore, we argue that optimization of observational information *via* adaptive sampling may play a crucial role in the improvement of the short- and medium-range forecasts. The impact of the initial error or the accuracy of the initial state on the forecast accuracy is less obvious after 3 months when model errors start dominate. Hence, additional observations assimilated into analysis providing initial state for the forecasts may have little impact on the forecast skills after 3 months. Increased accuracy of the long-range forecasts can be achieved with improved modeling techniques.

## Data availability statement

The raw data supporting the conclusions of this article will be made available by the authors, without undue reservation.

## Author contributions

EC – design of the study and numerical experiments, editing the manuscript. AB – preparation and running numerical experiments, development of HYCOM-TSIS, data processing. SM – design of the numerical experiments, editing the manuscript. DD – original draft preparation, data processing and analysis, preparation and running numerical experiments, preparation of figures, design of numerical experiments. All authors participated in discussions and interpretation of the model results, contributed to the writing of the manuscript and approved the submitted version.

## Funding

We acknowledge support from the Gulf Research Program of the National Academies of Sciences, Engineering, and Medicine under award numbers 2000009966 and 2000013149. The content is solely the responsibility of the authors and does not necessarily represent the official views of the Gulf Research Program or the National Academies of Sciences, Engineering, and Medicine.

## Acknowledgments

We acknowledge Julio Sheinbaum (CICESE) for his help with accessing NEMO data and Ashwanth Srinivasan (Tendral) for providing support with TSIS. We acknowledge our colleagues participating in UGOS-1 and the NASEM UGOS Standing Committee for helpful discussions and ideas on model predictability shared during project meetings. We thank Michael McDonald (FSU) for providing IT support during this

project. Numerical simulations were performed on FSU RCC supercomputing facilities.

## Conflict of interest

The authors declare that the research was conducted in the absence of any commercial or financial relationships that could be construed as a potential conflict of interest.

## Publisher's note

All claims expressed in this article are solely those of the authors and do not necessarily represent those of their affiliated organizations, or those of the publisher, the editors and the reviewers. Any product that may be evaluated in this article, or claim that may be made by its manufacturer, is not guaranteed or endorsed by the publisher.

## References

- Abascal, A. J., Sheinbaum, J., Candela, J., Ochoa, J., and Badan, A. (2003). Analysis of flow variability in the Yucatan channel. *J. Geophys. Res.* 108 (C12), 3381. doi: 10.1029/2003JC001922
- Bleck, R. (2002). An oceanic general circulation model framed in hybrid isopycnal-Cartesian coordinates. *Ocean Model.* 37, 55–88. doi: 10.1016/S1463-5003(01)00012-9
- Boer, G. J. (2000). A study of atmosphere-ocean predictability on long time scales. *Climate Dynamics*. 16, 469–477. doi: 10.1007/s003820050340
- Charney, J. G., Fleagle, R. G., Lally, V. E., Riehl, H., and Wark, D. Q. (1966). The feasibility of a global observation and analysis experiment. *Bull. Am. Meteorol. Soc.* 47, 200–220. doi: 10.1175/1520-0477-47.3.200
- Chassignet, E. P., Smith, L. T., Halliwell, G. R., and Bleck, R. (2003). North Atlantic simulation with the HYbrid coordinate ocean model (HYCOM): Impact of the vertical coordinate choice, reference density, and thermobaricity. *J. Phys. Oceanogr.* 33, 2504–2526. doi: 10.1175/1520-0485(2003)033<2504:NASWTH>2.0.CO;2
- Cooper, M., and Haines, K. (1996). Altimetric assimilation with water property conservation. *J. Geophys. Res.* 101 (C1), 1059–1077. doi: 10.1029/95JC02902
- Dalcher, A., and Kalnay, E. (1987). Error growth and predictability in operational ECMWF forecasts. *Tellus A: Dynamic Meteorol. Oceanogr.* 39 (5), 474–491. doi: 10.3402/tellusa.v39i5.11774
- Damien, P., Sheinbaum, J., de Fommervault, O. P., Jouanno, J., Linacre, L., and Duteil, O. (2021). Do loop current eddies stimulate productivity in the gulf of Mexico? *Biogeosciences* 18, 4281–4303. doi: 10.5194/bg-18-4281-2021
- DelSole, T. (2004). Predictability and information theory. part I: Measures of predictability. *J. Atmospheric Sci.* 61 (20), 2425–2440. doi: 10.1175/1520-0469(2004)061<2425:PAITPI>2.0.CO;2
- Donohue, K., Watts, D., Hamilton, P., Kennelly, M., and Lugo-Fernández, A. (2016b). Gulf of Mexico loop current path variability. *Dyn. Atmos. Ocean* 76, 174–194. doi: 10.1016/j.dynatmoce.2015.12.003
- Donohue, K. A., Watts, D. R., Hamilton, P., Leben, R., and Kennelly, M. (2016a). Loop current eddy formation and baroclinic instability. *Dynamics Atmosphere Oceans* 76 (2), 195–216. doi: 10.1016/j.dynatmoce.2016.01.004
- Dubuisson, M.-P., and Jain, A. K. (1994). A modified hausdorff distance for object matching. *Pattern Recognition* 1, 566–568. doi: 10.1109/ICPR.1994.576361
- Dukhovskoy, D. S., Leben, R. R., Chassignet, E. P., Hall, C., Morey, S. L., and Nedbor-Gross, R. (2015a). Characterization of the uncertainty of loop current metrics using a multidecadal numerical simulation and altimeter observations. *Deep-Sea Res. I* 100, 140–158. doi: 10.1016/j.dsr.2015.01.005
- Dukhovskoy, D. S., Ufnoske, J., Blanchard-Wrigglesworth, E., Hiester, H. R., and Proshutinsky, A. (2015b). Skill metrics for evaluation and comparison of sea ice models. *J. Geophys. Res.* 120, 5910–5931. doi: 10.1002/2015JC010989
- Dussin, R., Barnier, B., Brodeau, L., and Molines, J. M. (2016). *Drakkar forcing set DFS5*. MyOcean Report. Available at: [https://www.drakkar-ocean.eu/publications/reports/report\\_DFS5v3\\_April2016.pdf](https://www.drakkar-ocean.eu/publications/reports/report_DFS5v3_April2016.pdf).
- Edson, J. B., Jampana, V., Weller, R. A., Bigorre, S. P., Plueddemann, A. J., Fairall, C. W., et al. (2013). On the exchange of momentum over the open ocean. *J. Phys. Oceanogr.* 43 (8), 22. doi: 10.1175/jpo-d-12-0173.1
- Fujii, Y., Rémy, E., Zuo, H., Oke, P., Halliwell, G., Gasparin, F., et al. (2019). Observing system evaluation based on ocean data assimilation and prediction systems: On-going challenges and a future vision for designing and supporting ocean observational networks. *Front. Mar. Sci.* 6. doi: 10.3389/fmars.2019.00417
- Goessling, H. F., and Jung, T. (2018). A probabilistic verification score for contours: Methodology and application to Arctic ice-edge forecast, q. *J. R. Meteor. Soc.* 144, 735–743. doi: 10.1002/qj.3242
- Gower, J. F. R., and King, S. A. (2011). Distribution of floating sargassum in the gulf of Mexico and the Atlantic ocean mapped using MERIS'. *Int. J. Remote Sens.* 32 (7), 1917–1929. doi: 10.1080/01431161003639660
- Halliwell, G. R. (2004). Evaluation of vertical coordinate and vertical mixing algorithms in the HYbrid-coordinate ocean model (HYCOM). *Ocean Model.* 7, 285–322. doi: 10.1016/j.ocemod.2003.10.002
- Hamilton, P., Donohue, K., Hall, C., Leben, R. R., Quian, H., Sheinbaum, J., et al. (2014). Observations and dynamics of the loop current. *OCS Study BOEM 5015-006 New Orleans LA* 2014, 417.
- Hiester, H. R., Morey, S. L., Dukhovskoy, D., Chassignet, E. P., Kourafalou, V. H., and Hu, C. (2016). A topological approach for quantitative comparisons of ocean model fields to satellite ocean color data. *Methods Oceanogr.* 17, 232–250. doi: 10.1016/j.mio.2016.09.005
- Krause, P., Boyle, D. P., and Bäse, F. (2005). Comparison of different efficiency criteria for hydrological model assessment. *Adv. Geosciences* 5, 89–97. doi: 10.5194/advge-5-89-2005
- Krishnamurthy, V. (2019). Predictability of weather and climate. *Earth Space Sci.* 6, 1043–1056. doi: 10.1029/2019EA000586
- Lahoz, W. A., and Schneider, P. (2014). Data assimilation: Making sense of earth observation, front. *Environ. Sci. Sec. Atmospheric Sci.* 2, 1–28. doi: 10.3389/fenvs.2014.00016
- Large, W. G., McWilliams, J. C., and Doney, S. C. (1994). Oceanic vertical mixing: A review and a model with a nonlocal boundary layer parameterization. *Rev. Geophys.* 32 (4), 363–403. doi: 10.1029/94RG01872
- Latif, M., Anderson, D., Barnett, T., Cane, M., Kleeman, R., Leetmaa, A., et al. (1998). A review of the predictability and prediction of ENSO. *J. Geophysical Res.* 103 (C7), 375–314. doi: 10.1029/97JC03413
- Laxenaire, R., Chassignet, E. P., Dukhovskoy, D., and Morey, S. L. (2023). Impact of upstream variability on the loop current dynamics in numerical simulations of the gulf of Mexico. *Front. Mar. Sci.* 10. doi: 10.3389/fmars.2023.1080779
- Leben, R. R. (2005). "Altimeter-derived loop current metrics," in *Circulation in the gulf of Mexico: Observations and models*. Eds. W. Sturges and A. Lugo-Fernandez (AGU, Washington: American Geophysical Union). doi: 10.1029/161GM15

- Lellouche, J.-M., Greiner, E., Romain, B.-B., Gilles, G., Angelique, M., Marie, D., et al. (2021). The Copernicus global 1/12° oceanic and Sea ice GLORYS12 reanalysis. *Front. Earth Sci.* 21. doi: 10.3389/feart.2021.698876
- Lermusiaux, P. F. J., Chiu, C.-S., Gawarkiewicz, G. G., Abbot, P., Robinson, A. R., Miller, R. N., et al. (2006). Quantifying uncertainties in ocean predictions. *Oceanography* 19 (1), 92–105. doi: 10.5670/oceanog.2006.93
- Lermusiaux, P. F. J., Subramani, D. N., Lin, J., Kulkarni, C. S., Gupta, A., Dutt, A., et al. (2017). A future for intelligent autonomous ocean observing systems. *The sea. J. Marine Res.* 75 (6), 765–813. doi: 10.1357/002224017823524035
- Liu, Y., Weisberg, R. H., Lenes, J. M., Zheng, L., Hubbard, K., and Walsh, J. J. (2016). Offshore forcing on the “pressure point” of the West Florida shelf: Anomalous upwelling and its influence on harmful algal blooms. *J. Geophys. Res. Oceans* 121, 5501–5515. doi: 10.1002/2016JC011938
- Lorenz, E. (1965). A study of the predictability of a 28-variable atmospheric model. *Tellus* 17 (3), 321–333. doi: 10.1111/j.2153-3490.1965.tb01424.x
- Lorenz, E. N. (1982). Atmospheric predictability experiments with a large numerical model. *Tellus* 34, 505–513. doi: 10.3402/tellusa.v34i6.10836
- Lorenz, E. N. (1984). “Some aspects of atmospheric predictability,” in *Problems and prospects in long and medium range weather forecasting*. Eds. D. M. Burridge and E. Kallen (Berlin: Springer-Verlag), 1–20.
- Madec, G., Bourdallé-Badie, R., Bouttier, P.-A., Bricaud, C., Bruciaferri, D., Calvert, D., et al. (2017). *NEMO ocean engine (Version v3.6)*. Notes Du Pôle De Modélisation De L’institut Pierre-simon Laplace (IPSL), Zenodo. doi: 10.5281/zenodo.1472492
- Melsom, A., Palerme, C., and Muller, M. (2019). Validation metrics for ice edge position forecasts. *Ocean Sci.* 15, 615–630. doi: 10.5194/os-15-615-2019
- Metzger, E. J., Smedstad, O. M., Thoppil, P. G., Hurlburt, H. E., Cummings, J. A., Wallcraft, A. J., et al. (2014). US Navy operational global ocean and Arctic ice prediction systems. *Oceanography* 27 (3), 32–43. doi: 10.5670/oceanog.2014.66
- Mittermaier, M. P. (2008). The potential impact of using persistence as a reference forecast on perceived forecast skill. *Weather Forecasting* 23 (5), 1022–1031. doi: 10.1175/2008WAF0007037.1
- Mooers, C. N. K., Zaron, E. D., and Howard, M. K. (2012). “Final report for phase I: Gulf of Mexico 3-d operational ocean forecast system pilot prediction project,” in *Final report to research partnership to secure energy for America*. Houston, TX, 149.
- Murphy, S. J., Hurlburt, H. E., and O’Brien, J. J. (1999). The connectivity of eddy variability in the Caribbean Sea, the gulf of Mexico, and the Atlantic ocean. *JGR* 104 (C1), 1431–1453. doi: 10.1029/1998JC000010
- National Academies of Sciences, E., & Medicine (2018). “Understanding and predicting the gulf of Mexico loop current,” in *Critical gaps and recommendations* (Washington, DC: The National Academies Press). doi: 10.17226/24823
- Niraula, B., and Goessling, H. F. (2021). Spatial damped anomaly persistence of the sea ice edge as a benchmark for dynamical forecast systems. *J. Geophysical Research: Oceans* 126, e2021JC017784. doi: 10.1029/2021JC017784
- Oey, L.-Y., Ezer, T., Foristall, G., Cooper, C., DiMarco, S., and Fan, S. (2005). An exercise in forecasting loop current and eddy frontal positions in the gulf of Mexico. *GRL* 32, L12611. doi: 10.1029/2005GL023253
- Schneider, T., and Griffies, S. M. (1999). A conceptual framework for predictability studies. *J. Climate* 12, 3133–3155. doi: 10.1175/1520-0442(1999)012<3133:ACFFPS>2.0.CO;2
- Selph, K. E., Swalethorp, R., Stukel, M. R., Kelly, T. B., Knapp, A. N., Fleming, K., et al. (2022). Phytoplankton community composition and biomass in the oligotrophic gulf of Mexico. *J. Plankton Res.* 44 (5), 618–637. doi: 10.1093/plankt/fbab006
- Shay, L. K., Goni, G. J., and Black, P. G. (2000). Effects of a warm oceanic feature on hurricane opal. *Mon. Wea. Rev.* 128, 1366–1383. doi: 10.1175/1520-0493(2000)128<1366:EOAWOF>2.0.CO;2
- Sheinbaum, J., Candela, J., Badan, A., and Ochoa, J. (2002). Flow structure and transports in the Yucatan channel. *Geophys. Res. Lett.* 29 (3), 1040. doi: 10.1029/2001GL0139990
- Srinivasan, A., Chin, T. M., Chassignet, E. P., Iskandarani, M., and Groves, N. (2022). A statistical interpolation code for ocean analysis and forecasting. *J. Atm. Oc. Techn* 39, 367–386. doi: 10.1175/JTECH-D-21-0033.1
- Thoppil, P. G., Frolov, S., Rowley, C. D., Reynolds, C. A., Jacobs, G. A., Metzger, E. J., et al. (2021). Ensemble forecasting greatly expands the prediction horizon for ocean mesoscale variability. *Commun. Earth Environ.* 2, 89. doi: 10.1038/s43247-021-00151-5
- Vukovich, F. M., and Maul, G. (1985). Cyclonic eddies in the eastern gulf of Mexico. *J. Phys. Oceanogr.* 15 (1), 105–117. doi: 10.1175/1520-0485(1985)015<0105:CEITEG>2.0.CO;2
- Walker, N. D., Pilley, C. T., Raghunathan, V. V., D’Sa, E. J., Leben, R. R., Hoffmann, N. G., et al. (2011). “Impacts of loop current frontal cyclonic eddies and wind forcing on the 2010 gulf of Mexico oil spill,” in *Monitoring and modeling the deepwater horizon oil spill: A record-breaking enterprise*. Eds. Y. Liu, A. MacFadyen, Z.-G. Ji and R. H. Weisberg (Washington, DC: American Geophysical Union), 103–116. doi: 10.1029/2011GM001120
- Weisberg, R. H., Zheng, L., and Liu, Y. (2017). On the movement of deepwater horizon oil to northern gulf beaches. *Ocean Model.* 111, 81–97. doi: 10.1016/j.ocemod.2017.02.002
- Weisberg, R., Zheng, L., and Peebles, E. (2014). Gag grouper larvae pathways on the West Florida shelf. *Continental Shelf Res.* 88, 11–23. doi: 10.1016/j.csr.2014.06.003
- Wilks, D. (2006). *Statistical methods in atmospheric sciences. 2nd ed* Vol. 91 (Oxford, UK: Academic Press), 648.
- Zavala-Hidalgo, J., Morey, S., and O’Brien, J. (2003). Cyclonic eddies northeast of the campeche bank from altimetry data. *J. phys. Oceanogr.* 33 (3), 623–629. doi: 10.1175/1520-0485(2003)033<0623:CENOTC>2.0.CO;2
- Zeng, X., Li, Y., and He, R. (2015). Predictability of the loop current variation and eddy shedding process in the gulf of Mexico using an artificial neural network approach. *J. Atmospheric Oceanic Technol.* 32 (5), 1098–1111. doi: 10.1175/JTECH-D-14-00176.1
- Zerangue, B. A., Hahn, M. B., Riches, T. J., Maclay, D. M., and Wilson, M. G. (2022). “U.S. outer continental shelf gulf of Mexico region oil and gas production forecast: 2022-2031,” in *OCS report BOEM 2022-022* (New Orleans: U.S. Department of the Interior Bureau of Ocean Energy Management Gulf of Mexico OCS Region Office of Resource Evaluation), 28.



## OPEN ACCESS

## EDITED BY

Jacopo Chiggiato,  
National Research Council (CNR), Italy

## REVIEWED BY

Zhiwei Zhang,  
Ocean University of China, China  
Matthieu Le Hénaff,  
University of Miami, United States  
Evan Mason,  
Spanish National Research Council (CSIC),  
Spain

## \*CORRESPONDENCE

Gaston Manta

✉ gmanta@ucsd.edu

RECEIVED 01 February 2023

ACCEPTED 09 May 2023

PUBLISHED 25 May 2023

## CITATION

Manta G, Durante G, Candela J, Send U,  
Sheinbaum J, Lankhorst M and Laxenaire R  
(2023) Predicting the Loop Current  
dynamics combining altimetry and deep  
flow measurements through the Yucatan  
Channel.  
*Front. Mar. Sci.* 10:1156159.  
doi: 10.3389/fmars.2023.1156159

## COPYRIGHT

© 2023 Manta, Durante, Candela, Send,  
Sheinbaum, Lankhorst and Laxenaire. This is  
an open-access article distributed under the  
terms of the [Creative Commons Attribution  
License \(CC BY\)](https://creativecommons.org/licenses/by/4.0/). The use, distribution or  
reproduction in other forums is permitted,  
provided the original author(s) and the  
copyright owner(s) are credited and that  
the original publication in this journal is  
cited, in accordance with accepted  
academic practice. No use, distribution or  
reproduction is permitted which does not  
comply with these terms.

# Predicting the Loop Current dynamics combining altimetry and deep flow measurements through the Yucatan Channel

Gaston Manta<sup>1\*</sup>, Giovanni Durante<sup>2</sup>, Julio Candela<sup>2</sup>, Uwe Send<sup>1</sup>,  
Julio Sheinbaum<sup>2</sup>, Matthias Lankhorst<sup>1</sup> and Rémi Laxenaire<sup>3,4,5</sup>

<sup>1</sup>Scripps Institution of Oceanography, University of California, San Diego, La Jolla, CA, United States,

<sup>2</sup>Departamento de Oceanografía Física, Centro de Investigación Científica y de Educación Superior de Ensenada (CICESE), Ensenada, Mexico, <sup>3</sup>Center for Ocean-Atmospheric Prediction Studies, Florida State University, Tallahassee, FL, United States, <sup>4</sup>Laboratoire de Météorologie Dynamique, LMD-IPSL, UMR 8539, École Polytechnique, ENS, CNRS, Paris, France, <sup>5</sup>Laboratoire de l'Atmosphère et des Cyclones (LACy, UMR 8105 CNRS, Université de la Réunion, Météo-France), Université de La Réunion, Saint-Denis de La Réunion, France

The Loop Current is the main mesoscale feature of the Gulf of Mexico oceanic circulation. With peak velocities above  $1.5 \text{ m s}^{-1}$ , the Loop Current and its mesoscale eddies are of interest to fisheries, hurricane prediction and of special concern for the security of oil rig operations in the Gulf of Mexico, and therefore understanding their predictability is not only of scientific interest but also a major environmental security issue. Combining altimetric data and an eddy detection algorithm with 8 years of deep flow measurements through the Yucatan Channel, we developed a predictive model for the Loop Current extension in the following month that explains 74% of its variability. We also show that 4 clusters of velocity anomalies in the Yucatan Channel represent the Loop Current dynamics. A dipole with positive and negative anomalies towards the western side of the Channel represents the growing and retracted phases respectively, and two tripole shape clusters represent the transition phases, the one with negative anomalies in the center associated with 50% of the eddy separation events. The transition between these clusters is not equally probable, therefore adding predictability. Finally, we show that eddy separation probability begins when the Loop Current extends over 1800 km ( $\sim 27.2^\circ\text{N}$ ), and over 2200 km of extension, eddy detachment and reattachment is more frequent than separation. These results represent a step forward towards having the best possible operational Loop Current forecast in the near future, incorporating near real-time data transmission of deep flow measurements and high resolution altimetric data.

## KEYWORDS

Yucatan Channel, Loop Current, Gulf of Mexico, eddy shedding, mooring, satellite altimetry



## 1 Introduction

The Gulf of Mexico is a sea in the North Atlantic that is about 1700 km wide, connected to the Caribbean Sea and the North Atlantic through the Yucatan Channel and Florida Straits, respectively. The Yucatan Channel is wider (200 km) and deeper (2040 m) than the Florida Straits, which is 150 km wide and about 1400 m deep between Havana and the Florida Keys, but only 800 m between Miami and Bimini, and its topography is also more complex (Sturges and Evans, 1983). In a very first approximation, at seasonal/annual scales, a mean of about 27.2 Sv enters the Gulf through the Yucatan Channel, as the Loop Current, and goes out into the North Atlantic through the Florida Straits (Candela et al., 2019).

The Loop Current is the main mesoscale dynamic feature of the Gulf of Mexico (Figure 1), having a major impact on the circulation and its variability (Leben, 2005). The Loop Current carries warm

and saline Caribbean waters into the Gulf and sheds large anticyclonic eddies at irregular intervals, ranging from 6 to 12 months, with occasional longer shedding interval of 18 months (Sturges and Leben, 2000; Oey et al., 2003; Leben, 2005; Laxenaire et al., 2023). The eddy shedding is mostly driven by barotropic instability (e.g. Yang et al., 2023), and the retreat latitude of the Loop Current after an eddy shedding is linearly correlated with the time to the following shedding (Lugo-Fernández and Leben, 2010). Altimetric data allows to identify the Loop Current dynamics and also to identify and track the shedding of eddies (e.g. Hall and Leben, 2016). With peak velocities above  $1.5 \text{ m s}^{-1}$ , the Loop Current and its mesoscale eddies are of interest to many activities and of special concern for the security to oil rig operations in the Gulf of Mexico, particularly over the Sigsbee escarpment. Therefore understanding its predictability is not only of scientific interest but also a major environmental concern (National Academies of Sciences, Engineering, Medicine et al., 2018).

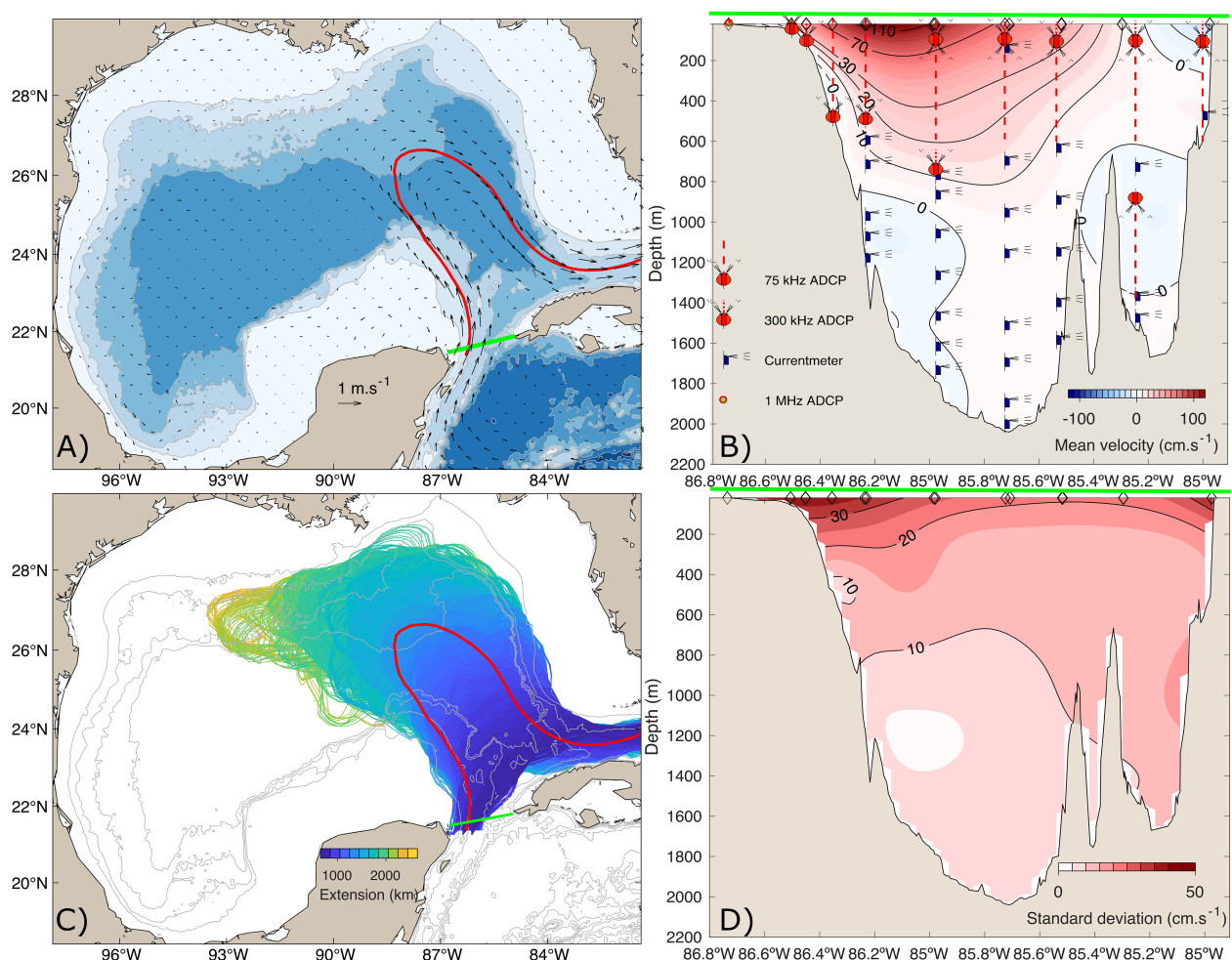


FIGURE 1

(A) Map of the Gulf of Mexico. Shaded colors show the bathymetry, while black vectors are the altimeter-derived mean geostrophic velocity. The Loop Current mean position also tracked from altimetry is shown in red, and the mooring array location in green. (B) Section of the Yucatan Channel. Shaded colors show the mean velocity through the channel ( $\text{cm s}^{-1}$ ) computed from 8 years of gridded *in-situ* observations. The instruments used in each mooring are also sketched. Modified from (Candela et al., 2019). (C) Loop Current position in the Gulf of Mexico from 29 years of daily altimetry data. The color scale represents the extension (in km) of each day. The Loop Current mean position also tracked from altimetry is shown in red, and the mooring array location in green. (D) Standard deviation ( $\text{cm s}^{-1}$ ) of the mean velocity across Yucatan Channel from 8 years of continuous *in-situ* observations from moorings as shown in (C).

The Yucatan Channel has been identified as a crucial section to monitor in order to understand and forecast the Loop Current extension/retraction processes and eddy shedding events (Reid, 1972; Candela et al., 2002; Sheinbaum et al., 2002; Athié et al., 2012; Hall and Leben, 2016; Hamilton et al., 2016). Given its relevance, mooring arrays have been deployed in the Yucatan Channel since 1999, in what is called the CANEK project (Ochoa et al., 2003). This mooring section allowed us to study the whole vertical and horizontal flow structure, its variability and its mean state over relatively long periods of time (Sheinbaum et al., 2002; Abascal et al., 2003; Athié et al., 2015; Candela et al., 2019). The main feature of the velocity field in the Yucatan section is the Yucatan Current, whose horizontal displacements are highly correlated with the first two principal components of the empirical orthogonal function (EOF) analysis applied to the velocity field (Abascal et al., 2003). Hence, these horizontal displacements of the Yucatan Current contribute the larger part of the variability along the entire section (Abascal et al., 2003; Candela et al., 2003; Sheinbaum et al., 2016; Athié et al., 2020). The characteristics of the flow variability through the Yucatan section present a relatively weak annual and semiannual cycle, explaining 19% and 32% of the transport variance respectively (Athié et al., 2020).

Previous modeling efforts suggest that both the surface and deep flow contribute to the predictability of the Loop Current (Oey, 1996; Vazquez et al., 2023), as it was proposed by Maul (1977), and tested later by Bunge et al. (2002) through observational *in-situ* and satellite data. Still, the predictability of the Loop Current evolution from the flow at the Yucatan Channel is far from well understood. Therefore, the objective of this manuscript is to use the *in-situ* observations of the flow variability through Yucatan Channel combined with altimetric data to understand and predict the Loop Current extension and eddy separation events.

## 2 Data

### 2.1 Gridded *in-situ* data: the CANEK database

We used an optimal interpolation product generated by Durante et al. (2023) from observational mooring array data. The dataset provides ocean currents (speed and direction) in the Yucatan Channel throughout the water column. The instrumentation on the moorings is a combination of Acoustic Doppler Current Profilers (ADCPs) and current meters in a configuration with up to ten moorings in the array as shown in Figure 1. The data cover the time period from July 2012 to July 2020, achieving more than 8 years with 99.9% of temporal coverage from hourly measurements. The mooring array was serviced approximately once per year, configurations changed slightly between deployments, and more moorings were added in the 2018–2020 period. See Candela et al. (2019) for details about each of the moorings deployments, instruments and configurations.

Before the spatial gridding procedure, standard processing and data quality management is carried out. Then, a gridding process is done using the optimal interpolation method (Bretherton et al., 1976; Roemmich, 1983). Gaussian spatial auto-correlation functions are implemented with decorrelation scales of 70 km and 500 m in the horizontal and vertical axis, respectively. Then, spatial mapping is performed onto a regular grid with 0.03° horizontal and 20 m vertical resolution at hourly time step. Daily means used here were computed from hourly means.

### 2.2 Satellite data

This study uses gridded satellite altimetry data distributed by Copernicus Marine Environment Monitoring Service. The data are the DT-2018 version from the Ssalto/Duacs multi-mission processing system that combines observations from multiple satellite missions (Capet et al., 2014; Pujol et al., 2016; Ballarotta et al., 2019), and gridded in space and time to 0.25° horizontal and daily temporal resolution. Here, the properties of absolute dynamic topography and derived surface geostrophic velocity are used, and the study area encompasses the entire Gulf of Mexico over the period 1993–2021.

## 3 Methods

### 3.1 Loop Current metrics and mesoscale eddies detection

Loop Current identification and metrics were computed using two different methods: The first one, following Hamilton et al. (2000) and widely used since then (e.g. Leben, 2005; Gopalakrishnan et al., 2013), consists of tracking the 0.17 m sea level contour connecting the Yucatan Channel with the Florida Straits in the Gulf after removing data outside the Gulf and the daily spatial mean as a way to eliminate the effect of homogeneous surface heating (from now on, the 0.17 m method). Some of the output metrics are the Loop Current extension (length measured in km), and northward (°) and westward (°) maximum extensions (Figures 1, 2).

The second method to identify the Loop Current was developed by Laxenaire et al. (2023). It consists of tracking the sea level streamline associated with maximum geostrophic velocity that connects the Yucatan Channel to the Straits of Florida (from now on, the <V> method). According to the authors, the method ensures that the Loop Current enters and exits the Gulf of Mexico and is more objective. Also, we noticed that it is more robust to unrealistic abrupt changes due to interruptions in the 0.17 m contour (Figure 2).

The method by Laxenaire et al. (2023) also provides an eddy detection algorithm named TOEddies (Chaigneau et al., 2011; Pegliasco et al., 2015; Laxenaire et al., 2018) and therefore, quantitative information on the eddies' interaction with the Loop Current. The TOEddies algorithm is also altimetry based and tracks enclosed streamlines of absolute dynamic topography, assuming

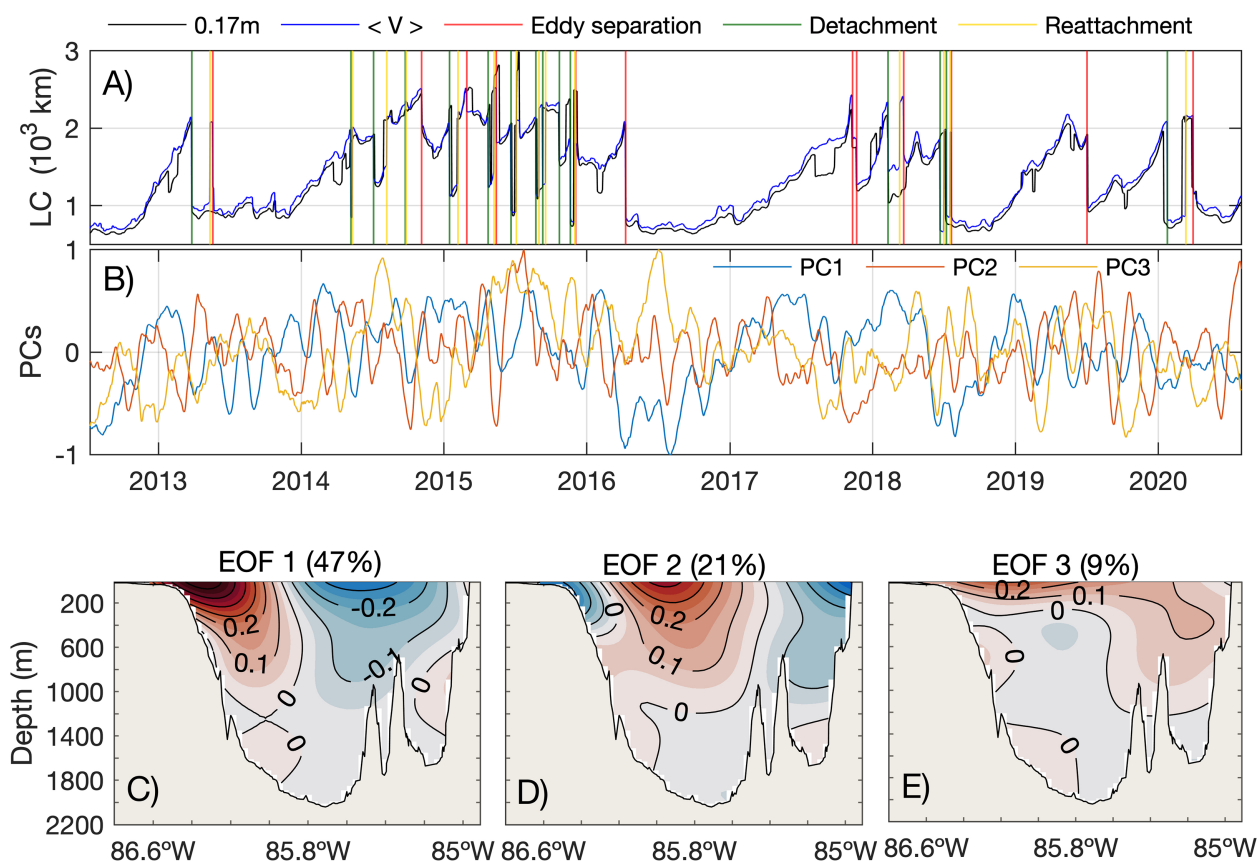


FIGURE 2

(A) Time-series of the Loop Current extension (km) from two different methods. The 0.17 m contour method is colored in black and the maximum gradient method in blue. Vertical red lines show each time an eddy was separated from the Loop Current, while green and yellow show detachment and reattachment events, respectively. (B) Empirical orthogonal function analysis of the *in-situ* flow measurements through the Yucatan Channel. The lines show the first 3 Principal Components, while (C, D, E), the spatial structure of the EOFs, with the explained variance on top.

geostrophic balance. It has been validated by comparing it with other eddy detection algorithms (e.g. Chelton et al., 2011) and *in-situ* observations from drifters (Lumpkin, 2016). The centers of the eddies are identified as extrema of the absolute dynamic topography, and the largest closed streamlines correspond to the boundary of these eddies. The eddy contour associated with the maximum azimuthal velocity, used as the eddy boundary in this study, is also identified. The eddies detected each day are then linked by trajectories if there is a superposition of the surface occupied by them between two time steps. This superposition method, developed by Pegliasco et al. (2015), allows the identification of merging and splitting of eddies.

Following Leben (2005), eddy shedding events by the Loop Current are classified into two groups: an eddy detachment is followed by a reattachment to the Loop Current, while an eddy separation is defined as the final detachment of an eddy from the Loop Current with no later reattachment. In Laxenaire et al. (2023), a comparison is made between the eddy separations obtained by this TOEddies and with respect to the method by Hall and Leben (2016), obtaining very similar results. A detailed description of the algorithm for the detection of eddies and the Loop Current extension can be found in Laxenaire et al. (2018) and Laxenaire et al. (2023), respectively.

### 3.2 *in-situ* data, smoothing and comparison with altimetry

A 21-day low-pass filter was applied to the interpolated mooring data product, in order to have a consistent time resolution between the mooring measurements and the effective time resolution of the altimeter used to detect the Loop Current (Ballarotta et al., 2019). The window for the low-pass filter was selected by finding the maximum correlation between altimetry and the different centered moving mean windows of the *in-situ* data (Figure 3). Then, the moving average window was applied to the mooring data using the current day and the previous 21 days in order to make this applicable to prediction using real-time data.

To estimate the correlation between mapped mooring velocities and altimetry derived geostrophic surface velocities, we first interpolated the altimetry data (25 km horizontal resolution) into the Yucatan section grid (5 km horizontal resolution) and rotated the vectors 10° anticlockwise in order to obtain the velocity through the channel. Then, we computed a linear regression between the interpolated across-channel altimetry geostrophic velocity and the mooring velocity product at each longitude point and over the entire water column, applying an independent linear regression at each depth point. The result was plotted as a section of the Pearson

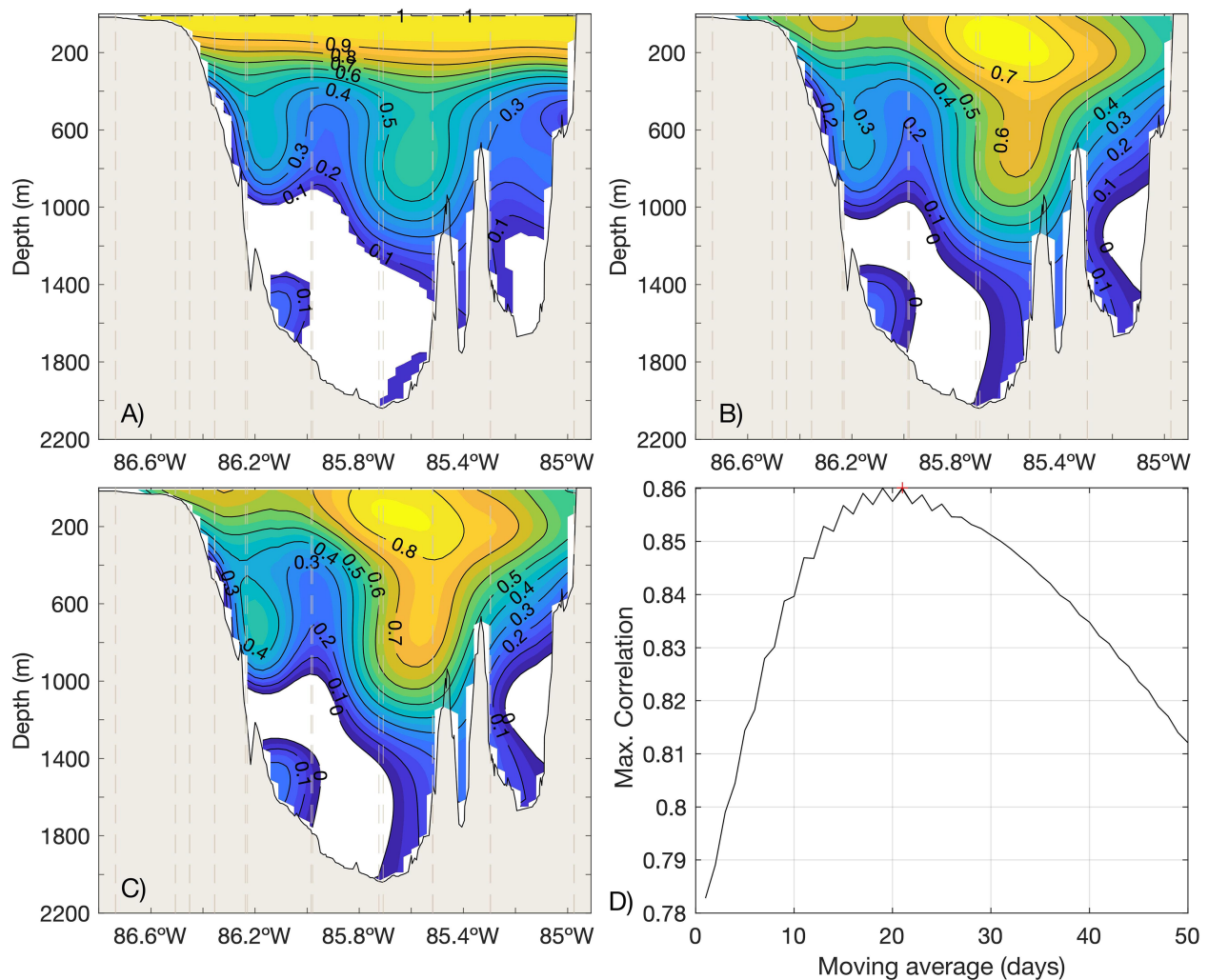


FIGURE 3

Pearson correlation coefficient for the linear regression between each gridded point from *in-situ* current measurements and: (A) co-located surface *in-situ* measurements (i.e. with the surface current at the same longitude), (B) the closest altimetric surface velocity data point, and (C) the closest altimetric data with a 21-day moving mean. (D) Maximum Pearson correlation coefficient with altimetry as a function of the low pass filtering of the *in-situ* data.

correlation coefficient ( $r$ ). The same analysis was applied for the mooring surface velocity with all the water column data points at each longitude in order to compare the vertical extension of the correlation from the mooring product and altimetry derived geostrophic approximation. Statistical significance of all correlation pairs was tested with a Student T-test ( $\alpha=0.01$ ).

### 3.3 Empirical orthogonal function (EOF) and cluster analyses

With the objective of understanding the spatio-temporal variability of the flow through the Yucatan Channel and its relationship with the Loop Current extension and eddy shedding, EOF and cluster analyses were computed from the 8 years of through-channel gridded mooring velocity anomalies. The anomalies were calculated by subtracting the long term mean,

as there were no substantial differences to removing the seasonal mean. EOFs were scaled by dividing/multiplying by the maximum value of the Principal Components (PCs) in order to obtain nondimensional PCs ranging from -1 to 1 and EOF maps with  $\text{m s}^{-1}$  units. For clustering, the Ward method was used to generate the clusters, although other methods were tested too, with results being robust (e.g. using k-means). The Ward method prioritizes coherence within groups by minimizing the sum of variances within-groups (Wilks, 2011). 2944 days of observations were used, with a total of 3231 variables (grid points with data), and 4 clusters were retained. With the time-series of the clustering, we also constructed a Markov chain transition model to analyze the probability transition between the clusters through time. Clustering and their transition probability is a common technique used in atmospheric and ocean sciences to describe and predict for example weather regimes (e.g. Arizmendi et al., 2022).



### 3.4 Predictive model of the Loop Current and eddy shedding

The predictive model of the Loop Current extension was constructed by implementing a multiple linear regression, optimizing the lowest root mean square error (RMSE) between the observed and predicted time-series and retaining only statistically significant variables as predictors. The model was trained with the first two thirds of the data (5.3 years) in order to test it with the last third (2.7 years). Four input variables capture the main changes of the flow associated with the predictability of the Loop Current extension. Two of the predictive variables of the model are the meridional component of surface geostrophic velocity from altimetry averaged in the areas defined by those points above the 99.5 percentile and those below the 0.05 percentile on the Pearson correlation map between the Loop Current extension and meridional velocity, respectively. Averaging these areas with 13 grid points each provided better skill than any single point. The other 2 predictive variables were taken from the gridded velocity product by automatically identifying the points of maximum and minimum correlation in the Yucatan section at different depths, and then retaining only the points that actually contributed to improve the skill of the model by being more correlated with the Loop Current extension than with surface altimetry at that Longitude. Finally, we selected the best compromise of vertically aligned points in what could be a mooring array. The analysis was repeated for every time interval, and the selected model was the one with highest correlation and lag, which turned out to be 30 days.

Accurately predicting an eddy separation event with at least one month lead time represents a major challenge, as it depends not only on the Loop Current but also on the evolution of the mesoscale field of the Gulf of Mexico. Here, two analyses were carried out that contribute to the eddy separation predictability. The first one was analyzing the relative frequency of the Loop Current extension during all days and only during those days before an eddy separation or detachment took place. The second analysis consisted in determining the probability of an eddy separation or detachment depending on the cluster configuration of the flow anomalies in Yucatan Channel.

## 4 Results

### 4.1 Descriptive analysis of the Loop Current and Yucatan flow

The Loop Current metrics show similar results from the two different methods of the 0.17 m contour and the streamline associated with maximum velocity ( $\langle V \rangle$ ), with a mean extension of 1449 and 1495 km and standard deviation of 487 and 466 km, respectively (Figures 1C; 2A). Even though the time-series are very similar, the correlation is 0.86, thus explaining 74% of the variance, and a root mean square error (RMSE) of 262 km between the two time-series is observed.

The events identified by the eddy detection algorithm are marked in Figure 2A. This shows that almost all the abrupt changes in the Loop Current extension (e.g. >100km/10 days) are associated with eddy shedding events (separation, detachment or reattachment). Apart from detachment and reattachment events, the Loop Current shows a repeated cycle in which it grows slowly from a retracted phase (<1000km) until it reaches an extended phase of about 1800–2600 km, when an eddy separation occurs and the system goes back to the retracted phase. This cycle can take between some months and up to 2 years (Figure 2A).

TOEddies detected 48 separation events between 1993 and 2021, 12 within the overlap period with *in-situ* measurements made on 2013/5/20, 2014/11/5, 2015/2/28, 2015/5/15, 2015/12/4, 2016/4/9, 2017/11/10, 2017/11/21, 2018/3/21, 2018/7/21, 2019/7/3, and 2020/3/30. Also, 56 detachment/reattachment events were detected by TOEddies during the altimetric period, and 15 overlapped with the gridded product in the Yucatan Channel. All the gridded total velocities and velocity anomalies on the Yucatan Channel, and the altimetric maps with the Loop Current and eddy detection can be seen in the Video S1.

The flow through the Yucatan Channel is dominated by the Yucatan Current, represented by the intense northward flow West of 85.4°W, with a maximum mean velocity at the surface of 1.14 m s<sup>-1</sup> decaying to 0 m s<sup>-1</sup> at about 800 m (Figure 1B). Below 800 m, the system shows velocities close to 0 m s<sup>-1</sup> and mostly southward, although the standard deviation exceeds the mean (0.05–0.1 m s<sup>-1</sup>). Close to the surface, the standard deviation increases with a maximum over the western slope (>0.3 m s<sup>-1</sup>; Figure 1D), as seen in earlier studies (Sheinbaum et al., 2002; Athié et al., 2015; Candela et al., 2019).

Three EOFs explain 77% of the variance of the Yucatan flow across the Channel. The first EOF explains 47% of the variance and shows a dipole structure centered at about 86°W, with surface values up to 0.6 m s<sup>-1</sup> near the surface, decaying to almost 0 m s<sup>-1</sup> at 1000 m depth (Figures 2B, C). The second EOF has a similar vertical structure, but it is a tripole and explains 21% of the variance (Figure 2D). These first two EOFs are associated with the westward-eastward displacements of the Yucatan Current, as already reported by (Abascal et al., 2003), who identified the first two EOFs as a “propagating signal” connected to the meandering and movement of the Yucatan Current core across the Yucatan Channel. The third EOF explains 9% of the variance and is the only one of the three with a change of sign in the vertical structure, especially well defined where the core of the Yucatan Current is located at 86.1°W, describing changes in the baroclinicity of the current (Figure 2E). The first EOF is the only one significantly correlated with the 206 Loop Current extension ( $r=0.44$ ).

### 4.2 *In situ* data, smoothing and comparison with altimetry

Gridded velocities through Yucatan Channel show over 0.95 correlation with the currents below everywhere in the upper 100 m section, decaying uniformly to a correlation of 0.5 at 400 m depth. A

portion of this vertical auto-correlation is explained by the gridding method. Below 400 m, considerable zonal differences are observed with two regions of relatively high vertical correlation at 85.4°W and 86.2°W above 0.4 and two regions of relatively low correlation below 0.2 at 86° W and East of 85.2°W. Below 1000 m, no significant correlation is observed essentially where the mean flow is negative on both sides of the channel except for a small region at about 1400–1800 m at 86°W, where a weak significant correlation exists (Figure 3A).

Altimetry-derived geostrophic velocity through the Yucatan Channel is significantly correlated with the surface gridded mooring velocities and shows a similar vertical correlation structure. The main difference observed in the upper 200 m with respect to the gridded mooring data correlation is that the Pearson coefficient values are about 0.1–0.2 lower, and also that zonal differences are observed in the upper layers, with higher correlations observed at 85.5°W and 86.1°W and decreasing towards the shelf at both boundaries, reaching values below 0.6 at the surface. Another difference between the correlation with surface *in-situ* measurements and with altimetry derived velocities is that the maximum correlation between altimetry and the gridded mooring product is not observed at the surface, but at 190 m depth. Between 400 and 1000m of depth, the correlation of *in-situ* measurements with altimetry is higher than with *in-situ* surface measurements (Figures 3B, C). The maximum correlation (0.86) is found after applying a 21 day running mean to the gridded data (Figure 3D).

### 4.3 Yucatan flow anomalies during growth, eddy separation, and retracted phase

The results of the cluster analysis of the velocity anomalies are shown in Figure 4. The composites of the 4 clusters show a similar anomaly structure to the positive and negative phases of the first two EOFs. Clusters 2 and 4 have similar structure as the first EOF, a dipole with positive and negative anomalies oriented west-east for phase 4, and east-west for phase 1. The top panel shows that they are associated with a retracted and a growing phase of the Loop Current, respectively (Figure 4A, Table 1). Clusters 1 and 3 have similar structure as the second EOF, a tripole with a centered positive anomaly and negative anomalies towards the sides for the cluster 1, and the opposite for the cluster 3 (Figures 4B, D). These clusters are associated with the shift between phases 2 and 4, as they have more transitions and are less persistent than clusters 2 and 4 (Table 1).

Descriptive statistics of the clusters show relevant results: Cluster 4, hereinafter also called the growing phase, is the one associated with the largest mean extension of the Loop Current (1633 km), and the only one with a positive net mean growth of the Loop Current, about 6.1 km day<sup>-1</sup> (Table 1). Cluster 2, hereinafter also called the retracted phase, stands out as the one associated with the lowest mean extension of the Loop Current (932 km), and the phase with the least transitions (12). Both clusters 2 and 4 are the most persistent ones, with a mean duration of 38 and 47 days, respectively (Table 1).

Clusters 3 and 1 are the transition clusters, being the less persistent ones. Nonetheless, cluster 3 is more frequent than the retracted phase of cluster 2, as the Loop Current often alters between cluster 3 and 4 during the extended phase before changing to the retracted phase of cluster 2 (e.g. 2014 to 2016 in Figure 4A). Cluster 3 is also the one with highest probability of eddy separation. 50% of the separations occur during cluster 3 while it is present 26% of the time (Table 1). Both transition clusters can represent a weakening or a strengthening of the Yucatan Current depending on whether the system is shifting from the retracted phase towards the growth phase or vice versa. Markov chain analysis indicates that these are not equally probable, and that cluster 1 is more associated with the transition from the retracted towards the extended phase (Table 1). Markov chain transition probability also shows that no transition is observed between cluster 2 (retracted phase) and 4 (extended phase).

The most probable cycle beginning from the retracted phase is towards Cluster 1, then to the growing phase and then to cluster 3. cluster 3 shows a very similar transition probability towards the other three clusters. Due to this last part of the loop phases 3 and 4 are where the most time is spent, even if 2 and 4 are the ones with more persistence. The retracted phase, although persistent, is the one with the least transitions, so the system alters frequently between the growing and transition phases and sometimes migrates towards the retracted phase after a separation event (Figure 4B, Table 1).

### 4.4 Predicting the Loop Current extension and eddy shedding

Horizontal (from altimetry) and vertical section (from Yucatan Channel mapped observations) distributions of the Pearson correlation coefficient between the Loop Current extension and the flow at each grid point 30 days before are shown in Figure 5. Both the horizontal map and the Yucatan Channel section display a dipole pattern, with positive correlation westward of the middle of the Yucatan Channel and negative towards the East. For the altimetric field, maximum and minimum correlation are observed downstream of the Yucatan Channel ( $> |0.6|$ ), decaying northward of 25°N (Figure 5A).

Maximum and minimum correlation values in the Yucatan Channel are observed near the surface ( $> |0.5|$ ). The vertical extension of the correlation in the Yucatan Channel with respect to the surface is about 1000 m. Although it tends to decrease towards the deep, this is not the case at every longitude. For example, at 86.2°W, the upper 1000 m show positive correlation, with relative maxima from the surface to 800 m deep. The correlation sign does not change through the water column for each longitude point in most for the channel, except for the mid depths (1000–1400 m) at the boundaries. In particular, the negative correlation at this depth implies that as the Yucatan Current extends it not only shifts westward but also gets shallower. Below 1400 m the correlation shows the same sign as at the surface, with a relative maximum at 1530 m 86.05°W of 0.38 (Figure 5B).

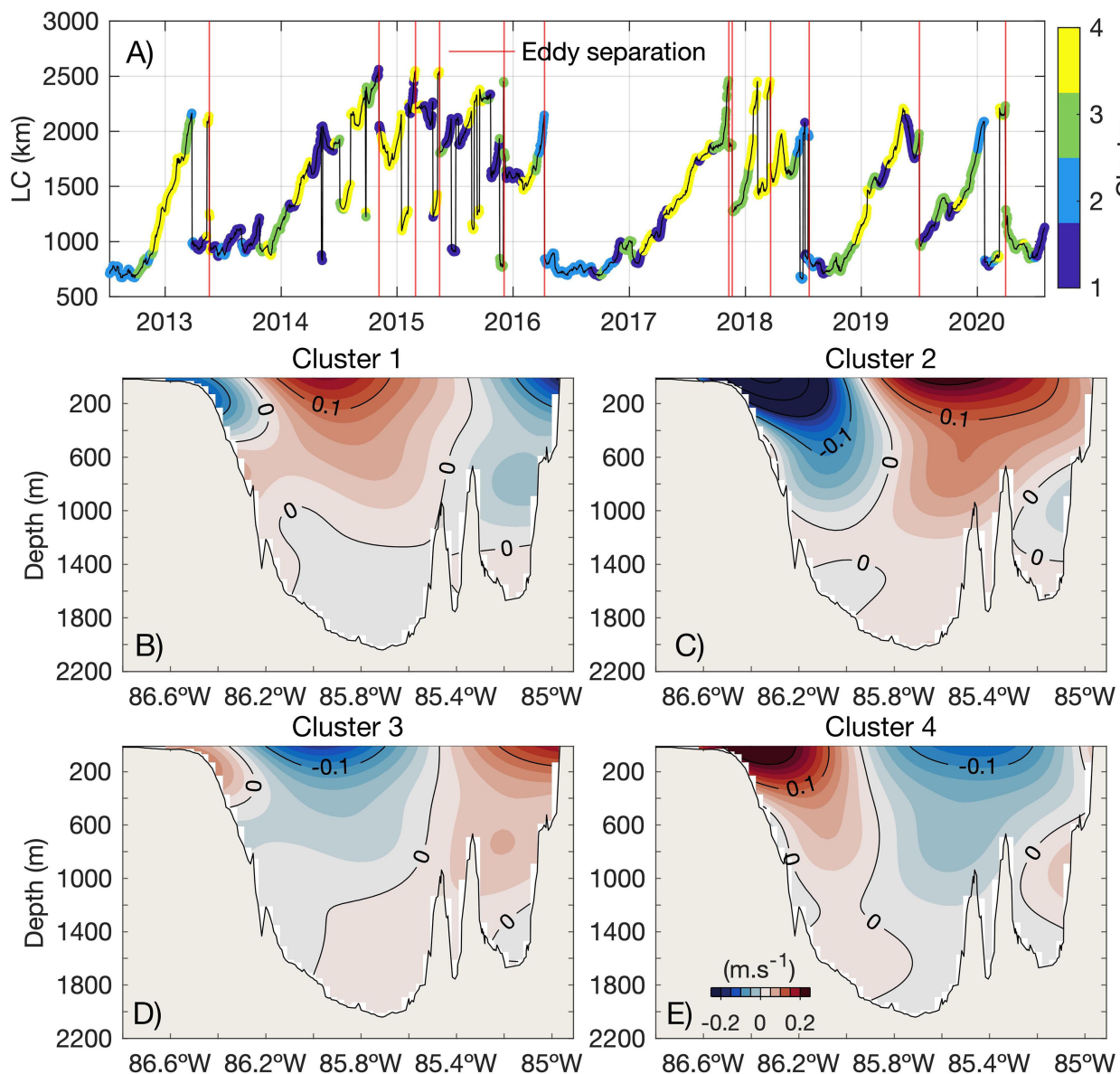


FIGURE 4

(A) Loop Current extension (km) time-series (in black) during the period with moorings in the Yucatan Channel. Each color in the time-series represents the corresponding cluster during that period based on the flow anomalies through the Yucatan Channel. Vertical red lines show each time an eddy was separated from the Loop Current. The composite of the velocity anomalies ( $m.s^{-1}$ ) of each cluster is plotted in (B–E).

A multiple linear regression model, based on the first 2/3 of the data record, explains 74% of the variance of the Loop Current extension ( $km$ ) 30 days ahead ( $t_{30}$ ), and a RMSE of 338 km, using four input variables as in equation 1:

$$LC(t_{30}, km) = 1100 + 369v_1 - 579v_2 + 2403v_3 - 2946v_4 \quad (1)$$

where all predictors are in  $m.s^{-1}$  and at  $t_0$   $v_1$  and  $v_2$  are the altimetric geostrophic velocity averaged over the region above the 99.5 and below the 0.05 percentile of highest/lowest correlation, respectively (marked with a cyan line in Figure 5A), and  $v_3$  and  $v_4$  are the *in-situ* velocities at 1170 m and 1530 m deep Yucatan Channel at 86.1°W, marked with cyan circles in Figure 5B.

The Loop Current extension is well predicted during the growth and retracted phases, and generally also when there is a large drop

in the Loop Current extension associated with an eddy separation. Both drops of July 2018 and January 2020 are due to the separation of large eddies and are captured by the model despite the fact that the gridded mooring data for the last third of the measurement period (Dec 2017 to August 2020) were not considered for estimating the regression coefficients. In the entire period the model fails to accurately predict the detachment and reattachment of eddies (Figure 5C).

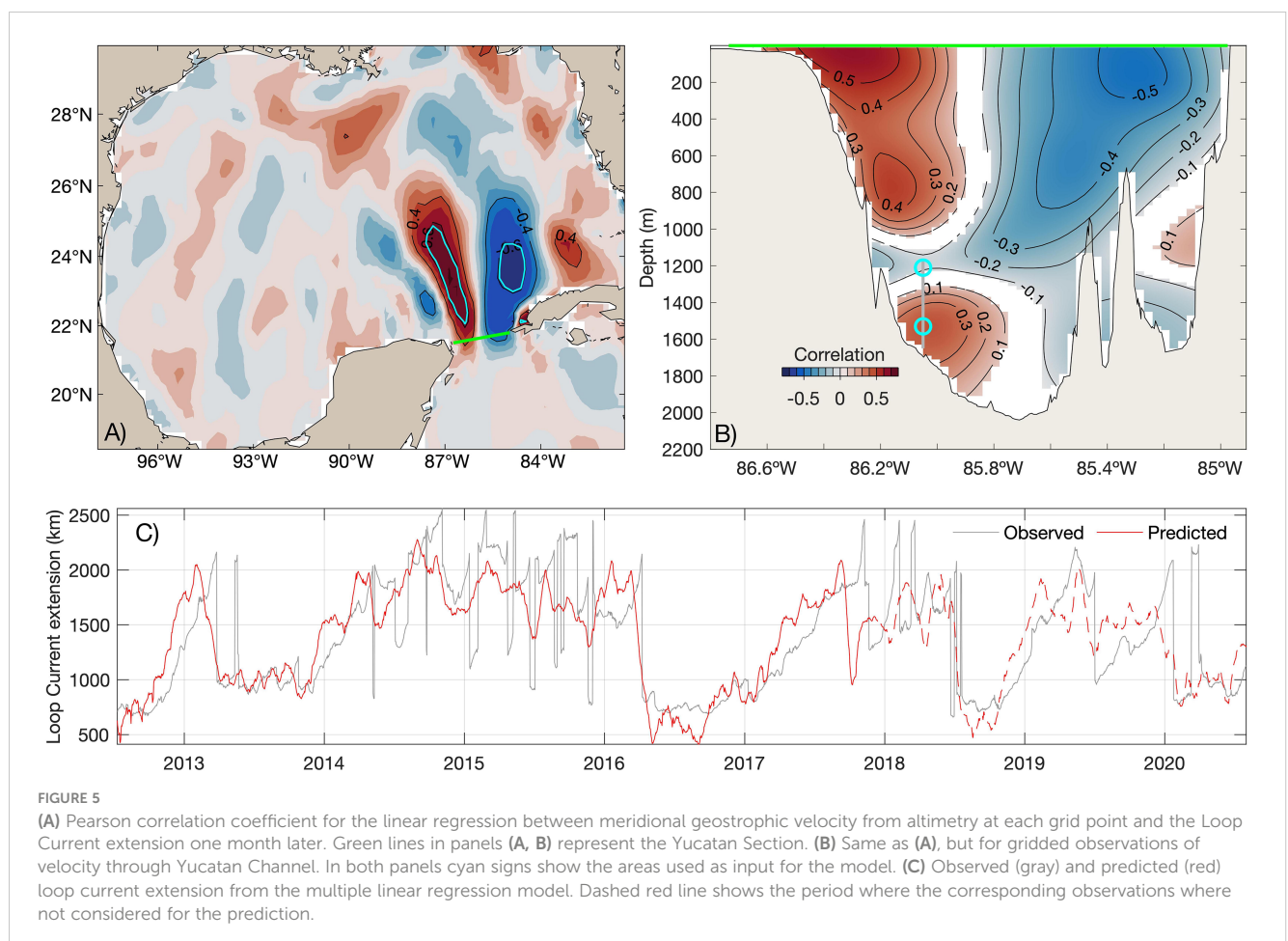
A tipping point related to eddy shedding probability is observed when the Loop Current extends 1800 km. This is the most frequent extension of the Loop Current that is reached during the growth/charge phase, and also where the shedding events start to be probable, as almost no separation or detachment is observed at extensions below 1800 km. 1800 km corresponds to a maximum

TABLE 1 Descriptive statistics of the four clusters based on velocity anomalies through the Yucatan Channel.

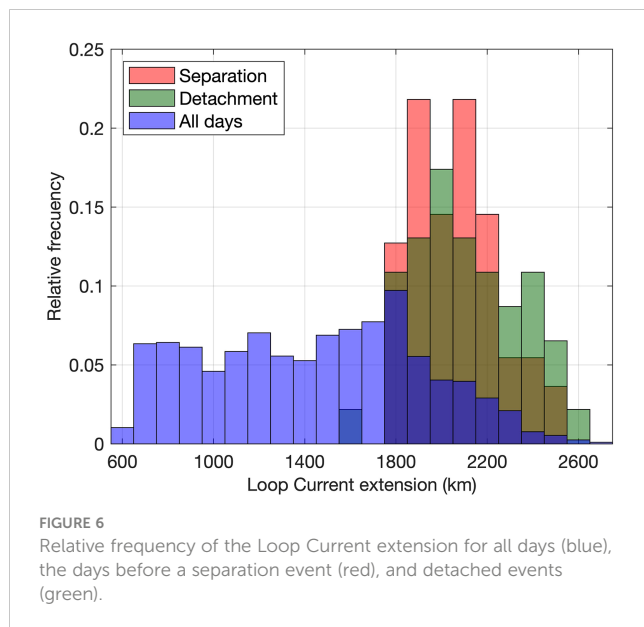
	1	2	3	4
Mean Loop Current extension (km)	1375	932	1337	1633
Time en each phase (%)	27	15	26	32
Persistence (days)	30	38	33	47
Maximum duration (days)	73	168	111	127
Loop Current change ( $\text{km day}^{-1}$ )	-1.7	-6.3	-1.3	6.1
Transitions to the cluster	26	12	23	20
Eddy separation (%)	8	17	50	25
Transition to cluster 1 (%)	0	16	32	52
Transition to cluster 2 (%)	75	0	25	0
Transition to cluster 3 (%)	40	30	0	30
Transition to cluster 4 (%)	40	0	60	0

northern reach of the Loop Current at  $27.3^{\circ}\text{N}$ , as the interval 600 km ( $24^{\circ}\text{N}$ ) - 2100 km ( $28^{\circ}\text{N}$ ) shows a linear increase of about 375 km of the Loop Current extension for every 1 degree increase in the maximum northern extent. The separations and detachments are also significantly different in their occurrence probability according to the Loop Current extension. At ranges between 1800 and 2300

km, the separation is more probable, while above 2300 km a detachment/reattachment is more probable (Figure 6). At extensions over 2100 km, the Loop Current has usually reached the shelf break of the Northern Gulf of Mexico and starts to extend mostly westward (Figure 1C). Over 56% of the shedding events are reattached, while 46% are actually separations and lose contact







forever with the Loop Current. 50% of the reattachments occurs within the first 12 days, and 95% within the first 2 months.

The flow anomalies through Yucatan Channel can also give predictability for the eddy separation and detachment, not only by predicting the Loop Current extension. Cluster 3, a tripole with negative anomalies in the core of the Yucatan Current, is observed prior to the separation events in 50% of the cases, although cluster 3 represents 26% of the time, and therefore it is more probable to observe a separation event when the Loop Current is over 1800 km of extension and shifts to Cluster 3. This is consistent with the results by Athié et al. (2012, 2015) who report an eastward shift of the Yucatan Current core prior to several eddy separations.

## 5 Discussion and conclusions

The deep flow measurements through the Yucatan Channel combined with altimetry data predict the Loop Current extension with a correlation of 0.86. The remaining unexplained variance, 26%, is of similar magnitude as the difference between the two Loop Current extension detection methods used. Therefore, correctly identifying the Loop Current extension probably is as important for its predictability as improving the predictive model.

Our results are consistent with previous research. Vazquez et al. (2023) showed that assimilating subsurface observations from moorings and altimetry significantly improved the model hindcasts and forecasts for the Loop Current extension, and also the eddy detachment. Bunge et al. (2002) demonstrate that filtering the deep transport time-series at Yucatan Channel with a 20 day running mean increases the correlation with the Loop Current extension by 0.21 with a lag of 8.5 days. Zeng et al. (2015) used an artificial neural network approach and an EOF decomposition of altimetry data to predict the Loop Current evolution and the shedding of an Loop Current eddy four weeks in advance, as in this research.

Our results are also consistent with (Wang et al., 2019; Wang et al., 2021), who also used machine learning to predict the Loop

Current evolution and Loop Current Eddy shedding events with satisfactory results up to 12 weeks in advance. Chiri et al. (2019) implemented auto-regressive logistic regression models to predict the evolution of 8 Loop Current patterns, using as input data bi-weekly averages of altimetry data but also wind stress curl in the Gulf of Mexico, and in the Caribbean Sea, and sea level pressure anomalies over the North Atlantic. For a specific case for the year 2016, the authors managed to predict the Loop Current pattern evolution 3 months in advance. This 1 to 3 months window of predictability fits the operational scope for the objectives of the phase 3 of the Understanding Gulf Ocean Systems program (UGOS-3), and one challenge for the near future will be to combine the published approaches and datasets in order get the best possible predictability skill of the Loop Current extension and eddy shedding.

The main strength of the predictive model developed here is identifying the regions that have high forecast skill, firstly from altimetry, and then adding those deep flow measurements that effectively contribute to improve the predictability. Another strength of the predictive model is that the deep flow measurements can be reduced to a few locations which could be locations of moored observations, away from the near-surface intense flow that represents a challenge for operational mooring arrays. This is of particular interest for the objectives of one of the UGOS-3 projects, where pressure-sensing inverted echo sounders (PIES) transmitting data in real-time will be tested in the Yucatan Channel for deep flow observations.

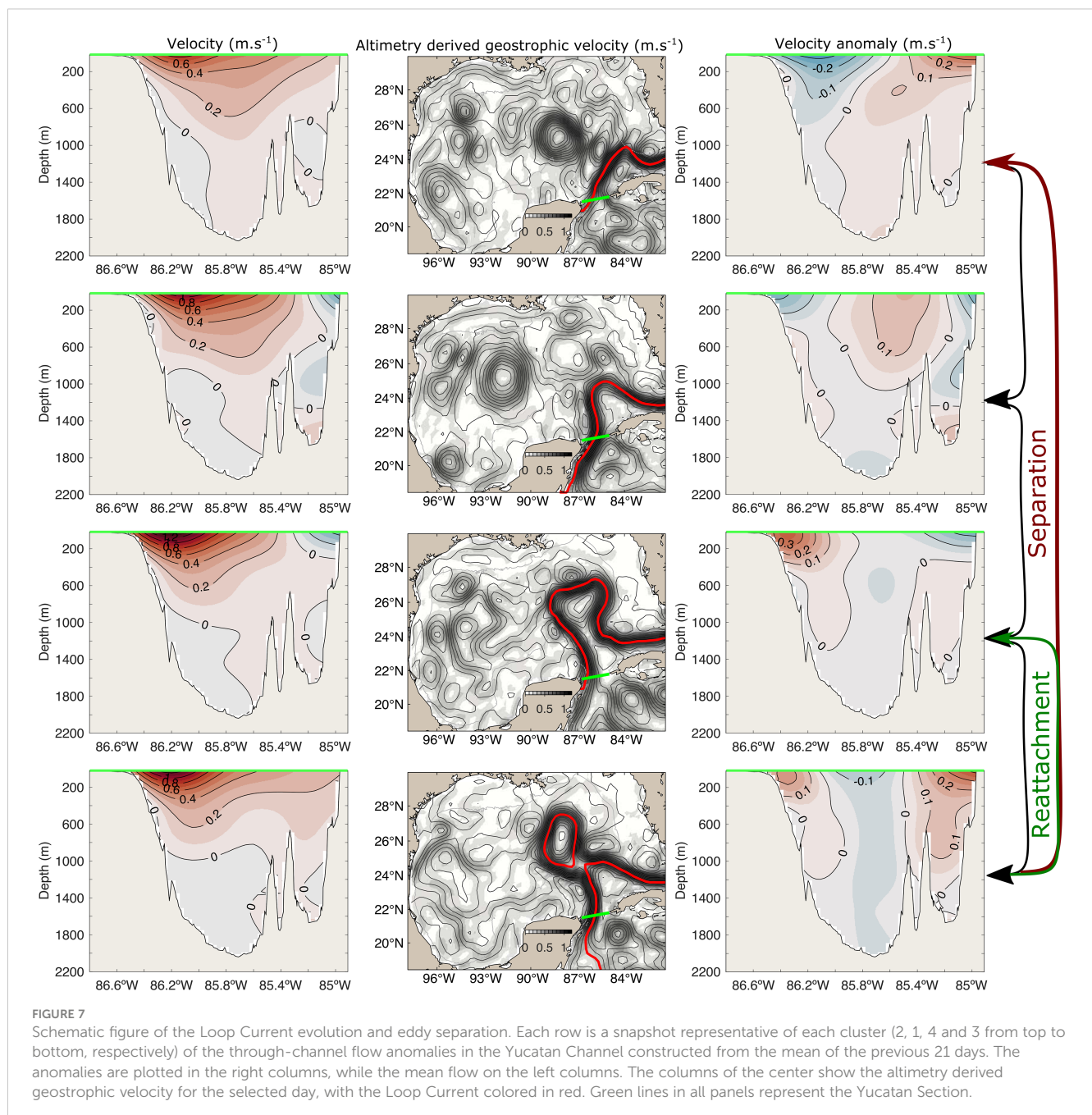
The smoothing of the *in-situ* data to match the effective temporal resolution of the altimetry improved the predictability of the Loop Current. Maximum correlation with altimetry was not found in the upper layers where ageostrophic currents are considerable, but below 100 m depth, as observed in other regions (e.g. Manta et al., 2022). As a consequence of the altimetric detection of the Loop Current, a resulting limitation of this analysis is that the potential contribution of the higher frequencies (e.g. variability within two weeks) from *in-situ* data cannot be used.

High-frequency predictability implies also a challenge due to the limited resolution of the altimetric data, especially for predicting the detachment/reattachment events when the Loop Current is highly extended (>2000km) reaching north of 26°N. Although the Loop Current extension itself can act as a predictor, these events seem to be driven mainly by mesoscale eddy interactions in the North of the Gulf of Mexico, rather than by substantial changes in the flow anomalies in the Yucatan Channel over the previous weeks. However, this is a subject of intense discussion in the community since many detachments and separations have been linked with perturbations (eddies) coming from the Caribbean (Abascal et al., 2003; Athié et al., 2012; Athié et al., 2015; Sheinbaum et al., 2016). Predicting trajectories of the cyclonic eddies that constrain the Loop Current using TOEddies or any related eddy tracking algorithm could contribute to improve the predictability of these detachment/reattachment events in the future, especially if the upcoming data from the SWOT satellite allows us to better resolve the small cyclonic structures. As has been shown in previous studies, cyclonic eddies in the Gulf of Mexico can either block the growth

of the Loop Current or favor the shedding of anticyclonic eddies from the Loop Current (Schmitz, 2005; Chérubin et al., 2006; Zavala-Hidalgo et al., 2006; Sheinbaum et al., 2016). A similar behavior has been identified for the Kuroshio Loop Current in the Luzon Strait (Zhang et al., 2017), making this region interesting to compare with in the future. Even though we are still not able to predict the detachment/reattachment events, we were able to show that the probability of an eddy separation or detachment/reattachment depends on the Loop Current extension which we can predict one month in advance, and that a tripole shape anomaly in the Yucatan Channel with negative values in the center of the Channel is observed before a separation event in 50% of the cases (Figure 7).

## 5.1 Conclusions

- We developed a predictive model of the Loop Current extension explaining 74% of the variance combining altimetry data and deep flow measurements at 1530 m and 1210 m deep in the Yucatan Channel at 86°W.
- 4 clusters of velocity anomalies through the Yucatan Channel represent the Loop Current dynamics. A dipole with positive and negative anomalies towards the western side of the Channel represents the growing and retracted phase of the Loop Current, and two tripole-shaped clusters represent the transition phases, with the one with negative



anomalies in the center associated with 50% of the eddy separation events. The transitions between these clusters are not equally probable, thereby adding predictability.

- Eddy shedding probability begins when the Loop Current extends over 1800 km, at which time it is situated near the slope in the northern Gulf. Beyond 2200 km extension, topography limits the direction of growth to mostly towards the west, and detachment and reattachment of eddies becomes more frequent than an eddy separation with other methods.
- Altimetry-derived geostrophic velocities are significantly correlated with *in-situ* flows in Yucatan Channel in the upper 1000 m. Nevertheless, high frequency (less than 2 weeks) events are not properly resolved by altimetry, making *in-situ* measurements not only of the deep flow but also the upper flow valuable to sample.
- These results will hopefully help to better resolve and predict the Loop Current dynamics in an operational way in the near future, once near real-time data of deep flow derived from the UGOS-3 project and high resolution altimetry from the SWOT satellite mission are available.

## Data availability statement

The CANEK dataset is online and available on <https://zenodo.org/record/7865542>. Requests to access these datasets should be directed to CANEK.CICESE@gmail.com.

## Author contributions

All authors contributed to the conception, design of the study and writing. GM also did the analysis and most of the writing. GD also did the Yucatan Channel data processing. All authors contributed to the article and approved the submitted version.

## Funding

Research reported in this publication was supported by the Gulf Research Program of the National Academies of Sciences, Engineering, and Medicine under award numbers 2000011057 and 200013145. Funding of the gridded data base used in this study comes from CICESE internal funds. Partial funding also comes from the National Council of Science and Technology of Mexico, Mexican Ministry of Energy, Hydrocarbon Trust,

project 201441, as part of the Gulf of Mexico Research Consortium (CIGoM).

## Acknowledgments

The data set used in this study was generated by JC, P.I. of the CICESE-CANEK Project for more than 25 years, who sadly passed away in November 2022. He was a wonderful human being and an outstanding scientist who contributed ideas and work that made this study possible. We wish to dedicate this article in his memory.

## Conflict of interest

The authors declare that the research was conducted in the absence of any commercial or financial relationships that could be construed as a potential conflict of interest.

## Publisher's note

All claims expressed in this article are solely those of the authors and do not necessarily represent those of their affiliated organizations, or those of the publisher, the editors and the reviewers. Any product that may be evaluated in this article, or claim that may be made by its manufacturer, is not guaranteed or endorsed by the publisher.

## Author disclaimer

The content is solely the responsibility of the authors and does not necessarily represent the official views of the Gulf Research Program or the National Academies of Sciences, Engineering, and Medicine.

## Supplementary material

The Supplementary Material for this article can be found online at: <https://www.frontiersin.org/articles/10.3389/fmars.2023.1156159/full#supplementary-material>

### SUPPLEMENTARY VIDEO 1

Left panel show the flow through the Yucatan Channel, and the right panel the anomalies. Both are the average of the previous 21 days. The middle panel shows the evolution of absolute dynamic topography in the Gulf of Mexico. Red line shows the tracked Loop Current extension, while magenta and cyan contours show the tracked anticyclonic and cyclonic eddies, respectively. The title of the middle panel also shows the date and the Loop Current extension for that day.

## References

Abascal, A., Sheinbaum, J., Candela, J., Ochoa, J., and Badan, A. (2003). Analysis of flow variability in the yucatan channel. *J. Geophysical Research: Oceans* 108. doi: 10.1029/2003JC001922

Arizmendi, F., Trinchin, R., and Barreiro, M. (2022). Weather regimes in subtropical south america and their impacts over uruguay. *Int. J. Climatology* 42, 9253–9270. doi: 10.1002/joc.7816



- Athié, G., Candela, J., Ochoa, J., and Sheinbaum, J. (2012). Impact of Caribbean cyclones on the detachment of loop current anticyclones. *J. Geophysical Research: Oceans* 117. doi: 10.1029/4052011JC007090
- Athié, G., Sheinbaum, J., Candela, J., Ochoa, J., Pérez-Brunius, P., and Romero-Arteaga, A. (2020). Seasonal variability of the transport through the Yucatan channel from observations. *J. Phys. Oceanography* 50, 343–360. doi: 10.1175/jpo-d-18-0269.1
- Athié, G., Sheinbaum, J., Leben, R., Ochoa, J., Shannon, M. R., and Candela, J. (2015). Interannual variability in the Yucatan channel flow. *Geophysical Res. Lett.* 42, 1496–1503. doi: 10.1002/2014GL062674
- Ballarotta, M., Ubelmann, C., Pujol, M.-I., Taburet, G., Fournier, F., Legeais, J.-F., et al. (2019). On the resolutions of ocean altimetry maps. *Ocean Sci.* 15, 1091–1109. doi: 10.5194/os-15-1091-2019
- Bretherton, F. P., Davis, R. E., and Fandry, C. (1976). A technique for objective analysis and design of oceanographic experiments applied to MODE-73. In *Deep Sea Res. Oceanographic Abstracts* 23, 559–582. doi: 10.1016/0011-7471(76)90001-2
- Bunge, L., Ochoa, J., Badan, A., Candela, J., and Sheinbaum, J. (2002). Deep flows in the Yucatan channel and their relation to changes in the loop current extension. *J. Geophysical Research: Oceans* 107, 26–1–26–7. doi: 10.1029/2001JC001256
- Candela, J., Ochoa, J., Sheinbaum, J., López, M., Pérez-Brunius, P., Tenreiro, M., et al. (2019). The flow through the gulf of Mexico. *J. Phys. Oceanography* 49, 1381–1401. doi: 10.1175/jpo-d-18-0189.1
- Candela, J., Sheinbaum, J., Ochoa, J., Badan, A., and Leben, R. (2002). The potential vorticity flux through the Yucatan channel and the loop current in the gulf of Mexico. *Geophysical Res. Lett.* 29, 16–1–16–4. doi: 10.1029/2002GL015587
- Candela, J., Tanahara, S., Crepon, M., Barnier, B., and Sheinbaum, J. (2003). Yucatan Channel flow: observations versus clipper atl6 and mercator pam models. *J. Geophysical Research: Oceans* 108. doi: 10.1029/2003JC001961
- Capet, A., Mason, E., Rossi, V., Troupin, C., Faugère, Y., Pujol, I., et al. (2014). Implications of refined altimetry on estimates of mesoscale activity and eddy-driven offshore transport in the Eastern boundary upwelling systems. *Geophysical Res. Lett.* 41, 7602–7610. doi: 10.1002/2014GL061770
- Chaigneau, A., Marie, L. T., Gérard, E., Carmen, G., and Oscar, P. (2011). Vertical structure of mesoscale eddies in the eastern south pacific ocean: a composite analysis from altimetry and argo profiling floats. *J. Geophysical Research: Oceans* 116. doi: 10.1029/2011JC007134
- Chelton, D. B., Schlax, M. G., and Samelson, R. M. (2011). Global observations of nonlinear mesoscale eddies. *Prog. Oceanography* 91, 167–216. doi: 10.1016/j.pocean.2011.01.002
- Chérubin, L. M., Morel, Y., and Chassignet, E. P. (2006). Loop current ring shedding: the formation of cyclones and the effect of topography. *J. Phys. Oceanography* 36, 569–591. doi: 10.1175/jpo2871.1
- Chiri, H., Abascal, A. J., Castaneda, S., Antolínez, J. A. A., Liu, Y., Weisberg, R. H., et al. (2019). Statistical simulation of ocean current patterns using autoregressive logistic regression models: a case study in the gulf of Mexico. *Ocean Model.* 136, 1–12. doi: 10.1016/j.ocemod.2019.02.010
- Durante, G., Candela, J., and Sheinbaum, J. (2023). *Canek database v0: gridded data from a mooring section across the yucatan channel*. (Zenodo) doi: 10.5281/zenodo.7865542
- Gopalakrishnan, G., Cornuelle, B. D., Hoteit, I., Rudnick, D. L., and Owens, W. B. (2013). State estimates and forecasts of the loop current in the gulf of Mexico using the mitgcm and its adjoint. *J. Geophysical Research: Oceans* 118, 3292–3314. doi: 10.1002/jgrc.20239
- Hall, C. A., and Leben, R. R. (2016). Observational evidence of seasonality in the timing of loop current eddy separation. *Dynamics Atmospheres Oceans* 76, 240–267. doi: 10.1016/j.dynatmoce.2016.06.002
- Hamilton, P., Berger, T., Singer, J., Waddell, E., Churchill, J., Leben, R., et al. (2000). *DeSoto canyon eddy intrusion study, final report. volume II: tech. rep* (New Orleans, LA: US Dept. of the Interior, Minerals Management Service), ISBN: .
- Hamilton, P., Lugo-Fernández, A., and Sheinbaum, J. (2016). A loop current experiment: field and remote measurements. *Dynamics Atmospheres Oceans* 76, 156–173. doi: 10.1016/j.dynatmoce.2016.01.005
- Laxenaire, R., Chassignet, E., Dukhovskoy, D., and Morey, S. L. (2023). Impact of upstream variability on the loop current dynamics in numerical simulations of the gulf of Mexico. *Front. Mar. Sci.* 10, 176. doi: 10.3389/fmars.2023.1080779
- Laxenaire, R., Speich, S., Blanke, B., Chaigneau, A., Pegliasco, C., and Stegner, A. (2018). Anticyclonic eddies connecting the Western boundaries of Indian and Atlantic oceans. *J. Geophysical Research: Oceans* 123, 7651–7677. doi: 10.1029/2018jc014270
- Leben, R. R. (2005). *Altimeter-derived loop current metrics* Vol. 463 (American Geophysical Union (AGU), 181–201. doi: 10.1029/161GM15
- Lugo-Fernández, A., and Leben, R. R. (2010). On the linear relationship between loop current retreat latitude and eddy separation period. *J. Phys. Oceanography* 40, 2778–2784. doi: 10.1175/2010JP04354.1
- Lumpkin, R. (2016). Global characteristics of coherent vortices from surface drifter trajectories. *J. Geophysical Research: Oceans* 121, 1306–1321. doi: 10.1002/2015JC011435
- Manta, G., Speich, S., Barreiro, M., Trinchin, R., de Mello, C., Laxenaire, R., et al. (2022). Shelf water export at the brazil-malvinas confluence evidenced from combined in situ and satellite observations. *Front. Mar. Sci.* 9. doi: 10.3389/fmars.2022.857594
- Maul, G. A. (1977). The annual cycle of the gulf loop current part i: observations during a one-year time series. *J. Mar. Res.* 35, 29–47.
- National Academies of Sciences, Engineering, Medicine, et al. (2018). *Understanding and predicting the gulf of Mexico loop current: critical gaps and recommendations* (National Academies Press).
- Ochoa, J., Badan, A., Sheinbaum, J., and Candela, J. (2003). “Canek: measuring transport in the yucatan channel,” in *Nonlinear processes in geophysical fluid dynamics* (Dordrecht: Springer), 275–286.
- Oey, L.-Y. (1996). Simulation of mesoscale variability in the gulf of Mexico: sensitivity studies, comparison with observations, and trapped wave propagation. *J. Phys. Oceanography* 26, 145–174. doi: 10.1175/1520-0485(1996)026<0145: SOMVIT>2.0.CO;2
- Oey, L.-Y., Lee, H.-C., and Schmitz, W. J. Jr. (2003). Effects of winds and Caribbean eddies on the frequency of loop current eddy shedding: a numerical model study. *J. Geophysical Research: Oceans* 108. doi: 10.1029/2002JC001698
- Pegliasco, C., Chaigneau, A., and Morrow, R. (2015). Main eddy vertical structures observed in the four major Eastern boundary upwelling systems. *J. Geophysical Research: Oceans* 120, 6008–6033. doi: 10.1002/2015JC010950
- Pujol, M.-I., Faugère, Y., Taburet, G., Dupuy, S., Pelloquin, C., Ablain, M., et al. (2016). DUACS DT2014: the new multi-mission altimeter data set reprocessed over 20 years. *Ocean Sci.* 12, 1067–1090. doi: 10.5194/os-12-1067-2016
- Reid, R. O. (1972). “A simple dynamic model of the loop current,” in *Contributions on the physical oceanography of the gulf of Mexico*, vol. II. (Gulf Publishing Co), 157–159.
- Roemmich, D. (1983). Optimal estimation of hydrographic station data and derived fields. *J. Phys. Oceanography* 13, 1544–1549. doi: 10.1175/1520-0485(1983)013<1544: OEOHSD>2.0.CO;2
- Schmitz, W. J. Jr. (2005). *Cyclones and westward propagation in the shedding of anticyclonic rings from the loop current* (American Geophysical Union (AGU), 241–261. doi: 10.1029/161GM18
- Sheinbaum, J., Athié, G., Candela, J., Ochoa, J., and Romero-Arteaga, A. (2016). Structure and variability of the Yucatan and loop currents along the slope and shelf break of the Yucatan channel and campeche bank. *Dynamics Atmospheres Oceans* 76, 217–239. doi: 10.1016/j.dynatmoce.2016.08.001
- Sheinbaum, J., Candela, J., Badan, A., and Ochoa, J. (2002). Flow structure and transport in the Yucatan channel. *Geophysical Res. Lett.* 29, 10–1–10–4. doi: 10.1029/2001GL013990
- Sturges, W., and Evans, J. (1983). On the variability of the loop current in the gulf of Mexico. *J. Mar. Res.* 41, 639–653. doi: 10.1357/002224083788520487
- Sturges, W., and Leben, R. (2000). Frequency of ring separations from the loop current in the gulf of Mexico: a revised estimate. *J. Phys. Oceanography* 30, 1814–1819. doi: 10.1175/1520-0485(2000)030<1814:forsft>2.0.co;2
- Vazquez, H. J., Gopalakrishnan, G., and Sheinbaum, J. (2023). Impact of yucatan channel subsurface velocity observations on the gulf of Mexico state estimates. *J. Phys. Oceanography* 53, 506 361–385. doi: 10.1175/JPO-D-21-0213.1
- Wang, Z.-F., Sun, L., Li, Q.-Y., and Cheng, H. (2019). Two typical merging events of oceanic mesoscale anticyclonic eddies. *Ocean Sci.* 15, 1545–1559. doi: 10.5194/os-15-1545-2019
- Wang, J. L., Zhuang, H., Chérubin, L., Muhamed Ali, A., and Ibrahim, A. (2021). Loop current ssh forecasting: a new domain partitioning approach for a machine learning model. *Forecasting* 3, 570–579. doi: 10.3390/forecast3030036
- Wilks, D. S. (2011). *Statistical methods in the atmospheric sciences* Vol. vol. 100 (Academic press).
- Yang, H., Yang, C., Liu, Y., and Chen, Z. (2023). Energetics during eddy shedding in the gulf of Mexico. *Ocean Dynamics*, 73 (2), 1–12. doi: 10.1007/s10236-023-01538-y
- Zavala-Hidalgo, J., Morey, S., O'Brien, J., and Zamudio, L. (2006). On the loop current eddy shedding variability. *Atmósfera* 19, 41–48.
- Zeng, X., Li, Y., and He, R. (2015). Predictability of the loop current variation and eddy shedding process in the gulf of Mexico using an artificial neural network approach. *J. Atmospheric Oceanic Technol.* 32, 1098–1111. doi: 10.1175/JTECH-D-14-00176.1
- Zhang, Z., Zhao, W., Qiu, B., and Tian, J. (2017). Anticyclonic eddy sheddings from kuroshio loop and the accompanying cyclonic eddy in the northeastern south china sea. *J. Phys. Oceanography* 47, 1243–1259. doi: 10.1175/JPO-D-16-0185.1





## OPEN ACCESS

## EDITED BY

Steven L. Morey,  
Florida Agricultural and Mechanical  
University, United States

## REVIEWED BY

Wei Huang,  
Oak Ridge National Laboratory (DOE),  
United States  
Charly De Marez,  
California Institute of Technology,  
United States

## \*CORRESPONDENCE

Paul A. Ernst

✉ pernst@seoe.sc.edu

RECEIVED 07 March 2023

ACCEPTED 17 May 2023

PUBLISHED 31 May 2023

## CITATION

Ernst PA, Subrahmanyam B, Trott CB and  
Chaigneau A (2023) Characteristics of  
submesoscale eddy structures within  
mesoscale eddies in the Gulf of Mexico  
from 1/48° ECCO estimates.  
*Front. Mar. Sci.* 10:1181676.  
doi: 10.3389/fmars.2023.1181676

## COPYRIGHT

© 2023 Ernst, Subrahmanyam, Trott and  
Chaigneau. This is an open-access article  
distributed under the terms of the [Creative  
Commons Attribution License \(CC BY\)](#). The  
use, distribution or reproduction in other  
forums is permitted, provided the original  
author(s) and the copyright owner(s) are  
credited and that the original publication in  
this journal is cited, in accordance with  
accepted academic practice. No use,  
distribution or reproduction is permitted  
which does not comply with these terms.

# Characteristics of submesoscale eddy structures within mesoscale eddies in the Gulf of Mexico from 1/48° ECCO estimates

Paul A. Ernst<sup>1\*</sup>, Bulusu Subrahmanyam<sup>1</sup>, Corinne B. Trott<sup>2</sup>  
and Alexis Chaigneau<sup>3</sup>

<sup>1</sup>School of the Earth, Ocean and Environment, University of South Carolina, Columbia, SC, United States,

<sup>2</sup>Naval Research Laboratory, Stennis Space Center, MS, United States, <sup>3</sup>LEGOS, CNES, CNRS, IRD, UPS,  
Université de Toulouse, Toulouse, France

Submesoscale oceanic structures (<10–20 km) such as eddies and fronts are often difficult to describe given the influence of the mesoscale. In order to characterize the surface signatures of submesoscale structures, we utilize a custom spatial filtering function to separate the meso- and large-scale sea surface height (SSH) signal from the small scale SSH signal of 1/48° high resolution estimates provided by NASA's Estimating the Circulation and Climate of the Oceans (ECCO) project. In this study, we use ECCO estimates from a 14-month global simulation between September 2011 and November 2012 with a 2 km horizontal grid spacing in the Gulf of Mexico. We then use an eddy detection and tracking algorithm to identify persistent circular features on both scales, giving rise to an atlas of submesoscale eddy-like variabilities (SEVs). We briefly investigate the geographic and temporal variability of SEVs as a whole before collocating SEVs inside mesoscale eddies, allowing us to evaluate the characteristics of internal SEVs and the impact of SEVs on mesoscale eddies. We find that SEVs, both anticyclonic and cyclonic, are ubiquitous inside mesoscale eddies with lifetimes longer than a week, accounting for an average of 10–20% of the spatial area and eddy kinetic energy of mesoscale eddies. We also show that internal SEVs are persistently associated with temperature and salinity anomalies in both eddy centers and edges of up to 0.1 °C and 0.05 psu, with anticyclonic internal SEVs being warmer and fresher while cyclonic internal SEVs are colder and saltier. Finally, we examine the life cycle of an anticyclonic Loop Current eddy, demonstrating that the number and intensity of internal SEVs within increases as the eddy approaches separation from the Loop Current until a maximum is obtained just after separation. In light of forthcoming submesoscale SSH observations from NASA's Surface Water and Ocean Topography (SWOT) mission, our results showcase the variability of submesoscale eddy structures and their possible implications for biogeochemical cycling, the inverse energy cascade, and Loop Current prediction techniques.

## KEYWORDS

submesoscale, eddies, mesoscale, energy cascade, Gulf of Mexico, high resolution modelling simulations, loop current, satellite oceanography

# 1 Introduction

Mesoscale eddies are ubiquitous in the world's oceans, accounting for significant fractions of the total transport of upper ocean properties (Zhang et al., 2014; Xia et al., 2022). Much is known regarding mesoscale eddies thanks to the maturity of satellite altimetry, allowing global, daily measurements of sea surface height (SSH) at a  $\frac{1}{4}^\circ$  spatial resolution since the launch of TOPEX/Poseidon in 1992 (Fu et al., 1994). Measurements of eddy behavior and fluxes on a global scale are therefore limited to this scale, leaving the smallest eddies defined by SSH to a radius of roughly 25 km. It is for this reason, and the fact that the diameter of these eddies often lies close to the baroclinic Rossby radius of deformation, that many recent publications choose 20–30 km as the cutoff point of the mesoscale and the beginning of the so-called submesoscale (Zhang & Qiu, 2018; Drushka et al., 2019; Gula et al., 2019; Zhang Y. et al., 2019; de Marez et al., 2020a; Morvan et al., 2020).

A variety of methods have been utilized to study eddy dynamics at the submesoscale, including using higher resolution observational ocean color, radar, gliders, drifters, and sea surface temperature (SST) datasets (Zamuda et al., 2016; Drushka et al., 2019; Zhang Y. et al., 2019; Ni et al., 2021). However, pending the first scientific data released to the public from the Surface Water and Ocean Topography mission, the main tool for studying submesoscale eddies on a regional scale remains the use of high resolution model simulations (Durand et al., 2010). Such models, coupled with observations where possible, have been used to study several elements of submesoscale eddies, including their likely generation mechanisms, interactions with topography, roles in the energy budget, influence on vertical transports, and more (Morvan et al., 2019; Tedesco et al., 2019; D'Addezio et al., 2020; Cao et al., 2021).

Of particular interest is the behavior of submesoscale phenomena embedded into and around mesoscale eddies. These include filaments, fronts, and other instabilities, all of which alter the characteristics of the mesoscale (Brannigan et al., 2017). Such submesoscale alterations can contribute to mixing and energy dissipation within the overall mesoscale eddy, increasing vertical heat transport below the depth of the mixed layer (Bracco et al., 2019; Garabato et al., 2022; Wang et al., 2022). Given the importance of understanding mesoscale eddy dynamics, it is clear that a greater understanding of the possible submesoscale influences underlying currently visible mesoscale eddies is needed.

One region where submesoscale influences may play a major role in mesoscale dynamics is the Gulf of Mexico (GoM). The Loop Current and its associated eddies, termed Loop Current Eddies (LCEs) have significant implications for the circulation within the basin, with individual eddies lasting for months to years while interacting with, *e.g.*, hurricanes, oil spills, and phytoplankton blooms (Leben & Born, 1993; Liu et al., 2009; Liu et al., 2011; Jaimes et al., 2016; Wang et al., 2019). As a result, understanding the submesoscale structures present within mesoscale eddies in the GoM may lead to new insights into mesoscale processes. For example, Haza et al. (2016) demonstrate tracer leakage across mesoscale structures in the GoM due to submesoscale activity,

while Meunier et al. (2018) report observations of intrathermocline eddies (ITEs) within an LCE, likely formed through intense mixing and ensuing Rossby adjustment.

In this study, we aim to investigate the characteristics of submesoscale structures within mesoscale eddies in the GoM. We separate the spatial scales of a high-resolution model simulation provided by the Estimating the Circulation and Climate of the Oceans (ECCO) project using a purpose-designed filtering process. This provides us with the means to algorithmically detect persistent Eulerian structures on both the large- and small-scales of the GoM. By collocating small scale structures within mesoscale eddies, we are able to track small-scale structures with eddy-like characteristics over time, allowing us to ultimately characterize the impact that these small scale, eddy-like structures have on the surface signatures (dynamic height, temperature, salinity) of mesoscale eddies in the GoM.

# 2 Materials and methods

## 2.1 Numerical simulation and domain

In this study, we use the ECCO project's (<https://ecco-group.org>)  $1/48^\circ$  run of the Massachusetts Institute of Technology general circulation model (MITgcm) on the Lat-Lon-Cap (LLC) 4320 grid (Marshall et al., 1997; Adcroft et al., 2004; Forget et al., 2015). The final product, often referred to by LLC4320, has hourly temporal resolution, 90 vertical levels, a nominal horizontal grid resolution in the Gulf of Mexico of roughly 2 km, and an effective resolution of roughly 8 km. This resolution was achieved through a series of progressively finer-scale models originally derived from an adjoint-method state estimate constrained to observations between 2009 and 2011 (Menemenlis et al., 2008). The forcings for this simulation were both atmospheric and tidal, including the 16 most significant tidal components, although this tidal forcing has been demonstrated to be overestimated by a factor of 1.1121 (Arbic et al., 2022). The simulation is global, covering 14 months from September 13<sup>th</sup>, 2011 through November 15<sup>th</sup>, 2012. It has previously been used to study submesoscale dynamics throughout the world (*e.g.* Rocha et al., 2016; Qiu et al., 2018; Chereskin et al., 2019).

While we utilize the entire temporal domain, we constrain our spatial domain to the Gulf of Mexico ( $18^\circ\text{N}$  -  $32^\circ\text{N}$ ,  $80^\circ\text{W}$  -  $100^\circ\text{W}$ ). As in Brokaw et al. (2020), we define the Loop Current region over which Eddy Kinetic Energy (EKE, calculated as  $\frac{1}{2}(U^2 + V^2)$ , where  $U$  and  $V$  are the zonal and meridional components of surface velocity) is calculated to be between  $21.5^\circ\text{N}$  -  $28^\circ\text{N}$  and  $81^\circ\text{W}$  -  $90^\circ\text{W}$ .

## 2.2 Separation of scales

We separate the mesoscale ("large") from the submesoscale ("small") using a filtration and removal technique used to similar effect by Rosso et al. (2015) and D'Addezio et al. (2020). We first smooth the original simulation data ("total scale") using a specific low-pass filter, then remove the low-pass output from the total scale

to achieve the small scale. In this study, our focus is on the spatial scale of less than 25 km (below the current spatial scale resolved by satellite altimeters), and so we aim for a window design that can efficiently separate the large scale from the small scale with comparatively minimal large scale contamination. Given that contamination between scales will persist regardless of the filtering technique, we match D'Addezio et al. (2020) in referring to the filtered fields as “large” and “small” instead of “mesoscale” and “submesoscale” where appropriate.

While a perfectly clean separation is impossible due to the continuity of scales within oceanic power spectra, one must choose an appropriate window to smooth with, *i.e.* one with sharper roll off at the filter transfer function. In this work, we utilize the Dolph–Chebyshev window (Lynch, 1997). This is a window with a steep roll off that guarantees minimal main lobe width for a given ripple ratio (Yao et al., 2014). As a result, it is theoretically more effective at achieving a separation of scales than a more gradually tapering window using a Parzen or Gaussian kernel. For our purposes, the Dolph–Chebyshev window is constructed with a filter size of 71 pixels (*i.e.* a half-power window of 30 pixels) and a sidelobe magnitude factor of 100. Our results are only weakly sensitive to the sidelobe magnitude factor, while a change in the filter size directly alters the frequency at which the filter operates. We also acknowledge that this is just one possible combination of parameters to achieve our desired result: a higher sidelobe magnitude factor could be used with a large filter size or vice versa and similar results may logically be obtained.

The operation of our filtering method as applied to our model's SSH data is displayed in Figure 1: Figure 1A is an example of the unfiltered SSH data in a restricted region of the GoM, Figure 1B is the large-scale result after the convolution of SSH with the Dolph–Chebyshev window, Figure 1C is the small-scale result after subtracting Figure 1B from Figure 1A, and Figure 1D demonstrates the crossover point in the normalized power spectra between Figures 1B, C. Given the crossover point near 25 km, we are confident that our procedure is effectively isolating the submesoscale and removing most mesoscale contamination. However, mesoscale energies do clearly still exist within our small-scale, so our results must be considered in this context.

## 2.3 Eddy detection and tracking

In order to detect eddy-like features, we employ an eddy detection and tracking algorithm first developed by Chaigneau et al. (2008; Chaigneau et al., 2009), expanded by Pegliasco et al. (2015), and employed by Trott et al. (2018; Trott et al., 2019), Roman-Stork et al. (2021; Roman-Stork et al., 2023), and Ernst et al. (2022). Notably for our purposes, this algorithm was also successfully used by Brokaw et al. (2020) to examine mesoscale eddy characteristics in the GoM. This algorithm detects eddies using closed contours of SSH. We use SSH instead of other fields (*i.e.* Vorticity or the Okubo-Weiss parameter) as SSH will provide the best comparison to forthcoming SWOT data, which is limited by

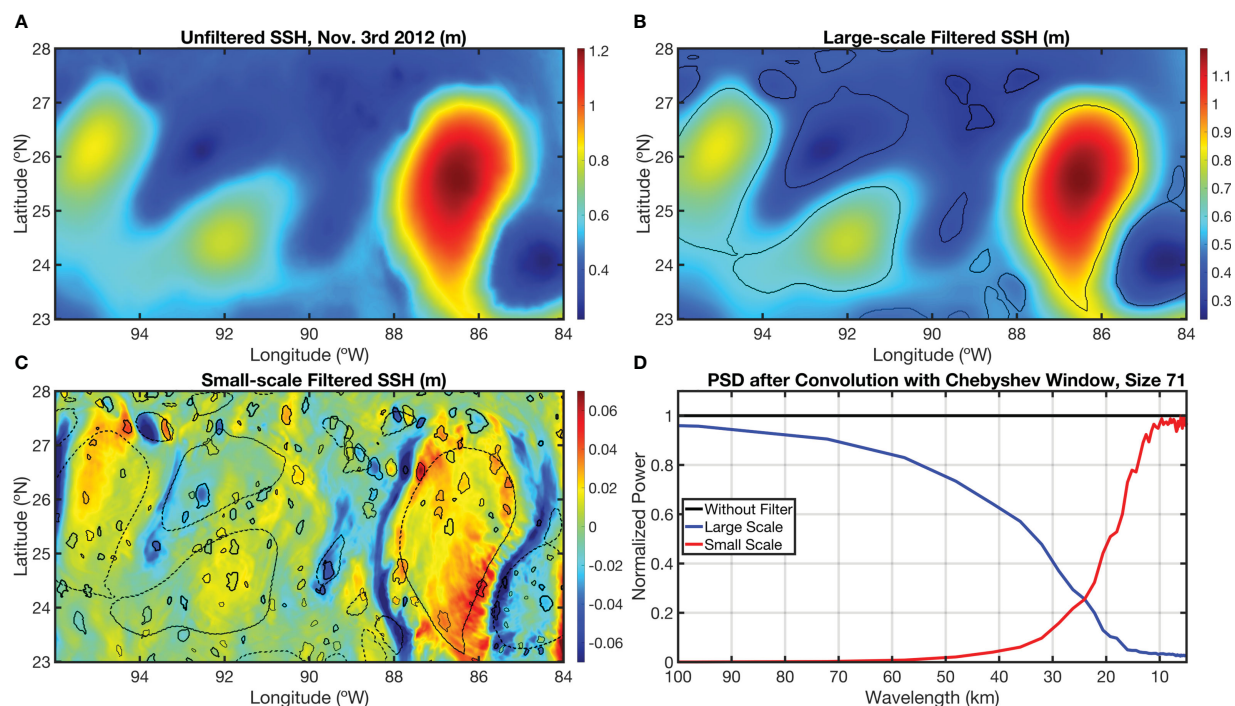


FIGURE 1

The SSH fields (m) in the central Gulf of Mexico for Nov. 3<sup>rd</sup>, 2012, showcasing the filtering process and eddy detection methodologies. (A) The total scale model outputs; (B) the large scale filtered SSH after convolution with the Dolph–Chebyshev window and corresponding mesoscale eddy edge detections (black lines); (C) the small scale filtered SSH after subtracting (B) from (A) along with both detections of large and small scale eddies (black lines). (D) The normalized power spectrum for the large scale field (in blue) and the small scale field (in red) demonstrating a crossover point near 25 km.

noise effects such that only SSH will be effective below a 25 km resolution (Chelton et al., 2019; Chelton et al., 2022). Upon isolating local extrema in the SSH field (maxima for anticyclonic eddies and minima for cyclonic eddies), closed contours are drawn around them and expanded until the closed contour breaks, resulting in the final eddy edge detections laying upon the largest closed contours. This method does not require an arbitrary threshold for initial detection and results in a more accurate eddy shape than traditional thresholded methods.

Eddy trajectories over time are formed based upon a cost function that compares overlapping contours from adjacent time steps. Those overlapping closed contours that are minimally costed based upon radius, amplitude, and EKE are considered to be a part of the same trajectory. For more information on this cost function, see Pegliasco et al. (2015) or Trott et al. (2018). Given the hourly nature of the estimates used in this study, we discard any eddy trajectories that are not coherent over at least a 12 hour timespan. This helps reduce the likelihood of false instantaneous detections and retains features that are coherent in the Eulerian sense over at least this length of time.

For additional accuracy in the context of elongated false detections upon fronts, we apply a shape-constraining test that compares the length of the longest axis across the center (major axis) to the shortest axis across the center (minor axis) of each eddy. In this context, the ratio of the major axis to the minor axis determines the circularity of the eddy: a ratio of 1 indicates a perfect circle. We choose a cutoff ratio of 0.35, which helps eliminate most of the frontal structures and filaments within our results. This is broadly similar to the classic circularity test (see Kurian et al., 2011 for details) and achieves comparable results to their circularity threshold of 50% shape error, e.g. Figure 1C. The ratio test is significantly faster computationally than the circularity test over a high resolution domain given the simplicity of the calculation and the number of eddies detected versus the need to draw and compare a perfect circle to every contour.

Eddies are detected and tracked on both the large and small scale fields (see Figures 1B–C). Large scale eddies are hereafter referred to as ‘mesoscale’ eddies, while small scale eddy-like features are referred to as submesoscale eddy-like variabilities or SEVs. Large scale features are not tracked on the unfiltered field, as submesoscale variabilities can interrupt the formation of closed contours and falsely reduce or eliminate detections of eddy contours.

Given that these smaller scale features do not often have rotation velocities that exceed their translation velocities, it is unlikely that these can trap fluids for greater lengths of time. While they may still provide loci for particle attraction, deflection, and leakage, they are isolated through the filtering process, not prevalent in the total-scale, and as of yet lack observation from satellite altimetry, so we will not refer to SEVs as true coherent submesoscale vortices. In a physical sense, the process of SEV classification is meant to extract eddies with a predominant submesoscale signature. However, this will also include other persistent submesoscale circular structures. We address the most likely causes and classifications of SEVs in Section 4.1.

## 3 Results

### 3.1 Mean characteristics of SEVs

Before an understanding of the characteristics of SEVs internal to mesoscale eddies can be constructed, the general distributions of eddy properties must be noted. In this way, we may draw comparisons between the performance of the LLC4320 simulation and both observations and other operational models (Brokaw et al., 2020). In keeping with a comparison to established eddy characteristics in the GoM, we annotate the locations of eddy generation, called generation numbers, the locations of all eddy detections, eddy radius, eddy amplitude, and EKE (Figure 2).

We find that the characteristics of the mesoscale-filtered eddies closely match those of both altimetry and the Hybrid Coordinate Ocean Model (HYCOM) as reported by Brokaw et al. (2020). There is a locus of eddy generation for Anticyclonic Eddies (AEs) in the extended Loop Current region (Figure 2A); these eddies propagate westward, with large radii ( $> 125$  km), amplitudes ( $> 25$  cm), and EKEs ( $> 0.2 \text{ m}^2 \text{ s}^{-2}$ ) reported in the central to western GoM (Figures 2B–E). CEs, meanwhile, are less frequent and more prevalent throughout the basin’s edges (Figures 2F, G), with a notable persistently large CE in the southwest (Figure 2H). We find that our model does overestimate the EKE intensity of central GoM eddies as compared to observations, but that the relative distribution of properties is otherwise comparable.

The occurrences of SEVs, both AE and CE, are spread across the entire basin but are concentrated in the center and east with certain pixels of the Loop Current generating over 200 SEVs over the course of the 14-month simulation (Figures 2K, L, P, Q). SEV radii are near uniform, with the entire basin averaging 7–8 km (Figures 2M, R) while there is a trend for SEV amplitudes and EKEs to follow the path of the extended Loop Current and its LCEs (Figures 2N, O, S, T). High amplitudes and EKEs are also exhibited to the north of the LCE track and along the western coast of the GoM. It is worth noting that the areas of highest EKE intensity only outline the extended Loop Current and not its retracted state, mirroring the energy analysis of Loop Current instabilities conducted by Yang et al. (2020). Given that submesoscale eddies are often generated by such instabilities, it follows that SEVs would be observed along the Loop Current front (Buckingham et al., 2017). Beyond the geographic distribution of SEV characteristics, it is helpful to examine the timewise variability of SEVs over the 14-month duration of the simulation (Figure 3).

The number of SEVs across the basin is relatively consistent, with a grouping around 280 SEVs of each rotational tendency per day (Figures 3A, F). That stated, there is some degree of variability present, with the highest number of SEVs observed in January ( $\sim 320$ ) and the lowest number in April–June ( $\sim 250$ ) before rising slightly ( $\sim 280$ ) to the end of the simulation. SEV amplitudes are consistently lower than those of mesoscale eddies at around 2 cm (calculated between the eddy center and contour, Figures 3B, G) which follows from the magnitude of the submesoscale filtered SSH field being roughly an order of magnitude less than the large-scale field (Figures 1B, C). Between the middle of October and the end of March, the amplitude and EKE of SEV-CEs nearly double those of



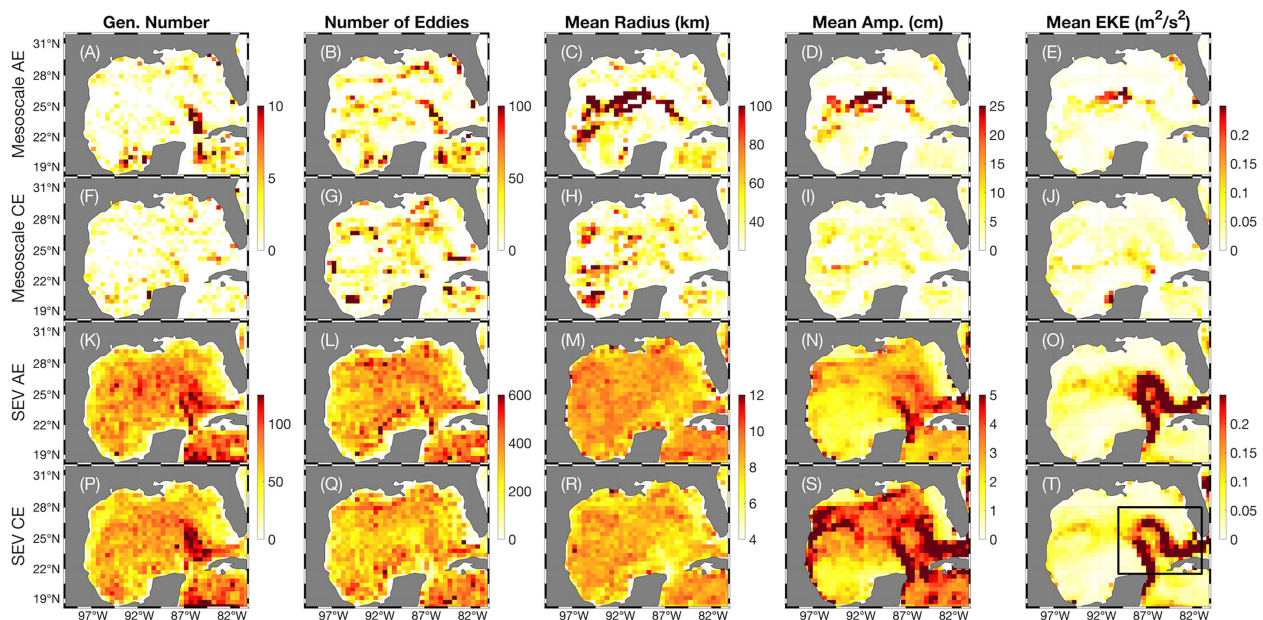


FIGURE 2

The properties of all mesoscale eddies and SEVs broken down geographically by eddy center location and binned into  $\frac{1}{2}^\circ$  pixels. (A–E) The generation number, *i.e.* number of eddies originated in the pixel, the number of all eddy detections, the mean eddy radius (km), the mean eddy amplitude (cm), and the mean EKE ( $\text{m}^2 \text{s}^{-2}$ ) for all mesoscale AEs. (F–J) As in (A–E) but for mesoscale CEs. (K–O) As in (A–E) but for SEV-AEs. (P–T) As in (A–E) but for SEV-CEs. The black box in (T) denotes the Loop Current region.

SEV-AEs even as SEV-AE amplitude increases, while median SEV-CE radius actually declines below that of the median SEV-AE radius (Figures 3C, D, H, I). This is most likely due to the increase in instabilities caused during the generation and separation of a major LCE, as we discuss later.

Finally, we note that the EKE of the Loop Current itself follows a periodic pattern that matches with fortnightly tidal variability associated with neap and spring tides (Figures 3E, J). Once this variability is removed, it is clear that the EKE of the Loop Current reaches its greatest extents between February–May 2012 and

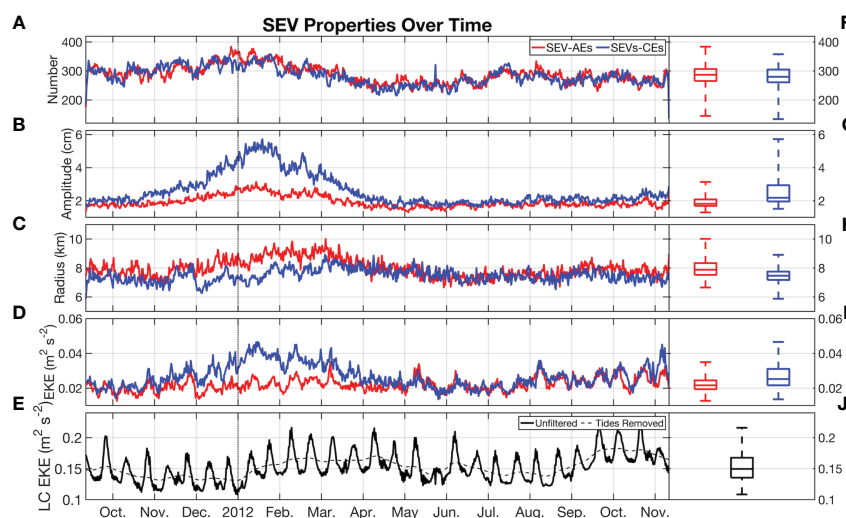


FIGURE 3

The properties of all SEVs over time from the beginning of the model simulation to its end, separated into AEs and CEs and binned into 12-hour increments. (A) The number of eddies per increment; (B) the median eddy amplitude (cm); (C) the median eddy radius (km); (D) the median eddy EKE ( $\text{m}^2 \text{s}^{-2}$ ). (E) The EKE for the Loop Current region as defined by Brokaw et al. (2020):  $21.5^\circ\text{N} - 28^\circ\text{N}$  and  $81^\circ\text{W} - 90^\circ\text{W}$ , both with and without tidal variability (as removed by a low-pass Gaussian filter with a half-window of 28 days). (F–J) As in (A–E) but using a box plot to show the median, quartiles, and extremes of the data upon which the time series is constructed.

September–November 2012. These coincide with the periods of greatest Loop Current extension during the simulation. To investigate how the intensity of the Loop Current and the tidal frequencies interact with the characteristics displayed in Figure 3, we perform a wavelet coherence analysis using the analytic Morlet wavelet (Figure 4, Grinsted et al., 2004).

The primary period of coherence between the energetics of the Loop Current and the characteristics of SEVs occurs in the 10–20 day range, with some degree of significant coherence across all

properties at some point during the simulation. Among the characteristics highlighted, amplitude and EKE are most frequently significant, with the EKE of the Loop Current and the EKE of SEV-AEs being persistently in phase (rightward pointing phase arrows) throughout the entire simulation. By contrast, the amplitudes of most SEVs, where notable, lie either slightly against phase or lagged by 90 degrees (downward pointing arrows). In this context, the most important implication is that the fortnightly tidal cycle is immediately influencing the EKE of SEVs.

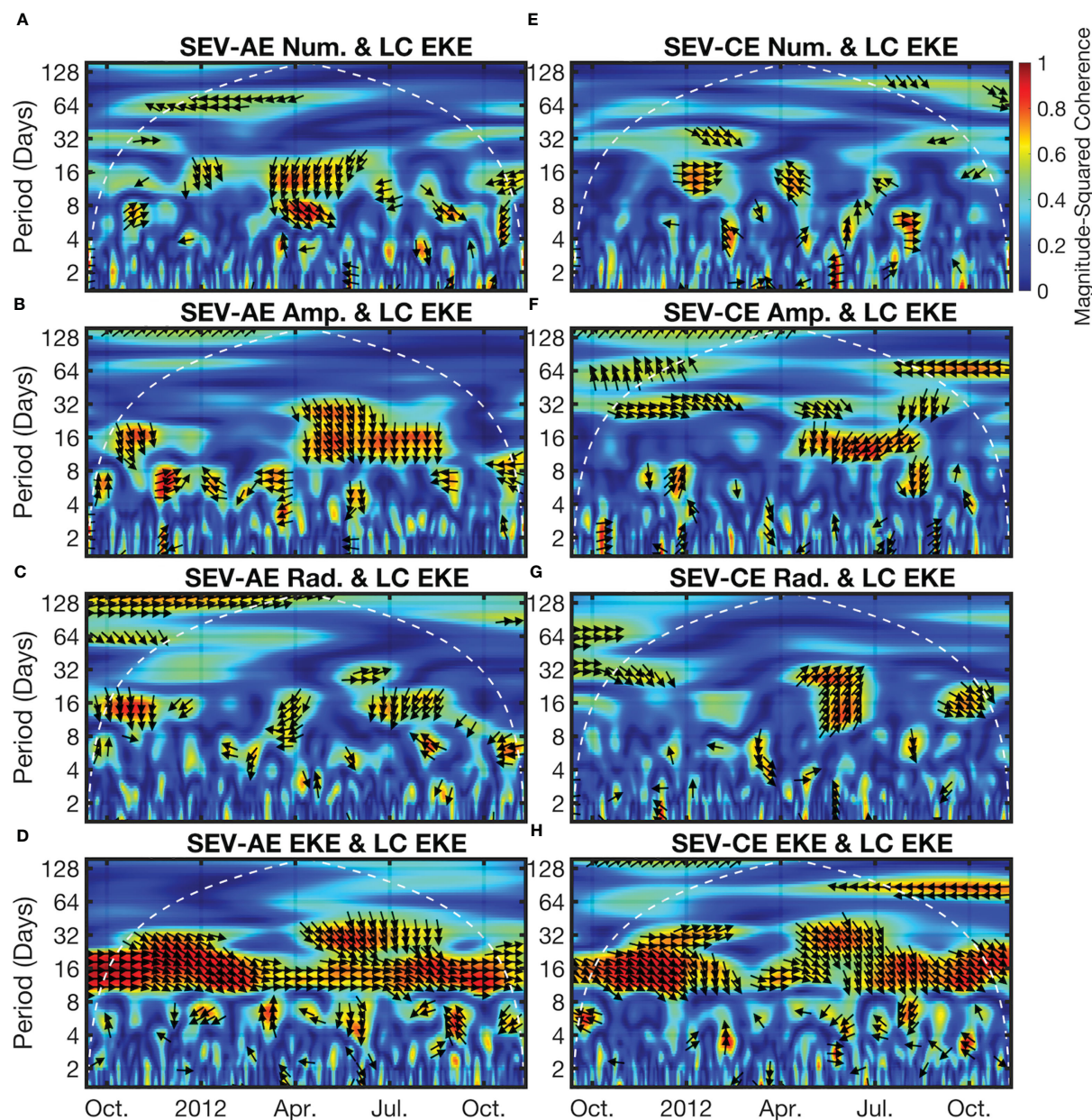


FIGURE 4

The magnitude-squared wavelet coherence computed using the analytic Morlet wavelet between each of the time series in Figures 3A–D, E. The white dashed line shows the cone of influence, after which edge effects dominate, while the black arrows show the direction of phase for coherence > 0.5. Rightward-facing arrows indicate the time series are in-phase, leftward facing arrows indicate the time series are anti-phase, downward facing arrows generally indicate that the first time series leads the second by 90 degrees, and upward facing arrows generally indicate that the second time series leads the first by 90 degrees. (A–D) The coherence between SEV-AEs number, amplitude, radius, and EKE time series and the Loop Current time series. (E–H) As in (A–D) but for SEV-CEs.



## 3.2 Characteristics of internal SEVs

With the general properties of SEVs laid out in the previous section, we may turn our attention to the prospect of SEVs internal to mesoscale eddies. In this analysis, we collocate SEVs whose contours enclose an area that is within a ‘parent’ mesoscale eddy. There are therefore 4 combinations of SEVs and mesoscale eddies: SEV-AEs within mesoscale AEs (abbreviated M-AE where appropriate), SEV-CEs within M-AEs, SEV-AEs within mesoscale CE (abbreviated M-CE where appropriate), and SEV-CEs within mesoscale CE. Of the 54,330 SEV-AE trajectories identified, 8,958 (16.5%) contain at least one timestep where they are mostly within a mesoscale eddy; of the 54,951 SEV-CE trajectories identified, 7,346 (13.4%) contain at least one timestep where they are identified within a mesoscale eddy. Thus, around 85% of SEV trajectories belong outside mesoscale eddies. For mesoscale eddies, 1038 of the total 1266 (81.99%) of M-AEs contain at least one SEV internally during their lifetimes. For M-CEs, 622 of the 789 (78.83%) M-CEs identified contain at least one SEV internally. It is worth noting that of the ~20% of mesoscale eddies that do not contain an SEV at any point in their lifetimes, none of them have a lifetime of greater than 7 days, indicating that all long lived eddies are subject to SEV-based variability at some point in their lives. On average, internal SEV-AEs (CEs) live for 2.8 (2.5) days, spending an average of 1.8 (1.6) of those days within a mesoscale eddy and propagating an average of 14.3 (12.7) km away from their origin point. The longest lived internal SEV-AE (CE) lasts for 61.5 (96.0) days and propagates 245.6 (295.6) km away from its origin. The other mean characteristics of SEVs are given in Table 1.

Overall, while there is substantial variance in all parameters, SEVs within M-CEs have the longest lives, SEVs within M-AEs have the highest EKEs, and SEV-CEs have greatest amplitudes. We break these characteristics down geographically in the same manner as all SEVs (Figure 5).

We note that the geographic distribution of internal SEVs within M-AEs closely follows the track of LCEs (Figures 5A–B, F–G), with an additional increased concentration within the western Caribbean Sea. M-CE internal SEVs are most frequent within the southwestern corner of the GoM, corresponding to an intense, persistent M-CE (Figures 5K–L, P–Q). Three other loci of SEV-CE formation are notable: the eastern bend of the Loop Current, the tip of the extended Loop Current, and the northern Caribbean. As before, these all correspond to M-CE hotspots, both in our simulation (Figure 2) and in observations (Brokaw et al., 2020). Internal SEVs of all types on the boundaries are

comparatively rare. This may be due in part to the filtering process, since results towards the boundaries are less reliable where there is insufficient data to fill the full filter window and so there are less mesoscale eddy detections. The distribution, then, of internal SEVs closely follows the areas of large parent eddy formation, an unsurprising result. The same trends are seen in the amplitude and EKE of internal SEVs, though it is notable that the most intense M-CE, SEV-CEs are found not in the extended Loop Current but at the base of the Loop Current, itself not a hotspot of M-CE EKE (Figure 5T). The properties of internal SEVs are further laid out over the duration of the dataset in Figure 6.

We note a much more intense variability in the characteristics of internal SEVs as opposed to all SEVs, with the number of daily internal SEVs at one point dropping to just 4, causing the median radius spike at the end of May (Figures 6A, C). In contrast to Figure 3, there is also a prolonged period of time where internal SEV-AE numbers exceed those of SEV-CEs between the beginning of January and mid-May. After this point, the number of all internal SEVs never exceeds 50 of either type, despite having regularly exceeded this value previously. During this second half of the simulation, internal SEV-AE EKE rises, more often exceeding that of internal SEV-CEs. The increase in SEV-CE amplitude between December and March is also present here, though with more inherent variability (Figure 6B). As in Figure 4, we wish to determine whether there is significant coherence between the energy of the Loop Current and the energy of SEVs (Figure 7).

While there is significant coherence at the 32-day period near the beginning of the simulation for all non-EKE characteristics, there is a distinct lack of coherence at the 16-day period for EKE as there was in Figure 4 (Figures 7D, H). Interestingly, there is a particularly strong coherence between internal SEV-CE number and the 16 day period between February and April, with the phase arrows showing both the number of SEV-CEs leading Loop Current EKE (upwards arrows) and the two being anti-phase. This is the only relation of all those seen in Figures 4, 7 that demonstrates a significant lead from SEV properties to Loop Current properties. This also partially coincides with the increase in SEV-CE amplitudes observed in Figures 3, 6, indicating a possible relationship between the generation of instabilities in the Loop Current and its strength. However, there is no significant coherence between internal SEV-CE amplitudes and Loop Current EKE at this time. With the general characteristics of internal SEVs established, we turn our attention to the relationship between the properties of parent mesoscale eddies and their internal SEVs (Figure 8).

TABLE 1 The arithmetic means and standard deviations of Internal SEV lifetimes (column 1), radii (column 2), amplitudes (column 3), and EKE (column 4) for SEV-AEs internal to mesoscale AEs (row 1), SEV-CEs internal to mesoscale AEs (row 2), SEV-AEs internal to mesoscale CE (row 3) and SEV-CEs internal to mesoscale CE (row 4).

	Lifetime (days)	Radius (km)	Amplitude (cm)	EKE ( $\text{m}^2 \text{s}^{-2}$ )
M-AE, SEV-AE	$5.5 \pm 7.3$	$9.2 \pm 4.3$	$2.3 \pm 1.8$	$0.10 \pm 0.14$
M-AE, SEV-CE	$5.0 \pm 8.0$	$8.2 \pm 3.7$	$3.0 \pm 2.5$	$0.073 \pm 0.088$
M-CE, SEV-AE	$6.5 \pm 8.5$	$9.4 \pm 4.5$	$2.6 \pm 2.0$	$0.033 \pm 0.054$
M-CE, SEV-CE	$7.5 \pm 12.8$	$9.8 \pm 4.8$	$3.9 \pm 3.1$	$0.055 \pm 0.094$

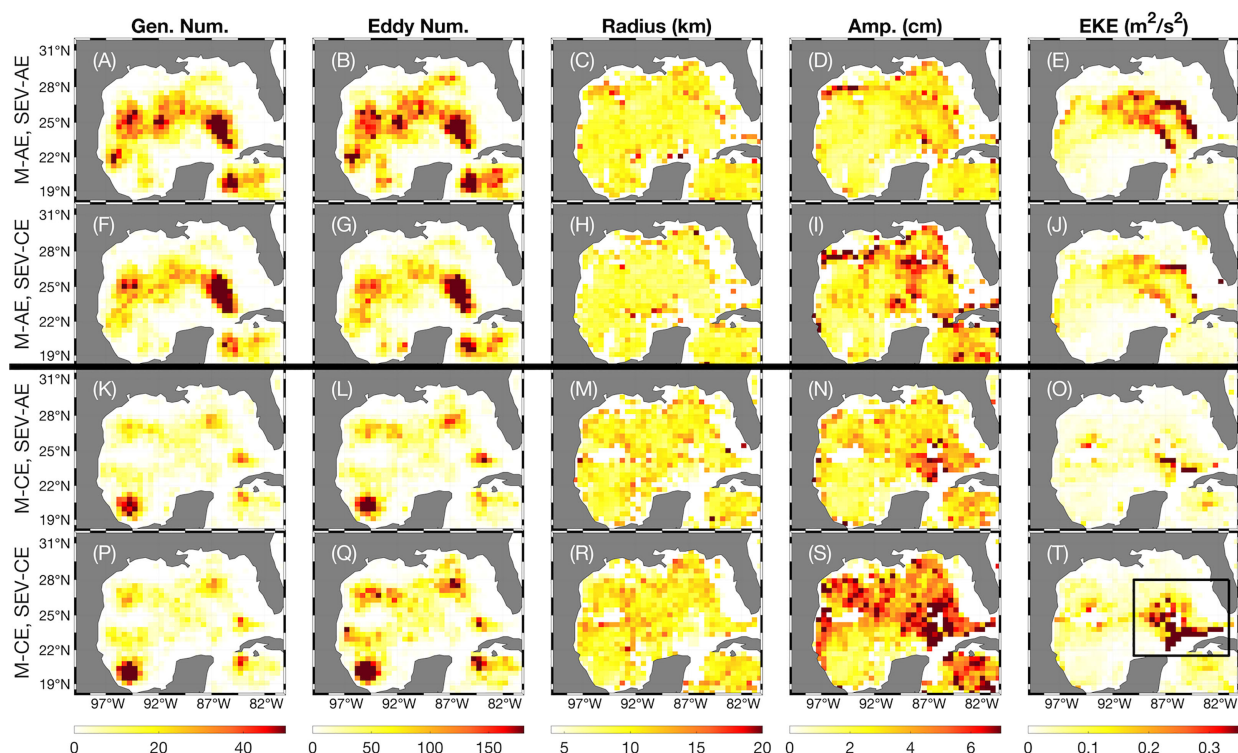


FIGURE 5

The geographic properties, as in Figure 2, for each type of internal SEV-outer mesoscale eddy combination pair. (A–E) The generation number, the mean eddy radius (km), the mean eddy amplitude (cm), and the mean EKE ( $\text{m}^2 \text{s}^{-2}$ ) for all SEV-AEs internal to mesoscale AEs. (F–J) As in (A–E) but for SEV-CEs internal to mesoscale AEs. (K–O) As in (A–E) but for SEV-AEs internal to mesoscale CEs. (P–T) As in (A–E) but for SEV-CEs internal to mesoscale CEs. The black box in (T) denotes the Loop Current region.

The lifespans of internal SEVs range between the minimum coherence interval (12 hours) and 80 days, with the longest-lived SEVs being those CEs internal to mesoscale CEs (Figures 8A–D). In particular, due to the length of the simulation, there are a handful of major mesoscale eddies that remain coherent for over half of the simulation, standing out clearly as sources of internal SEVs. There are in fact two mesoscale eddies whose lifespans cover the entirety of the simulation, one AE and one CE. The CE in particular is clearly visible in Figure 8D, as it contains a large number of long-lived internal SEVs. While some longer lived SEVs are present in shorter lived mesoscale eddies, demonstrating the capability for submesoscale structures to persist through the dissipation of a mesoscale eddy, all longer lived (lifespan > 10 days) SEVs whose trajectories are over 50% internal to mesoscale eddies are logically only found in longer-lived mesoscale eddies. The overall correlation between SEV and mesoscale eddy lifetimes is not significant ( $p < 0.05$ ).

The same relationship does not hold true for radius (Figures 8E–H) or amplitude (Figures 8I–L), with the mean radius of SEVs (~8 km) remaining relatively constant for all radii of parent eddy with very low  $R^2$  values on a slightly negative trend; trends for radius and amplitude are also not statistically significant. Amplitude for SEVs internal to M-AEs follows a dipolar pattern, with a grouping of SEVs in low-amplitude M-AEs (~5 cm) and another in high-amplitude M-AEs (~23 cm). By contrast, SEVs internal to M-CEs mostly cluster around 10 cm in the parent eddy, without a spike in SEV number at lower amplitudes. Finally, the

relationship between SEV and mesoscale eddy EKE is mostly focused around the origin, with lower EKE mesoscale eddies unable to host SEVs of higher EKE, and the number of high-EKE SEVs peaking around a parent eddy mean EKE of around  $0.03 \text{ m}^2 \text{s}^{-2}$  in all cases (Figures 8M–P). All correlations between SEV and mesoscale eddy EKEs are statistically significant. Another important element to examine in the relationship between mesoscale eddies and SEVs is how this relation changes over the course of the parent eddy lifetime (Figure 9).

Based upon the statistics of our mesoscale eddy detections, we separate the parent mesoscale eddies into classes based upon their maximum radii: 25–75 km covers eddies up until roughly the mean, 76–125 km covers eddies between 1 and 2 standard deviations above the mean, and 126+ km covers eddies with maximum radii above 2 standard deviations above the mean. For all sizes of mesoscale eddies, we catalogue the number of internal SEV-AEs and SEV-CEs along with the percent of the parent eddy that is taken up by the internal SEVs in both spatial area and EKE. We find in all sizes of mesoscale eddies that the number of internal SEVs begins to rise at around 80% through the parent eddy's lifetime. Towards the end of an average large eddy lifetime, between 8 to 9 internal SEVs of each type are expected as the eddy decoheres (Figures 9E–F). The EKE and area shares only slightly increase during this time, without the same rapid increase. A notable exception is in mid-size M-CEs, where SEV-CE EKE share rises to 35% of the parent eddy total (Figure 9D).



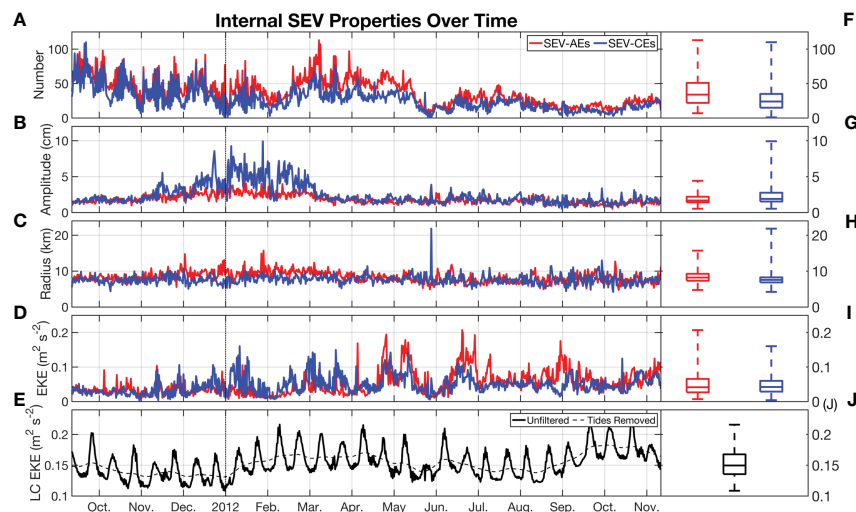


FIGURE 6

The time series of SEV properties, exactly as in Figure 3, but for only internal SEVs. Loop Current EKE is repeated without alterations. (A) The number of eddies per increment; (B) the median eddy amplitude (cm); (C) the median eddy radius (km); (D) the median eddy EKE ( $\text{m}^2 \text{s}^{-2}$ ). (E) The EKE for the Loop Current region both with and without tidal variability. (F–J) As in (A–E) but using a box plot to show the median, quartiles, and extremes of the data upon which the time series is constructed.

In all cases, the same rotation direction between SEV and mesoscale eddy (CE-CE or AE-AE) is more likely to be found within an eddy, rather than the counterrotating opposite (CE-AE or AE-CE). Similarly, the EKE and area shares are dominated by same-direction rotating pairs, with an average value for same-direction pairs lying between 10 and 20% of the parent eddy, while opposite-direction pairs average between 0 and 10% for all eddy sizes. One last anomaly is in the lowest sample size category, large M-CEs: there are intense spikes in SEV-CE EKE share at the beginning and middle of the M-CE normalized lifetime (Figure 9F). Given that the figure shown is of an arithmetic mean, this is more likely to be contaminated by a handful of outliers; however, the values shown (76.7% at the beginning and 67.9% in the mid-life) are too high for a single outlier to be fully responsible. Additionally, we do see an early-life trend for higher SEV-CE EKE share in smaller M-CEs (Figures 9B, D). This indicates that there may be a relationship between M-CE and SEV-CE EKE in the formation stages in addition to death stages; this relationship is not present in M-AEs and SEV-AEs. While the previous figures have indicated the characteristics of SEVs inside of parent eddies, the probabilities of the locations of the SEVs have yet to be interrogated. We examine this distribution in Figure 10.

The rows of Figure 10 are broken down as in Figure 9 for eddies of increasing maximum radii. The greatest probability of SEV occurrence is for M-CEs and SEV-CEs, where there is over a 25% chance of finding an SEV-CE at any given timestep in the center of any given M-CE (Figures 10D, H, L). This likelihood decreases away from the center of the eddy until a minimum is reached beyond 1 radius of the M-CE. Given that the size of SEVs is relatively consistent between 6 and 12 km, while the size of mesoscale eddies varies considerably, it follows that the probabilities of SEVs in larger mesoscale eddies would take up less of the overall eddy in the composite. However, the overall shape of the pattern is

the same. A similar pattern is observed for M-AEs and SEV-AEs, although the likelihood is halved and the distribution is flattened longitudinally (Figures 10A, E, I). Furthermore, the pattern for M-AEs is more diffuse, reaching beyond the first radius of the M-AE for smaller eddies. It also worth noting that some of the “SEVs” observed in the centers of same-type rotation pairs are actually the centers of the original mesoscale eddy leaking through the filter.

The more intriguing of the probability patterns are those found on opposite-type rotation pairs. While the most rare to find in one particular point in the eddy, M-AEs and SEV-CEs exhibit a ringed pattern focused on the edge of the first eddy radius, gradually shifting inside the radial edge as eddy size increases (Figures 10B, F, J). This is most intense on the northern and southern edges. In a similar way, M-CEs and SEV-AEs exhibit a stricter dipolar pattern with two loci to the direct north and south of the eddy center and lying once again on or slightly in from the first eddy radius (Figures 10C, G, K). Interestingly, smaller M-CEs have a larger focus of SEV-AE activity on their southern edge; however, this reverses for larger eddies, with a more intense focus of SEV-AEs on the northern edge. In both opposite-type pairs, the center of the eddy is the least likely location for an SEV to occur, with a probability close to 0. The impacts of SEVs on mesoscale eddies may be evaluated not only through their location within mesoscale eddies, but also with their temperature and salinity signatures at the surface. We begin with sea surface temperature anomalies (SSTAs) of SEVs, computed as the difference between the center SST and the mean SST out to a distance of 3 radii (Figure 11).

The general trend of the anomalies of the SEVs are as expected: the cyclonic, upwelling motion of SEV-Ces in all cases create a negative SSTA versus the background, while the anticyclonic, downwelling motion of SEV-AEs create a positive SSTA. This is most intense in the case of M-CEs, where SEV-AEs are associated with an SSTA of up to  $0.06^\circ\text{C}$  and SEV-CEs are associated with an

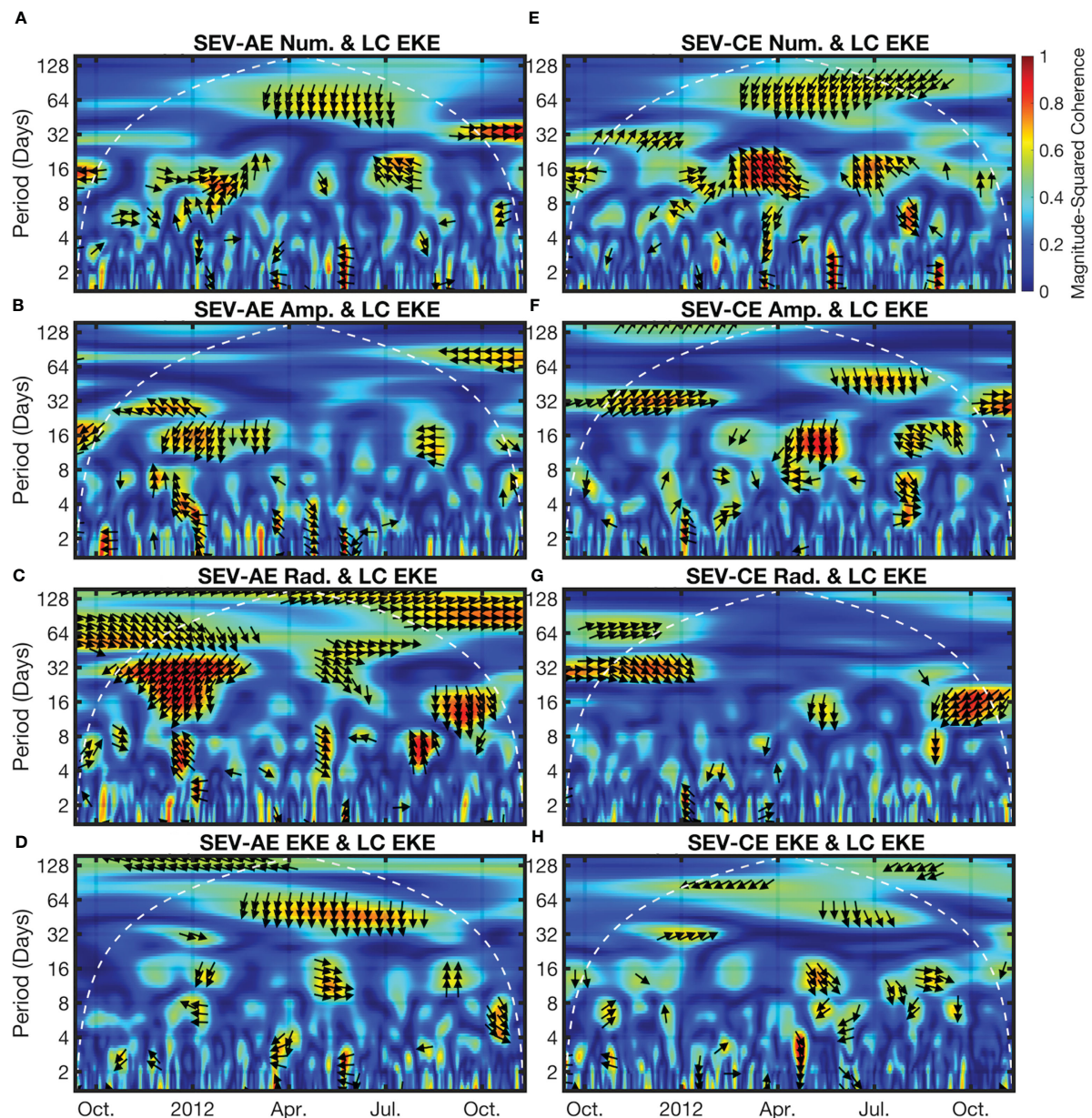


FIGURE 7

The Morlet wavelet coherence, exactly as in Figure 4, but for the internal SEV time series in Figure 6. The white dashed line shows the cone of influence, after which edge effects dominate, while the black arrows show the direction of phase for coherence > 0.5. (A–D) The coherence between internal SEV-AEs number, amplitude, radius, and EKE time series and the Loop Current time series. (E–H) As in (A–D) but for internal SEV-CEs.

SSTA of up to  $-0.07^{\circ}\text{C}$  (Figures 11C, D, G, H, K, L). By contrast, the anomalies associated with M-AE internal SEVs are less intense but still present (Figures 11A, B, E, F, I, J). For all combinations, the anomalies are generally an order of magnitude less than those SSTAs associated with mesoscale eddies from observations (Brokaw et al., 2020). The general shape of the background SST is also comparable to those from observations, with a cooler flank generally to the north and a warmer flank to the south, attributable to the warmer Loop Current bringing warmer water to the south. As with SSTA, we compute the sea surface salinity anomalies (SSSAs) for SEVs of each type (Figure 12).

Interestingly, none of the SEVs exhibit a clear SSSA at their centers. Rather, each combination leads to a different arrangement of anomalies around the SEV center. In general, M-AEs and SEV-AEs lead to a negative SSSA to the direct east of the SEV center, being more intense with larger M-AEs (Figures 12A, E, I) while M-AEs and SEV-CEs demonstrate a positive SSSA to the east, with the most intense anomalies associated with mid-size eddies (Figures 12B, F, J). A similar set of patterns is exhibited for M-CEs and their constituent SEVs. However, the most intense SSSAs for M-CEs and both SEV-AEs and SEV-CEs is in smaller eddies rather than large ones (Figures 12C, D). While these patterns are

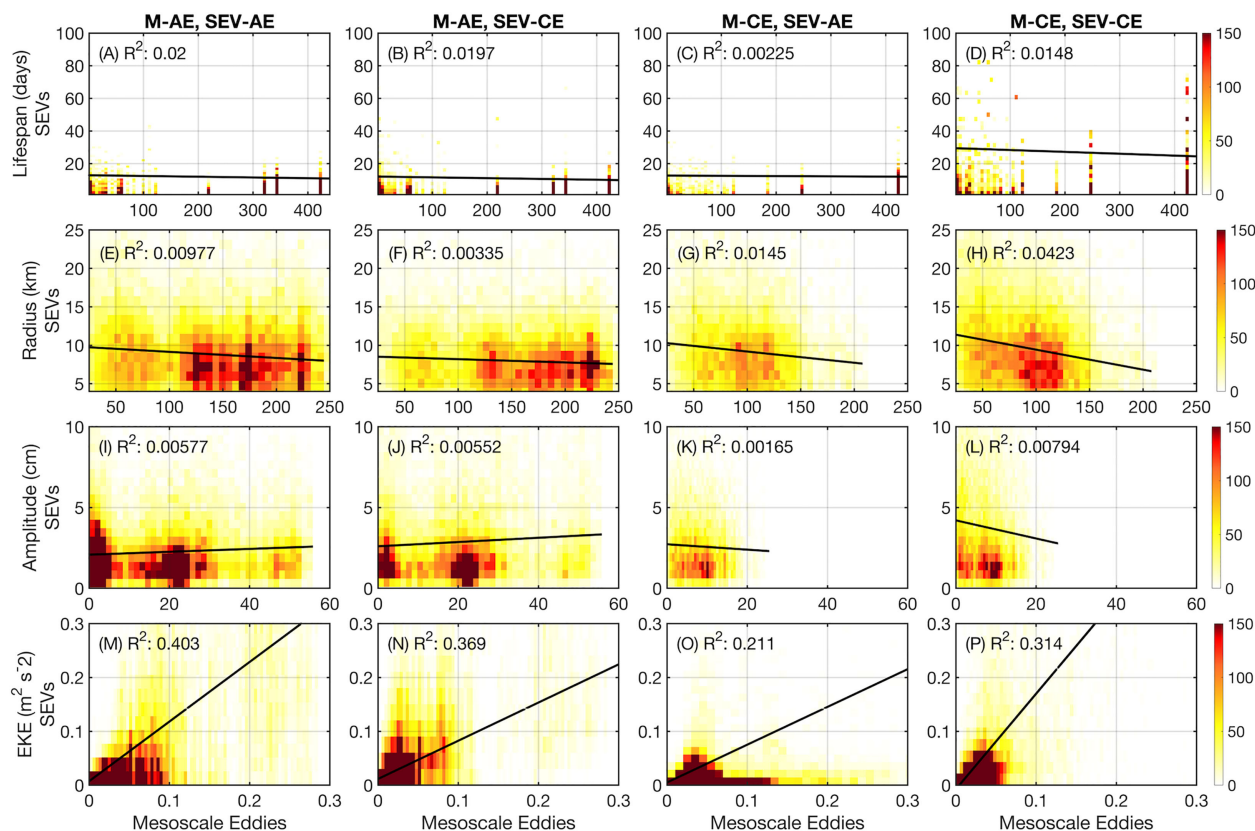


FIGURE 8

The binned histograms, in number of eddies, between the coincident properties of parent mesoscale eddies (x-axes) and their internal SEVs (y-axes) for each type of internal SEV-outer mesoscale eddy combination pair (columns 1–4). (A–D) The lifespans (days) of SEVs versus their parent mesoscale eddy lifespans. (E–H) The radii (km) of SEVs versus their parent mesoscale eddy radii. (I–L) The amplitudes (cm) of SEVs versus their parent mesoscale eddy amplitudes. (M–P) The EKEs ( $\text{m}^2 \text{s}^{-2}$ ) of SEVs versus their parent mesoscale eddy EKEs. Linear regressions are shown as black lines with  $R^2$  values annotated.

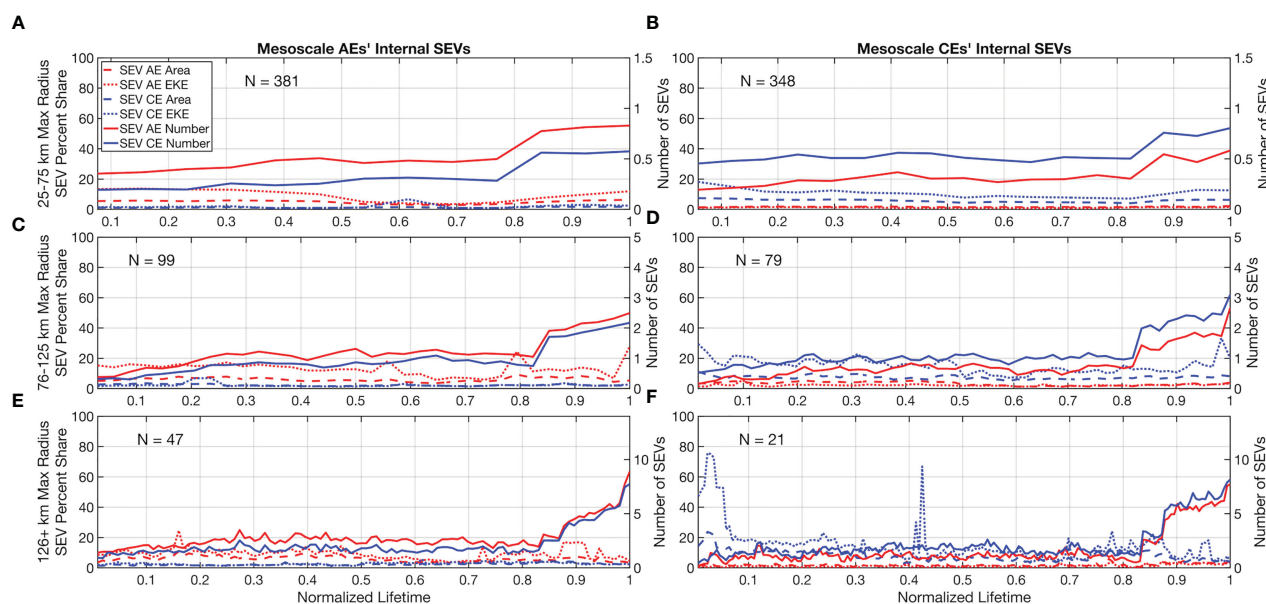


FIGURE 9

The numbers, fractions of parent eddy area, and fractions of parent eddy EKE taken up by internal SEVs over the normalized lifespan of their parent eddies. Number of parent eddies in each figure is shown. The left y-axes depict the percentage statistics, while the right y-axis depicts the number of SEVs. (A) The statistics for parent AEs with a maximum trajectory radius of between 25 and 75 km. (B) As in (A) but for parent CEs. (C) As in (A) but for eddies whose maximum radius lies between 76 and 125 km. (D) As in (C) but for parent CEs. (E) As in (A) but for eddies whose maximum radius lies above 126 km. (F) As in (E) but for parent CEs.



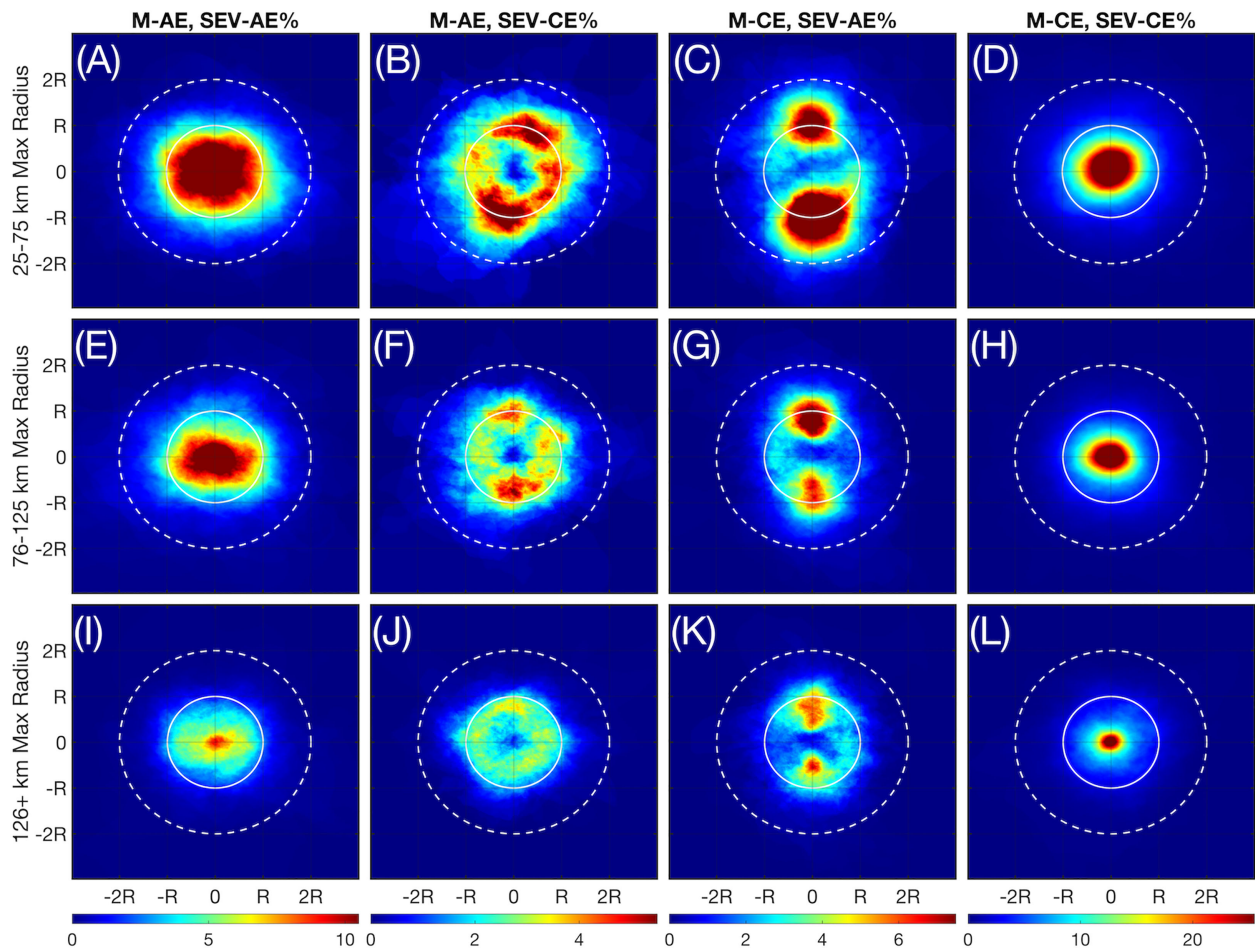


FIGURE 10

The locational composites for all instances of internal SEVs, showing the likelihood of a SEV covering a given pixel in a mesoscale eddy in percentage points for each type of internal SEV-outer mesoscale eddy combination pair. (A–D) The composites for eddies of maximum radius between 25 and 75 km. (E–H) As in (A–D) but for eddies of maximum radius between 76 and 125 km. (I–L) As in (A–D) but for eddies whose maximum radius lies above 126 km.

similar in some respects to the patterns exhibited by observed mesoscale eddies in the GoM, such as the fact that the eddy center does not show a clear anomaly and that fresher water tends to originate to the north due to the Mississippi river outflow, the off-center anomaly is unusual (Brokaw et al., 2020).

As our results have indicated, internal SEVs are most often found within large eddies and induce anomalies in both SSTA and SSSA while they are present. Therefore, the last analysis we conduct is on the subject of the relationship between LCEs and SEVs using the major LCE of the simulation (Figure 13).

This LCE is noteworthy for being identifiable from the beginning of the simulation (as the Loop Current begins in an extended state) all the way through the end, not actually dissipating during the duration of the simulation. It separates fully from the Loop Current in early February before propagating westward and resting on the western boundary. This particular LCE was the fourth AE identified by the eddy detection algorithm, and so is assigned the identifier AE4. Over the course of its life, AE4 always has at least 3 SEVs inside it, with at least 4% of its area and EKE devoted to these SEVs (Figure 13A). We showcase three snapshots of AE4 in relation

to the Loop Current: one snapshot as the Loop Current is still extending in January (Figure 13B, E), one just after separation in late February (Figure 13C, F), and one a month after separating in late March (Figure 13D, G). As shown by the dashed lines in Figure 13A, these dates coincide with a middle, high, and low relative internal SEV composition respectively. We therefore observe that the SEVs reach a peak intensity inside AE4 just after separation from the Loop Current and rapidly fall thereafter as AE4 begins propagating westward.

## 4 Discussion

In our results we have emphasized the characteristics of SEVs and their relationships with mesoscale eddies. Generally, SEVs are short-lived (on the order of a week lifetime) structures that are ubiquitous in long-lived (longer than a week lifetime) mesoscale eddies. They are most concentrated in the Loop Current and in the LCEs that spawn from it, but their general characteristics are similar across all types of eddies. SEVs increase in number both in the



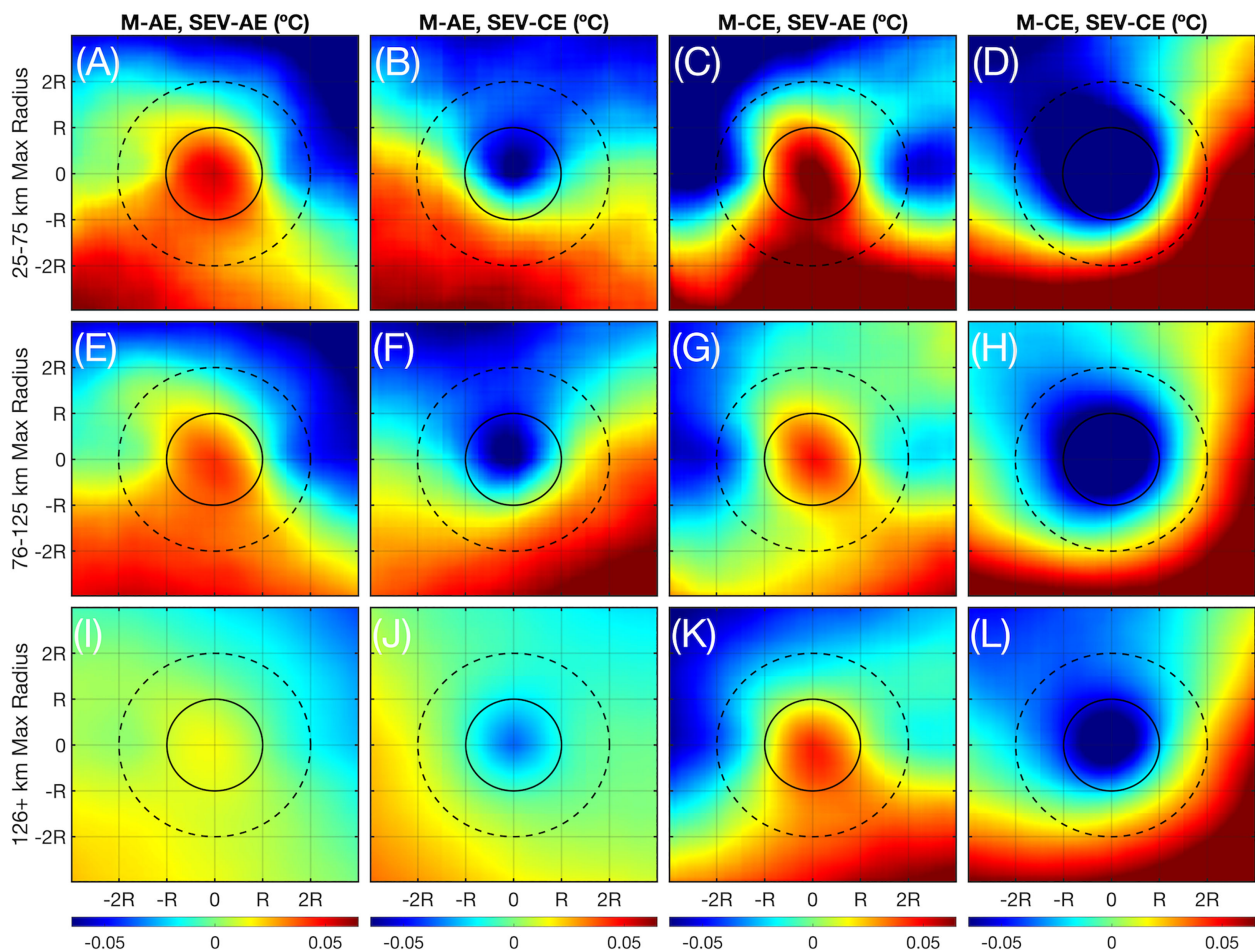


FIGURE 11

The composites for all SST anomalies ( $^{\circ}\text{C}$ ) associated with internal SEVs (difference between center SEV temperature and mean temperature computed up to 3 radii) for each type of internal SEV-outer mesoscale eddy combination pair. (A–D) The composites for eddies of maximum radius between 25 and 75 km. (E–H) As in (A–D) but for eddies of maximum radius between 76 and 125 km. (I–L) As in (A–D) but for eddies whose maximum radius lies above 126 km.

splitting of LCEs from the Loop Current as well as towards the end of the lifetimes of mesoscale eddies. The amplitude of SEV-CEs in particular is a strong signal produced by an extending Loop Current about to shed an LCE (Figures 3B, 5B). The EKE of such SEVs strongly follows a fortnightly tidally induced signal apparent in the Loop Current. It is possible that, as suggested by previous literature, some of these SEVs are produced by barotropic tides near the coast (Callendar et al., 2011; Nakamura et al., 2012). Regardless of when they appear, SEVs induce submesoscale temperature and salinity variabilities in their parent mesoscale eddies. With this general breakdown, however, arises questions that we have not yet fully addressed in our analysis.

#### 4.1 Proposed generation mechanisms of SEVs

We begin with an assessment of likely SEV generation mechanisms. One explanation particularly relevant for SEV-AEs, previously described by Brannigan (2016) and observed by

Brannigan et al. (2017), is symmetric instabilities in the mixed layer. In this process, an instability is generated in the mixed layer, primarily driven by vertical buoyancy fluxes and vertical velocity shear, ultimately leading to a negative potential vorticity region at the surface. The number of filaments and structures generated through this process are shown to be highly resolution-dependent, first resolvable at the 2-km scale. As this is the scale resolved by our simulation, filaments, fronts, and eddy-like structures associated with symmetric instabilities may be associated with SEV-AEs found in the cores of M-AEs. Symmetric instabilities are also observed by de Marez et al., (2020b) to act at the northern edge of a simulated eddy, which then induces diapycnal mixing. Therefore, symmetric instabilities may explain the dipolar distribution of SEV-AEs within M-CEs. However, the coastal nature of the most numerous SEV-AEs within M-CEs (i.e. Figure 5K, L, P, Q) may also play a role in forcing this distribution. The intense vertical velocities associated with such structures, robust throughout studies of the submesoscale, may explain also the coherency of the SSTA observed in their cores (Figure 11).

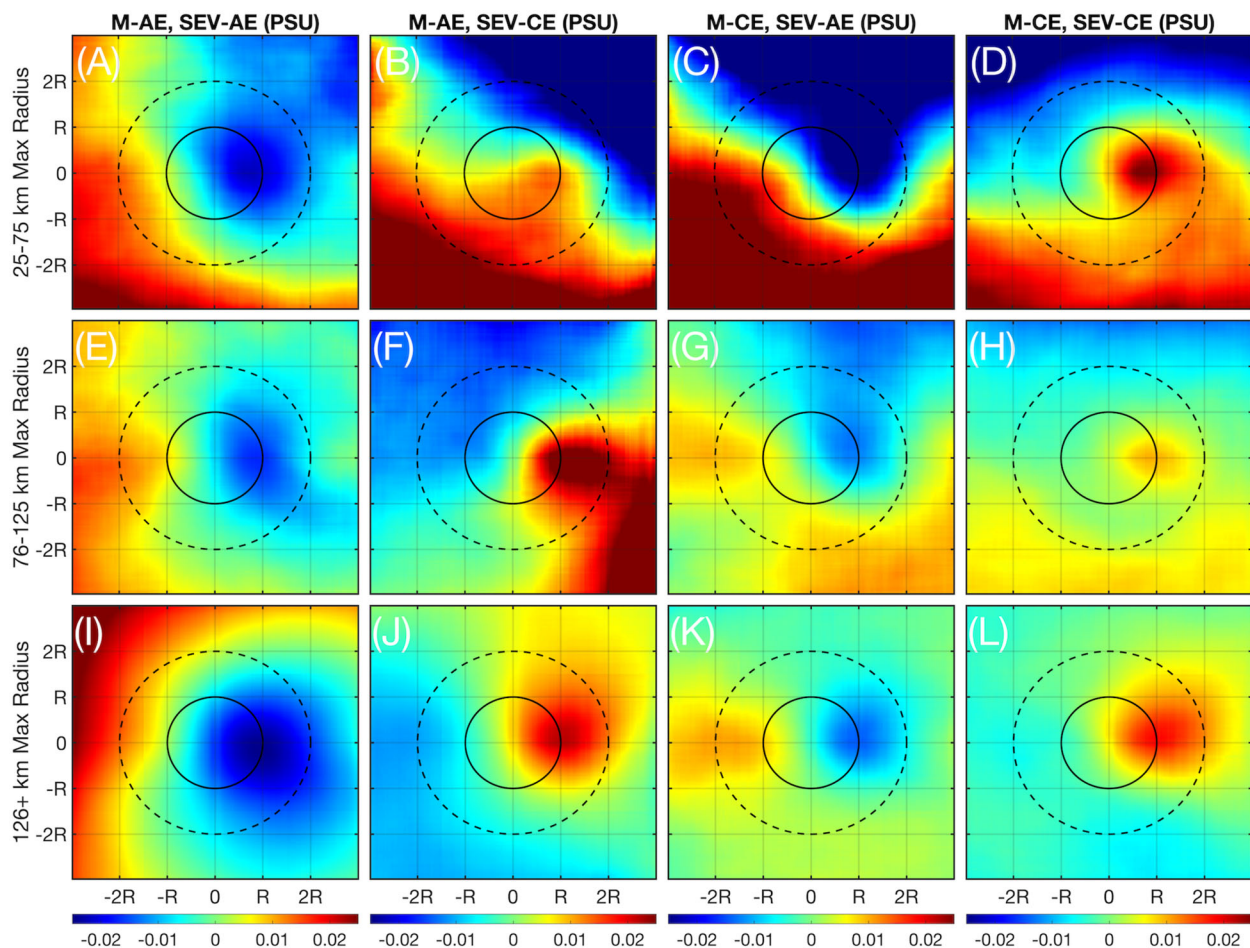


FIGURE 12

The composites for all SSS anomalies (PSU) associated with internal SEVs (difference between center SEV salinity and mean salinity computed up to 3 radii) for each type of internal SEV-outer mesoscale eddy combination pair. (A–D) The composites for eddies of maximum radius between 25 and 75 km. (E–H) As in (A–D) but for eddies of maximum radius between 76 and 125 km. (I–L) As in (A–D) but for eddies whose maximum radius lies above 126 km.

Symmetric instabilities as a possible cause for SEV generation is also supported by the instability analysis of [Lahaye and Zeitlin \(2015\)](#), but alongside baroclinic and barotropic instabilities. The dominance of baroclinic and barotropic instabilities in the generation of submesoscale structures is likewise supported by the observations of [Buckingham et al. \(2017\)](#). Similarly, [Yang et al. \(2020\)](#) report that baroclinic instabilities play a particular role in the genesis of eddies in the Loop Current region. They also observe a mechanical energy transfer between mesoscale eddies and high frequency frontal eddies as a part of an inverse energy cascade, an observation similarly reported by [Lazaneo et al. \(2022\)](#). The presence of SEVs, aligning with those frontal eddies described by [Yang et al. \(2020\)](#) correlates with the splitting of the LCE from the Loop Current as described previously ([Figure 13](#)). Therefore, through both baroclinic instabilities and the ensuing frontogenesis (*i.e.* [Garabato et al., 2022](#)), the generation of SEVs may indicate an intensification of the inverse energy cascade; this most likely varies in conjunction with the forward energy cascade on a seasonal basis, as highlighted by [Yang et al. \(2021\)](#). The

concept that the inverse energy cascade might be uniquely prevalent for internal SEVs is supported by the findings in our [Figure 9](#), as SEVs increase in number the closer a mesoscale eddy is to decoherence. These SEVs, particularly those of opposite sign that gather on eddy boundaries, may also play a role similar to the submesoscale structures noted by [Haza et al. \(2016\)](#), causing leakage across eddy boundaries. An eddy with more such SEVs, therefore, can be expected to fracture from within due to baroclinic and barotropic instabilities at and below the mixed layer expressed as a part of same-rotation type SEVs. At the same time, such an eddy might be leaking fluid to without due to symmetric instabilities and frontogenesis expressed by opposite-rotation type SEVs, possibly in a process similar to that described by [Barkan et al. \(2019\)](#) and [Verma et al. \(2019\)](#). The non-baroclinic processes are likely intensified as a mesoscale eddy approaches topographic features ([Rosso et al., 2015](#); [Morvan et al., 2019](#); [Morvan et al., 2020](#)). Lastly, it is worth noting that based upon the season and location of SEV formation the motions and predominant EKE that characterize SEVs may be either primarily balanced or unbalanced in terms of



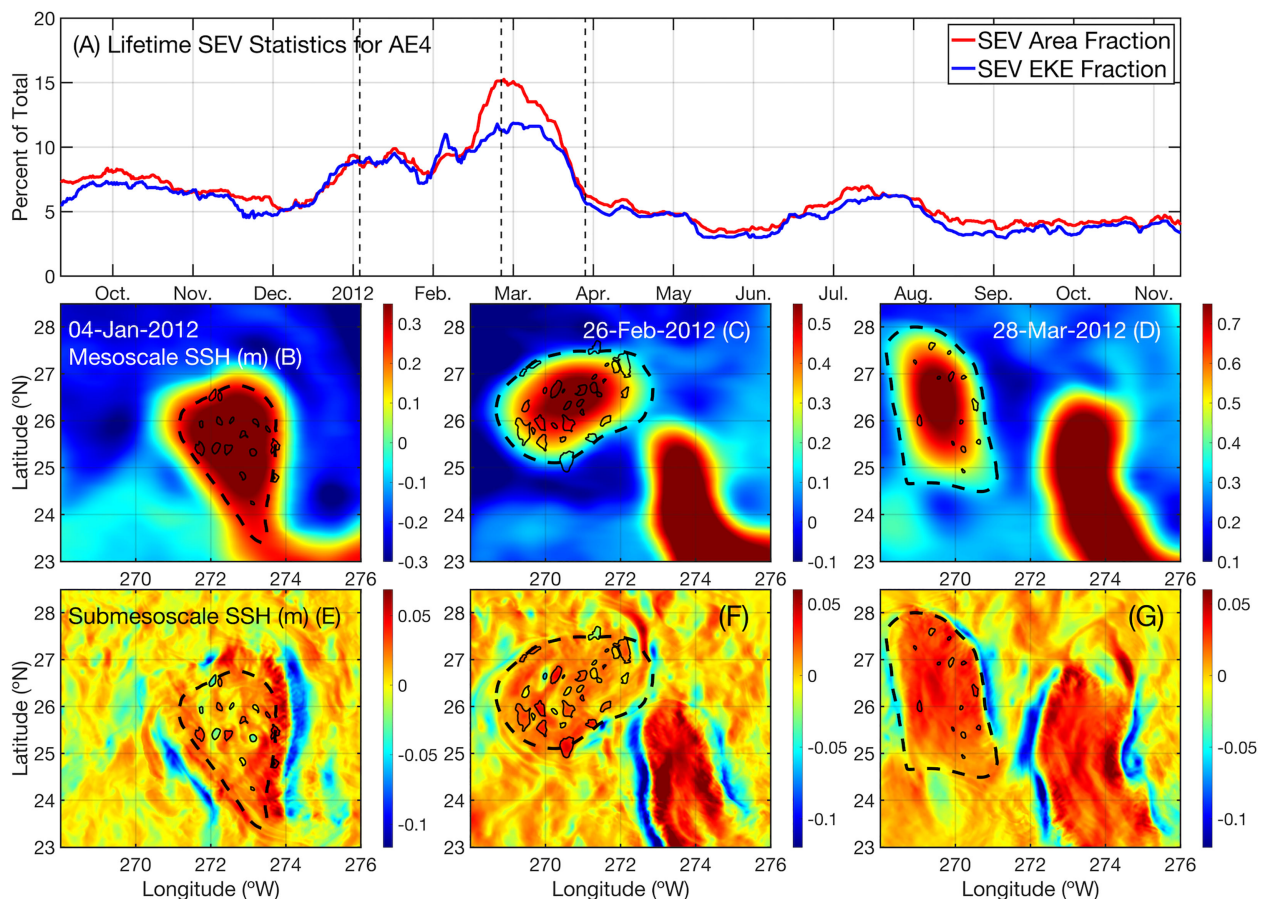


FIGURE 13

The separation of the Loop Current Eddy AE trajectory #4, or AE4. (A) The percent of AE4's area and EKE taken up by SEVs over its lifespan, with black dashed lines showing the dates of the following snapshots. (B) The large-scale SSH (m) field associated with Jan. 4<sup>th</sup>, 2012 showing AE4 (dashed line) and its internal SEVs (solid lines). (C) As in (B) but for Feb. 26<sup>th</sup>, 2012. (D) As in (B) but for Mar. 28<sup>th</sup>, 2012. (E–G) As in (B–D) but showing the small-scale SSH (m) field instead.

dissipation vs. atmospheric forcings; the reader is referred to [Cao et al. \(2023\)](#) for a more complete discussion on the nature of such motions as manifested in our model simulations.

## 4.2 SSSA anomaly patterns

While the SSTA patterns described in [Figure 11](#) match those ascribed both to mesoscale eddies in the GoM and the dynamics of submesoscale vertical heat transport, the dynamical meaning behind the SSSA patterns of [Figure 12](#) are less clear ([Brokaw et al., 2020](#); [Wang et al., 2022](#)). As previously noted, in fact, the observed patterns are opposite of those expected in such structures from a theoretical standpoint. The SSSA signature associated with AEs is typically associated with an increased surface salinity, while the surface expression of CE is more often associated with a decrease in surface salinity as described in mesoscale eddies throughout the world's oceans ([Melnichenko et al., 2017](#)). The patterns seen in [Figure 12](#), however, show an opposite effect, as SEV-AEs are associated with more intense freshwater anomalies and SEV-CEs are associated with more intense salinity anomalies.

In both cases, the dipolar structure is expected, but the intensity of the poles are reversed.

The answer may be found in the work of [Zhang X. et al. \(2019\)](#). In this study, the formation of a submesoscale eddy is observed as a result of baroclinic instability in a slumping salinity front. The authors find that, due to the fresher surface layer, upwelling induced by the eddy resulted in a more saline surface layer. In the same fashion, large submesoscale salinity variations on the order of 0.05 psu at the surface as observed by [Drushka et al. \(2019\)](#) might be expected in the GoM due to the river plume of the Mississippi river. In effect, the decidedly fresher surface water of the GoM, especially towards its northern edge, is likely entrained by SEV-AEs, decreasing salinity adjacent to the SEV core. At the same time, SEV-CEs are responsible for upwelling through the surface layer, allowing for a more saline surface. This allows for frontal compensation across the GoM as described for freshwater-influenced regions by [Spiro Jaeger and Mahadevan \(2018\)](#). An intriguing connection here is made by [Kobashi and Hetland \(2020\)](#): the Mississippi river outflow is partially controlled by anthropogenic factors and remote interannual variabilities, e.g. the El Niño Southern Oscillation. As a result, SEVs and other structures often associated with salinity fronts may

introduce an element of remote forcing into SEV variability. However, as the authors conclude, there is as of yet insufficient evidence to prove a significant link exists, especially at the under observed submesoscale.

### 4.3 Broader implications

The ubiquity of SEVs in the GoM and mesoscale eddies suggests that SEVs may play an important role in the biogeochemical cycling and chlorophyll dispersal within the Gulf. For example, frontal eddy structures have already been observed in the Florida Straits using ocean color data (Zhang Y. et al., 2019). At the same time, mesoscale eddies in the Gulf have been shown to aid in the dispersal of chlorophyll-a as eddies interact and break plumes apart (Toner et al., 2003). SEVs and the frontal dynamics associated with them likely play a role in the advection and vertical movement of nutrients into and away from the surface layer, influencing the distribution of phytoplankton blooms and hypoxic zones (Rabalais et al., 2002). Internal SEVs and leakage associated with them may also complicate the transport of freshwater away from the river plume with future implications for the spread of pollutants (Özgökmen et al., 2016).

Another implication of SEV-induced variability in the Gulf is that on tropical cyclone strength. Warm sea surface temperatures associated with mesoscale eddies have been observed to correlate with an increase in storm strength (Jaimes et al., 2016). LCEs have also been drained of heat and forcibly dissipated through air-sea interactions with hurricanes (Potter et al., 2021). As we demonstrate here, the submesoscale variability of both the Loop Current and LCEs changes dramatically depending on life cycle stage. Future observations will serve to clarify the role that submesoscale oceanic variability plays in the intensification and feedbacks associated with hurricane growth.

Finally, machine learning based approaches have already demonstrated skill in the prediction of the separation of LCEs (Wang et al., 2019). The most prevalent of these approaches utilizes high resolution SSH time series to extract hidden patterns that lead to LCE separation spatiotemporal predictions. Greater resolution data and an increased understanding of the submesoscale dynamics within that data may improve the accuracy and skill of future predictions, as the separation of an LCE from the Loop current involves interactions across both the mesoscale and submesoscale that cannot be properly discerned from previously available data (Yang et al., 2020).

## 5 Conclusion

In this study, we have used a tailor-made filtering approach to efficiently separate the spatial scales in a high resolution modelling simulation. Through the use of an automated eddy detection and tracking algorithm, we have identified regions that, through shape, persistence, and SSH anomalies, behave like eddies. These so-called SEVs were then evaluated both across the entire spatiotemporal domain and in the context of mesoscale eddies, where SEVs were collocated within mesoscale eddy contours. To our knowledge, this

is the first time this has been done algorithmically on a basin-wide scale. Through describing the characteristics of SEVs, particularly those internal to mesoscale eddies, we demonstrate that SEVs are typically responsible for up to 15% of the internal variability in terms of EKE, SSS, SST, and SSH in mesoscale eddies of all sizes throughout the GoM. We show that SEVs also correlate with the extensions of the Loop Current, with the number of SEVs internal to an LCE reaching a maximum just after separation from the loop current occurs. These findings have implications for biogeochemical processes in the Gulf, as well as Loop Current and LCE separation forecasting. Given our results' dependence on our model's resolution as demonstrated by previous studies, further observations are required to validate and confirm them. The SWOT mission, already in orbit and undergoing calibration and validation, promises to provide the first wide-scale SSH measurements of an effective resolution capable of resolving these SEVs.

### Data availability statement

Publicly available datasets were analyzed in this study. This data can be found here: The National Aeronautics and Space Administration (NASA) Estimating the Circulation & Climate of the Ocean (ECCO) Data Portal, [https://data.nas.nasa.gov/ecco/data.php?dir=/eccodata/llc\\_4320](https://data.nas.nasa.gov/ecco/data.php?dir=/eccodata/llc_4320).

### Author contributions

BS managed the computational resources, funding acquisition, and lab space. All authors contributed to the conceptualization and design of the study. PE managed the data and wrote the software. All authors contributed to the formulation of the analysis. PE wrote the original draft of the manuscript. All authors contributed to the manuscript revision. All authors contributed to the article and approved the submitted version.

### Funding

Research reported in this manuscript was supported by the Gulf Research Program of the National Academies of Sciences, Engineering, and Medicine under award #2000013149. The content is solely the responsibility of the authors and does not necessarily represent the official views of the Gulf Research Program or the National Academies of Sciences, Engineering, and Medicine. PE was funded by the U.S. Department of Defense Science, Mathematics, and Research for Transformation (SMART) Scholarship and the University of South Carolina Presidential Fellowship.

### Acknowledgments

This has NRL contribution number NRL-JA-7320-23-5876. Approved for public release, distribution is unlimited. We thank the editor and three reviewers for their suggestions that significantly improved the quality of the final work.



## Conflict of interest

The authors declare that the research was conducted in the absence of any commercial or financial relationships that could be construed as a potential conflict of interest.

The handling editor SM declared a shared consortium GOFFISH with the author BS at the time of review.

## References

- Adcroft, A., Hill, C., Campin, J.-M., Marshall, J., and Heimbach, P. (2004). "Overview of the formulation and numerics of the MIT GCM," in *Proceedings of the ECMWF seminar series on numerical methods, recent developments in numerical methods for atmosphere and ocean modeling* (ECMWF: Shinfield Park, Reading).
- Arbic, B. K., Elipot, S., Brusch, J. M., Menemenlis, D., Ponte, Aurélien L., Shriver, J. F., et al. (2022). Near-surface oceanic kinetic energy distributions from drifter observations and numerical models. *J. Geophysical Research: Oceans* 10, e2022JC018551. doi: 10.1029/2022JC018551
- Barkan, R. M., Molemaker, J., Srinivasan, K., McWilliams, J. C., and D'Asaro, E. A. (2019). The role of horizontal divergence in submesoscale frontogenesis. *J. Phys. Oceanography* 6, 1593–1618. doi: 10.1175/JPO-D-18-0162.1
- Bracco, A., Liu, G., and Sun, D. (2019). Mesoscale-submesoscale interactions in the gulf of Mexico: from oil dispersion to climate. *Chaos Solitons Fractals* 119, 63–72. doi: 10.1016/j.chaos.2018.12.012
- Brannigan, L. (2016). "Intense submesoscale upwelling in anticyclonic eddies." *Geophysical Res. Lett.* 43, 3360–3369. doi: 10.1002/2016GL067926
- Brannigan, L., Marshall, D. P., Naveira, A. C., Garabato, A. J., Nurser, G., and Kaiser, J. (2017). Submesoscale instabilities in mesoscale eddies. *J. Phys. Oceanography* 12, 3061–3085. doi: 10.1175/JPO-D-16-0178.1
- Brokaw, R. J., Subrahmanyam, B., Trott, C. B., and Chaigneau, A. (2020). Eddy surface characteristics and vertical structure in the gulf of Mexico from satellite observations and model simulations. *J. Geophysical Research: Oceans* 2, e2019JC015538. doi: 10.1029/2019JC015538
- Buckingham, C. E., Khaleel, Z., Lazar, A., Martin, A. P., Allen, J. T., Naveira Garabato, A. C., et al. (2017). Testing munk's hypothesis for submesoscale eddy generation using observations in the north Atlantic. *J. Geophysical Research: Oceans* 8, 6725–6745. doi: 10.1002/2017JC012910
- Callendar, W., Klymak, J. M., and Foreman, M. G. G. (2011). Tidal generation of Large Sub-mesoscale eddy dipoles. *Ocean Sci.* 4, 487–502. doi: 10.5194/os-7-487-2011
- Cao, H., Fox-Kemper, B., and Jing, Z. (2021). Submesoscale eddies in the upper ocean of the kuroshio extension from high-resolution simulation: energy budget. *J. Phys. Oceanography* 7, 2181–2201. doi: 10.1175/JPO-D-20-0267.1
- Cao, H., Fox-Kemper, B., Jing, Z., Song, X., and Liu, Y. (2023). Towards the upper-ocean unbalanced submesoscale motions in the oleaner observations. *J. Phys. Oceanography* 4, 1123–1138. doi: 10.1175/JPO-D-22-0134.1
- Chaigneau, A., Eldin, Gérard, and Dewitte, B. (2009). Eddy activity in the four major upwelling systems from satellite altimetry–2007). *Prog. Oceanography Eastern Boundary Upwelling Ecosystems: Integr. Comp. Approaches* 1, 117–123. doi: 10.1016/j.pocean.2009.07.012
- Chaigneau, A., Gizolme, A., and Grados, C. (2008). Mesoscale eddies off Peru in altimeter records: identification algorithms and eddy spatio-temporal patterns. *Prog. Oceanography Northern Humboldt Curr. System: Ocean Dynamics Ecosystem Processes Fisheries* 2, 106–119. doi: 10.1016/j.pocean.2008.10.013
- Chelton, D. B., Samelson, R. M., and Farrar, J.T. (2022). The effects of uncorrelated measurement noise on SWOT estimates of Sea surface height, velocity, and vorticity. *J. Atmospheric Oceanic Technol.* 7, 1053–1083. doi: 10.1175/JTECH-D-21-0167.1
- Chelton, D. B., Schlax, M. G., Samelson, R. M., Farrar, J.T., Jeroen Molemaker, M., McWilliams, J. C., et al. (2019). Prospects for future satellite estimation of small-scale variability of ocean surface velocity and vorticity. *Prog. Oceanography* 173, 256–350. doi: 10.1016/j.pocean.2018.10.012
- Chereskin, T. K., Rocha, C. B., Gille, S. T., Menemenlis, D., and Passaro, M. (2019). Characterizing the transition from balanced to unbalanced motions in the southern California current. *J. Geophysical Research: Oceans* 3, 2088–2109. doi: 10.1029/2018JC014583
- D'Addezio, J. M., Jacobs, G. A., Yaremchuk, M., and Souopgui, I. (2020). Submesoscale eddy vertical covariances and dynamical constraints from high-resolution numerical simulations. *J. Phys. Oceanography* 4, 1087–1115. doi: 10.1175/JPO-D-19-0100.1
- de Marez, C., Carton, X., Corréard, Stéphanie, L'Hégaret, P., and Morvan, M. (2020a). Observations of a deep submesoscale cyclonic vortex in the Arabian Sea. *Geophysical Res. Lett.* 13, e2020GL087881. doi: 10.1029/2020GL087881
- de Marez, C., Meunier, T., Morvan, M., L'Hégaret, P., and Carton, X. (2020b). Study of the stability of a Large realistic cyclonic eddy. *Ocean Model.* 146, 101540. doi: 10.1016/j.ocemod.2019.101540
- Drushka, K., Asher, W. E., Sprintall, J., Gille, S. T., and Hoang, C. (2019). Global patterns of submesoscale surface salinity variability. *J. Phys. Oceanography* 7, 1669–1685. doi: 10.1175/JPO-D-19-0018.1
- Durand, M., Fu, L.-L., Lettenmaier, D. P., Alsdorf, D. E., Rodriguez, E., and Esteban-Fernandez, D. (2010). The surface water and ocean topography mission: observing terrestrial surface water and oceanic submesoscale eddies. *Proc. IEEE* 5, 766–779. doi: 10.1109/JPROC.2010.2043031
- Ernst, P. A., Subrahmanyam, B., and Trott, C. B. (2022). Lakshadweep High propagation and impacts on the Somali current and eddies during the southwest monsoon. *J. Geophysical Research: Oceans* 3, e2021JC018089. doi: 10.1029/2021JC018089
- Forget, G., Campin, J.-M., Heimbach, P., Hill, C. N., Ponte, R. M., and Wunsch, C. (2015). ECCO version 4: an integrated framework for non-linear inverse modeling and global ocean state estimation. *Geoscientific Model. Dev.* 10, 3071–3104. doi: 10.5194/gmd-8-3071-2015
- Fu, L.-L., Christensen, E. J., Yamarone, C. A.Jr., Lefebvre, M., Ménard, Y., Dorrer, M., et al. (1994). TOPEX/POSEIDON mission overview. *J. Geophysical Research: Oceans* 99, 24369–24381. doi: 10.1029/94JC01761
- Garabato, A. C.N., Yu, X., Callies, Jörn, Barkan, R., Polzin, K. L., Frajka-Williams, E. E., et al. (2022). Kinetic energy transfers between mesoscale and submesoscale motions in the open ocean's upper layers. *J. Phys. Oceanography* 52, 75–97. doi: 10.1175/JPO-D-21-0099.1
- Gristed, A., Moore, J. C., and Jevrejeva, S. (2004). Application of the cross wavelet transform and wavelet coherence to geophysical time series. *Nonlinear Processes Geophysics* 11, 561–566. doi: 10.5194/npg-11-561-2004
- Gula, J., Blacic, T. M., and Todd, R. E. (2019). Submesoscale coherent vortices in the gulf stream. *Geophysical Res. Lett.* 5, 2704–2714. doi: 10.1029/2019GL081919
- Haza, A. C., Özgökmen, T. M., and Hogan, P. (2016). Impact of submesoscales on surface material distribution in a gulf of Mexico mesoscale eddy. *Ocean Model.* 107, 28–47. doi: 10.1016/j.ocemod.2016.10.002
- Jaimes, B., Shay, L. K., and Brewster, J. K. (2016). Observed air-Sea interactions in tropical cyclone Isaac over loop current mesoscale eddy features. *Dynamics Atmospheres Oceans Loop Curr. Dynamics Experiment* 76, 306–324. doi: 10.1016/j.jdynatmoce.2016.03.001
- Kobashi, D., and Hetland, R. (2020). Reproducibility and variability of submesoscale frontal eddies on a broad, low-energy shelf of freshwater influence. *Ocean Dynamics* 70, 1377–1395. doi: 10.1007/s10236-020-01401-4
- Kurian, J., Colas, F., Capet, X., McWilliams, J. C., and Chelton, D. B. (2011). Eddy properties in the California current system. *J. Geophysical Research: Oceans* 116, doi: 10.1029/2010JC006895
- Lahaye, Noé, and Zeitlin, V. (2015). Centrifugal, barotropic and baroclinic instabilities of isolated ageostrophic anticyclones in the two-layer rotating shallow water model and their nonlinear saturation. *J. Fluid Mechanics* 762, 5–34. doi: 10.1017/jfm.2014.631
- Lazaneo, C. Z., Calil, P. H. R., Tandon, A., and da Silveira, I. C. A. (2022). Submesoscale coherent vortices in the south Atlantic ocean: a pathway for energy dissipation. *J. Geophysical Research: Oceans* 127, e2020JC017099. doi: 10.1029/2020JC017099
- Leben, R. R., and Born, G. H. (1993). Tracking loop current eddies with satellite altimetry. *Adv. Space Res.* 13, 325–333. doi: 10.1016/0273-1177(93)90235-4
- Liu, X., Wang, M., and Wei, S. (2009). A study of a hurricane Katrina-induced phytoplankton bloom using satellite observations and model simulations. *J. Geophysical Research: Oceans* 114, doi: 10.1029/2008JC004934
- Liu, Y., Weisberg, R. H., Hu, C., Kovach, C., and Riethmüller, R. (2011). "Evolution of the loop current system during the deepwater horizon oil spill event as observed with drifters and satellites," in *Geophysical monograph series*, vol. 195. Eds. Y. Liu, A. MacFadyen, Z.-G. Ji and R. H. Weisberg (Washington, D. C: American Geophysical Union), 91–101. doi: 10.1029/2011GM001127

- Lynch, P. (1997). The dolph–chebyshev window: a simple optimal filter. *Monthly Weather Rev.* 125, 655–660. doi: 10.1175/1520-0493(1997)125<0655:TDCWAS>2.0.CO;2
- Marshall, J., Adcroft, A., Hill, C., Perelman, L., and Heisey, C. (1997). A finite-volume, incompressible navier stokes model for studies of the ocean on parallel computers. *J. Geophysical Research: Oceans* 102, 5753–5766. doi: 10.1029/96JC02775
- Melnichenko, O., Amores, A., Maximenko, N., Hacker, P., and Potemra, J. (2017). Signature of mesoscale eddies in satellite Sea surface salinity data. *J. Geophysical Research: Oceans* 122, 1416–1424. doi: 10.1002/2016JC012420
- Menemenlis, D., Campin, J.-M., Heimbach, P., Hill, C., Lee, T., Nguyen, A., et al. (2008). ECCO2: high resolution global ocean and Sea ice data synthesis. *AGU Fall Meeting* 31.
- Meunier, T., Tenreiro, M., Pallás-Sanz, E., Ochoa, J., Ruiz-Angulo, A., Portela, E., et al. (2018). Intrathermocline eddies embedded within an anticyclonic vortex ring. *Geophysical Res. Lett.* 15, 7624–7633. doi: 10.1029/2018GL077527
- Morvan, M., Carton, X., Corréard, Stéphanie, and Baraille, Rémy (2020). Submesoscale dynamics in the gulf of Aden and the gulf of Oman. *Fluids* 5, 146. doi: 10.3390/fluids5030146
- Morvan, M., L'Hégaret, P., Carton, X., Gula, J., Vic, Clément, de Marez, C., et al. (2019). The life cycle of submesoscale eddies generated by topographic interactions. *Ocean Sci.* 15, 1531–1543. doi: 10.5194/os-15-1531-2019
- Nakamura, T., Matthews, J. P., Awaji, T., and Mitsudera, H. (2012). Submesoscale eddies near the kuril straits: asymmetric generation of clockwise and counterclockwise eddies by barotropic tidal flow. *J. Geophysical Research: Oceans* 117. doi: 10.1029/2011JC007754
- Ni, Q., Zhai, X., Wilson, C., Chen, C., and Chen, D. (2021). Submesoscale eddies in the south China Sea. *Geophysical Res. Lett.* 48, e2020GL091555. doi: 10.1029/2020GL091555
- Özgökmen, T. M., Chassignet, E. P., Dawson, C. N., Dukhovskoy, D., Jacobs, G., Ledwell, J., et al. (2016). “Over what area did the oil and gas spread during the 2010 deepwater horizon oil spill?” *Oceanography* 29, 96–107. doi: 10.5670/oceanog.2016.74
- Pegliasco, C., Chaigneau, A., and Morrow, R. (2015). Main eddy vertical structures observed in the four major Eastern boundary upwelling systems. *J. Geophysical Research: Oceans* 9, 6008–6033. doi: 10.1002/2015JC010950
- Potter, H., Hsu, C.-Y., and DiMarco, S. F. (2021). Rapid dissipation of a loop current eddy due to interaction with a severe gulf of Mexico hurricane. *Ocean Dynamics* 71, 911–922. doi: 10.1007/s10236-021-01471-y
- Qiu, Bo, Chen, S., Klein, P., Wang, J., Torres, H., Fu, L.-L., et al. (2018). Seasonality in transition scale from balanced to unbalanced motions in the world ocean. *J. Phys. Oceanography* 48, 591–605. doi: 10.1175/JPO-D-17-0169.1
- Rabalais, N. N., Turner, R.E., and Wiseman, W. J. (2002). Gulf of Mexico hypoxia, A.K.A. “The dead zone.” *Annu. Rev. Ecol. Systematics* 1, 235–263. doi: 10.1146/annurev.ecolsys.33.010802.150513
- Rocha, C. B., Gille, S. T., Chereskin, T. K., and Menemenlis, D. (2016). Seasonality of submesoscale dynamics in the kuroshio extension. *Geophysical Res. Lett.* 43, 11,304–11,311. doi: 10.1002/2016GL071349
- Roman-Stork, H. L., Byrne, D. A., and Leuliette, E. W. (2023). MESI: a multiparameter eddy significance index. *Earth Space Sci.* 10, e2022EA002583. doi: 10.1029/2022EA002583
- Roman-Stork, H. L., Subrahmanyam, B., and Trott, C. B. (2021). Mesoscale eddy variability and its linkage to deep convection over the bay of Bengal using satellite altimetric observations. *Adv. Space Research 25 Years Prog. Radar Altimetry* 68, 378–400. doi: 10.1016/j.asr.2019.09.054
- Rosso, I., Hogg, A. M., Kiss, A. E., and Gayen, B. (2015). Topographic influence on submesoscale dynamics in the southern ocean. *Geophysical Res. Lett.* 4, 1139–1147. doi: 10.1002/2014GL062720
- Spiro Jaeger, G., and Mahadevan, A. (2018). Submesoscale-selective compensation of fronts in a salinity-stratified ocean. *Sci. Adv.* 4, e1701504. doi: 10.1126/sciadv.1701504
- Tedesco, P., Gula, J., Ménesguen, C., Penven, P., and Krug, M. (2019). “Generation of submesoscale frontal eddies in the agulhas current.” *J. Geophysical Research: Oceans* 124, 7606–7625. doi: 10.1029/2019JC015229
- Toner, M., Kirwan, A. D.Jr., Poje, A. C., Kantha, L. H., Müller-Karger, F. E., and Jones, C. K. R. T. (2003). Chlorophyll dispersal by eddy-eddy interactions in the gulf of Mexico. *J. Geophysical Research: Oceans* 108. doi: 10.1029/2002JC001499
- Trott, C. B., Subrahmanyam, B., Chaigneau, A., and Delcroix, T. (2018). Eddy tracking in the northwestern Indian ocean during southwest monsoon regimes. *Geophysical Res. Lett.* 13, 6594–6603. doi: 10.1029/2018GL078381
- Trott, C. B., Subrahmanyam, B., Chaigneau, A., and Roman-Stork, H. L. (2019). Eddy-induced temperature and salinity variability in the Arabian Sea. *Geophysical Res. Lett.* 5, 2734–2742. doi: 10.1029/2018GL081605
- Verma, V., Pham, H. T., and Sarkar, S. (2019). The submesoscale, the finescale and their interaction at a mixed layer front. *Ocean Model.* 140, 101400. doi: 10.1016/j.ocemod.2019.05.004
- Wang, Q., Dong, C., Dong, J., Zhang, H., and Yang, J. (2022). Submesoscale processes-induced vertical heat transport modulated by oceanic mesoscale eddies. *Deep Sea Res. Part II: Topical Stud. Oceanography* 202, 105138. doi: 10.1016/j.dsr2.2022.105138
- Wang, J. L., Zhuang, H., Chérubin, L. M., Ibrahim, A. K., and Muhamed Ali, A. (2019). Medium-term forecasting of loop current eddy Cameron and eddy Darwin formation in the gulf of Mexico with a divide-and-Conquer machine learning approach. *J. Geophysical Research: Oceans* 8, 5586–5606. doi: 10.1029/2019JC015172
- Xia, Q., Li, G., and Dong, C. (2022). Global oceanic mass transport by coherent eddies. *J. Phys. Oceanography* 52, 1111–1132. doi: 10.1175/JPO-D-21-0103.1
- Yang, Y., McWilliams, J. C., Liang, X.S., Zhang, H., Weisberg, R. H., Liu, Y., et al. (2021). Spatial and temporal characteristics of the submesoscale energetics in the gulf of Mexico. *J. Phys. Oceanography* 51, 475–489. doi: 10.1175/JPO-D-20-0247.1
- Yang, Y., Weisberg, R. H., Liu, Y., and Liang, X.S. (2020). Instabilities and multiscale interactions underlying the loop current eddy shedding in the gulf of Mexico. *J. Phys. Oceanography* 50, 1289–1317. doi: 10.1175/JPO-D-19-0202.1
- Yao, W., Teng, Z., Tang, Q., and Zuo, P. (2014). Adaptive dolph–chebyshev window-based s transform in time-frequency analysis. *IET Signal Process.* 9, 927–937. doi: 10.1049/iet-spr.2013.0400
- Zamuda, Aleš, Daniel, José, Sosa, Hernández, and Adler, L. (2016). Constrained differential evolution optimization for underwater glider path planning in Submesoscale eddy sampling. *Appl. Soft Computing* 42, 93–118. doi: 10.1016/j.asoc.2016.01.038
- Zhang, X., Dai, H., Zhao, J., and Yin, H. (2019). Generation mechanism of an observed submesoscale eddy in the chukchi Sea. *Deep Sea Res. Part I: Oceanographic Res. Papers* 148, 80–87. doi: 10.1016/j.dsr.2019.04.015
- Zhang, Y., Hu, C., Liu, Y., Weisberg, R. H., and Kourafalou, V. H. (2019). Submesoscale and mesoscale eddies in the Florida straits: observations from satellite ocean color measurements. *Geophysical Res. Lett.* 22, 13262–13270. doi: 10.1029/2019GL083999
- Zhang, Z., and Qiu, Bo (2018). Evolution of submesoscale ageostrophic motions through the life cycle of oceanic mesoscale eddies. *Geophysical Res. Lett.* 45, 11,847–11,855. doi: 10.1029/2018GL080399
- Zhang, Z., Wang, W., and Qiu, Bo (2014). Oceanic mass transport by mesoscale eddies. *Science* 345, 322–324. doi: 10.1126/science.1252418



## OPEN ACCESS

## EDITED BY

Ruoying He,  
North Carolina State University,  
United States

## REVIEWED BY

Baptiste Mourre,  
Balearic Islands Coastal Ocean Observing  
and Forecasting System (SOCIB), Spain  
Laurent Marcel Cherubin,  
Florida Atlantic University, United States

## \*CORRESPONDENCE

Efraín Moreles

✉ moreles@cmar.unam.mx

<sup>†</sup>These authors share first authorship

RECEIVED 20 September 2022

ACCEPTED 26 May 2023

PUBLISHED 10 July 2023

## CITATION

Higuera-Parra S, Moreles E,  
Olvera-Prado ER and Zavala-Hidalgo J  
(2023) Stratification variability in the  
Yucatan Channel and its relationship with  
the Loop Current System.  
*Front. Mar. Sci.* 10:1049662.  
doi: 10.3389/fmars.2023.1049662

## COPYRIGHT

© 2023 Higuera-Parra, Moreles,  
Olvera-Prado and Zavala-Hidalgo. This is an  
open-access article distributed under the  
terms of the [Creative Commons Attribution  
License \(CC BY\)](https://creativecommons.org/licenses/by/4.0/). The use, distribution or  
reproduction in other forums is permitted,  
provided the original author(s) and the  
copyright owner(s) are credited and that  
the original publication in this journal is  
cited, in accordance with accepted  
academic practice. No use, distribution or  
reproduction is permitted which does not  
comply with these terms.

# Stratification variability in the Yucatan Channel and its relationship with the Loop Current System

Susana Higuera-Parra<sup>1†</sup>, Efraín Moreles<sup>2\*†</sup>,  
Erick R. Olvera-Prado<sup>3</sup> and Jorge Zavala-Hidalgo<sup>3</sup>

<sup>1</sup>Facultad de Ciencias, Universidad Nacional Autónoma de México, Mexico City, Mexico, <sup>2</sup>Instituto de Ciencias del Mar y Limnología, Unidad Académica Procesos Oceánicos y Costeros, Universidad Nacional Autónoma de México, Mexico City, Mexico, <sup>3</sup>Instituto de Ciencias de la Atmósfera y Cambio Climático, Universidad Nacional Autónoma de México, Mexico City, Mexico

The non-seasonal stratification variability in the upper 400 m of the Yucatan Channel (YC) and its relationship with the Loop Current System is studied based on the analysis of long-term timescales not yet resolved in observational studies. Daily outputs from a 22-year free-running simulation performed with the HYbrid Coordinate Ocean Model were used, and the variability modes of the squared buoyancy frequency were estimated using Empirical Orthogonal Functions. Intrinsic ocean dynamics is the primary determinant of the dominant spatial and temporal variability of hydrography and dynamics in the YC. The leading mode, described by a vertical dipole at the western YC section with timescales of 1.5–7.5 years, is mainly determined by the Yucatan Current (YCu) variability. There is a strong connection between YCu dynamics, the upper YC hydrography, the Loop Current (LC) intrusion into the Gulf of Mexico, the detachment of Loop Current Eddies (LCEs), and cyclonic anomalies surrounding the LC. Intense eastward displacements of the YCu are associated with intense stratification anomalies in the western YC, the presence of cyclonic anomalies surrounding the LC southwest margin, detachments of LCEs with larger-than-average diameter, and intense LC retreat; before these eddy detachments, the LC metric values are lower than their average ones. Atmospheric forcing induces more complexity in YC dynamics and the Loop Current System; it produces a significant high-frequency signal that modifies their low-frequency behavior. The relationships found in this work could contribute to a better understanding of the upwelling development on the eastern Yucatan shelf.

## KEYWORDS

stratification variability, Yucatan Current, Loop Current, Gulf of Mexico, Empirical Orthogonal Functions, HYbrid Coordinate Ocean Model

# 1 Introduction

The Gulf of Mexico significantly influences different physical, ecological, biogeochemical, and geological processes in the North Atlantic. Extensive research has been conducted on characterizing the mean state and variability of the hydrography and ocean circulation of the Gulf, essential for better understanding its dynamics, diversity, and productivity under actual and future conditions (Sturges et al., 2005; Jochens and DiMarco, 2008; Yoskowitz et al., 2013; Moreles et al., 2021). The main circulation pattern and source of variability in the Gulf is the Loop Current System, consisting of the Loop Current (LC), which originates in the Yucatan Channel (YC) as the Yucatan Current (YCu), and the Loop Current Eddies (LCEs) (Schmitz et al., 2005; Sturges et al., 2005; NASEM, 2018; Hamilton et al., 2019). Figure 1 shows schematic representations of the main circulation features in the eastern Gulf of Mexico and relevant physiographic characteristics.

There is a strong relationship between YCu dynamics and YC hydrography (Candela et al., 2002; Ezer et al., 2003; Marín et al., 2008; Lin et al., 2009; Athie et al., 2011; Athié et al., 2012; Ramos-Musalem, 2013; Sheinbaum et al., 2016; Androulidakis et al., 2021), which significantly influences the region's vital ecological and biogeochemical processes, e.g., the macro-nutrient and oxygen supply over the continental shelf and coral reef ecosystem (Gruber, 2011; Jacox and Edwards, 2011; Carrillo et al., 2016; Reyes-Mendoza et al., 2019; Androulidakis et al., 2021). Merino (1997), Reyes-Mendoza et al. (2016), and Jouanno et al. (2018) found that the interaction of the YCu with the Yucatan shelf establishes bottom Ekman pumping, which

may contribute to the water upwelling with temperatures between 16.0–22.5°C at the northeastern tip of the Yucatan Peninsula. Enríquez and Mariño-Tapia (2014) found that the northeastward displacement of the YCu path enhances the Yucatan upwelling; Carrillo et al. (2016) related the isopycnals uplift in that region with an intensified YCu northward flow; Jouanno et al. (2018) suggested a relationship between a strengthened LC flow along the eastern Yucatan shelf and the enhancement of the Yucatan upwelling associated with higher stratification in the middle of the water column.

Relationships between the dynamics in the YC region and the Loop Current System behavior have also been explored: the structure of the YC transport and LC dynamics (Sheinbaum et al., 2002; Abascal et al., 2003; Ezer et al., 2003; Lin et al., 2009; Athié et al., 2015; Moreles et al., 2021), LC frontal eddies (Zavala-Hidalgo et al., 2003; Schmitz, 2005; Le Hénaff et al., 2012), cyclones blocking the LC (Zavala-Hidalgo et al., 2006), vorticity flux through the YC and LC dynamics (Candela et al., 2002; Oey, 2004), and relationships between YCu longitudinal displacements and LCE detachments (Ezer et al., 2003; Marín et al., 2008; Athie et al., 2011; Athié et al., 2012; Sheinbaum et al., 2016; Androulidakis et al., 2021). Roughly 90% of the water transport through the YC occurs above 400 m depth (Rousset and Beal, 2010; Candela et al., 2019), where the stratification is the strongest and has the highest variability related to the YCu flow structure. Therefore, significant relationships exist between YCu dynamics, the upper YC stratification, and the Loop Current System behavior.

Previous research has outlined meaningful relationships between YCu dynamics, upper YC hydrography, and the Loop

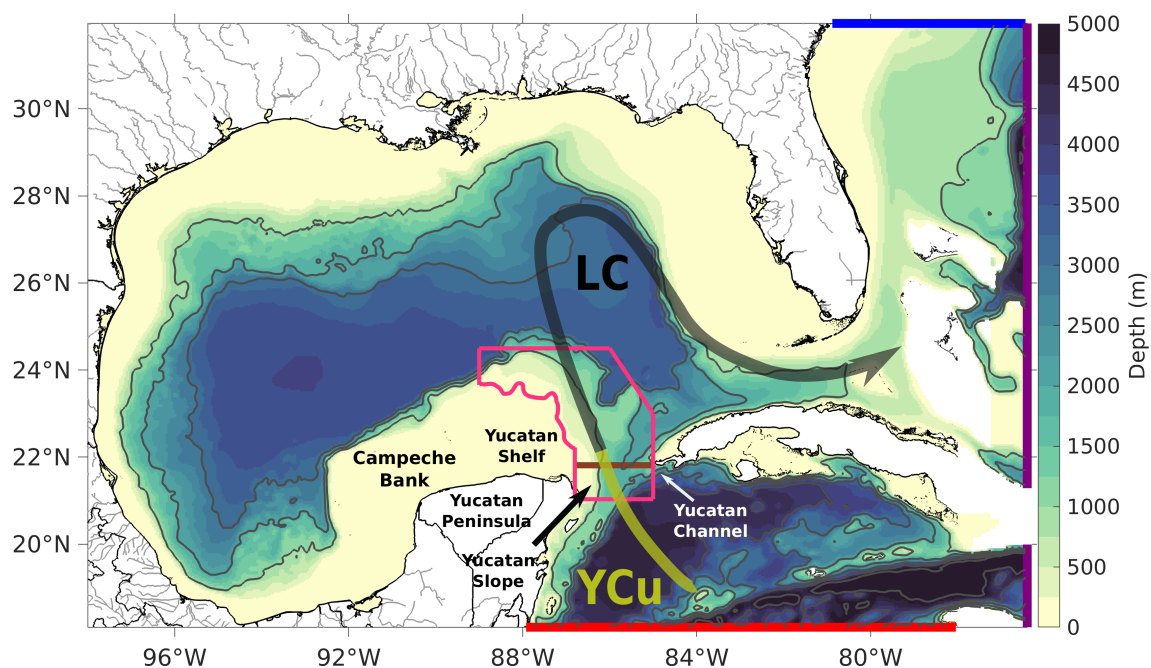


FIGURE 1

Map of the horizontal domain used to simulate the Gulf of Mexico hydrodynamics. Blue, purple, and red lines indicate the north, east, and south open boundaries. The main circulation features in the eastern Gulf and relevant physiographic characteristics are also represented. The brown line at 21.81° N indicates the transect used to analyze stratification variability across the Yucatan Channel. The pink polygon encloses the domain A1 (roughly south-limited by the 100m isobath) used to compute sea surface height anomalies. The gray contours represent the 1000, 2000, and 3000 m isobaths.



Current System. However, these relationships need to be further investigated. Relationships obtained with simplified and theoretical models must be verified in more complex and realistic simulations or using long-term observations. An in-depth analysis of the YC stratification is still needed, which defines its long-term nature, spatial and temporal variability, relationship with YCu dynamics and the Loop Current System behavior, and causal relationships. Such an analysis is urgently needed due to the expected increase in the Gulf upper ocean stratification associated with climate change (Gruber, 2011; Yamaguchi and Suga, 2019). Exploring these processes is crucial to understanding the Loop Current System and predicting its response to climate change (Moreles et al., 2021).

This work aims to characterize the dominant non-seasonal stratification variability across the YC and its connection with YCu dynamics and the Loop Current System behavior. In order to achieve this aim, long-term free-running simulations of the Gulf hydrodynamics performed with an oceanic general circulation model were implemented to obtain statistically and physically consistent relationships between those processes. Statistical modes of variability were obtained from the buoyancy frequency squared using the Empirical Orthogonal Functions analysis. Also, analyses of different hydrographic variables across the YC and the LC metrics were conducted to identify relationships between those processes and to obtain insights into the causal relationships of the YC stratification. Simulations with incremental complexity and realism were implemented to achieve these goals: that is, the previously outlined analyses were first carried out considering only ocean dynamics and then incorporating the effects of atmospheric forcing, i.e., including mass, momentum, and energy fluxes between the ocean and the atmosphere.

## 2 Methods and data

### 2.1 The numerical simulations

In order to adequately represent the long-term statistics of the intrinsic YC stratification variability, long-term data with sufficient spatial and temporal sampling are needed. Long-term free-running simulations performed with oceanic general circulation models are valuable tools to achieve this goal, as they provide physically consistent descriptions of ocean dynamics satisfying the primitive equations. According to Morey et al. (2020), the HYbrid Coordinate Ocean Model, the Regional Ocean Modeling System, and the MIT General Circulation Model have the necessary dynamics to realistically represent and adequately describe the hydrodynamics of the Gulf of Mexico, its mean circulation, its deep circulation, and its variability.

In this study, the HYbrid Coordinate Ocean Model was used to simulate the Gulf of Mexico hydrodynamics, as it provides optimal simulation of coastal and open-ocean circulation features given its generalized hybrid vertical coordinate system (Bleck, 2002; Chassignet et al., 2007). A free-running simulation was

configured with a horizontal domain of  $[98^{\circ}\text{W}, 77^{\circ}\text{W}] \times [18^{\circ}\text{N}, 32^{\circ}\text{N}]$  (Figure 1), a spatial resolution of  $1/25^{\circ}$  ( $\sim 3.8\text{--}4.2$  km), and 41 hybrid vertical layers, which are mainly isopycnal layers in the open ocean below the mixed layer and  $z$ -layers above it. The model bathymetry is a blended product that incorporates the one from the HYbrid Coordinate Ocean Model Consortium (hycom.org), the General Bathymetric Chart of the Oceans, and observations collected during several cruises. Monthly climatology river inflow is simulated at 40 locations along the coast, no data assimilation was used, and no tidal dynamics was incorporated. The simulations were nested within the  $1/12^{\circ}$  Global Ocean Forecasting System 3.1 reanalysis GLBv0.08-53.X (HYCOM-GOFS3.1, n.d.) using monthly open boundary conditions from a climatology of 22 years (1994–2015) of the model.

Twin simulations with incremental complexity and realism were performed to help obtain an in-depth description of the analyzed processes and reveal causal relationships between them. The main characteristics of each simulation and their differences are indicated below:

- Experiment without atmospheric forcing (NoAF). It focused on stratification variability attributable to ocean conditions in the absence of atmospheric forcing, referred to in this study as “intrinsic ocean dynamics.” Thus, it did not incorporate atmospheric forcing given by energy and momentum fluxes between the ocean and the atmosphere and river inflow.
- Experiment with atmospheric forcing (AF). It expanded the analysis by considering a more realistic experiment that included atmospheric forcing. The atmospheric forcing was obtained from the Climate Forecast System Reanalysis from 1994–2015 (NCEP-CFSR, n.d.), which comprises hourly fields of 10 m wind speed, 2 m air temperature, 2 m atmospheric humidity, surface shortwave and longwave heat fluxes, surface atmospheric pressure, and precipitation. Wind stress is computed *via* bulk formulae during the model execution considering the speed of ocean currents.

Both experiments share the same initial conditions. They were initialized from the mean state of January 1994 of the global reanalysis, with their target densities along the vertical inherited from the global reanalysis, and they were run from 1994–2015 (22 years) to be consistent with the boundary conditions. Instantaneous daily outputs were recorded and used for the analysis.

Experiment AF is the most realistic simulation; it represents the control run and is thus the one that was validated. The validation of variables related to stratification is shown in the [Supplementary Material](#). Olvera-Prado et al. (2022) thoroughly validated this experiment, including mean circulation and transport, the Loop Current System, and energy fields. The conjoint validation showed a good agreement between the simulation outputs and observations. The validation results provide very high confidence in obtaining accurate and credible results.

## 2.2 Stratification measure

As a stratification measure, the buoyancy frequency squared ( $N^2$ ) was considered (Gill, 1982; Jackett and McDougall, 1995),

$$N^2 = -g \frac{1}{\rho_\theta} \frac{d\rho_\theta}{dz}, \quad (1)$$

where  $g$  is the acceleration of gravity,  $\rho_\theta$  is the locally referenced potential density, and  $z$  is the vertical coordinate (negative downwards from the sea surface).  $N^2$  measures the stability of a parcel of fluid, where the stability and instability conditions are given by positive and negative values of  $N^2$ , respectively. This variable was computed along a latitudinal transect across the YC at 21.81°N, which was selected to represent the variability and dynamics at the YC (brown line in Figure 1). The SeaWater library of EOS-80 seawater properties (Morgan and CSIRO, 1994; Jackett and McDougall, 1995) was used to compute  $N^2$  from daily model outputs of temperature and salinity fields. Daily  $N^2$  profiles were obtained in the upper 400 m (from 5 to 395 m depth), with a vertical resolution of 10 m and longitudinally interpolated every 0.02°.

In order to reduce small-scale spatial variations in  $N^2$ , each  $N^2$  profile was smoothed using a low-pass Lanczos filter with a cut-off frequency of 1/3 and 3 weights. The variability analysis focuses on the mesoscale, i.e., ocean signals with horizontal scales of 50–500 km and time scales of 10–100 days (CTOH, 2013). Therefore, the  $N^2$  time series were time-filtered using a low-pass Lanczos filter with a 45-day cut-off period and 61 weights; this filter will be called the mesoscale temporal filter.

## 2.3 Analysis of stratification variability and description of the Loop Current System

The YC stratification variability was analyzed from the  $N^2$  field using the Empirical Orthogonal Functions (EOFs) technique. This technique derives the dominant patterns of variability from a field, characterizing its state in terms of statistical modes of variability, which contain a fraction of the total variance of the data. Each mode is represented by a spatial pattern and its evolution time series or principal component (PC) (Storch and Zwiers, 1999). The trend and annual cycle were removed from the  $N^2$  field, its corresponding covariance matrix was constructed, and its variability modes were obtained. Results refer to the upper section of the YC, calculated at the latitudinal transect shown in Figure 1, and do not necessarily reflect the whole dynamics in the YC.

The proportion of the total variance of the data explained by a particular mode is represented by its proportion of explained variance, given by

$$1 - \frac{\text{Var}(P - F)}{\text{Var}(P)}, \quad (2)$$

where  $P$  is the original data and  $F$  is its reconstruction using a particular mode. The regions with a large proportion of explained variance are the most significant in describing the associated spatial patterns.

The description and time monitoring of the Loop Current System were addressed using the LC metrics proposed by Hamilton et al. (2000), who used a specific contour of the sea surface height as a proxy for the LC location. From the location of the LC, its metrics can be calculated: its northernmost latitude ( $LC_{NL}$ ), westernmost longitude ( $LC_{WL}$ ), length ( $LC_L$ ), and area ( $LC_A$ ). By plotting the LC metrics as time series, the LC intrusion is identified by a sustained increase in the time series, whereas the LCE detachment events are identified with the local minima in the series after an extended LC intrusion. Then, the LCE metrics can be calculated: the shedding period ( $LCE_P$ ) and diameter ( $LCE_D$ ) of the LCEs and the LC retreat latitude ( $LC_{RL}$ ), i.e., the LC northernmost latitude after the LCE detachment.

The LCE detachment events with and without reattachments to the mean LC flow were identified; the LCE detachments not followed by a reattachment to the mean LC flow were called LCE separations. The relationship between the YC stratification variability and LC evolution was examined by comparing the resulting PC time series and LC metrics.

## 3 Results

### 3.1 Spatial variability of stratification in the Yucatan Channel

The primary mechanism that forces the YC stratification variability is the transport through the YC, mainly determined by the YCu. YCu dynamics is a crucial determinant of the vertical and horizontal hydrographic structure on the eastern coast of the Yucatan Peninsula (Enríquez and Mariño-Tapia, 2014; Carrillo et al., 2016; Reyes-Jiménez et al., 2023). Geostrophic balance arguments allow outline relationships between the zonal position of the YCu core ( $YCu_{zp}$ ), YCu transport, sea surface slope, and uplifting of isotherms (Athie et al., 2011; Athié et al., 2012; Athié et al., 2015). Since the structure of the meridional velocity through the YC strongly influences the YC stratification, a description of the spatial variability of the meridional velocity through the YC is first presented (Figure 2) and then referred to when describing the EOFs of  $N^2$  (Figure 3). By contrasting the results for experiments NoAF and AF, it is possible to evaluate the influence of atmospheric forcing on different oceanic processes in the YC.

Figure 2 shows a monthly climatology of meridional velocity through the YC for experiments NoAF and AF, considering the 22 years of simulation. The velocity amplitude is represented in color scale, with red and blue representing northward and southward velocity, respectively, whereas yellow contours indicate specific isotachs. For both experiments, two main velocity structures are identified. The first is a very intense northward current in the western YC, associated with the YCu, which is very persistent throughout the year. The second is a less intense southward current near Cuba, present all year round.

For experiment NoAF (panels of the first column in Figure 2), the variations in the velocity structures are mainly associated with the YCu; thus, the dominant variability is located in the western YC and is the following:

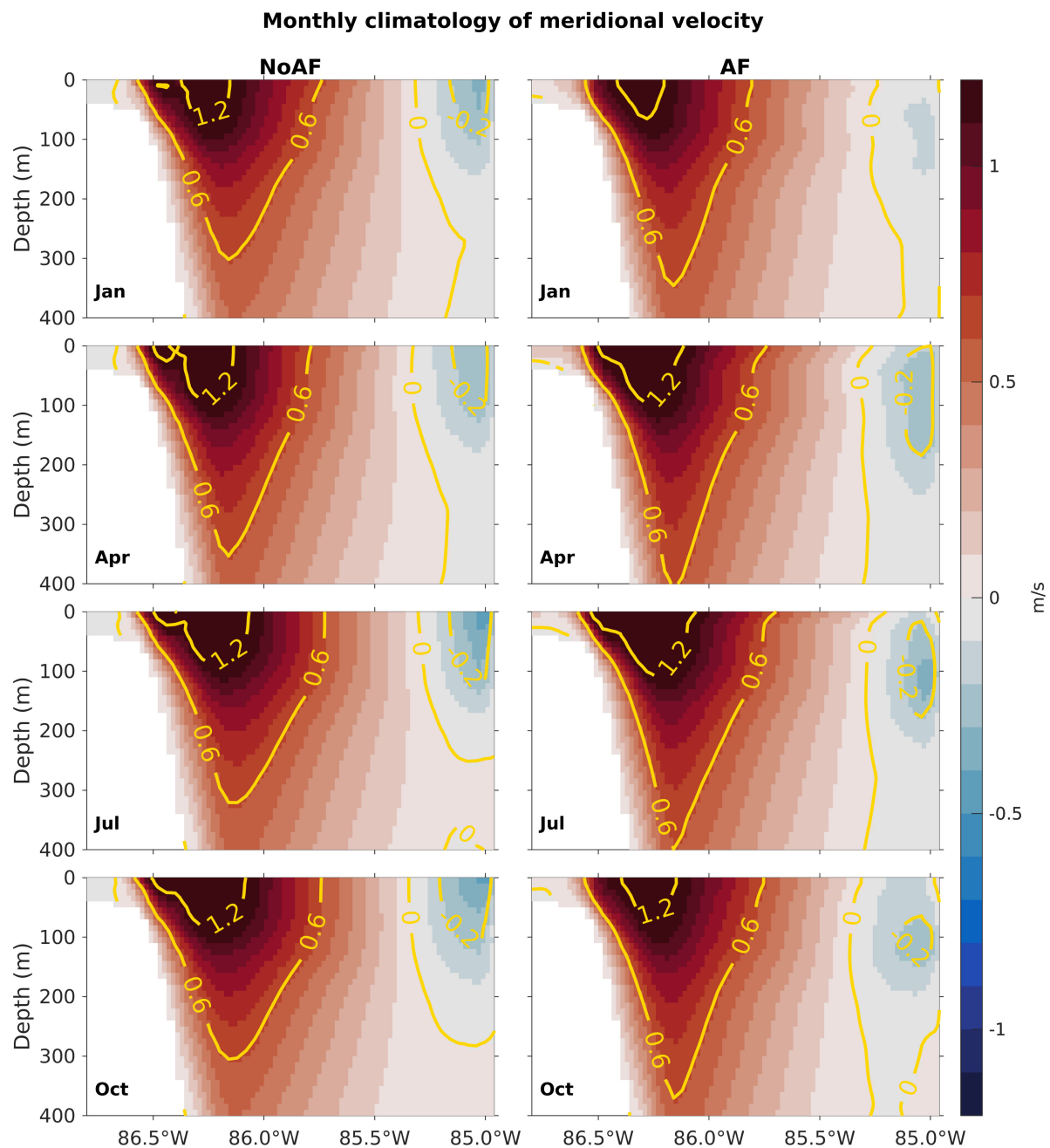


FIGURE 2

Monthly climatology of meridional velocity through the Yucatan Channel for experiments NoAF and AF. The velocity amplitude is represented in color scale, where red and blue represent northward and southward velocity, respectively. Yellow contours indicate the isotachs of -0.2, 0.0, 0.6, and 1.2 m/s.

1. The YCu core, delimited by the 0.6 m/s isotach (Athie et al., 2011), extends horizontally from the middle YC (around 85.7°W) to the Yucatan slope and extends vertically from the surface to about 300 m depth, reducing its width with depth. In spring, the YCu core has its minimum width, reaching up to 85.78°W on the surface, and reaches its maximum depth of about 360 m. As the year progresses, its horizontal extension slightly increases, and its vertical extension decreases, reaching its minimum depth of just 300 m in winter.
2. The structure of the southward current near Cuba is very persistent, without appreciable variations throughout the year. It is confined east of 85.4°W mainly in the upper 180 m of the water column, with intensities of about 0.2 m/s.

For experiment AF (panels of the second column in Figure 2), in contrast to experiment NoAF (panels of the first column in Figure 2), the YCu core reaches greater depths, and the southward current near Cuba exhibits significant variations throughout the year. The inclusion of atmospheric forcing

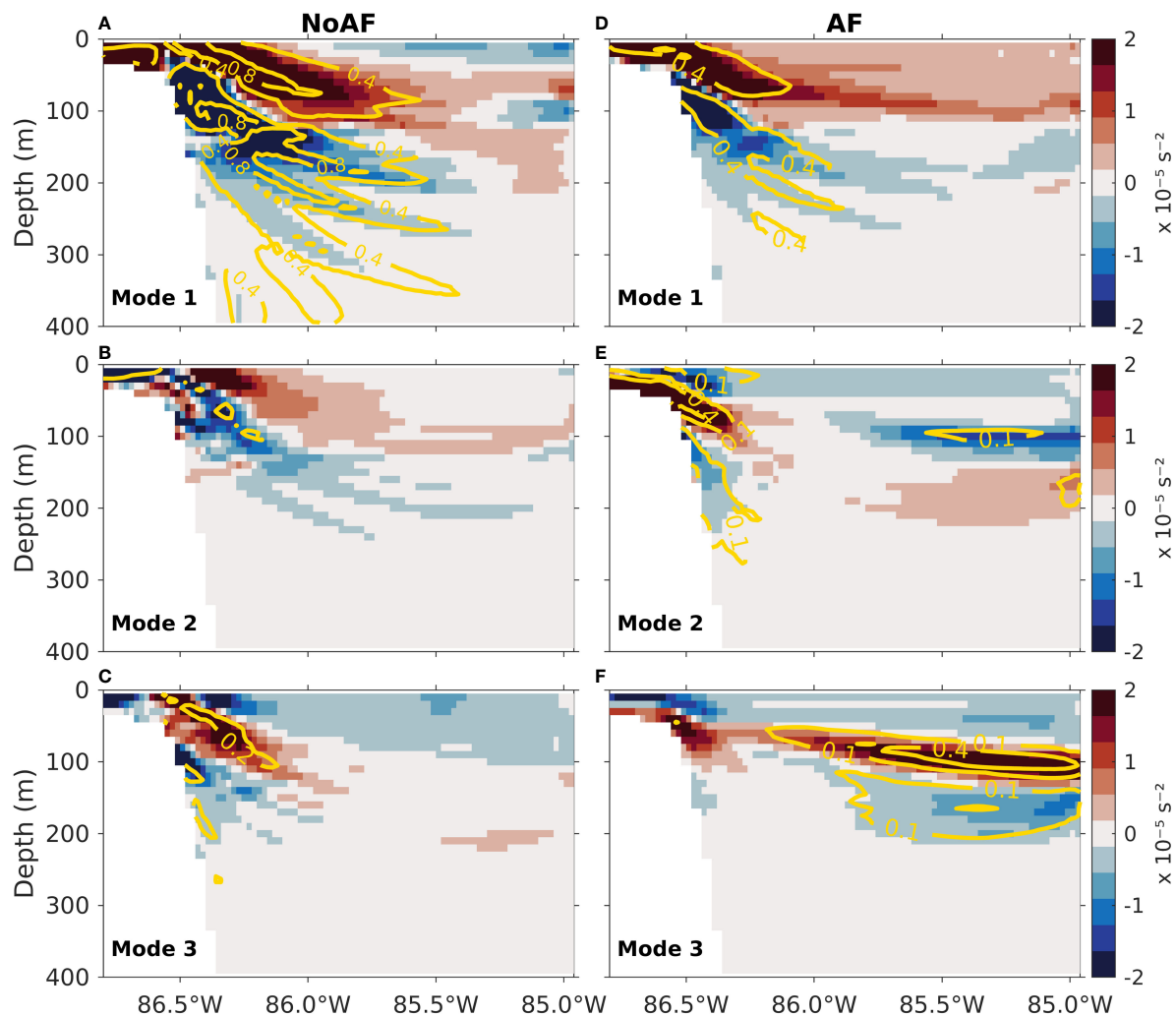


FIGURE 3

Spatial patterns of the first three EOFs of  $N^2$  for experiments NoAF (A–C) and AF (D–F). The pattern amplitude is represented in color scale, and yellow contours represent its proportion of explained variance.

modified the YCu with a non-seasonal behavior and established a seasonal variation of the southward current near Cuba. The variations in the velocity structures are the following:

1. In winter, the horizontal and vertical extension of the YCu core is the minimum, reaching up to 85.8°W on the surface and 350 m in depth. In spring, the YCu core increases its horizontal extension and reaches its maximum depth of more than 400 m. During summer, the YCu core reaches its maximum horizontal extension and slightly decreases its depth to about 400 m. In fall, the YCu core starts decreasing its horizontal extension and continues decreasing its vertical extension until reaching their minima in winter.
2. The southward current near Cuba is confined east of 85.4°W as in experiment NOAF, but with a vertical extension strongly varying throughout the year. During winter, the current is feeble and extends from 50–150 m depth. It intensifies during spring, reaching its maximum vertical extension from 0–250 m depth. During summer and fall, it

weakens and reduces its vertical extension until reaching their minima in winter.

Now, the most important variability modes of  $N^2$  are analyzed. Table 1 shows the contained variance in the first three modes, which constitute a non-degenerate set according to the rule of thumb of North et al. (1982).

- For experiment NoAF, a high percentage of the variance of  $N^2$  is contained in the first mode (54%), representing the dominant variability of YCu upper stratification. The high variance contained in the first mode evidences the YCu upper stratification as a discernible mechanism, with most of the processes involved in its dynamics encompassing a single mode of variability. Results suggest that the stratification variability determined by ocean dynamics is non-complex and easy to describe. Hence, it is possible to associate the principal mode of variability with relevant physical processes, like the LC.



- When including atmospheric forcing, the stratification variance is distributed in a larger number of modes. Even three modes of experiment AF are not enough to gather the contained variance in the principal mode of experiment NoAF. Atmospheric forcing adds relevance to the higher-order modes and produces a more complex stratification variability, making it more difficult to associate physical processes with the resulting variability.

The spatial patterns of the EOFs of  $N^2$  (Figure 3) are expected to identify the regions with high variability in the meridional velocity (Figure 2). Figure 3 shows the spatial patterns of the first three modes of  $N^2$  for experiments NoAF and AF, in which the pattern amplitude is represented in color scale, and yellow contours represent its proportion of explained variance. The spatial patterns are described below:

1. The spatial pattern of the first mode in experiment NoAF (Figure 3A) consists of a well-defined structure of two anomalies with opposite signs at the western region, in the upper 250 m: an upper positive anomaly (the red-colored region) ranging from near the surface over the Yucatan slope to around 100 m depth at 85.5°W, and a lower negative one (the blue-colored region) extending from 50 m depth at 86.5°W to around 200 m depth at 85.5°W.
2. In experiment AF, the same bipolar spatial pattern occurs in the first mode but with a lower horizontal extension (Figure 3D).
3. In experiment NoAF, the spatial variability of modes 2 and 3 (Figures 3B, C) is located in the western YC and displays characteristics similar to mode 1. However, the regions with a large proportion of explained variance are small.
4. In contrast to experiment NoAF, the higher-order variability patterns are drastically modified in experiment AF when adding atmospheric forcing. Mode 2 mainly describes the variability of a positive anomaly in the western YC between 15 m depth and the Yucatan shelf (Figure 3E). Mode 3 shows high variability in the eastern YC (Figure 3F); it represents a bipolar anomaly consisting of an upper positive anomaly between 60 and 120 m depth and a lower negative one between 130 and 210 m depth. Variations in the intensity and extension of the

southward current near Cuba (panels of the second column in Figure 2) may account for this variability. However, due to the small contained variance in Mode 3 in experiment AF (Figure 3F), its association with observed hydrodynamics variability in the eastern region must be addressed cautiously.

Since the high variance contained in the first mode for experiments NoAF and AF (Table 1) and their similitude (Figures 3A, D), these patterns are suggested to represent the fundamental and dominant variability of the YC stratification without and with atmospheric forcing. These results add to the evidence supporting YCu dynamics, specifically the variations in the YCu core, as the mechanism determining the dominant variability of the YC stratification.

### 3.2 Dominant variability of stratification and hydrography in the Yucatan Channel

This subsection analyzes, for experiments NoAF and AF, the timescales and relationships between the following processes:

1. The dominant variability of the YC stratification described by the principal component of the first mode (PC1).
2. The YCu core's behavior. This is described by the time series of  $YCu_{zp}$ , calculated as the longitude where the vertical average of the meridional velocity from the surface to 130 m depth along the computing transect reaches its maximum value. Similar to the processing of the  $N^2$  data, the annual cycle was removed from this series, and the resulting anomalies were time-filtered using the mesoscale temporal filter. Figures 4A, F show the time series of PC1 and  $YCu_{zp}$ .
3. The western YC hydrography. This was analyzed through Hovmuller diagrams of velocity and temperature at specific depths and longitudes across the YC. As illustrative cases, the meridional (Figures 4B, G) and zonal (Figures 4C, H) velocity components at 60 m depth and the temperature above the Yucatan slope at 86.42°W (Figures 4D, I) were calculated. To fully appreciate the physical characteristics of these fields, they are shown without the annual cycle removed in the Hovmuller diagrams but with the corresponding mesoscale temporal filtering.

The dominant variability of the YC stratification shows notable differences when considering intrinsic oceanic dynamics and when considering the effects of incorporating atmospheric forcing:

- In experiment NoAF, the PC1 (Figure 4A) shows interannual variability. It remains negative and close to zero most of the time, corresponding to a negative and weak phase of the spatial stratification pattern in the western YC (Figure 3A). Most of the time, there are weak stratification anomalies: negative ones at the upper 100 m and positive ones between

TABLE 1 Percentage of the total variance contained in the first three modes of  $N^2$  for experiments NoAF and AF.

	Experiment NoAF (without atmospheric forcing)	Experiment AF (with atmospheric forcing)
Mode 1	54	24
Mode 2	17	16
Mode 3	5	11
Cumulative	76	51

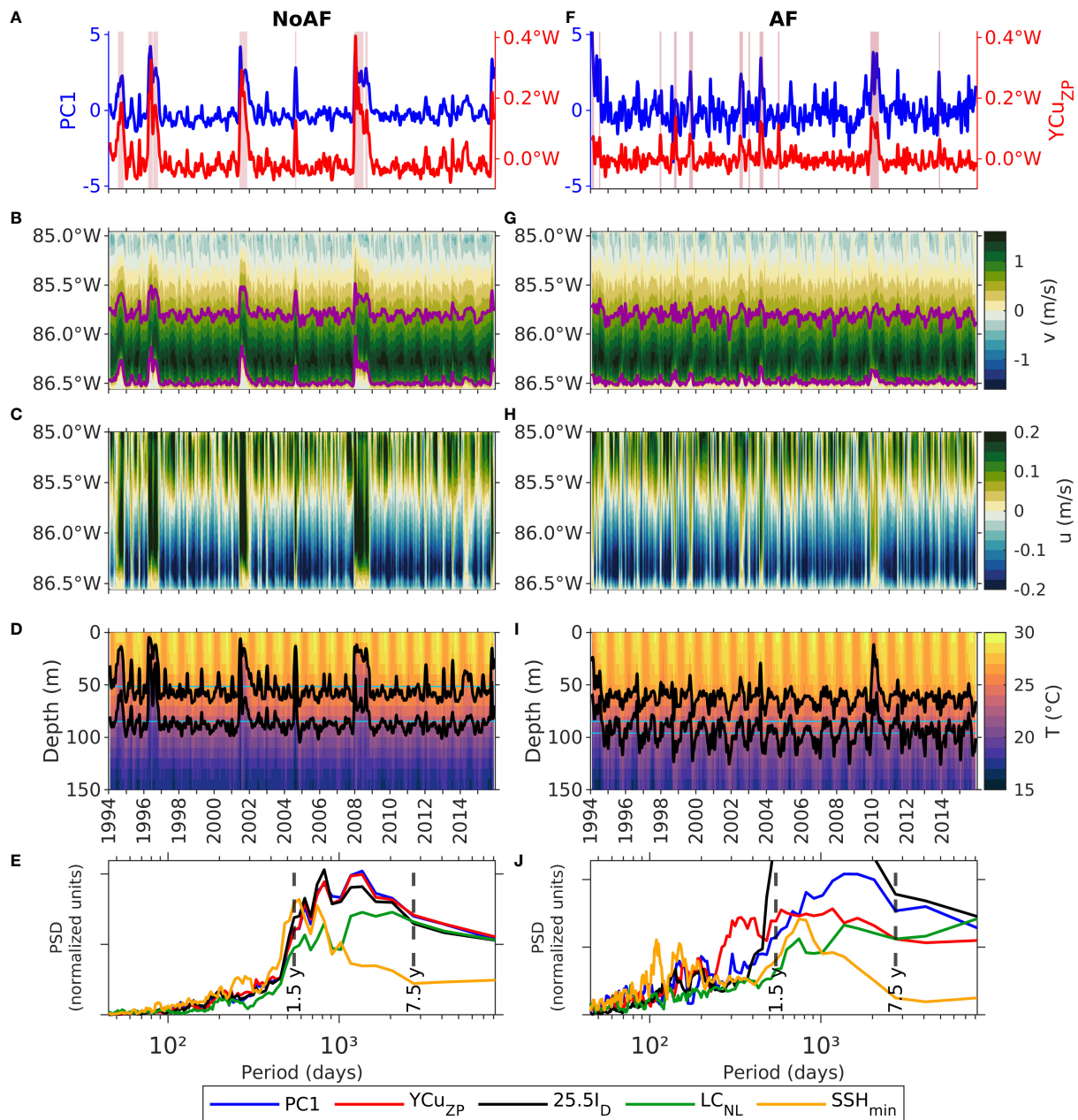


FIGURE 4

(A) Time series of the first principal component (PC1) and anomalies of the zonal position of the YCu core (YCu<sub>ZP</sub>) for experiment NoAF, with the +YCu<sub>ZP</sub> events pink-shaded. (F) Same as figure A for experiment AF. (B) Hovmuller diagram of meridional velocity at 60 m depth across the YC, highlighting the 0.6 m/s isotachs for experiment NoAF. (G) Same as figure B for experiment AF. (C) Hovmuller diagram of zonal velocity at 60 m depth across the YC for experiment NoAF. (H) Same as figure C for experiment AF. (D) Hovmuller diagram of temperature at 86.42°W across the YC, highlighting the 22.0 and 25.5°C-isotherms (black lines) and their corresponding mean depth (blue lines) for experiment NoAF. (I) Same as figure D for experiment AF. (E) Power spectral density (PSD) of the anomalies of: PC1, YCu<sub>ZP</sub>, depth of 25.5°C-isotherm (25.5I<sub>D</sub>), LC northernmost latitude (LC<sub>NL</sub>), and SSH<sub>min</sub>, for experiment NoAF. (J) Same as figure E for experiment AF.

50 and 200 m depth. At irregular time intervals, an intense positive signal in PC1 stands out. This signal characterizes intense stratification anomalies in the western YC: positive ones at the upper 100 m and negative ones between 50 and 200 m depth.

- The PC1 in experiment AF (Figure 4F) shows interannual variability and a strong high-frequency signal. PC1 exhibits high positive values at irregular intervals, in which the

spatial pattern of stratification in the western YC is very similar in both experiments: intense positive stratification anomalies at the upper 100 m and negative ones between 50 and 200 m depth. The PC1 oscillates rapidly around zero, and consequently, the associated spatial pattern of stratification changes rapidly over time (Figure 3D); there is no preferred stratification state, as there is when only intrinsic ocean dynamics is considered.

A crucial dynamical factor in YC dynamics is the YCu core displacement (represented by  $YCu_{zp}$ ), which has very different behavior in experiments NoAF and AF:

- In both experiments, the YCu core is confined between the same longitudes; its west and east limits are located around 86.5°W and 85.8°W, respectively. In experiment NoAF (Figure 4B), west and east limits displace eastward consistently, producing intense eastward displacements of up to 0.4°W.
- In experiment AF (Figure 4G), the west limit displaces eastward, but the east limit displaces both westward and eastward. In some periods, such displacements are inconsistent, reducing the width and overall eastward displacements of the YCu core, with maximum displacements of about 0.1°W. Atmospheric forcing induces complex mass counterflows at the eastern YC (Figure 2), resulting in a non-corresponding behavior of the west and east limits of the YCu core (Figures 4B, G).
- The duration of the eastward displacements of the YCu core is also affected when including atmospheric forcing. In experiment NoAF, the displacements can last almost a year (Figures 4A–C), whereas, in experiment AF, the displacements are not maintained beyond a few months (Figures 4F–H).

There is a clear connection between  $YCu_{zp}$  and PC1; in general, increments in  $YCu_{zp}$  are concurrent with increments in PC1 (Figures 4A, F). The events of noticeable eastward displacements of the YCu core were identified by periods with  $YCu_{zp}$  values above the 90th percentile lasting 25 or more days. These events will be referred to as the  $+YCu_{zp}$  events (pink-shaded periods in Figures 4A, F); they occurred in 1994, 1996, 2001, 2004, and 2008 in experiment NoAF, and in 1994, late 1997, 1998, 1999, 2002, 2003, 2004, 2010, and late 2013 in experiment AF. The characteristics of the  $+YCu_{zp}$  events are mainly associated with the YCu core behavior, as described above. Compared to experiment NoAF, in experiment AF, there are more  $+YCu_{zp}$  events with shorter occurrence periods, shorter duration, and lower intensity.

The eastward displacements of the YCu core and the YC stratification variability are also connected with YC hydrography. Figures 4D, I show, for both experiments, a Hovmuller diagram of temperature at 86.42°W across the YC (above the Yucatan slope), highlighting the 22.0 and 25.5°C-isotherms with black lines. In both experiments, the depth of the isotherm shows interannual variability, with an emphasized seasonal behavior in experiment AF caused by the seasonal air-sea fluxes as was shown by Jouanno et al. (2018).

- The 22.0°C and 25.5°C-isotherms' depth in experiment NoAF significantly rises during the  $+YCu_{zp}$  events (Figure 4D), with amplitude variations of 5–70 m and 20–100 m, respectively.
- In experiment AF, the 22.0°C and 25.5°C-isotherms are deeper and exhibit higher vertical variations than in

experiment NoAF (Figure 4I). The 25.5°C-isotherm has variations from 10 to 80 m, whereas the 22.0°C-isotherm has variations from 60 to 125 m. The larger vertical extent of the YCu core (panels of the second column in Figure 2) may be associated with the lower vertical position of the isotherms in experiment AF. Rises of the isotherms are concurrent with the most intense or long-lasting  $+YCu_{zp}$  events. Results indicate a strong connection between these three phenomena in the YC.

Figure 5 shows two standard similarity measures, the root mean square similarity and Pearson's correlation (Cassisi et al., 2012), between different variables associated with the processes of interest, where 1 indicates the maximum similarity. This figure evinces the close connection between the processes described above. The similarity between PC1,  $YCu_{zp}$ , and 25.5I<sub>D</sub> is very high for experiment NoAF, with mean values of 0.76 and 0.94 for the root mean square similarity and Pearson's correlation, respectively. For experiment AF, the similarity is slightly lower due to the complex interactions induced by atmospheric forcing, with mean values of 0.56 and 0.69 for the root mean square similarity and Pearson's correlation, respectively. The similarity measures give a rough estimation of the relative importance of atmospheric forcing on the connection between the eastward displacements of the YCu core and the stratification and hydrography at the upper YC. The similarity analysis also included LC<sub>NL</sub> and SSH<sub>min</sub>, but their description is addressed in section 3.3.

Finally, the temporal variability of these processes was also analyzed in the frequency domain through their spectra (Figures 4E, J), which were estimated using a multitaper approach with the annual cycle removed from the 22-year time series.

- When isolating intrinsic ocean dynamics (experiment NoAF), the dominant variability of the YC stratification (PC1), the YCu core's behavior ( $YCu_{zp}$ ), and the western YC hydrography (25.5I<sub>D</sub>) exhibit the same spectral variance characteristics; they share the same temporal behavior. None of these processes have evident periodicity. They mainly vary over long timescales, with negligible short-term variations. Most of their spectral variance is concentrated in the 1.5–7.5 years period band, with relative maxima at about 2.2 and 3.5 years; the high spectral variance content in this period band is associated with the interannual period between the  $+YCu_{zp}$  events. The high similarity between the spectral variance content of these processes indicates that their time persistence is very similar. Since the YCu is the primary mechanism determining the stratification and hydrography in the YC, it is suggested that the observed 1.5–7.5 year variability in the dominant stratification variability and western YC hydrography has its origin in YCu dynamics, specifically in the variation, location, and displacements of the YCu core.
- In general, including atmospheric forcing (experiment AF) preserves the dominant spectral variance content in the 1.5–

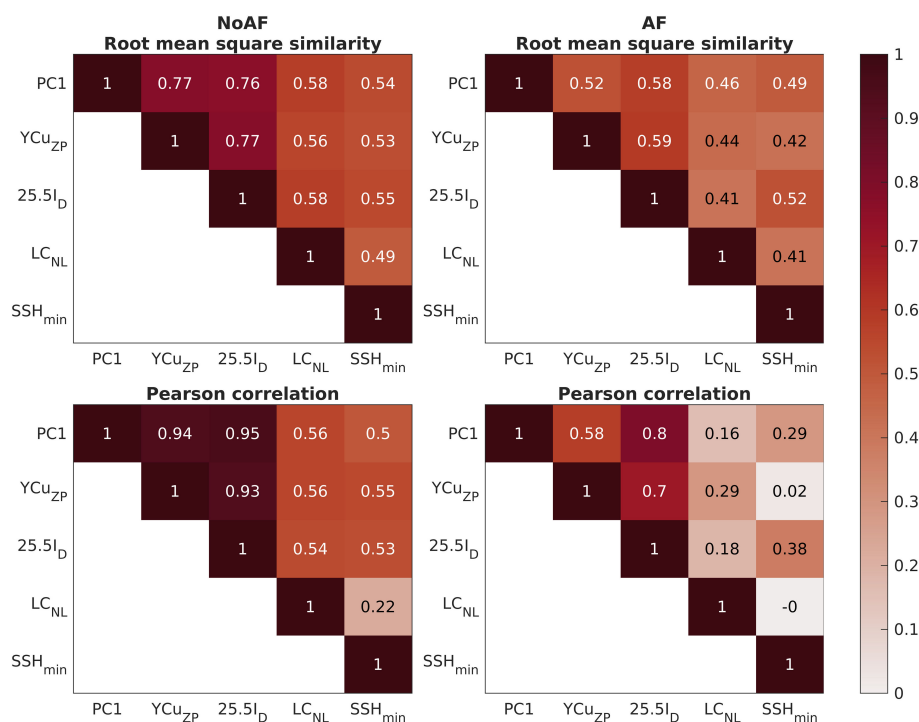


FIGURE 5

Similarity measures between different variables of interest for experiments NoAF and AF. All the time series are standardized anomalies except PC1. The time series 25.5I<sub>D</sub>, LC<sub>NL</sub>, and SSH<sub>min</sub> were multiplied by -1 to calculate the similarity measures.

7.5 years period band of experiment NoAF. However, as expected, atmospheric forcing modifies the dynamics in a rich and complex manner, resulting in the appearance of high-frequency signals. The high spectral variance content in the 1.5-7.5 years period band is similar and clearly identifiable in the YC stratification and the western YC temperature, regardless they now exhibit short-term variations mainly in periods shorter than five months. On the other hand, variations longer than three years are now de-emphasized in the YCu core's behavior, and variations shorter than one year are significant. The connection between these processes is still appreciable, but modifications in YCu dynamics by including atmospheric forcing weaken such connection in the long-term, and complex dynamics appears on shorter time scales.

### 3.3 Stratification and circulation in the Yucatan Channel and the Loop Current System

#### 3.3.1 Relationships between the Yucatan Current and the Loop Current

This subsection explores the conjoint variability of the YCu core's dynamics, the YC western section hydrography, and the Loop Current System behavior. The aim is to provide robust relationships between these phenomena and gain insights into possible mechanisms of transmission of information between them,

specifically during the +YCu<sub>ZP</sub> events. A thorough analysis of the dynamical mechanisms of the LC and the formation and detachment of LCEs (causal relationships) is proposed for future research.

In order to explore those relationships, a Hovmuller diagram of YCu<sub>ZP</sub> from 21.0°N to 22.5°N (Figures 6A, D), time series of PC1 and LC<sub>NL</sub> (Figures 6B, E), and an area chart of SSH<sub>min</sub> (Figures 6C, F) were calculated for both experiments. SSH<sub>min</sub> represents the minimum of sea surface height (SSH) anomaly in the domain A1 (see Figure 1); in this series, the annual cycle was removed, and the mesoscale temporal filter was applied. In Figure 6, the +YCu<sub>ZP</sub> events are pink-shaded, and vertical dashed lines indicate LCE separations. This figure shows an appreciable correspondence between YCu<sub>ZP</sub>, PC1, and LC<sub>NL</sub> for the entire simulation period in experiment NoAF; in experiment AF, the correspondence is less appreciable for the entire simulation period but clearly appreciable during the +YCu<sub>ZP</sub> events (see also Figures 4, 5).

During the +YCu<sub>ZP</sub> events in experiment NoAF, the YCu core experiences intense eastward displacements beyond 85.9°W in its northern section at 22.5°N and moderate ones in its southern section at 21°N (Figure 6A). In contrast, the YCu is more north-south oriented in experiment AF, with moderate displacements in its northern section and null ones in its southern section (Figure 6D), only reaching 86.0°W for a short period in 1998, late 2003, and 2010. During the +YCu<sub>ZP</sub> events, in both experiments, there is a concurrence of intense eastward displacements of the YCu (Figures 6A, D), intense stratification anomalies in the western YC section (positive ones at the upper 100 m and negative ones between



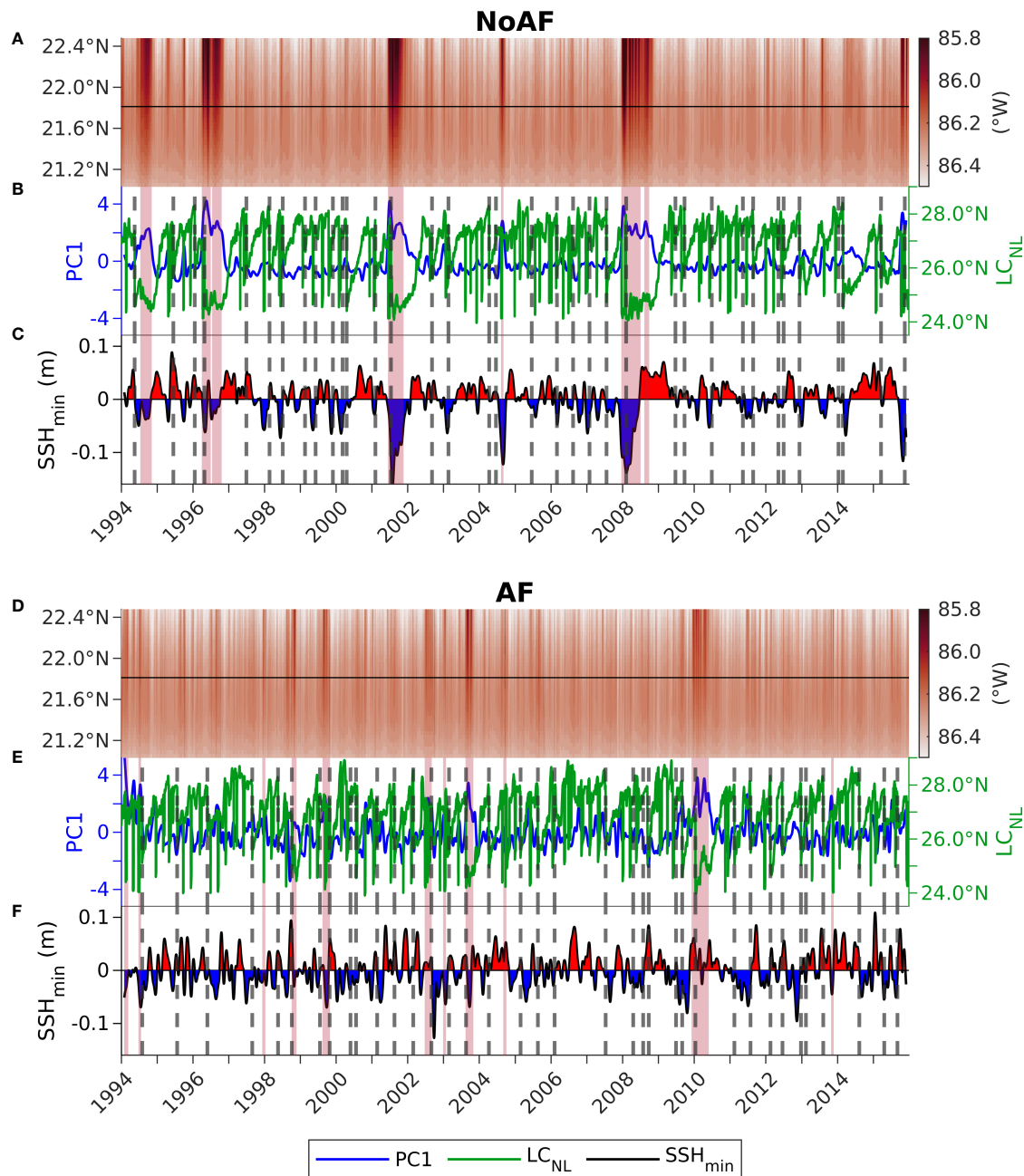


FIGURE 6

(A) Hovmuller diagram of YCu<sub>ZP</sub> from 21.0°N and 22.5°N, (B) time series of PC1 and LC<sub>NL</sub>, and (C) area chart of SSH<sub>min</sub> in domain A1 for experiment NoAF. (D–F) Same as figures (A–C) but for experiment AF. In panels (A, D), the horizontal black line is at 21.81°N, where the EOF analysis of stratification was performed. The +YCu<sub>ZP</sub> events are pink-shaded, and vertical dashed lines indicate LCE separations.

50 and 200 m depth) (Figures 6B, E), detachments of big LCEs, and intense LC retreat (Figures 6C, F). The concurrence between these processes also occurs in some LCE detachment events not identified as +YCu<sub>ZP</sub>, characterized by a weak or short-lasting (< 25 days) eastward displacement of the YCu core. Such events occurred in 1995, 1998, 2003, 2012, 2013, and 2014 in experiment NoAF, and in 1995, 1996, 2000, 2005, and 2011 in experiment AF.

The above relationships between the YCu core behavior, YC hydrography, and the Loop Current System behavior can be readily appreciable by observing the oceanic conditions before and during a

+YCu<sub>ZP</sub> event. These conditions are typical for all the +YCu<sub>ZP</sub> events in experiments NoAF and AF but atypical for the overall system behavior, and they appear associated with specific mechanisms in the YC and inside the Gulf of Mexico. Figure 7 shows the oceanic conditions before and during the +YCu<sub>ZP</sub> event of 1996 for experiment NoAF. Previous conditions display the YCu core very close to the Yucatan eastern shelf at the YC section (Figure 7A), isotherms lowered above the Yucatan slope (Figure 7B), the maximum stratification located to the east of the Yucatan slope where the isotherms are squeezed (Figure 7C), and a

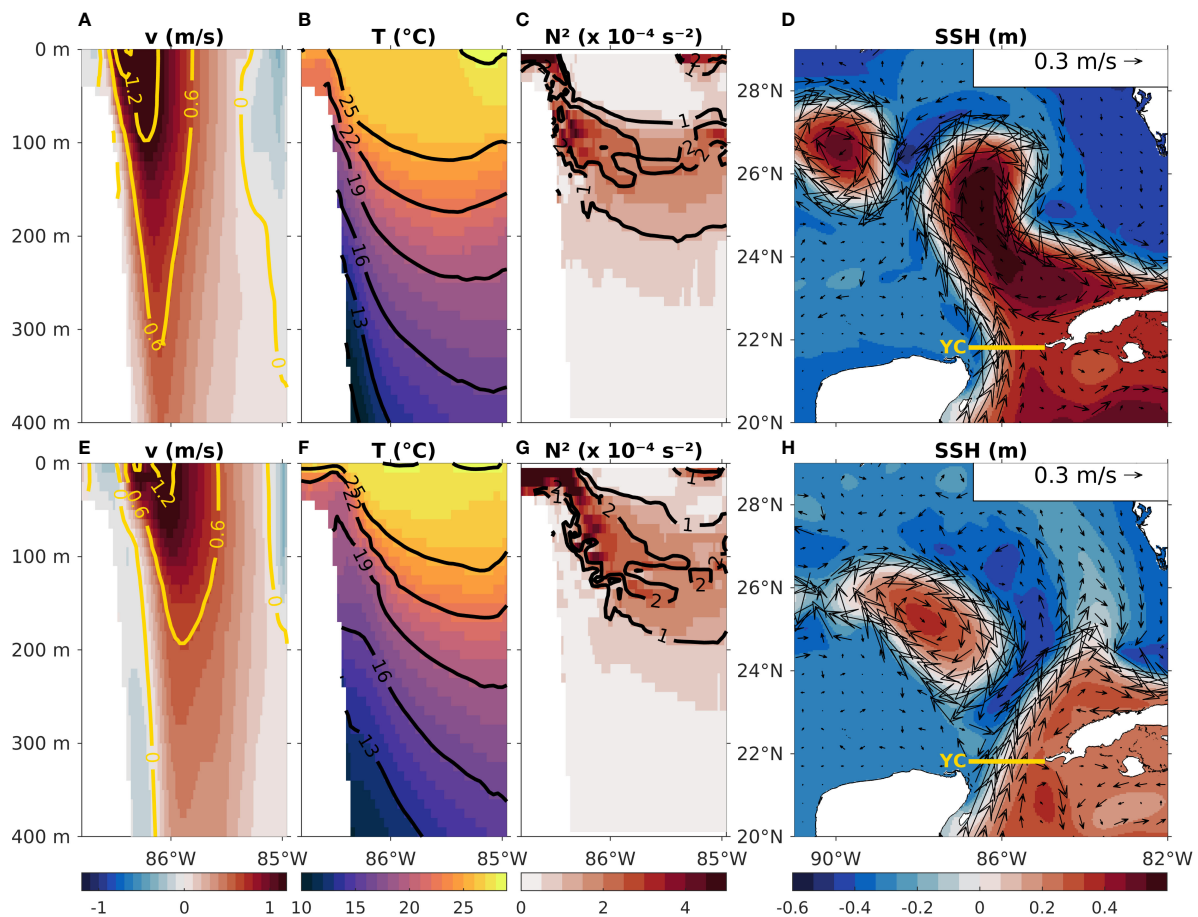


FIGURE 7

Instantaneous daily fields of the state of the ocean before (panels A–D) and during (panels E–H) the +YCu<sub>ZP</sub> event of 1996 (days 64 and 140) in experiment NoAF. Vertical sections of (A, E) meridional velocity, (B, F) temperature, and (C, G)  $N^2$  in the upper 400 m along a latitudinal transect across the YC at 21.81°N. (D, H) Sea surface height and surface velocity field in the eastern Gulf of Mexico.

northwestward extended LC (Figure 7D). During the +YCu<sub>ZP</sub> event, the YCu core displaces away from the Yucatan eastern shelf (Figure 7E), isotherms are uplifted above the Yucatan slope (Figure 7F), the maximum of stratification is located above 100 m depth where the isotherms are squeezed when uplifted (Figure 7G), the YCu path deviates northeastward, and a big LCE detaches (Figure 7H). After the detachment, the YCu core displaces westward, the isotherms descend, and the stratification maximum descends above the Yucatan slope. An animation of this +YCu<sub>ZP</sub> event is provided in the [Supplementary Material](#). A similar figure and animation corresponding to the +YCu<sub>ZP</sub> event of 2003 in experiment AF are also included in the [Supplementary Material](#).

Now that the results regarding LC<sub>NL</sub> and SSH<sub>min</sub> have been presented, the similarity and spectral analyses shown in Figures 4 and 5 can be concluded. For both experiments, there is a high similarity between PC1, YCu<sub>ZP</sub>, 25.5I<sub>D</sub>, LC<sub>NL</sub>, and SSH<sub>min</sub> (Figures 4–6), with a prevalent 1.5–7.5 year variability among them (Figures 4E, J). However, the variability of LC<sub>NL</sub> and SSH<sub>min</sub> exhibits important differences concerning the remaining

variables. The spectral variance of LC<sub>NL</sub> is similar to that of PC1, YCu<sub>ZP</sub>, and 25.5I<sub>D</sub> for experiment NoAF, with most of it contained in the 1.5–7.5 years period band but not as high as for the other variables (Figure 4E). By including atmospheric forcing (experiment AF), the low-frequency signal is preserved in LC<sub>NL</sub>, but it includes high-frequency energy in periods below five months and in the periods previously mentioned for the other processes (Figure 4J). The spectral variance of SSH<sub>min</sub> is not concentrated in the 1.5–7.5 years period band (Figures 4E, J). Most of its spectral variance is contained in the 1.5–2.5 years period band for both experiments, with the addition of high-frequency energy in periods below seven months for experiment AF.

Additional characteristics in the Loop Current System behavior were identified for the two experiments. Figure 8 shows the LC metric values on the day before each LCE detachment and the LCE metric values on the detachment day for all the LCE detachment events. The gray lines correspond to all LCE detachments, the red lines correspond to the +YCu<sub>ZP</sub> events, and the blue line represents the mean values of all the LCE detachments, which are:

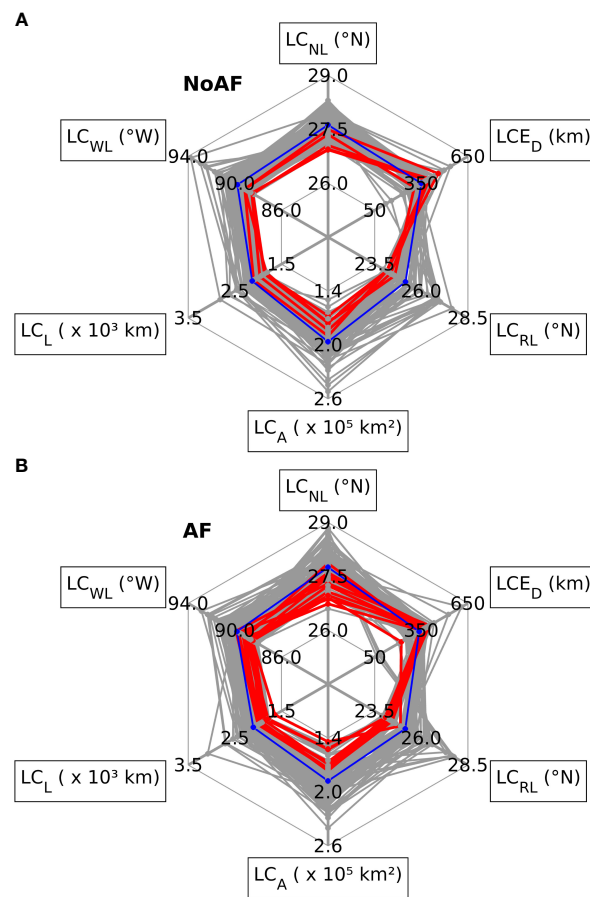


FIGURE 8

LC metric values on the day before LCE detachments and the LCE metrics on the day of LCE detachments for experiments (A) NoAF and (B) AF. The gray lines correspond to all LCE detachments, the red lines correspond to the +YCu<sub>ZP</sub> events, and the blue line represents the mean values of all the LCE detachments. Abbreviations: LC<sub>NL</sub>, LC northernmost latitude; LC<sub>WL</sub>, LC westernmost longitude; LC<sub>L</sub>, LC length; LC<sub>A</sub>, LC area; LC<sub>RL</sub>, LC retreat latitude; LCE<sub>D</sub>, LCE diameter.

- Experiment NoAF. LC<sub>NL</sub>, 27.62°N; LC<sub>WL</sub>, 89.78°W; LC<sub>L</sub>, 2127 km; LC<sub>A</sub>, 1.96 x 10<sup>5</sup> km<sup>2</sup>; LC<sub>RL</sub>, 25.15°N; LCE<sub>D</sub>, 350 km.
- Experiment AF. LC<sub>NL</sub>, 27.75°N; LC<sub>WL</sub>, 89.82°W; LC<sub>L</sub>, 2104 km; LC<sub>A</sub>, 1.88 x 10<sup>5</sup> km<sup>2</sup>; LC<sub>RL</sub>, 25.14°N; LCE<sub>D</sub>, 336 km.

The percentage differences in the LC and LCE metrics of experiment AF relative to experiment NoAF are less than 1% for LC<sub>NL</sub>, LC<sub>WL</sub>, LC<sub>L</sub>, and LC<sub>RL</sub>, whereas the percentage differences are 4% for LC<sub>A</sub> and LCE<sub>D</sub>. By including atmospheric forcing, LCE activity increased from 95 detachments with 36 separations in experiment NoAF to 110 detachments with 37 separations in experiment AF. On average, the LC reaches higher latitudes in experiment AF than in experiment NoAF, whereas the average LC<sub>RL</sub> is very similar in both experiments; however, the LCE<sub>D</sub> is not bigger in experiment AF than in experiment NoAF.

Similar conditions characterize the LCE detachments during the +YCu<sub>ZP</sub> events in both experiments. Before a LCE detachment, the LC metric values are lower than their average ones; when the LCE

detaches, LC<sub>RL</sub> is lower, and LCE<sub>D</sub> is higher than their average values (Figure 8). After the LCE detachments in all the +YCu<sub>ZP</sub> events, three scenarios are possible:

1. The detached LCE re-attaches to the main LC flow, and the +YCu<sub>ZP</sub> event ends. Events occurred in 2004 in experiment NoAF, and in early 1994, late 1997, early 2003, 2004, and 2013 in experiment AF.
2. The LCE detachment is followed by a sequence of one or more reattachments and detachments, ending in a LCE separation; all of these detachments are associated with the same event of YCu eastward displacement. Events occurred in 1996, 2001, and 2008 in experiment NoAF, and in mid-1994, 1999, and mid-2002 in experiment AF.
3. The detached LCE does not reincorporate into the LC, representing a LCE separation. Events occurred in 1994 in experiment NoAF, and in late 1998, late 2003, and 2010 in experiment AF.

### 3.3.2 Yucatan Current dynamics, the Loop Current, and peripheral cyclonic anomalies

The relationships identified between YCu dynamics, the upper YC hydrography, the Loop Current System behavior, and cyclonic anomalies surrounding the LC suggest the existence of underlying physical mechanisms playing significant roles in transmitting information between YCu dynamics and the LC behavior. Interactions of the LC with peripheral cyclonic anomalies at its west margin are a potential underlying mechanism influencing the LC intrusion, YCu path deviation, and LCE detachment (Zavala-Hidalgo et al., 2002; Zavala-Hidalgo et al., 2003; Schmitz et al., 2005; Chérubin et al., 2006; Zavala-Hidalgo et al., 2006; Athié et al., 2012; Le Hénaff et al., 2012; Garcia-Jove et al., 2016; Jouanno et al., 2016; Sheinbaum et al., 2016).

The role of peripheral cyclonic anomalies on the relationship between YCu dynamics and the LC behavior, focusing on the +YCu<sub>zp</sub> events, was explored through the evolution of SSH and surface velocity fields in the eastern Gulf of Mexico. The area charts of SSH<sub>min</sub> in Figures 6C, F show that the occurrence of the +YCu<sub>zp</sub> events is associated with the presence of cyclonic anomalies surrounding the LC southwest margin (with high negative values of SSH<sub>min</sub>), which usually precede or coincide with a LCE detachment. The influence of peripheral cyclonic anomalies on YCu dynamics and the LC behavior is readily appreciable in the overall variability of experiment NoAF and less appreciable in experiment AF. Nonetheless, due to the dynamical correspondence between the dominant variability in experiments NoAF and AF, the influence of this mechanism is expected to operate similarly without and with atmospheric forcing.

A thorough analysis of the evolution of the cyclonic anomalies surrounding the LC during the +YCu<sub>zp</sub> events revealed the general behavior of this mechanism:

1. When the LC has a substantial northward intrusion, two cyclonic anomalies of varying intensity appear surrounding the LC, one at the northeastern Yucatan shelf and the other at the eastern margin of the LC (Figures 9A, D). The anomaly in the west is described by the negative values of SSH<sub>min</sub> in the area charts of Figures 6C, F.
2. The YCu displaces eastward; the more intense the YCu displacement in its northern section, the stronger the resulting curvature on the LC west margin and the development of an LC necking. Then, both cyclonic anomalies squeeze the LC, and a LCE detachment is induced (Figures 9B, E).
3. The resulting LCE detachment may be followed by a sequence of one or more reattachment-detachments and a final eddy separation, in which the cyclonic anomalies surrounding the LC evolve to either merge or weaken separately (Figures 9C, F). Additional cyclonic anomalies at the southwestern and eastern margins of the LC participate in the following LCE detachments and separation.

In some +YCu<sub>zp</sub> events, particular behavior of the YCu and LC is observed for those long-lasting events that occurred in 1994,

1996, 2001, and 2008 in experiment NoAF; and for those that occurred in late 1998, late 2003, and 2010 in experiment AF:

1. Following a LCE separation, the LC remains retracted for several months, reaching its minimum northernmost latitude: 24.06°N in experiment NoAF and 24.00°N in experiment AF.
2. During the retracted phase of the LC, the YCu path remains northeastward-oriented, with the isotherms uplifted above the Yucatan slope and the associated high stratification anomaly at the western YC section above 100 m depth (Figures 4, 6). Such behavior, more intense in experiment NoAF than in experiment AF, coincides with the prolonged presence of an intense cyclonic anomaly north of the LC blocking its intrusion into the Gulf (Figures 9C, F). This cyclonic anomaly resulted from merging the cyclonic anomalies surrounding the LC that led to the LCE separation (Figures 9A, B, D, E).
3. The subsequent gradual LC intrusion coincides with the westward displacement of the YCu core, the lowering of the isotherms above the Yucatan slope, and a weak negative stratification anomaly at the western YC section above 100 m depth (Figures 4, 6).
4. The prolonged LC retraction and gradual northward intrusion led to an extended detachment period (342–462 days in experiment NoAF and 184–303 days in experiment AF) of the subsequent LCE, which is longer than the average period of all detachments (84 days in experiment NoAF and 73 days in experiment AF).
5. During the event of 1998 in experiment AF, no intense cyclonic formations at the southwestern margin of the LC were observed (Figures 9G–I). The LCE separation was mainly associated with a cyclonic anomaly north of the LC, fed by a set of cyclonic anomalies from the northeastern Yucatan shelf that traveled around the LC.

Also, a significant behavior was identified for the events of weak or short-lasting (< 25 days) YCu eastward displacement, previously mentioned in subsection 3.3.1. Compared to the +YCu<sub>zp</sub> events, in those events, LCE detachments usually coincide with a weaker cyclonic anomaly at the southwestern margin of the LC and (or) a LC necking occurring in a higher latitude. In these events, the LC necking is insufficient to induce a LCE detachment, and the southwestern cyclonic anomaly displaces northwestward, preventing an intense YCu eastward displacement. The 2014 event in experiment NoAF (Figures 9J–L) exemplifies this mechanism. During the LCE detachment, the YCu core is slightly eastward displaced with a weak and loosely organized cyclonic anomaly at the northeastern Yucatan shelf, associated with a slight increase in the PC1 series (Figures 6A–C).

Results suggest that peripheral cyclonic anomalies and their interaction with the LC relate to YCu dynamics, the upper YC hydrography, and the Loop Current System behavior. Intense and well-organized cyclonic anomalies at the northeastern Yucatan shelf are associated with the isotherms' uplift above the Yucatan shelf's



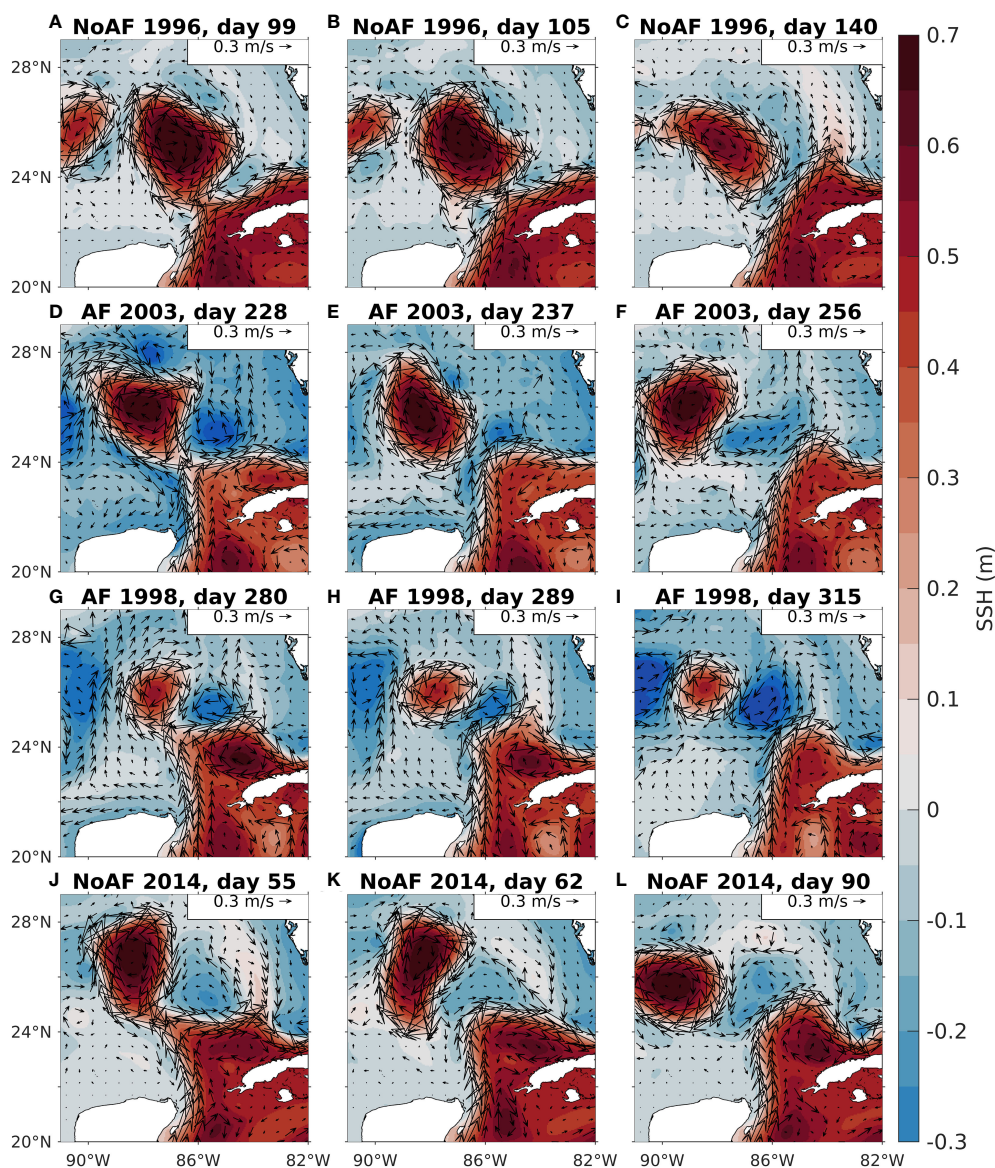


FIGURE 9

SSH and surface velocity fields in the eastern Gulf of Mexico, showing three main stages during the +YCu<sub>zp</sub> events of (A–C) 1996 in experiment NoAF, (D–F) 2003 in experiment AF, (G–I) 1998 in experiment AF, and (J–L) 2014 in experiment NoAF. The mean was removed from the SSH field to reduce the bias associated with seasonal height variations due to upper-ocean warming and cooling.

eastern slope, a stratification increase above 100 m depth at the western YC section, specific conditions of LC intrusion prior to the detachment of a big LCE, and an intense LC retreat. Absent or weak cyclonic anomalies deviate the system from this behavior.

## 4 Discussion

This work identified and described the most important non-seasonal spatial and temporal variability patterns of the YC upper stratification, considering long-term timescales not yet addressed by observational analyses. This study also revealed significant characteristics of the upper YC hydrography, YCu dynamics, the

Loop Current System behavior, the cyclonic anomalies surrounding the LC, and the relationships between them.

Implementing twin simulations of the Gulf of Mexico hydrodynamics, without and with atmospheric forcing, allowed us to evaluate the effect of atmospheric forcing on different oceanic processes in the YC and the Gulf interior associated with the LC behavior. Atmospheric forcing excited additional eigenmodes of ocean dynamics associated with higher variability of the upper flow at the eastern YC, originating in the ocean-atmosphere interaction (Hasselmann, 1976; Grötzner et al., 1999). Consequently, it is impossible to easily track the resulting oceanic variability in terms of atmospheric variability and to *a priori* identify the resulting oceanic spectral variance. Compared to the variability only

associated with ocean dynamics, atmospheric forcing induces a more complex behavior of YC dynamics and the Loop Current System. It produces a significant high-frequency signal and modifies the low-frequency behavior of those phenomena, which in the middle and long term means a more complex behavior of them and probably a reduction in their predictability. This result is consistent with previous ones that showed that simple models show more predictability of the LC (e.g., [Moreles et al. \(2021\)](#)) and that more complex models exhibit an increased variability.

Atmospheric forcing induces variability in periods around 8–15 months on YCu<sub>zp</sub>, with consistent spectral variance on period bands of 4.5–5.5 and 6–8 months; these periods are close to those of 5.6, 8.4 and 11.2 months found by [Ezer et al. \(2003\)](#) for the YCu flow position from 4-year model results. The findings of [Jouanno et al. \(2018\)](#) of high spectral variance around period bands of 180–365 and 60–100 days on Yucatan upwelling variability are supported by our results, with the addition that this variability is strongly related to that of YCu<sub>zp</sub>. Atmospheric forcing also induces interannual variability and high-frequency signal with periods shorter than five months in the LC behavior, which has been previously studied. [Sheinbaum et al. \(2016\)](#) found intense low-frequency (40–100 days) eddy kinetic energy peaks along the water column associated with LCE detachments. [Donohue et al. \(2016\)](#) found that SSH variability associated with LC's northern front is dominated by LC advance and retreat, with most of its variance in periods longer than 100 days; at higher frequencies, most of the contained variance is found at the band of 40–100 days, with peaks during LCE events, and confined eastward of the Mississippi Fan. Atmospheric forcing has a small influence on the temperature and salinity of the water masses of the YCu, due to the relatively short time (around three days) that it takes a water mass in the YCu to move while the YCu flows along the Northwestern Caribbean Sea.

Since atmospheric forcing mainly modifies the higher-order variability modes of YC stratification and has a moderate effect on YC dynamics, results suggest that ocean dynamics is the primary determinant of the dominant spatial and temporal variability of the hydrography and dynamics in the YC. By isolating intrinsic ocean dynamics, an evident dominant mode of YC stratification variability arose, very similar to the dominant one when including atmospheric forcing. The dominant modes have an associated spatial pattern describing a dipole in the western YC, with most of their spectral variance concentrated in the 1.5–7.5 years period band, which originates in the variation, location, and displacements of the YCu core. The findings of this work complement previous ones that showed that the YCu is the dominant source of YC dynamics variability ([Ezer et al., 2003](#); [Marín et al., 2008](#); [Athie et al., 2011](#); [Sheinbaum et al., 2016](#)) and that of [Carrillo et al. \(2016\)](#) who found that the YCu determines the spatial distribution of thermohaline properties in the northeastern tip of the Yucatan Peninsula.

The relationship between the eastward displacement of the YCu path and the isotherms' uplifting at the upper western YC, previously found by [Enríquez and Mariño-Tapia \(2014\)](#), was corroborated in this study, showing it is a recurrent pattern that

could be related to the cold nutrient-rich water upwelling at Yucatan northeastern coast ([Enríquez and Mariño-Tapia, 2014](#); [Carrillo et al., 2016](#); [Reyes-Mendoza et al., 2016](#); [Jouanno et al., 2018](#)). The upper stratification at the western YC, the zonal position of the YCu core, and the vertical thermal structure above the Yucatan slope evolve in the same low-frequency timescales; the connection between them is strong without and with atmospheric forcing. Our work can contribute to a better understanding of the upwelling development on the eastern Yucatan shelf, which has significant dynamical and biological implications for the region ([Merino, 1997](#); [Abascal et al., 2003](#); [Carrillo et al., 2016](#); [Jouanno et al., 2018](#); [Reyes-Jiménez et al., 2023](#)). Studies of upper stratification are especially relevant in describing and forecasting mixing processes, oxygen and nutrient supply in the upper ocean, ocean uptake of greenhouse gasses, and local primary productivity ([Gruber, 2011](#); [Jacox and Edwards, 2011](#)). Since regional ocean circulation is of primary importance in the variability of YC upper stratification, long-term studies are needed to evaluate the effects that changes in YC dynamics, such as the expected 20–25% reduction of YCu transport during the 21st century ([Liu et al., 2012](#); [Moreles et al., 2021](#)), could have on the stratification and the consequent ecological and biogeochemical impact in the region.

Using observations from the 2003–2015 period, [Varela et al. \(2018\)](#) found an eastward trend of the YCu zonal position relative to the 1993–2003 period, probably associated with a cooling trend of the sea surface temperatures in the Yucatan shelf's north coast during 1982–2015. Since our simulations were forced by climatological boundary conditions, we do not expect to see this eastward tendency. Our results indicate that eastward displacements of the YCu are an intrinsic part of its variability. If the YCu transport structure is maintained over time at its climatological values, neither a long-term eastward trend in its zonal position nor a cooling trend in temperature is expected to occur. Long-term simulations of the Gulf hydrodynamics incorporating interannual variability on the boundary conditions could shed light on these processes. Our methodological approach could serve as a basis for analyzing the effects of the expected changes in upper ocean stratification for different time horizons due to climate change.

The LC evolution is strongly related to its dynamical conditions at the YC, as previously evinced ([Candela et al., 2002](#); [Lin et al., 2009](#); [Athié et al., 2012](#); [Sheinbaum et al., 2016](#); [Androulidakis et al., 2021](#); [Moreles et al., 2021](#)). The identified relationship between the eastward displacement of the YCu core and LCE detachments relates to previous studies suggesting these processes are connected with vorticity anomalies from the northwestern Caribbean Sea crossing the YC ([Abascal et al., 2003](#); [Marín et al., 2008](#); [Athie et al., 2011](#); [Athié et al., 2012](#); [Sheinbaum et al., 2016](#); [Androulidakis et al., 2021](#)). We conducted preliminary analyses (not shown) of the vorticity flux in latitudinal sections along the YCu west margin without obtaining conclusive results, so further analyses are required to explore this relationship in detail and corroborate it.

The relationships between the cyclonic anomalies at the northeastern Yucatan shelf, the eastward displacement of the YCu

core, LC intrusion, and LCE detachment support the results documented in previous observational and numerical works. Using simulation outputs from the Navy Coastal Ocean Model, Zavala-Hidalgo et al. (2002) described the formation of cyclones at the Campeche Bank and the LC east margin and their relationship to the LC necking during a LCE detachment. Later, Zavala-Hidalgo et al. (2003) associated the cyclone genesis at the Campeche Bank with the last stage of a big LCE detachment when the LC west margin displaces eastwards; Zavala-Hidalgo et al. (2006) described some mechanisms associated with the LC blocking by a large cyclone. These mechanisms were identified and described in experiments NoAF and AF, deepening our understanding of the physical system under study. The intense YCu eastward displacement and strong curvature on the LC west margin during the +YCu<sub>ZP</sub> events could partially account for the generation of the cyclonic anomalies at the Yucatan shelf through local instabilities, as found by Chérubin et al. (2006). Additional research is needed to elucidate the origin, coherence, trajectories, and dissipation of such cyclonic anomalies and eventually reveal their causal dynamics.

The observed concurrent variability of different dynamical processes at the YC section and the Gulf interior allows us to suggest that the interaction of the LC with peripheral cyclones could be a potential mechanism associated with the transmission of information between YCu dynamics and the LC behavior, especially during LCE detachments. This study raised some questions: Could the cyclonic features at the Yucatan shelf be fed by cyclonic anomalies passing through the YC from the northwestern Caribbean Sea, as Jouanno et al. (2016) suggested? Could the related vorticity flux account for the eastward displacement of the YCu core and the isotherms' uplift over the eastern slope of the Yucatan shelf? In order to respond to these questions, a thorough analysis of the potential vorticity flux through the YC and in meridional and zonal transects at the northeastern Yucatan shelf is proposed for future research.

A thorough analysis of the variability of wind stress, remote forcings, or heat and evaporation fluxes in the Gulf of Mexico could help provide a complete description of the stratification variability at the Yucatan Channel and the relative importance of its different driving mechanisms. Additionally, circulation and dynamics in the entire Gulf, including changes in its stratification, should significantly impact the Yucatan Channel dynamics. Such analyses are beyond the scope of this work and are proposed for future research.

## 5 Conclusions

This work described the non-seasonal dominant variability of the upper stratification at the Yucatan Channel; the regions with high variability and their timescales were identified. The stratification variability at the Yucatan Channel is mainly associated with the Yucatan Current variability, in agreement with previous research. In addition, we found and described new features of this system. Ocean dynamics is the primary determinant

of the dominant hydrography variability and dynamics in the Yucatan Channel. The most important stratification variability modes are strongly connected with the hydrography and dynamics at the Yucatan Channel and the Loop Current System. We found physically consistent and statistically significant relationships between the variability at the Channel, eastward displacement of the Yucatan Current, the Loop Current intrusion, the detachment of big Loop Current Eddies, and the development of cyclonic anomalies at the northeastern Yucatan shelf. The influence of atmospheric forcing on such relationships and mechanisms was also addressed; it excited additional eigenmodes of ocean dynamics, producing significant high-frequency variability in YC dynamics and the Loop Current System, resulting in a more complex behavior of them and probably reducing their predictability in the middle and long term.

We expect our results will help expand our knowledge of the different dynamical processes occurring in the region, including those with biological relevance, such as the upwelling on the eastern Yucatan shelf. The results can be used as a baseline for further studies exploring the response of the above relationships to changes in stratification and transport of the Yucatan Current due to climate change. For future work, it is suggested to reproduce the analysis in an even more realistic setting by incorporating interannual variability into the model's open boundary conditions.

## Data availability statement

The datasets presented in this study can be found in online repositories. The names of the repository/repositories and accession number(s) can be found below: <http://metadata.icmyl.unam.mx/handle/20.500.12201/11339>.

## Author contributions

SH-P validated the HYCOM simulations, analyzed and interpreted the data, created the figures, and wrote and revised the manuscript. EM conceived and designed the study, validated the HYCOM simulations, analyzed and interpreted the data, wrote and revised the manuscript, and acquired funding. EO-P implemented and validated the HYCOM simulations, analyzed and interpreted the data, and revised the manuscript. JZ-H interpreted the data and revised the manuscript. All authors contributed substantially to this work and approved it for publication.

## Funding

This research was funded by UNAM-PAPIIT IA104320, the Instituto de Ciencias del Mar y Limnología of the Universidad Nacional Autónoma de México (grants 626 and 101), and by the Mexican National Council for Science and Technology—Mexican



Ministry of Energy—Hydrocarbon Fund, project 201441. This is a contribution of the Gulf of Mexico Research Consortium (CIGoM). We acknowledge PEMEX's specific request to the Hydrocarbon Fund to address the environmental effects of oil spills in the Gulf of Mexico.

## Acknowledgments

The authors acknowledge the support of the participants in the project UNAM-PAPIIT IA104320: Luis Zamudio, María E. Osorio-Tai, Oscar Navarro-Sánchez, Jenny Vázquez-Ramírez, Pavel Oropeza-Alfaro, and Juan Nieblas-Piquero. SH-P thanks the support provided by UNAM-PAPIIT IA104320 and the Universidad Nacional Autónoma de México to complete her undergraduate studies. EO-P thanks the support provided by the program of postdoctoral fellowships UNAM-DGAPA. The authors acknowledge the reviewers for their valuable comments, which significantly improved this work.

## References

- Abascal, A. J., Sheinbaum, J., Candela, J., Ochoa, J., and Badan, A. (2003). Analysis of flow variability in the Yucatan Channel. *J. Geophysical Research: Oceans* 108 (C12), 3381. doi: 10.1029/2003JC001922
- Androulidakis, Y., Kourafalou, V., Olascoaga, M., Beron-Vera, F., Le Hénaff, M., Kang, H., et al. (2021). Impact of Caribbean anticyclones on Loop Current variability. *Ocean Dynamics* 71, 935–956. doi: 10.1007/s10236-021-01474-9
- Athié, G., Candela, J., Ochoa, J., and Sheinbaum, J. (2012). Impact of Caribbean cyclones on the detachment of Loop Current anticyclones. *J. Geophysical Research: Oceans* 117 (C3), C03018. doi: 10.1029/2011JC007090
- Athié, G., Candela, J., Sheinbaum, J., Badan, A., and Ochoa-de-la Torre, J. (2011). Yucatan Current variability through the Cozumel and Yucatan channels. *Cienc. Marinas* 37, 471–492. doi: 10.7773/cm.v37i4A.1794
- Athié, G., Sheinbaum, J., Leben, R., Ochoa, J., Shannon, M. R., and Candela, J. (2015). Interannual variability in the Yucatan Channel flow. *Geophysical Res. Lett.* 42 (5), 1496–1503. doi: 10.1002/2014GL026274
- Bleck, R. (2002). An oceanic general circulation model framed in hybrid isopycnal-Cartesian coordinates. *Ocean Model.* 4, 55–88. doi: 10.1016/S1463-5003(01)00012-9
- Candela, J., Ochoa, J., Sheinbaum, J., López, M., Pérez-Brunius, P., Tenreiro, M., et al. (2019). The flow through the Gulf of Mexico. *J. Phys. Oceanography* 49, 1381–1401. doi: 10.1175/JPO-D-18-0189.1
- Candela, J., Sheinbaum, J., Ochoa, J., Badan, A., and Leben, R. (2002). The potential vorticity flux through the Yucatan Channel and the Loop Current in the Gulf of Mexico. *Geophysical Res. Lett.* 29 (22), 16-1–16-4. doi: 10.1029/2002GL015587
- Carrillo, L., Johns, E., Smith, R., Lamkin, J., and Largier, J. (2016). Pathways and hydrography in the Mesoamerican Barrier Reef System Part 2: Water masses and thermohaline structure. *Continental Shelf Res.* 120, 41–58. doi: 10.1016/j.csr.2016.03.014
- Cassisi, C., Montalto, P., Aliotta, M., Cannata, A., and Pulvirenti, A. (2012). “Similarity Measures and Dimensionality Reduction Techniques for Time Series Data Mining,” in *Advances in data mining knowledge discovery and applications*. Ed. A. Karahoca (Rijeka: IntechOpen), 71–96. doi: 10.5772/49941
- Chassignet, E. P., Hurlburt, H. E., Smedstad, O. M., Halliwell, G. R., Hogan, P. J., Wallcraft, A. J., et al. (2007). The HYCOM (HYbrid Coordinate Ocean Model) data assimilative system. *J. Mar. Syst.* 65, 60–83. doi: 10.1016/j.jmarsys.2005.09.016
- Chérubin, L. M., Morel, Y., and Chassignet, E. P. (2006). Loop Current ring shedding: the formation of cyclones and the effect of topography. *J. Phys. Oceanography* 36, 569–591. doi: 10.1175/JPO2871.1
- CTOH. (2013). *What are Mesoscale Processes?* Available at: <http://ctoh.legos.obs-mip.fr/applications/mesoscale/what-are-mesoscale-processes> (Accessed December, 2022).
- Donohue, K., Watts, D., Hamilton, P., Leben, R., Kennelly, M., and Lugo-Fernández, A. (2016). Gulf of Mexico Loop Current path variability. *Dynamics Atmospheres Oceans* 76, 174–194. doi: 10.1016/j.dynatmoce.2015.12.003
- Enriquez, C., and Mariño-Tapia, I. (2014). “Mechanisms driving a coastal dynamic upwelling,” in *Proceedings of the 17th Physics of Estuaries and Coastal Seas (PECS) Conference*, Porto de Galinhas, Pernambuco, Brazil.
- Ezer, T., Oey, L.-Y., Lee, H.-C., and Sturges, W. (2003). The variability of currents in the Yucatan Channel: Analysis of results from a numerical ocean model. *J. Geophysical Research: Oceans* 108 (C1), 3012. doi: 10.1029/2002JC001509
- García-Jové, M., Sheinbaum, J., and Jouanno, J. (2016). Sensitivity of Loop Current metrics and eddy detachments to different model configurations: The impact of topography and Caribbean perturbations. *Atmosfera* 29, 235–265. doi: 10.20937/ATM.2016.29.03.05
- Gill, A. (1982). “Atmosphere-Ocean Dynamics,” in *International geophysics*, 1 edn. (United States of America: Academic Press), vol. 30.
- Grötzner, A., Latif, M., Timmermann, A., and Voss, R. (1999). Interannual to Decadal Predictability in a Coupled Ocean–Atmosphere General Circulation Model. *J. Climate* 12, 2607–2624. doi: 10.1175/1520-0442(1999)012<2607:ITDPIA>2.0.CO;2
- Gruber, N. (2011). Warming up, turning sour, losing breath: ocean biogeochemistry under global change. *Philos. Trans. R. Soc. A: Mathematical Phys. Eng. Sci.* 369, 1980–1996. doi: 10.1098/rsta.2011.0003
- Hamilton, P., Berger, T. J., Singer, J. J., Waddell, E., Churchill, J. H., Leben, R. R., et al. (2000). “Desoto Canyon Eddy Intrusion Study, Final Report, Volume II. tech. rep., OCS study MMS 2000-080” in *U.S. Dept. of the Interior, Minerals Management Service, Gulf of Mexico OCS Region*, New Orleans, Louisiana. (United States Department of the Interior), 275.
- Hamilton, P., Bower, A., Furey, H., Leben, R., and Pérez-Brunius, P. (2019). The Loop Current: Observations of Deep Eddies and Topographic Waves. *J. Phys. Oceanography* 49, 1463–1483. doi: 10.1175/JPO-D-18-0213.1
- Hasselmann, K. (1976). Stochastic climate models Part I. *Theory. Tellus* 28, 473–485. doi: 10.1111/j.2153-3490.1976.tb00696.x
- HYCOM-GOFS3.1 HYCOM Consortium for Data Assimilative Modeling. GOFS 3.1: 41-layer HYCOM + NCODA global. Available at: <https://www.hycom.org/data/glbv0pt08/expt-53ptx> (Accessed November 15, 2021).
- Jackett, D. R., and McDougall, T. J. (1995). Minimal adjustment of hydrographic profiles to achieve static stability. *J. Atmospheric Oceanic Technol.* 12, 381–389. doi: 10.1175/1520-0426(1995)012<0381:MAOHTP>2.0.CO;2
- Jacox, M. G., and Edwards, C. A. (2011). Effects of stratification and shelf slope on nutrient supply in coastal upwelling regions. *J. Geophysical Research: Oceans* 116 (C3), C03019. doi: 10.1029/2010JC006547
- Jochens, A. E., and DiMarco, S. F. (2008). Physical oceanographic conditions in the deepwater Gulf of Mexico in summer 2000–2002. *Deep Sea Res. Part II: Topical Stud. Oceanography* 55, 2541–2554. doi: 10.1016/j.dsr2.2008.07.003
- Jouanno, J., Ochoa, J., Pallàs-Sanz, E., Sheinbaum, J., Andrade-Canto, F., Candela, J., et al. (2016). Loop current frontal eddies: formation along the campeche bank and impact of coastally trapped waves. *J. Phys. Oceanography* 46, 3339–3363. doi: 10.1175/JPO-D-16-0052.1

## Conflict of interest

The authors declare that the research was conducted in the absence of any commercial or financial relationships that could be construed as a potential conflict of interest.

## Publisher's note

All claims expressed in this article are solely those of the authors and do not necessarily represent those of their affiliated organizations, or those of the publisher, the editors and the reviewers. Any product that may be evaluated in this article, or claim that may be made by its manufacturer, is not guaranteed or endorsed by the publisher.

## Supplementary material

The Supplementary Material for this article can be found online at: <https://www.frontiersin.org/articles/10.3389/fmars.2023.1049662/full#supplementary-material>



- Jouanno, J., Pallàs-Sanz, E., and Sheinbaum, J. (2018). Variability and Dynamics of the Yucatan Upwelling: High-Resolution Simulations. *J. Geophysical Research: Oceans* 123 (2), 1251–1262. doi: 10.1002/2017JC013535
- Le Hénaff, M., Kourafalou, V. H., Morel, Y., and Srinivasan, A. (2012). Simulating the dynamics and intensification of cyclonic Loop Current frontal eddies in the Gulf of Mexico. *J. Geophysical Research: Oceans* 117 (C2), C02034. doi: 10.1029/2011JC007279
- Lin, Y., Greatbatch, R. J., and Sheng, J. (2009). A model study of the vertically integrated transport variability through the Yucatan Channel: Role of Loop Current evolution and flow compensation around Cuba. *J. Geophysical Research: Oceans* 114 (C8), C08003. doi: 10.1029/2008JC005199
- Liu, Y., Lee, S.-K., Muhling, B. A., Lamkin, J. T., and Enfield, D. B. (2012). Significant reduction of the Loop Current in the 21st century and its impact on the Gulf of Mexico. *J. Geophysical Research: Oceans* 117 (C5), C05039. doi: 10.1029/2011JC007555
- Marín, M., Candela, J., Sheinbaum, J., Ochoa, J., and Badan, A. (2008). On the near surface momentum balance in the yucatán Channel. *Geofísica Internacional* 47, 57–75. doi: 10.22201/igeof.00167169p.2008.47.1.67
- Merino, M. (1997). Upwelling on the Yucatan shelf: hydrographic evidence. *J. Mar. Syst.* 13 (1), 101–121. doi: 10.1016/S0924-7963(96)00123-6
- Morelos, E., Zavala-Hidalgo, J., Martínez-López, B., and Ruiz-Angulo, A. (2021). Influence of stratification and yucatan current transport on the loop current eddy shedding proces. *J. Geophysical Research: Oceans* 126, e2020JC016315. doi: 10.1029/2020JC016315
- Morey, S. L., Gopalakrishnan, G., Sanz, E. P., Souza, J. M. A. C. D., Donohue, K., Pérez-Brunius, P., et al. (2020). Assessment of numerical simulations of deep circulation and variability in the gulf of mexico using recent observations. *J. Phys. Oceanography* 50, 1045–1064. doi: 10.1175/JPO-D-19-0137.1
- Morgan, P. P. CSIRO (1994). *SEAWATER : a library of MATLAB computational routines for the properties of sea water / phillip p. Morgan* (Australia:CSIRO Marine Laboratories Hobart, Tas), 37 pp.
- NASEM. (2018). “National Academies of Sciences, Engineering, and Medicine,” in *Understanding and predicting the Gulf of Mexico Loop Current: critical gaps and recommendations* (Washington, DC: The National Academies Press). doi: 10.17226/24823
- NCEP-CFSR. *HYCOM Consortium for Data Assimilative Modeling*. NCEP CFSR. Available at: <https://www.hycom.org/dataserver/ncep-cfsr> (Accessed November 15, 2021).
- North, G. R., Bell, T. L., Cahalan, R. F., and Moeng, F. J. (1982). Sampling errors in the estimation of empirical orthogonal functions. *Monthly Weather Rev.* 110, 699–706. doi: 10.1175/1520-0493(1982)110<0699:SEITEO>2.0.CO;2
- Oey, L.-Y. (2004). Vorticity flux through the Yucatan Channel and Loop Current variability in the Gulf of Mexico. *J. Geophysical Research: Oceans* 109 (C10), C10004. doi: 10.1029/2004JC002400
- Olvera-Prado, E. R., Romero-Centeno, R., Zavala-Hidalgo, J., Morelos, E. and , and Ruiz-Angulo, A. (2022). Contribution of the wind and Loop Current Eddies to the circulation in the southern Gulf of Mexico. *ESS Open Arch.* doi: 10.22541/essoar.167214412.29537730/v1
- Ramos-Musale, K. (2013). Estudio numérico de los forzamientos que generan la surgencia de Yucatán. (Bsc. Thesis). UNAM Mexico, 95.
- Reyes-Jiménez, T., Athié, G., Enriquez, C., Sheinbaum, J., Mariño-Tapia, I., Marín-Hernández, M., et al. (2023). Triggering mechanisms of the Yucatan upwelling. *Continental Shelf Res.* 255, 104910. doi: 10.1016/j.csr.2022.104910
- Reyes-Mendoza, O., Herrera-Silveira, J., Mariño-Tapia, I., Enriquez, C., and Largier, J. L. (2019). Phytoplankton blooms associated with upwelling at Cabo Catoche. *Continental Shelf Res.* 174, 118–131. doi: 10.1016/j.csr.2018.12.015
- Reyes-Mendoza, O., Mariño-Tapia, I., Herrera-Silveira, J. A., Ruiz-Martínez, G., Enriquez, C. E., and Largier, J. L. (2016). The Effects of Wind on Upwelling off Cabo Catoche. *J. Coast. Res.* 32, 638–650. doi: 10.2112/JCOASTRES-D-15-00043.1
- Rousset, C., and Beal, L. M. (2010). Observations of the Florida and Yucatan Currents from a Caribbean Cruise Ship. *J. Phys. Oceanography* 40, 1575–1581. doi: 10.1175/2010JPO4447.1
- Schmitz, W. J. (2005). “Cyclones and Westward Propagation in the Shedding of Anticyclonic Rings from the Loop Current,” in *Circulation in the Gulf of Mexico: Observations and Models*. Eds. W. Sturges and A. Lugo-Fernandez (American Geophysical Union), vol. 17, 241–261. doi: 10.1029/161GM18
- Schmitz, W. J., Biggs, D. C., Lugo-Fernandez, A., Oey, L.-Y., and Sturges, W. (2005). “A Synopsis of the Circulation in the Gulf of Mexico and on its Continental Margins,” in *Circulation in the Gulf of Mexico: Observations and Models*. Eds. W. Sturges and A. Lugo-Fernandez, vol. 2, 11–29. (American Geophysical Union). doi: 10.1029/GM161
- Sheinbaum, J., Athié, G., Candela, J., Ochoa, J., and Romero-Arteaga, A. (2016). Structure and variability of the Yucatan and Loop Currents along the slope and shelf break of the Yucatan Channel and Campeche bank. *Dynamics Atmospheres Oceans* 76, 217–239. doi: 10.1016/j.dynatmoce.2016.08.001
- Sheinbaum, J., Candela, J., Badan, A., and Ochoa, J. (2002). Flow structure and transport in the Yucatan Channel. *Geophysical Res. Lett.* 29, 10–1–10–4. doi: 10.1029/2001GL013990
- Storch, H. v., and Zwiers, F. W. (1999). *Statistical Analysis in Climate Research*. (Cambridge:Cambridge University Press). doi: 10.1017/CBO9780511612336
- Sturges, W., Lugo-Fernández, A., and Shargel, M. (2005). Introduction to Circulation in the Gulf of Mexico. *Circulation in the Gulf of Mexico: Observations and Models* (American Geophysical Union (AGU)), 1–10. doi: 10.1029/161GM02
- Varela, R., Costoya, X., Enriquez, C., Santos, F., and Gómez-Gesteira, M. (2018). Differences in coastal and oceanic SST trends north of Yucatan Peninsula. *J. Mar. Syst.* 182, 46–55. doi: 10.1016/j.jmarsys.2018.03.006
- Yamaguchi, R., and Suga, T. (2019). Trend and variability in global upper-ocean stratification since the 1960s. *J. Geophysical Research: Oceans* 124 (12), 8933–8948. doi: 10.1029/2019JC015439
- Yoskowitz, D., Leon, C., Gibeaut, J., Lupher, B., Lopez, M., Santos, C., et al. (2013). *Gulf 360: State of the Gulf of Mexico. tech. rep., harte research institute for Gulf of Mexico studies* (Texas: Texas A&M University-Corpus Christi).
- Zavala-Hidalgo, J., Morey, S., and O'Brien, J. (2002). “On the formation and interaction of cyclonic eddies with the Loop Current using NCOM and a suite of observations,” in *OCEANS '02 MTS/IEEE*, Vol. 3, 1463–1466. doi: 10.1109/OCEANS.2002.1191853
- Zavala-Hidalgo, J., Morey, S. L., and O'Brien, J. J. (2003). Cyclonic Eddies Northeast of the Campeche Bank from Altimetry Data. *J. Phys. Oceanography* 33, 623–629. doi: 10.1175/1520-0485(2003)033<0623:CENOTC>2.0.CO;2
- Zavala-Hidalgo, J., Morey, S. L., O'Brien, J. J., and Zamudio, L. (2006). On the Loop Current eddy shedding variability. *Atmósfera* 19, 41–48.



## OPEN ACCESS

## EDITED BY

Ruoying He,  
North Carolina State University,  
United States

## REVIEWED BY

Wei Huang,  
Oak Ridge National Laboratory (DOE),  
United States  
Matthieu Le Hénaff,  
University of Miami, United States

## \*CORRESPONDENCE

Efraín Moreles  
✉ moreles@cmarl.unam.mx

RECEIVED 06 October 2022

ACCEPTED 06 June 2023

PUBLISHED 28 July 2023

## CITATION

Moreles E (2023) Variability of the southern  
Gulf of Mexico and its predictability and  
stochastic origin.  
*Front. Mar. Sci.* 10:1063293.  
doi: 10.3389/fmars.2023.1063293

## COPYRIGHT

© 2023 Moreles. This is an open-access  
article distributed under the terms of the  
[Creative Commons Attribution License  
\(CC BY\)](https://creativecommons.org/licenses/by/4.0/). The use, distribution or  
reproduction in other forums is permitted,  
provided the original author(s) and the  
copyright owner(s) are credited and that  
the original publication in this journal is  
cited, in accordance with accepted  
academic practice. No use, distribution or  
reproduction is permitted which does not  
comply with these terms.

# Variability of the southern Gulf of Mexico and its predictability and stochastic origin

Efraín Moreles\*

Instituto de Ciencias del Mar y Limnología, Unidad Academica Procesos Oceánicos y Costeros,  
Universidad Nacional Autónoma de México, Mexico City, Mexico

The variability of surface and deep layers in the southern Gulf of Mexico and their predictability and stochastic origin are studied. Considering separated and coupled layers analyses, the most important variability modes were estimated via Empirical Orthogonal Functions using daily isopycnic layer-thickness anomalies from a 21-year free-running simulation of the Gulf hydrodynamics performed with the HYbrid Coordinate Ocean Model. There is a separation between the principal and higher-order coupled variability. The deep layer strongly determines the variability throughout the water column for the principal coupled variability: the timescales and long-term persistence are mainly associated with deep dynamics. Higher-order coupled variability has no clear association with surface or deep dynamics. Deep dynamics is likely to influence the subsequent evolution of surface dynamics; however, an evident causality relationship between them was not found. No vertical correspondence between surface and deep isopycnal fluctuations was found. The principal coupled variability mode is described by a surface region in the southwest where the Campeche Gyre occurs and a deep region in the center of the basin extending to the north. The predictability was estimated through the decorrelation times of the variability modes. The predictability of deep variability is three times that of surface variability, with 30.5-month predictability for the principal deep mode. Layer coupling evinced the role of the deep ocean in generating long-term variability by extending the predictability of the principal surface mode 2.6-fold, from 10.6 to 27.2 months. Strong evidence is provided for the stochastic origin of the principal variability, suggesting it can be described using linear dynamics in terms of a fast and a slow component.

## KEYWORDS

isopycnic layers, separated and coupled variability, long-term persistence, empirical orthogonal functions, hybrid coordinate ocean model

## 1 Introduction

The sustainable management of global marine resources requires knowing the ocean circulation and characterizing its mean state, its variability in different temporal and spatial scales, and its stability to different perturbations (Schmitt, 2018). In this way, it will be possible to understand and predict the changes in the physical, ecological, and chemical

processes occurring in the oceans, making it possible to face and attend to the possible impacts of these changes in different aspects affecting humankind (Cooley et al., 2022). In the North Atlantic Ocean, the Gulf of Mexico (GoM) is a sea of prime importance; it is the ninth-largest water body in the world (NOAA, 2008), located between the coasts of Mexico, the United States, and Cuba (Figure 1). The GoM represents a vast source of natural resources, with a unique ecological diversity and a variety of coastal ecosystems, which sustain much of its economic activity, one of the most robust worldwide (Adams et al., 2004; NOAA, 2008; Yoskowitz et al., 2013). The state, circulation, and dynamics of the GoM play a significant role in defining the weather and climate of the region (Muller-Karger et al., 2015). The development and behavior of different meteorological phenomena (e.g., hurricanes and autumn-winter cold fronts) and oceanic productivity are strongly influenced by air-sea interaction, the upper ocean heat content, mixed layer depth, transport of heat and salt, dissolved matter, and exchange of mass, momentum, and nutrients between different water masses (Morey et al., 2005; Martínez-López and Zavala-Hidalgo, 2009; Muller-Karger et al., 2015; Judt et al., 2016; NASEM, 2018; Portela et al., 2018).

This study focuses on the southern GoM (Figure 1), a very relevant region in the GoM due to the regular exploration and exploitation of oil and gas developed there (Adams et al., 2004; NOAA, 2008; Yoskowitz et al., 2013) and because it contains some of the most important coral reefs of the GoM (NOAA, 2008; Yoskowitz et al., 2013; Gil-Agudelo et al., 2020). Consequently, studies on mixing processes, dispersion of tracers and pollutants, interchange of tracers between continental shelf waters and the deep ocean, particle dispersion, and ecosystem conservation in the southern GoM are needed (Zavala-Sansón et al., 2017; Gil-Agudelo et al., 2020; Guerrero et al., 2020). The southern GoM circulation is very complex and does not exhibit a clear monthly or seasonal variability pattern; it is composed of many circulation patterns occurring at different spatial scales, lasting from some

weeks to a few months (Monreal-Gómez and Salas-de León, 1997; Zavala-Hidalgo et al., 2003; Vázquez de la Cerda et al., 2005; Vukovich, 2007; Dubranna et al., 2011; Pérez-Brunius et al., 2013; Hamilton et al., 2016; Zavala-Sansón et al., 2017; Zavala-Sansón, 2019). The circulation and its associated variability result from the interaction of different ocean mesoscale circulation processes occurring there: a semi-permanent cyclonic circulation referred to as the Campeche Gyre (Monreal-Gómez and Salas-de León, 1997; Vázquez de la Cerda et al., 2005; Pérez-Brunius et al., 2013), a seasonal circulation in the form of an intense alongshore current at the western margin of the basin (Zavala-Hidalgo et al., 2003; Dubranna et al., 2011), and the aperiodic arrival of Loop Current Eddies (Vidal et al., 1992; Vukovich, 2007; Pérez-Brunius et al., 2013; Meza-Padilla et al., 2019).

Observational (Vázquez de la Cerda et al., 2005; Pérez-Brunius et al., 2013) and simplified theoretical and numerical studies (Zavala-Sansón, 2019) have revealed different characteristics of ocean variability in the southern GoM. Vázquez de la Cerda et al. (2005) characterized the mean circulation and variability of the southern GoM using satellite-derived sea surface data, hydrographic data at 425, 800, and 1500 m depth, and drifter and float measurements at 900 m depth. They identified significant circulation patterns in the region, along with their seasonal and non-seasonal variability, temporal variations, and possible associated forcings, emphasizing the Campeche Gyre. Pérez-Brunius et al. (2013) analyzed the surface circulation of the southern GoM using three years of data from surface drifters, current meter moorings (deployed at 500 and 2000 m depth), and satellite altimetry. They observed important effects of Loop Current Eddies on the variability of the Campeche Gyre, whose size and location are delimited by the bathymetry of the region, evincing the relevance of potential vorticity conservation and the equivalent-barotropic model to describe the Gyre dynamics. Zavala-Sansón (2019) used equivalent-barotropic modeling to examine the formation of the Campeche Gyre considering its barotropic

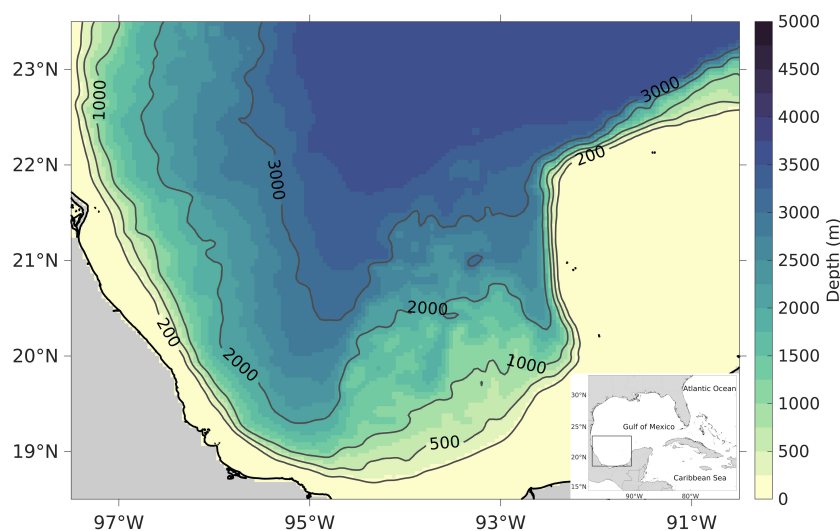


FIGURE 1

The Gulf of Mexico with a zoom in its southern region. The gray contours represent the 200, 500, 1000, 2000, and 3000 m isobaths.

vertical structure. He found that the formation of the Gyre is consistent with equivalent-barotropic dynamics and that it is topographically confined according to the shape of the geostrophic contours.

Previous studies have outlined different aspects of the variability, dynamics, and associated forcings of the southern GoM in great detail at the surface and, to a lesser extent, at depths greater than 1000–1200 m. Due to the limited temporal and spatial coverage of data records used in those studies, a comprehensive depiction of deep GoM dynamics still needs to be completed. It remains to be proved if the variability patterns found are persistent, episodic, or representative of GoM dynamics in the long term. Previous research indicated a significant relationship between surface and deep variability in the GoM, with distinctive surface and deep features. Olvera-Prado et al. (2023) studied the coupling between surface and deep layer variability across the entire GoM using thickness data of isopycnic layers from a long-term numerical simulation; they found a strong connection between the layers and associations between the variability modes with recurrent circulation patterns in both layers. However, due to the characteristics of southern GoM dynamics and the implemented methodology, it was not possible to find its regional variability modes. Hence, a thorough description of southern GoM variability throughout the water column has yet to be accomplished.

This work aims to study the extent and characteristics of southern GoM variability throughout the water column, considering the separated variability of a surface and a deep layer and their corresponding coupled variability. Specifically, the following subjects are investigated:

1. The coupling timescales between surface and deep variability.
2. The spatial structure of surface, deep, and coupled variability.
3. The dominant timescales and predictability of surface, deep, and coupled variability.
4. The stochastic origin of southern GoM variability.

In order to achieve these goals, outputs from a 21-year free-running simulation (a simulation without ocean data assimilation) of the GoM hydrodynamics were used. The variability modes were estimated from the layer-thickness field of a surface and a deep isopycnic layer, considering separated and coupled layers analyses. The resulting modes' spatial structure, dominant timescales, predictability, and stochastic origin were examined.

## 2 Methods

### 2.1 Estimation of the variability modes

Oceanic general circulation models are robust and reliable tools for studying the circulation and dynamics of the oceans (Grötzner et al., 1999; Zavala-Hidalgo et al., 2003; Meza-Padilla et al., 2019;

Morey et al., 2020; Olvera-Prado et al., 2023). Oceanic general circulation models are robust and reliable tools for studying the circulation and dynamics of the oceans. The characteristics of the numerical models allow for obtaining data continuously. Depending on the physics the models can resolve and the available computing resources to execute them, it is possible to obtain long-term data (several decades) with higher spatial and temporal resolutions than those typical in observations. Specifically, free-running simulations provide a physically consistent description of ocean dynamics that satisfies the primitive equations, allowing a better understanding of ocean dynamics (Morey et al., 2020). This work used the outputs of a 21-year free-running simulation of the GoM hydrodynamics performed with the HYbrid Coordinate Ocean Model (HYCOM), whose characteristics can be reviewed in Olvera-Prado et al. (2023). The simulation covers the period 1992–2012; the horizontal domain covers the region  $[98^{\circ}\text{W}, 77^{\circ}\text{W}] \times [18^{\circ}\text{N}, 32^{\circ}\text{N}]$ , with a  $1/25^{\circ}$  of horizontal resolution and 27 hybrid vertical layers. The validation of such numerical simulation showed that the simulated GoM hydrodynamics and hydrography are consistent with those obtained using ocean altimetry and *in-situ* observations (Olvera-Prado et al., 2023).

The most important variability modes were estimated from daily isopycnic layer-thickness anomalies of a surface and a deep layer *via* the Empirical Orthogonal Functions (EOFs) (Storch and Zwiers, 1999). The surface layer comprises the layers with density values from 17.25 to 26.52, ranging from 0–250 m approximately; the deep layer comprises the isopycnal 27.74 and ranges from 1000–1800 m approximately. The isopycnic layers' selection is based on the representation of the deep GoM basins as a two-layer system described by Hamilton et al. (2018), in which the  $6^{\circ}\text{C}$  isotherm divides the upper (0– $\sim 1000$  m) and lower (below  $\sim 1000$ – $1200$  m) layers. In this work, the combined thickness of the surface and deep layers does not cover the total depth of the ocean, so they are not in physical contact; the reason for doing this was to prevent the surface and deep layer fluctuations from mirroring each other, allowing exploring their vertical connection. In addition, the thickness choice of the surface and deep layers made it possible to capture the most energetic component of the variability in each layer, accentuate thickness fluctuations, and reduce the ocean bottom effects on the deep fluctuations.

The variability analysis focuses on the mesoscale, i.e., ocean signals with space scales of 50–500 km and timescales of 10–100 days (CTOH, 2013). Thus, the data were filtered to enhance the mesoscale signal using a low-pass Lanczos filter considering different cutoff periods and a two-dimensional convolution filter considering different space windows. The following study cases were analyzed:

- Case 1: 30-day time filtering and 23 km space filtering.
- Case 2: 30-day time filtering and 69 km space filtering.
- Case 3: 30-day time filtering and 87 km space filtering.
- Case 4: 90-day time filtering and 23 km space filtering.
- Case 5: 90-day time filtering and 69 km space filtering.



However, only the results for Case 2 are shown since it is the most representative of the mesoscale. The trend and annual cycle were removed from the time series of layer-thickness at each grid point, and the correlation matrix was constructed for the surface and deep layers separately. The correlation matrix is the covariance matrix of the standardized anomalies of the data (Wilks, 2019). The variability analyses intend to identify the intercorrelation between the thickness anomalies in the same layer and between the surface and deep layers (characterized by the correlation matrix); they do not intend to identify the strongest variations of thickness anomalies (characterized by the covariance matrix). The following analyses were performed:

1. Separated analysis. It considered an EOF analysis for each layer separately. This work referred to the resulting variability as “separated variability”.
2. Coupled analysis. It considered an EOF analysis for the surface and deep layers data concatenated into a single matrix. This work referred to the resulting variability as “coupled variability”.

In the separated and coupled EOF analyses, the corresponding vector time series  $\vec{X}(\vec{x}, t)$  can be expanded in terms of its spatial patterns,  $\vec{e}^k(\vec{x})$ , and their time-varying coefficients,  $\alpha_k(t)$ , also called the principal components (PCs),

$$\vec{X}(\vec{x}, t) = \sum_k \alpha_k(t) \vec{e}^k(\vec{x}), \quad (1)$$

where  $\vec{x}$  denotes the spatial coordinates,  $t$  denotes time, and  $k$  runs over the dimension of  $\vec{X}(\vec{x}, t)$ . Since  $\vec{e}^k$  is orthogonal to each other, the regions well explained by each spatial pattern are different. A common approach to identify the regions well explained by a particular set of EOFs  $\{\vec{e}^m\}$  is to compute its proportion of explained variance (PEV),

$$\text{PEV}(\vec{x}) = 1 - \frac{\text{var}(\vec{X} - \sum_m \alpha_m \vec{e}^m)}{\text{var}(\vec{X})}, \quad (2)$$

where  $\text{var}$  denotes variance. Similar to  $\vec{e}^k$ , PEV can also be displayed as a map. Since the PEV represents the proportion of the total variance of the data explained by a particular set of EOFs, the spatial patterns are significant only in the regions with large PEV; these regions are statistically meaningful and were used to describe the spatial variability of the southern GoM. Generally, the regions with large EOF amplitude coincide with those with large PEV.

## 2.2 Predictability timescale

The predictability timescales of southern GoM variability were estimated by analyzing the characteristic properties of the PCs of each EOF analysis using time series analysis techniques (Storch and Zwiers, 1999; Box et al., 2015; Brooks, 2019). It was supposed that the predictability skill of southern GoM variability depends on the persistence of the PCs. The PCs can be grouped into processes with

long or short memory depending on the persistence of their current values. In long-memory processes, the current value tends to persist during long periods, resulting in processes with long-term persistence; in short-memory processes, the values persist during shorter periods (Storch and Zwiers, 1999; Brooks, 2019). Thus, the skillfulness of the persistence forecasts is greater for long-memory processes than for short-memory processes and is highly determined by their corresponding auto-correlation functions (Storch and Zwiers, 1999).

The predictability timescale for each mode of southern GoM variability was estimated using a measure of the decorrelation time  $\tau$  of the corresponding PC for each EOF analysis,

$$\tau = 1 + 2 \sum_{k=1}^{\infty} \rho^2(k), \quad (3)$$

where  $\rho(k)$  is the auto-correlation function of the corresponding PC at discrete lag  $k$ . This work supposes that autoregressive processes of order  $p$ , or AR( $p$ ) processes, can describe the PCs. AR( $p$ ) processes are an important class of time series models (Brooks, 2019), widely used in climate research because they represent discretized versions of ordinary differential equations (Storch and Zwiers, 1999) and because they are helpful in modeling and predicting a variable of interest using only its own and past values, without the necessity of specifying a theoretical model of its behavior (Brooks, 2019). With this approach, an AR( $p$ ) process was fitted to each PC following Box et al. (2015), the theoretical auto-correlation functions of the fitted AR processes were obtained by solving the Yule-Walker equations following Storch and Zwiers (1999), and their predictability timescales were estimated using Equation (3).

Trenberth (1985) proposed the decorrelation time given by Equation (3) as an indicator of the persistence timescale of the corresponding time series and its associated processes. DelSole (2001) showed that Equation (3) arises naturally in statistical sampling theory and provides an accurate predictability estimate for oscillatory auto-correlation functions. Buckley et al. (2019) used this definition of the decorrelation time to estimate the predictability timescales for sea surface temperature and upper-ocean heat content in the North Atlantic. Because  $\tau$  is based solely on the local auto-correlation function, it can be interpreted as a lower bound on the predictability timescale since skillful predictions, at least as long as  $\tau$ , can be made using linear regression, where the inclusion of additional predictors can extend the predictability timescale (Buckley et al., 2019).

## 2.3 Stochastic origin of variability

The stochastic origin of variability is based on the stochastic null hypothesis of climate variability proposed by Hasselmann (1976), which says that the long-term (or low-frequency) variability of a system can be understood as the integrated response of it driven by high-frequency fluctuations. The stochastic climate model of Hasselmann can be derived via a statistical dynamical model in terms of a fast (e.g., atmosphere) and a slow (e.g., ocean) component of the climate system (Storch and Zwiers, 1999), resulting in that, to first order, the long-term variability can be explained by an AR(1) process.

The AR(1) process is commonly taken as the null hypothesis to explain long-term variability (Grötzner et al., 1999; Storch and Zwiers, 1999; Dommenget and Latif, 2002). Several hypothesis tests have been developed to investigate the adequacy of this null hypothesis in describing long-term variability. The following two hypothesis tests were used to investigate the stochastic origin of southern GoM variability, considering the PCs of each EOF analysis (subsection 3.4). This work fitted an AR(1) process to each PC following Box et al. (2015). The fitted AR(1) process represents the null AR(1) process, and its spectrum represents the corresponding null AR(1) spectrum, that is, the reference spectrum against which the PC spectrum was compared and used to perform the hypothesis tests.

- Wilks (2019) describes a hypothesis test whose null hypothesis states that the arising of the process of interest from a given null process cannot be rejected at a specified level if its largest spectral coefficient does not rise above the corresponding rejection limit curve of the null spectrum. This work examined the statistical significance of the largest spectral peak in the sample spectrum of each PC considering rejection limits at the 0.01 level in each null AR(1) spectrum.
- Dommenget and Latif (2002) developed a statistical test to test if the power spectral density (PSD) increase of a process of interest is consistent with a fitted AR process. It assumes that the sample spectral coefficients of the process of interest are random fluctuations around the spectral coefficients of the null spectrum based on a test quantity  $T$  defined as

$$T = \frac{1}{\ln(\sigma_{spec})} \sqrt{\sum_{i=2}^N \frac{[\log(s_i) - \log(t_i)]^2}{N-1}}, \quad (4)$$

- where  $s_i$  are the spectral coefficients of a PC,  $t_i$  are the spectral coefficients of the corresponding null AR(1) spectrum,  $N$  is the number of spectral coefficients, and  $\sigma_{spec}$  is the standard deviation of  $s_i$ . The confidence levels relative to the statistical distribution of the test quantity are derived using Monte Carlo statistics; in this work, such levels were derived from 100000 realizations of null AR(1) processes. The hypothesis test was implemented to the sample spectra of each PC up to the frequency of 12 cpy (30 days) to avoid possible discrepancies by the application of the low-pass Lanczos filter to the PC series.

### 3 Results

#### 3.1 Surface-deep coupling timescales of southern GoM variability

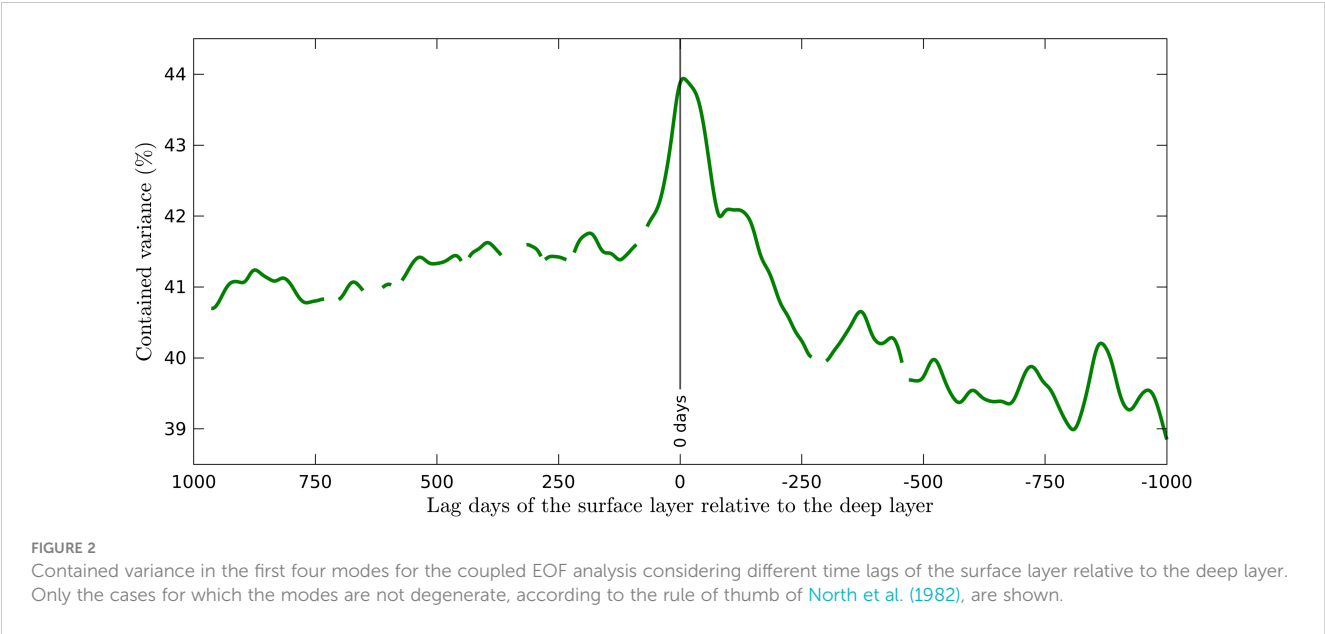
This subsection analyzes the correlation between the variability of the surface and deep layers for different time lags between them.

The objective is to investigate the timescales in which surface and deep variability are strongly connected, for which a coupled EOF analysis was performed considering lags from 1000 to −1000 days of the surface layer relative to the deep layer. For example, a lag of 250 days means that the surface layer is shifted forward in time 250 days relative to the deep layer. For the lags of ±1000 days, the resulting time series corresponds to a reduction of 13% in the total length of the analyzed data.

Figure 2 shows the contained variance in the first four modes considering different time lags of the surface layer relative to the deep layer (the results are very similar for the other study cases mentioned in subsection 2.1); the figure only shows the results when the set of modes is not degenerate according to the rule of thumb of North et al. (1982). The contained variance is taken as a measure of the coupling's strength between surface and deep variability for a given lag: a high variance corresponds to strong coupling, whereas a small variance corresponds to weak coupling. The percentage of the total variance contained in the first four modes varies little (from 39–44%) for lags from 1000 to −1000 days of the surface layer relative to the deep layer; the southern GoM variability is very complex, resulting in a non-evident coupling between its surface and deep variability. The most intense coupling for a particular state of surface variability at a given time is found with the concurrent and quasi-concurrent states of deep variability. The coupling between surface variability and deep variability is slightly higher for previous states of deep variability than for subsequent states of it, which could suggest that deep variability precedes surface variability and that the deep layer is more likely to influence the subsequent evolution of the surface layer than the other way around. Nonetheless, since the suggested direction of information transmission between the layers was obtained through purely statistical analysis, additional specific analyses are required to establish causality relationships between the deep and surface layers.

In order to perform an analysis of coupled variability in the southern GoM resulting in coupled modes with the highest possible contained variance, a coupled EOF analysis with a zero-day lag between the surface and deep layers was considered. Given the chosen zero-day lag, the coupled analysis describes concurrent spatial variability between the surface and deep layers; it identifies surface and deep regions spatially connected and the characteristics of that connection.

The distribution of contained variance in each mode for the separated and coupled EOF analyses (Table 1) indicates that southern GoM variability is a complex process. The total variance is distributed in many modes, and no single mode contains a considerable portion of it. For the separated analyses, the first mode contains a quarter of the total variance; the contained variance in the first mode is slightly smaller for the coupled analysis. The decrease in contained variance for the higher-order modes is smaller for the surface layer, then for the deep layer, and ultimately for the coupled layers; such behavior can be transferred to the ability to define the corresponding variability. Because the contained variance in the first four modes is significant for the separated and coupled EOF analyses, it is assumed that these modes describe the predominant southern GoM variability well and that the study of it can be adequately addressed via EOFs decomposition.



3.2 Spatial patterns of southern GoM variability

What characteristics would the spatial patterns obtained from the isopycnic layer-thickness field have? In the surface layer, the isopycnic layer-thickness contours are a good proxy of circulation since they closely follow the flow streamlines; thus, the EOFs reflect where the main circulation variability occurs. In the deep layer, the isopycnic layer-thickness contours are not a good circulation proxy (Cushman-Roisin et al., 1990; Olvera-Prado et al., 2023). Nonetheless, since the isopycnic layer-thickness structure throughout the water column responds to pressure gradients, layer-thickness variability (and thus the associated EOFs) is expected to reflect regions with high circulation variability in each layer. Moreover, due to the weak deep GoM stratification, a bathymetry-influenced deep variability, strongly governed by the conservation of potential vorticity, is also expected. Accordingly, a description of surface and deep circulation variability of the southern GoM is first presented (Figure 3) and then referred to when describing the EOFs (Figure 4).

Figure 3 shows a monthly climatology of vertically averaged currents in a surface layer (0-250 m) and a deep layer (1000-1500 m) for the 21 years of simulation. The brown lines in the deep layer

maps represent planetary potential vorticity ( $f/H$ ) contours, where  $f$  is the local Coriolis parameter, and  $H$  is the bottom depth. In the surface layer, the currents' speed is approximately three times greater than in the deep layer, with significant changes in the circulation patterns throughout the year, in contrast to the more persistent deep circulation. The changes in surface circulation patterns (panels of the first column in Figure 3) can be described as follows:

1. In the region north of 20.5°N and west of 93.5°W, an intense and well-defined anticyclonic circulation occurs during winter and summer. During fall, the circulation in the region (95.0°W, 93.5°W) × (20.5°N, 23.0°N) is cyclonic, with a weak intensity in its interior and southern branch. During spring, the region (95.0°W, 93.5°W) × (20.5°N, 23.0°N) is occupied by a dipole, with a cyclone and an anticyclone oriented from north to south; the circulation is weak in the interior and the eastern branch of the dipole.
2. The circulation in the region east of 93.5°W and north of 22.0°N is intense and northeasterly during winter and summer, weak and anticyclonic during fall, and intense and easterly during spring. The circulation changes in the

TABLE 1 Distribution of contained variance in the first four modes for the separated and coupled EOF analyses.

Mode	Surface layer	Deep layer	Coupled layers
1	24	26	19
2	16	12	10
3	12	8	8
4	10	6	7
Total	62	52	44

The values are given in percentage.

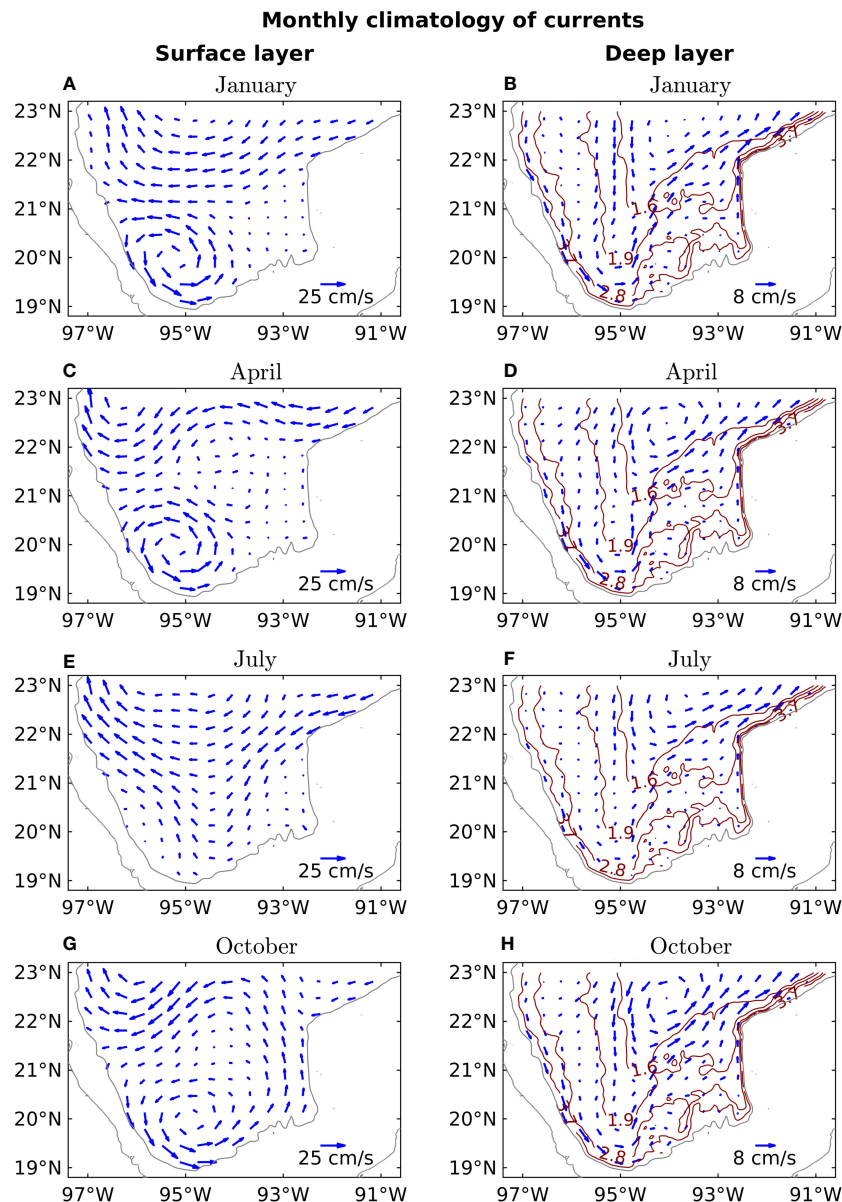


**FIGURE 3**  
Monthly climatology of vertically averaged currents in the southern Gulf of Mexico in a surface layer (0–250 m) and a deep layer (1000–1500 m) derived from the HYCOM simulation. The brown lines in the deep layer maps represent the planetary potential vorticity contours in  $(\text{s}\cdot\text{m})^{-1}$ .

northern region are probably associated with the arrival or generation of cyclonic and anticyclonic mesoscale features (Zavala-Sansón et al., 2017; Guerrero et al., 2020).

3. The circulation in the region  $(93.5^{\circ}\text{W}, 92.5^{\circ}\text{W}) \times (20.0^{\circ}\text{N}, 22.0^{\circ}\text{N})$  is feeble and northerly during most of the year, but during fall, it is intense and southerly.
4. To the southeast of the basin, west of  $94.0^{\circ}\text{W}$  and south of  $21.0^{\circ}\text{N}$ , there is a cyclonic circulation, the Campeche Gyre (Vázquez de la Cerda et al., 2005; Pérez-Brunius et al., 2013; Zavala-Sansón, 2019). During winter and spring, the Gyre is intense and located to the northwest; it weakens until its dissipation in summer; in fall, the Gyre re-forms in a southeast location.

The circulation patterns in the deep layer (panels of the second column in Figure 3) have small variations throughout the year, reaching their minimum intensity during summer. The circulation is aligned with the planetary potential vorticity contours with a cyclonic rotation sense: west of  $95.0^{\circ}\text{W}$ , the currents go from north to south, and east of  $95.0^{\circ}\text{W}$ , the currents go from south to north. The circulation in the southeast region, where the bathymetry is abrupt, is weak, with few changes throughout the year. The changes in deep circulation patterns can be described as follows:

1. In the region north of  $21.0^{\circ}\text{N}$  and east of  $95.0^{\circ}\text{W}$ , roughly limited by the  $1.6 (\text{s}\cdot\text{m})^{-1}$  planetary potential vorticity contour, there is an intense and well-defined cyclonic



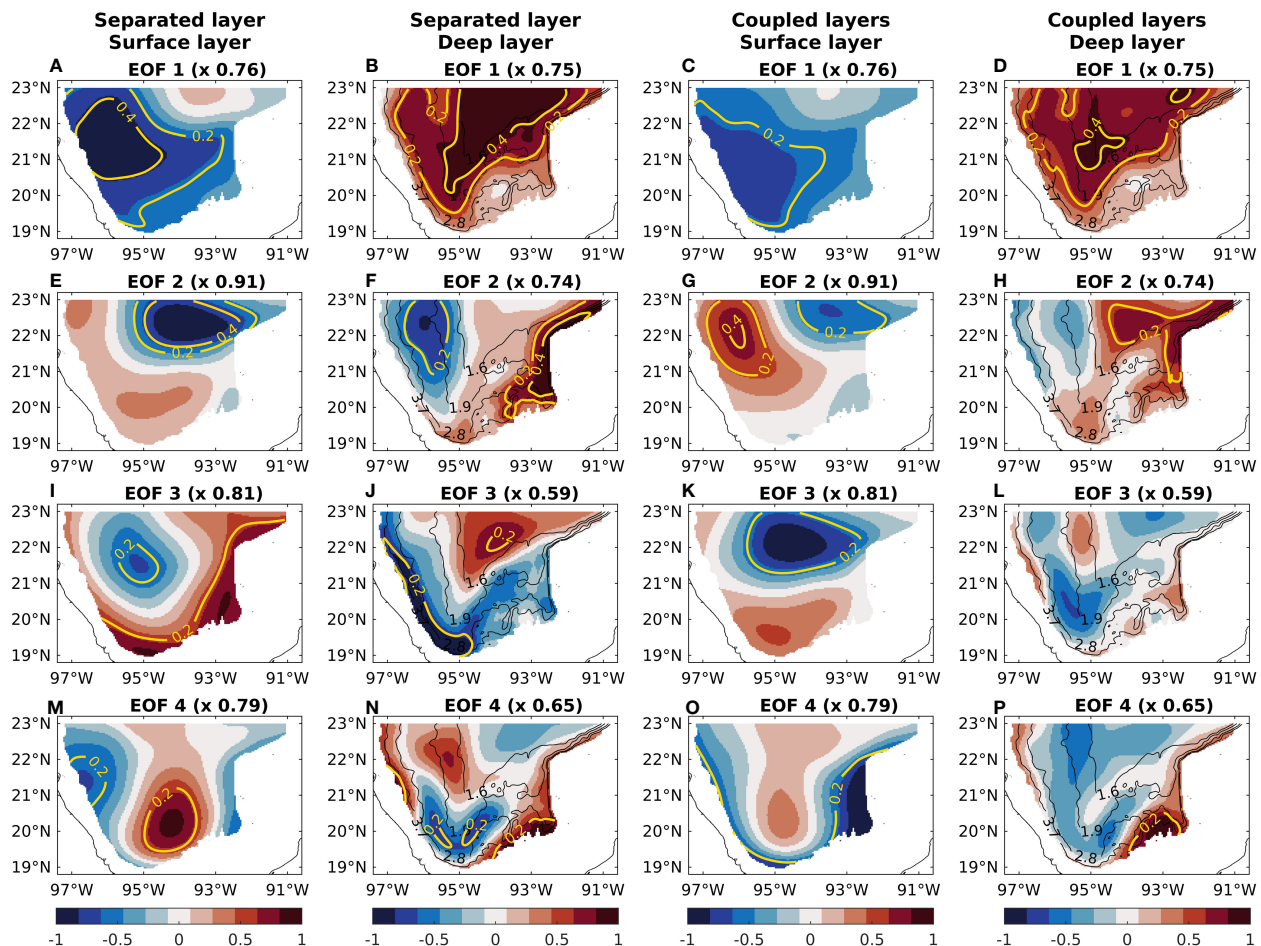


FIGURE 4

First four EOFs of the surface and deep layers for the separated and coupled EOF analyses. The EOF amplitude is shown in color scale, and yellow contours represent the proportion of explained variance of each EOF. The black lines in the deep layer maps represent the planetary potential vorticity contours in  $(\text{s}\cdot\text{m})^{-1}$ .

circulation throughout the year. This circulation is shifted to the south during spring and fall, whereas it is shifted to the northeast during winter and summer.

2. In the region between  $(96.5^{\circ}\text{W}, 95.0^{\circ}\text{W})$  and north of  $20.0^{\circ}\text{N}$ , there is a year-round northerly circulation, with a weak western branch and an intense eastern branch. The western branch circulation strengthens during spring and weakens during winter, summer, and fall; the eastern branch strengthens during winter and fall and weakens during spring and summer.
3. The circulation intensity in the eastern boundary north of  $20.0^{\circ}\text{N}$  and the western boundary varies throughout the year. It strengthens during winter and fall and weakens during spring and summer.
4. The intensity of the cyclonic circulation along  $19.5^{\circ}\text{N}$  and between  $(95.5^{\circ}\text{W}, 94.5^{\circ}\text{W})$  remains intense most of the year except during summer.

Figure 4 shows the first four EOFs of the surface and deep layers for the separated and coupled EOF analyses. The EOF amplitude is

shown in color scale, and yellow contours represent the PEV of each EOF. Due to the thickness data processing (subsection 2.1), the EOFs are assumed to represent the mesoscale variability in each layer adequately.

First, the separated variability modes are described (panels of the first and second columns in Figure 4). The first four EOFs in both layers are well-defined and recognizable, and together they occupy the entire basin. As expected, the EOFs identify regions with high circulation variability in both layers (Figure 3); they rank variability modes based on their contained variance but are not expected to identify individual dynamical modes (Storch and Zwiers, 1999; Monahan et al., 2009). In the deep layer, the bathymetry influences the variability; layer-thickness variations align with the planetary potential vorticity contours and intensify along bottom slopes. The spatial variability modes are described below:

1. The principal variability in the surface layer (Figure 4A), mainly located in the northwest, is associated with variations in the anticyclonic circulation north of  $20.5^{\circ}\text{N}$  and west of  $94.5^{\circ}\text{W}$  (panels of the first column in Figure 3).

The principal variability in the deep layer (Figure 4B), covering a wide area north of 20.0°N, is associated with latitudinal shifts of the long-scale cyclonic circulation in that region (panels of the second column in Figure 3).

2. The spatial pattern of the second mode in the surface layer (Figure 4E) shows high variability in the region east of 95.0°W and north of 21.5°N, associated with changes in the intensity and direction of the circulation in the northern region (panels of the first column in Figure 3). The spatial pattern in the deep layer (Figure 4F) shows high variability along 96.0°W and north of 21°N and along the eastern basin boundary, mainly associated with variations in the circulation intensity in those regions (panels of the second column in Figure 3).
3. The third mode in the surface layer (Figure 4I) reflects variability along the eastern and southern boundaries, which is associated with changes in the intensity and direction of the circulation in that region (panels of the first column in Figure 3). In the deep layer (Figure 4J), the variability is located along the western boundary, which is associated with variations in circulation intensity in that region; and in a spot centered at (94.0°W, 22.0°N), associated with latitudinal shifts of the cyclonic circulation in that region (panels of the second column in Figure 3).
4. The spatial pattern of the fourth mode (Figure 4M) shows high surface variability in a spot centered at (94.0°W, 20.0°N), which is associated with changes in the intensity and direction of the circulation in that region (panels of the first column in Figure 3). The deep variability (Figure 4N) is represented by a lobe form centered at (95.0°W, 19.5°N), which is associated with intensity variations of the cyclonic circulation in that region (panels of the second column in Figure 3).

The spatial patterns of coupled variability (panels of the third and fourth columns in Figure 4) differ from those of separated variability (panels of the first and second columns in Figure 4), which could indicate a significant connection between the surface and deep layers. By comparing the spatial structure and time evolution of coupled and separated variability, it is possible to obtain insights into the dynamics of southern GoM variability throughout the water column. The first four EOFs in the surface layer (panels of the third column in Figure 4) are well-defined, recognizable, and significant (they have spatial regions with appreciable PEV). However, only the first two modes in the deep layer (panels of the fourth column in Figure 4) are significant; the third and fourth modes lack spatial regions with appreciable PEV, indicating that higher-order surface variability has no connection with deep variability. Results also show no vertical correspondence between surface and deep layer-thickness variations; the fluctuations of deep isopycnals do not mirror those of surface isopycnals. The spatial variability modes are described below:

1. The principal coupled variability in the surface layer (Figure 4C), described by a confined southwestern region

where the Campeche Gyre occurs, is associated with the strengthening and dissipation of the Campeche Gyre and with its latitudinal and longitudinal shifts (panels of the first column in Figure 3). In the deep layer (Figure 4D), the variability is mainly described by a small region centered at (95.0°W, 21.5°N), associated with the southernmost intrusion of the cyclonic circulation in that region; and by a wide region north of 20.0°N, associated with long-scale variations of the cyclonic circulation in the region east of 95.0°W and north of 20.0°N (panels of the second column in Figure 3). The deep pattern is very similar to that of the first mode of the separated deep layer.

2. The spatial pattern of the second mode in the surface layer (Figure 4G), described by a zonal dipole north of 21.0°N, is associated with variations in the circulation in the northern region (panels of the first column in Figure 3). In the deep layer (Figure 4H), the spatial pattern shows high variability in the northeast, which is associated with variations in the circulation intensity along the eastern boundary and with latitudinal shifts of the cyclonic circulation east of 95.0°W and north of 21.0°N (panels of the second column in Figure 3).
3. The third coupled mode in the surface layer (Figure 4K) is very similar to the second separated mode in the surface layer (Figure 4E). The fourth coupled mode in the surface layer (Figure 4O) shows high variability in the southeastern region, associated with variations in the circulation intensity in that region. These surface modes have no associated deep modes (Figures 4L, P) since these are not recognizable due to their marginal PEV.

### 3.3 Predictability of southern GoM variability and associations between separated and coupled variability

The predictability timescales of southern GoM variability were estimated by considering the decorrelation time (subsection 3.2) of each PC for the separated and coupled EOF analyses. The fitting of an AR model to each PC resulted in an AR(5) for each. Figure 5 shows the predictability timescales for the first four variability modes of the surface, deep, and coupled layers; the predictability timescales of the PCs are representative of the characteristic timescales of the corresponding spatial variability. The shortest predictability timescales are for the surface layer, with values from 1.4 to 10.6 months, which reminds the dominant timescales of mesoscale variability in the southern GoM (Vázquez de la Cerda et al., 2005; Pérez-Brunius et al., 2013; Zavala-Sansón et al., 2017). The deep layer has the longest predictability timescales, with almost three times the scales of the surface layer, from 3.0 to 30.5 months. Deep variability is more persistent and changes in longer timescales than surface variability, in agreement with the temporal change of surface and deep currents (monthly climatology of currents shown in Figure 3).

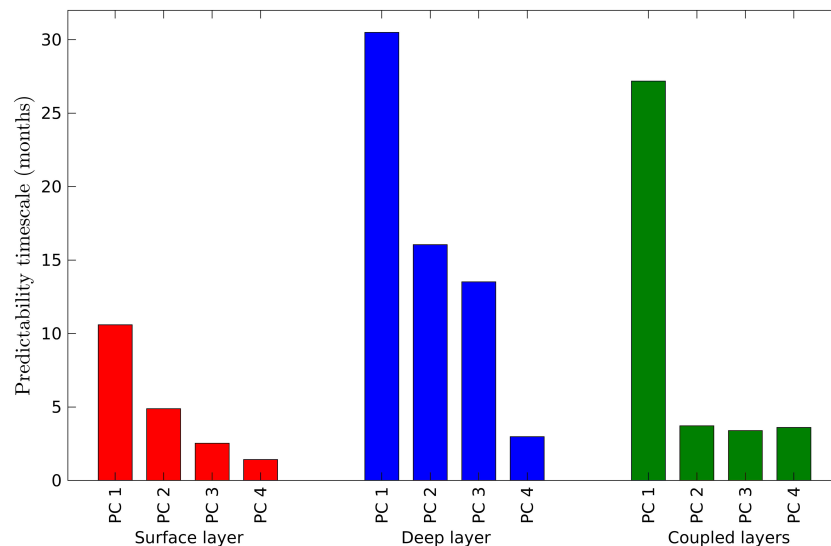


FIGURE 5

Predictability timescales of the first four principal components (PCs) for the surface, deep, and coupled layers.

The predictability timescales of the coupled layers depend on the coupling's strength of the surface and deep layers. The predictability timescales for the coupled layers lie between those for the surface and deep layers but closer to those of the deep layer, with values from 3.4 to 27.2 months (Figure 5). Such behavior indicates that the memory of the coupled system resides in the deep layer but only for the first variability mode. By coupling a system composed of a fast (the surface ocean layer in this study) and a slow (the deep ocean layer in this study) component, the predictability of the fast component can be extended by coupling it with the slow component (Hasselmann, 1976; Grötzner et al., 1999; Dommenges and Latif, 2002). Nevertheless, the intensity of the coupled system's high-frequency internal noise could weaken the coupling's strength and drastically reduce its predictability timescale. The predictability timescales for the coupled system have the following behavior (Figure 5):

- First mode. The long predictability timescale for this mode suggests an intense surface-deep coupling, in which both layers evolve conjointly with a predictability timescale of 27.2 months. The predictability timescale in the surface layer was substantially extended by a factor of 2.6 compared with that of the separated surface layer, resulting in a very similar timescale to that of the separated deep layer. The predictability timescale in the deep layer is very similar to that of the separated deep layer (30.5 months).
- Higher-order modes. The surface-deep coupling is not strong enough to extend the predictability timescales in the surface layer with respect to those obtained in the separated analysis. Such weak surface-deep coupling resulted in predictability timescales in the deep layer similar to those of the separated surface layer.

The previous analysis indicated a connection between the surface and deep layers in the southern GoM, in which the

coupled variability (variability throughout the water column) is more similar to the deep variability, at least for the principal variability mode. In order to explore further the connection of coupled variability with surface and deep variability, the similarity between each coupled PC and each surface and deep PC was examined considering two standard similarity measures, the root mean square similarity and Pearson's correlation, where 1 indicates the maximum similarity (Cassisi et al., 2012). Figure 6 shows the similarity analysis, which helps reveal the coupling's strength between coupled and separated variability. The first three coupled PCs have a clear and dominant association with a separated PC. The coupled PC 1 is mainly associated with the deep PC 1. The coupled PC 2 is highly associated with the deep PC 2. The coupled PC 3 is mainly associated with the surface PC 2; from the previous analysis of spatial variability, it is an expected result since the third coupled mode in the surface layer (Figure 4K) is practically the same as the second separated mode in the surface layer (Figure 4E).

The connection between coupled and separated variability is also appreciable in the time domain. Figure 7 shows the time series of the first three PCs of coupled layers with their corresponding associated PCs of separated layers. Their temporal nature is described below.

- The PCs for the first variability mode of the coupled and deep layers (Figure 7A) are very similar, as are their corresponding spatial patterns (Figures 4D, B). The PCs evolve in long timescales, with negative or positive values maintained for extended periods, although their wiggles do not always coincide; they are very time persistent and have the longest predictability timescale among all the variability modes (Figure 5).
- The PC for the second coupled variability mode evolves with more accentuated short-term variations and has a high similitude with the deep PC 2 (Figure 7B). Such short-term

variations in both PCs resulted in a low time persistence and short predictability timescales (Figure 5) of their associated spatial patterns (Figures 4F, G, H).

- The PC for the third coupled mode is practically the same as for the second surface mode (Figure 7C); their corresponding spatial patterns (Figures 4K, E) are also practically the same. Due to the evolution with high-frequency variations of these modes, their time persistence is low, and their predictability timescales are short (Figure 5).

There is a similarity between the variability modes obtained in the coupled and separated layers analyses. Nevertheless, some coupled modes differ from all those obtained in the separated layers analyses, suggesting that these result from the surface-deep coupling. Examples of this coupling are the spatial pattern of the first mode in the surface layer (Figure 4C) and the patterns of the second mode in both layers (Figures 4G, H).

### 3.4 Stochastic origin of southern GoM variability

As a preamble to analyze the stochastic origin of southern GoM variability, the distinctive timescales of surface, deep, and coupled variability of the southern GoM were revisited using the spectra of their PCs (Figure 8). Figure 8 shows the sample spectra (cyan lines) and multitaper spectra (blue lines) of the first four PCs for the separated and coupled EOF analyses, with their corresponding null AR(1) spectra (solid red lines) and rejection limits at the 0.01 level

(dashed red lines). The multitaper method consistently estimates a process's true PSD by averaging a set of modified periodograms obtained using several tapers as windowing functions, reducing spectral leakage (Thomson, 1982). In terms of the PSD of a process, the longer the memory of the process, the higher its values for frequencies approaching zero. The principal variability mode for the separated and coupled layers (Figures 8A–C) varies over long timescales. The PSD of the PC increases with decreasing frequency (a typical red noise process), leading to the associated spatial patterns (Figures 4A–D) being long-term persistent. The long-term persistence of the principal mode is stronger in the deep layer (Figure 8B) than in the surface layer (Figure 8A), showing the well-known fact that the deep layer evolves in longer timescales than the surface layer. The PSD increase of the principal mode of the coupled layers (Figure 8C) is very similar to that of the deep layer (Figure 8B), indicating that the timescales of coupled variability are similar to those of deep variability.

In agreement with the predictability timescales analysis (Figure 5), the higher-order variability is not long-term persistent; the PSD of the associated PCs does not consistently increase with decreasing frequency (Figures 8D–L). In the surface layer (Figures 8D, G, J), a significant portion of the PSD is concentrated in the three-month to one-year period band, with a small decrease for periods longer than one year. The PSD increase in the deep layer (Figures 8E, H, K) has a small bump in the one-month to three-month period band and a pronounced decrease for periods longer than one year. For the coupled layers (Figures 8F, I, L), a large portion of the PSD is concentrated in the three-month to

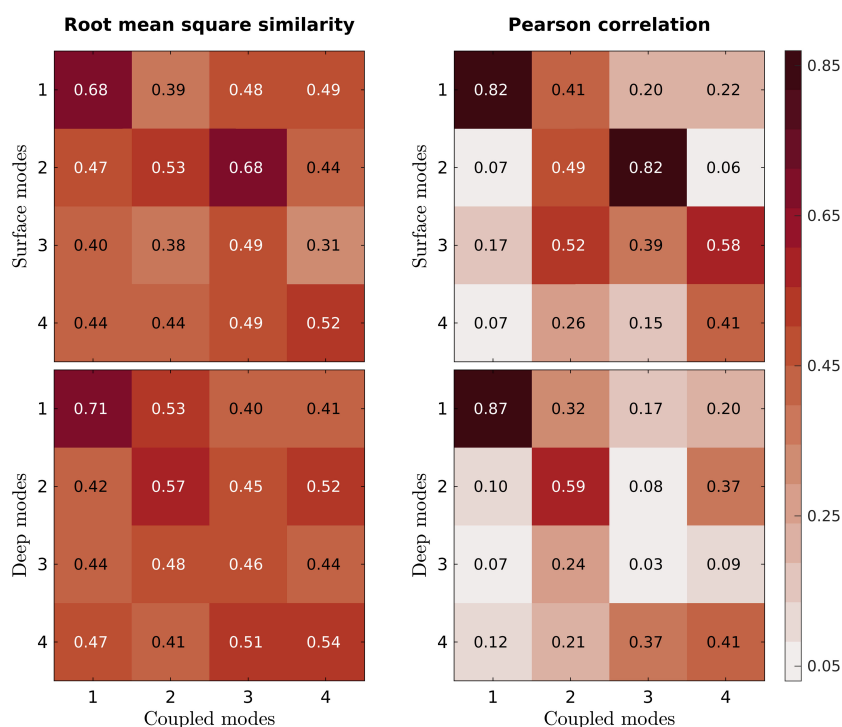


FIGURE 6

Similarity measures for each combination of principal components (PCs) considering the separated and coupled EOF analyses of southern GoM variability. For Pearson's correlation, its absolute value is shown.



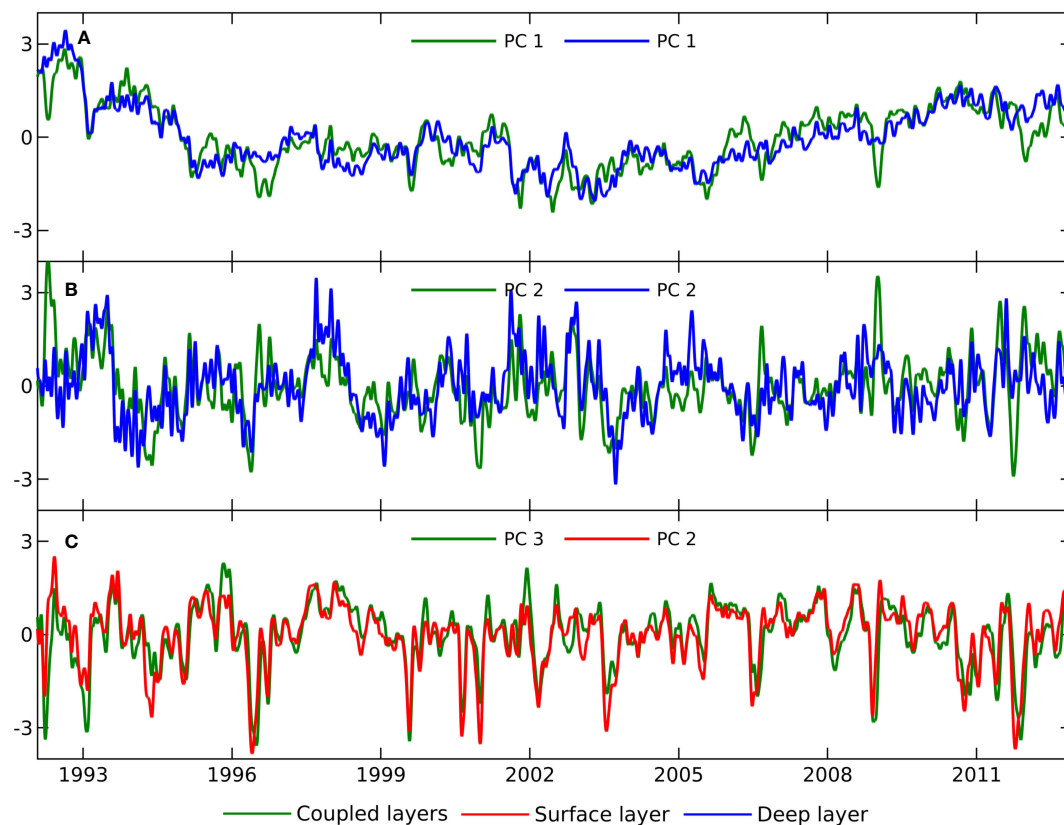


FIGURE 7

Time series of the first three principal components (PCs) of coupled layers with their corresponding associated PCs of separated layers. (A) Coupled PC 1 and deep PC 1. (B) Coupled PC 2 and deep PC 2. (C) Coupled PC 3 and surface PC 2.

one-year period band, with a small decrease for periods longer than one year. In summary, higher-order coupled modes vary on similar timescales to higher-order surface modes but without an associated correspondence between the modes of the same order.

When considering coupled variability of the southern GoM, there is a separation between its principal and higher-order modes (Figures 2 and 4–8). Its principal variability (timescales and long-term persistence) is mainly associated with its deep dynamics; the deep layer strongly determines the principal variability throughout the water column. Its higher-order variability has surface and deep dynamics characteristics, with no clear association with one of them.

Now it is the turn to explore the stochastic origin of the long-term variability of the southern GoM, considering the two hypothesis tests described in subsection 2.3. First, the analysis was performed considering the hypothesis test described by Wilks (2019). For this, the spectra of the PCs and the spectra of the AR(1) models fitted to each of them (the null AR(1) spectra of the PCs) shown in Figure 8 were used. All the PC spectra do not rise above their AR(1) rejection limits at frequencies lower than 0.5 cpy (periods longer than two years), but they do rise above them at frequencies higher than 0.5 cpy (periods shorter than two years). Thus, the simplest stochastic model adequately describes only the long-term variability of the surface, deep, and coupled layers in the southern GoM. The high thermal inertia of the isopycnal layers acts as a memory, integrating short-

term random variations and carrying energy to the long term in the manner described by Hasselmann (1976), producing a reddened spectrum consistent with an AR(1) process at frequencies lower than 0.5 cpy. On the other hand, the PC spectra deviate from their corresponding null AR(1) spectra at frequencies higher than 0.5 cpy. Southern GoM variability in timescales from some weeks to a couple of years is strongly affected by the episodic occurrence of different mesoscale circulation processes (Vázquez de la Cerda et al., 2005; Pérez-Brunius et al., 2013; Zavala-Sansón et al., 2017; Guerrero et al., 2020), which could explain the PC spectra deviations described above.

The results of the hypothesis test proposed by Dommenget and Latif (2002) are shown in Table 2, considering null AR(1) and AR(2) spectra and a rejection limit at the 0.05 level. The PSD increase of each first PC is consistent with an AR(1) process, indicating that their source of long-term variability can be associated only with short-term random variations. The principal variability mode of the surface, deep, and coupled layers agrees with the stochastic null hypothesis of Hasselmann (1976); they can be described using a linear dynamics approach in terms of a fast and a slow component, with the involved dynamical processes grouped in one of those components (Storch and Zwiers, 1999). The random origin of the principal variability of the southern GoM does not mean that it is not predictable at all; only a completely random process such as AR(0) is not predictable at all. The performed fitting

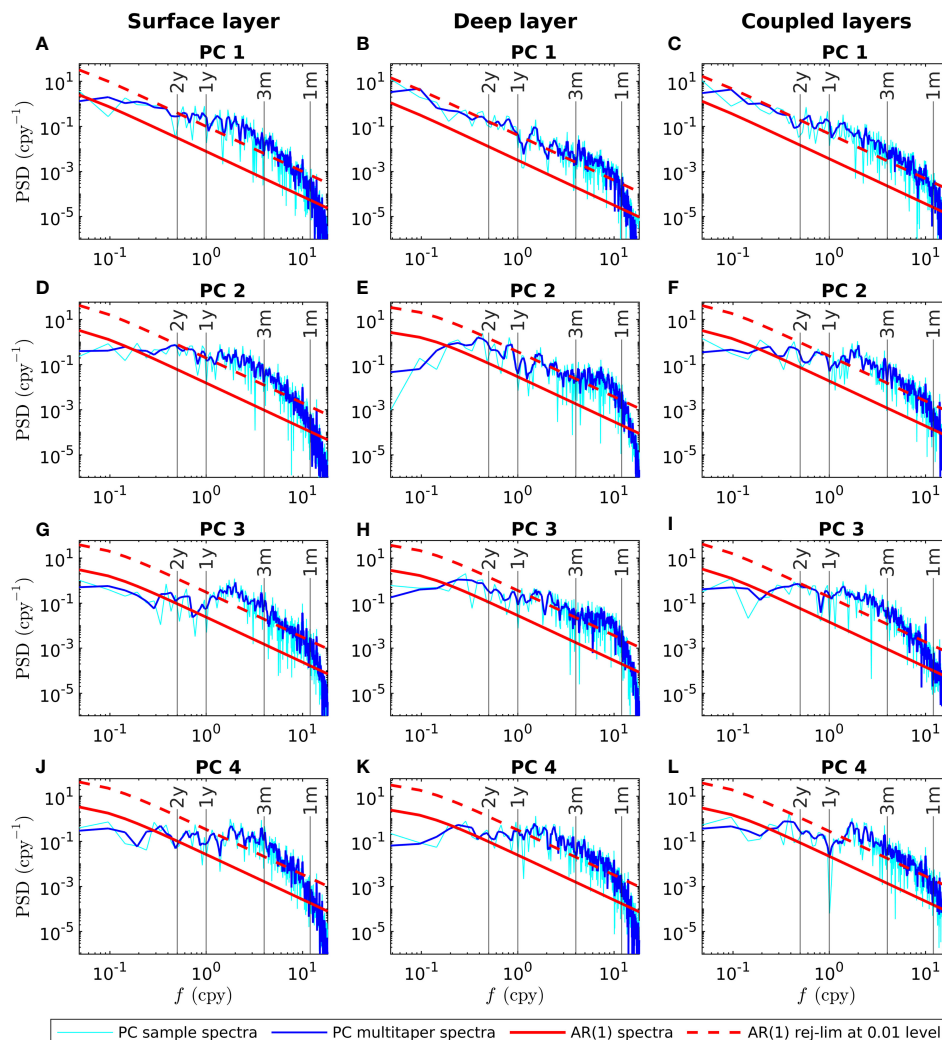


FIGURE 8

Sample spectra (cyan lines) and multitaper spectra (blue lines) of the first four principal components (PCs) for the separated and coupled EOF analyses. The spectra of the AR (1) models fitted to each PC (the null AR(1) spectra) are plotted using solid red lines, with their corresponding rejection limits at the 0.01 level plotted using dashed red lines. PSD stands for power spectral density.

of higher-order AR models to the PCs to estimate their predictability timescales (Figure 5) does not invalidate the results concerning the stochastic origin of southern GoM variability, as these methodologies have different objectives. A precise fitting of an AR model to a time series attempts to describe most of its wiggles, but this does not necessarily correspond to improving the description of its dynamics.

The higher-order variability modes are not consistent with AR(1) processes (Table 2). These modes contain a more complex variability structure than the dominant ones, linear dynamics cannot explain them, and higher-order AR processes are needed to describe them. The different sources of southern GoM variability can be involved in such behavior, like surface-layer processes (e.g., atmosphere-ocean fluxes, advection and circulation of adjacent regions, and entrainment of sub-layers), a range of circulation features with a strong interaction between them (Zavala-Sansón et al., 2017; Guerrero et al., 2020), and topographic effects ruling to a certain extent the circulation throughout the water column (Pérez-

Brunius et al., 2013; Zavala-Sansón, 2019). However, the higher-order variability can be adequately described using AR(2) processes, indicating that their dynamics is somewhat more complex than a linear one.

## 4 Discussion

This study explored different characteristics of southern GoM variability, providing realistic, robust, physically consistent, and statistically significant results. The choice of data and its processing were necessary to address the objectives posed for this work. Implementing climatological open boundary conditions (flow at the open boundaries without interannual variability) in the numerical simulation (Olvera-Prado et al., 2023) did not affect the reproducibility of southern GoM variability since it is mainly determined by wind stress (Gutiérrez de Velasco and Winant, 1996; DiMarco et al., 2005; Vázquez de la Cerda et al., 2005), eddy-driven

TABLE 2 Hypothesis test results for the stochastic origin of southern GoM variability, considering the first four principal components (PCs) for the separated and coupled EOF analyses.

Layers	PC	H <sub>0</sub> : Stochastic origin of variability described by an AR(1) process	H <sub>0</sub> : Stochastic origin of variability described by an AR(2) process
Surface layer	1	Failure to reject H <sub>0</sub>	Failure to reject H <sub>0</sub>
	2	Rejection of H <sub>0</sub>	Failure to reject H <sub>0</sub>
	3	Rejection of H <sub>0</sub>	Failure to reject H <sub>0</sub>
	4	Rejection of H <sub>0</sub>	Rejection of H <sub>0</sub>
Deep layer	1	Failure to reject H <sub>0</sub>	Failure to reject H <sub>0</sub>
	2	Rejection of H <sub>0</sub>	Failure to reject H <sub>0</sub>
	3	Rejection of H <sub>0</sub>	Failure to reject H <sub>0</sub>
	4	Rejection of H <sub>0</sub>	Rejection of H <sub>0</sub>
Coupled surface-deep layers	1	Failure to reject H <sub>0</sub>	Failure to reject H <sub>0</sub>
	2	Rejection of H <sub>0</sub>	Failure to reject H <sub>0</sub>
	3	Rejection of H <sub>0</sub>	Failure to reject H <sub>0</sub>
	4	Rejection of H <sub>0</sub>	Failure to reject H <sub>0</sub>

H<sub>0</sub> represents the null hypothesis that was tested.

vorticity fluxes (Vidal et al., 1992; Ohlmann et al., 2001; Meza-Padilla et al., 2019), and the bathymetry of the region (Pérez-Brunius et al., 2013; Zavala-Sansón, 2019). These processes were adequately implemented and represented in the numerical simulation (Olvera-Prado et al., 2023). This work did not address the variability occurring on the basin boundaries and that with spatial and temporal scales smaller than mesoscale, such as that associated with barotropic waves (Abolfazli et al., 2020; Gómez-Valdivia and Parés-Sierra, 2020).

This work used the EOFs technique to describe the mesoscale variability throughout the water column in the southern GoM by identifying its most important surface, deep, and coupled modes. Although the EOFs are not expected to identify individual dynamical modes (Storch and Zwiers, 1999; Monahan et al., 2009), they helped suggest a dynamical connection between surface and deep variability, including the timescales in which they are strongly connected. The findings of this work complement those of Pérez-Brunius et al. (2013), Hamilton et al. (2016), Hamilton et al. (2018), and Pérez-Brunius et al. (2018).

The coupling between surface and deep variability depends on the relative evolution of the deep layer with respect to the surface layer: it is maximal for the concurrent and quasi-concurrent states of deep variability, quasi-constant for previous states, and decreasing for subsequent states. The results suggest that deep dynamics is likely to influence the subsequent evolution of surface dynamics but do not demonstrate a causality relationship between them. A separation between the principal and higher-order coupled variability was found: the timescales and long-term persistence are mainly associated with deep dynamics for the principal variability, whereas higher-order variability has no clear association with surface or deep dynamics. The connection between the surface and deep layers is more complex than considering that due to the

geographical isolation of the deep GoM from adjacent seas, the deep layer will evolve according to the surface layer's behavior (Welsh and Inoue, 2000). The energy driving the deep circulation and dynamics comes from the surface layer; however, deep layer dynamics and the bathymetric configuration influence the dynamics and circulation throughout the water column in the southern GoM (Pérez-Brunius et al., 2013; Zavala-Sansón, 2019).

No vertical spatial correspondence between the surface and deep layers was found; the fluctuations of deep isopycnals do not mirror those of surface isopycnals. These results indicate that the circulation and dynamics throughout the water column in the southern GoM are more complex than those resulting from considering it as a two-layer system (Hamilton et al., 2018), in which, given the weak deep stratification, it is expected that the fluctuations of deep isopycnals mirror those of surface isopycnals. Thus, theoretical and simplified studies of the southern GoM using a two-layer system (e.g., Moreles et al., 2021) could be limited in adequately representing its variability and circulation patterns throughout the entire water column, being more appropriate to consider a more complex layer regime.

The principal coupled mode in the surface layer is described by a confined region in the southwest where the Campeche Gyre occurs. In the coupled EOF analysis of this work, that region was the only one statistically meaningful according to the PEV values; in the EOF analysis of Vázquez de la Cerda et al. (2005) using sea surface height anomalies, more statistically meaningful regions were obtained. This surface variability pattern is connected with deep variability in the center and a wide region in the north in the deep layer. These patterns only resulted in the coupled analysis using the data correlation matrix. Thus, they resulted from the intercorrelation between the surface and deep layers and are relevant to the dominant dynamics throughout the water column

in the southern GoM. The finding of these patterns seems remarkable due to their very persistent nature (predictability timescale of 27.2 months) and possible connection with the Campeche Gyre dynamics (subsection 3.2). The influence of bathymetric characteristics (topographic control) on the development and evolution of the Campeche Gyre described by Pérez-Brunius et al. (2013) and Zavala-Sansón (2019) could be associated with the causal role of deep dynamics on surface dynamics suggested in this work. However, further research is needed to elucidate this relationship.

This work adds to those of Kolodziejczyk et al. (2011), Pérez-Brunius et al. (2013), and Pérez-Brunius et al. (2018) by providing the predictability timescales of the most important modes of southern GoM variability in terms of their decorrelation times. Using the decorrelation time to measure predictability produces well and robust results compared with other techniques, as Buckley et al. (2019) showed, and provides a proper interpretation of the persistence of a process (Trenberth, 1985; Storch and Zwiers, 1999). An application of the stochastic climate model of Hasselmann (1976) to the southern GoM was implemented. By coupling the surface ocean layer (the fast component of the system with a short memory) with a deep ocean layer (the slow component of the system with a long memory), the predictability timescale of the principal surface variability mode was extended to a much longer scale than that obtained by considering the layer separately, similar to what is done in coupled ocean-atmosphere studies (Grötzner et al., 1999; Dommenges and Latif, 2002; Moreles and Martínez-López, 2016). The predictability timescale of the principal variability mode in the surface layer was extended by a factor of 2.6, from 10.6 to 27.2 months, highlighting the persistent nature of this coupled pattern.

Strong evidence was provided for the stochastic origin of the dominant southern GoM variability throughout the water column. Despite the great variety of dynamical processes involved in southern GoM dynamics, its dominant variability can be described using linear dynamics in terms of the simplest AR process. The description of the higher-order variability in terms of the simplest AR process was prevented by different processes, among which the following are suggested: strong mesoscale dynamics, high-intensity variations of the fast component, short memory of the slow component, and weak surface-deep coupling. The nature of such processes could lead the long-term variability of a system to deviate from the stochastic null hypothesis of Hasselmann (1976), as found by Grötzner et al. (1999), Dommenges and Latif (2002), Moreles and Martínez-López (2016), and Buckley et al. (2019). The separation of the dynamics of the variability modes in a fast and a slow component implies that statistical models can be constructed to analyze their potential predictability (Storch and Zwiers, 1999); however, such construction is proposed for future research.

Applying EOF analysis in a coupled manner, as was done in this work, may help represent unknown deep variability in terms of

known surface variability and eventually complement the development of ocean data assimilation systems throughout the water column by projecting surface information to deep layers in a statistically consistent manner (Chapman and Charantonis, 2017; Manucharyan et al., 2021; Sonnewald et al., 2021).

## 5 Conclusions

This work studied two major aspects of southern GoM dynamics: variability and predictability. It described the surface, deep, and coupled surface-deep variability of the southern GoM, its predictability timescales, and its stochastic origin. Relevant characteristics of the surface-deep coupling and dynamics of the southern GoM were provided. A strong connection was found between surface and deep variability, with particular and varied temporal and spatial characteristics related to the dominant circulation. The deep ocean's role in generating long-term variability and its influence on the surface ocean's behavior was described. This work adds support to the simplest stochastic model as a promising paradigm to approach variability and predictability in the climate system, emphasizing the utility of long-term free-running simulations and multivariate statistical analyses to address the variability and predictability of the climate system. Finally, it provides strong evidence for the stochastic origin of southern GoM variability, which has important implications for its description. We hope the methodology developed in this study can be improved and applied to other ocean basins.

This work provides further insights into the southern GoM dynamics and is complementary to others focusing on GoM dynamics; it also outlines some general implications for modeling, forecasting, and assimilation systems of the southern GoM. However, many questions remain to be answered, and further research using alternative and specific methodologies needs to be conducted to fully discern the GoM dynamics throughout the water column. An in-depth analysis of the dynamical connection throughout the water column in the southern GoM, specifically regarding the Campeche Gyre dynamics, is proposed for future research.

## Data availability statement

Publicly available datasets were analyzed in this study. This data can be found here: The Zenodo repository [<https://doi.org/10.5281/zenodo.5605092>].

## Author contributions

EM conceived and designed the study, acquired funding, analyzed and interpreted the data, created the figures, wrote and revised the manuscript, and approved the submitted version.



## Funding

This work was supported by UNAM-PAPIIT IA104320 and by the Instituto de Ciencias del Mar y Limnología of the Universidad Nacional Autónoma de México (grant 626).

## Acknowledgments

The author acknowledges Aurea De Jesús for her helpful discussions and valuable comments. Juan Nieblas-Piquero computed the monthly climatology of vertically averaged currents in the southern Gulf of Mexico, represented in Figure 3; Susana Higuera-Parra created Figure 1. The HYCOM simulation and its validation used in this study are a contribution of the Gulf of Mexico Research Consortium (CIGoM). The author thanks the reviewers for their valuable comments, which significantly improved this work.

## References

- Abolfazli, E., Liang, J.-H., Fan, Y., Chen, Q. J., Walker, N. D., and Liu, J. (2020). Surface gravity waves and their role in ocean-atmosphere coupling in the Gulf of Mexico. *J. Geophys. Res.: Oceans* 125, e2018JC014820. doi: 10.1029/2018JC014820
- Adams, C. M., Hernández, E., and Cato, J. C. (2004). The economic significance of the Gulf of Mexico related to population, income, employment, minerals, fisheries and shipping. *Ocean Coast. Manage.* 47, 565–580. doi: 10.1016/j.ocecoaman.2004.12.002
- Box, G., Jenkins, G., Reinsel, G., and Ljung, G. (2015). *Time Series Analysis: Forecasting and Control*. 5 edn (San Francisco: Wiley).
- Brooks, C. (2019). *Introductory Econometrics for Finance*. 4 edn (Cambridge: Cambridge University Press). doi: 10.1017/9781108524872
- Buckley, M. W., DelSole, T., Lozier, M. S., and Li, L. (2019). Predictability of north Atlantic Sea surface temperature and upper-ocean heat content. *J. Climate* 32, 3005–3023. doi: 10.1175/JCLI-D-18-0509.1
- Cassisi, C., Montalto, P., Aliotti, M., Cannata, A., and Pulvirenti, A. (2012). “Similarity measures and dimensionality reduction techniques for time series data mining,” in *Advances in Data Mining Knowledge Discovery and Applications*. Ed. A. Karahoca (Rijeka: IntechOpen). doi: 10.5772/49941
- Chapman, C., and Charantonis, A. A. (2017). Reconstruction of subsurface velocities from satellite observations using iterative self-organizing maps. *IEEE Geosci. Remote Sens. Lett.* 14, 617–620. doi: 10.1109/LGRS.2017.2665603
- Cooley, S., Schoeman, D., Bopp, L., Boyd, P., Donner, S., Ghebrehewet, D., et al. (2022). “Oceans and coastal ecosystems and their services,” in *Climate Change 2022: Impacts, Adaptation and Vulnerability. Contribution of Working Group II to the Sixth Assessment Report of the Intergovernmental Panel on Climate Change*. Eds. H.-O. Pörtner, D. C. Roberts, M. Tignor, E. S. Poloczanska, K. Mintenbeck, A. Alegria, et al. (Cambridge, UK and New York, NY, USA: Cambridge University Press), 379–550. doi: 10.1017/9781009325844.005
- CTOH (2013) *Center for Topographic studies of the Ocean and Hydrosphere. What are Mesoscale Processes?* Available at: <http://ctoh.legos.obs-mip.fr/applications/mesoscale/what-are-mesoscale-processes> (Accessed 2023-05-05).
- Cushman-Roisin, B., Tang, B., and Chassignet, E. P. (1990). Westward Motion of mesoscale eddies. *J. Phys. Oceanogr.* 20, 758–768. doi: 10.1175/1520-0485(1990)020<0758:WMOME>2.0.CO;2
- DelSole, T. (2001). Optimally persistent patterns in time-varying fields. *J. Atmospheric Sci.* 58, 1341–1356. doi: 10.1175/1520-0469(2001)058<1341:OPPTV>2.0.CO;2
- DiMarco, S. F., Nowlin, W. D. Jr., and Reid, R. O. (2005). “A statistical description of the velocity fields from upper ocean drifters in the Gulf of Mexico,” in *Circulation in the Gulf of Mexico: Observations and Models*. Eds. W. Sturges and A. Lugo-Fernandez (American Geophysical Union), 101–110. doi: 10.1029/161GM08
- Dommenget, D., and Latif, M. (2002). Analysis of observed and simulated SST spectra in the midlatitudes. *Climate Dynamics* 19, 277–288. doi: 10.1007/s00382-002-0229-9
- Dubrunna, J., Pérez-Brunius, P., López, M., and Candela, J. (2011). Circulation over the continental shelf of the western and southwestern Gulf of Mexico. *J. Geophys. Res.: Oceans* 116, C08009. doi: 10.1029/2011JC007007
- Gil-Agudelo, D. L., Cintra-Buenrostro, C. E., Brenner, J., González-Díaz, P., Kiene, W., Lusic, C., et al. (2020). Coral reefs in the Gulf of Mexico large marine ecosystem: Conservation status, challenges, and opportunities. *Front. Mar. Sci.* 6. doi: 10.3389/fmars.2019.00807
- Gómez-Valdivia, F., and Parés-Sierra, A. (2020). Seasonal upper shelf circulation along the central Western Gulf of Mexico: A preferential upcoast flow reinforced by the recurrent arrival of Loop Current eddies. *J. Geophys. Res.: Oceans* 125, e2019JC015596. doi: 10.1029/2019JC015596
- Grötzner, A., Latif, M., Timmermann, A., and Voss, R. (1999). Interannual to decadal predictability in a coupled ocean-atmosphere general circulation model. *J. Climate* 12, 2607–2624. doi: 10.1175/1520-0442(1999)012<2607:ITDPIA>2.0.CO;2
- Guerrero, L., Sheinbaum, J., Mariño-Tapia, I., González-Rejón, J. J., and Pérez-Brunius, P. (2020). Influence of mesoscale eddies on cross-shelf exchange in the western Gulf of Mexico. *Continental Shelf Res.* 209, 104243. doi: 10.1016/j.csr.2020.104243
- Gutiérrez de Velasco, G., and Winant, C. D. (1996). Seasonal patterns of wind stress and wind stress curl over the Gulf of Mexico. *J. Geophys. Res.: Oceans* 101, 18127–18140. doi: 10.1029/96JC01442
- Hamilton, P., Bower, A., Furey, H., Leben, R. R., and Pérez-Brunius, P. (2016). *Deep Circulation in the Gulf of Mexico: A Lagrangian Study*. (New Orleans, Louisiana Hamilton2016: U.S. Dept. of the Interior Bureau of Ocean Energy Management, Gulf of Mexico OCS Region), 289.
- Hamilton, P., Leben, R., Bower, A., Furey, H., and Pérez-Brunius, P. (2018). Hydrography of the Gulf of Mexico using autonomous floats. *J. Phys. Oceanogr.* 48, 773–794. doi: 10.1175/JPO-D-17-0205.1
- Hasselmann, K. (1976). Stochastic climate models part i. theory. *Tellus* 28, 473–485. doi: 10.1111/j.2153-3490.1976.tb00696.x
- Judt, F., Chen, S. S., and Curcic, M. (2016). Atmospheric forcing of the upper ocean transport in the Gulf of Mexico: From seasonal to diurnal scales. *J. Geophys. Res.: Oceans* 121, 4416–4433. doi: 10.1002/2015JC011555
- Kolodziejczyk, N., Ochoa, J., Candela, J., and Sheinbaum, J. (2011). *Deep currents in the Bay of Campeche*. *J. Phys. Oceanogr.* 41, 1902–1920. doi: 10.1175/2011JPO4526.1
- Manucharyan, G. E., Siegelman, L., and Klein, P. (2021). A deep learning approach to spatiotemporal Sea surface height interpolation and estimation of deep currents in geostrophic ocean turbulence. *J. Adv. Modeling Earth Syst.* 13, e2019MS001965. doi: 10.1029/2019MS001965
- Martínez-López, B., and Zavala-Hidalgo, J. (2009). Seasonal and interannual variability of cross-shelf transports of chlorophyll in the Gulf of Mexico. *J. Mar. Syst.* 77, 1–20. doi: 10.1016/j.jmarsys.2008.10.002
- Meza-Padilla, R., Enriquez, C., Liu, Y., and Appendini, C. M. (2019). Ocean circulation in the Western Gulf of Mexico using self-organizing maps. *J. Geophys. Res.: Oceans* 124, 4152–4167. doi: 10.1029/2018JC014377
- Monahan, A. H., Fyfe, J. C., Ambaum, M. H. P., Stephenson, D. B., and North, G. R. (2009). Empirical orthogonal functions: The medium is the message. *J. Climate* 22, 6501–6514. doi: 10.1175/2009JCLI3062.1
- Monreal-Gómez, M., and Salas-de León, D. (1997). “Circulación y estructura termohalina del Golfo de México,” in *Contribuciones a la Oceanografía Física en México, Monografía*, vol. 3. Ed. M. Lavin-Peregrina (Unión Geofísica Mexicana), 183–199.
- Moreles, E., and Martínez-López, B. (2016). Analysis of the simulated global temperature using a simple energy balance stochastic model. *Atmósfera* 29, 279–297. doi: 10.20937/ATM.2016.29.04.01

## Conflict of interest

The author declares that the research was conducted in the absence of any commercial or financial relationships that could be construed as a potential conflict of interest.

## Publisher's note

All claims expressed in this article are solely those of the authors and do not necessarily represent those of their affiliated organizations, or those of the publisher, the editors and the reviewers. Any product that may be evaluated in this article, or claim that may be made by its manufacturer, is not guaranteed or endorsed by the publisher.

- Moreles, E., Zavala-Hidalgo, J., Martínez-López, B., and Ruiz-Angulo, A. (2021). Influence of Stratification and Yucatan Current Transport on the Loop Current Eddy Shedding Process. *J. Geophys. Res.: Oceans* 126, e2020JC016315. doi: 10.1029/2020JC016315
- Morey, S. L., Gopalakrishnan, G., Sanz, E. P., Souza, J. M. A. C. D., Donohue, K., Pérez-Brunius, P., et al. (2020). Assessment of numerical simulations of deep circulation and variability in the Gulf of Mexico using recent observations. *J. Phys. Oceanogr.* 50, 1045–1064. doi: 10.1175/JPO-D-19-0137.1
- Morey, S. L., Zavala-Hidalgo, J., and O'Brien, J. J. (2005). "The seasonal variability of continental shelf circulation in the northern and Western Gulf of Mexico from a high-resolution numerical model," in *Circulation in the Gulf of Mexico: Observations and Models*. Eds. W. Sturges and A. Lugo-Fernandez (American Geophysical Union), 203–218. doi: 10.1029/161GM16
- Muller-Karger, F. E., Smith, J. P., Werner, S., Chen, R., Roffer, M., Liu, Y., et al. (2015). Natural variability of surface oceanographic conditions in the offshore Gulf of Mexico. *Prog. Oceanogr.* 134, 54–76. doi: 10.1016/j.pocean.2014.12.007
- NASEM (2018). *National Academies of Sciences, Engineering, and Medicine*. (Washington, DC: The National Academies Press). doi: 10.17226/24823
- NOAA (2008). National ocean service. *Gulf of Mexico at a Glance* (Washington, D.C., U.S. Department of Commerce, National Oceanic and Atmospheric Administration), 30.
- North, G. R., Bell, T. L., Cahalan, R. F., and Moeng, F. J. (1982). Sampling errors in the estimation of empirical orthogonal functions. *Monthly Weather Rev.* 110, 699–706. doi: 10.1175/1520-0493(1982)110<0699:SEITEO>2.0.CO;2
- Ohlmann, J. C., Niiler, P. P., Fox, C. A., and Leben, R. R. (2001). Eddy energy and shelf interactions in the Gulf of Mexico. *J. Geophys. Res.: Oceans* 106, 2605–2620. doi: 10.1029/1999JC000162
- Olvera-Prado, E. R., Moreles, E., Zavala-Hidalgo, J., and Romero-Centeno, R. (2023). Upper–lower layer coupling of recurrent circulation patterns in the Gulf of Mexico. *J. Phys. Oceanogr.* 53, 533–550. doi: 10.1175/JPO-D-21-0281.1
- Pérez-Brunius, P., Furey, H., Bower, A., Hamilton, P., Candela, J., García-Carrillo, P., et al. (2018). Dominant circulation patterns of the deep Gulf of Mexico. *J. Phys. Oceanogr.* 48, 511–529. doi: 10.1175/JPO-D-17-0140.1
- Pérez-Brunius, P., García-Carrillo, P., Dubranna, J., Sheinbaum, J., and Candela, J. (2013). Direct observations of the upper layer circulation in the southern Gulf of Mexico. *Deep Sea Res. Part II: Topical Stud. Oceanogr.* 85, 182–194. doi: 10.1016/j.dsr2.2012.07.020
- Portela, E., Tenreiro, M., Pallas-Sanz, E., Meunier, T., Ruiz-Angulo, A., Sosa-Gutiérrez, R., et al. (2018). Hydrography of the central and Western Gulf of Mexico. *J. Geophys. Res.: Oceans* 123, 5134–5149. doi: 10.1029/2018JC013813
- Schmitt, R. W. (2018). The ocean's role in climate. *Oceanography* 31, 32–40. doi: 10.5670/oceanog.2018.225
- Sonnwald, M., Lguensat, R., Jones, D. C., Dueben, P. D., Brajard, J., and Balaji, V. (2021). Bridging observations, theory and numerical simulation of the ocean using machine learning. *Environ. Res. Lett.* 16, 073008. doi: 10.1088/1748-9326/ac0eb0
- Storch, H. V., and Zwiers, F. W. (1999). *Statistical Analysis in Climate Research* (Cambridge: Cambridge University Press). doi: 10.1017/CBO9780511612336
- Thomson, D. (1982). Spectrum estimation and harmonic analysis. *Proc. IEEE* 70, 1055–1096. doi: 10.1109/PROC.1982.12433
- Trenberth, K. E. (1985). Persistence of daily geopotential heights over the southern hemisphere. *Monthly Weather Rev.* 113, 38–53. doi: 10.1175/1520-0493(1985)113<0038:PODGHO>2.0.CO;2
- Vázquez de la Cerdá, A. M., Reid, R. O., DiMarco, S. F., and Jochens, A. E. (2005). "Bay of Campeche circulation: An update," in *Circulation in the Gulf of Mexico: Observations and models*. Eds. W. Sturges and A. Lugo-Fernandez (American Geophysical Union), 279–293. doi: 10.1029/161GM20
- Vidal, V. M. V., Vidal, F. V., and Pérez-Molero, J. M. (1992). Collision of a Loop Current anticyclonic ring against the continental shelf slope of the western Gulf of Mexico. *J. Geophys. Res.: Oceans* 97, 2155–2172. doi: 10.1029/91JC00486
- Vukovich, F. M. (2007). Climatology of ocean features in the Gulf of Mexico using satellite remote sensing data. *J. Phys. Oceanogr.* 37, 689–707. doi: 10.1175/JPO2989.1
- Welsh, S. E., and Inoue, M. (2000). Loop Current rings and the deep circulation in the Gulf of Mexico. *J. Geophys. Res.: Oceans* 105, 16951–16959. doi: 10.1029/2000JC900054
- Wilks, D. (2019). *Statistical Methods in the Atmospheric Sciences. 4 edn* (Elsevier Science).
- Yoskowitz, D., Leon, C., Gibeau, J., Lupher, B., Lopez, M., Santos, C., et al. (2013). *Gulf 360: State of the Gulf of Mexico* (Texas: Harte Research Institute for Gulf of Mexico Studies, Texas A&M University-Corpus Christi), 52.
- Zavala-Hidalgo, J., Morey, S. L., and O'Brien, J. J. (2003). Seasonal circulation on the western shelf of the Gulf of Mexico using a high-resolution numerical model. *J. Geophys. Res.: Oceans* 108, 3389. doi: 10.1029/2003JC001879
- Zavala-Sansón, L. (2019). Nonlinear and time-dependent equivalent-barotropic flows. *J. Fluid Mechanics* 871, 925–951. doi: 10.1017/jfm.2019.354
- Zavala-Sansón, L., Pérez-Brunius, P., and Sheinbaum, J. (2017). Point source dispersion of surface drifters in the southern Gulf of Mexico. *Environ. Res. Lett.* 12, 024006. doi: 10.1088/1748-9326/aa537c



## OPEN ACCESS

## EDITED BY

Julio Sheinbaum,  
Centro de Investigación Científica y de  
Educación Superior de Ensenada (CICESE),  
Mexico

## REVIEWED BY

Wei Huang,  
Oak Ridge National Laboratory (DOE),  
United States  
Jorge Zavala-Hidalgo,  
Universidad Nacional Autónoma de  
México, Mexico  
Efrain Moreles,  
National Autonomous University of Mexico,  
Mexico

## \*CORRESPONDENCE

Xingchen Yang  
✉ xxy181@miami.edu

RECEIVED 20 September 2022

ACCEPTED 13 September 2023

PUBLISHED 13 October 2023

## CITATION

Yang X, Le Hénaff M, Mapes B and  
Iskandarani M (2023) Dynamical  
interactions between Loop Current  
and Loop Current Frontal Eddies in a  
HYCOM ensemble of the circulation  
in the Gulf of Mexico.  
*Front. Mar. Sci.* 10:1048780.  
doi: 10.3389/fmars.2023.1048780

## COPYRIGHT

© 2023 Yang, Le Hénaff, Mapes and  
Iskandarani. This is an open-access article  
distributed under the terms of the [Creative  
Commons Attribution License \(CC BY\)](#). The  
use, distribution or reproduction in other  
forums is permitted, provided the original  
author(s) and the copyright owner(s) are  
credited and that the original publication in  
this journal is cited, in accordance with  
accepted academic practice. No use,  
distribution or reproduction is permitted  
which does not comply with these terms.

# Dynamical interactions between Loop Current and Loop Current Frontal Eddies in a HYCOM ensemble of the circulation in the Gulf of Mexico

Xingchen Yang<sup>1,2\*</sup>, Matthieu Le Hénaff<sup>3,4</sup>, Brian Mapes<sup>1</sup>  
and Mohamed Iskandarani<sup>1</sup>

<sup>1</sup>Rosenstiel School of Marine, Atmospheric, and Earth Science, University of Miami, Miami, FL, United States,

<sup>2</sup>Research Center for Intelligent Supercomputing, Zhejiang Laboratory, Hangzhou, China,

<sup>3</sup>Cooperative Institute for Marine and Atmospheric Studies, University of Miami, Miami, FL, United States,

<sup>4</sup>Atlantic Oceanographic and Meteorological Laboratory (NOAA), Miami, FL, United States

The dynamics of the Loop Current (LC) system in the Gulf of Mexico (GoM), specifically during the shedding of Eddy Franklin in 2010, is investigated using an ensemble of simulations. The ensemble members differed in their initial conditions of the West Florida Cyclonic Eddy (WFCE), which in turn significantly influences the timing and occurrence of the Loop Current Eddy (LCE) detachment. The results reveal that a stronger and larger WFCE leads to an early LCE detachment, while a weaker and smaller WFCE results in late or even no detachment within the 60-day simulation period. The initial WFCE's size and strength are also found to impact the evolution of Campeche Bank Cyclonic Eddies (CBCE). The intrusion of a large and strong WFCE into the LC leads to a rapid growth of potential vorticity (PV) over the eastern Campeche Bank (CB), associated with the formation of a CBCE. In addition, ensemble members with stronger and larger WFCE generally agree with mooring data regarding the velocity evolution over the eastern CB, as well as the CBCE's northeastward offshore displacement. Our results suggest that the size and strength of the WFCE may serve as predictors of the formation of a CBCE and of an LCE detachment occurrence. This finding has implications for future studies and forecasting methodologies for the GoM circulation.

## KEYWORDS

Loop Current, ensemble simulations, Campeche Bank cyclonic eddy, West Florida cyclonic eddy, potential vorticity, teleconnection

# 1 Introduction

The Loop Current (LC) dominates the oceanic flow in the Gulf of Mexico (GoM) as it is its most energetic feature. The LC enters the Gulf through the Yucatan Channel and exits through the Florida Straits before it becomes the Gulf Stream. The path of the LC is highly variable. It can flow directly from the Yucatan Channel to the Florida Straits, which is usually referred to as the ‘port to port’ state (Schmitz, 2005). The LC can also have an extended state when its northern tip intrudes northward into the eastern GoM basin. The extended state LC sheds an anticyclonic LC eddy (LCE) intermittently at irregular intervals (Schmitz, 2003). The LCEs may re-attach to and detach from the LC several times before the final detachment (Schmitz, 2005). After the final detachment, the LCE propagates westwards, and the LC retreats depending on the size of the detached LCE (Leben, 2005).

Given its dynamic and highly variable nature, understanding the LC system’s dynamics is vital for improving the LC circulation forecasts in the GoM, and thereby providing valuable information for marine operations in the GoM such as: pollutant transport (Walker et al., 2011; Le Hénaff et al., 2012b), hurricane intensification (Bao et al., 2000; Jaimes et al., 2006), and oil platform operations (National Academies of Sciences et al., 2018). The dynamical processes and mechanisms involved in LCE sheddings have been the subject of many observational, theoretical and modeling studies. Modeling studies reveal that both baroclinic and barotropic instabilities play roles in the separation process of LCEs (Hurlburt and Thompson, 1982; Cherubin et al., 2005). Pichevin and Nof (1997) proposed the momentum imbalance paradox for explaining eddy separation. Analysis of the observations from the CANEK program (Candela et al., 2002) revealed that potential vorticity (PV) flux anomaly at the Yucatan Channel may serve as a useful indicator of Loop Current variability, including Loop Current extension, retraction, and eddy shedding (Candela et al., 2003; Oey, 2004). A nearly linear relationship between the Loop Current retreat latitude and the subsequent separation period was found via altimeter-derived LC metrics (Leben, 2005). By analyzing hydrographic data, Sturges and Evans (1983) indicated that the north-south fluctuations in the Loop Current position are correlated with the sea level at the coast and presumably with coastal currents. Deep eddies and deep flows are found to influence the LCE shedding process as well (Oey, 2008; Chang and Oey, 2011). Observational data has also linked LCE detachments to eddies or perturbations coming from the Caribbean Sea (Athié et al., 2012; Androulidakis et al., 2021; Le Hénaff et al., 2023; Ntaganou et al., 2023) and pulses of increased transport through the Florida Straits (Sturges et al., 2010).

Previous studies have revealed the important roles that the Loop Current Frontal Eddies (LCFEs) play in the LC dynamics and its detachment. The observation of these cold, cyclonic eddies along the LC edge was first documented by Cochrane (1972). Vukovich & Maul (1985) found that, on the eastern side of the LC, LCFEs have diameters in the range of 80–120 km and reach at least 1000 m

depth. According to the authors, these eddies can move westward and lead to an LCE detachment or separation. Fratantoni et al. (1998) used Sea Surface Temperature (SST) satellite data to reveal that a cyclonic eddy would stay longer near the Dry Tortugas when an LCE is shed. Zavala-Hidalgo et al. (2003) investigated cyclonic eddies over the northeast Campeche Bank (CB) and documented their formation and life cycle (either their decay or their north/northwest migration). They noted in particular that their formation coincides with LCE detachments. The LCE detachment types were categorized into two general modes by Schmitz (2005). One is primarily due to pinch-off by cyclones on the boundary of the LC, the other when the LC is being pulled apart by the westward propagation of its own tip. The numerical simulations of Androulidakis et al. (2014) confirmed the role of northern LCFE and CB LCFE in necking down the LC during LCE detachment. In addition, the bathymetry of the Mississippi Fan was found to play a role in intensifying LCFEs along the extended LC northern edge (Le Hénaff et al., 2012a). In their analysis of mooring data in both the northeast and southeast GoM, Hamilton et al. (2016) found that the steepening of the LC meanders leads to a pinch-off of LC eddies, and that the deep lower-layer eddies, constrained by the closed topography of the southeastern Gulf, appear to assist in achieving separation. Finally, Sheinbaum et al. (2016), using some of the same mooring observations, found that some LCE detachments are dominated by a cyclone associated with a meander through the southward flowing branch of the LC, e.g., Eddy Ekman and Eddy Franklin in 2010–2011, while during some other events (Eddy Cameron and Eddy Darwin in 2008–2009<sup>1</sup>, the CB cyclone appears to be nearly as strong as the ones coming from the eastern side of the LC.

While previous studies have explored the dynamics of the LC system, including the LCFEs and LCEs, there are still gaps in our understanding of this system. Specifically, in ocean model simulations, the influence of initial condition perturbations, on the subsequent development of LCFEs and the detachment of LCEs remains underexplored. Furthermore, the existence of a teleconnection between distinct LCFEs, that is, a distant interaction between LCFEs that ring the LC system and propagate along its rim, has not been seriously studied, although this possibility was brought up by Schmitz (2005).

This study attempts to fill these gaps by applying targeted ensemble simulations to investigate the dynamics of the LC system during the shedding of Eddy Franklin in 2010 (see Figure 1), with a particular emphasis on the impact of initial condition perturbations on the development of LCFEs and the detachment of LCEs. In addition, the possible teleconnection between distinct LCFEs is statistically investigated. The realism of the model outputs is also evaluated by comparing ensemble simulations with mooring observations. This study is a continuation of the work in Iskandarani et al. (2016) and Wang et al. (2018), aiming to provide deeper insights into the LC system’s

**Abbreviations:** \*Fully documented templates are available in the elsarticle package on CTAN.

<sup>1</sup> For the detailed information of these LCEs, please see the Woods Hole Gulf of Mexico Loop Current Eddies records website: <https://www.horizonmarine.com/loop-current-eddies>.



dynamics and its implications for the GoM circulation forecasts. The analysis herein shows that the initial condition perturbations have a significant impact on the LCE detachment and its timing, and that larger and stronger LCFEs are more likely to be followed by an LCE detachment. Moreover, when a large and strong LCFE intrudes into the LC from the east, a second LCFE on the western side of the LC is prone to form.

The layout of this article is as follows: Section 2 provides background information about the ensemble simulation and a description of the observational data. Section 3 presents the research results, including the impact of initial conditions on the LC system, the teleconnection found between LCFEs and a model-mooring data comparison. Section 4 provides a summary and a discussion.

## 2 Background/model description

### 2.1 HYCOM setup

The ensemble forecast we used was generated using the Hybrid Coordinate Ocean Model (HYCOM) (Bleck, 2002; Chassignet et al., 2003; Halliwell, 2004). The model configuration is described in Iskandarani et al. (2016). HYCOM uses a generalized vertical coordinate system to optimize the distribution of vertical computational layers so that they are isopycnic (sigma) in stratified regions, terrain-following in shallow coastal regions, and isobaric (z-level) in the unstratified mixed layer. The model used here has a horizontal grid resolution of  $1/25^\circ$  and 20 vertical layers<sup>2</sup>. Out of the vertical layers, 5 are purely z-levels at the top, and spread to about 20 m depth in the open ocean, ensuring a good representation of the upper ocean, while the other 15 layers are hybrid (z-levels, sigma or terrain-following depending on the stratification and on the location) to represent the rest of the water column. The computational domain is open along portions of its southern, eastern and northern boundaries, where values are provided by a lower resolution  $1/12^\circ$  North Atlantic HYCOM simulation (Chassignet et al., 2007). The model is forced by the 27km resolution Coupled Ocean Atmosphere Mesoscale Prediction System (COAMPS) atmospheric outputs<sup>3</sup>. The model has the same configuration as the GoM regional expt 20.1 experiment of HYCOM (McDonald, 2006) that was implemented in near realtime by the US Navy Research Laboratory (NRL) at the time of Eddy Franklin, which ensures that it is a robust model with realistic capabilities. In particular, the expt 20.1 experiment was used in several studies of the Deepwater Horizon oil spill (e.g. Mezić et al. (2010); Liu et al. (2011); Valentine et al. (2012); Le Hénaff et al.

(2012b)). The initial conditions for the model, prior to perturbations, are from the same expt 20.1 experiment which assimilates available satellite altimeter observations and *in situ* sea surface temperature (SST) as well as available *in situ* vertical temperature and salinity profiles from XBTs, ARGO floats and moored buoys. After adding perturbations, the model is then integrated forward in time without data assimilation.

### 2.2 The HYCOM Ensemble

Each member (or realization) of the ensemble, which is integrated for 60 days from May 1, 2010 to June 29, 2010, corresponds to a different initial condition in which the size and strength of the West Florida Cyclonic Eddy (WFCE) are modified with respect to the control run, which is the unperturbed simulation. The perturbation strategy is based on the Empirical Orthogonal Function (EOF) decomposition of the temporal evolution of the near-real time, data-assimilative expt20.1 experiment from which the present model configuration is derived. The EOF decomposition was computed over a 14-day period, which is expected to be dominated by changes in the LC and LCFEs (Iskandarani et al., 2016). The multivariate, 3-dimensional EOF decomposition is performed on two variables: the 3-dimensional ocean hydrostatic pressure increment in each model layer, and the sea surface height (SSH). The hydrostatic pressure increment is a good proxy for the ocean vertical structure, in particular the density gradients are associated with geostrophic currents, whereas the SSH incorporates the surface signature of the dynamical features of interest here, i.e. the LC and the associated eddies. The principal components of each mode were used to project the EOF modes to the model prognostic variables, i.e., temperature, salinity, velocities, layer thicknesses (Li et al., 2016). The perturbations consist in the first two leading EOF modes, and the strength of the perturbations to the HYCOM control was modulated by the amplitudes of the EOF modes which were considered uncertain. Iskandarani et al. (2016) shows that the two leading EOF modes mostly perturb the strength of the WFCE. This approach allows us to directly link the output of the simulation to only two uncertain parameters, as done by Iskandarani et al. (2016) and Wang et al. (2018), and provide the opportunity to investigate the relationship between the initial strength and size of the WFCE and the subsequent LC detachment and formation of the Campeche Bank Cyclonic Eddy (CBCE). The first two EOF modes have been found to be sufficient to represent the uncertainty in the Loop Current region from May 1, 2010 to May 30, 2010, when the first detachment of Eddy Franklin occurred (Iskandarani et al., 2016; Wang et al., 2018). Each ensemble member corresponds to a specified setting of the EOF modal amplitudes, referred to here as  $\xi_1$  and  $\xi_2$  (a value of 0 corresponds to not perturbing the control run whereas a value of  $\pm 1$  corresponds to adding and subtracting the EOF mode at full amplitude). Illustrations of the signature of these perturbations can be found in Iskandarani et al. (2016) (their Figures 1, 2 and 4) and Wang et al. (2018) (their Figure 8). The

<sup>2</sup> The details of the model configuration, including advection scheme, mixing, vertical structure, can be found in the HYCOM website: <https://www.hycom.org/data/goml0pt04/expt-20pt1>

<sup>3</sup> To access COAMPS model code and data, please see <https://cordc.ucsd.edu/projects/models/coamps/>.

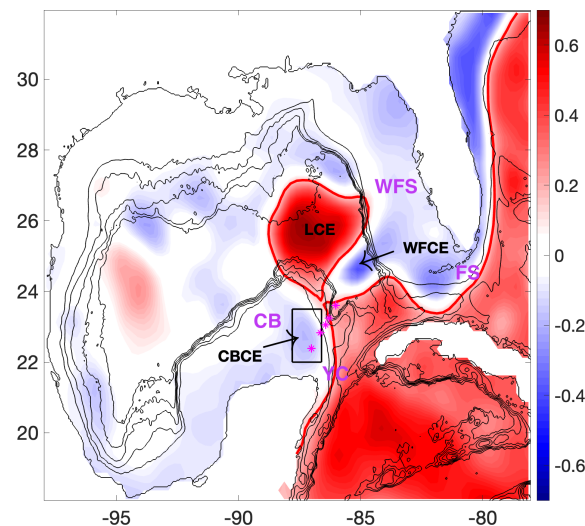


FIGURE 1

Altimetry sea surface height (SSH, m) during LCE Franklin detachment on 05/29/2010. The red line, which is 0.17 m SSH contour, delineates the edge of the LC. Two LCFEs are present on either side of the LC, the West Florida cyclonic eddy (WFCE) on the east flank of the LC and the Campeche Bank cyclonic eddy (CBCE) the west flank of the LC. The mooring stations described in Section 2.3 are marked in magenta asterisks. Acronyms of geographic features are in magenta text: West Florida Shelf (WFS), Florida Straits (FS), Yucatan Channel (YC) and Campeche Bank (CB). The rectangular region that contains the CBCE is the fixed region in which the spatially averaged potential vorticity of eastern CB is estimated in Section 3.1 and 3.2. The black lines are isobaths from 0 to 3000 m with 600 m intervals.

ensemble sampled the 2D uncertain amplitude space  $(\xi_1, \xi_2)$ <sup>4</sup> using a total of 49 realizations. The ensemble outputs are saved daily for 60 days from May 1st, 2010 to June 29, 2010. Previous studies showed that the actual LC contour derived from satellite observation generally fall within the envelope of this HYCOM ensemble contours within 30 days, which stresses the realism of the ensemble since the observational data appears to be a plausible realization of the model ensemble (Iskandarani et al., 2016; Wang et al., 2018).

## 2.3 Mooring data

The observation data used in our study is from the moorings of the Centro de Investigación Científica y de Educación Superior de Ensenada (CICESE) array in the Mexican waters of the GoM. The array was designed to investigate the flow over the Western Yucatan Channel and Campeche Bank and its role in the LC dynamics and LCE detachments (Sheinbaum et al., 2016). The Plataforma Este (PE, Eastern shelf) mooring section that we picked for the analysis crosses from the CB shelf break to depths between 2000 and 3500 m. Section PE is located in the region where CBCEs usually develop. The section consists of five moorings that use a variety of current measurement equipment, such as Acoustic Doppler Current Profilers and Nortek Aquadopp current meters. The moorings are off-shore from 100 km to 270 km. The coordinates of each PE

mooring station are listed on Table 2 in Athie et al. (2014). The mooring measurement depth is 100 m for the shallowest station, and it reaches about 3500 m depth for the deepest station. The vertical sampling deployment is at intervals of 300 m to 500 m. The PE section deployment covers over 22 months, from June 2009 to April 2011 (Athie et al., 2014).

## 3 Results

### 3.1 Potential vorticity anomaly analysis

Firstly, we investigate the impact of initial condition perturbations on the evolution of the LCFEs' structure and strength, using potential vorticity (PV) and PV anomaly (PVA) for the dynamical analysis. In geostrophic balance, an eddy is associated with a local extreme of PV (Ertel, 1942). In isopycnal coordinates, the PV of a fluid parcel within an isopycnal layer is given by

$$PV = \frac{\zeta + f}{h} \quad (1)$$

where  $\zeta$  is the relative vorticity of the fluid within the layer,  $h$  is the layer thickness, and  $f$  is the planetary vorticity. The PV includes information of both the vorticity dynamics (numerator) and the mass field (denominator). PVA is defined as the difference between PV and a reference PV state at rest (PV<sub>ref</sub>), which was chosen here to be the ocean at a location outside the LC and LCFE regions (calculation details of PV<sub>ref</sub> provided later on), normalized by the reference layer thickness  $H$

$$PVA = H(PV - PV_{\text{ref}}) = H\left(\frac{\zeta + f}{h} - \frac{f}{H}\right) \quad (2)$$

<sup>4</sup> The sampling was designed to minimize the error between a Polynomial Chaos surrogate and the sample via a Galerkin projection on polynomials of degree 6 in the variables  $\xi_1$  and  $\xi_2$ . See Figure 3 in Iskandarani et al. (2016) for the sampling points in the uncertain  $(\xi_1, \xi_2)$  space.

Hoskins et al. (1985) found that the presence of a PVA pole in a specific layer is associated with a circulation that extends to all layers, but which is more intense in that specific layer (a positive PVA pole being associated with a cyclonic circulation, while a negative PVA pole is associated with an anticyclonic circulation). That property means that the strengthening of the cyclonic structure, can be associated with an intensification of its PVA [see also Herbette et al. (2005); Meunier et al. (2010); Le Hénaff et al. (2012a)]. Thus, the PVA evolution of the LCFEs reveals the strengthening or weakening of the LCFEs' structures.

There are 20 hybrid layers in the original HYCOM output. To simplify the analysis, we group together those original layers with similar PVA patterns and come up with a simplified two-layer system. Previous studies have conducted similar layer simplification strategy to analyze the evolution of LCFE (Le Hénaff et al., 2012a; Androulidakis et al., 2014). To get the simplified system, we first project the model outputs onto purely isopycnal layers, using the same number of layers, as well as the same target densities as the native HYCOM grid. The projection on purely isopycnal layers is necessary, because the PV calculation requires the knowledge of isopycnal layer thicknesses. This projection procedure leads to the interpolation of fields only from the layers that were not isopycnal in the HYCOM configuration, i.e., layers that were based on  $z$  levels and sigma layers near steep topography. The new fields in the purely isopycnal layers are interpolated linearly between adjacent depths from the original HYCOM grid. To define  $PV_{ref}$  in our study, we select a date in the previous year in the same season when the LC is not as extended. On that date, we select a grid point in the eastern Gulf which is away from both the LC and LCFE regions, to estimate the reference PV, using outputs from the near-real time HYCOM expt\_20.1 reference experiment. The LC dynamics is absent from the location selected for estimating  $PV_{ref}$  location, and RV at the reference location is as close to zero as possible, so that the ocean state used to estimate  $PV_{ref}$  can be considered at rest when compared to the LC system. The same approach was used by Le Hénaff et al. (2012a) and Androulidakis et al. (2014) to study the evolution of the LCFEs and of the LC system.  $PV_{ref}$  in each isopycnal layer is calculated as  $PV_{ref,i} = \frac{f}{H_i}$ , where  $PV_{ref,i}$  is the reference PV corresponding to the  $i$ -th isopycnal layer, and  $H_i$  is the  $i$ -th HYCOM layer depth at the reference point.

After projecting the original hybrid HYCOM layers into purely isopycnal layers and after defining  $PV_{ref}$ , we estimate the PVA in each layer in order to identify the positive PVA regions along the west Florida Shelf and over the Campeche Bank corresponding to the cyclonic activities associated with the west Florida cyclonic eddy (WFCE) and the Campeche Bank cyclonic eddy (CBCE), respectively. After identifying the layers showing the high positive PVA signals associated with the cyclones under study, we reduce the number of layers in order to simplify the analysis of the evolution of the PV field. The isopycnal layers with a high positive PVA cores corresponding to WFCE and CBCE are grouped together. In our case, this method leads to a simplified analysis using two layers, where the LC and LCFEs signals are mainly in the upper layer. The upper layer groups the top 10 projected isopycnal layers of densities ranging from 1019.5 to 1025.77  $kg/m^3$  and extends as deep as 800 m in the study area, while the lower layer below extends to the GoM bottom. We then

evaluate the corresponding PVA for each simplified layer. We use vertically averaged velocity for the calculation of relative vorticity  $\zeta$ , and the layer thickness  $h$  is the sum of the thicknesses of all the isopycnal layers that constitute the simplified layer.

We focus on the evolution of LCFEs in several specific ensemble members with significantly different initial condition perturbations: realization 01 (hereafter RZ01) with the most negative perturbations [ $(\xi_1, \xi_2) = (-0.9491, -0.9491)$ ], realization 25 (hereafter RZ25) with no perturbation [ $(\xi_1, \xi_2) = (0, 0)$ ], a.k.a., the control run, and realization 49 (hereafter RZ49) with the most positive perturbations [ $(\xi_1, \xi_2) = (0.9491, 0.9491)$ ]. Figure 2 shows the upper layer PVA evolution of our simplified two-layer system for those three different realizations. The differences in PVA anomaly on the first day are due to the initial condition perturbations. RZ49 has the most positive PVA and the largest high positive PVA region to the north and northeast of the extended LC, while RZ01 has the least positive PVA and smallest high positive PVA region. The control run RZ25 has a moderate positive PVA strength and positive PVA size region. This illustrates how the initial condition perturbations perturb the strength of the WFCE, and also the northern cyclonic eddy (NCE) (Schmitz, 2005), which is located on the northern edge of the LC. A positive perturbation yields strong frontal eddies and vice versa. This relationship between perturbation and the strength of the LCFEs matches the results from Iskandarani et al. (2016), who found the same effect of the initial condition perturbations on the strength of the WFCE, albeit in the SSH signal. As time progresses, the positive PVA pattern corresponding to the WFCE moves southward along the west Florida shelf before it changes direction to intrude into the LC. On day 20, the three realizations differ in the degree to which the WFCE has intruded into the LC. RZ49 shows a WFCE with the most western longitudinal extension and whose PVA remains the most intense among the three realizations. When the perturbation is negative, in RZ01, the western intrusion of the WFCE into the LC is reduced along with its amplitude. On day 30, the WFCE in RZ01 moves south along the shelf, instead of intruding west into the LC, while its counterparts in RZ25 and RZ49 continue their westward intrusion. The WFCE in RZ49 still exhibits a stronger positive PVA than that in RZ25, and more importantly, the former has evolved into an extended tongue that intrudes further west than 88°W, which makes the LCE totally detached. Based on the 17-cm SSH contours (not shown) that Leben (2005) used to define the edge of the LC, on day 30 RZ49 has a detached LCE, RZ25 shows a nearly detached LCE, and RZ01 has no tendency of LCE detachment at all. It is also worth noticing the PVA evolution on the eastern edge of the CB. From day 1 to day 20, high PVA accumulates gradually over the eastern CB close to the Yucatan, as the LC is squeezed against the CB. The PVA evolution in this region is similar across the realizations during this period. On day 30, the three realizations show evident differences in PVA patterns over the eastern CB. In RZ25, the high positive PVA region along the eastern bank edge is more intense than that in RZ01, and in both realizations, it is oriented along the southeast-northwest direction, following the edge of the LC. In RZ49, this area of high PVA starts to move northeastward and to interact with the southwestward moving WFCE; this growing patch of high positive PVA eventually forms

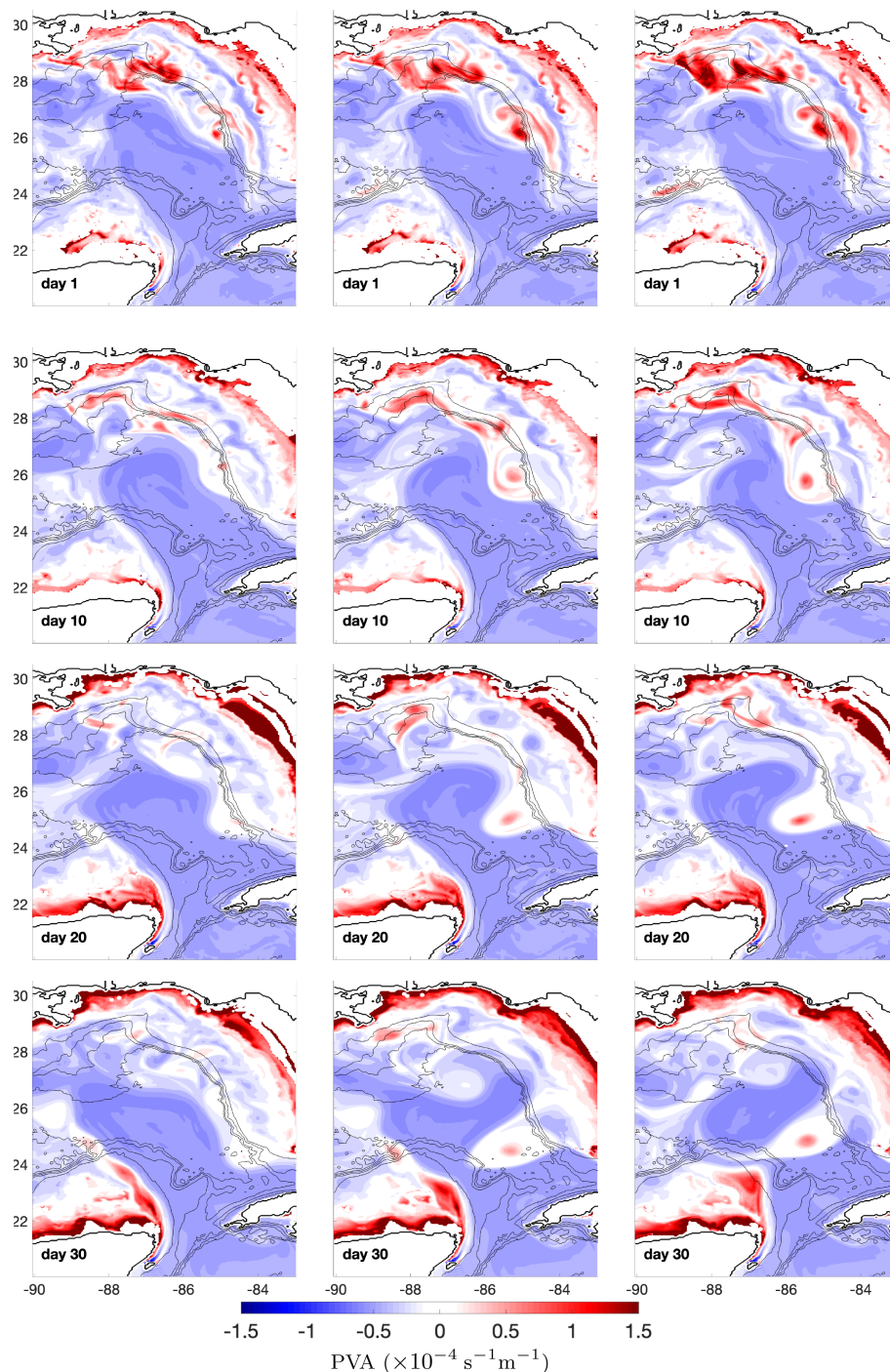


FIGURE 2

Upper layer PVA evolution for RZ01 (left column), RZ25 (center column), and RZ49 (right column). Coastlines are shown in black lines. Isobaths are shown in gray lines from 0 to 3500 m with 700 m intervals.

a CBCE. To sum up, [Figure 2](#) delivers the information that PV along the CB accumulates and finally forms a CBCE when the WFCE is strong and intrudes into the LC, while no CBCE forms when the WFCE is initially weak and LC intrusion does not happen. In Subsection 3.2, we perform an analysis of the teleconnection taking place between the WFCE and the CBCE.

[Figure 3](#) shows the evolution of the lower layer PVA for the three realizations. Realizations showing a strong WFCE signals in

the upper layer (see RZ25 on day 20 and 30, and RZ49 for day 10, 20 and 30) have corresponding strong pole in positive PVA in the lower layer. This indicates that the WFCE, once well developed, has a very coherent vertical structure, which is consistent with [Le Hénaff et al. \(2012a\)](#). All three realizations show a strong positive PVA belt along the eastern edge of the CB from day 1 to day 20. This belt stretches from the eastern shelf along the Yucatan Peninsula in the Caribbean Sea (20° N) to the northern tip of the CB (24°N).



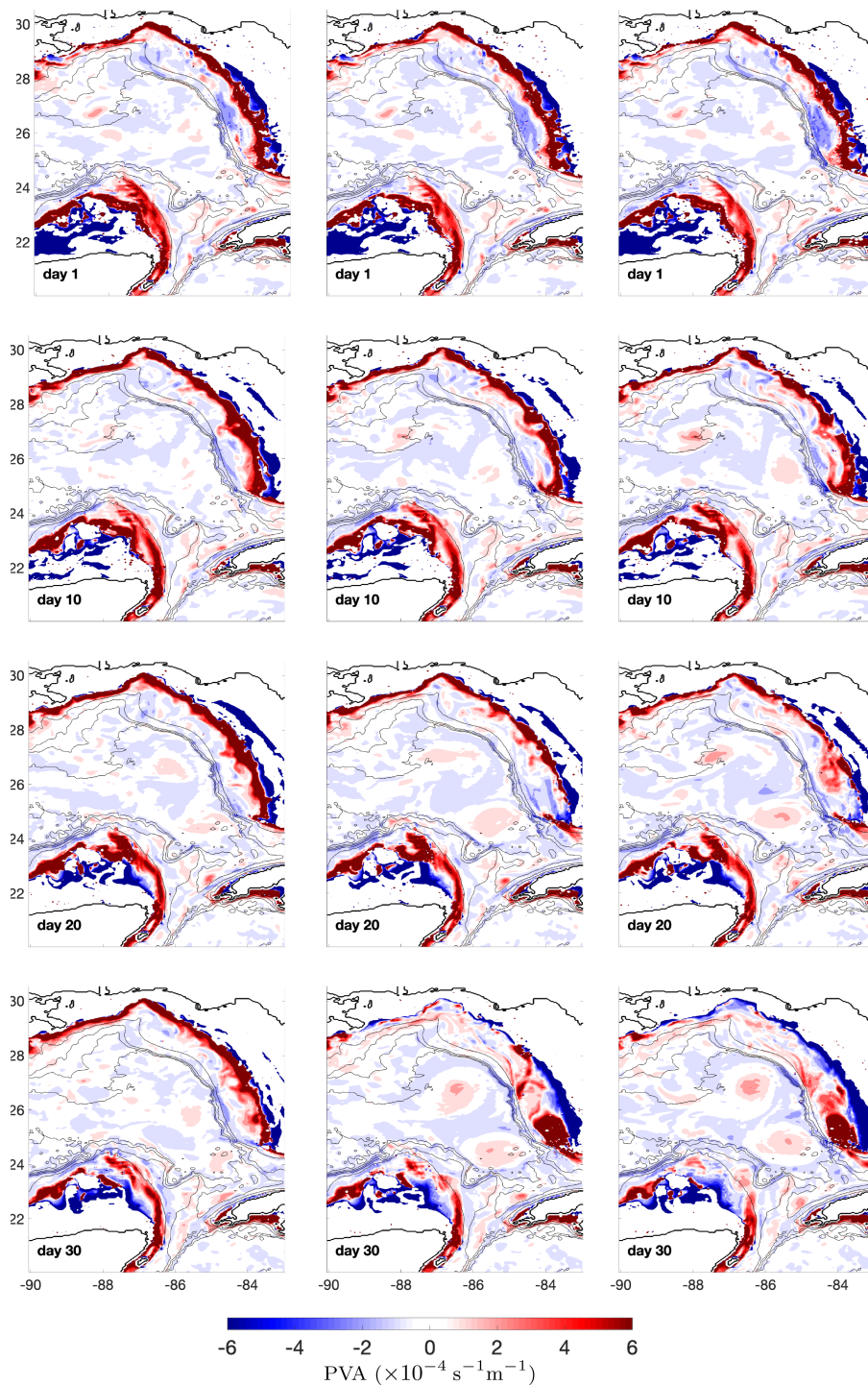


FIGURE 3  
same as Figure 2, for lower layer PVA evolution.

In RZ49, where CBCE is in development in the upper layer, this strong positive belt in the lower layer retracts (from 24°N to 23°N) on day 30. This indicates that, when the upper layer high positive PVA patch along the eastern CB starts to shift direction to the northeast, developing a CBCE (RZ49), its lower layer PVA structure erodes. While in the simulations that this upper layer PVA patch is oriented southeast-northwest (RZ01 and RZ25), the PVA belt in the lower layer does not erode.

Figure 4 presents the evolution of the ensemble upper layer PVA standard deviation<sup>5</sup> as a measure of the uncertainty in the PVA in the simplified upper layer associated with the variability

<sup>5</sup> The ensemble standard deviation were calculated using the Polynomial Chaos surrogate, see Le Maître and Knio (2010) and Iskandarani et al. (2016) for details.

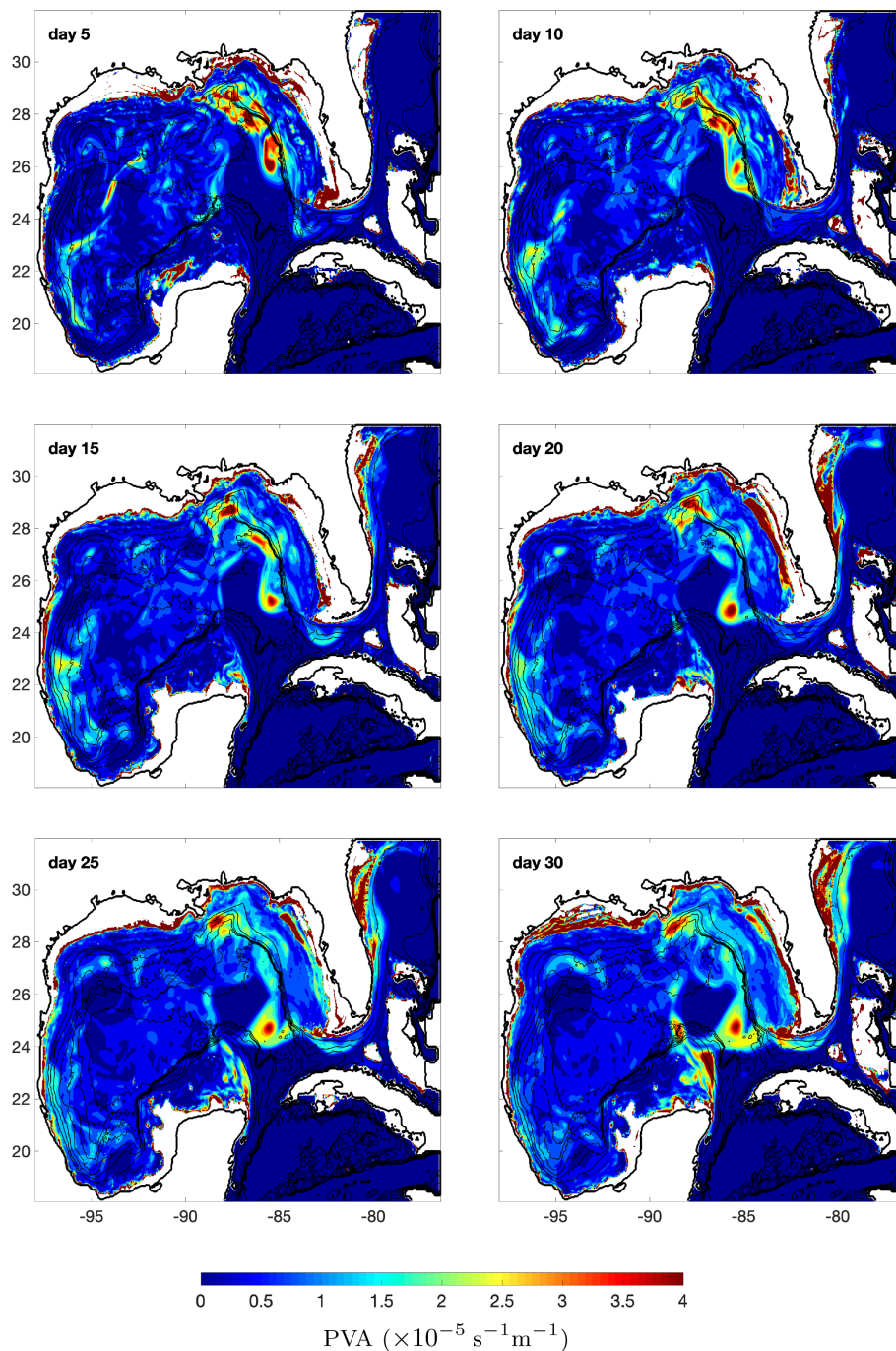
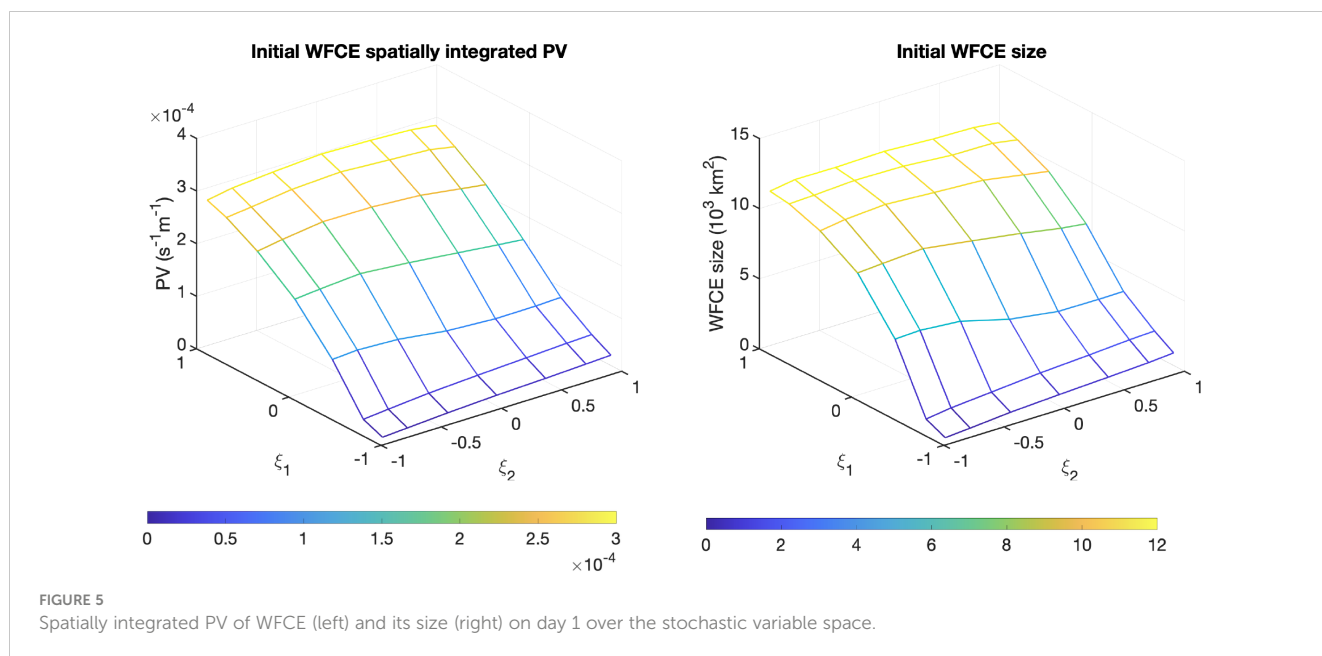


FIGURE 4

Ensemble standard deviation of PVA in the upper layer. The black lines are isobaths from 0 to 4000 m with 500 m intervals.

of the ensemble of initial conditions. In the early stage (from day 5 to day 20), the PVA uncertainty is mainly located to the north and northeast of the LC. The region of high PVA variance east of the LC is due to the different strength and size of the WFCE across realizations. At day 25, a noticeably high PVA variance region starts to form over the eastern CB, and becomes significant on day 30. It reflects that a CBCE has formed in some realizations while fail to form in other realizations. This corresponds to the difference in the CBCE formation and the LCE detachment across the different realizations.

We now investigate the relationship between the EOF perturbation stochastic amplitudes,  $\xi_1$  and  $\xi_2$ , the initial size and strength of the WFCE, and the later development of CBCE. We use the -28 cm SSH to define the edge of the WFCE region as in [Hiron et al. \(2020\)](#) where this contour level was found to be a good and convenient proxy for attractive Lagrangian Coherent Structures (closed patterns of high negative values of the finite-size Lyapunov exponent). [Figure 5](#) shows the response surfaces of the initial area size and strength (defined as the spatially integrated PV) of the WFCE at day 1 to changes in the stochastic amplitudes  $\xi_1$  and  $\xi_2$ . The two



quantities show a strong dependence to the amplitude of the first EOF mode  $\xi_1$ . With an increase of  $\xi_1$ , both the size and strength of WFCE increase evidently. With different values of  $\xi_1$ , the initial strength of WFCE can vary from  $0.07 \times 10^{-4}$  to  $2.98 \times 10^{-4} \text{ s}^{-1} \text{ m}^{-1}$ , the initial size of WFCE from  $0.23 \times 10^3$  to  $11.6 \times 10^3 \text{ km}^2$ . By contrast, the WFCE is quite insensitive to changes in  $\xi_2$ . The difference in sensitivity of the WFCE characteristics to the two perturbation modes can be explained by the spatial signature of these EOF modes: mode 1 has a strong signature on the initial WFCE, whereas the signature of mode 2 in the WFCE is not as strong (see Iskandarani et al. (2016), their Figure 1). In addition, the explained variance of EOF mode 2 is quite small compared to that of EOF mode 1 (Iskandarani et al., 2016). As a result,  $\xi_2$ , the amplitude of mode 2, has little impact on WFCE, and EOF 1 makes the largest contributions to the perturbation of the initial size and strength of WFCE.

Figure 6 shows the temporal evolution of the response surface of the spatially integrated PV over the eastern CB (see Figure 1), where we found that the PVA variance increases after day 25 (see Figure 4). On day 5, the averaged PV over this region is insensitive to changes in  $\xi_1$  or  $\xi_2$ . As time progresses, however, the dependence of the area-integrated PV on  $\xi_1$  starts to appear whereby an increase in  $\xi_1$  leads to an increase of the area-integrated PV. The area-integrated PV remains largely insensitive to changes in the amplitude of the second mode  $\xi_2$  throughout the duration of the experiment albeit for slight positive correlation. Although the change of the area-integrated PV along the  $\xi_1$  axis is not monotonic in some realizations, it is obvious that the increase in PV over the CB since day 25 is strongly associated with increasing  $\xi_1$ , that is an increase in the size and strength of the WFCE. The area-integrated PV of all realizations increases with time, with the largest increase associated with those realizations with a strong and large initial WFCE (high  $\xi_1$ ). Figure 6 confirms that, although the initial impact of the 1st EOF mode perturbation is confined to the northeast of the LC, it leads to a stronger subsequent PV development southwest of the LC along the eastern CB.

### 3.2 Teleconnection between LCFEs

The initial condition perturbations modify the PVA in the northeastern GoM and modulates the strength of the WFCE. These same perturbations do not impact the PVA over the eastern CB until 25 days later when differences between realizations starts to appear, especially along the CB. In order to investigate whether the PV evolution over the eastern CB can be correlated with other processes in the GoM, we estimate the covariance between the spatially averaged upper layer PV over the eastern CB on day 30 ( $22.4^\circ \text{ N}$  to  $23.8^\circ \text{ N}$ ,  $86.6^\circ \text{ W}$  to  $87.8^\circ \text{ W}$ , see the rectangular region in Figure 1) and the SSH with lagged time over the whole GoM.

For two variables  $X$  and  $Y$ , the covariance is estimated as

$$\text{cov}(X, Y) = \frac{1}{N-1} \sum_{n=1}^N (X_n - \bar{X})(Y_n - \bar{Y}) \quad (3)$$

For covariance between the spatially averaged PV over eastern CB on day  $t$ ,  $PV_{CB}^t$ , and the SSH at a grid  $(i, j)$  with  $\tau$  days lag,  $SSH_{ij}^{t-\tau}$ , the empirical covariance between them is

$$\text{cov}(PV_{CB}^t, SSH_{ij}^{t-\tau}) = \frac{\sum_{n=1}^N (PV_{CB,n}^t - \overline{PV_{CB}^t})(SSH_{ij,n}^{t-\tau} - \overline{SSH_{ij}^{t-\tau}})}{N-1} \quad (4)$$

Where  $PV_{CB,n}^t$  is the spatially averaged PV of CBCE on day  $t$  for realization number  $n$ ,  $SSH_{ij,n}^{t-\tau}$  is SSH value at grid point  $(i, j)$  with  $\tau$  days lag for realization number  $n$ ,  $\overline{PV_{CB}^t} = \frac{1}{N} \sum_{r=1}^N PV_{CB,n}^t$ ,  $\overline{SSH_{ij}^{t-\tau}} = \frac{1}{N} \sum_{r=1}^N SSH_{ij,n}^{t-\tau}$ ,  $N$  is the total number of realizations.

Figure 7 shows the covariance between this averaged PV on day 30, and the lagged SSH (SSH on day 5, 10, 15, 20, 25 and 30) over the entire GoM. The covariance is normalized by the maximum and minimum values so that all the values fall between -1 and 1. On day



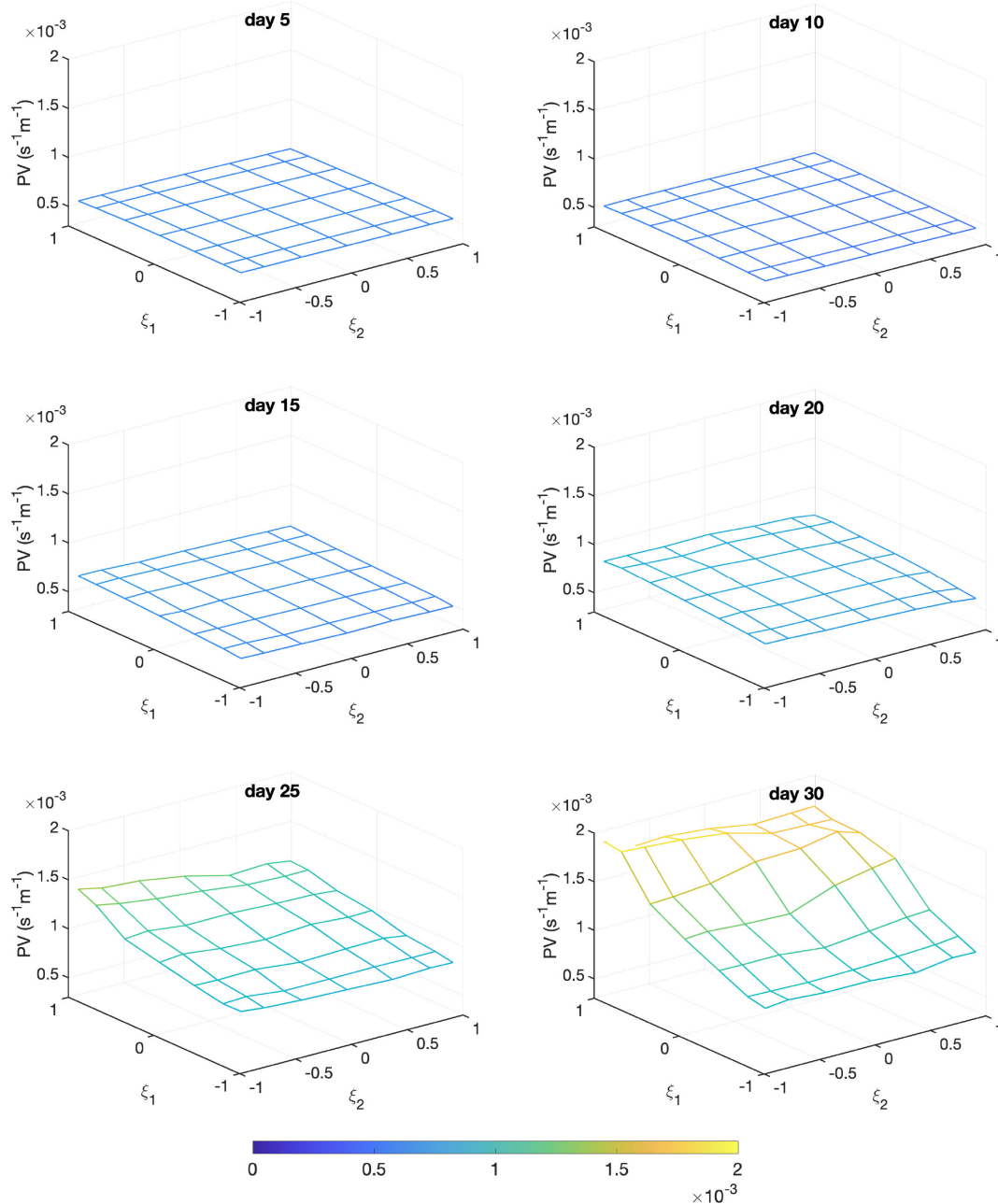


FIGURE 6  
Evolution of spatially integrated PV over the eastern CB in the stochastic variable ( $\xi_1, \xi_2$ ) space.

5, i.e., at -25 day lag, negative covariance regions is present on the northeast side of the LC and these regions overlap with the front of the WFCE shown in SSH contours. As time progresses, this negative covariance strengthens and the associated region moves along with the WFCE front. The ensemble mean SSH contours are shown as well, in black lines. On day 25, i.e., at -5 day lag, on the north and east side of this negative covariance region, noticeable positive covariance emerges, which coincide with the LC edges that have been displaced westward by an intruding WFCE. On day 30, i.e., at 0 day lag, the negative covariance region extends to the east side of the CB, while the positive covariance regions intensify. Since a cyclonic eddy is associated with a negative SSH anomaly and an

anti-cyclonic is associated with a positive SSH anomaly, a negative covariance with the SSH of a cyclonic eddy corresponds to a positive relationship with the strength of that eddy. This covariance analysis stresses the statistical teleconnection that exists between the signatures of both LCFES at various times, i.e., the CBCE around the time of its formation and the WFCE during the previous 25 days.

Figure 8 is the scatterplot of initial WFCE strength versus area-integrated PV over the eastern CB. The red circles are realizations without an LCE detachment occurs and the blue circles are realizations where an LCE detachment occurs. The correlation coefficient  $r$  between both variables is already high on day 1, and



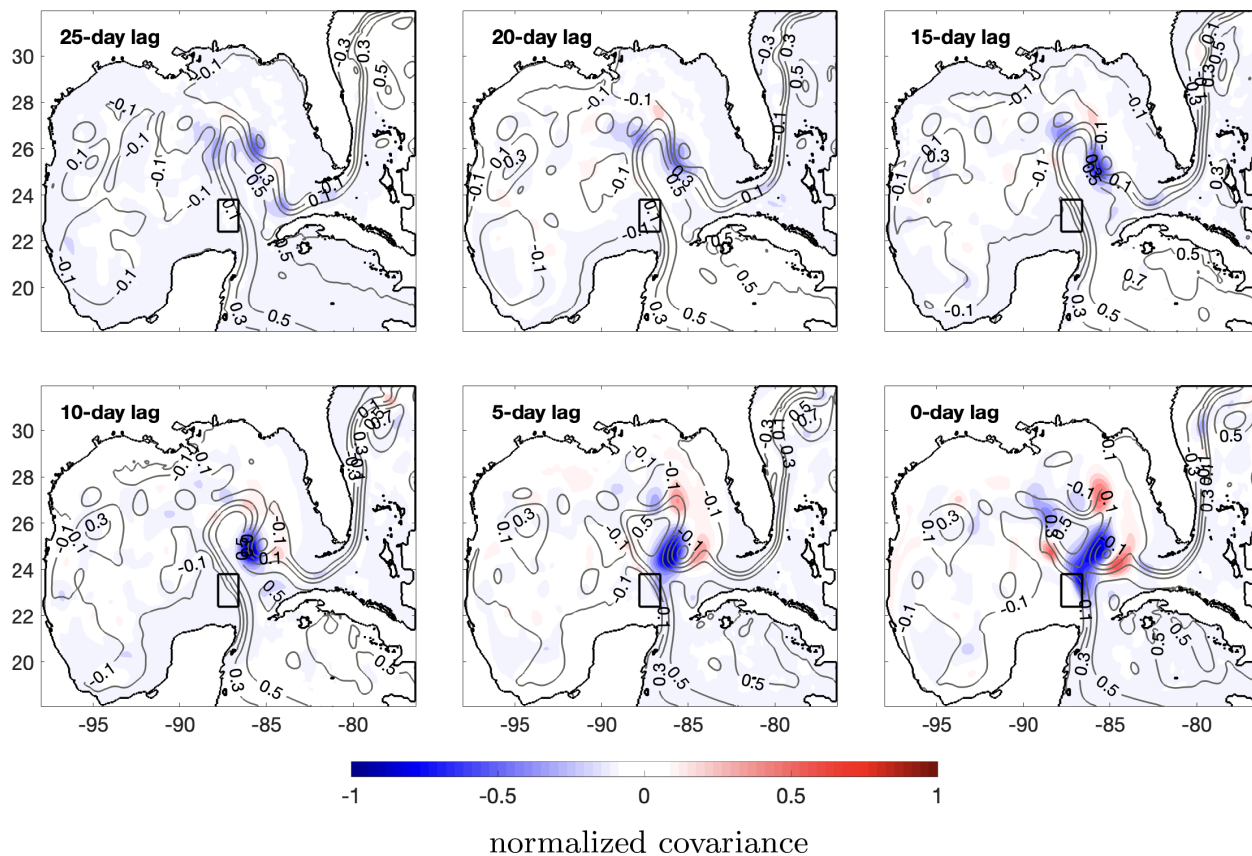


FIGURE 7

Covariance between the spatially averaged upper layer PV over the eastern CB on day 30 (the spatially averaged area shown in rectangular region in each subplot, and in Figure 1 as well) and the lagged SSH (SSH on day 5, 10, 15, 20, 25 and 30) over the GoM. The covariance is normalized by the maximum and minimum values so that all the values fall between -1 and 1. The ensemble mean SSH contours are shown in gray lines marked with SSH values (in m). The coastlines are shown in black lines.

reaches its peak value of 0.945 on day 30. The correlation weakens slightly on day 35 but still exhibits a high correlation coefficient. Figure 9 is the scatterplot of the initial WFCE size versus the eastern CB strength. The result is quite similar to that of Figure 8. The correlation between the initial WFCE size and the eastern CB strength remains high throughout all the forecast days and it peaks on day 30. The positive correlation between the initial WFCE size and the integrated PV over the eastern CB, illustrative of a teleconnection between both eddies, is verified in Figures 8, 9. Another phenomenon that is revealed in Figures 8, 9 is that the realizations with an LCE detachment start with an initially higher WFCE strength and size, and end with a higher eastern CB integrated PV value, than those without LCE detachment. In the realizations without an LCE detachment, the initial integrated PV values of WFCE are all lower than  $1.5 \times 10^{-4} \text{ s}^{-1} \text{ m}^{-1}$ . Most of the PV values are greater than  $1.5 \times 10^{-4} \text{ s}^{-1} \text{ m}^{-1}$  for realizations with an LCE detachment, except for three realizations, whose PV values are around  $0.8 \times 10^{-4} \text{ s}^{-1} \text{ m}^{-1}$ . Similarly, in terms of the initial WFCE size, the realizations without an LCE detachment have small WFCE sizes that are always smaller than  $6 \times 10^3 \text{ km}^2$ . The initial WFCE size is greater than  $6 \times 10^3 \text{ km}^2$  for the realizations with an LCE detachment, with 3 exceptions, which are all around  $4 \times 10^3 \text{ km}^2$ . In terms of the eastern CB integrated PV value (y axis values in Figures 8, 9), all the

realizations with an LCE detachment have PV values greater than  $4.0 \times 10^{-4} \text{ s}^{-1} \text{ m}^{-1}$  on day 35, while all the realizations without an LCE detachment have PV values lower than  $4.0 \times 10^{-4} \text{ s}^{-1} \text{ m}^{-1}$ . By contrast, on day 1, the eastern CB integrated PV values are similar across all realizations.

In Subsection 3.1, we showed that a CBCE develops only when a WFCE is strong enough to intrude into the LC. The statistical analysis performed in this subsection confirms that a teleconnection exists between both eddies, during the LCE detachment process, by which the growing PV on the eastern CB is positively related with the strength of WFCE and the distance between them. In other words, a more intense WFCE approaching the CB will lead to increase in the PV over the eastern CB and favor the formation of a CBCE.

### 3.3 LCE detachment criterion

This subsection presents the investigation of the conditions and timing of the LCE detachment. Among the 49 ensemble realizations, 29 realizations led to an LCE detachment; no such detachment occurs for the remaining 20 realizations in the 60-day simulation period. Figure 10 shows the relationship between the

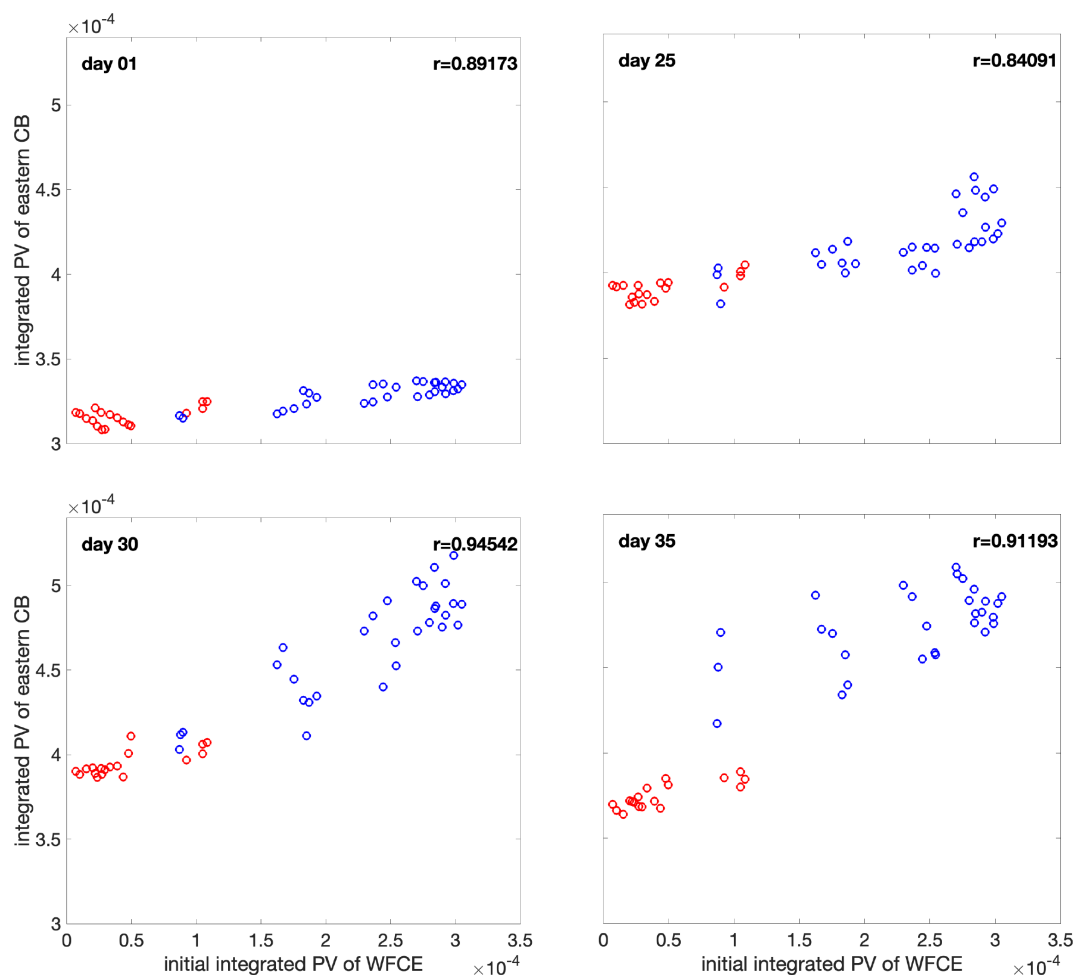


FIGURE 8

Scatterplots of integrated PV ( $s^{-1}m^{-1}$ ) over the eastern CB (see box on Figure 1) on day 01, 25, 30 and 35 against the initial day 01 integrated PV of the WFCE. Red circles are realizations without an LCE detachment. Blue circles are realizations with an LCE detachment.

LCE detachment day and the amplitude of the first perturbation  $\xi_1$ , since there is little dependency on  $\xi_2$ . We can see that in the scatterplot, there is a noticeable negative trend between these two variables. The more positive  $\xi_1$  value, the sooner the LCE detachment. In other words, a larger  $\xi_1$  accelerates the LCE detachment process. The PVA plots on Figures 2, 3 also suggest that the positive initial perturbation is associated with a more unstable LC system, i.e. with large meanders and strong PVA poles. This finding shows that the initial conditions, in particular the strength of the WFCE, have a role on the behavior of the LC system, i.e., the LCE detachment occurrence and timing. This may be useful for LC system forecasting.

We also trace the trajectory of WFCEs in all the ensemble realizations. We find that when an LCE detaches, the western extension of WFCE is always west of  $85.6^\circ$  W (not shown). In the realizations without an LCE detachment, the WFCE is always east of  $85.6^\circ$  W (when the WFCE moves south to  $26^\circ$  N). This is in agreement with mechanisms described by Schmitz (2005), and it reveals that in order to trigger an LCE detachment, the WFCE needs to extend at least west to  $85.6^\circ$ W.

We also present the LCE detachment in altimetry SSH data, to verify that the eddy detachment process that we found in the ensemble of simulations is realistic. Figure 11 shows the altimetry SSH evolution for Eddy Franklin in 2010 (upper row) and Eddy Icarus 2011 (lower row). These two eddy detachment events exhibit WFCEs with similar sizes before the WFCEs start to intrude into the LC. These two events also share a similar LCE detachment mechanism, with the WFCE making the major contribution to the initial eddy detachment. The timespans from the WFCE intrusion to the LCE detachment are similar as well, in these two events, with 26 days for Franklin, and 21 days for Icarus. More generally, the involvement of a strong WFCE and of a growing CBCE, as is the focus of our study, is consistent with Schmitz (2005), who studied and described a large number of LCE detachment sequences.

### 3.4 Observation-model comparison

In this subsection, we compare the ensemble outputs with mooring observation data to investigate how the initial condition

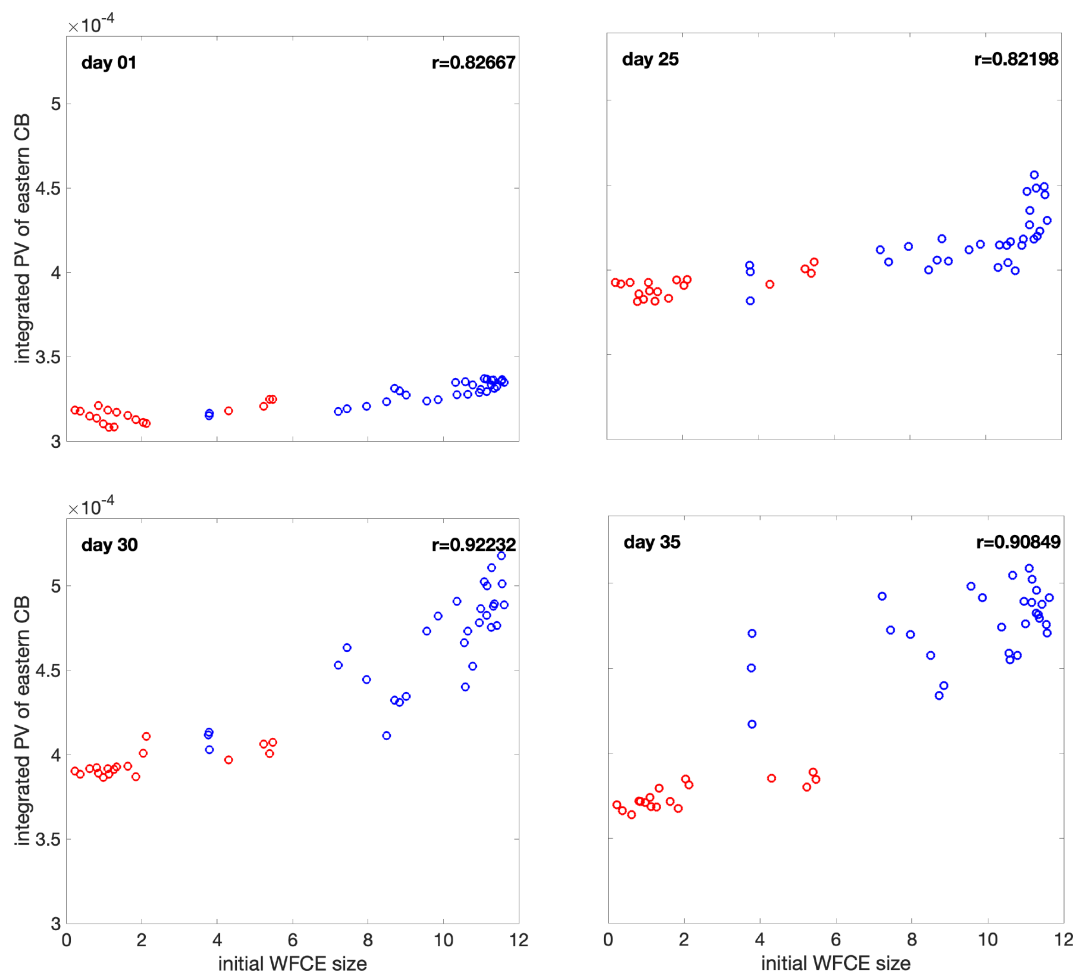


FIGURE 9  
Scatterplots of integrated PV ( $s^{-1}m^{-1}$ ) over the eastern CB (see box on Figure 1) on day 01, 25, 30 and 35 against initial size ( $10^3 km^2$ ) of the WFCE. Red dots are realizations without an LCE detachment. Blue dots are realizations with an LCE detachment.

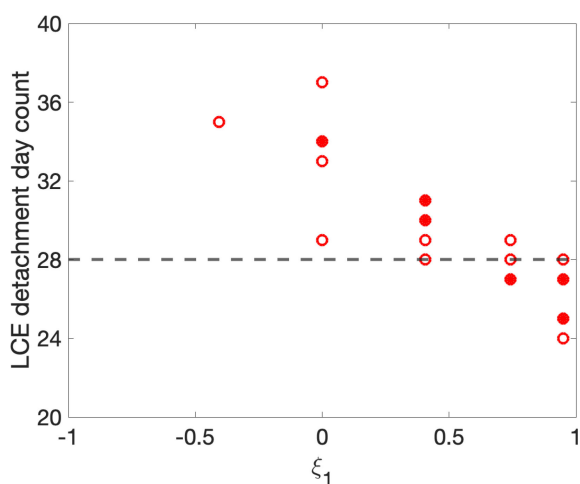


FIGURE 10  
LCE detachment day against  $\xi_1$ . Circles are single realizations. Solid dots are multiple realizations that are overlapped. The horizontal dashed line (day 28) is the day that the LCE actually detached based on altimetry data.

perturbations impact the realism of the model outputs, in light of our results from the ensemble modeling, in particular related to the detachment or not of an LCE.

To make the mooring observation and model outputs comparable in both time and space, we take the daily mean of the PE section mooring data to match the date of the daily HYCOM outputs. Then we use linear and bi-linear interpolation to interpolate the model data onto the mooring locations.

Firstly, we make model-observation comparison of the current velocity components tangential and normal to the mooring line (See Figure 1 for the locations of the mooring stations from PE1 to PE5. See Table 2 in Athie et al. (2014) for the coordinates of each PE mooring station). The comparison of the normal velocity component (normal with respect to the mooring array, i.e. along the dominant current direction) at shallow depth (50 to 60 m) for each mooring station is shown in Figure 12. In the beginning of the comparison period, the ensemble of realizations yield values that are very close to each other and generally capture the observed trend, if not the exact observed values. The ensemble starts to diverge around day 25. Apart from mooring PE5 where no model realization follows the observed trends, a subset of realizations

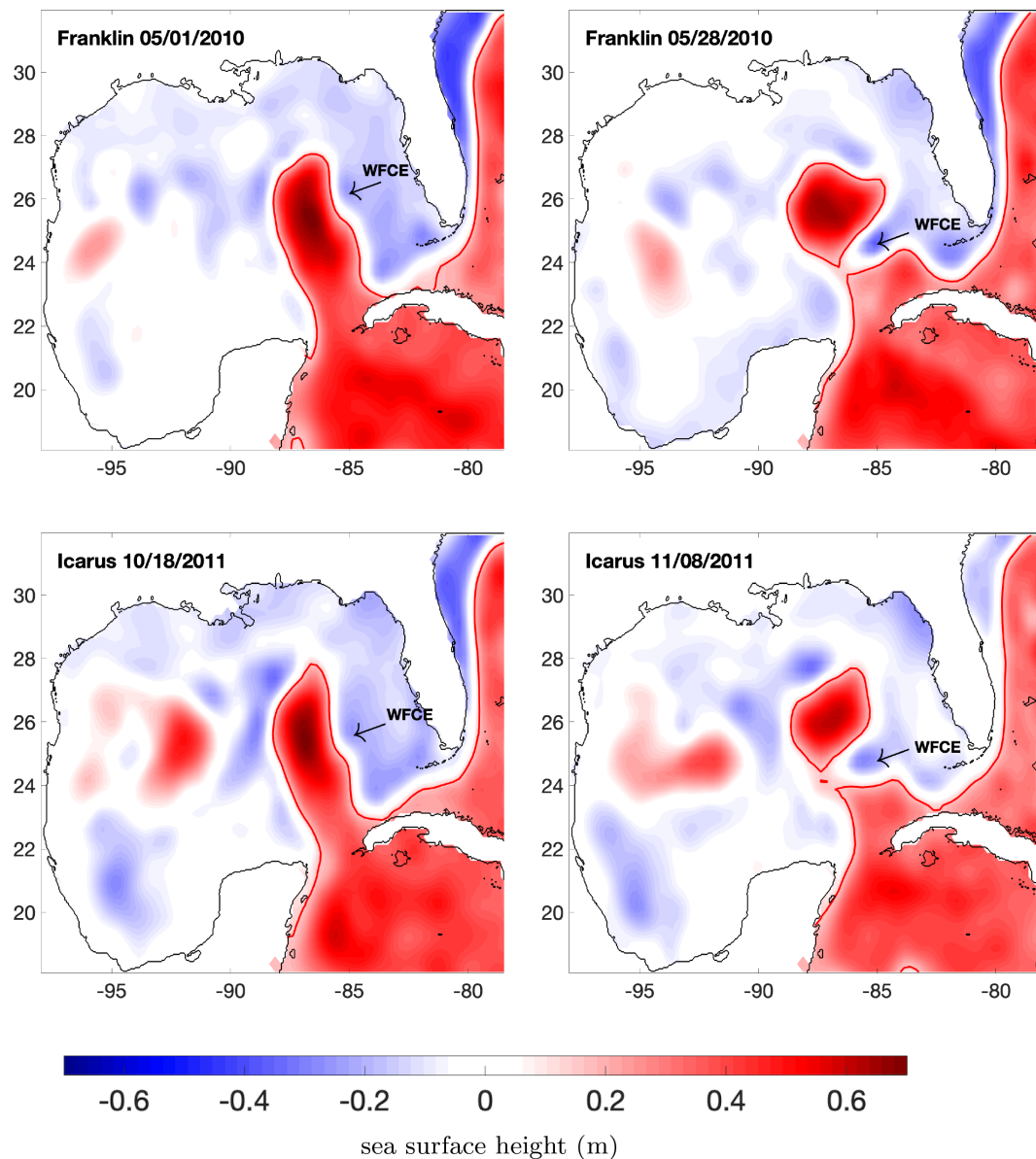


FIGURE 11

Altimetry-derived SSH (m) for Eddy Franklin in 2010 and Icarus in 2011. The black line is the coastline. The red line is 0.17 m SSH contour, which is the edge of the LC (Leben, 2005). The WFCE that is intruding into the LC and causing the LCE detachment is marked by an arrow and the mention "WFCE".

tends to generally compare reasonably well with the observations or their trends (blue lines), while other realizations deviate from the observations (red lines). Compared to the blue realization group, the red group generally shows small variations through time, and fails to capture the characteristics of the observations. Overall, the model realizations in which an LCE detachment occurs are closer to the observations or their trend than the ones in which there is no LCE detachment. Since an LCE detachment was actually observed (Figure 10, on day 28), this comparison shows that the simulations with a strong initial WCCE, which leads to an LCE detachment, provide a reasonable representation of the early stages of the

shedding process of Eddy Franklin, and that our ensemble is adapted to study the sensitivity of this process to initial conditions.

We also compare the relative vorticity (RV) between the ensemble members and the mooring array observations. Due to the lack of salinity data in the moorings, it is not possible to estimate the PV. Since the mooring data are aligned on a straight line, we can only measure the across-line component of the RV  $\frac{dU_n}{dx_i}$ , where  $dU_n$  is the difference in normal velocities  $U_n$  between two adjacent mooring stations (i.e., PE1 and PE2, PE2 and PE3, etc), and  $dx_i$  is the distance between these stations. Figure 13 presents the vertical section of the RV from mooring data and from the three



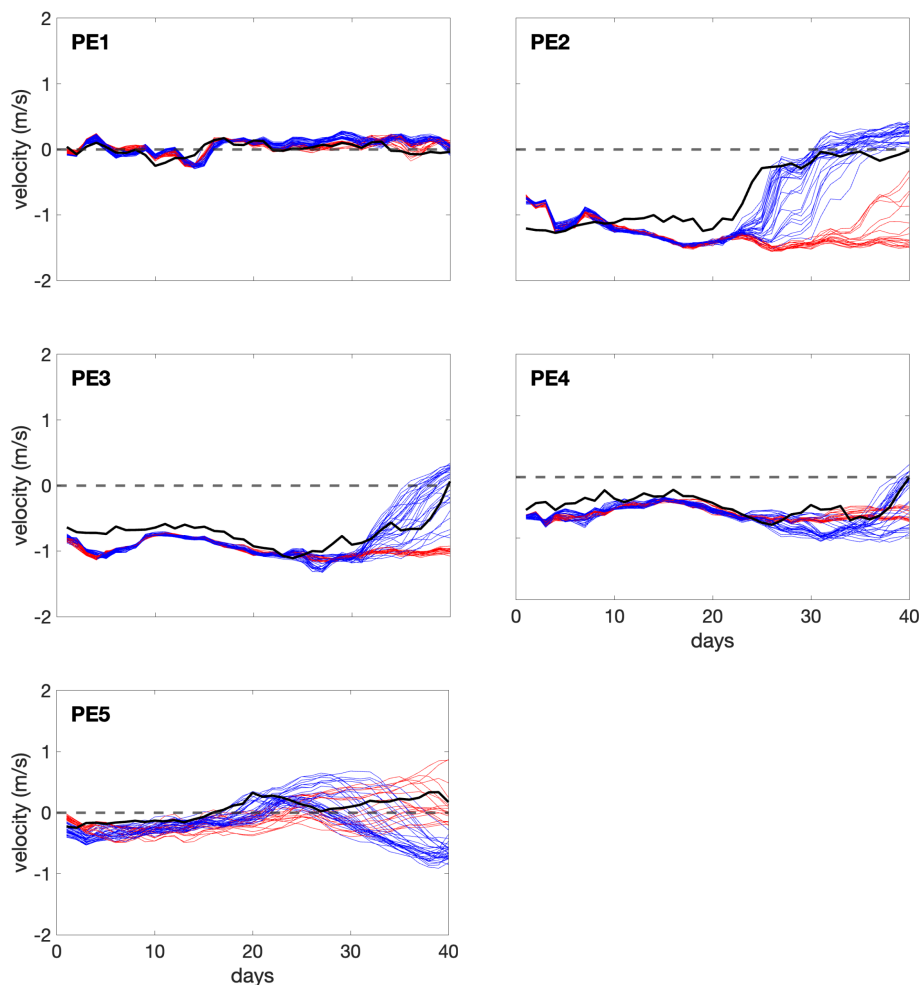


FIGURE 12

Comparison of model and mooring data for the normal (with respect to the mooring array) velocity  $U_n$  for each mooring station at depth 50~60 m. The realizations with an LCE detachment are in blue color. The realizations without an LCE detachment are in red color. The bold black lines are the observed velocities from the mooring array. The horizontal dashed line is the line of zero velocity.

representative ensemble realizations on day 1. The observation exhibits high positive RV formed near the surface, over the shallow region along the CB, while the simulations all present high positive RV at depth, close to the shelf break. Figure 14 shows that the observed positive RV structure is shifted eastwards on day 25, and that this offshore displacement appears barotropic. In the simulations, the deep patch of positive RV lifts upwards and the RV structure in RZ49 has become very similar to the one in the observations. On day 30 (Figure 15), the patch of positive RV in the observation extends eastwards at depth, and gradually becomes smaller when closer to the surface, with the core of the structure (highest RV) near the surface, over the CB shelf break. Among the three simulations, RZ49 matches with the observation very well regarding the positive RV structure. Based on SSH values, RZ49 shows an LCE that detaches on May 27th, which is very close to May 28th, the LCE actual detachment altimetry observations. This comparison confirms that the simulations in which an LCE detachment takes place, thanks to realistic initial conditions, compare well with the observations throughout the study period.

## 4 Summary and discussion

This paper analyses the impacts of perturbing the initial conditions in an ensemble simulation of the LC system whose main goal was forecasting the detachment of LCE Franklin. By targeting specific aspects of the initial conditions, namely the size and strength of the WFCE, the ensemble is used to investigate the dynamic impacts of such perturbations on LC detachments. The methodology adopted allowed us to build a direct relationship between two uncertain parameters controlling the initial perturbations and their subsequent impact on the ensuing LC circulation. The spatial distribution of the perturbations was obtained through an EOF decomposition of a 14-day time series of a realistic model representation of the GoM where the dominant modes reflect the variability of the LC frontal dynamics (Iskandarani et al., 2016). The two uncertain parameters,  $\xi_1$  and  $\xi_2$ , consisted of the amplitude of the two dominant modes. Our research finds that both the WFCE and CBCE are perturbed by the first variability mode. More positive value of  $\xi_1$  yields stronger

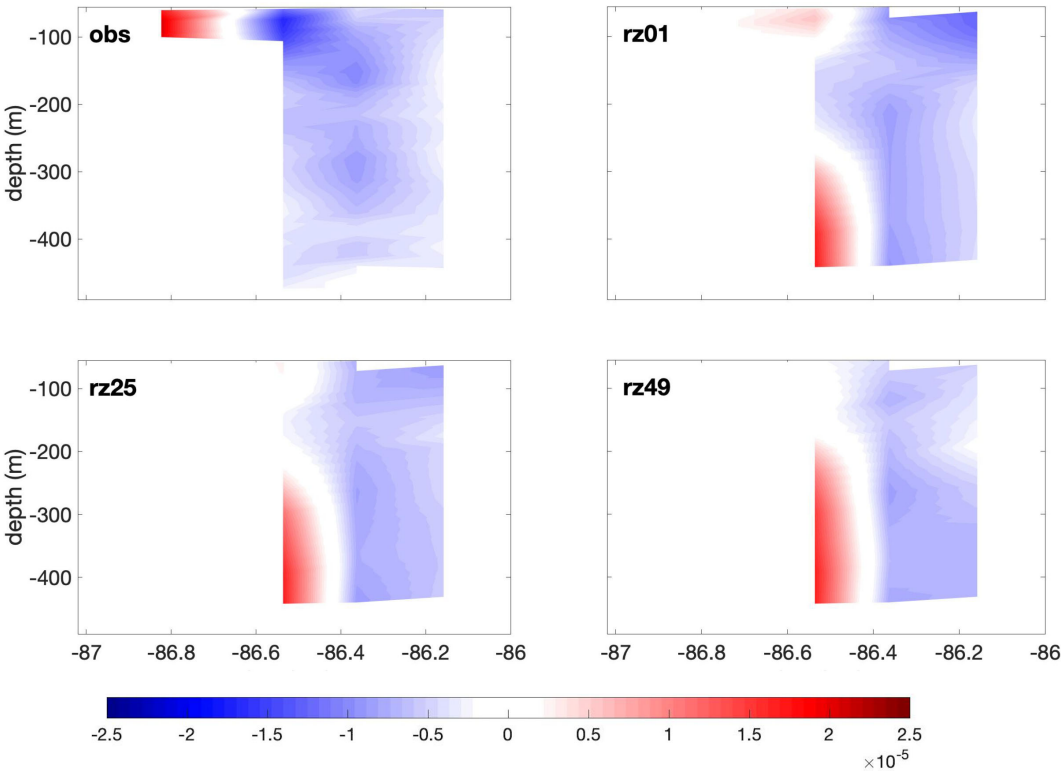


FIGURE 13  
Vertical section of the RV ( $s^{-1}$ ) over the eastern CB on day 1 for mooring data (upper left), rz 01 (upper right), rz 25 (lower left) and rz 49 (lower right).

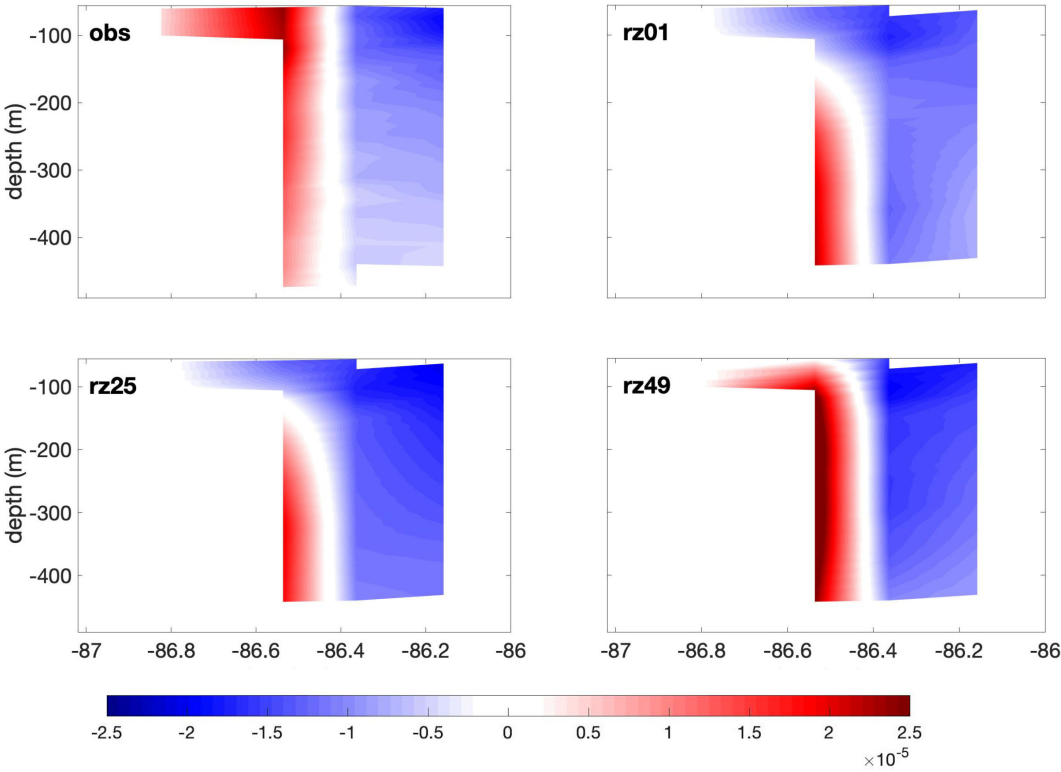


FIGURE 14  
same as Figure 13, on day 25.

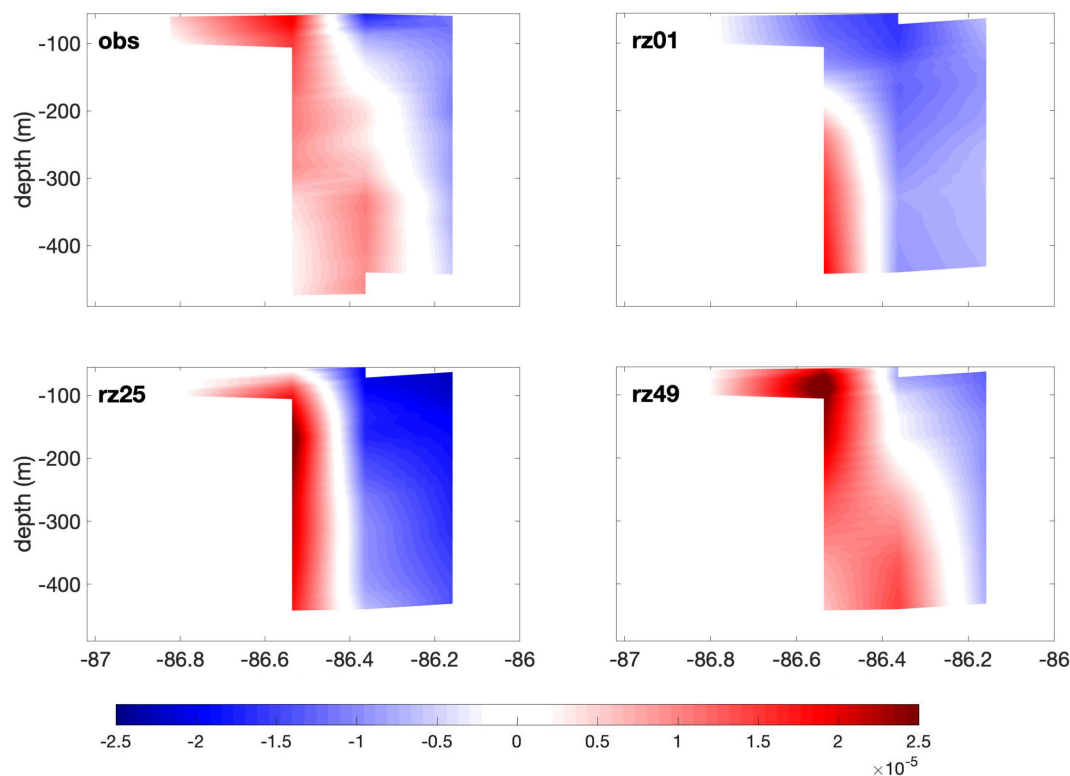


FIGURE 15  
same as Figure 13, on day 30.

WFCE immediately and stronger CBCE around 25 days later. The strong LCFEs consequently favor the detachment of an LCE. Meanwhile, the LCFEs are quite insensitive to changes in  $\xi_2$ .

This teleconnection between the CBCE and the WFCE during the LCE detachment process has been confirmed by a statistical analysis, in which we found that the PV growing on east of the CB is positively correlated with the strength of the WFCE and the distance between those PV poles. In the ensemble realizations analysis, we found that a strong WFCE leads to the formation of a CBCE, while a CBCE does not form when the WFCE weak or small. Combining those findings, we draw the conclusion that the more intense WFCE and the closer it is approaching to the CB, the more cyclonic PV will gather east of the CB. The approaching strong WFCE strengthens a forming CBCE which can subsequently intrude into the LC from its western side.

The ensemble members all share the same boundary conditions in the Caribbean Sea, so that the differences appearing in the CB region in the ensemble of simulations only come from the perturbations of the initial conditions. Considering that these perturbations are insignificant in the CB region, but that their signature is in the strength of the WFCE, the formation of a CBCE around and after day 25 can be attributed to the initial strength of the WFCE. If the formation of the CBCE was independent from the initial strength of the WFCE, the surface response of the PV amplitude in the CB region to the initial perturbation amplitudes would remain flat throughout the simulations, unlike what is seen on Figure 6. Moreover, the scatterplots relating the PV values in the

CB region to the initial WFCE strength or size would show scattered values for each subplot, without pattern and without any high correlation values, unlike what is seen on Figures 8, 9. These considerations make it clear that there exists a teleconnection between the CBCE and the WFCE in our study case of the formation of Eddy Franklin. Hiron et al. (2022) revealed that during LCE detachment, some of the WFCE water originates from the outer band of the LC front. In particular, small cyclonic eddies along the northern edge of the LC were found to merge and form a larger frontal eddy on the eastern side of the LC. This is indicative of a connection between small LCFEs along the LC and the formation of a WFCE. However, that connection is directed by the advective time scales along the edge of the LC and implies physical contact (through merging), whereas in the present study the connection is remote between two distinct eddies that do not necessarily merge.

Comparing the model outputs with mooring velocity observations along the eastern CB, we found that those ensemble realizations with relatively strong initial WFCE (realizations with LCE detachment) generally capture the characteristics of the observation evolution. The high RV corresponding to the CBCE formation in the observation is first visible at the surface, while in model simulations it appears to be lifted from deep region. However, as the time increases, the simulations successfully represent the eastward displacement of the high RV structure. The realizations with an LCE detachment present positive RV structures that are quite similar to the observations after around day 25.

Another significant phenomenon that we find through this investigation is that the initial state (size and strength) of the WFCE determines the evolution of the CBCE and the occurrence of the LCE detachment around 25 days and later. A strong and large WFCE leads to an LCE detachment and the formation of a CBCE along the eastern flank of the CB. By contrast, a weak and small WFCE in the northeastern side of the LC does not trigger an LCE detachment, or the formation of a CBCE. This result is consistent with [Le Hénaff et al. \(2014\)](#), in which the authors show that only intense WFCEs appear to participate in LC detachments. Our results suggest that the state of the WFCE may be a predictor of the LC system evolution. The size and strength of WFCE when it's present on the northeastern flank of the LC, can determine whether a CBCE will develop later on, and whether a LC detachment will occur or not. Moreover, since we have found that a stronger and larger initial WFCE leads to an earlier LCE detachment date ([Figure 10](#)), it might be possible to estimate the approximate date of an upcoming LCE detachment, after a well-formed WFCE is identified on the northeastern flank of the LC with a measurement of its size or strength. This suggestion is based on the study case of the formation of Eddy Franklin, but the sequence of eddy presence observed in our study case at the beginning of the shedding process was observed in the shedding process of Eddy Icarus, which followed Eddy Franklin in 2011, and is more generally consistent with the descriptive study of [Schmitz \(2005\)](#). In addition, [Sheinbaum et al. \(2016\)](#) mentioned that, for certain LCE detachments, the strength of the CBCE matches that of the WFCE, unlike during the Eddy Franklin shedding; it is worthwhile to investigate to what extent the teleconnection between LCFEs identified in our study is preserved under the latter scenario. Further research needs to be conducted on multiple LCE detachment events, in order to construct and test a valid relationship between the WFCE state and the LCE detachment process.

## Author's note

The content is solely the responsibility of the authors and does not necessarily represent the official views of the Gulf Research Program or the National Academies of Sciences, Engineering, and Medicine.

## Data availability statement

The raw data supporting the conclusions of this article will be made available by the authors, without undue reservation.

## Author contributions

XY, MI and MLH conceived of the presented idea. XY and MLH performed the computations. MI supervised the findings of this work. XY, MI and MLH analyzed the results from the investigation and made conclusions. BM provides suggestions during the conduction of the investigation. XY wrote the paper with comments from all other authors. All authors contributed to the article and approved the submitted version.

## Funding

This research was made possible by the support of the National Science Foundation Award 1639722 and ONR grant N000141912671. MLH received partial support for work on this publication by NOAA/AOML and was supported in part under the auspices of the Cooperative Institute for Marine and Atmospheric Studies (CIMAS), a cooperative institute of the University of Miami and NOAA (agreement NA20OAR4320472). Research reported in this publication was partially supported by the Gulf Research Program of the National Academies of Sciences, Engineering, and Medicine under the Grant Agreement number 2000011056 and the Grant Agreement number 2000013149.

## Acknowledgments

The mapped altimetry products were produced by Ssalto/Duacs and distributed by the Copernicus Marine Environment Marine Service.

## Conflict of interest

The authors declare that the research was conducted in the absence of any commercial or financial relationships that could be construed as a potential conflict of interest.

## Publisher's note

All claims expressed in this article are solely those of the authors and do not necessarily represent those of their affiliated organizations, or those of the publisher, the editors and the reviewers. Any product that may be evaluated in this article, or claim that may be made by its manufacturer, is not guaranteed or endorsed by the publisher.



## References

- Androulidakis, Y., Kourafalou, V., Le Hénaff, M., Kang, H., and Ntaganou, N. (2021). The role of mesoscale dynamics over northwestern Cuba in the loop current evolution in 2010, during the deepwater horizon incident. *J. Mar. Sci. Eng.* 9, 1–26. doi: 10.3390/jmse9020188
- Androulidakis, Y., Kourafalou, V. H., and Le Hénaff, M. (2014). Influence of frontal cyclone evolution on the 2009 (ekman) and 2010 (franklin) loop current eddy detachment events. *Ocean Sci.* 10, 947–965. doi: 10.5194/os-10-947-2014
- Athié, G., Candela, J., Ochoa, J., and Sheinbaum, J. (2012). Impact of caribbean cyclones on the detachment of loop current anticyclones. *J. Geophysical Research: Oceans* 117. doi: 10.1029/2011JC007090
- Athie, G., Sheinbaum, J., Romero, A., Ochoa, J., and Candela, J. (2014). “Measurements in the Yucatan-Campeche area in support of the Loop Current dynamics study,” in *Technical Report*, Bureau of Ocean Energy Management, Gulf of Mexico OCS Region, New Orleans. (New Orleans, Louisiana: United States. Department of the Interior), 159pp.
- Bao, J., Wilczak, J., Choi, J., and Kantha, L. (2000). Numerical simulations of air-sea interaction under high wind conditions using a coupled model: A study of hurricane development. *Monthly Weather Rev.* 128, 2190–2210. doi: 10.1175/1520-0493(2000)128<2190:NSOASI>2.0.CO;2
- Bleck, R. (2002). An oceanic general circulation model framed in hybrid isopycnal-cartesian coordinates. *Ocean Model.* 4, 55–88. doi: 10.1016/S1463-5003(01)00012-9
- Candela, J., Sheinbaum, J., Ochoa, J., Badan, A., and Leben, R. (2002). The potential vorticity flux through the yucatan channel and the loop current in the gulf of Mexico. *Geophysical Res. Lett.* 29, 16–11. doi: 10.1029/2002GL015587
- Candela, J., Tanahara, S., Crepon, M., Barnier, B., and Sheinbaum, J. (2003). Yucatan channel flow: Observations versus clipper atl6 and mercator pam models. *J. Geophysical Research: Oceans* 108. doi: 10.1029/2003JC001961
- Chang, Y.-L., and Oey, L.-Y. (2011). Loop current cycle: coupled response of the loop current with deep flows. *J. Phys. Oceanography* 41, 458–471. doi: 10.1175/2010JO4479.1
- Chassignet, E. P., Hurlburt, H. E., Smedstad, O. M., Halliwell, G. R., Hogan, P. J., Wallcraft, A. J., et al. (2007). The hycom (hybrid coordinate ocean model) data assimilative system. *J. Mar. Syst.* 65, 60–83. doi: 10.1016/j.jmarsys.2005.09.016
- Chassignet, E. P., Smith, L. T., Halliwell, G. R., and Bleck, R. (2003). North atlantic simulations with the hybrid coordinate ocean model (hycom): Impact of the vertical coordinate choice, reference pressure, and thermobaricity. *J. Phys. Oceanography* 33, 2504–2526. doi: 10.1175/1520-0485(2003)033<2504:NASWTH>2.0.CO;2
- Cherubin, L. M., Sturges, W., and Chassignet, E. P. (2005). Deep flow variability in the vicinity of the yucatan straits from a high-resolution numerical simulation. *J. Geophysical Research-Oceans* 110, C04009. doi: 10.1029/2004JC002280
- Cochrane, J. D. (1972). Separation of an anticyclone and subsequent developments in the loop current (1969). *Contributions Phys. Oceanography Gulf Mexico* 2, 91–106.
- Ertel, H. (1942). Ein neuer hydrodynamischer wirbelsatz. *Met. Z.* 59, 277–281.
- Fratantoni, P. S., Lee, T. N., Podesta, G. P., and Muller-Karger, F. (1998). The influence of loop current perturbations on the formation and evolution of tortugas eddies in the southern straits of florida. *J. Geophysical Research: Oceans* 103, 24759–24779. doi: 10.1029/98JC02147
- Halliwell, G. R. (2004). Evaluation of vertical coordinate and vertical mixing algorithms in the hybrid-coordinate ocean model (hycom). *Ocean Model.* 7, 285–322. doi: 10.1016/j.ocemod.2003.10.002
- Hamilton, P., Lugo-Fernández, A., and Sheinbaum, J. (2016). A loop current experiment: Field and remote measurements. *Dynamics Atmospheres Oceans* 76, 156–173. doi: 10.1016/j.dynatmoce.2016.01.005
- Herbette, S., Morel, Y., and Arhan, M. (2005). Erosion of a surface vortex by a seamount on the  $\beta$  plane. *J. Phys. oceanography* 35, 2012–2030. doi: 10.1175/JPO2809.1
- Hiron, L., de la Cruz, B. J., and Shay, L. K. (2020). Evidence of loop current frontal eddy intensification through local linear and nonlinear interactions with the loop current. *J. Geophysical Research: Oceans* 125, e2019JC015533. doi: 10.1029/2019JC015533
- Hiron, L., Miron, P., Shay, L. K., Johns, W. E., Chassignet, E. P., and Bozec, A. (2022). Lagrangian coherence and source of water of loop current frontal eddies in the gulf of Mexico. *Prog. Oceanography* 208, 102876. doi: 10.1016/j.pocean.2022.102876
- Hoskins, B. J., McIntyre, M. E., and Robertson, A. W. (1985). On the use and significance of isentropic potential vorticity maps. *Q. J. R. Meteorological Soc.* 111, 877–946. doi: 10.1002/qj.49711147002
- Hurlburt, H. E., and Thompson, J. D. (1982). The dynamics of the loop current and shed eddies in a numerical model of the gulf of Mexico. *Elsevier Oceanography Ser.* 34, 243–297. doi: 10.1016/S0422-9894(08)71247-9
- Iskandarani, M., Le Hénaff, M., Thacker, W. C., Srinivasan, A., and Knio, O. M. (2016). Quantifying uncertainty in gulf of Mexico forecasts stemming from uncertain initial conditions. *J. Geophysical Research: Oceans* 121, 4819–4832. doi: 10.1002/2015JC011573
- Jaimes, B., Shay, L. K., Uhlhorn, E., Cook, T. M., Brewster, J., Halliwell, G., et al. (2006). Influence of loop current ocean heat content on Hurricanes Katrina, Rita, and Wilma. In *Proceedings of the 27th Conference on Hurricanes and Tropical Meteorology*. (Monterey, CA, USA), 24–28.
- Leben, R. R. (2005). Altimeter-derived loop current metrics. *Geophysical Monograph-American Geophysical Union* 161, 181. doi: 10.1029/161GM15
- Le Hénaff, M., Kourafalou, V. H., Androulidakis, Y., Ntaganou, N., and Kang, H. (2023). Influence of the caribbean sea eddy field on loop current predictions. *Front. Mar. Sci.* 10, 1129402. doi: 10.3389/fmars.2023.1129402
- Le Hénaff, M., Kourafalou, V. H., Dussurget, R., and Lumpkin, R. (2014). Cyclonic activity in the eastern gulf of Mexico: Characterization from alongtrack altimetry and in situ drifter trajectories. *Prog. Oceanography* 120, 120–138. doi: 10.1016/j.pocean.2013.08.002
- Le Hénaff, M., Kourafalou, V. H., Morel, Y., and Srinivasan, A. (2012a). Simulating the dynamics and intensification of cyclonic loop current frontal eddies in the gulf of Mexico. *J. Geophysical Research: Oceans* 117. doi: 10.1029/2011JC007279
- Le Hénaff, M., Kourafalou, V. H., Paris, C. B., Helgers, J., Aman, Z. M., Hogan, P. J., et al. (2012b). Surface evolution of the deepwater horizon oil spill patch: combined effects of circulation and wind-induced drift. *Environ. Sci. Technol.* 46, 7267–7273. doi: 10.1021/es301570w
- Le Maître, O., and Knio, O. M. (2010). *Spectral methods for uncertainty quantification: with applications to computational fluid dynamics* (Berlin: Springer Science & Business Media).
- Li, G., Iskandarani, M., Le Hénaff, M., Winokur, J., Le Maître, O. P., and Knio, O. M. (2016). Quantifying initial and wind forcing uncertainties in the gulf of Mexico. *Comput. Geosciences* 20, 1133–1153. doi: 10.1007/s10596-016-9581-4
- Liu, Y., Weisberg, R. H., Hu, C., and Zheng, L. (2011). Tracking the deepwater horizon oil spill: A modeling perspective. *Eos Trans. Am. Geophysical Union* 92, 45–46. doi: 10.1029/2011EO60001
- McDonald, M. (2006) *Hycom + ncoda gulf of Mexico 1/25° analysis (goml0.04/expt 20.1)*. Available at: <http://www.hycom.org/data/goml0pt04>.
- Meunier, T., Rossi, V., Morel, Y., and Carton, X. (2010). Influence of bottom topography on an upwelling current: Generation of long trapped filaments. *Ocean Model.* 35, 277–303. doi: 10.1016/j.ocemod.2010.08.004
- Mezić, I., Loire, S., Fonoberov, V. A., and Hogan, P. (2010). A new mixing diagnostic and gulf oil spill movement. *Science* 330, 486–489. doi: 10.1126/science.1194607
- National Academies of Sciences, et al. (2018). *Understanding and predicting the gulf of Mexico loop current: critical gaps and recommendations* (Washington, DC: National Academies Press). doi: 10.17226/24823
- Ntaganou, N., Kourafalou, V., Beron-Vera, F. J., Olascoaga, M. J., Le Hénaff, M., and Androulidakis, Y. (2023). Influence of caribbean eddies on the loop current system evolution. *Front. Mar. Sci.* 10, 961058. doi: 10.3389/fmars.2023.961058
- Oey, L.-Y. (2004). Vorticity flux through the yucatan channel and loop current variability in the gulf of Mexico. *J. Geophysical Research-Oceans* 109. doi: 10.1029/2004JC002400
- Oey, L.-Y. (2008). Loop current and deep eddies. *J. Phys. Oceanography* 38, 1426–1449. doi: 10.1175/2007JP03818.1
- Pichevin, T., and Nof, D. (1997). The momentum imbalance paradox. *Tellus* 49A, 298–319. doi: 10.3402/tellusa.v49i2.14484
- Schmitz, J. W. J. (2003). “Notes on the circulation in and around the gulf of Mexico,” in *A review of the deep water circulation*, vol. i. (TX, USA: Texas A&M University Press, College Station).
- Schmitz, J. W. J. (2005). Cyclones and westward propagation in the shedding of anticyclonic rings from the loop current. *Washington DC Am. Geophysical Union Geophysical Monograph Ser.* 161, 241–261. doi: 10.1029/161GM18
- Sheinbaum, J., Athié, G., Candela, J., Ochoa, J., and Romero-Arteaga, A. (2016). Structure and variability of the yucatan and loop currents along the slope and shelf break of the yucatan channel and campeche bank. *Dynamics Atmospheres Oceans* 76, 217–239. doi: 10.1016/j.dynatmoce.2016.08.001
- Sturges, W., and Evans, J. (1983). On the variability of the loop current in the gulf of Mexico. *J. Mar. Res.* 41, 639–653. doi: 10.1357/002224083788520487
- Sturges, W., Hoffmann, N. G., and Leben, R. R. (2010). A trigger mechanism for loop current ring separations. *J. Phys. Oceanography* 40, 900–913. doi: 10.1175/2009JP04245.1
- Valentine, D. L., Mezić, I., Ma’ce’si’c, S., Crnjari’c’-Zic’, N., Ivi’c, S., Hogan, P. J., et al. (2012). Dynamic autoinoculation and the microbial ecology of a deep water hydrocarbon irruption. *Proc. Natl. Acad. Sci.* 109, 20286–20291. doi: 10.1073/pnas.1108820109
- Vukovich, F. M., and Maul, G. A. (1985). Cyclonic eddies in the eastern gulf of Mexico. *J. Phys. Oceanography* 15, 105–117. doi: 10.1175/1520-0485(1985)015<0105:CEITEG>2.0.CO;2
- Walker, N. D., Pilley, C. T., Raghunathan, V. V., D’Sa, E. J., Leben, R. R., Hoffmann, N. G., et al. (2011). Impacts of loop current frontal cyclonic eddies and wind forcing on the 2010 gulf of Mexico oil spill. *Monit. Modeling Deepwater Horizon Oil Spill: A Record-Breaking Enterprise* 195, 103–116. doi: 10.1029/2011GM001120
- Wang, S., Li, G., Iskandarani, M., Le Hénaff, M., and Knio, O. M. (2018). Verifying and assessing the performance of the perturbation strategy in polynomial chaos ensemble forecasts of the circulation in the gulf of Mexico. *Ocean Model.* 131, 59–70. doi: 10.1016/j.ocemod.2018.09.002
- Zavala-Hidalgo, J., Morey, S. L., and O’Brien, J. J. (2003). Cyclonic eddies northeast of the campeche bank from altimetry data. *J. Phys. oceanography* 33, 623–629. doi: 10.1175/1520-0485(2003)033<0623:CENOTC>2.0.CO;2



## OPEN ACCESS

## EDITED BY

Weifeng (Gordon) Zhang,  
Woods Hole Oceanographic Institution,  
United States

## REVIEWED BY

Huijie Xue,  
University of Maine, United States  
Nabi Allahdadi,  
North Carolina State University, United States

## \*CORRESPONDENCE

Erick R. Olvera-Prado  
✉ [erolvera@izt.uam.mx](mailto:erolvera@izt.uam.mx)

RECEIVED 14 March 2023

ACCEPTED 29 January 2024

PUBLISHED 15 February 2024

## CITATION

Olvera-Prado ER, Morey SL and  
Chassignet EP (2024) Contribution of the  
wind and Loop Current eddies to the  
circulation in the western Gulf of Mexico.  
*Front. Mar. Sci.* 11:1185849.  
doi: 10.3389/fmars.2024.1185849

## COPYRIGHT

© 2024 Olvera-Prado, Morey and Chassignet.  
This is an open-access article distributed under  
the terms of the [Creative Commons Attribution  
License \(CC BY\)](https://creativecommons.org/licenses/by/4.0/). The use, distribution or  
reproduction in other forums is permitted,  
provided the original author(s) and the  
copyright owner(s) are credited and that the  
original publication in this journal is cited, in  
accordance with accepted academic  
practice. No use, distribution or reproduction  
is permitted which does not comply with  
these terms.

# Contribution of the wind and Loop Current eddies to the circulation in the western Gulf of Mexico

Erick R. Olvera-Prado<sup>1,2,3\*</sup>, Steven L. Morey<sup>3,4</sup>  
and Eric P. Chassignet<sup>3</sup>

<sup>1</sup>Departamento de Ingeniería de Procesos e Hidráulica, CBI, Universidad Autónoma Metropolitana - Iztapalapa, Mexico City, Mexico, <sup>2</sup>Instituto de Ciencias de la Atmósfera y Cambio Climático, Universidad Nacional Autónoma de México, Mexico City, Mexico, <sup>3</sup>Center for Ocean-Atmospheric Prediction Studies, Florida State University, Tallahassee, FL, United States, <sup>4</sup>School of the Environment, Florida Agricultural and Mechanical University, Tallahassee, FL, United States

The roles of the Loop Current (LC) and associated eddies in driving the circulation of the Gulf of Mexico (GoM) have been investigated for several decades from different perspectives. Nevertheless, a clear understanding of the relative contributions of the wind forcing and the Loop Current eddies (LCEs) to the GoM circulation and variability remain lacking. In this study, the roles of these two factors in sustaining the less well-known western GoM upper-layer (~1000 m) circulation are investigated with two numerical experiments using the HYbrid Coordinate Ocean Model (HYCOM). First, we examine the relative contributions of the wind and LCEs in setting the mean circulation in the western GOM. We then perform a vorticity balance to analyze the relative importance of the physical processes, including the wind stress, involved in sustaining the western GoM circulation. The results show that the wind stress contributes to a mean anticyclonic circulation in the central and northwestern Gulf, while in the southwestern subregion both wind and LCEs combine to induce a cyclonic circulation, highlighting the role of wind stress curl and topographic confinement. The vorticity balance analysis conducted in the upper layer of the western basin shows that planetary vorticity and stretching are primarily responsible for the balance in time scales longer than weeks, and their co-variability are good indicators of LCEs entering the central and northwestern subregions. However, the southwestern subregion is primarily driven by vortex stretching. Mean advection of vorticity and planetary vorticity are also contributors to the time-averaged vorticity field. Since the wind stress is distributed over the upper layer of the GoM, direct input of vorticity in the regional vorticity balance is negligible, but it does play a role through the vortex stretching term. The results also suggest that wind forcing acts to produce larger, faster moving, and longer-lived anticyclonic eddies that impact the western Gulf and modulate the circulation over monthly timescales.

## KEYWORDS

Gulf of Mexico, Loop Current eddies, wind forcing, ocean modeling, vorticity balance

# 1 Introduction

The Gulf of Mexico (GoM) is a semi-enclosed sea located in the western Atlantic Ocean, connected with the Caribbean Sea through the Yucatan Channel and with the North Atlantic Ocean through the Florida Straits (Figure 1). The circulation in the basin is forced at the surface by the wind stress, and to a lesser degree by heat and freshwater fluxes, and at the Yucatan Channel by the Yucatan Current. The Yucatan Channel flow is driven by the western boundary current of the North Atlantic Subtropical Gyre, an anticyclonic circulation forced by the northward compensation of the Sverdrup transport due to the wind stress curl, and the surface component of the meridional overturning cell (Schmitz et al., 2005), yielding a mean transport of  $27.0 \pm 0.5$  Sv ( $1 \text{ Sv} = 10^6 \text{ m}^3 \text{ s}^{-1}$ ) (Athié et al., 2015; Rousset and Beal, 2010; Sheinbaum et al., 2002). In the eastern GoM, the Yucatan Current enters the GoM through the Yucatan Channel and forms an anticyclonic looping circulation, the Loop Current (LC), which, in its extended phase, intrudes further north and episodically sheds large warm-core anticyclonic vortices called Loop Current eddies (LCEs). These LCEs have a time interval between separation events (referred to as LCE separation period) observed to range from a few weeks to 18–19 months (Sturges and Leben, 2000; Leben, 2005; Vukovich, 2012). LCEs have diameters of about 300 km or more (Vukovich, 2012), an average westward propagation speed of  $4.4 \pm 2.9$  km/day (Leben, 2005; Vukovich, 2007) and lifetimes of months to approximately a year (Elliott, 1982; Frolov et al., 2004). The LC exits the basin through the Florida Straits becoming the Florida Current and then the Gulf Stream.

The upper layer circulation of the western Gulf is commonly described in two subregions with different behavior: the northwestern region is dominated by an anticyclonic circulation and the presence of mesoscale eddies (LCEs) (Vidal et al., 1994), and the Bay of Campeche in the south, characterized by a cyclonic circulation known as the Campeche Gyre (Vázquez de la Cerda et al., 2005;

Perez-Brunius et al., 2013; Olvera-Prado et al., 2023b). It has been shown that circulation on the shelves presents strong seasonality driven by the wind (Zavala-Hidalgo et al., 2003; Morey et al., 2005). Through an analysis using self-organizing maps, Meza-Padilla et al. (2019) extracted circulation patterns from modeled salinity and current fields in the western GoM and confirmed the dominant role of LCEs over local and regional dynamics as suggested by previous studies. By comparing different sources of observational data, Sturges (2020) found that the mean near-surface flow in the southwestern GoM depicts an east-west direction with values  $\sim 10$  cm/s or more, and no clear evidence of a near-surface return flow back to the east. In the northwestern part, the author found that mean flow is not significantly different from zero, and transport to the west from LCEs is possibly returned in a deep boundary flow driven by the rectification of deep topographic Rossby waves.

Vázquez de la Cerda et al. (2005) presented strong evidence of a mean cyclonic gyre in the Bay of Campeche likely forced by the positive wind stress curl that prevails in this region throughout the year (Figure 2F), using oceanographic observations available at the time. Other studies suggest that the LCEs collapsing against the western boundary influence the cyclonic circulation in the Bay in an irregular manner. Vidal et al. (1992), concluded that the collision of a LCE with the southwestern continental shelf led to a transfer of mass and angular momentum to the south, thereby producing a cyclonic eddy. Also, Romanou et al. (2004) suggest that the cyclonic circulation in the Bay is caused by accretion of cyclones generated in the western Gulf by interaction of LCEs with the continental slope. Using a set of observations, Perez-Brunius et al. (2013) provided further evidence that the cyclonic gyre is vertically coherent, extending below 1000 m and confined to the deep western basin. The authors concluded that the cyclonic gyre results from the contributions of wind stress curl and topographic confinement via conservation of potential vorticity in an equivalent barotropic flow but suggest the need to determine the role the wind plays in the

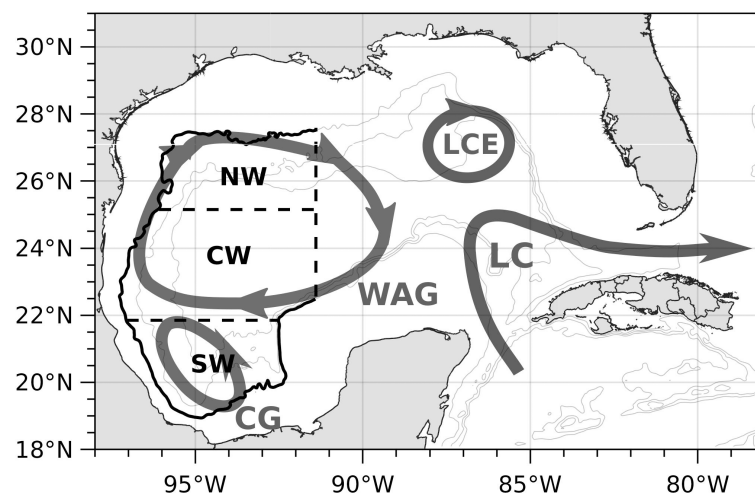


FIGURE 1

Schematic of the major upper layer circulation patterns in the GoM: The Loop Current (LC), Loop Current eddy (LCE), the Western Anticyclonic Gyre (WAG) and the Campeche Gyre (CG). The boundaries of the three western subregions are also shown in in black lines. The gray contours represent the 1000-, 2000-, and 3000-m isobaths.



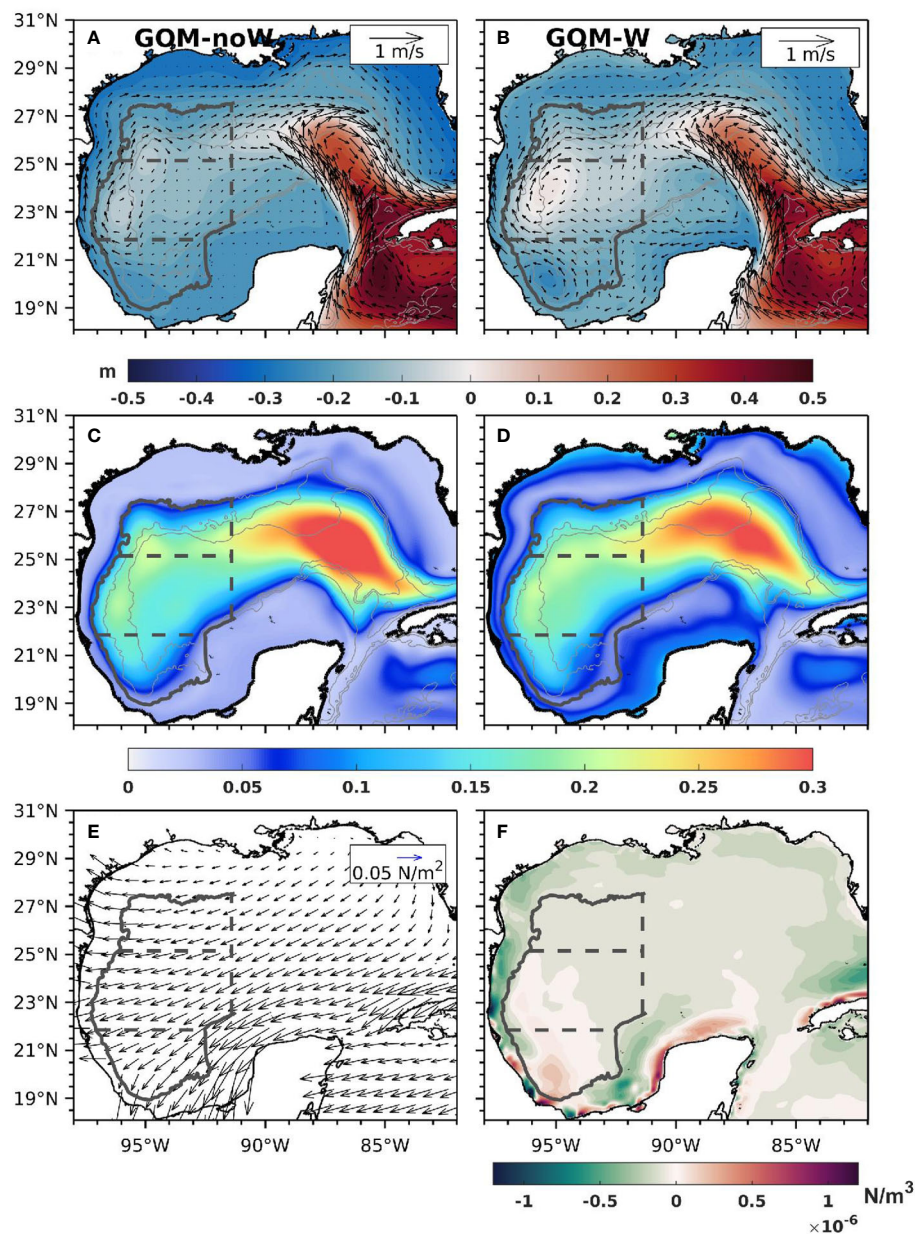


FIGURE 2

(A, B) Mean surface velocity vectors and SSH contours for experiments GOM-noW and GOM-W respectively; standard deviation of the SSH from (C) GOM-noW and (D) GOM-W (E) mean wind stress vectors and (F) mean wind stress curl. Gray contours in a-d represent the 1000-, 2000-, and 3000-m isobaths.

seasonal modulation of the cyclonic circulation. Their data also suggest that the intraseasonal variability of the surface currents are mainly due to changes in the position, size and intensity of the cyclonic gyre, influenced by energetic LCEs impacting the western boundary. Using a set of numerical simulations, [Olvera-Prado et al. \(2023b\)](#) found that the wind is the dominant factor modulating the seasonal variability of the Campeche Gyre. The LCEs and associated cyclonic circulations also contribute to the non-seasonal component of the flow in the Bay of Campeche when they collide with the western boundary.

Comparatively, studies on the relative contributions of the wind and the LC-induced circulation for the entire GoM are scarce. Early

studies suggested that the wind stress ([Figure 2E](#)) and basin geometry of the GoM seem suitable for the development of a Western Boundary Current from the combined effects of LCEs and large-scale wind stress curl forcing ([Figure 2F](#)) ([Sturges and Blaha, 1976](#)), although the relative importance of such forcings was not fully understood. Fundamental work by [Elliott \(1982\)](#) of LC versus wind energy sources indicate that although the energy contribution of the wind stress and LC rings is about the same ( $2.8 \times 10^4 \text{ Jm}^{-2}$  and  $5.1 \times 10^4 \text{ Jm}^{-2}$ , respectively), the wind stress energy is a basin-wide value, whereas the ring's available potential energy is concentrated into a smaller length scale consistent with the north-south scale of the current. Contrary to [Elliott \(1982\)](#)



deductions, Sturges (1993) examined their relative contribution by focusing on the annual cycle of the estimated flow as deduced from a compilation of ship drift data and concluded that the western boundary current is driven by the annual variation in wind stress curl augmented by Ekman Pumping, with the flow along the current strongest in July and weakest in October. He also found evidence that LCEs shed from the Loop Current had no annual periodicity, so they make no significant contribution to the long-term annual signal. Vidal et al. (1999), through an analysis of the geostrophic circulation in the western Gulf during summer in 1985, found that the western boundary current is formed by conservation of angular momentum produced by the collision of LCEs against the western boundary and concluded that in the presence of a LCE, the wind-driven background circulation is overwhelmed. Lee and Mellor (2003) noted that, in addition to wind forcing, their model-determined anticyclonic upper-level circulation in the western Gulf is strongly influenced by the average contribution of LCEs propagating to the west while dispersing anticyclonic vorticity. The bulk of these previous studies suggest that seasonal flow in the western GoM is wind forced, but that a detailed quantitative determination of the partitioning between the wind and eddy contributions to the mean flow is needed (Perez-Brunius et al., 2013; Zavala-Hidalgo et al., 2014).

In this study, we investigate the relative importance of the wind and the LCEs in driving the circulation of the western GoM using a set of two long-term, free-running numerical simulations conducted with the HYbrid Coordinate Ocean Model (HYCOM), in which we isolate the effects of these processes to discern their relative contributions. First, the separate and joint effect of the wind and LCEs is examined through calculation of a circulation index in three subregions defined over deep waters (>1000 m) in the western GoM: north-western (NW), central-western (CW), and south-western (SW) (Figure 1). Results from this calculation show that wind forcing reverses the mean circulation in the NW subregion from weakly cyclonic in the non-wind forced simulation to weakly anticyclonic, similarly enhances the anticyclonic circulation in the CW subregion, and forces the cyclonic circulation in the SW subregion. Next, a vorticity balance is performed over these subregions to analyze the contributions of the different terms in the balance and their relationships with the physical processes occurring in the region, including the wind and LCEs. This analysis clarifies the relative roles of wind forcing and eddies in governing the vorticity budget of the upper 1000 m in the western GoM subregions. Wind forcing impacts the vorticity budget through the vortex stretching, with eddies contributing to the modulation of the vorticity on monthly timescales. The layout of this paper is as follows: In section 2, the numerical setup is described, together with a quantification of the impact of atmospheric forcing on LCE metrics. The relative contributions of the wind and LCEs to the circulation of the western GoM are addressed in section 3. In section 4, a vorticity balance analysis is used to infer the roles of different processes in sustaining the circulation of the western GoM over different time scales. Finally, a summary of the results and conclusions are presented in section 5.

## 2 Methods and data

### 2.1 The numerical simulations

To address the contributions of the wind and mesoscale processes to the circulation in the western GoM, two free-running (i.e., no data assimilation) simulations were conducted in the GoM region with HYCOM (Wallcraft et al., 2009). HYCOM uses a generalized hybrid vertical coordinate system that allows vertical coordinates to follow isopycnal layers in the deep stratified ocean and transition to pressure coordinates or terrain-following coordinates in unstratified regions or coastal areas, respectively (Bleck and Boudra, 1981; Bleck, 2002; Chassignet et al., 2003; Chassignet et al., 2006). The regional HYCOM GoM domain is equivalent to the one used by Dukhovskoy et al. (2015) and Laxenaire et al. (2023), configured from 18°N to 32°N and 98°W to 77°W (Figure 1), therefore covering the northwestern Caribbean Sea and part of the western North Atlantic Ocean, with a 1/25° horizontal resolution (~3.8–4.2 km) and 36 hybrid vertical layers, which are mainly isopycnal layers in the open ocean below the mixed layer and z-layers within it. Both simulations use monthly climatology open boundary conditions constructed from the 22-year (1994–2015) 1/12° Global Ocean Forecasting System 3.1 reanalysis GLBb0.08-53.X (Metzger et al., 2017). The target densities, which define the vertical grid in the model, are inherited from the global reanalysis. Sea surface salinity and sea surface temperature are restored to monthly climatological values from the Generalized Digital Environmental Model v. 4.

Both simulations share the specifications mentioned above, however, their main features are listed below:

- Experiment GOM-W is the control run since it is the most realistic simulation with wind forcing. Following spin-up, hourly 10-m wind speed is prescribed using the Climate Forecast System Reanalysis (Saha et al., 2010) from 1997–2015 that has a horizontal resolution of 38 km. The wind stress  $\tau$  is calculated using bulk formulae during model run time taking into account the surface current speed.

$$\tau = \rho C_D |U_{10} - U_{curr}| (U_{10} - U_{curr}) \quad (1)$$

where  $\tau$  is the wind stress vector,  $\rho$  is the density of the air,  $U_{10}$  is the wind vector at 10 m,  $U_{curr}$  is the ocean surface velocity vector, and  $C_D$  is obtained from an approximation to the COARE 3.0 bulk algorithm (Fairall et al., 2003).

- Experiment GOM-noW is the model experiment with no wind forcing. The wind forcing is turned off to discern the influence of LCEs in the absence of wind forcing.

With the approach described above, we ensure that both experiments are equivalent, except for the wind. The input of vorticity through wind forcing was shown by Ohlmann et al. (2001) to be of the same order of magnitude as LCEs on long time scales. They estimated that the mean vorticity flux along the western GoM due to LCEs is  $6.3 \times 10^{-14} \text{ s}^{-2}$ , while the mean vorticity flux due to wind stress curl in the same region is  $4.0 \times 10^{-14} \text{ s}^{-2}$ .

Both experiments were initialized from the global reanalysis mean state for January 1994, and they were run from 1994 to 2015

(22 years) with outputs saved daily. The vertical viscosity and diffusivity through the water column are prescribed with the K-profile parameterization (KPP; Large et al., 1994). The KPP parameters take into account the contributions of: a) resolved shear instability, b) unresolved shear instability due to the background wave field, and c) double diffusion. For more details on the numerical setup, the reader is referred to Dukhovskoy et al. (2015); Laxenaire et al. (2023), and Olvera-Prado et al. (2023b). The control experiment (GOM-W) was thoroughly validated against altimetry and *in-situ* observations in Olvera-Prado et al. (2023b). The evaluation showed realistic LC variability, including LC

extension (Figures 3E, F) and area (Figures 3G, H), and distribution of LCE separation period (Figure 3C), monthly occurrence (Figure 3D) and trajectories (Figures 3A, B). The Yucatan Channel flow structure and transport comparisons with data were also in good agreement. Finally, the model was shown to successfully resolve the mean deep circulation patterns and energy fields previously reported by observational studies. It is important to note that since identical open boundary conditions are prescribed in both simulations, and owing to the facts stated above, the role of the wind in modifying some of the LC and LCE characteristics can be isolated and, thus, evaluated.

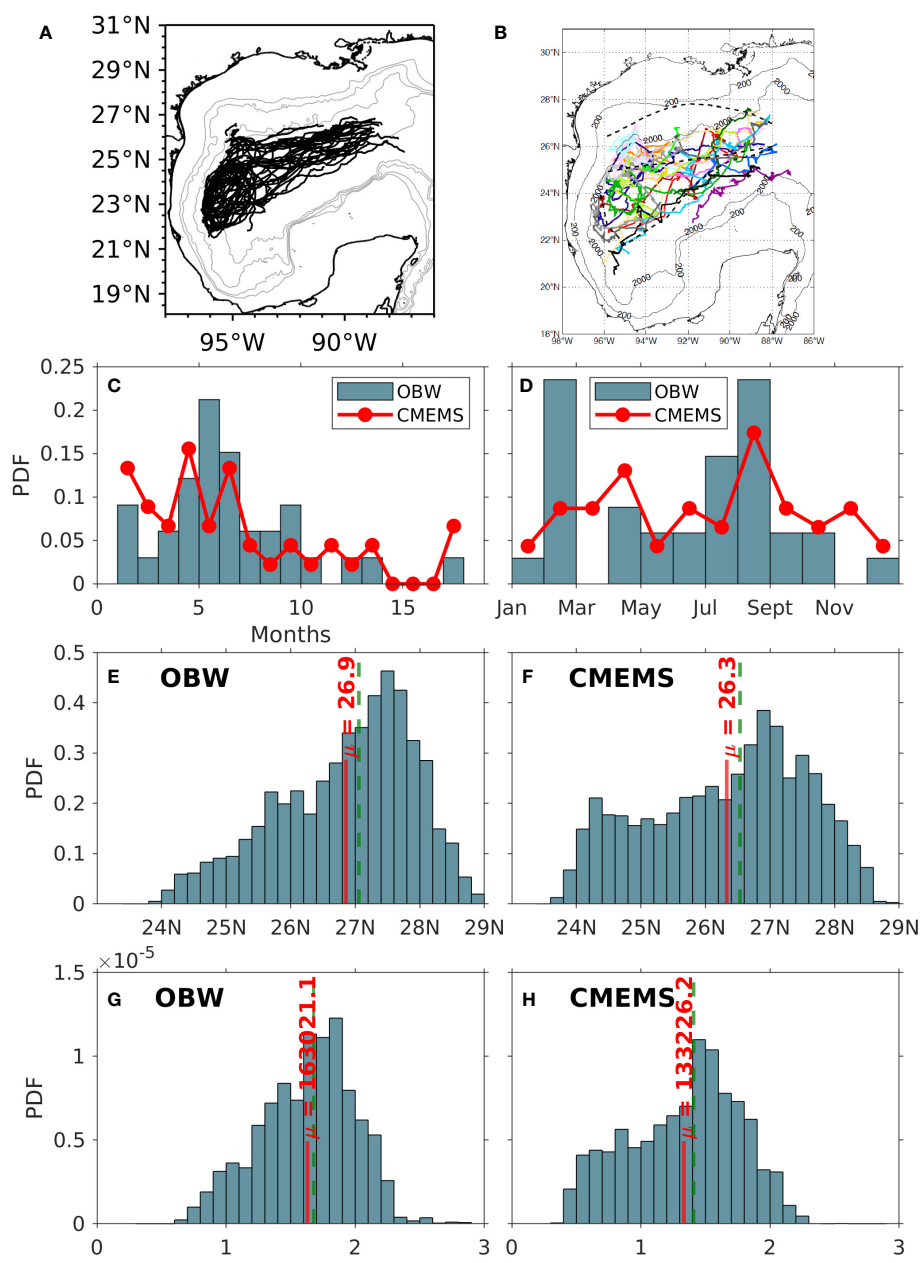


FIGURE 3

Trajectories of every LCE from (A) HYCOM and (B) observations (from Donohue et al. (2008)). Comparison between OBW model control run outputs and the CMEMS database for normalized histograms of (C) LCE separation period and (D) monthly occurrence. Normalized histograms of LC northernmost latitude penetration from (E) model outputs and (F) CMEMS. Normalized histograms of LC area ( $\times 10^5$  km<sup>2</sup>) from (G) model outputs and (H) CMEMS (from Olvera-Prado et al., 20023b).

The impact of the wind forcing on LCE metrics was evaluated by tracking the LC and LCE fronts using the 0.17-m contour in the 22-year record of the demeaned sea surface height (SSH) fields for experiments GOM-W and GOM-noW (Leben, 2005; Dukhovskoy et al., 2015; Olvera-Prado et al., 2023b). Results from the objective tracking technique identified a total of 37 and 36 separation events for experiments GOM-W and GOM-noW, respectively. The mean LCE separation period, which is the time between two consecutive separation events, is 7 months with a median of 6.2 months for experiment GOM-W. Meanwhile for experiment GOM-noW, the mean separation period is 7 months with a median of 6.6 months. Overall, there is good agreement in the distribution of the LCE separation period between experiment GOM-W and the observations (Sturges and Leben, 2000).

Although the shape and size of a mesoscale eddy generally evolve during its life cycle, here the area of the LCE is used as an overall measure of size and provides some insight on the impact of wind forcing on the LCEs. Table 1 shows the mean LCE area from detachment until death for experiments GOM-W and GOM-noW. The mean value of each distribution indicates that GOM-W LCEs are, on average, slightly bigger with wind forcing when compared to GOM-noW ( $3.75 \times 10^4 \text{ km}^2$  versus  $3.22 \times 10^4 \text{ km}^2$ ). The mean lifetimes for the LCEs are roughly 252 and 237 days with standard deviations of 122 and 103 days for experiments GOM-W and GOM-noW, respectively (Table 1). These values fall within published estimates of ~6 months to one year (Elliott, 1982; Frolov et al., 2004). Mean westward propagation speeds are 3.6 and 3.12 km/day with standard deviations of 1.31 and 0.78 km/day for GOM-W and GOM-noW, respectively. These results are comparable to several previous observational and numerical studies (Leben, 2005; Vukovich, 2007, and more) based on the westward long Rossby wave speed around these latitudes. The above suggests that, statistically, the cumulative effect of the local large-scale wind tends to increase the LCE size, lifespan, speed and distance traveled before dissipation, as well as to modify the eddy shedding period. This means that the eddies in the simulation with atmospheric forcing (GOM-W) are likely to more strongly impact the circulation in the western Gulf, which is consistent with the increase seen in SSH variability along the LCE westward pathway in the GOM-W simulation over the GOM-noW simulation (Figure 2). The SSH variability is, however, smaller in GOM-W when compared to the GOM-noW experiment (Figure 2) in agreement with Chaichitehrani and He (2024) who state that the wind stress work over the GoM is negative due to the relative wind stress (Equation 1) and associated eddy killing effect (Larrañaga et al., 2022).

It is important to note that, since the background wind-driven circulation is absent in the western Gulf of Mexico when the wind

forcing is turned off, one does expect differences in the time evolution of the LC and LCE characteristics as shown above. This is not an entirely new result, since Oey et al. (2003) found that the wind-induced transport fluctuations through the Greater Antilles Passages cause LCE shedding to be more frequent (3–7 months). Meanwhile Chang and Oey (2012) found that the seasonal signal of the wind over the GoM and Caribbean Sea can modify the Yucatan Channel transport, inducing favorable conditions for eddy shedding in summer and winter. More recently, Chaichitehrani and He (2024), using a set of atmospheric and oceanic reanalysis, confirmed the role of the easterly winds over the Caribbean Sea in modulating the Yucatan Channel transport, which in turn is correlated with major eddy shedding events. The impact of the wind stress curl in the western Gulf of Mexico on the eddy pathway and mean circulation is further discussed in section 3.

## 2.2 Circulation index

To quantify the circulation in the Gulf, an index is computed over the pre-defined subregions of the western Gulf (Figures 1 and 2) over deep waters (>1000 m): north-western (NW), central-western (CW), and south-western (SW). The definition of these subregions is based on the analysis of Vukovich (2007), who defines three mean paths in the GoM (northern, central and southern paths, his figure 17) based on the paths that LCEs follow during their western propagation once they separate from the LC and whose final fates fall within the subregions. We choose to compute the index over the upper 1000 m, since it represents a typical depth of the main thermocline in the GoM and the Atlantic (Liu and Tanhua, 2021), where the signature of the wind-driven currents like the LC (and the Gulf Stream) extends. Furthermore, the 1000 m depth also corresponds to the depth of the first baroclinic mode crossing and, thus, we can assume that the circulation in the GoM is reasonably well represented by a two-layer system with an upper layer of 1000 m (Hamilton, 2009). We can then compute the depth-averaged area-integrated relative vorticity of the upper layer, i.e., the Circulation Index (CI). According to the Stokes' theorem, the circulation (Equation 2),  $\Gamma$ , defined by the line integral of the velocity field around a closed curve  $C$ , can be computed from the area integral of the vorticity over the area enclosed by the curve  $A$  as

$$\Gamma \equiv \oint_C \mathbf{u} \cdot d\mathbf{s} = \int_A (\nabla \times \mathbf{u}) \cdot d\mathbf{A} \quad (2)$$

For this calculation, the 1000 m depth-averaged velocities are used and  $\Gamma$  becomes the CI. The CI is computed individually in each of the western basin subregions delimited by the dashed lines in Figures 1 and 2: NW, CW and SW.

TABLE 1 Mean LCE properties for experiments GOM-noW and GOM-W.

Experiment	# events	Area ( $\times 10^4 \text{ km}^2$ )	Lifespan (days)	Translation speed (km/day)	Distance (km)
GOM-W	38	3.79 (1.66)	255 (118)	3.5 (1.27)	1412 (450)
GOM-noW	36	3.22 (1.66)	237 (103)	3.12 (0.78)	1285 (311)

Numbers in parentheses indicate the standard deviations.

## 2.3 Upper ocean vorticity balance

Analysis of the vorticity budget through calculation of the different terms in the vorticity equation has been used to elucidate the roles of different physical processes in governing the circulation of many ocean regions in numerical model studies (e.g., Boudra and Chassignet, 1988; Murray et al., 2001; Azevedo Correia de Souza et al., 2015). Understanding the upper ocean vorticity balance in the GoM provides insight into the conditions under which the circulation is driven by certain processes, such as those associated with the wind and the LCEs. For this study, the vorticity balance Equation 3 is derived from the momentum equation given by

$$\begin{aligned} \frac{\partial \mathbf{v}}{\partial t} + \nabla \cdot \frac{\mathbf{v}^2}{2} + (\zeta + f)\mathbf{k} \times \mathbf{v} \\ = -\nabla M + \alpha \frac{\partial \tau}{\partial p} + (\Delta p)^{-1} \nabla \cdot (\nu \Delta p \nabla \mathbf{v}) \end{aligned} \quad (3)$$

where  $\mathbf{v}$  is the horizontal velocity vector ( $u, v$ ),  $\zeta$  is the relative vorticity,  $f$  is the Coriolis parameter,  $\mathbf{k}$  is vertical unit vector,  $M = z + \rho\alpha$  is the Montgomery Potential,  $\alpha$  is the specific volume of water,  $\tau$  is the wind stress,  $\nu$  is the horizontal turbulent viscosity and  $\Delta p$  is the layer thickness. Taking the vertical component from the curl of Equation 3, yields the differential form of the relative vorticity equation. Then, it is possible to estimate the contribution of different forcing terms to the vorticity balance, calculated at each model grid point.

$$\begin{aligned} \frac{\partial \zeta}{\partial t} = \underbrace{-\mathbf{v} \cdot \nabla \zeta}_{ADV} - \underbrace{\nu \beta}_{BETA} - \underbrace{(\zeta + f) \cdot \nabla \cdot \mathbf{v}}_{STRCH} \\ + \underbrace{\alpha \nabla \times \tau_z}_{WIND} + \underbrace{\nabla \times \{(\Delta p)^{-1} \nabla \cdot (\nu \Delta p \nabla \cdot \mathbf{v})\}}_{VISC} \end{aligned} \quad (4)$$

where, in addition to the terms described above,  $\beta$  is the meridional gradient of  $f$ . On the right hand side of Equation 4, the first term is the advection of relative vorticity (ADV); the second term is the advection of planetary vorticity (BETA); the third term is the vortex stretching (STRCH); the fourth term is the wind stress curl (WIND) and the fifth term is the viscous stress curl (VISC). Equation 4 is then discretized in a similar fashion to the Boudra and Chassignet (1988) application for the Agulhas region, i.e.,

$$\begin{aligned} \frac{\partial \zeta}{\partial t} = -\overline{u^{xy} \Delta_x \zeta^x} - \overline{v^{xy} \Delta_y \zeta^y} - \overline{v^{xy} \Delta_y f^y} - (\zeta + f) \Delta_x u + \Delta_y v^{xy} \\ + \alpha (\Delta_x \{(\Delta p^y)^{-1} \tau_y\} - \Delta_y \{(\Delta p^x)^{-1} \tau_x\}) \\ + \nu (\Delta_x \{\Delta_x^2 v + \Delta_y^2 v\} - \Delta_y \{\Delta_x^2 u + \Delta_y^2 u\}) \end{aligned} \quad (5)$$

where the  $\Delta_{(x,y)}$  () operator is the difference between () at neighboring grid points divided by the  $(x,y)$ -directions grid distance. Similarly  $\overline{()}$  is an average of () over consecutive grid points.

## 3 Contribution of wind and LCEs to the GoM mean circulation

We first address the relative importance of the wind and eddy-driven circulation in the GoM by examining the mean circulation obtained averaging the 22 years of daily output for each experiment. Figure 2 shows the maps of mean surface velocity and SSH for experiments GOM-noW (a) and GOM-W (b).

Experiment GOM-noW depicts a narrow area of high pressure, extending from the LC through the central-western subregion which mimics the south-west trajectory of LCEs once they detach from the LC, represented by light blue color (negative anomalies after demeaning). An interesting result is the absence of a surface cyclonic circulation associated with a low in dynamic height representing the Campeche Gyre in the Bay of Campeche for experiment GOM-noW. This suggests that the latter is primarily wind-driven (Figure 4). Experiment GOM-W shows a broader anticyclonic circulation over the central- and north-western subregions (Figure 2B) located from 90°W to the western boundary and from 20°N to the northern boundary of the domain covering an area of approximately 700 x 500 km. This difference with GOM-noW is consistent with the role of the negative wind stress curl that prevails over the region (Figure 2F). In the Bay of Campeche, bound to the west, the semi-permanent cyclonic circulation is shown with center at 95.5°W, 20°N and is represented by dark blue (a low in dynamic height) in Figure 2B. Higher values of SSH standard deviation extending westward of 90°W is a manifestation of the larger and longer-lived LCEs found in the wind-forced simulation (Figures 2C, D).

The time series of CI (not shown) for the GOM-W and GOM-noW experiments show no marked seasonal cycle; therefore, we focus on the average CI value for each subregion represented with a bar chart in Figure 5. Focusing first on the NW subregion, it is observed that experiment GOM-noW produce a cyclonic circulation on average with mean CI =  $0.8 \times 10^4 \text{ m}^2/\text{s}$ , while for experiment GOM-W, the mean CI is =  $-0.5 \times 10^4 \text{ m}^2/\text{s}$  meaning that the average circulation is anticyclonic. Now, if the western GoM circulation can be thought as an eddy-induced flow superimposed over the wind driven circulation, it could be said that in the NW subregion the eddy-driven flow is slightly cyclonic on average, and changes to slightly anticyclonic with the inclusion of wind. Second, in the CW subregion, both experiments produce an anticyclonic circulation (negative CI mean), somewhat expected since it is observed on the horizontal maps of time-averaged velocity and SSH. The anticyclonic circulation is somewhat stronger in the presence of wind (experiment GOM-W). Using the same analogy as above, it could be said that wind tends to strengthen the anticyclonic circulation as seen in the more negative value of the mean CI of experiment GOM-W (red bar). Finally, in the SW subregion, both experiments produce a cyclonic circulation on



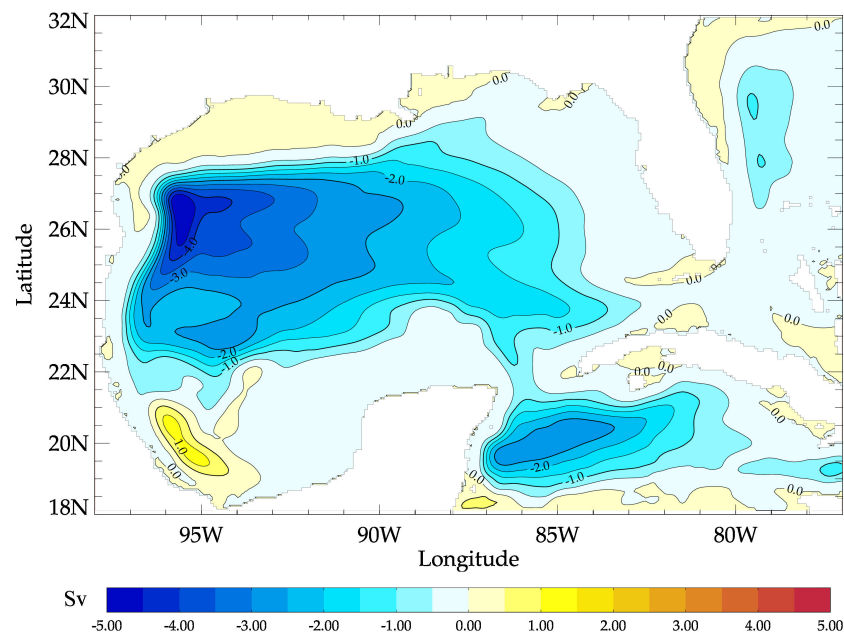


FIGURE 4  
Wind-induced linear Sverdrup circulation computed as in Townsend et al. (2000).

average (positive CI mean) verifying the presence of the quasi-permanent gyre in the western region, a result also expected. It is noteworthy, however, that the CI is more positive in the experiment with wind (GOM-W) by a factor of approximately 3 times the standard deviation, demonstrating the importance of the wind stress curl in strengthening the Campeche Gyre. This result suggests that the Campeche gyre is the result of the contribution of, at least, 2 processes: one being the strong cyclonic circulation produced by the positive wind stress curl that prevails over the region throughout the year (Figures 2F, 4) and the other the average contribution of the large cyclones accompanying the LCEs that eventually enter the Bay (Olvera-Prado et al., 2023b).

The relative role of the wind stress in determining the circulation of the western GoM can be further understood by considering the linear response of the ocean to the large-scale, low-frequency wind forcing, or the Sverdrup circulation (Figure 4) as in Townsend et al. (2000). Barotropic Sverdrup transport streamlines show an anticyclonic circulation strongest in the NW subregion (about 5 Sv) weakening over the CW subregion. This result is consistent with the reversing of the mean circulation from weakly cyclonic to anticyclonic with the addition of wind to the nonlinear HYCOM simulation and slightly strengthening the anticyclonic circulation in the CW subregion (Figure 5). A strong barotropic Sverdrup circulation is induced by the wind in the SW subregion, again consistent with the profound strengthening of the cyclonic circulation in this region when wind forcing is added to the nonlinear HYCOM simulation (Figure 5).

## 4 The vorticity balance in the western Gulf of Mexico

### 4.1 Time-mean vorticity balance

Determining the dominant balances of terms of the vorticity equation aids in understanding the physical mechanisms that govern the mean and variability of the circulation. This analysis examines the time-mean upper-layer vorticity balance in the NW, CW, and SW subregions of the GoM extending seaward of the 1000 m isobath. First, all the variables of Equation 5 are depth-averaged over the upper 30 layers of the model, corresponding to an upper layer extending down to a mean depth of approximately 1000 m, with the exception of the wind stress  $\tau$ , which is a surface variable.

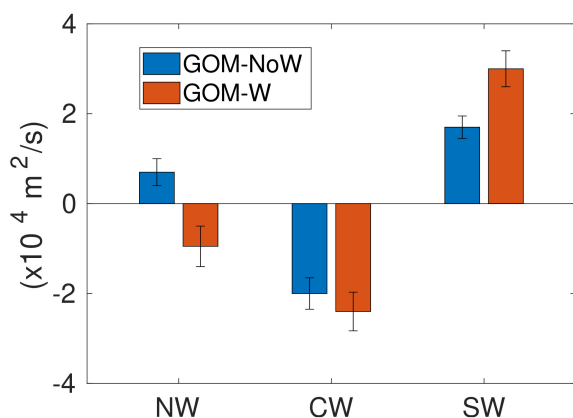


FIGURE 5  
Mean circulation index computed in the three sub-regions for experiments GOM-noW (blue) and GOM-W (red). Error bars indicate one standard deviation.

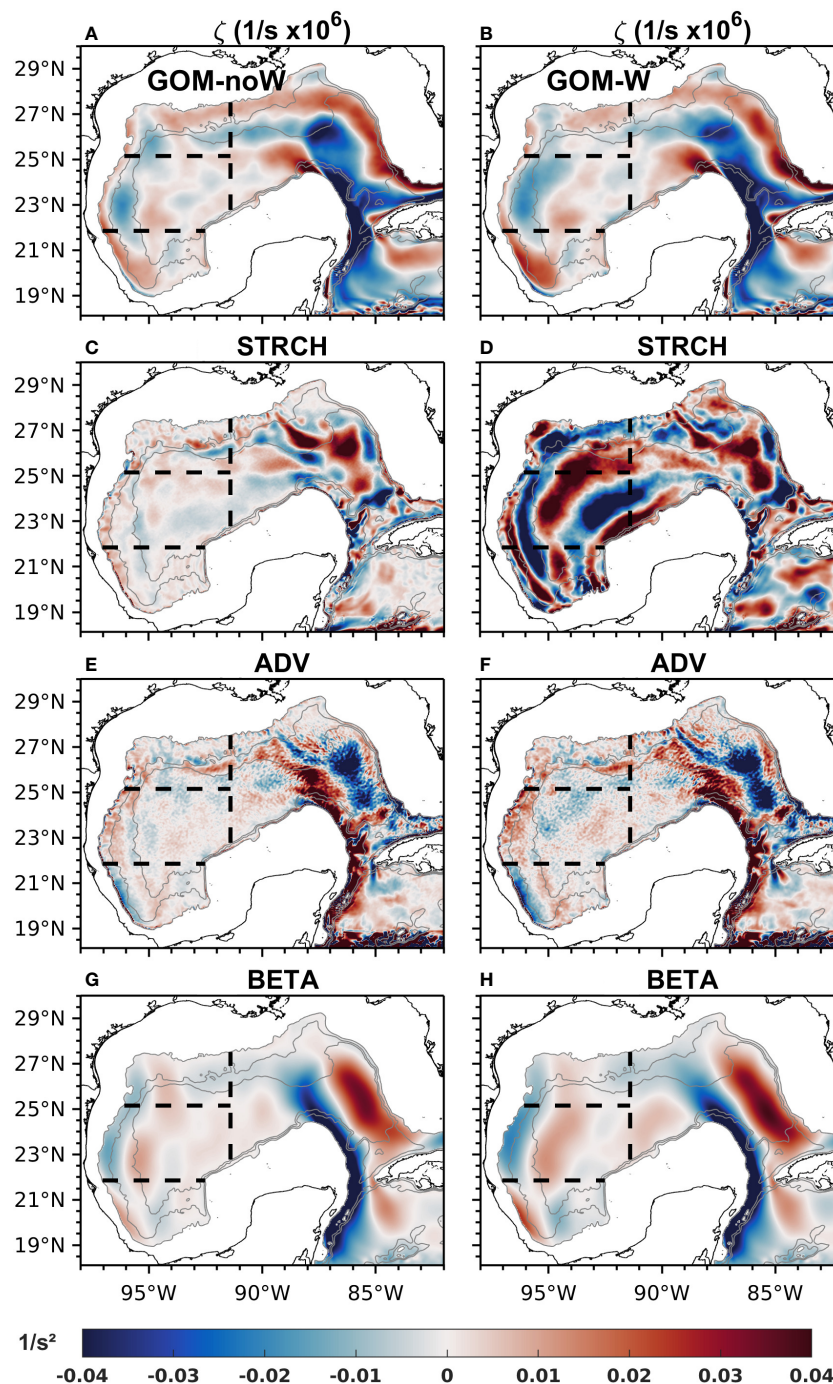


FIGURE 6

Mean maps of upper-layer relative vorticity derived from modeled velocity for experiments (A) GOM-noW and (B) GOM-W; stretching for (C) GOM-noW and (D) GOM-W; advection of vorticity for (E) GOM-noW and (F) GOM-W and; planetary vorticity advection for (G) GOM-noW and (H) GOM-W. Gray contours represent the 1000, 2000 and 3000 m isobaths, and black dashed lines the limits of the NW, CW and SW subregions.

Then, the time-averaged spatial fields of the terms in Equation 5 are compared for experiments GOM-noW and GOM-W.

Focusing on the western Gulf, the mean relative vorticity for experiment GOM-noW (Figure 6A) shows an anticyclonic maximum in the CW subregion (negative values in blue) centered at 96°W and 23°N, which is accompanied with small regions of negative and positive relative vorticity. In fact, a secondary maximum of cyclonic vorticity (positive values in red) is observed

to the east of the anticyclonic maximum. The location of this secondary maximum suggests that it may be the result of two processes, one is the barotropic signature of the Sigsbee Abyssal Gyre (Perez-Brunius et al., 2018), a feature that has been recently found to be well-resolved in non-data assimilative HYCOM simulations (Morey et al., 2020; Olvera-Prado et al., 2023a), and the other process may involve the cyclones that accompany the LCEs and form directly to their north, traveling clockwise

surrounding it and which eventually enter the southern region (Frolov et al., 2004; Olvera-Prado et al., 2023b). In the SW subregion, the cyclonic vorticity maximum in the western Bay of Campeche is consistent with the relatively weaker net cyclonic circulation mentioned earlier for this simulation, and there is even a small area with anticyclonic vorticity just to the north that could be produced by LCEs colliding with the western boundary and whose southern rim penetrates into the SW subregion. The NW subregion seems to be influenced by the LCEs traveling on a northern path and reaching the western boundary.

Experiment GOM-W (Figure 6B) also depicts a region of strong anticyclonic vorticity dominating in the CW subregion, being consistent with the mean circulation on the western boundary of Figure 2B and with the region where most of the LCEs dissipate (LCs paths not shown). This structure is stronger and more organized compared to experiment GOM-noW. In the SW subregion, the cyclonic vorticity maximum in the western region is also consistent with the Campeche Gyre, but with larger magnitude than the GOM-noW experiment. The NW subregion shows no very defined pattern, only a pair of cyclonic anticyclonic regions that could be the result of the average contribution of wind and LCEs.

The relative vorticity structure over the LC region depicts similar patterns in both experiments, a strong anticyclonic vorticity core surrounded by a cyclonic vorticity band produced by the cyclones formed around the front of the LC. This average structure suggests the dominance of the LC system over the role of the wind in the eastern region.

The horizontal maps of the STRCH, ADV and BETA terms averaged over the 22-year period are shown in Figures 6C, E, G for experiment GOM-noW. The average contribution of advection (Figure 6E) reveals paths of advected anticyclonic and cyclonic vorticity (blue and red respectively) through the CW and NW subregions, with a north-south orientation, presumably responsible for the anticyclonic maximum and part of the secondary cyclonic maximum shown in Figure 6A. Also, the SW subregion shows an area of advection of cyclonic vorticity, which contributes to the cyclonic vorticity maximum in that region. Similarly, the advection of planetary vorticity (Figure 6G) seems to be responsible for conveying part of the anticyclonic vorticity carried by LCEs northward, once they reach the western boundary (around 96.5° W and confined mainly within the CW and NW subregions) and part of the cyclonic vorticity carried southward by the cyclones formed to the north of LCEs once they reach the western boundary (around 95° W within the CW and NW subregions). Being a second-order derivative, the vorticity gradient present in the ADV term is highly sensitive to noise, producing a noisier ADV field, which can be seen in Figure 6E while the planetary vorticity advection term, a first order derivative, presents a smoother pattern (Figure 6G). However, it is somewhat noticeable that the meridionally-oriented bands of positive and negative BETA on the western part of the CW and NW subregions are balanced partially by ADV. The above is reasonable given the fact that these two terms are also highly balanced over the LC region, an interesting fact beyond the aim of this study but certainly important to mention.

The mean map of the STRCH term (Figure 6C) shows similar magnitude values as ADV and BETA terms in the western GoM, but with no clear pattern that could be related to a particular physical process.

The horizontal maps of the vorticity balance STRCH, ADV and BETA terms for experiment GOM-W are shown in Figures 6D, F, H. In general, ADV and BETA terms have similar mean patterns and behavior to those for experiment GOM-noW, but with higher magnitude values. The meridionally-oriented bands of positive and negative BETA are compensated partially by the ADV term. On the other hand, the mean contribution of the STRCH term to the mean vorticity field is stronger and depicts a defined pattern in GOM-W. The map shows strong paths of anticyclonic and cyclonic vorticity oriented in a northeast-southwest direction in the NW and CW subregions. These paths propagate down to the SW subregion, where a strong core of positive vorticity is located in the Campeche Gyre region. The fact that this particular distribution of paths appears with such strength in the wind-driven experiment (GOM-W), suggests that the paths are directly related to the isopycnal interface displacement and associated velocity field of the wind-driven circulation in the western Gulf (Figure 4) and, therefore, the STRCH term can be a mechanism for the input of vorticity through wind stress (e.g., Ekman pumping).

Results of the vorticity analysis also indicate that the contributions of the WIND and VISC terms to the mean vorticity field are negligible in both experiments; therefore, these maps are not presented. For the WIND term in GOM-W, the main reason for this result is that the wind stress effect is distributed over a large depth and that its contribution is cumulative. Overall, the presence of a well-organized (mean) circulation indicates that the dominant contribution to mean upper-layer relative vorticity is stretching, advection of vorticity and planetary vorticity advection.

## 4.2 Time-varying vorticity balance

Analyses of the mean state and vorticity balances in the GoM do not yield a complete picture of the processes controlling the circulation due to its highly variable nature. The GoM circulation exhibits strong variability at high frequencies due to synoptic variability, monthly periods associated with its energetic mesoscale activity and long period variability due to seasonal and interannual modulation of inflow conditions and atmospheric forcing. The analysis in this section now focuses on the vorticity balances at high frequencies (daily time scales) through inspection of instantaneous values of the terms of the vorticity equation, and at lower frequencies associated with mesoscale activity.

Figures 7A–H shows the horizontal maps of relative vorticity  $\zeta$ , STRCH, ADV and BETA terms for experiments GOM-noW and GOM-W respectively. The maps are for the simulation day August 8, 2000 for GOM-noW (a, c, e and g), when two LCEs are located inside the CW subregion, and for the simulation day March 15, 2005 for GOM-W (b, d, f and h), a time when the LC depicts an intermediate stage, a LCE is just detached from the LC and another



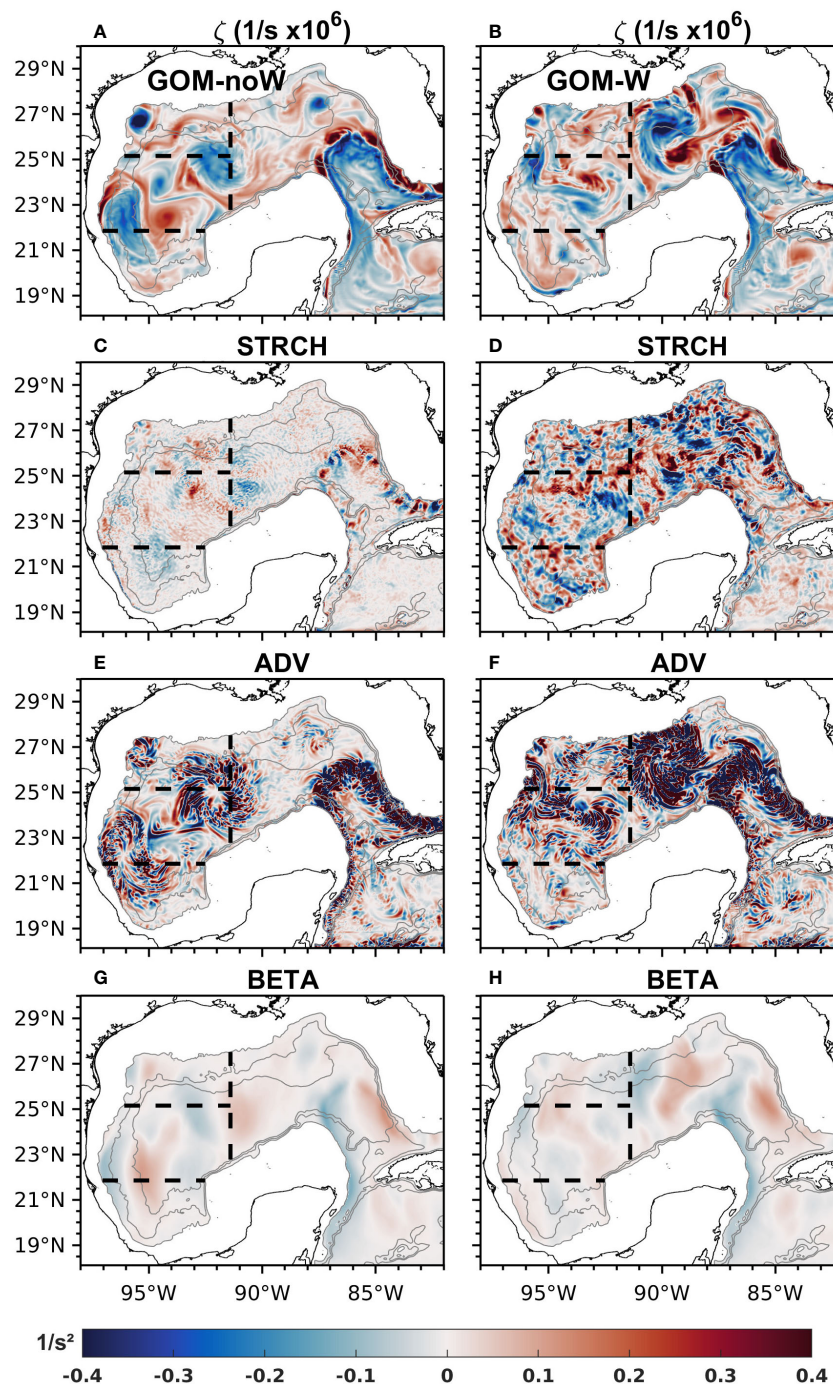


FIGURE 7

Instantaneous maps of upper-layer relative vorticity derived from modeled velocity for experiments (A) GOM-noW (August 8<sup>th</sup>, 2000) and (B) GOM-W (March 15<sup>th</sup>, 2005); stretching for (C) GOM-noW and (D) GOM-W; advection of vorticity for (E) GOM-noW and (F) GOM-W and; planetary vorticity advection for (G) GOM-noW and (H) GOM-W. Gray contours represent the 1000, 2000 and 3000 m isobaths, and black dashed lines the limits of the NW, CW and SW subregions. Although the dates differ between experiments, the aim is to show the variability and magnitude of the fields rather than directly compare them.

LCE is located in the CW subregion. (Note that the dates presented here correspond to dates of wind forcing and are used for convenience to refer to particular model times. However, because there is no data assimilation in these experiments, model results should not be directly compared to observations for these or any particular times). From these maps, one can observe large

magnitudes of the terms representing advection of relative vorticity and planetary vorticity over regions of strong currents like the LC or LCEs in both experiments. The BETA term has smaller magnitudes compared to the advection of relative vorticity, but with less small-scale variability and thus appearing more coherent with the mesoscale circulation features. In particular, the



dominance of the meridional velocity in the BETA term leads to defined patterns of negative and positive values found to the left and right sides of the LCE and LC due to the anticyclonic circulation (taking into account the negative sign in front of the term in Equation 4).

Instantaneous maps of the STRCH term reveal generally higher magnitudes and spatial variability in the GOM-W (Figure 7C) simulation compared to the GOM-noW (Figure 7D) simulation, which confines the higher spatial variability to a region over the LC and LCE. The differences in the STRCH terms in the GOM-W simulation can only be due to small-scale wind-induced processes, such as frontal eddies or meanders traversing the periphery of the larger mesoscale features.

In order to look into the time-varying balance at longer time scales typical of the mesoscale variability in the Gulf, time series of the terms in Equation 4 are first constructed by integrating them over each subregion for the whole 22-year record of daily model output. Then, a 30-day running mean filter is applied to the whole set of time series in the three subregions for GOM-noW and GOM-

W (Figures 8E, F). Primarily, the balance in both cases is a combination of vortex stretching, planetary vorticity advection and advection of vorticity and to a lesser extent to viscous stress curl and wind stress curl in GOM-noW. Figures 8B, D, F show that in the three subregions, the contribution of the STRCH (green line) dominates, since it is the term that exhibits larger amplitude and variability, especially in the NW and CW. However, in the NW and CW subregions BETA (blue line) also becomes important in some time periods. In fact, it can be seen that for periods of ~2-3 months length, BETA balances STRCH. The advection of vorticity (pink line) in GOM-W occurs either because it balances STRCH when it and BETA are out of phase or to help BETA compensate STRCH when its amplitude is high. There are a few exceptions with periods when BETA is negligible and ADV compensates STRCH entirely. In GOM-noW (Figures 8A, C, E), STRCH, BETA and ADV depict the same behavior as in GOM-W, except that the latter still shows remnants of high-frequency variability after the filter was applied. In both experiments, typical values of vortex stretching, and planetary vorticity advection are around  $\pm 1 \times 10^{10} \text{ m}^2 \text{ s}^{-2}$  with

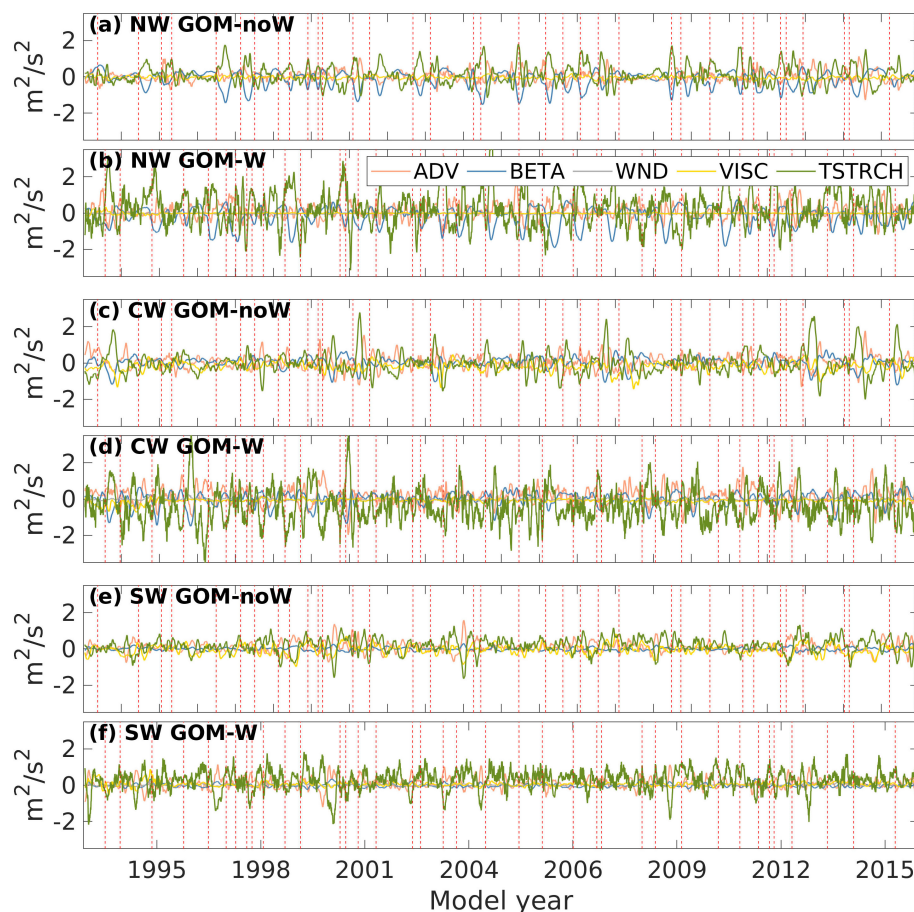


FIGURE 8

Time series of low-pass filtered spatially-integrated advection of vorticity (pink line), advection of planetary vorticity (blue line), stretching (green line), wind stress curl (gray line) and viscous stress curl (yellow line); for experiment GOM-noW, for the (A) NW (C) CW and (E) SW subregions; and for experiment GOM-W, for the (B) NW (D) CW and (F) SW regions. All values are multiplied by  $\times 10^{-10}$ . Red vertical dashed lines indicate the LCEs shedding dates for the corresponding experiment.

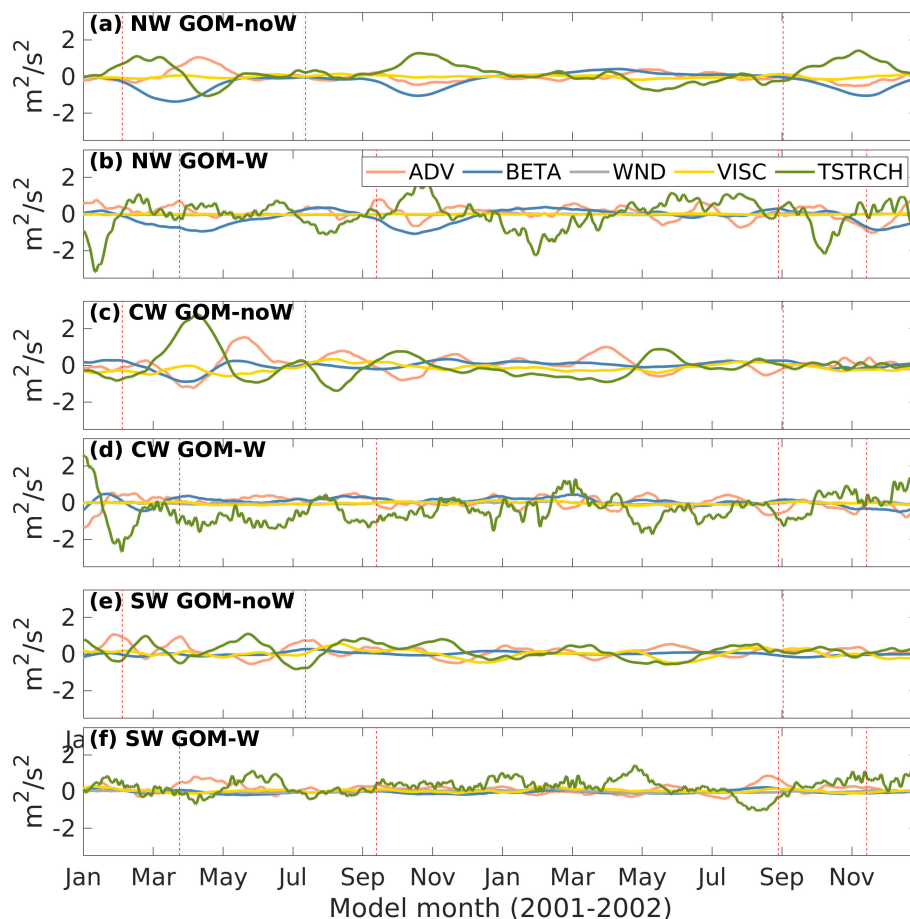


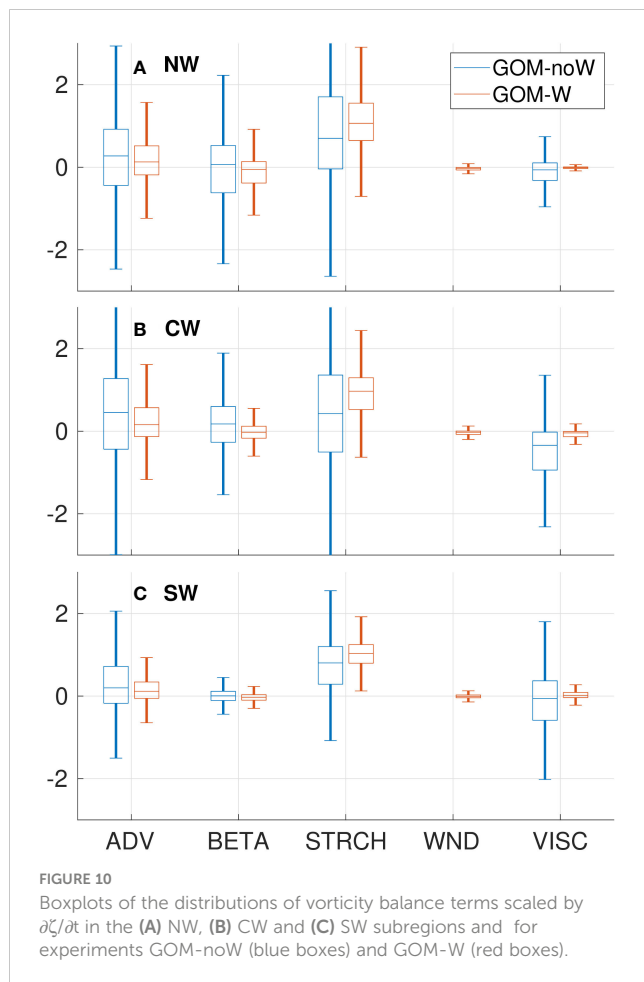
FIGURE 9  
Same as Figure 8 but zoomed-in for model years 2001-2002.

maximum values of  $\pm 2 \times 10^{10} \text{ m}^2 \text{ s}^{-2}$ , while advection of vorticity does not increase above  $\pm 0.5 \times 10^{10} \text{ m}^2 \text{ s}^{-2}$  in most of the cases. On the other hand, wind stress curl (gray line) in GOM-W shows values an order of magnitude smaller and its contribution to the balance becomes important in apparent atmospheric events, presumably during storms such as cold fronts or tropical cyclones. A zoomed-in figure of the time series is shown in Figure 9 for model years 2001-2002.

To assess the importance of the different terms in the vorticity balance over long time scales and how they compare between experiments, a scale analysis was performed for the low-pass filtered data of GOM-noW and GOM-W for the whole 22-year simulation. The scale analysis consists of dividing each term by the sum of them i.e.,  $\partial\zeta/\partial t$  as defined in Equation 4, in order to ascertain how much of the variability is explained by each term. Figure 10 shows box plots of the distribution of scaled terms for each subregion for the filtered time series. The wide distributions of STRCH in both experiments confirm its dominance in impacting the variability in the three subregions. It can reach values as high as 5 times  $\partial\zeta/\partial t$ , with an exception for the CW subregion in GOM-noW (blue box plots) where ADV becomes equally important as STRCH. ADV and BETA show secondary

importance and distributions behave similarly between GOM-noW and GOM-W. WIND and VISC contributions to the vorticity balance can be considered negligible. An interesting result is that the distributions of the vorticity balance terms show a smaller variability for GOM-W than for GOM-noW in the three subregions, which is mainly due to the fact that the amplitude and variability of  $\partial\zeta/\partial t$  is larger for GOM-W (not shown); this fact suggests that circulation remains more persistent through the year in the absence of wind forcing.

Now the question arises as to what ocean process is responsible for the first-order balance between STRCH and BETA lasting around 2-3 months, especially because these events happen with apparently no periodicity. Our hypothesis is that these events could be related to mesoscale features like LCEs. Therefore, we focus on a single event happening in 2005 of the GOM-W simulation, to shed more light into the problem. Figure 11 shows the instantaneous horizontal maps of ADV, BETA and STRCH terms for May 2005 for the control experiment (GOM-W), when a LCE is entering the NW subregion, along with the time series of BETA, STRCH and ADV in which the vertical red line indicates the time when the snapshots are shown. Also, the gray thick contours show the 0.17 m contour representing the LCE and LC cores. It can be observed that



when the eddy is entering the region, BETA becomes more negative and STRCH more positive, balancing each other; this suggests that the northward velocity in the region becomes stronger and the water column stretches due to the arrival of the deepened isopycnals within the eddy. It also can be seen that, although ADV is not entirely insignificant in the NW subregion (Figure 9A), its time series does not show a distinctive behavior during the period the LCE enters the region (Apr-Jul), but it does later on when it becomes important and balances the STRCH term. It is important to note that LCEs have a direct influence in the CW and NW subregions compared to the SW subregion, where they rarely enter with a sufficiently strong circulation, since they have already experienced some dissipation. Consequently, the BETA term becomes less important in the SW subregion.

## 5 Summary and conclusions

The Gulf of Mexico is one of the most studied regions in the world ocean, even so, there is still a need to better understand the mechanisms that govern the circulation in the region. One example is the western Gulf, where the circulation over deep waters responds to the large-scale, low-frequency winds and the migration of LCEs in a complex way. We used two multi-year,

free-running numerical simulations configured for the Gulf of Mexico using HYCOM in order to help us better understand the role of the wind, LCEs and other processes in the circulation of the Gulf but in particular the upper layer (<1000 m) in the western region. The results show that there is an indirect effect of the wind on the circulation leading to an increase of the LCE size, lifespan, speed and distance traveled. Although the scope of the present study is not to understand the mechanisms behind this behavior, the fact that LCEs tend to stay longer in the western GoM in the presence of wind means that the region is exposed to more vorticity input through LCEs. Therefore, we can expect that, for instance, the BETA term in the vorticity balance becomes more important more frequently in experiment GOM-W.

We computed a circulation index (CI), which is the depth-averaged and horizontally integrated relative vorticity for the three subregions in the western Gulf, to estimate the relative contributions of the wind and LCEs on the mean circulation of each subregion. Although the physics of the ocean model is nonlinear, the results show that the effect of these factors is approximately additive as long as the western GoM circulation is thought as an eddy-induced flow superimposed over a wind-driven circulation. We found that, in the NW subregion the LCEs produce a mean cyclonic flow in the absence of wind. When the wind is added, the circulation changes to weakly anticyclonic. In the CW subregion. Mean anticyclonic flow induced by the wind tends to enhance the comparatively weaker anticyclonic flow induced by LCEs. In the SW subregion LCEs and its associated eddy field can induce a cyclonic flow, which is enhanced by the wind.

We analyze the upper (~1000 m) ocean vorticity field in order to obtain a description of the contribution of different processes to the circulation in the three western subregions described above and at different time scales. The results show that stretching (STRCH), the advection of relative vorticity (ADV) and the advection of planetary vorticity (BETA) are the dominant terms transporting or moving around vorticity on average. This can be interpreted as the influence of the mesoscale activity generated by the LCEs and low-frequency (monthly time scale) wind variability. We speculate that the high-frequency (daily time scale) wind variability is responsible for the inertial currents present in the STRCH instantaneous field and in the area-integrated time series. We found that there is a primary balance between the low-pass filtered area-integrated time series of BETA and STRCH within the NW and CW subregions at irregular intervals. This balance is reached by means of isopycnal deepening and strengthen of the y-component of the velocity occurring whenever a LCE enters the eastern boundary of the NW or CW subregions, therefore the variability of these terms become a good indicator of LCEs entering the western Gulf. On the other hand, the scaling analysis helps to determine the relative importance of the STRCH and BETA terms on long time scales, as well as the more persistent cyclonic circulation in the Bay of Campeche compared with the CW and NW subregions. Finally, we found that the input of vorticity through wind stress curl (WIND) and

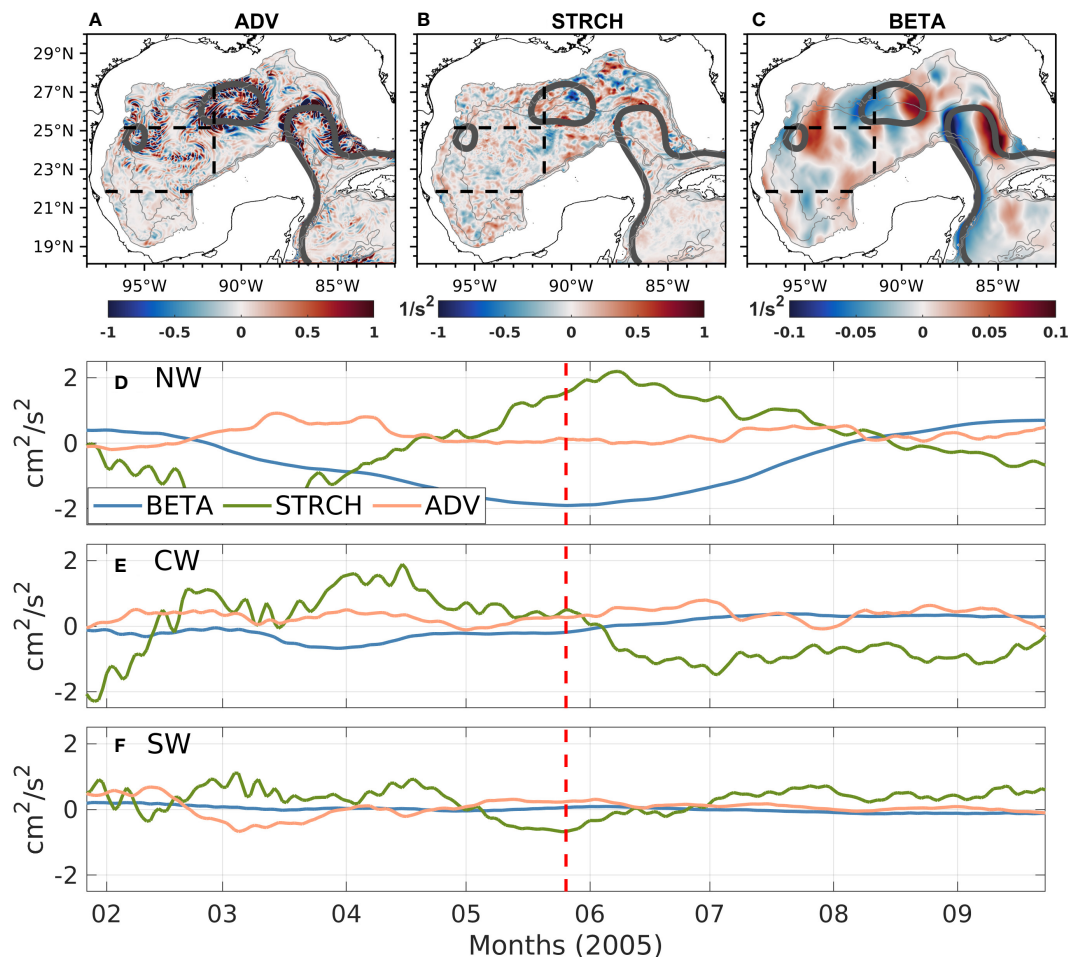


FIGURE 11

Instantaneous fields of (A) ADV, (B) STRCH and (C) BETA for 26th of May 2005 of experiment GOM-W; the time series are shown for the BETA, STRCH and ADV terms, for the (D) NW, (E) CW and (F) SW subregions. The vertical red line is centered on the date of the analysis.

viscous stress curl (VISC) are negligible. However, it is important to clarify that this fact does not mean that the contribution of wind to the circulation is null, it is just that its effect is integrated over a large depth ( $\sim 1000$  m), corresponding to the main thermocline depth, and that its contribution is cumulative.

Future studies can include separation of the vorticity balance terms into the mean and eddy components, and additional approaches to deepen our knowledge of the roles of the wind and LCEs in the western GoM circulation, such as performing new experiments to evaluate: (a) the impact of the current feedback to the wind forcing (Larrañaga et al., 2022), (b) the impact of the wind-SST coupling on the LC and LCE shedding and characteristics (Chelton et al., 2007), and (c) the impact on future climate on the GoM circulation (Liu et al., 2012).

## Data availability statement

The raw data supporting the conclusions of this article will be made available by the authors, without undue reservation.

## Author contributions

All authors designed the study, analyzed, interpreted the data, and contributed to the writing of the manuscript. EROP ran the numerical simulations. All authors contributed to the article and approved the submitted version.

## Funding

The author(s) declare financial support was received for the research, authorship, and/or publication of this article. EC and SM acknowledge support from the Gulf Research Program of the National Academies of Sciences, Engineering, and Medicine under award numbers 2000009966 and 2000013149. SM's contribution was also made possible by the National Oceanic and Atmospheric Administration (NOAA) Office of Education, Educational Partnership Program with Minority-Serving Institutions award #NA21SEC4810004 (NOAA Center for Coastal and Marine Ecosystems-II). The content is solely the responsibility of the authors



and does not necessarily represent the official views of the Gulf Research Program, the National Academies of Sciences, Engineering, and Medicine, or the U.S. Department of Commerce, NOAA.

## Acknowledgments

EROP thanks the National Council of Science and Technology of Mexico (CONACYT), the Office of Naval Research (ONR) and the Secretariat of Public Education (SEP) for supporting his PhD studies at the Center for Ocean-Atmospheric Prediction Studies, FSU. We acknowledge Jorge Zavala-Hidalgo and the Instituto de Ciencias de la Atmósfera y Cambio Climático, UNAM, for the use of the supercomputer Omoteotl to run the HYCOM simulations. EROP acknowledges Alexandra Bozec for her guidance and advice when conducting the numerical simulations with HYCOM.

## References

- Athié, G., Sheinbaum, J., Leben, R., Ochoa, J., Shannon, M. R., and Candela, J. (2015). Interannual variability in the Yucatan channel flow. *Geophysical Res. Lett.* 42 (5), 1496–1503. doi: 10.1002/2014GL062674
- Azevedo Correia de Souza, J. M., Powell, B., Castillo-Trujillo, A. C., and Flament, P. (2015). The vorticity balance of the ocean surface in Hawaii from a regional reanalysis. *J. Phys. Oceanography* 45 (2), 424–440. doi: 10.1175/JPO-D-14-0074.1
- Bleck, R. (2002). An oceanic general circulation model framed in hybrid isopycnal-cartesian coordinates. *Ocean Model.* 4 (1), 55–88. doi: 10.1016/S1463-5003(01)00012-9
- Bleck, R., and Boudra, D. B. (1981). Initial testing of a numerical ocean circulation model using a hybrid (quasi-isopycnal) vertical coordinate. *J. Phys. Oceanography* 11 (6), 755–770. doi: 10.1175/1520-0485(1981)011<0755:ITOANO>2.0.CO;2
- Boudra, D. B., and Chassignet, E. P. (1988). Dynamics of Agulhas retroflection and ring formation in a numerical model. part I: The vorticity balance. *J. Phys. Oceanography* 18 (2), 280–303. doi: 10.1175/1520-0485(1988)018<0280:DOARAR>2.0.CO;2
- Chaichitrahani, N., and He, R. (2024). Investigation of ocean environmental variables and their variations associated with major Loop Current eddy-shedding events in the Gulf of Mexico. *Deep Sea Res. Part II: Topical Stud. Oceanography* 213, 105354. doi: 10.1016/j.dsr2.2023.105354
- Chang, Y.-L., and Oey, L.-Y. (2012). Why does the Loop Current tend to shed more eddies in summer and winter?: seasonal Loop Current shedding. *Geophys. Res. Lett.* 39 (5), L05605. doi: 10.1029/2011GL050773
- Chassignet, E. P., Hurlburt, H. E., Smedstad, O. M., Halliwell, G. R., Wallcraft, A. J., Metzger, E. J., et al. (2006). Generalized vertical coordinates for eddy-resolving global and coastal ocean forecasts. *Oceanography* 19, 118–129. doi: 10.5670/oceanog.2006.95
- Chassignet, E. P., Smith, L. T., Halliwell, G. R., and Bleck, R. (2003). North atlantic simulations with the hybrid coordinate ocean model (hycom): Impact of the vertical coordinate choice, reference pressure, and thermobaricity. *J. Phys. Oceanography* 33 (12), 2504–2526. doi: 10.1175/1520-0485(2003)033<2504:NASWTH>2.0.CO;2
- Chelton, D. B., Schlax, M. G., and Samelson, R. M. (2007). Summertime coupling between sea surface temperature and wind stress in the California current system. *J. Phys. Oceanogr.* 37, 495–517. doi: 10.1175/JPO3025.1
- Donohue, K. A., Hamilton, P., Leben, R., Watts, R., and Waddell, E. (2008). Survey of deepwater currents in the northwestern Gulf of Mexico. *Tech. Rep. MMS* 2, 91.
- Dukhovskoy, D. S., Leben, R. R., Chassignet, E. P., Hall, C. A., Morey, S. L., and Nedbor-Gross, R. (2015). Characterization of the uncertainty of loop current metrics using a multidecadal numerical simulation and altimeter observations. *Deep-Sea Res. Part I* 100, 140–158. doi: 10.1016/j.dsr.2015.01.005
- Elliott, B. A. (1982). Anticyclonic rings in the Gulf of Mexico. *J. Phys. Oceanography* 12 (11), 1292–1309. doi: 10.1175/1520-0485(1982)012<1292:ARITGO>2.0.CO;2
- Fairall, C. W., Bradley, E. F., Hare, J. E., Grachev, A. A., and Edson, J. B. (2003). Bulk parameterization of air–sea fluxes: updates and verification for the COARE algorithm. *J. Climate* 16, 571–591. doi: 10.1175/1520-0442(2003)016<0571:BPOASF>2.0.CO;2
- Frolov, S. A., Sutyrin, G. G., Rowe, G. D., and Rothstein, L. M. (2004). Loop current eddy interaction with the western boundary in the Gulf of Mexico. *J. Phys. Oceanography* 34 (10), 2223–2237. doi: 10.1175/1520-0485(2004)034<2223:LCEIWT>2.0.CO;2
- Hamilton, (2009). Topographic Rossby waves in the Gulf of Mexico. *Prog. Oceanogr.* 82 (1), 1–31. doi: 10.1016/j.pcean.2009.04.019
- Large, W. G., McWilliams, J. C., and Doney, S. C. (1994). Oceanic vertical mixing: A review and a model with a nonlocal boundary layer parameterization. *Rev. Geophys.* 32 (4), 363–403. doi: 10.1029/94RG01872
- Larrañaga, M., Renault, L., and Jouanno, J. (2022). Partial control of the Gulf of Mexico dynamics by the current feedback to the atmosphere. *J. Phys. Oceanogr.* 52, 2515–2530. doi: 10.1175/JPO-D-21-0271.1
- Laxenaire, R., Chassignet, E. P., Dukhovskoy, D., and Morey, S. L. (2023). Impact of upstream variability on the Loop Current dynamics in numerical simulations of the Gulf of Mexico. *Front. Mar. Sci.* 10. doi: 10.3389/fmars.2023.1080779
- Leben, R. R. (2005). Altimeter-derived loop current metrics. In *Circulation in the Gulf of Mexico: Observations and Models* (eds W. Sturges and A. Lugo-Fernandez), 181–201. doi: 10.1029/161GM15
- Lee, H.-C., and Mellor, G. L. (2003). Numerical simulation of the gulf stream system: The loop current and the deep circulation. *Journal of Geophysical Research: Oceans*, 108(C2). Liu, Y., S.-K. Lee, B. A. Muhling, J. T. Lamkin, and XXXD. B. Enfield (2012). Significant reduction of the Loop Current in the 21st century and its impact on the Gulf of Mexico. *J. Geophys. Res.* 117, C05039. doi: 10.1029/2011JC007555
- Liu, M., and Tanhua, T. (2021). Water masses in the Atlantic Ocean: characteristics and distributions. *Ocean Sci.* 17, 463–486. doi: 10.5194/os-17-463-2021
- Liu, Y., Lee, S.-K., Muhling, B. A., Lamkin, J. T., and Enfield, D. B. (2012). Significant reduction of the Loop Current in the 21st century and its impact on the Gulf of Mexico. *J. Geophys. Res.* 117, C05039. doi: 10.1029/2011JC007555
- Metzger, E., Helber, R., Hogan, P., Posey, P., Thoppil, P., Townsend, T., et al. (2017). *Global ocean forecast system 3.1 validation testing*. 60.
- Meza-Padilla, R., Enriquez, C., Liu, Y., and Appendini, C. M. (2019). Ocean circulation in the western Gulf of Mexico using self-organizing maps. *J. Geophys. Res. Oceans* 124, 4152–4167. doi: 10.1029/2018JC014377
- Morey, S., Gopalakrishnan, G., Pallaz Sanz, E., Azevedo, C., Donohue, K., Perez-Brunius, P., et al. (2020). Assessment of numerical simulations of deep circulation and variability in the Gulf of Mexico using recent observations. *J. Phys. Oceanogr.* 50, 1045–1064. doi: 10.1175/JPO-D-19-0137.1
- Morey, S. L., Zavala-Hidalgo, J., and O'Brien, J. J. (2005). “The seasonal variability of continental shelf circulation in the northern and western Gulf of Mexico from a high-resolution numerical model,” in *Circulation in the Gulf of Mexico: Observations and Models*. Eds. W. Sturges and A. Lugo-Fernandez, 203–218. doi: 10.1029/161GM16
- Murray, C. P., Morey, S. L., and O'Brien, J. J. (2001). Interannual variability of upper ocean vorticity balances in the Gulf of Alaska. *J. Geophysical Research: Oceans* 106 (C3), 4479–4491. doi: 10.1029/1999JC000071
- Oey, L.-Y., Lee, H.-C., and Schmitz, W. J. Jr. (2003). Effects of winds and Caribbean eddies on the frequency of Loop Current eddy shedding: A numerical model study. *J. Geophys. Res.* 108, 3324. doi: 10.1029/2002JC001698
- Ohlmann, J. C., Niiler, P. P., Fox, C. A., and Leben, R. R. (2001). Eddy energy and shelf interactions in the Gulf of Mexico. *J. Geophys. Res. Oceans* 106 (C2), 2605–2620. doi: 10.1029/1999JC000162
- Olvera-Prado, E. R., Moreles, E., Zavala-Hidalgo, J., and Romero-Centeno, R. (2023a). “Upper–lower layer coupling of recurrent circulation patterns in the Gulf of Mexico,” in *Journal of Physical Oceanography*, vol. 53, 533–550. Available at: <https://>

## Conflict of interest

The authors declare that the research was conducted in the absence of any commercial or financial relationships that could be construed as a potential conflict of interest.

## Publisher's note

All claims expressed in this article are solely those of the authors and do not necessarily represent those of their affiliated organizations, or those of the publisher, the editors and the reviewers. Any product that may be evaluated in this article, or claim that may be made by its manufacturer, is not guaranteed or endorsed by the publisher.

[journals.ametsoc.org/view/journals/phoc/53/2/JPO-D-21-0281.1.xml](https://journals.ametsoc.org/view/journals/phoc/53/2/JPO-D-21-0281.1.xml). Retrieved Feb 14, 2023.

- Olvera-Prado, E. R., Romero-Centeno, R., Zavala-Hidalgo, J., Moreles, E., and Ruiz-Angulo, A. (2023b). Contribution of the wind, Loop Current Eddies, and topography to the circulation in the southern Gulf of Mexico. *Ocean Dynamics*. 73, 597–618. doi: 10.1007/s10236-023-01569-5
- Perez-Brunius, P., Furey, H., Bower, A., Hamilton, P., Candela, J., Garcia-Carrillo, P., et al. (2018). Dominant circulation patterns of the deep Gulf of Mexico. *J. Phys. Oceanography* 48 (3), 511–529. doi: 10.1175/JPO-D-17-0140.1
- Perez-Brunius, P., Garcia-Carrillo, P., Dubranna, J., Sheinbaum, J., and Candela, J. (2013). Direct observations of the upper layer circulation in the southern Gulf of Mexico. Deep Sea Research Part II: Topical Studies in Oceanography. *Modern Phys. Oceanography Professor H.T. Rossby* 85, 182–194. doi: 10.1016/j.dsr2.2012.07.020
- Romanou, A., Chassignet, E. P., and Sturges, W. (2004). Gulf of Mexico circulation within a high-resolution numerical simulation of the north atlantic ocean. *J. Geophysical Research: Oceans* 109, C01003. doi: 10.1029/2003JC001770
- Rousset, C., and Beal, L. M. (2010). Observations of the florida and yucatan currents from a caribbean cruise ship. *J. Phys. Oceanography* 40 (7), 1575–1581. doi: 10.1175/2010JPO4447.1
- Saha, S., Moorthi, S., Pan, H., Wu, X., Wang, J., and Nadiga, S. (2010). The NCEP climate forecast system reanalysis. *Bull. Am. Meteorological Soc.* 91 (8), 1015–1058. doi: 10.1175/2010BAMS3001.1
- Schmitz, W., Biggs, D., Lugo-Fernandez, A., Oey, L.-Y., and Sturges, W. (2005). A Synopsis of the Circulation in the Gulf of Mexico and on its Continental Margins. 11–29. doi: 10.1029/161GM03
- Sheinbaum, J., Candela, J., Badan, A., and Ochoa, J. (2002). Flow structure and transport in the Yucatan channel. *Geophysical Res. Lett.* 29 (3), 10–1–10–4. doi: 10.1029/2001GL013990
- Sturges, W. (1993). The annual cycle of the western boundary current in the Gulf of Mexico. *J. Geophysical Research: Oceans* 98 (C10), 18053–18068. doi: 10.1029/93JC01730
- Sturges, W. (2020). On the mean flow in the western Gulf of Mexico and a reappraisal of errors in ship-drift data. *J. Phys. Oceanography* 50 (7), 1983–1988. doi: 10.1175/JPO-D-19-0260.1
- Sturges, W., and Blaha, J. P. (1976). A western boundary current in the Gulf of Mexico. *Science* 192 (4237), 367–369. doi: 10.1126/science.192.4237.367
- Sturges, W., and Leben, R. (2000). Frequency of ring separations from the loop current in the Gulf of Mexico: A revised estimate. *J. Phys. Oceanography* 30 (7), 1814–1819. doi: 10.1175/1520-0485(2000)030<1814:FORSFT>2.0.CO;2
- Townsend, T. L., Hurlburt, H. E., and Hogan, P. J. (2000). Modeled Sverdrup flow in the North Atlantic from 11 different wind stress climatologies. *Dyn. Atmo. Ocean* 32 (3–4), 373–417. doi: 10.1016/S0377-0265(00)00052-X
- Vázquez de la Cerda, A. M., Reid, R. O., DiMarco, S. F., et al. (2005). “Bay of Campeche circulation: An update,” in *Circulation in the Gulf of Mexico: Observations and Models*. Eds. W. Sturges and A. Lugo-Fernandez (American Geophysical Union (AGU)), 279–293. doi: 10.1029/161GM20
- Vidal, V. M. V., Vidal, F. V., Hernandez, A. F., Meza, E., and Perez-Molero, J. M. (1994). Baroclinic flows, transports, and kinematic properties in a cyclonic-anticyclonic-cyclonic ring triad in the gulf of Mexico. *J. Geophysical Research: Oceans* 99 (C4), 7571–7597. doi: 10.1029/93JC03334
- Vidal, V. M. V., Vidal, F. V., Meza, E., Portilla, J., Zambrano, L., and Jaimes, B. (1999). Ring slope interactions and the formation of the western boundary current in the Gulf of Mexico. *J. Geophysical Research: Oceans* 104 (C9), 20523–20550. doi: 10.1029/1999JC900118
- Vidal, V. M. V., Vidal, F. V., and Perez-Molero, J. M. (1992). Collision of a loop current anticyclonic ring against the continental shelf slope of the western Gulf of Mexico. *J. Geophysical Research: Oceans* 97 (C2), 2155–2172. doi: 10.1029/91JC00486
- Vukovich, F. M. (2007). Climatology of ocean features in the Gulf of Mexico using satellite remote sensing data. *J. Phys. Oceanography* 37 (3), 689–707. doi: 10.1175/JPO2989.1
- Vukovich, F. (2012). Changes in the loop current’s eddy shedding in the period 2001–2010. *Int. J. Oceanography* 2012, 11–18. doi: 10.1155/2012/439042
- Wallcraft, A., Metzger, E., and Carroll, S. (2009). *Software design description for the HYbrid Coordinate Ocean Model (HYCOM), version 2.2*.
- Zavala-Hidalgo, J., Romero-Centeno, R., Mateos-Jasso, A., Morey, S. L., and Martinez-Lopez, B. (2014). The response of the Gulf of Mexico to wind and heat flux forcing: What has been learned in recent years? *Atmosfera* 27 (3), 317–334. doi: 10.1016/S0187-6236(14)71119-1
- Zavala-Hidalgo, J., Morey, S. L., and O’Brien, J. J. (2003). Seasonal circulation on the western shelf of the Gulf of Mexico using a high resolution numerical model. *J Geophys Res Oceans (1978-2012)* 108 (C12). doi: 10.1029/2003JC001879

# Frontiers in Marine Science

Explores ocean-based solutions for emerging global challenges

The third most-cited marine and freshwater biology journal, advancing our understanding of marine systems and addressing global challenges including overfishing, pollution, and climate change.

## Discover the latest Research Topics

[See more →](#)

### Frontiers

Avenue du Tribunal-Fédéral 34  
1005 Lausanne, Switzerland  
[frontiersin.org](https://frontiersin.org)

### Contact us

+41 (0)21 510 17 00  
[frontiersin.org/about/contact](https://frontiersin.org/about/contact)

